

NATIONAL AERONAUTICS AND SPACE ADMINISTRATION

Space Programs Summary 37-46, Vol. III

The Deep Space Network

For the Period May 1 to June 30, 1967

GPO PRICE \$ _____

CFSTI PRICE(S) \$ _____

Hard copy (HC) 3⁰⁰

Microfiche (MF) .65

ff 653 July 85

FACILITY FORM 602

N 67-36965	
(ACCESSION NUMBER)	(THRU)
251	1
(PAGES)	(CODE)
CR#88553	07
(NASA CR OR TMX OR AD NUMBER)	(CATEGORY)

JET PROPULSION LABORATORY
CALIFORNIA INSTITUTE OF TECHNOLOGY
PASADENA, CALIFORNIA

July 31, 1967

NATIONAL AERONAUTICS AND SPACE ADMINISTRATION

Space Programs Summary 37-46, Vol. III

The Deep Space Network

For the Period May 1 to June 30, 1967

JET PROPULSION LABORATORY
CALIFORNIA INSTITUTE OF TECHNOLOGY
PASADENA, CALIFORNIA

July 31, 1967

SPACE PROGRAMS SUMMARY 37-46, VOL. III

Copyright © 1967
Jet Propulsion Laboratory
California Institute of Technology

Prepared Under Contract No. NAS 7-100
National Aeronautics & Space Administration

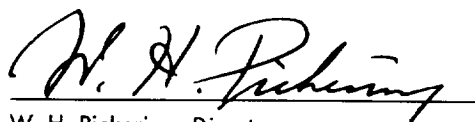
Preface

The Space Programs Summary is a six-volume bimonthly publication designed to report on JPL space exploration programs and related supporting research and advanced development projects. The titles of all volumes of the Space Programs Summary are:

- Vol. I. *The Lunar Program* (Confidential)
- Vol. II. *The Planetary-Interplanetary Program* (Confidential)
- Vol. III. *The Deep Space Network* (Unclassified)
- Vol. IV. *Supporting Research and Advanced Development* (Unclassified)
- Vol. V. *Supporting Research and Advanced Development* (Confidential)
- Vol. VI. *Space Exploration Programs and Space Sciences* (Unclassified)

The Space Programs Summary, Vol. VI, consists of: an unclassified digest of appropriate material from Vols. I, II, and III; an original presentation of the JPL quality assurance and reliability efforts, and the environmental- and dynamic-testing facility-development activities; and a reprint of the space science instrumentation studies of Vols. I and II.

Approved by:

A handwritten signature in dark ink, appearing to read "W. H. Pickering", is written over a horizontal line.

W. H. Pickering, Director

Jet Propulsion Laboratory

Contents

I. Introduction	1
II. Tracking and Navigational Accuracy Analysis	3
A. DSN Inherent Accuracy Project <i>T. W. Hamilton and D. W. Trask</i>	3
B. The Effects of Medium-Term Oscillator Stability on Two-Way Doppler Data Precision and Orbit Accuracy <i>D. W. Curkendall</i>	4
C. The Effects of Station and Probe Locations on the Information Content of a Single Pass of Doppler Data <i>J. F. Jordan</i>	8
D. Consistency of <i>Lunar Orbiter II</i> Ranging and Doppler Data <i>N. A. Mottinger and W. L. Sjogren</i>	19
E. Results of the Doppler-Ranging Calibration Experiment, Phase I <i>A. Liu</i>	23
F. Theoretical Basis for the Double Precision Orbit Determination Program: IX. Statistical Formulas <i>T. D. Moyer</i>	28
G. Sun-Earth Line Plots and DSN Planning <i>J. F. Gallagher</i>	36
References	47
III. Communications Research and Development	49
A. Digital Communication and Tracking: Specification of Parameters of Phase Locked Receivers at an Arbitrary Design Point <i>R. Tausworthe</i>	49
B. Digital Communication and Tracking: Analysis of the Tracking Loop of the <i>Mariner V</i> Ranging System <i>R. M. Gray</i>	53
C. Information Systems: Addition of Conditional-Compile Option to SDS FORTRAN-II and Real-Time-FORTRAN-II Compilers <i>W. B. Kendall</i>	56
D. Precision Time Synchronization Development: The Central Frequency Synthesizer <i>G. U. Barbani</i>	60
E. Efficient Antenna Systems: Ultracone <i>G. S. Levy, D. A. Bathker, R. E. Cormack and F. E. McCrea</i>	63
F. Improved RF Calibration Techniques: S-Band Ultracone RF Instrumentation <i>D. V. White and C. T. Stelzried</i>	67
G. Low Noise Receivers: Ultracone Maser Development <i>R. C. Clauss</i>	67

Contents (contd)

H. Improved RF Calibration Techniques: Daily System Noise Temperature Calibration With Ambient Termination <i>C. T. Stelzried</i>	72
I. Improved RF Calibration Techniques: WR 430 Waveguide Precision Rotary Vane Attenuator Calibration <i>T. Y. Orosi and C. T. Stelzried</i>	73
J. Efficient Antenna Systems: Venus DSS Polarization Tests <i>D. E. Neff</i>	82
K. Measurement of Signal Power in Real Time With an SDS 920 Computer <i>H. Mack, Jr.</i>	83
L. Advanced Development of Microwave Antenna Subsystems: 500-kW Component Prototypes <i>R. W. Hartop</i>	88
M. A 1-MHz Cleanup Loop for <i>Mariner Venus 67</i> Precision Ranging and Occultation Experiments <i>R. B. Crow</i>	89
References	93
IV. Communications Engineering	95
A. DSN 10-kW Transmitters <i>B. W. Harness and R. L. Leu</i>	95
B. Modification of a Cassegrain Cone Assembly To Reduce System Noise Temperature <i>R. W. Hartop</i>	101
C. Results of Signal Acquisition Dynamic Tests Performed at the DSS 11 MSFN Wing <i>R. L. Weber</i>	102
D. Four-Foot HA-Dec Time-Synchronization Antenna Mount <i>M. Kron</i>	109
E. Techniques for Evaluation of Antenna Reflector Structures—STAIR Computer Program <i>M. S. Katow</i>	113
F. Internal Alignment of the 210-ft Antenna Master Equatorial <i>H. McGinness</i>	115
References	119
V. Facility Engineering and Operations	121
A. Flight Project Support <i>R. M. Cuberly</i>	121
B. Facility Construction and Equipment Installation <i>R. M. Cuberly</i>	122

Contents (contd)

C. Venus DSS Operations	
<i>E. B. Jackson and A. L. Price</i>	123
D. Antenna Engineering	
<i>W. J. Kissane, R. McKee, A. Nicula, V. B. Lobb, J. Carpenter, and J. O. Breninger</i>	124
E. DSS 51 Equipment Replacement	
<i>R. C. Rydgig</i>	144
F. DSIF Station Control and Data Equipment	
<i>R. N. Flanders, E. Bann, G. Jenkins, C. M. Maretzo, A. T. Burke, and E. Garcia</i>	149
G. DSIF Phase I Monitor Program	
<i>R. N. Flanders</i>	152
H. Sustaining Engineering	
<i>P. T. Westmoreland, C. N. Wong, and H. W. Baugh</i>	155
I. Digital Tracking System	
<i>P. L. Lindley</i>	157
J. Hi-Rel Digital Modules	
<i>H. W. Baugh</i>	159
K. Transmission of Surveyor High-Speed Telemetry Data From DSS to SFOF	
<i>R. G. Polansky</i>	161
L. SFOF Data Processing System	
<i>R. G. Polansky</i>	164
M. SFOF Power System Reliability and Availability	
<i>D. C. Card</i>	172
Reference	174
VI. Multiple-Mission Telemetry System	175
A. Introduction	
<i>W. S. Baumgartner</i>	175
B. System Description	
<i>W. Frey</i>	176
C. System Performance and Analysis	
<i>M. H. Brockman, R. W. Burt, J. W. Layland, and G. M. Munson</i>	187
D. System Verification and Testing	
<i>M. A. Burow, L. Couvillon, and A. Vaisnys</i>	215
E. Equipment Description	
<i>J. W. Layland, R. G. Petrie, J. E. Stelzried, and J. K. Woo</i>	221
References	242

I. Introduction

The Deep Space Network (DSN) is a facility established by the NASA Office of Tracking and Data Acquisition under the system management and technical direction of JPL, and is responsible for two-way communications with unmanned spacecraft traveling approximately 10,000 miles from Earth to interplanetary distances. The DSN is distinct from other NASA networks such as the Space Tracking and Data Acquisition Network (STADAN), which tracks Earth-orbiting scientific and communication satellites, and the Manned Space Flight Network (MSFN), which tracks the manned spacecraft of the *Gemini* and *Apollo* programs.

The DSN performs four basic functions in support of each space flight project: tracking, data acquisition, command, and control. Tracking is the function of locating the spacecraft, calculating its distance, velocity, and position, and following its course. Data acquisition consists of the recovery of information from the spacecraft in the form of telemetry—the recorded measurements of the condition of, and the scientific data obtained by, the spacecraft. The command function involves the sending of signals to the spacecraft to guide it in its flight and to operate scientific and engineering equipment on board the spacecraft. Control refers to the making of command decisions from a central facility and to the overall direction of flight operations, including the network of ground stations, during a mission. Present facilities permit simul-

taneous control of a newly launched spacecraft and a second one already in flight. In preparation for the increased number of U.S. activities in space, a capability is being developed for simultaneous control of either two newly launched spacecraft plus two in flight, or four spacecraft in flight. With the advanced communications techniques now being implemented, it may soon be possible to obtain data from, and track spacecraft to, planets as far out in space as Jupiter.

The DSN supports, or has supported, the following NASA space exploration projects: *Ranger*, *Surveyor*, and *Mariner* (JPL); *Lunar Orbiter* (Langley Research Center); *Pioneer* (Ames Research Center); *Voyager*; and *Apollo* (Manned Spacecraft Center), as backup to the MSFN.

The main elements of the network are: the Deep Space Instrumentation Facility (DSIF), with space communications and tracking stations located around the world; the Ground Communications System (GCS), which provides communications between all elements of the DSN; and the JPL Space Flight Operations Facility (SFOF), the command and control center.

The DSIF is a worldwide chain of deep space stations that provide radio contact with the spacecraft (Table 1). JPL operates the U.S. and the Ascension Island stations. The overseas stations are normally staffed and operated

Table 1. Deep Space Instrumentation Facility

Deep Space Communication Complex (DSCC)	Deep Space Station (DSS)	DSS serial designation	Geodetic longitude, deg
Goldstone	Pioneer	11	243.1 E
	Echo	12	243.2 E
	Venus	13	243.2 E
	Mars	14	243.1 E
Canberra	Woomera	41	136.9 E
	Tidbinbilla	42	149.0 E
	Booroomba ^a	43	—
	Johannesburg	51	27.7 E
Madrid	Robledo	61	355.7 E
	Cebreros	62	355.6 E
	Rio Cofio ^a	63	—
	Cape Kennedy (Spacecraft Monitoring)	71	279.4 E
	Ascension Island (Spacecraft Guidance and Command)	72	345.7 E

^aStation not yet authorized.

by government agencies of the respective countries, with the assistance of U.S. support personnel. To maintain continuous mission coverage, the stations are placed approximately 120 deg apart in longitude around the Earth, so that the spacecraft is always within the field of view of at least one of the ground stations.

Radio contact with the spacecraft begins when it is poised on the launch pad at Cape Kennedy, and is maintained throughout the mission as the spacecraft passes from the field of view of one station to that of another. The Cape Kennedy tracking facility monitors the spacecraft during and immediately after launch. Later in the launch trajectory, while the spacecraft is relatively low in altitude, the signal is picked up by the 30-ft antenna at Ascension Island. Once the spacecraft is in orbit, the deep space stations with the large antennas, low-noise phase-lock receiving systems, and high-power transmitters take over radio communications and follow the vehicle to its destination. These stations obtain angular position, velocity (doppler), and distance (range) data for the spacecraft, and provide command control (up-link) and data reception (down-link) for the spacecraft. The standard 85-ft-diameter antennas in use at the deep space stations have gains of 53 db at 2295 MHz, permitting the receipt of significant data at distances as far as Mars. To improve the data-rate and distance capability, a 210-ft-diameter antenna having a gain of 61.81 ± 0.32 db at 2295 MHz has been built at DSS 14; two additional antennas of this size are planned for installation at overseas stations. In the

present configuration, with the exception of DSS 51 which has an S-band receiver-exciter subsystem, all stations are full S-band.

The DSN continuously conducts research and development of new components and systems to maintain a state-of-the-art capability. Therefore, the Goldstone DSCC is also used for extensive investigation of space tracking and telecommunications techniques, establishment of DSIF-spacecraft compatibility, and development of new DSIF hardware and software. New DSIF system equipment is installed and tested at the Goldstone DSCC before being accepted for systemwide integration into the DSIF. After acceptance for general use, it is classed as Goldstone Duplicate Standard (GSDS) equipment, thus standardizing the design and operation of identical items throughout the system.

The GCS, using facilities of the worldwide NASA Communications System (NASCOM), provides voice and teletype communications among the overseas DSIF stations, Goldstone, Cape Kennedy, and the SFOF. A special microwave link, which includes a video channel, is used between the SFOF and Goldstone to transmit critical data during a mission. Overseas communications are transmitted by land lines, submarine cables, microwave relays, high-frequency radio circuits, and even communication satellites.

Teletype is the primary means of transmitting tracking and telemetry data from the DSIF stations to the SFOF and sending predictions and other data to the stations. Voice circuits are used for transmission of high-priority communications other than data.

The SFOF at JPL is equipped with operations control consoles, status and operations displays, computers, and data-processing systems, and is the focal point of the DSN. From launch through mission completion, it is the control center for DSIF tracking and data-acquisition activities, as well as for spacecraft trajectory determinations, generation of the commands transmitted to the spacecraft, and analysis and interpretation of the data received.

Internal communications at the SFOF are maintained by means of telephones, voice intercom units, a public address system, closed-circuit TV, and other types of visual displays. Incoming spacecraft telemetry and tracking data from the deep space stations are automatically routed to the SFOF data-processing system, where special telemetry-processing equipment and high-speed digital computers convert the data into information for use by scientific experimenters and spacecraft engineers.

II. Tracking and Navigational Accuracy Analysis

A. DSN Inherent Accuracy Project, *T. W. Hamilton and D. W. Trask*

The DSN Inherent Accuracy Project was formally established by the DSN Executive Committee in July 1965. The objectives of the Project are:

- (1) Determination (and verification) of the inherent accuracy of the DSN as a radio navigation instrument for lunar and planetary missions.
- (2) Formulation of designs and plans for refining this accuracy to its practical limits.

Achievement of these goals is the joint responsibility of the Telecommunications Division (33) and the Systems Division (31) of JPL. To this end, regular monthly meetings are held to coordinate and initiate relevant activities. The Project leader and his assistant (from Divisions 31 and 33, respectively) report to the DSN Executive Committee, and are authorized to task Project members to (1) conduct analyses of proposed experiments, (2) prepare reports on current work, and (3) write descriptions of proposed experiments. The Project is further authorized to deal directly with those flight projects using the

DSN regarding data-gathering procedures that bear on inherent accuracy.

Technical work directly related to the Inherent Accuracy Project is presented in SPS 37-38, Vol. III, and in subsequent issues, and is continued in the following sections of this volume. The various data types and tracking modes provided by the DSIF in support of lunar and planetary missions are discussed in SPS 37-39, Vol. III, pp. 6-8. In this issue, the first comparison of doppler and ranging data obtained operationally during a lunar mission is presented. Although this is an interim analysis, the results do demonstrate the consistency of these two data types. Also, results from the first two tracks of data for the doppler-ranging calibration experiment are presented. The transponder differential delay versus temperature is clearly evident, and in these two cases masks any effects due to the ionosphere.

The concept of the information content of a single pass of doppler data from a distant spacecraft (Hamilton and Melbourne; SPS 37-39, Vol. III, pp. 18-23) is utilized in two of the articles in this issue. The first suggests a figure of merit that can be used in relating medium-term oscillator stability to navigational accuracy; the second relates

the information content to the relative probe-tracking station locations.

The series of articles on the theoretical basis of the double precision orbit determination program (DPODP) is continued with a description of the statistical formulas. These yield the covariance matrix of the solve-for parameters at an epoch and with respect to a body, both of which can be specified by the user. In addition, provisions are made for either exact or inexact constraints among the parameters. The final article in this section describes the sun-earth line plot which has proved useful in the planning activities of the DSN. Although some information is lost in a plot of this type, it has the capability of neatly and concisely displaying tracking coverage information over much longer periods of time than the conventional earth-probe orbit plots.

B. The Effects of Medium-Term Oscillator Stability on Two-Way Doppler Data Precision and Orbit Accuracy, D. W. Curkendall

1. Introduction and Motivation

The purpose of this article is twofold: (1) to establish that the medium-term drift characteristics of the tracking station's reference oscillator are of critical importance for the further refinement of the precision of DSN doppler tracking data, and (2) to present a simple figure of merit that permits the evaluation of the appropriateness of an arbitrary oscillator for reference use in terms of its characteristic power spectral density.

It is typically assumed that the coherent doppler system can measure range rate to an approximate accuracy of 1 mm/s over a 1-min smoothing time, and it is hoped that this figure can be refined to 0.5 mm/s for the 1973 time period. These numbers do not necessarily represent hardware limitations alone, but include error sources such as uncalibrated ionospheric effects and short-term pole wander uncertainties. To achieve these low numbers, it is necessary to assume that the reference oscillator does not contribute significantly to the effective noise.

In order to test the appropriateness of this assumption, it is useful to transform the range-rate error to its equivalent range-change error. A 1-min sample having a range-rate error of 1 mm/s implies that the range change during this interval is measured to an accuracy of 0.06 m. If we sum up these errors for an entire pass and employ the uncorrelated range-rate assumption that is usually made,

$$\begin{aligned}\sigma_{\Delta\rho} &= \sigma_{\dot{\rho}} \Delta t \sqrt{N} \\ &= 1.6 \text{ m}\end{aligned}\tag{1}$$

where Δt is the sampling interval and N is the number of samples per pass; i.e., the 1 mm/s noise level is equivalent to measuring the range change over a twelve-hour pass to an accuracy of 1.6 m. For comparison with this, the following expression for the range-change error due to oscillator instability (derived in SPS 37-41, Vol. III, pp. 42-47) is useful:

$$\sigma_{\Delta\rho_0} = \sigma_{\omega} \sqrt{\tau}\tag{2}$$

where τ is the round-trip light time to the probe and σ_{ω} is related to the height of the oscillator spectral content which was assumed to be flat; i.e.,

$$E[f_{\epsilon}(u)f_{\epsilon}(v)] = \sigma_{\omega}^2 \delta(u-v)$$

where

$f_{\epsilon}(t)$ is the departure from nominal of the oscillator's frequency at time t

E is the expectation operation

δ is the Dirac delta function

In SPS 37-43, Vol. III, pp. 37-39, two-way doppler data taken from *Pioneer VI* were used to determine σ_{ω} , which was found to be approximately

$$\sigma_{\omega} = 0.045 \text{ cycles} / \sqrt{s} \text{ at S-band}$$

which is equivalent to a frequency excursion of approximately 2 parts in 10^{11} for a 1-s averaging time.

If we employ this figure in Eq. (2) and assume τ to be 20 min, which is characteristic of near-Mars light time, we have

$$\sigma_{\Delta\rho_0} = 0.1 \text{ m}$$

which is considerably less than the 1.6 m, or even the 0.8 m for the projected 0.5 mm/s noise level. Taken in conjunction then, the two previous SPS articles cited in effect declare that the oscillator does not contribute significantly to the assumed noise levels. This appears quite conclusive, and it is—at least for the high frequency portion of the spectrum. However, the same conclusion cannot be reached for longer term drifts; this is

demonstrated by the following simple computation. The range-change error induced by the oscillator drift over a tracking period T is given by

$$\begin{aligned}\Delta\rho_\epsilon &= k \int_0^T f_\epsilon(t) - f_\epsilon(t-\tau) dt \\ &= k \left[\int_{T-\tau}^T f_\epsilon(t) dt - \int_{-\tau}^0 f_\epsilon(t) dt \right] \quad (3)\end{aligned}$$

Eq. (3), which is valid only for two-way coherent tracking, can be derived from inspection of the sketch (Fig. 1) and from the knowledge that the received error frequency, which is equivalent to the error frequency transmitted τ seconds earlier, is subtracted from the present f_ϵ by the station electronics. If we now think of f_ϵ as a slowly varying function during the pass, we have the approximate relation

$$\Delta\rho_\epsilon \approx k\tau [f_\epsilon(0) - f_\epsilon(T)]$$

Reliable estimates of Δf_ϵ for the rubidium standards in an operational configuration are sketchy, but a figure of 5 parts in 10^{12} or 0.0115 Hz is not unreasonable. Transforming to metric units ($k = 6.5$ cm/cycle), and again using $\tau = 1.2 \times 10^3$ s, we have

$$\Delta\rho_\epsilon = 0.8 \text{ m}$$

a figure equal to that of the total for the 0.5 mm/s noise level.

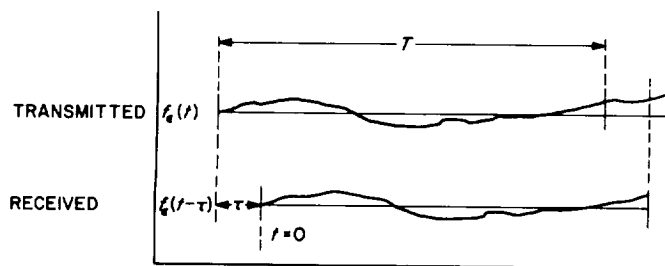


Fig. 1. Transmitted and received error frequencies

2. Degradation of Observable Estimates Due to Worst-Case Oscillator Drift Signatures

Here we shall further pursue the arguments introduced in Section 1 and assume certain worst-case drift signatures in order to determine the actual errors introduced in the orbital element estimates that are visible on a single pass of data.

In SPS 37-39, Vol. III, pp. 18-23, Hamilton and Melbourne derived the following approximate expression for the topocentric range rate:

$$\dot{\rho} = a + b \sin \omega t + c \cos \omega t + n(t) \quad (5)$$

where

- a is the geocentric range rate of the probe
- b is related to the declination
- c is related to the declination and right ascension
- ω is the Earth's angular velocity
- $n(t)$ is the noise on the observation

A regression is performed on Eq. (5), and the information content of the doppler is expressed in terms of the ability to determine the three coefficients, a , b , and c . Quoting Hamilton and Melbourne directly, Table 1 registers the precision of these estimates for a twelve-hour pass of data.

Table 1. Precision of coefficient estimates
 $\sigma_p = 1$ mm/s, 1-min samples

σ_a/ω	σ_b/ω	σ_c/ω
1.15 m	0.72 m	1.65 m

The procedure here will be to assume an additional measurement error (over and above the σ_p) which is induced by the oscillator, and to chart the degradation in the above parameter estimates. The oscillator will be assumed to drift within specified limits, but in such a manner as to produce $\dot{\rho}$ signatures indistinguishable from the observable coefficients. Differentiating Eq. (3) with respect to T , and reinterpreting T as an arbitrary time t during the pass, we have

$$\frac{d(\Delta\rho_\epsilon)}{dt} = \dot{\rho}_\epsilon = k [f_\epsilon(t) - f_\epsilon(t - \tau)] \quad (6a)$$

$$= \tau \frac{[f_\epsilon(t) - f_\epsilon(t - \tau)]}{\tau} \quad (6b)$$

$$\approx \tau \frac{df_\epsilon(t)}{dt} \quad (6c)$$

Again, in Eq. (6c), we have used the approximation that f_ϵ is slowly varying over the time τ . Thus it is trivial to

find the function $f_\epsilon(t)$ such that $\dot{\rho}_\epsilon$ appears identical to a, b, c .

For a ,

$$f_\epsilon(t)_a = d_a t \quad (7a)$$

For b ,

$$f_\epsilon(t)_b = d_b \cos \omega t \quad (7b)$$

For c ,

$$f_\epsilon(t)_c = d_c \sin \omega t \quad (7c)$$

Then, if we constrain the coefficients of Eq. (7) such that the maximum frequency departure at any time during the pass is no greater than a specified $\Delta f/f$, an evaluation of the worst-case signature can be obtained. For example, if the drift is linear (Eq. 7a), the real observation becomes

$$y = a + k\tau d_a$$

Then, assuming d_a to be a zero mean random variable uncorrelated with a , the accuracy to which a may be determined is degraded to

$$\sigma_a = \sqrt{\sigma_y^2 + k^2 \tau^2 \sigma_{d_a}^2}$$

This procedure was carried out for the forms given by Eqs. (7a) and (7b), and the results are displayed in Figs. 2 and 3. Here we have plotted σ_a/ω and σ_b/ω versus the maximum rms frequency departure in terms of $\Delta f/f$ for the two noise levels discussed earlier. Table 2 was taken directly from these figures and records the $\sigma_{\Delta f/f}$ associated with the desired signature to produce a 50% degradation in the orbital element. It is seen that significant loss of information occurs below the 5 parts in 10^{12} suggested drift specification in both parameters, even with

Table 2. Degradation of estimates

Parameter	Assumed noise level, mm/s	$\sigma_{\Delta f/f}$ for 50% increase in parameter
a	1	4×10^{-12}
a	0.5	3×10^{-12}
b	1	3.5×10^{-12}
b	0.5	1.5×10^{-12}

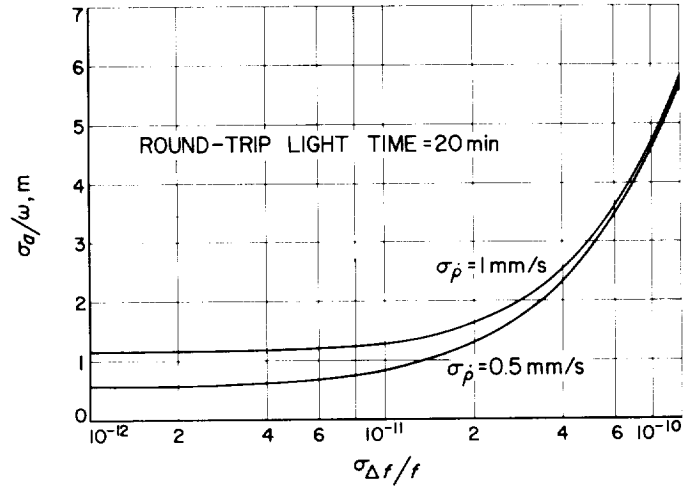


Fig. 2. Precision of range-rate measurement σ_a versus standard deviation of maximum frequency excursion $\sigma_{\Delta f/f}$ for linear drift

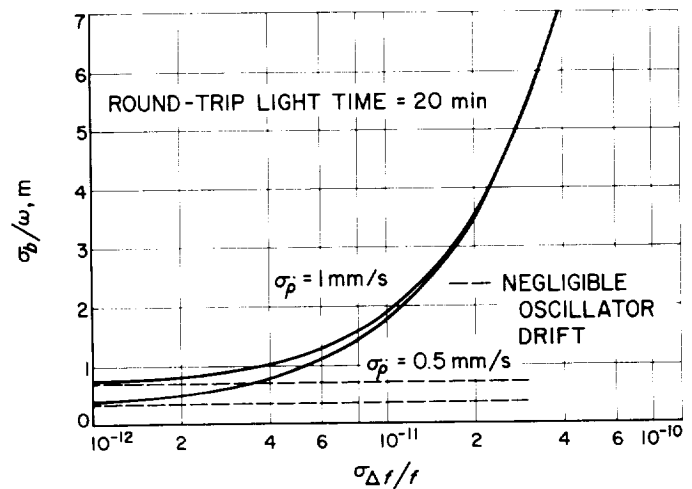


Fig. 3. Precision of declination measurement σ_b versus standard deviation of maximum frequency excursion $\sigma_{\Delta f/f}$ for a sinusoidal diurnal drift

the greater 1 mm/s noise figure. While these are worst-case numbers, neither a linear or a diurnal drift is a particularly unreasonable characteristic.

3. A General Oscillator Figure of Merit

In the preceding two sections, we have supplied what are believed to be persuasive arguments that the low frequency content of a tracking station's reference oscillator is of utmost importance to its evaluation as a tracking instrument, at least at interplanetary distances. In Section 1, the criterion of $\Delta \rho$ was used to show that

currently assumed drifts (up to 5 parts in 10^{12}) contribute significantly to the effective doppler noise figure used. In Section 2, we showed that there was a reasonable correspondence between the $\Delta\rho$ criterion and the worst-case performance. Here we return to the first criterion and present an equation for $\sigma_{\Delta\rho}$ in terms of the oscillator spectral content.

We may express this range-change measurement uncertainty as a general integral equation given below:

$$\sigma_{\Delta\rho}^2(T, \tau) = \int_{-\infty}^{\infty} K(\omega) G(\omega) d\omega \quad (8)$$

where

$G(\omega)$ is the spectral density of the oscillator spectrum at frequency ω , $\text{Hz}^2/\text{rad/s}$

$K(\omega)$ is the mean squared range-change error induced from a unit power density at ω , m^2/Hz^2

From Eq. (3), it may be derived that

$$K(\omega) = \frac{4k^2(1 - \cos \omega\tau)(1 - \cos \omega T)}{\omega^2} \quad (9)$$

A few observations can be made concerning Eq. (9). First, we see it is oscillatory in manner: for large T , nulls are reached at every $\omega = n2\pi/T$ and relative maxima occur at $(2n-1)\pi/T$. Although this presents a slight complication in interpretation, it is not severe. The limiting cases are easily treated:

$$K(\omega) \approx (k\omega \alpha T)^2 \quad \text{as } \omega \rightarrow 0$$

and the envelope of the maxima will decrease to zero as

$$K(\omega)_{\text{envelope}} = \frac{16k^2}{\omega^2} \quad \text{as } \omega \rightarrow \infty$$

Thus the sensitivity of the filter to either very low or high portions of the spectrum is essentially zero. Figure 4(a) plots this function for

$$T = 10 \text{ h}$$

$$\tau = 20 \text{ min}$$

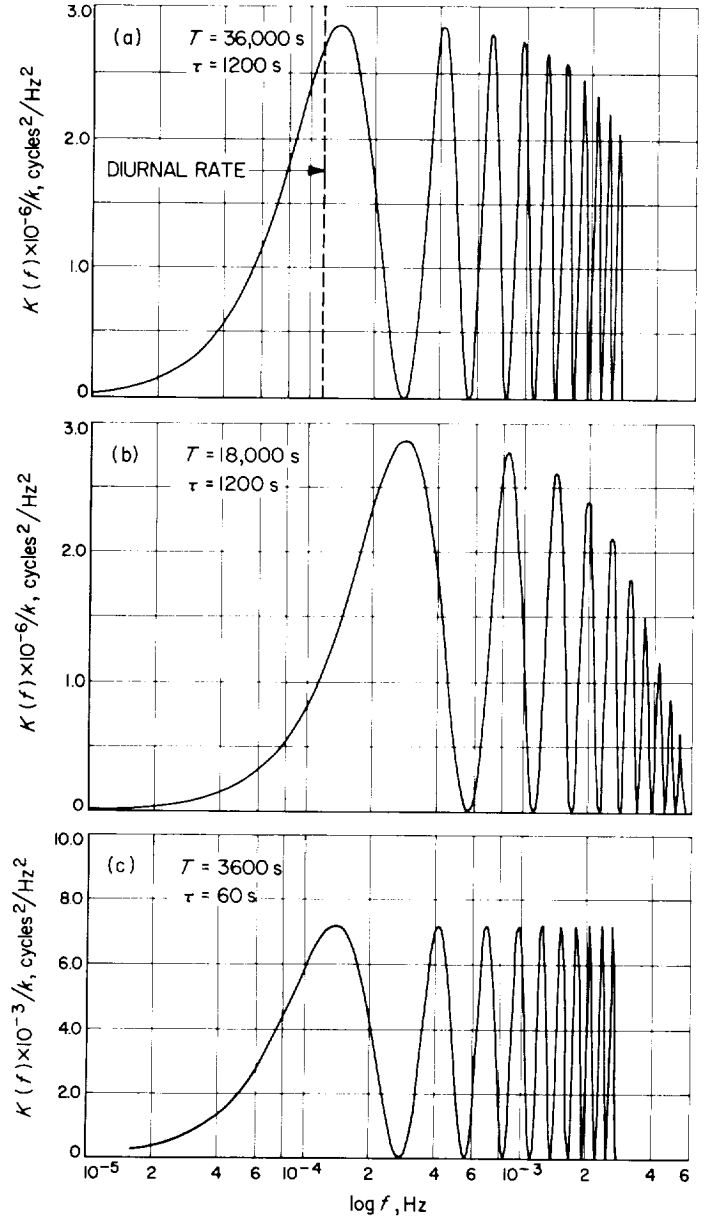


Fig. 4. Sensitivity of doppler count to oscillator noise power versus noise frequency

Figures 4(b) and 4(c) contain two variations of this basic case. The first, which halves the count time, attains about the same maximum value but is less sensitive to the extremely low frequencies. The second variation, which reduces light time to 1 min, retains the low frequency shape of the standard but has a much reduced sensitivity—a demonstration of the dependence of the previous results on the assumed light time.

It is thought that these figures have direct utility in determining the portion of the spectrum that must be

measured in order to specify tracking performance. In addition, it is possible to integrate Eq. (12) and achieve a closed-form solution for rms range-change error in certain idealized cases. Frequency standards of the rubidium class are often characterized as having a spectral content composed of two sources:

- (1) a white or flat component

$$G_1(\omega) = a$$

- (2) a flicker component

$$G_2(\omega) = b/\omega$$

From previous calculations, we already know that the form of the result for the first component is

$$\sigma_{\Delta\rho_w}^2 = \begin{cases} \sigma_{w^2}^2 \tau, & T \geq \tau \\ \sigma_{w^2}^2 T, & T \leq \tau \end{cases} \quad (10)$$

where

$$\sigma_{w^2}^2 = 4k^2\pi a$$

The flicker component gives rise to a nonstationary noise source with T , and is found to be¹

$$\sigma_{\Delta\rho_f}^2 = 8bk^2 \left[\frac{(\tau+T)^2}{4} \ln(\tau+T) + \frac{(\tau-T)^2}{4} \ln|\tau-T| - \frac{\tau^2}{2} \ln \tau - \frac{T^2}{2} \ln T \right] \quad (11)$$

Then, if the oscillator can be reasonably characterized by these two components, the desired figure of merit (expressed in meters of expected rms range-change error) is given simply by

$$FOM = \sqrt{\sigma_{\Delta\rho_w}^2 + \sigma_{\Delta\rho_f}^2} \quad (12)$$

¹The solution of Eq. (8) for this case was obtained by H. Lass.

C. The Effects of Station and Probe Locations on the Information Content of a Single Pass of Doppler Data, J. F. Jordan

1. Introduction

In SPS 37-39, Vol. III, pp. 18-23, Hamilton and Melbourne have shown that a space probe's geocentric radial velocity, its right ascension, and the cosine of its declination are the three major parameters that can be meaningfully measured from an observed pass of earth-based doppler data. The approximate accuracies to which these three parameters can be estimated from data taken over a tracking time interval corresponding to a station pass half-width of $\psi = 80$ deg are given in Eqs. (25), (26), and (27) of the Hamilton-Melbourne article.

It is recognized that the ideal maximum possible pass width of a given station observing a given space probe depends on the locations of both the station and the probe. In particular, the maximum pass half-width ψ is related to the station latitude ϕ and the probe geocentric declination δ by the following equations:

$$\left. \begin{aligned} \cos \psi &= -\tan \phi \tan \delta & \text{when } |\phi| + |\delta| < \frac{\pi}{2} \\ \cos \psi &= 0 & \text{when } |\phi| + |\delta| \geq \frac{\pi}{2} \end{aligned} \right\} \quad (1)$$

where ψ is in the first quadrant when δ and ϕ have the opposite signs and in the second quadrant when δ and ϕ have the same sign.

Perhaps the dependency of ψ on ϕ and δ can best be seen from a diagram of ϕ versus δ (due to Hamilton), showing contours of constant half-width and regions of total, partial, and no observability. The diagram is shown in Fig. 5.

The purpose of this article is to extend the Hamilton-Melbourne results to include the effects of the station and probe location dependent pass width. The sensitivity to the variable pass width is shown for the precision of estimates of the station location parameters as well as for the probe parameters mentioned above.

The results are then extended to the case of a full 24-h pass of data taken from two stations on the earth placed diametrically opposite each other. It should be noted that two such stations lie in opposite hemispheres, the geocentric latitude of one being the negative of the other, and that the probe is visible to one, and only one, station

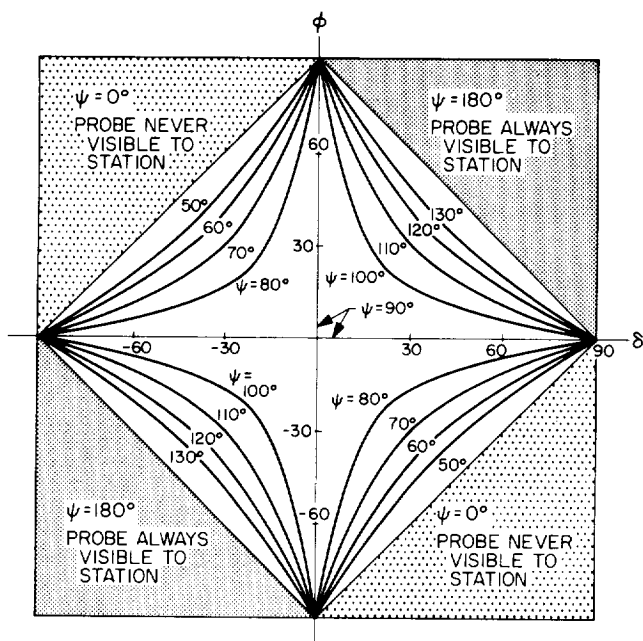


Fig. 5. Station latitude versus probe declination

at any given time during the 24-h pass. Hence, the pass half-width of one station ψ_1 and the pass half-width of the other station ψ_2 satisfy the relation $\psi_1 + \psi_2 = \pi$.

Finally, the characteristics of the results are discussed in terms of the observing capability of the present DSN.

2. The Mathematical Model

The observation model employed is identical to that used by Hamilton and Melbourne, with the observable—

the probe-station range rate—related to the parameters to be estimated by

$$\dot{\rho} = a + b \sin \omega t + c \cos \omega t + n \quad (2)$$

where

$$a = \dot{r}$$

$$b = r_s \omega \cos \delta$$

$$c = \omega t_0 r_s \omega \cos \delta$$

The symbol definitions used in the previous equation are identical to those used by Hamilton and Melbourne. For convenience, a list of definitions is given at the end of the article. In the numerical calculations, the following constants were used:

$$\sigma_{\dot{\rho}} = 0.001 \text{ m/s}$$

$$\omega = 7.27 \times 10^{-5} \text{ rad/s}$$

$$1 \text{ sample/min}$$

3. Results of the Single Station Pass of Data

The equations for the maximum likelihood estimates of a , b , and c , when observations of a space probe are made by one station, are given by Hamilton and Melbourne in Eqs. (11), (12), and (13) of their article, and the covariance matrix of the errors in the estimates is given in terms of ψ by Eq. (14); i.e.,

$$\Lambda = \frac{\sigma_{\dot{\rho}}^2}{N} \begin{bmatrix} \frac{1}{1-\rho_{13}^2} & 0 & \frac{-2 \sin \psi}{\psi \left(1 + \frac{1}{2\psi} \sin 2\psi\right) (1-\rho_{13}^2)} \\ 0 & \frac{2}{\left(1 - \frac{1}{2\psi} \sin 2\psi\right)} & 0 \\ \frac{-2 \sin \psi}{\psi \left(1 + \frac{1}{2\psi} \sin 2\psi\right) (1-\rho_{13}^2)} & 0 & \frac{2}{\left(1 + \frac{1}{2\psi} \sin 2\psi\right) (1-\rho_{13}^2)} \end{bmatrix} \quad (3)$$

where

$$\rho_{13}^2 = - \frac{2^{1/2} \sin \psi}{\psi \left(1 + \frac{1}{2\psi} \sin 2\psi\right)^{1/2}}$$

The variations of the precisions of the estimates of a , b , and c to the station and probe locations are shown on the dashed curves in Figs. 6, 7, and 8, respectively, in which σ_a/ω , σ_b/ω , and σ_c/ω are plotted versus δ for various

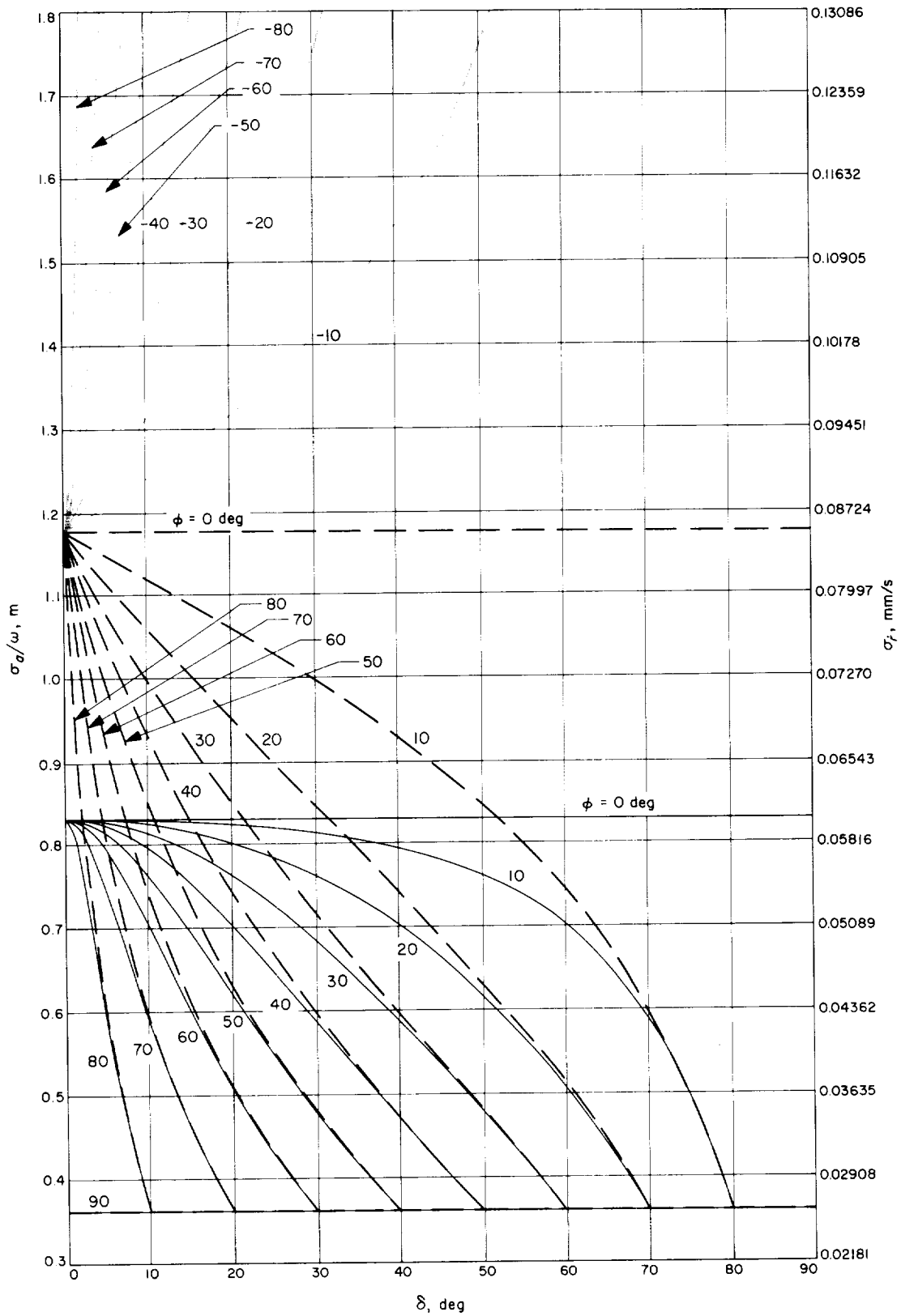


Fig. 6. Precision of estimates of a versus probe declination

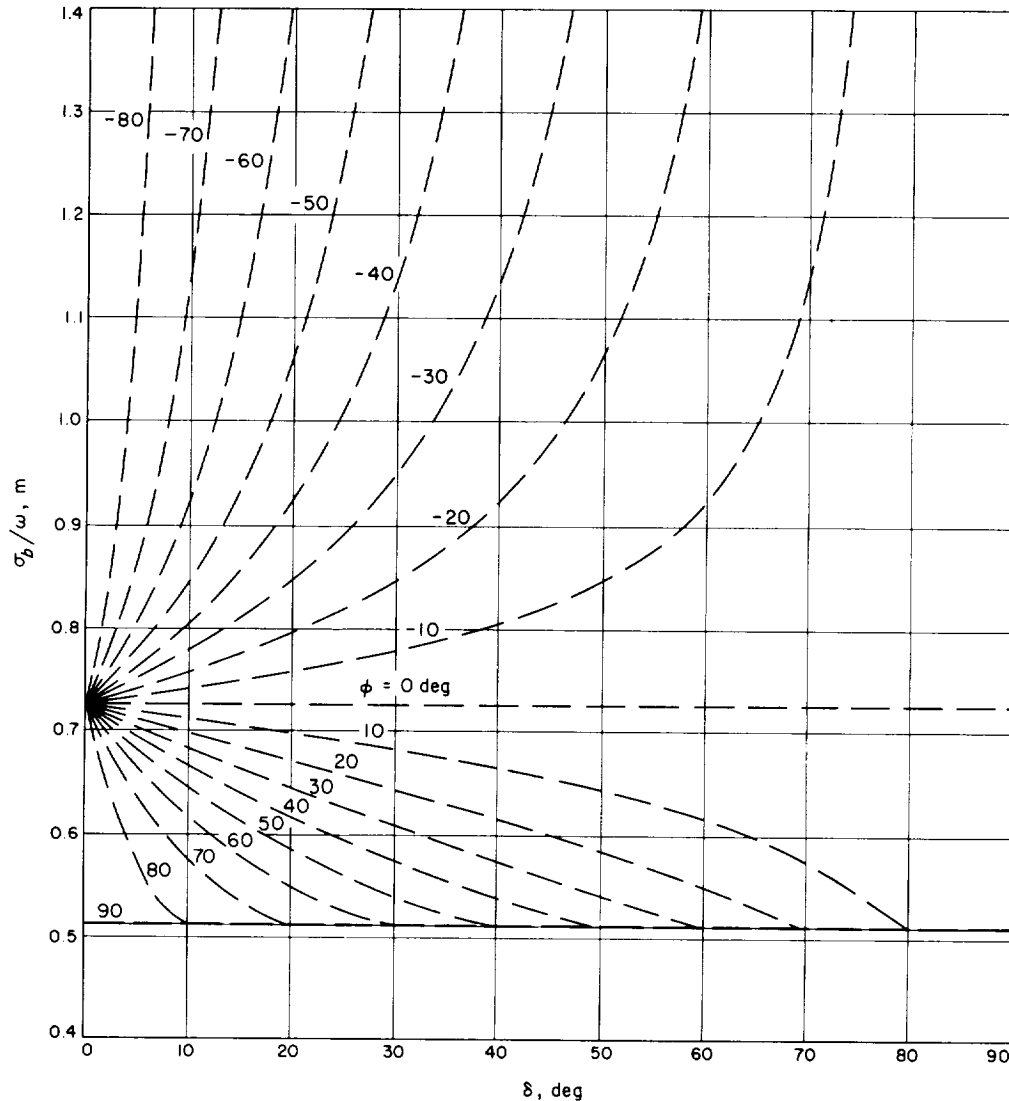


Fig. 7. Precision of estimates of b versus probe declination

values of ϕ . Probe locations for the curves are restricted to the northern celestial hemisphere, since the results for probes in the southern hemisphere are symmetric to those shown and can be obtained from the presented curves by substituting $-\delta$ for δ and $-\phi$ for ϕ . The point at which the various curves come together at $\delta = 0$ corresponds to a pass half-width of 90 deg. In the region below that point, the pass half-width $\psi > \pi/2$, and in the region above that point, $\psi < \pi/2$. Notice that for a station located with a latitude of about 35 deg (approximately Goldstone DSCC latitude), the precision of the estimates for observations of a probe with $\delta = 30$ deg is improved by about 20 to 40% over the precision of estimates of a probe in the equatorial plane, and the precision of estimates for a probe with $\delta = -30$ deg is degraded by about that same percentage. This effect is primarily due to the increased

pass half-width ($\psi \approx 105$ deg) when the probe and station are in the northern hemisphere, and to the decreased pass half-width ($\psi \approx 75$ deg) when the station and probe are in opposite hemispheres.

If the coordinates of the observed space probe are well known, the pass information content expressed by the covariance matrix in Eq. (3) can be mapped into the precision with which the station's longitude and its distance from the earth's spin axis r_s can be estimated. From Eq. (2) we have

$$\left. \begin{aligned} r_s &= \frac{b}{\omega \cos \delta} \\ \omega t_0 &= \frac{c}{b} \end{aligned} \right\} \quad (4)$$

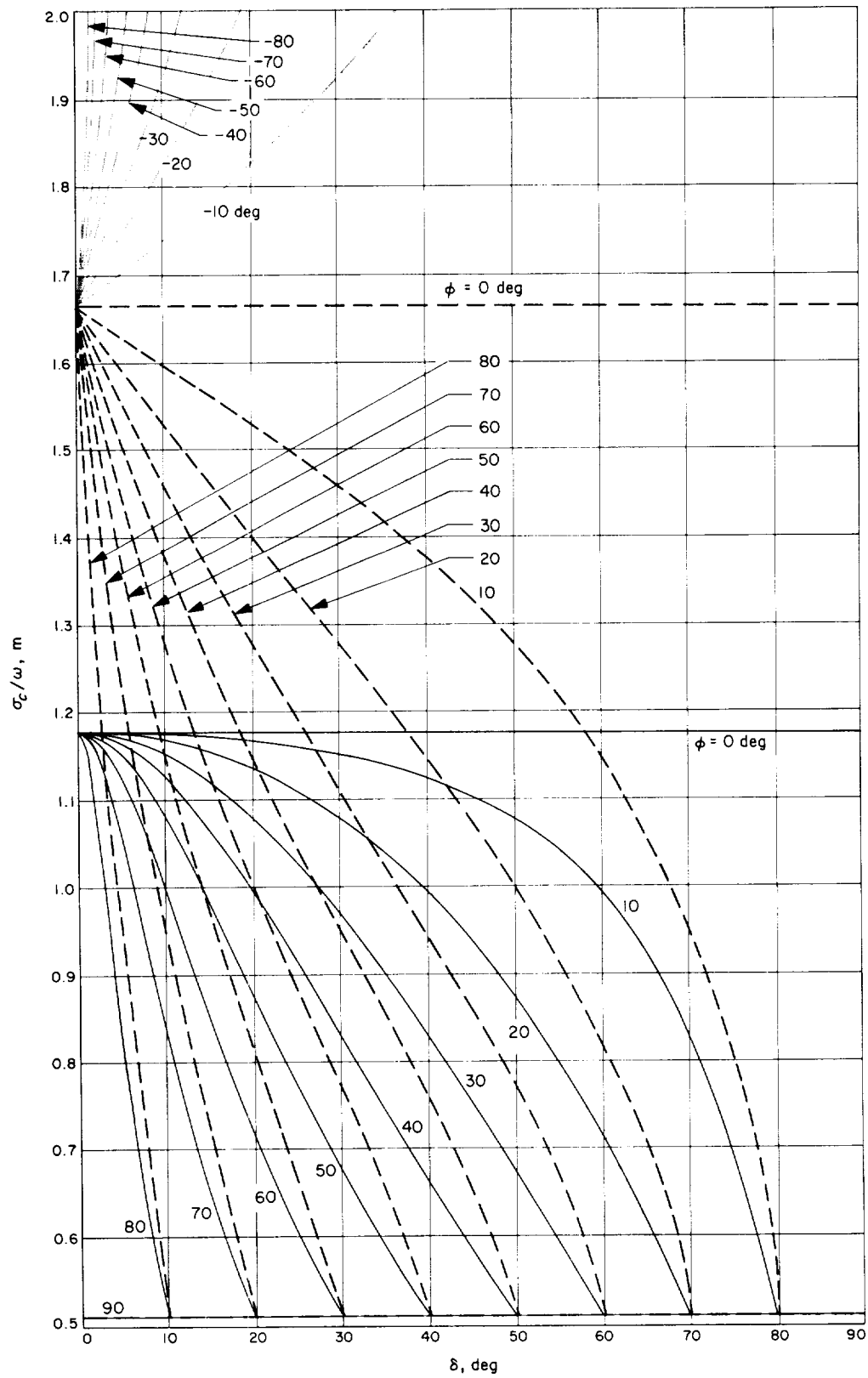


Fig. 8. Precision of estimates of c versus probe declination

By using the relation between the time of meridian crossing t_0 and the errors in station longitude and in universal time, given by Hamilton-Melbourne in Eq. (8), the following equations for the respective standard deviations of the errors in the estimates of r_s and λ can be derived:

$$\left. \begin{aligned} \sigma_{r_s} &= \frac{\sigma_b}{\omega \cos \delta} \\ r_s \sigma_\lambda &= \left[\left(\frac{\sigma_c}{\omega \cos \delta} \right)^2 + (r_s \omega \sigma_\xi)^2 \right]^{1/2} \end{aligned} \right\} \quad (5)$$

Figures 9 and 10 show the variation of σ_{r_s} and $r_s \sigma_\lambda$ with the declination of the observed probe δ for various values of ϕ . The curves indicate that the location of a station can best be established from tracking data of a probe slightly out of the equatorial plane and in the same hemisphere as the station.

If it is assumed that the tracking station is located by previous tracking to within the precision expressed by Eq. (5), and that over a single pass of data the precision in the station location remains constant and is not a dominant error source, then the standard deviation of the errors in the estimates of \dot{r} , α , and δ can be written as

$$\left. \begin{aligned} \sigma_{\dot{r}} &= \sigma_a \\ \sigma_\alpha &= \left\{ 2 \left[\left(\frac{\sigma_c}{r_s \omega \cos \delta} \right)^2 + (\omega \sigma_\xi)^2 \right] \right\}^{1/2} \\ \sigma_\delta &= \frac{2^{1/2} \sigma_b}{r_s \omega \sin \delta} \end{aligned} \right\} \quad (6)$$

where the factor of $2^{1/2}$ in the expressions for σ_α and σ_δ results from the allowance of station location errors. The variation of $\sigma_{\dot{r}}$ with δ can be obtained directly from the dashed curves in Fig. 6, and the variation of σ_α and σ_δ with δ , for various values of ϕ , is shown on the dashed curves in Figs. 11 and 12, respectively. It can be seen from the figures that both σ_α and σ_δ vary greatly with the probe declination. In the case of α , the variation is due mainly to pass-width variation; in the case of δ , the variation is due mainly to the fact that basically $\cos \delta$ is measured, and hence δ is virtually unobservable if the probe is near the equatorial plane.

4. Results of the Two-Station 24-h Pass of Data

Consider the two-station observing arrangement (discussed in the introduction) for the observation of a

space probe in the northern celestial hemisphere. The station in the northern hemisphere, called the primary station, has a geocentric latitude ϕ_1 , and the secondary station in the southern hemisphere is at latitude $\phi_2 = -\phi_1$. The longitudes of the respective stations satisfy the relation $\lambda_2 = -(\pi - \lambda_1)$.

The consecutive tracking of a single probe is performed by the two stations over a 24-h pass, and the covariance matrix of errors in the estimates of a , b , and c can be derived from the formula

$$\Lambda_{2\pi}^{-1} = \Lambda_1^{-1}(\psi_1, N_1) + \Lambda_2^{-1}(\psi_2, N_2) \quad (7)$$

where Λ_1 and Λ_2 are the individual error covariance matrices of estimates obtained from the two respective stations. By using the functional dependency of Λ on ψ and N (expressed in Eq. 3), and by carrying out the necessary algebraic manipulations, the following expression for $\Lambda_{2\pi}$ can be derived:

$$\Lambda_{2\pi} = \frac{\sigma_\rho^2}{N_{2\pi}} \begin{bmatrix} \frac{1}{1-\gamma^2} & 0 & \frac{2^{1/2}\gamma}{1-\gamma^2} \\ 0 & 2 & 0 \\ \frac{2^{1/2}\gamma}{1-\gamma^2} & 0 & \frac{2}{1-\gamma^2} \end{bmatrix} \quad (8)$$

with

$$\gamma = -\frac{2^{1/2} \sin \psi_1}{\pi/2}$$

$$N_{2\pi} = N_1 + N_2$$

where ψ_1 is the pass half-width of the primary station. Note that Eq. (8) is not dependent on the station positions at the start or end of the 24-h pass.

The variation of the precision to which a , b , and c can be measured from the two-station pass with δ is shown on the solid curves in Figs. 6, 7, and 8, respectively. Note that $\sigma_b/\omega = 0.513$ m for all values of ϕ and δ .

The accuracy to which the two stations can be located by observation of a single probe can be seen from Figs. 9 and 10, where, in all cases, the primary station is seen to be more precisely located than the secondary station.

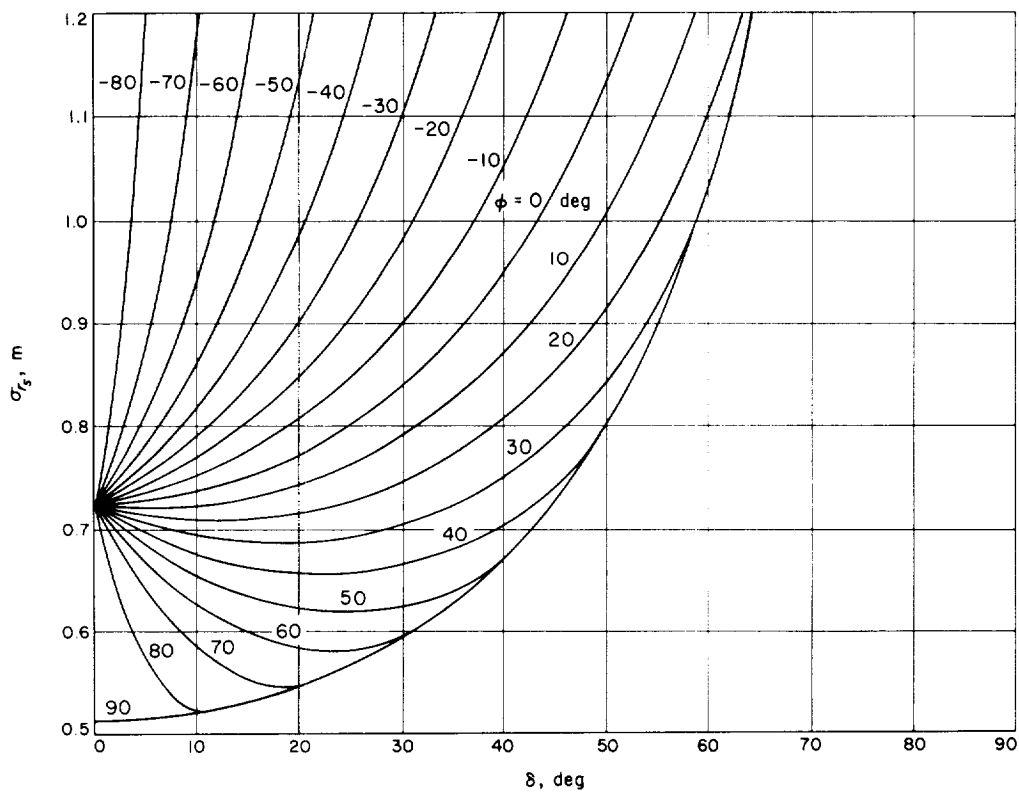


Fig. 9. Precision of estimates of r_s versus probe declination

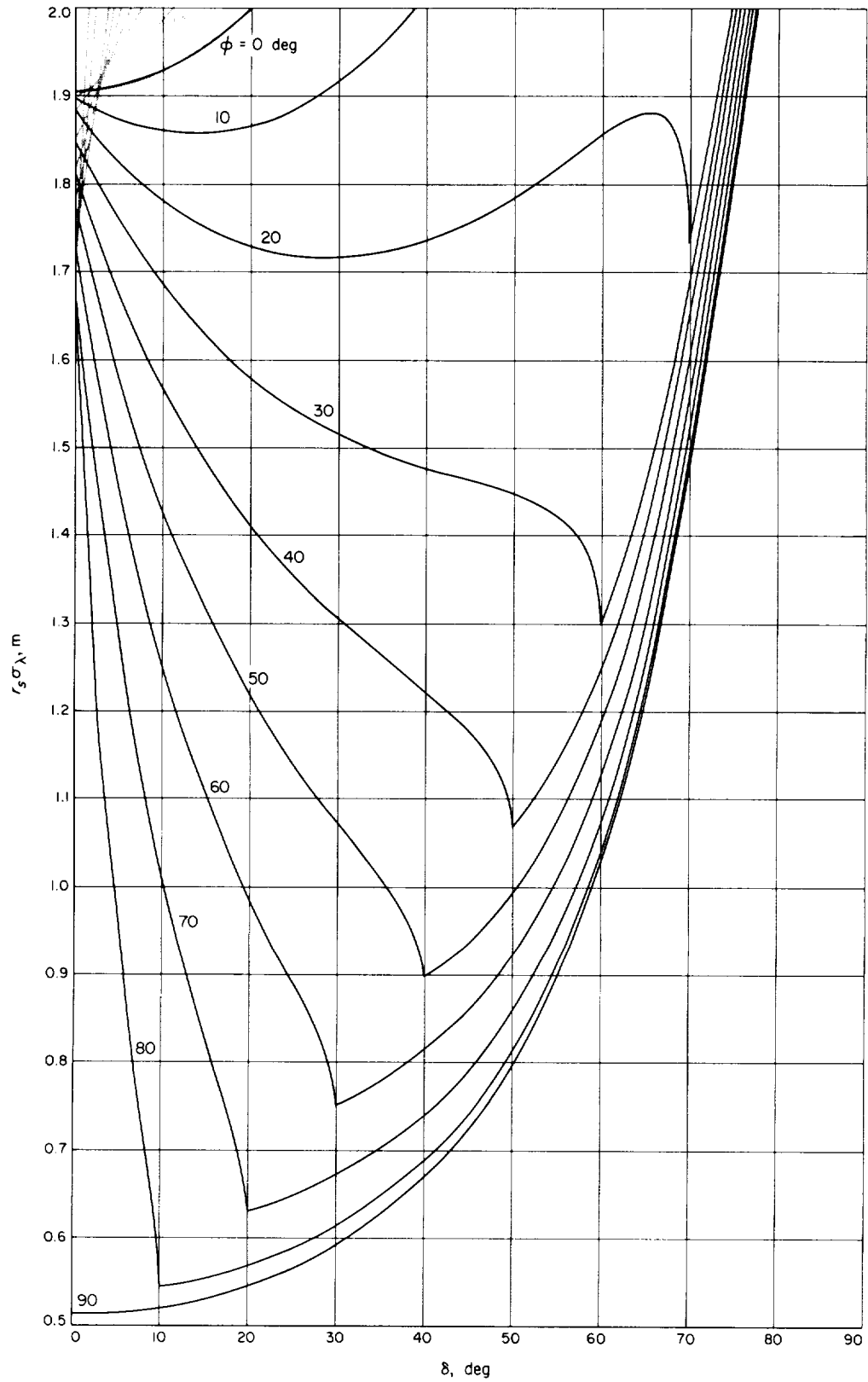


Fig. 10. Precision of estimates of station latitude versus probe declination

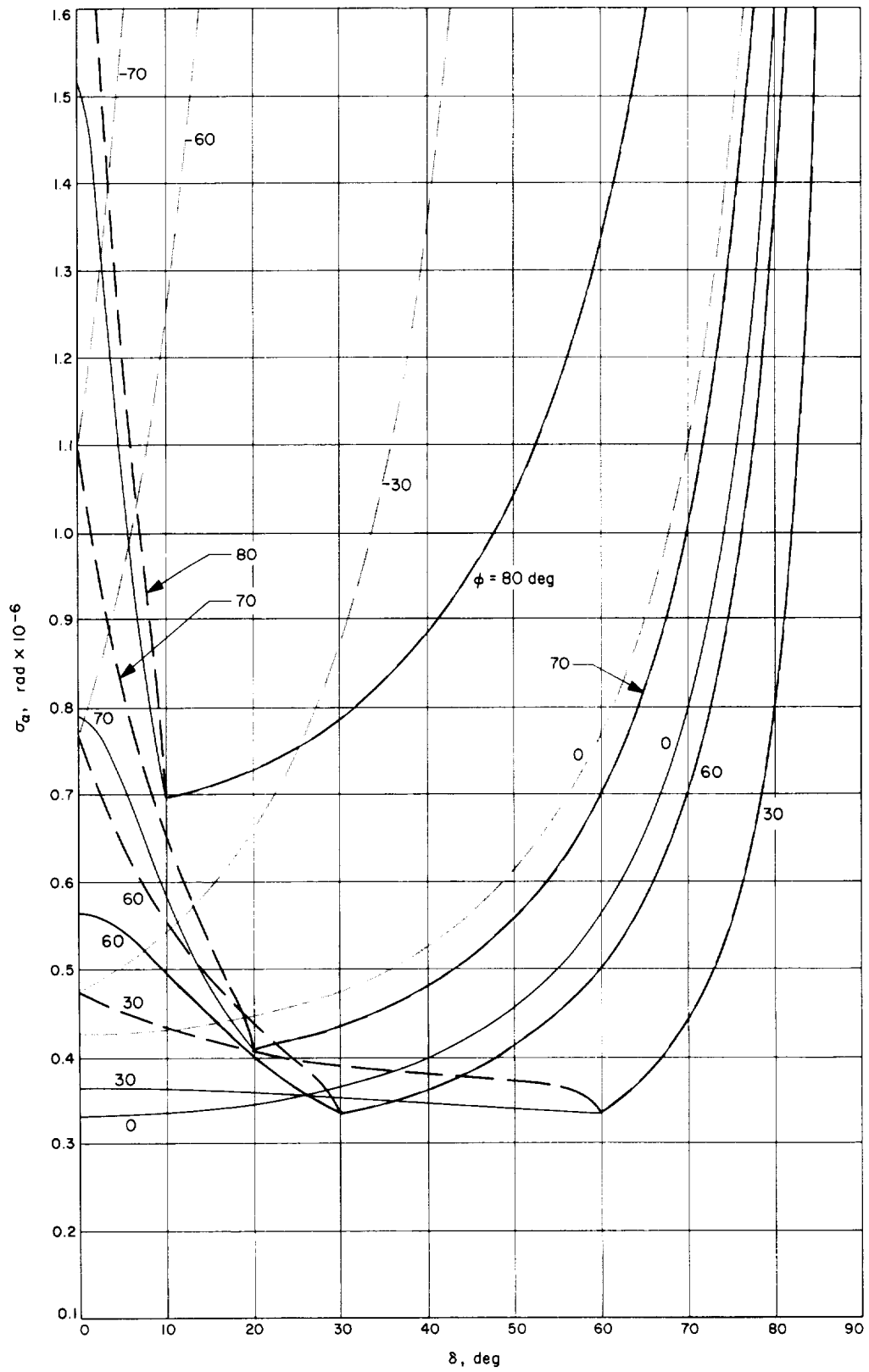


Fig. 11. Precision of right ascension estimates versus probe declination

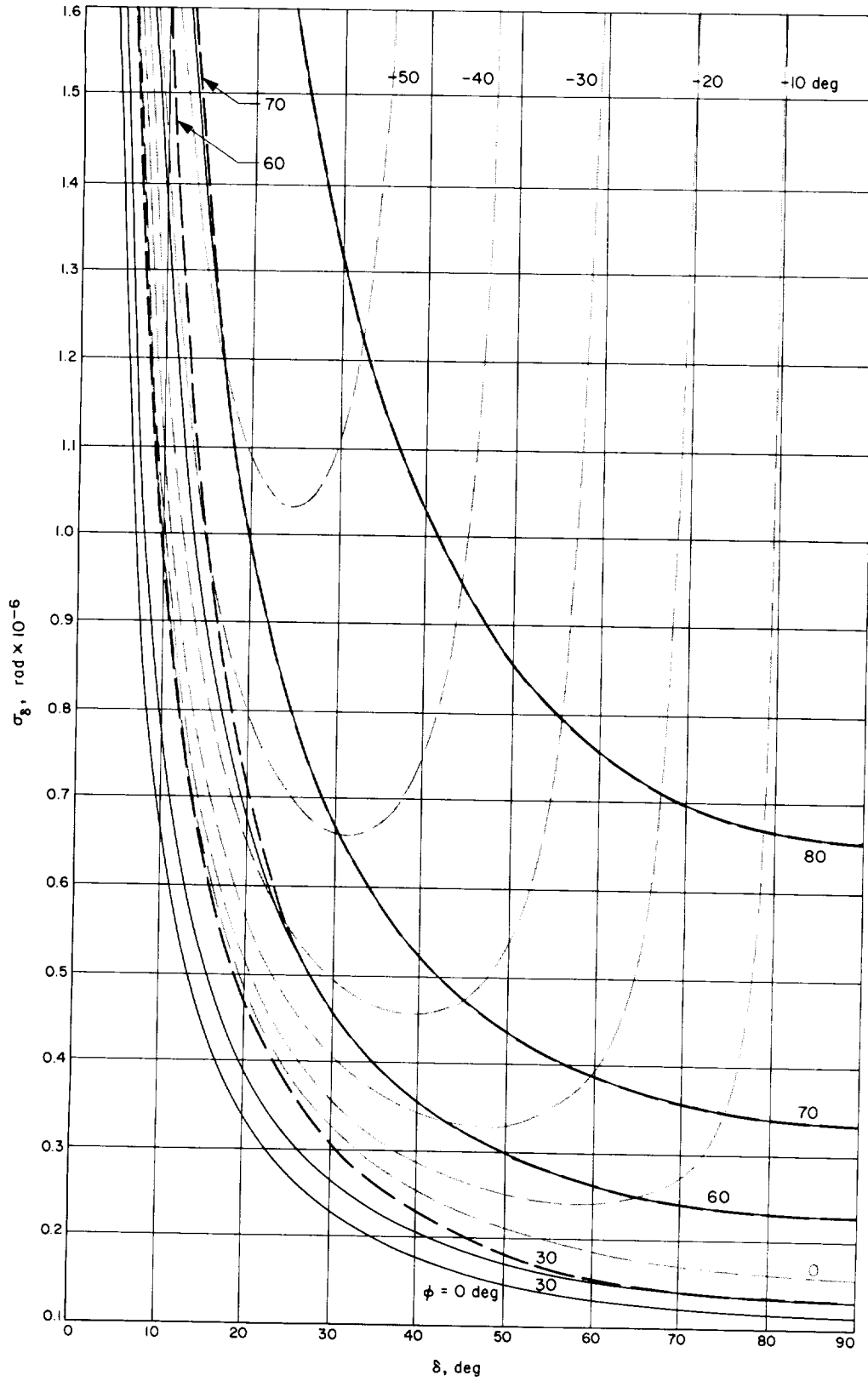


Fig. 12. Precision of declination estimates versus probe declination

If we assume that both stations are located to within the same precision—in particular, that given in Eq. (5)—the accuracy to which \dot{r} , α , and δ can be measured can be obtained for the two-station pass from Eq. (6), where σ_a , σ_b , and σ_c are obtained from the diagonal elements of the covariance matrix in Eq. (8). The variation of $\sigma_{\dot{r}}$ with δ can be directly obtained from the solid curves in Fig. 6, and the variations of σ_a and σ_b with δ are shown respectively on the solid curves in Figs. 11 and 12.

5. Comparison of the Single-Station and Two-Station Tracking Results

For a single station that is located near the equator ($\phi = 0$) and is observing a space probe on an interplanetary mission ($-30 \text{ deg} < \delta < 30 \text{ deg}$), the following approximate estimation accuracies are obtained:

$$\left. \begin{aligned} \sigma_{\dot{r}} &= 0.085 \text{ mm/s} \\ \sigma_a &= 4.3 \times 10^{-7} \text{ to } 4.8 \times 10^{-7} \text{ rad} \\ \sin \delta \sigma_b &= 1.6 \times 10^{-7} \text{ rad} \end{aligned} \right\} \quad (9)$$

depending on the declination of the probe. The numbers above correspond to a pass half-width of $\psi = 90 \text{ deg}$, and correspond roughly to the results given by Hamilton and Melbourne in Eqs. (25), (26), and (27). For two stations on the equator, the results are

$$\left. \begin{aligned} \sigma_{\dot{r}} &= 0.060 \text{ mm/s} \\ \sigma_a &= 3.6 \times 10^{-7} \text{ to } 3.4 \times 10^{-7} \text{ rad} \\ \sin \delta \sigma_b &= 1.1 \times 10^{-7} \text{ rad} \end{aligned} \right\} \quad (10)$$

Because of the doubling of the total tracking time, the accuracies expressed in Eq. (10) reflect an increase in precision by a factor of $1/2^{1/2}$ over the single-station results.

For a single station located at a latitude of $\phi = 30 \text{ deg}$, the following accuracies are obtained:

$$\left. \begin{aligned} \sigma_{\dot{r}} &= 0.15 \text{ to } 0.053 \text{ mm/s} \\ \sigma_a &= 8.5 \times 10^{-7} \text{ to } 3.8 \times 10^{-7} \text{ rad} \\ \sin \delta \sigma_b &= 2.0 \times 10^{-7} \text{ to } 1.5 \times 10^{-7} \text{ rad} \end{aligned} \right\} \quad (11)$$

depending on the declination of the probe. The two-station accuracies at $\phi = 30 \text{ deg}$ are

$$\left. \begin{aligned} \sigma_{\dot{r}} &= 0.060 \text{ to } 0.050 \text{ mm/s} \\ \sigma_a &= 3.7 \times 10^{-7} \text{ to } 3.5 \times 10^{-7} \text{ rad} \\ \sin \delta \sigma_b &= 1.3 \times 10^{-7} \text{ rad} \end{aligned} \right\} \quad (12)$$

which reflect an accuracy gain for the two-station results from 5 to 300%, depending on the declination of the probe. The main advantage of the two-station mode of tracking appears to be the protection it affords against a short or null pass width which sometimes occurs with one station.

6. Discussion of Results in Terms of the Present DSN

The various station locations (Table 3) of the network afford total viewing time of a space probe at any location; hence, the two-station results given in this article for $\phi = 20$ to 40 deg can be viewed as a rough approximation of the upper bound of the observing capability of the network. The solid-line curves in Figs. 6, 11, and 12 indicate good observing capability for \dot{r} , α , and δ for all interplanetary probes ($|\delta| < 30 \text{ deg}$), with the accuracies of the measurements of all three parameters improving with increasing probe declination.

Definition of symbols

ψ	maximum station pass half-width
ρ	noise-contaminated station-probe range rate
ω	angular velocity of earth
n	noise in doppler (range rate) tracking data
r_s	distance of station from earth spin axis
t_0	time when probe crosses station meridian
σ_p	standard deviation of data noise
N	number of doppler counts in pass
ϕ	station latitude
λ	station longitude
α	space probe right ascension
δ	space probe declination
r	space probe's radial distance from center of earth
ξ	error in universal time

Table 3. Geographic locations of the DSN

Geographic location	Approximate latitude, deg	Approximate longitude, deg
Barstow, Calif. (Goldstone DSCC)	+35	-116
Madrid, Spain (Madrid DSCC)	+40	-3
Johannesburg, South Africa (Johannesburg DSS)	-26	+27
Canberra, Australia (Tidbinbilla DSS)	-35	+149
Island Lagoon, Australia (Woomera DSS)	-31	-136

Table 4. Data summary for Lunar Orbiter II

DSS	Premidcourse				Postmidcourse			
	Doppler, 1/min		Ranging, 1/3 min		Doppler, 1/min		Ranging, 1/3 min	
	(1) Number of points	(2) Standard deviation, Hz	(3) Number of points	(4) Standard deviation, m	(1) Number of points	(2) Standard deviation, Hz	(3) Number of points	(4) Standard deviation, m
12	773	0.0045	32	10.3	931	0.0041	180	8.3
41	777	0.0077	193	4.6	914	0.0071	264	6.1
61	697	0.0053	123	6.3	871	0.0042	217	8.0
Total	2247	—	348	—	2716	—	661	—
Combined total of doppler points = 4963								
Combined total of ranging points = 1009								

D. Consistency of Lunar Orbiter II Ranging and Doppler Data, N. A. Mottinger and W. L. Sjogren

1. Introduction

Prior to the *Lunar Orbiter* missions there had been no deep space coherent ranging. In SPS 37-43, Vol. III, pp. 24-28, some initial results were given for tracking data obtained during the lunar orbit phase of these missions. This report deals with the 90 h of tracking in transit from the earth to the moon. The results illustrate that the doppler and ranging data are basically consistent and that the accuracy of the ranging data is on the order of 10 m. Residual plots (the difference between the actual ranging observables and the theoretical range values) are presented for the case of a trajectory determined from doppler data only and for the case where the ranging and doppler data are used together.

The estimated parameters obtained from *Lunar Orbiter II* when ranging data are used and when they are omitted are compared with previous *Ranger* and *Mariner* results. Station longitude uncertainty is reduced a magnitude with the use of ranging data, and spacecraft position along the ranging direction is reduced to a few meters. Subsequent reports on *Lunar Orbiters III* and *IV*² should build a very high degree of confidence in the DSN ranging system.

¹If *Lunar Orbiter E* is successfully launched and functions properly, these data will also be reported. Since *Lunar Orbiter I* had Canopus sensor problems, the data are continuously contaminated by the small forces from uncoupled attitude control jets; therefore, no reduction has been done.

2. Discussion

The tracking data for *Lunar Orbiter II* were obtained from three deep space stations: DSS 41 (Woomera, Australia); DSS 12 (Echo, Goldstone, California); and DSS 61 (Robledo, Madrid, Spain). The S-band two-way doppler and Mark I ranging data received at all three stations are presented in Table 4. The normal sample rate was one doppler point every 1 min and one independent range point every 3 min. The tracking period covers approximately 90 h of free flight (i.e., the entire period from injection near the earth to deboost into lunar orbit), with only one discontinuity caused by a motor burn (midcourse maneuver) approximately 41 h from injection.

The high frequency noise values³ are shown in columns 2 and 4 of Table 4, and also in the residual plots of Figs. 13 and 14. The noise on the doppler data is primarily due to quantization error, which is theoretically 0.0034 Hz for DSS 61 and DSS 12 and 0.0068 Hz for DSS 41,⁴ and compares favorably with the actual noise level shown in Table 4. There are a few periods in the Goldstone pass where some 10-s data are taken and the noise level is proportionally higher (i.e., postmaneuver residual plot at November 8, 19:00; November 10, 19:00; and November 10, 20:25 GMT).

The noise on the ranging data varies as a function of signal strength, the primary factor being phase jitter on

³Quoted uncertainties are 1 σ .

⁴DSS 41 counts only every other zero crossing, whereas DSS 12 and DSS 61 count every zero crossing.

the incoming coded signal. Some known biases that could easily exist in the ranging system include ionospheric changes over a pass of data (± 3 m) (only a constant was used to account for ionospheric effect), inaccuracy in station delay calibration and variation during a pass (± 2 m), single precision computer computations (± 4 m at lunar distance), editing program subtraction for 180-deg phase shift (± 5 m), inaccuracy in calibrating spacecraft transponder delay (± 3 m), and computer program integration error (unknown, but certainly ± 10 m or more). Therefore, ranging data could have a 25-m bias; it will be pointed out that this can corrupt the station location estimates, etc. The effectiveness of the ranging data on the estimate is a direct function of the assumed data weights.⁵ The weights used were 0.1 Hz on the 1-min doppler data and 15 m on the 3-min ranging data. The doppler data weight is fairly realistic; however, the ranging weight is rather optimistic and will undoubtedly be changed in future reductions.

The processing of the data was accomplished with the aid of the single precision orbit determination program (Ref. 1), and the procedure of combining the premidcourse data block with the postmidcourse data was the same as that outlined in Ref. 2. Essentially, the procedure is to fit only the premidcourse data and accumulate the normal equations at the injection epoch, and then to integrate the converged estimate to the midcourse epoch with a linear mapping of the inverted normal equation matrix (i.e., covariance matrix) to this time also. The estimate is then incremented with the best estimate of the maneuver, and the mapped covariance is corrupted in the velocity components and used *a priori* for the postmidcourse data fit.

During the initial reduction of ranging data in near-real time, it became evident that the doppler and ranging data were somewhat inconsistent (i.e., range residuals of 1 km or more). However, during postflight analysis it was noted that neglect of the solar pressure computation (not usually used in lunar real-time data reduction) caused the poor data comparison. Also, a poor lunar potential model which was stored into the computer program produced systematic errors on the order of 0.1 Hz at encounter. Corrections in these two areas brought the data into the fine agreement shown in the residual plots.

The parameters estimated in these computations were: the spacecraft position and velocity at an epoch, GM_{\oplus} ,

⁵The term weight is used as the standard deviation of an effective noise level (σ_{eff}) and is the inverse of W , the normally used weight notation; i.e., $W = 1/\sigma_{eff}$.

GM_{\odot} , a solar pressure constant, lunar ephemeris radial scale factor, and two components of station location for each of the three tracking stations. On the doppler-only fit, the ephemeris scale factor could not be estimated very well (i.e., 9 m, 1- σ uncertainty); as a result, when the scale factor moved off its original input estimate by some small portion of its uncertainty (i.e., 3.3 m), the ranging residuals picked up a time-varying bias, becoming larger as the spacecraft approached the moon. Therefore, it was decided to remove this parameter on the doppler-only fit and fix the scale factor at a consistent value with GM_{\oplus} and GM_{\odot} (i.e., $RE = K(GM_{\oplus} + GM_{\odot})^{1/3}$; $K = 86.313527 \text{ s}^{2/3}$). The residuals displayed are for the case where the scale factor is held fixed. The ephemeris used in the reduction was one of the latest JPL ephemerides⁶ with the updated mass ratios and Eckert's corrections.

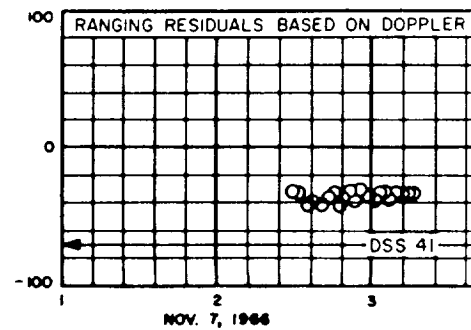
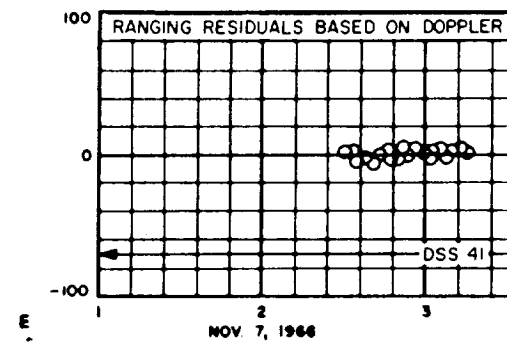
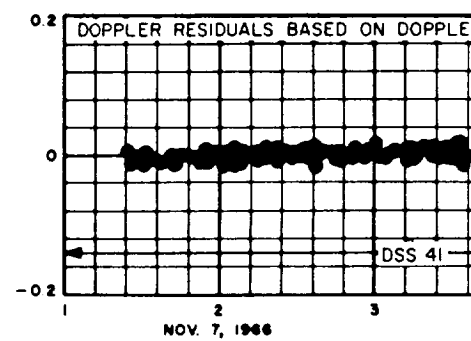
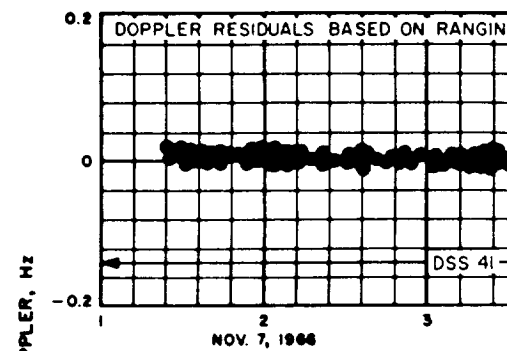
3. Results

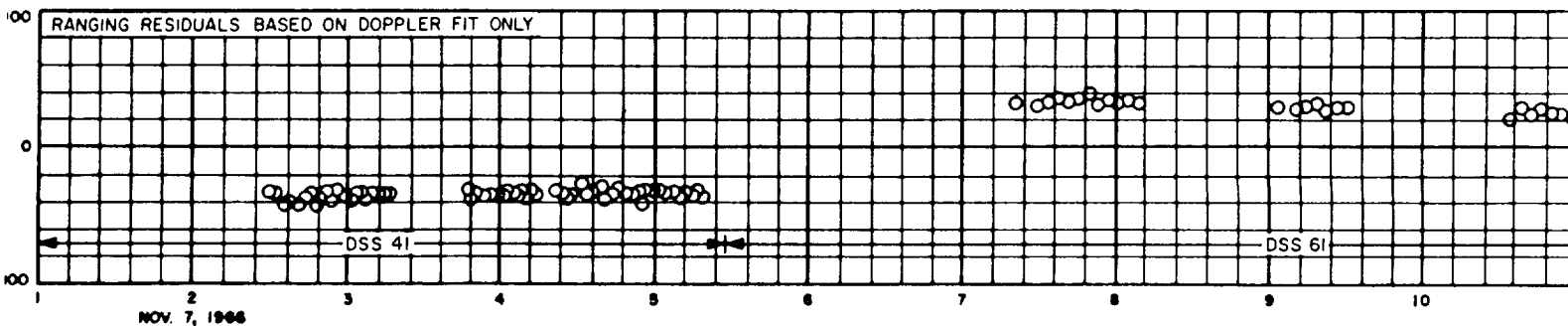
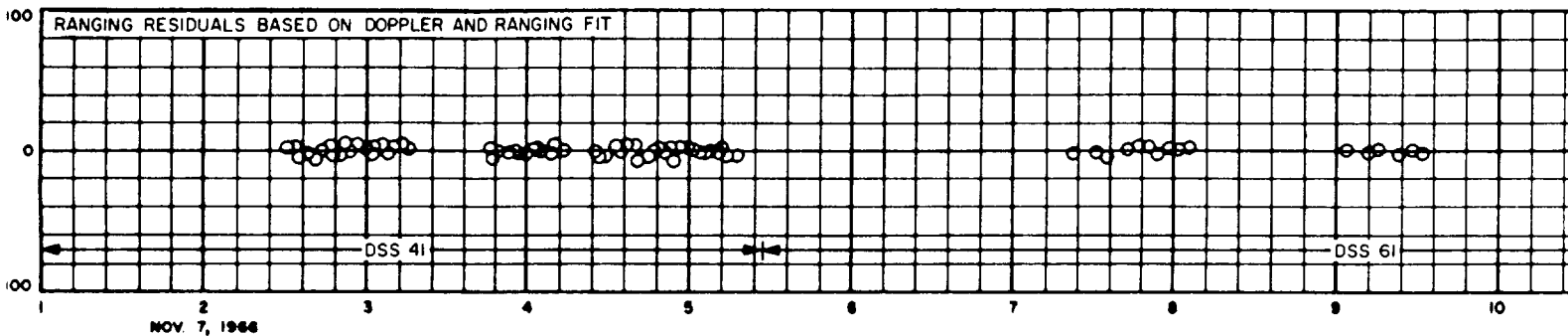
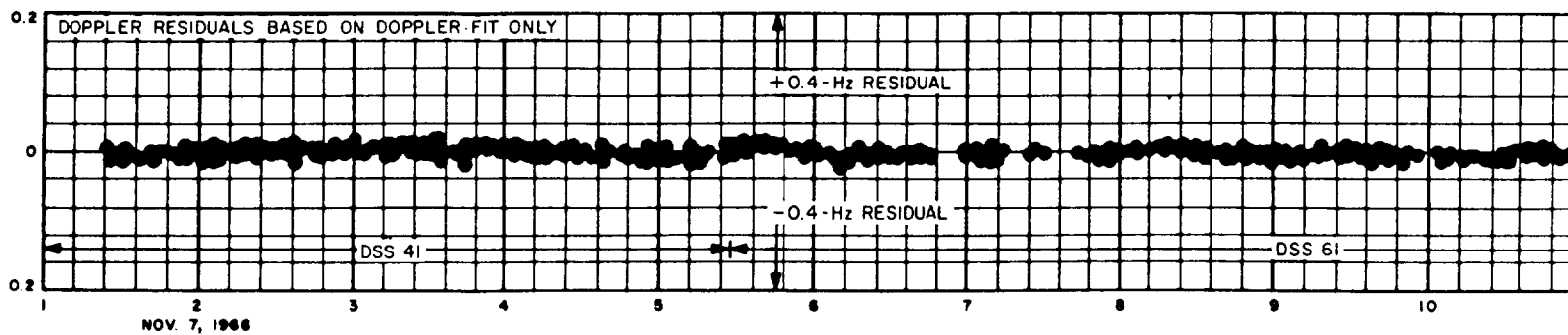
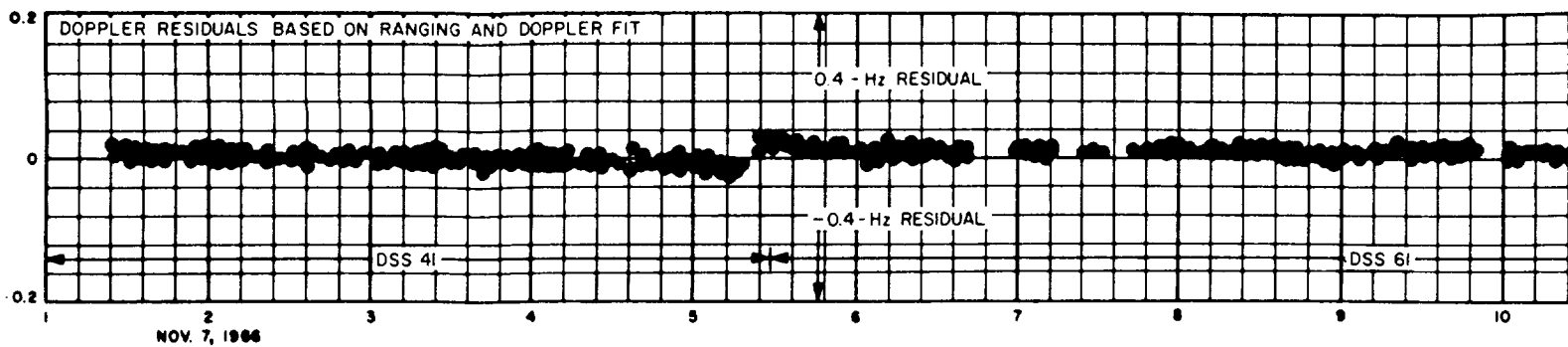
In Figs. 13 and 14, it can be noted that the ranging data residuals are good in both premidcourse and postmidcourse cases where only doppler data were being fit. In the premidcourse residuals (Fig. 13), for the doppler-only fit, ranging residuals are at a maximum of 40 m while the mean is about 20 m. Also, the three ranging blunder points at 07:00 on November 8 are not in the fit, but do appear on the plots.⁷ For the two times when 10-s data were being taken, 19:15 on November 8 and 20:12 on November 10, the higher noise present is caused by the increase in roundoff error due to the decreased averaging time. The 10-s data have a roundoff error six times greater than the normal count time of 60 s. Between the runs, a slight change was made in the data range span at the conclusion of the premidcourse doppler and ranging fit. This accounts for the absence of 10-s data in the doppler residuals.

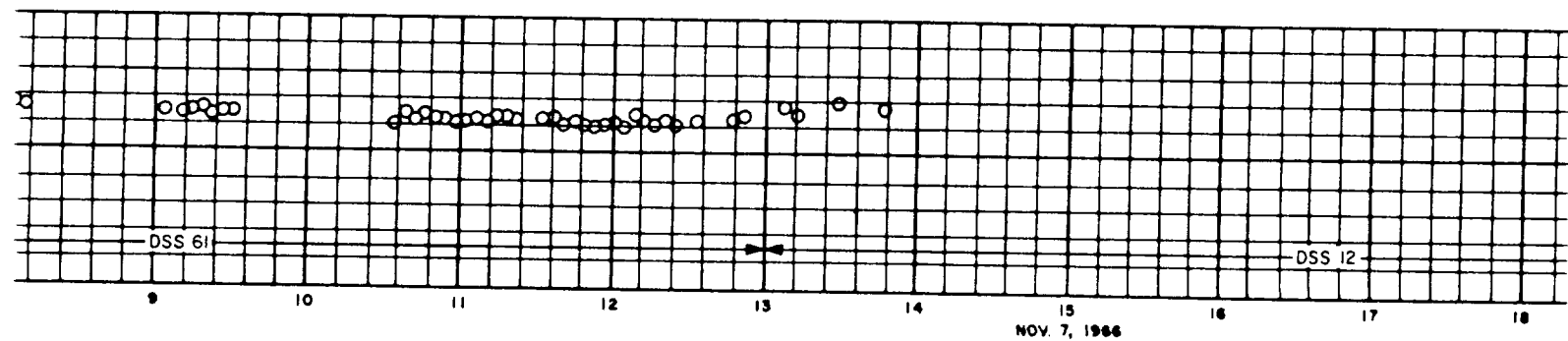
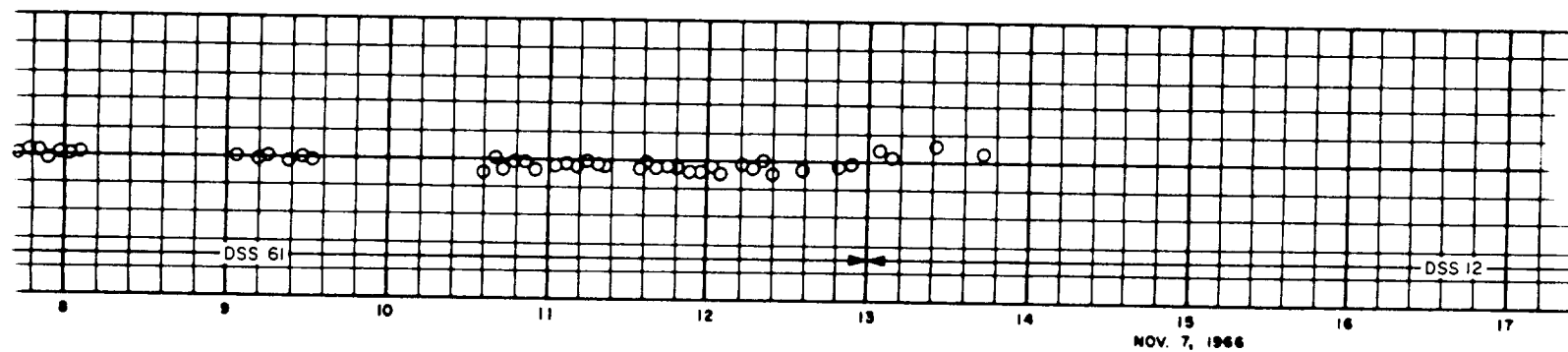
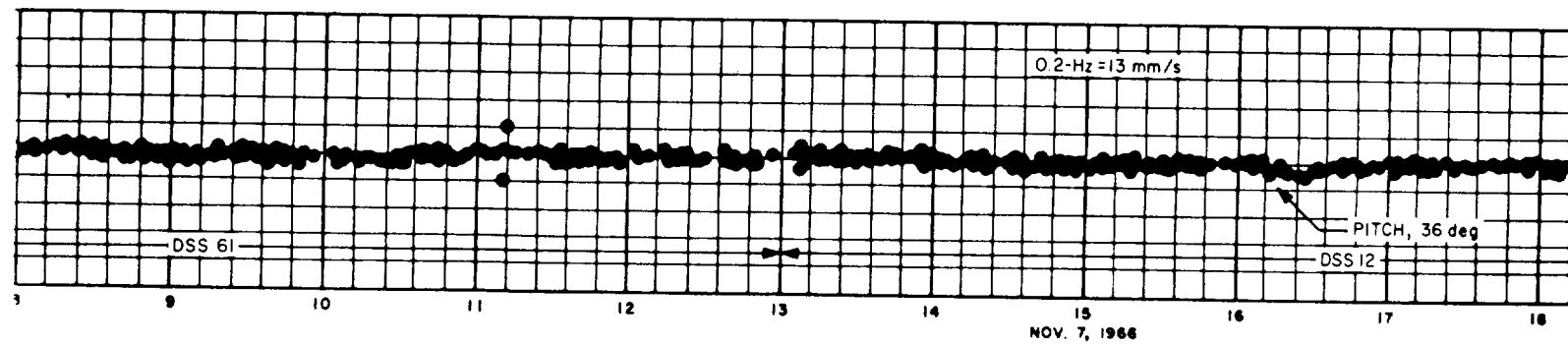
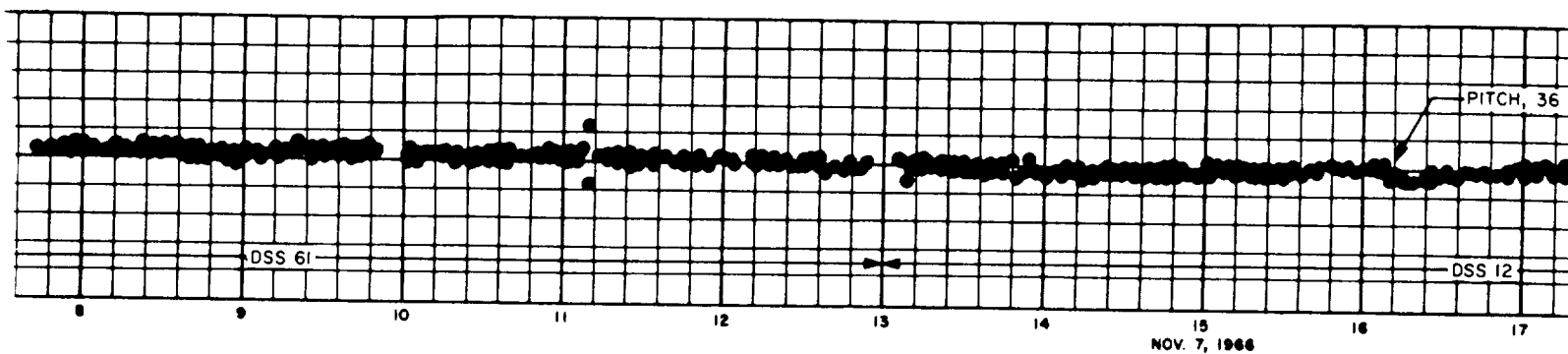
The postmidcourse range residuals (Fig. 14) show variations from 0 to 70 m, but generally follow the doppler results. These biases can be attributed to many causes, several of which were mentioned previously. Other biases may result from an incomplete theoretical model where additional perturbations have not been included, such as small forces from attitude control maneuvers (noted on plots), higher coefficients in lunar potential, and others unknown at this time.

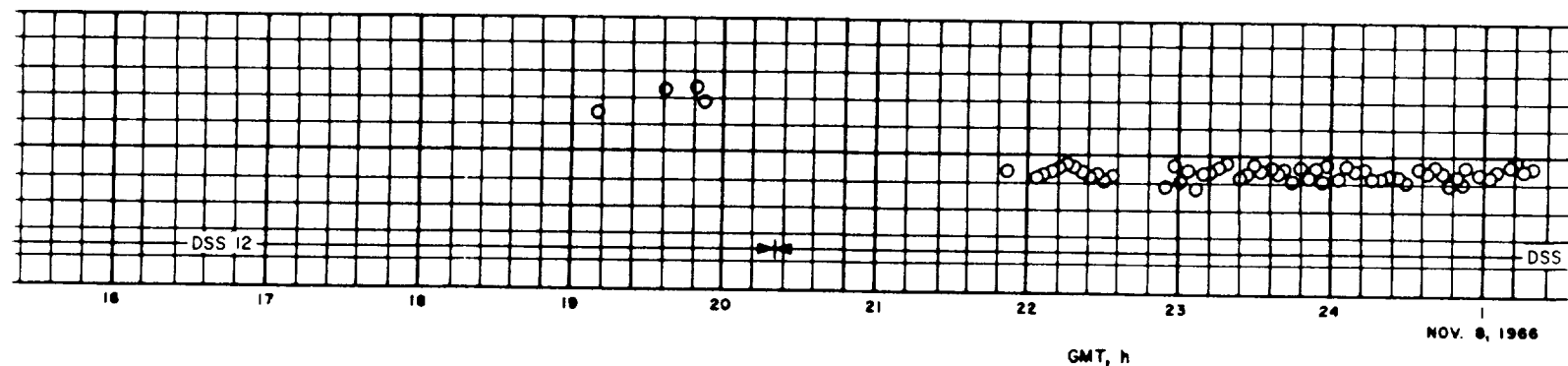
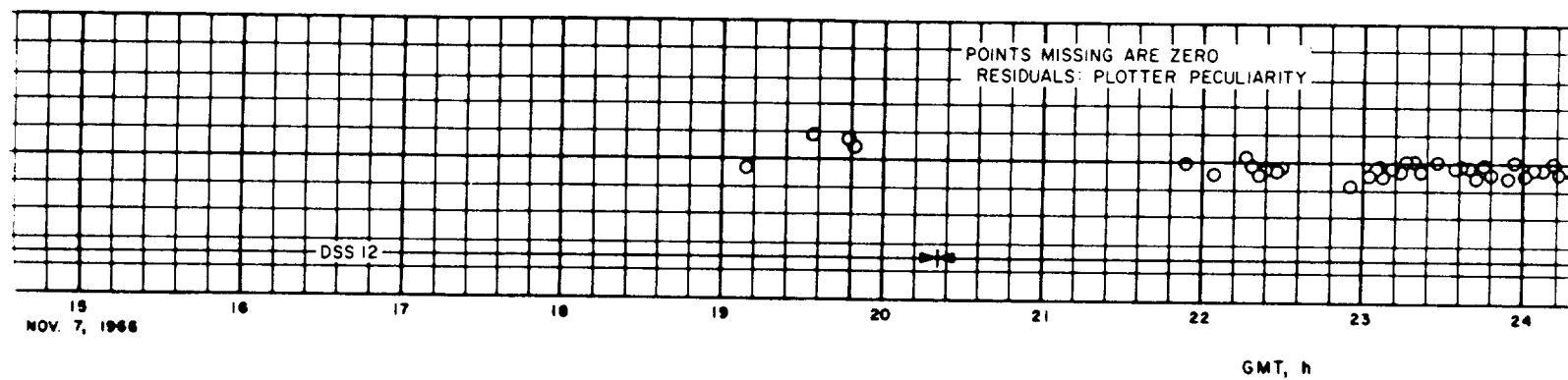
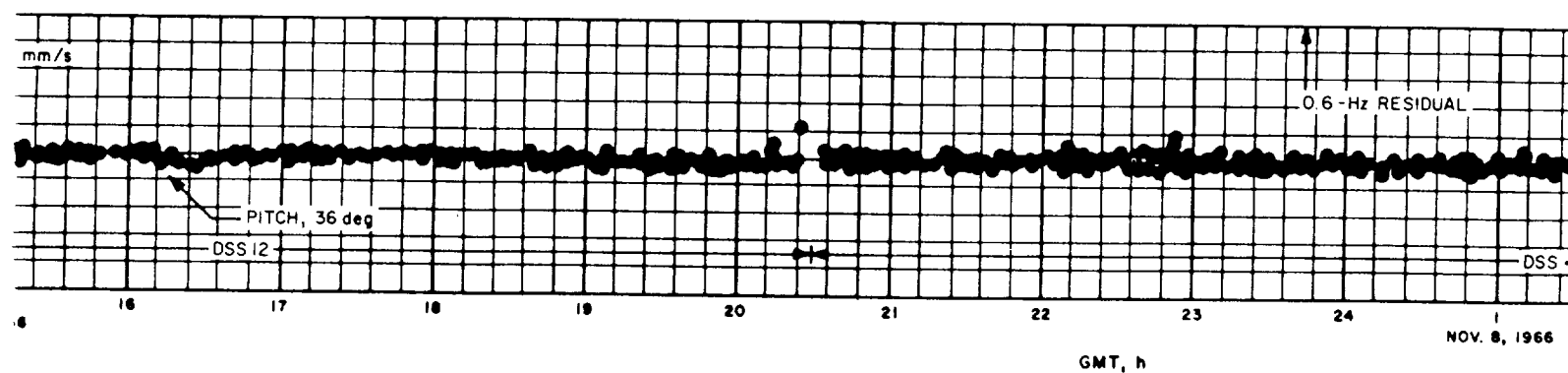
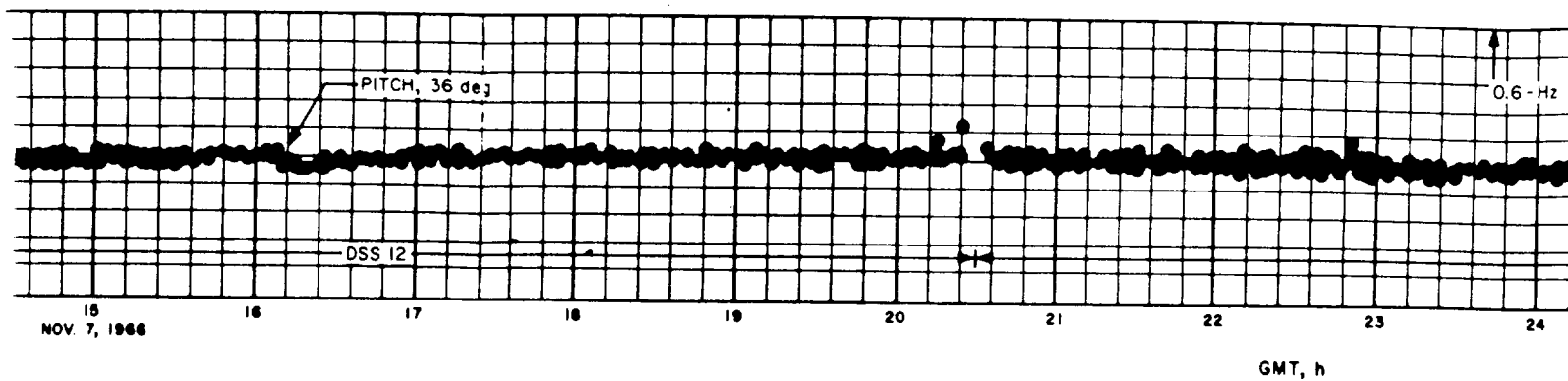
⁶Tape 9302, $RE = 6378.1503$.

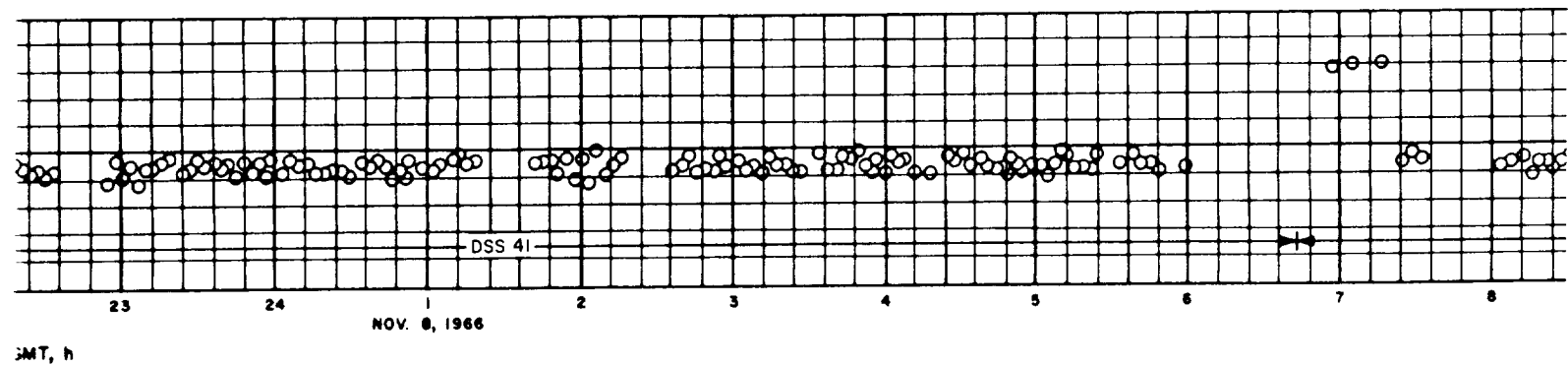
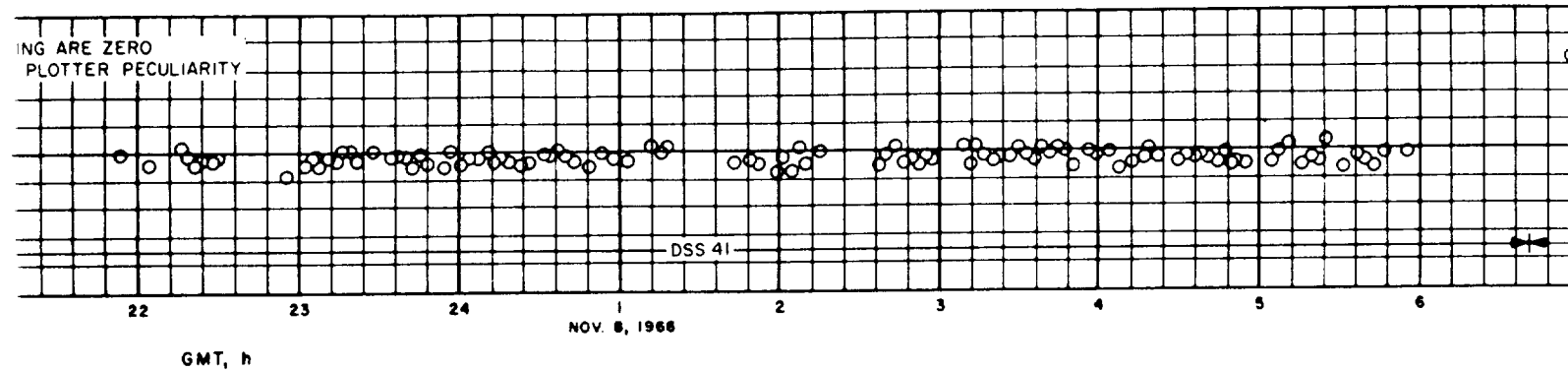
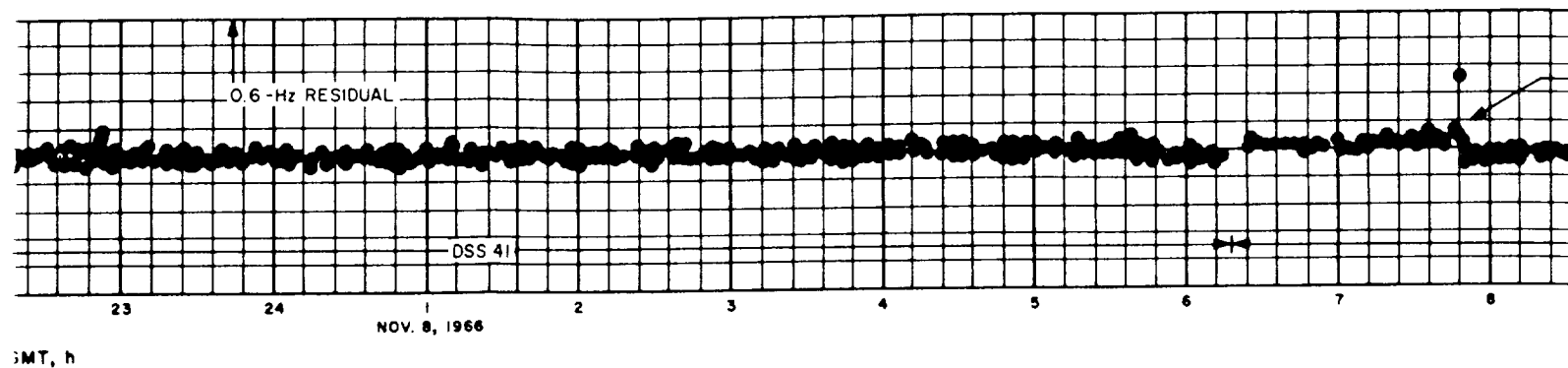
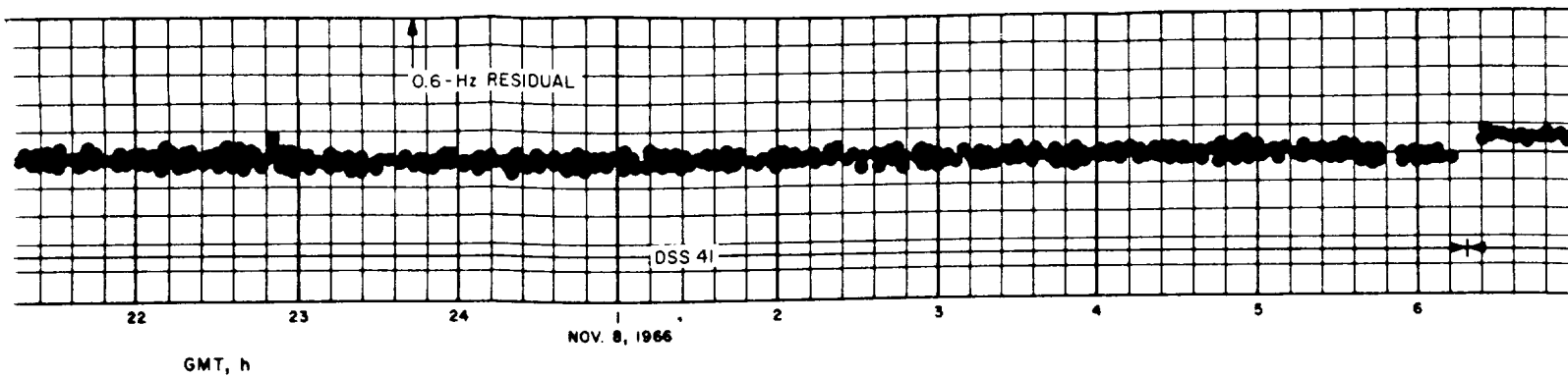
⁷Unfortunately, there are also three doppler residuals marked in Fig. 13 which are in the fit but are not on the plots. In future analyses they will be excluded from the fit, but their effect on these present results should be very small considering the large amount of data.

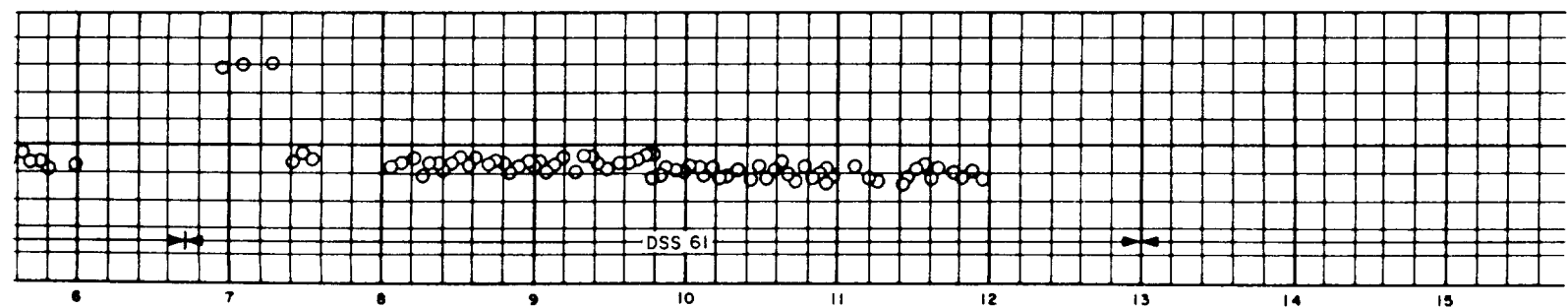
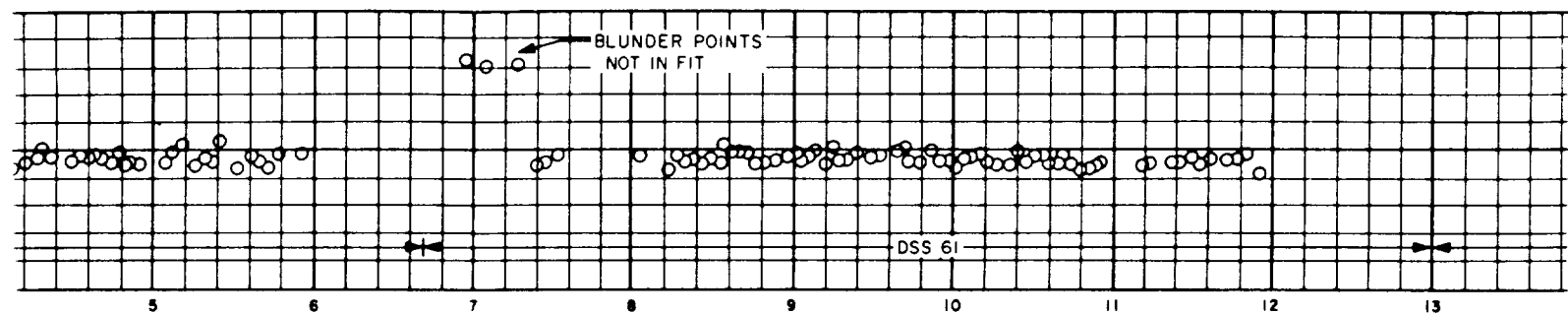
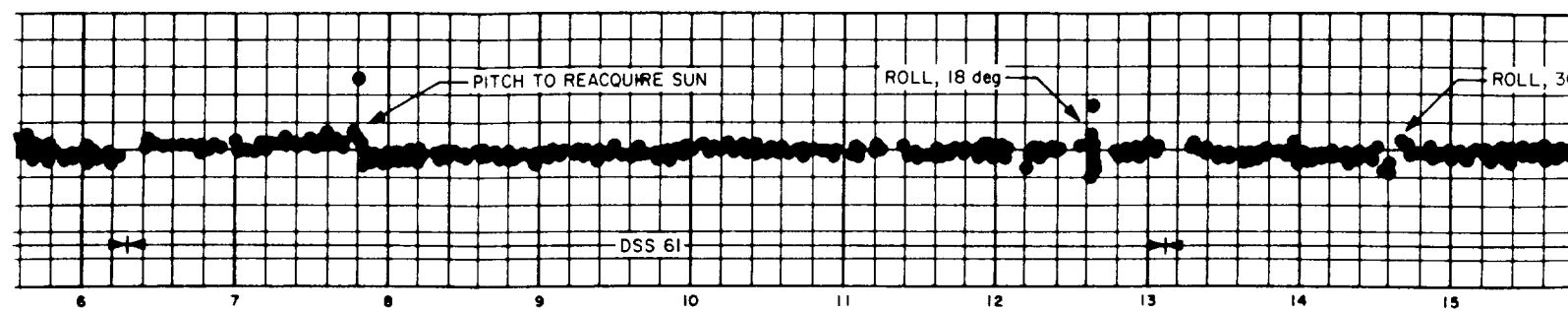
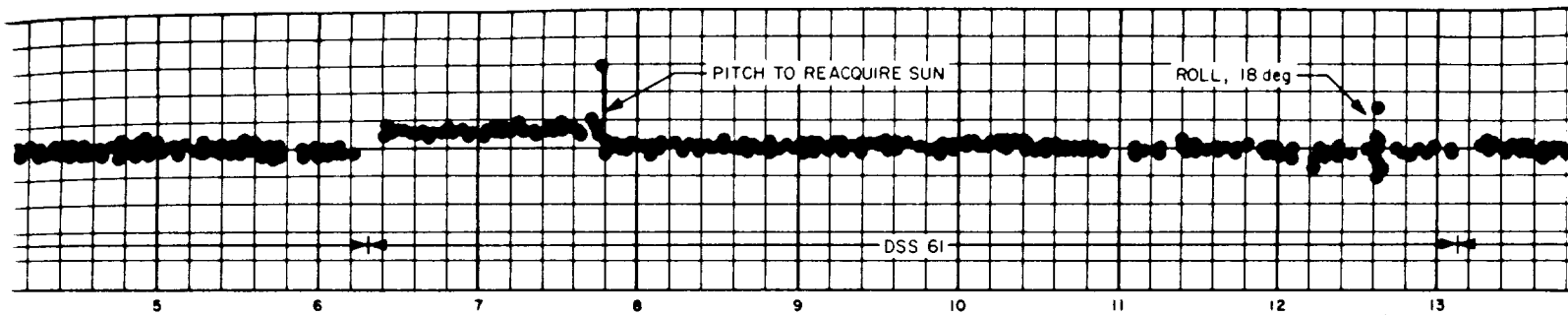












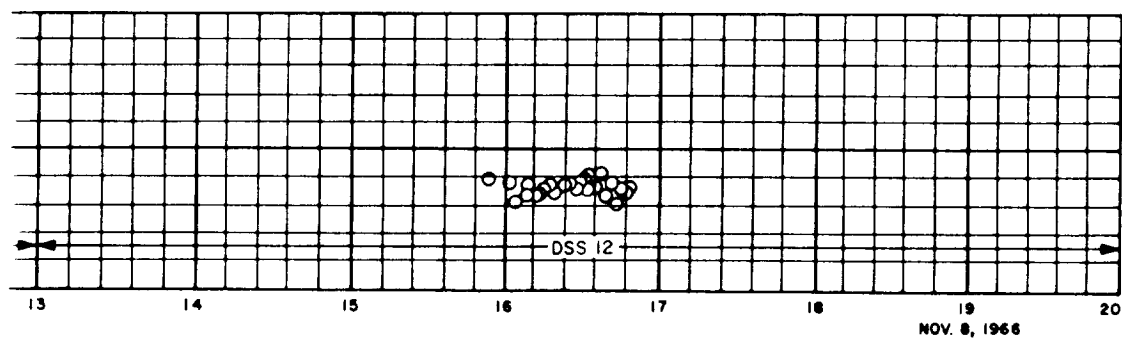
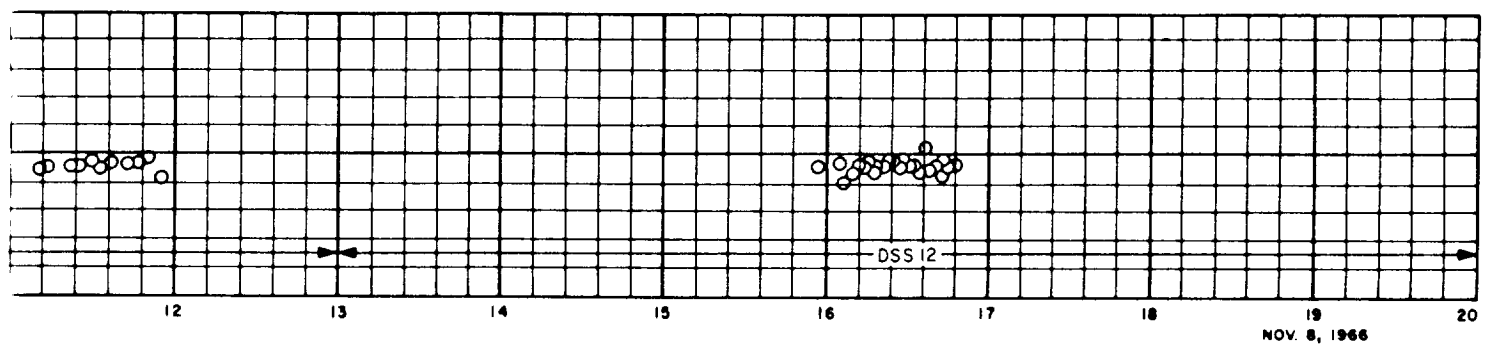
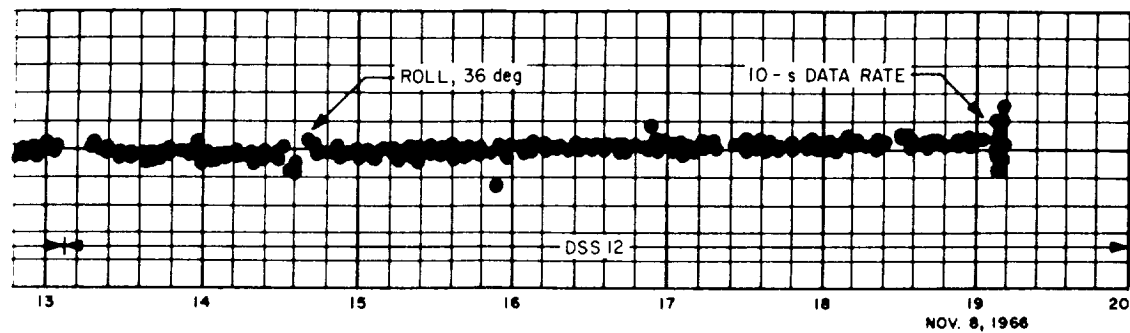
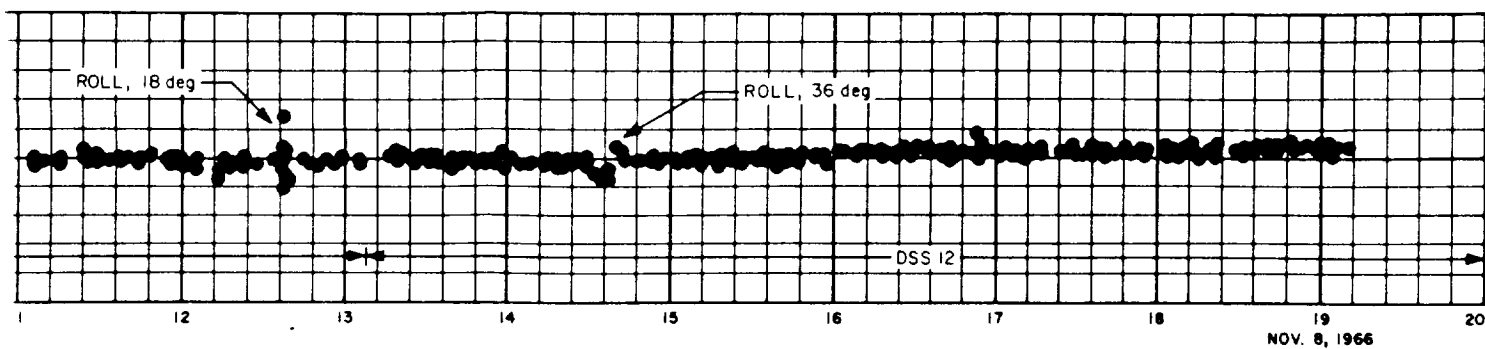


Fig. 13. Premaneuver residuals for Lunar Orbiter II

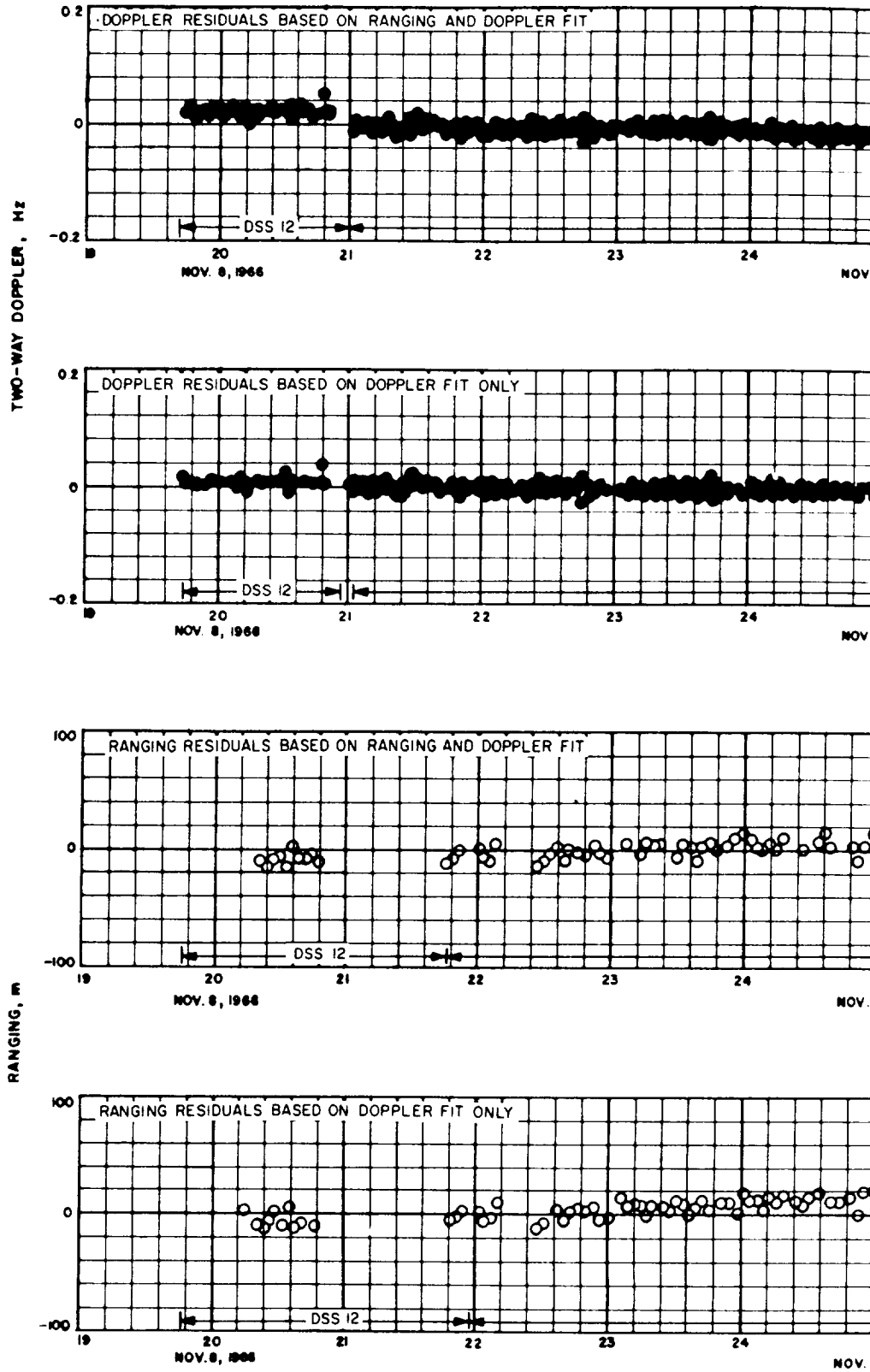
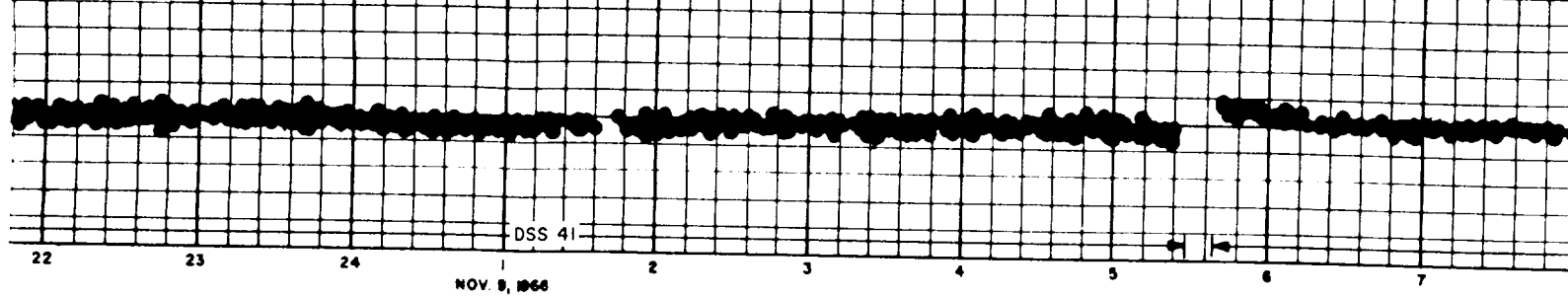
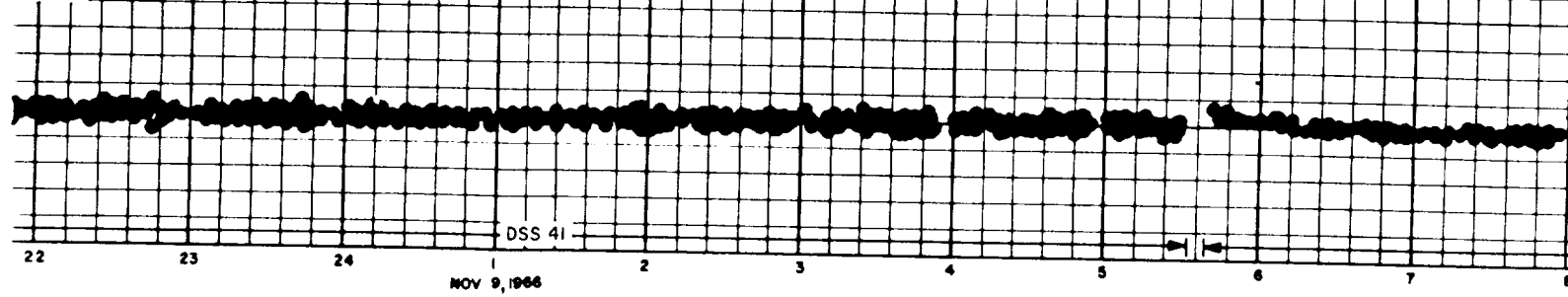


Fig 14. Postmaneuver residuals for Lunar Orbiter II

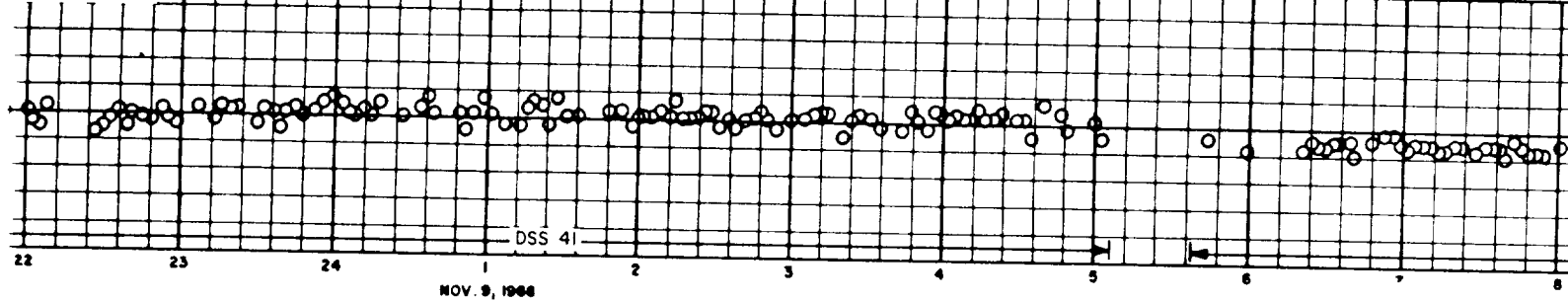
AND DOPPLER FIT



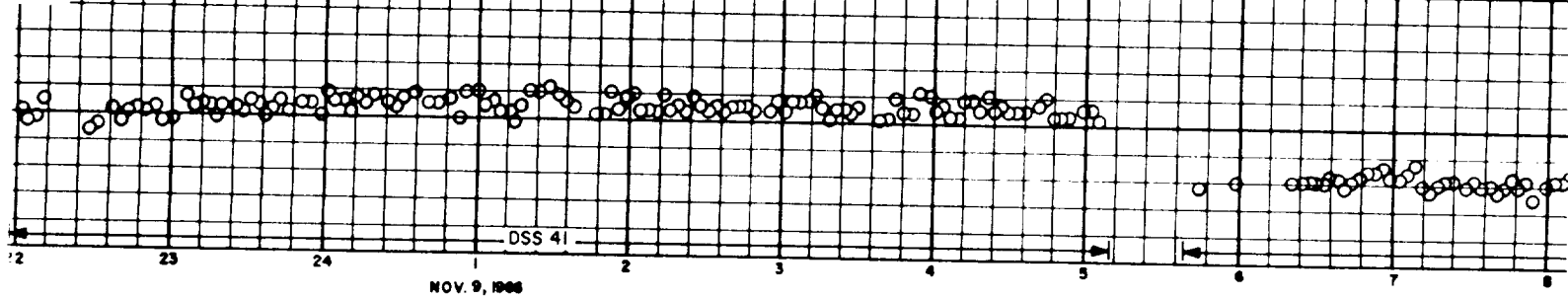
T ONLY



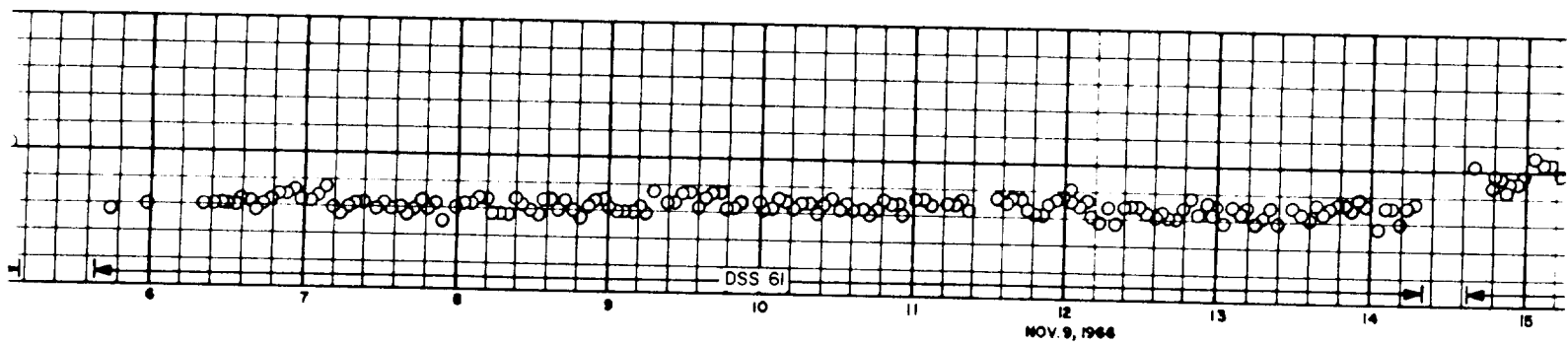
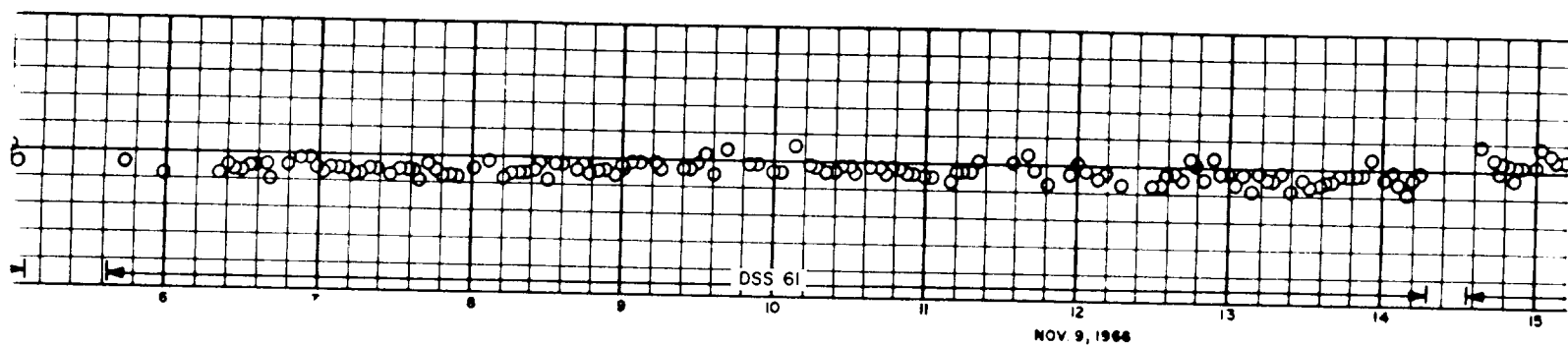
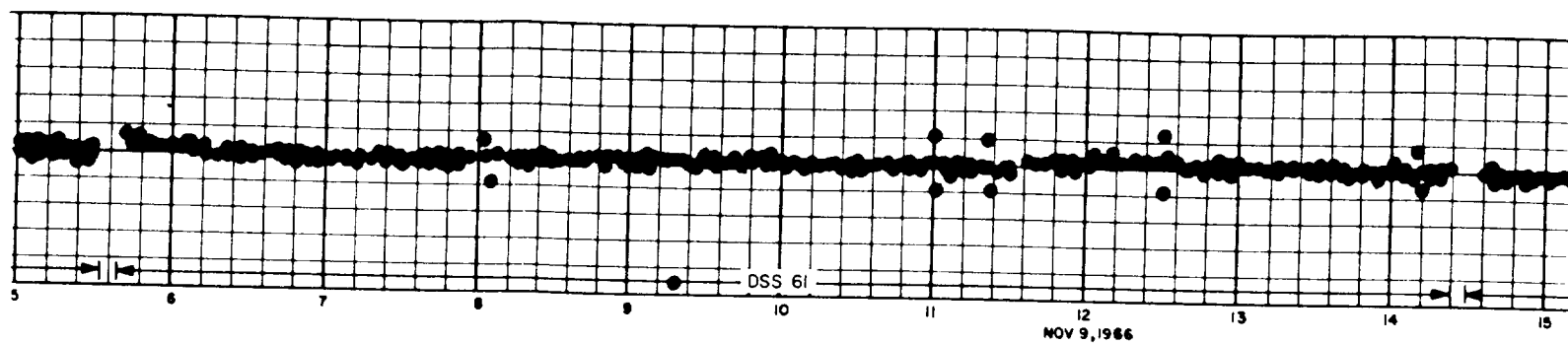
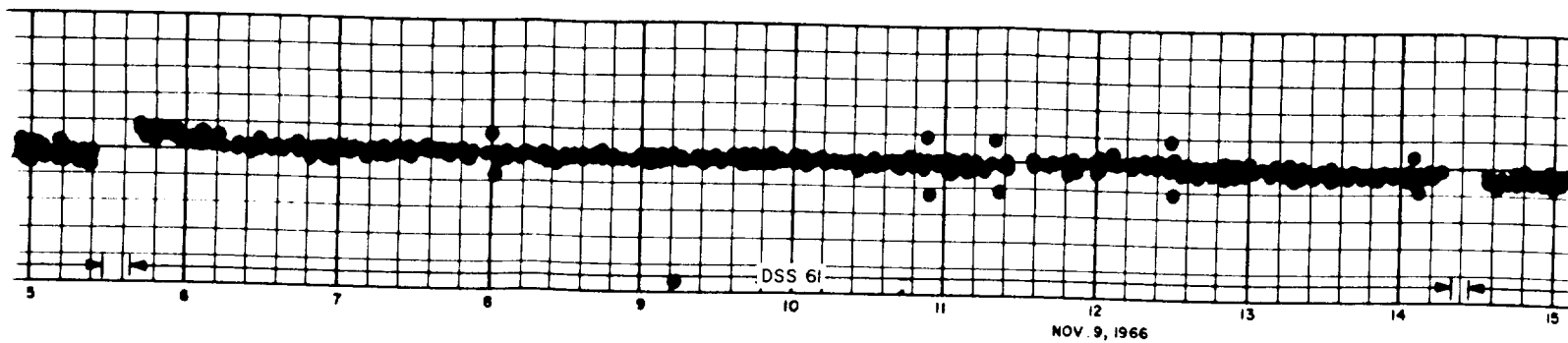
D DOPPLER FIT

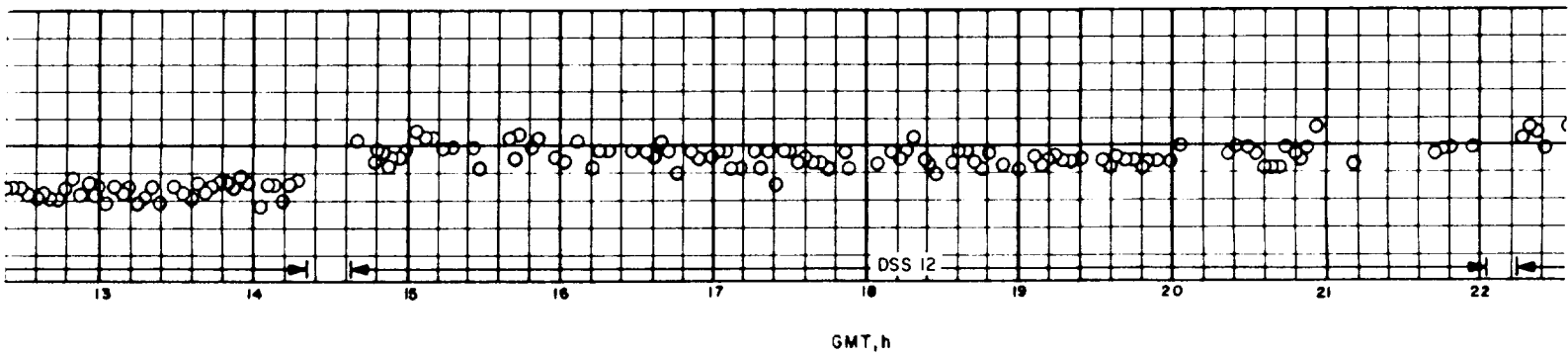
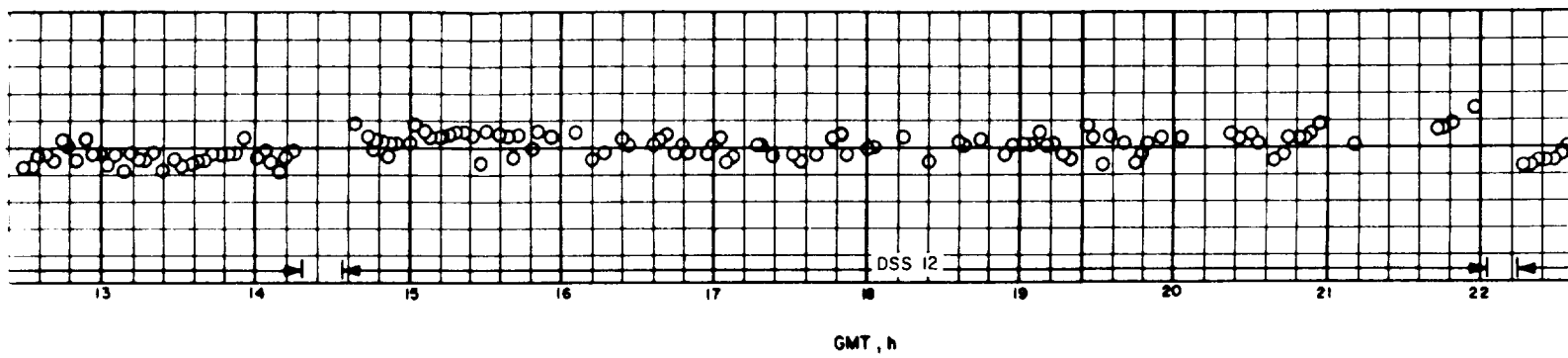
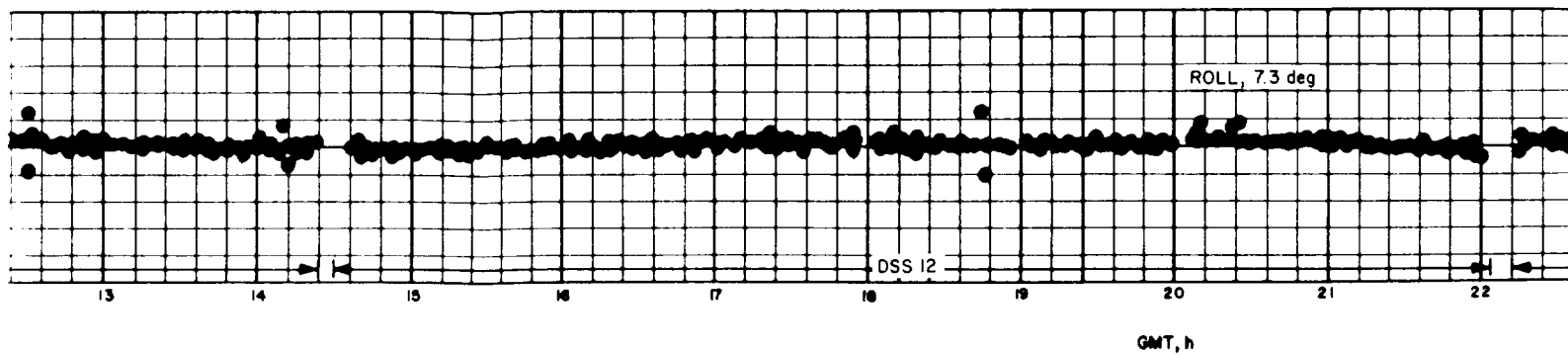
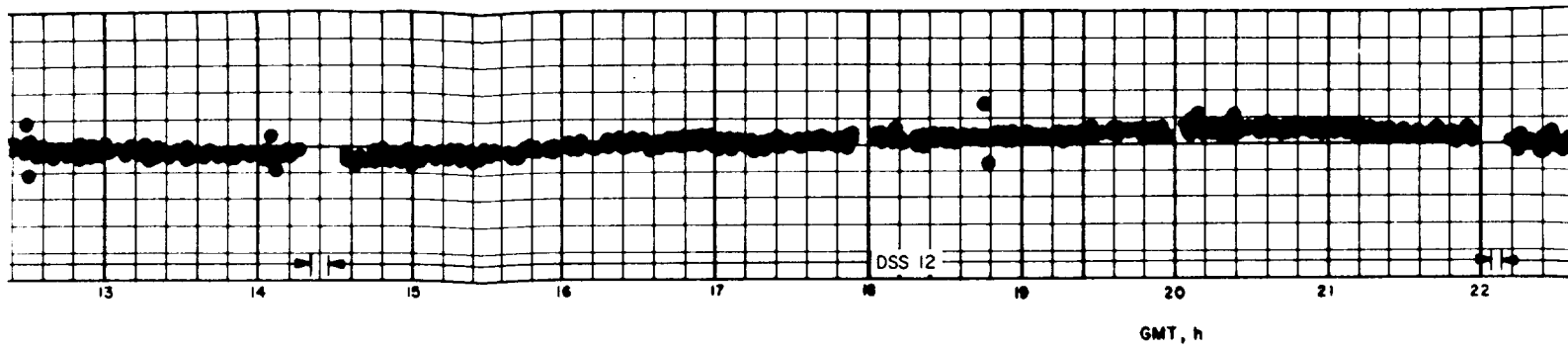


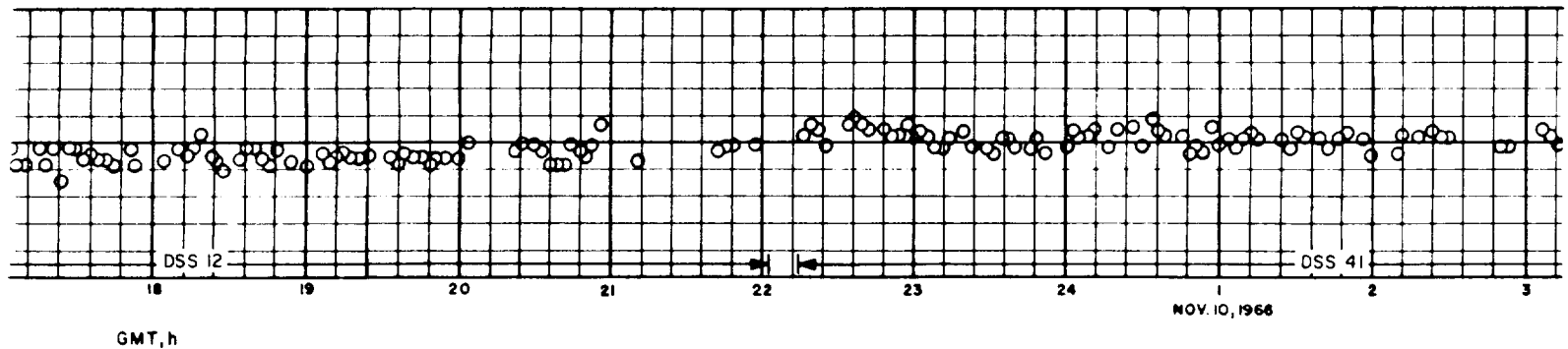
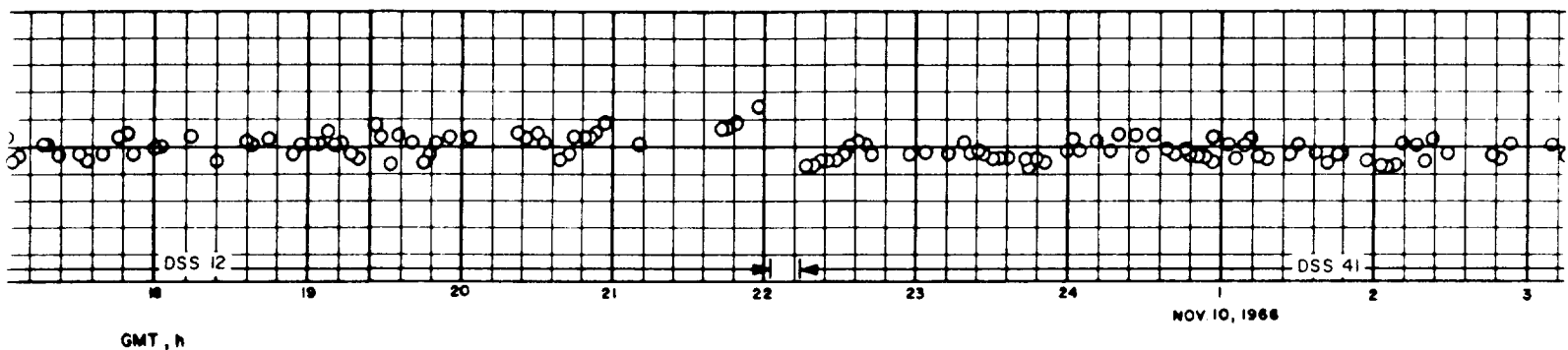
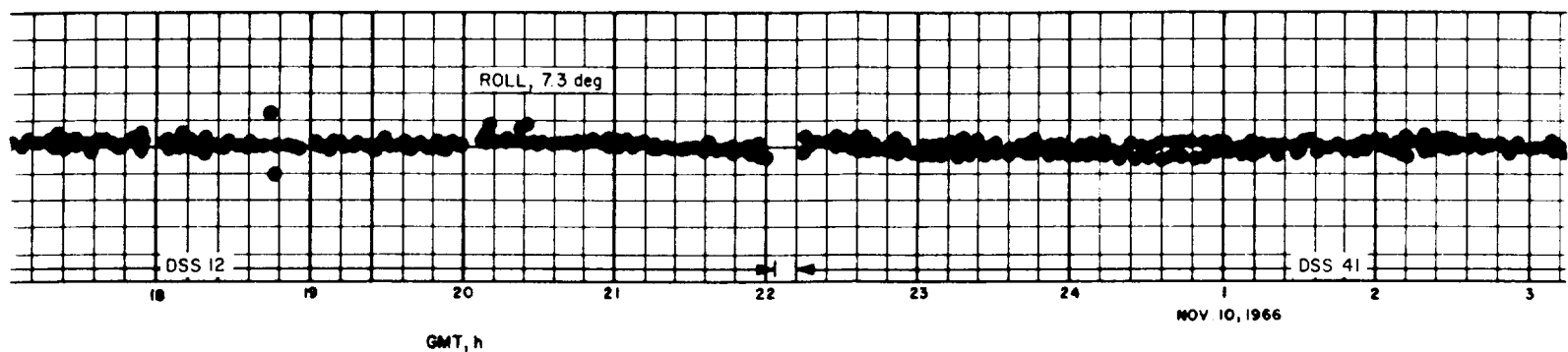
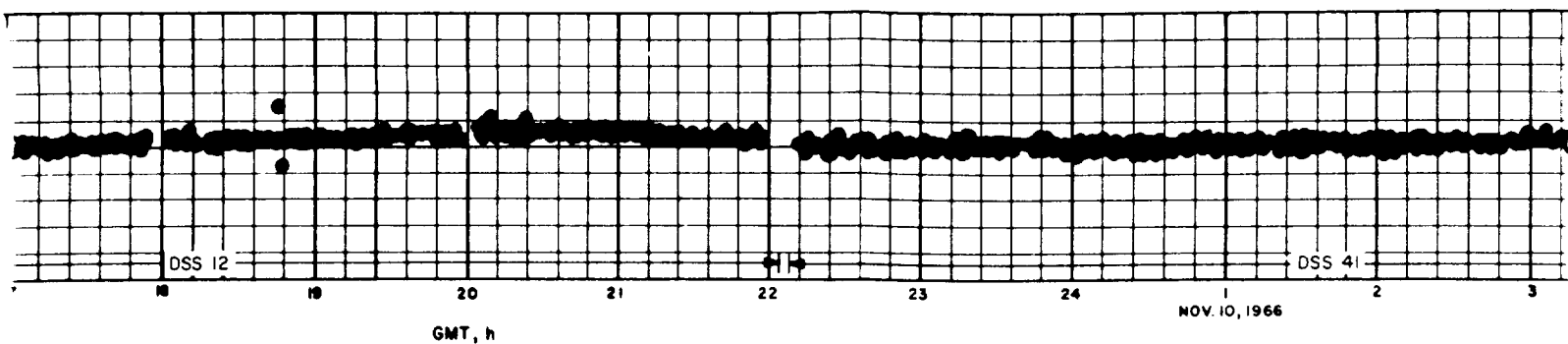
ONLY



or II

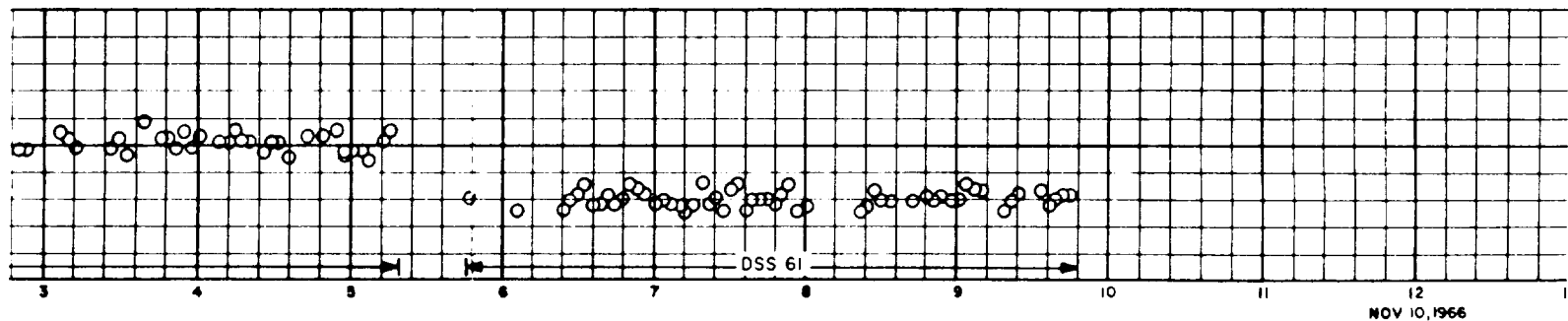
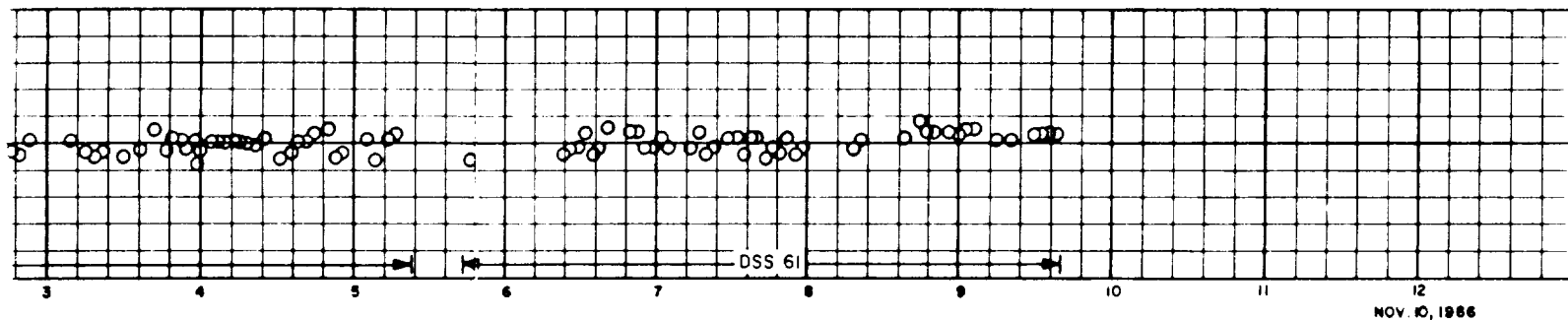
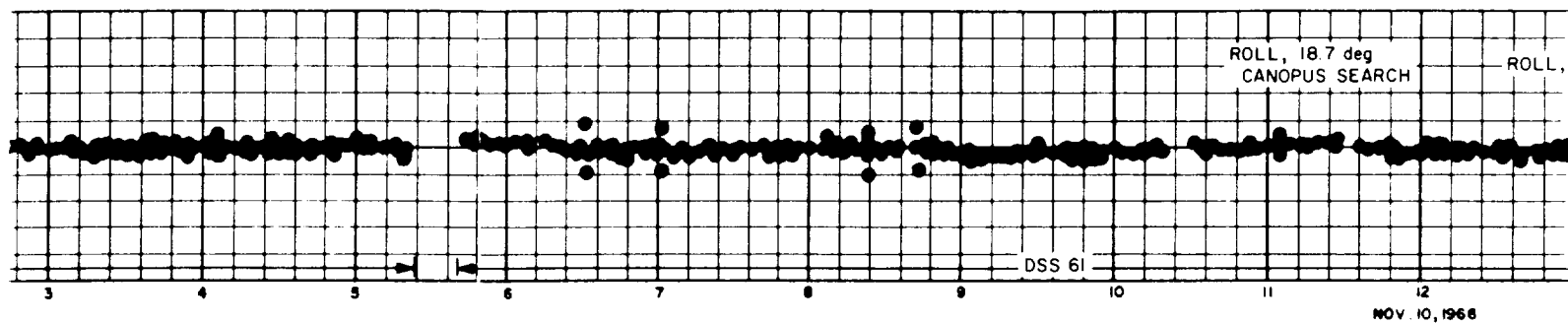
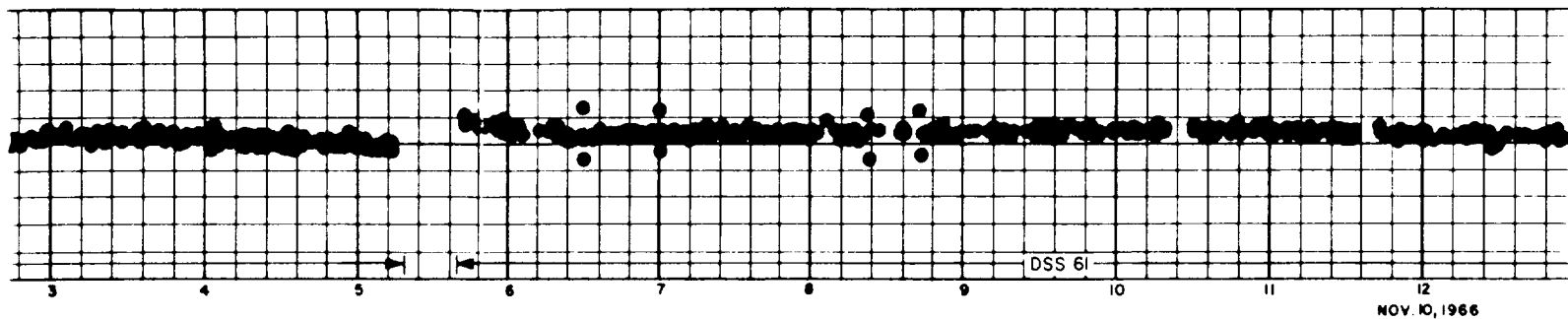






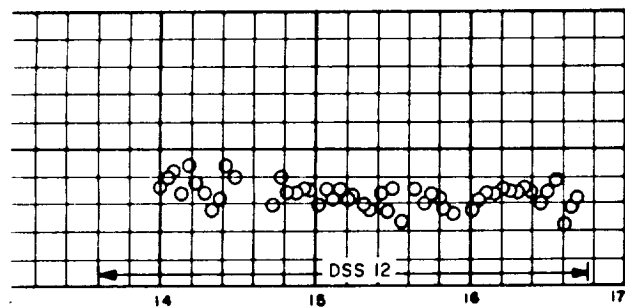
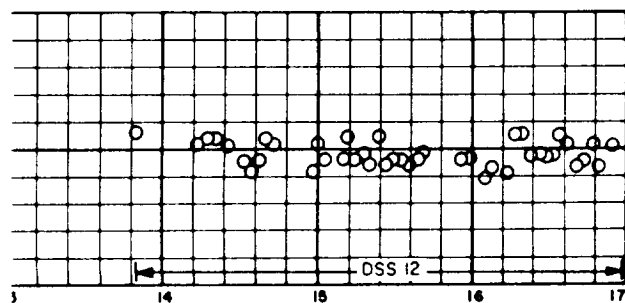
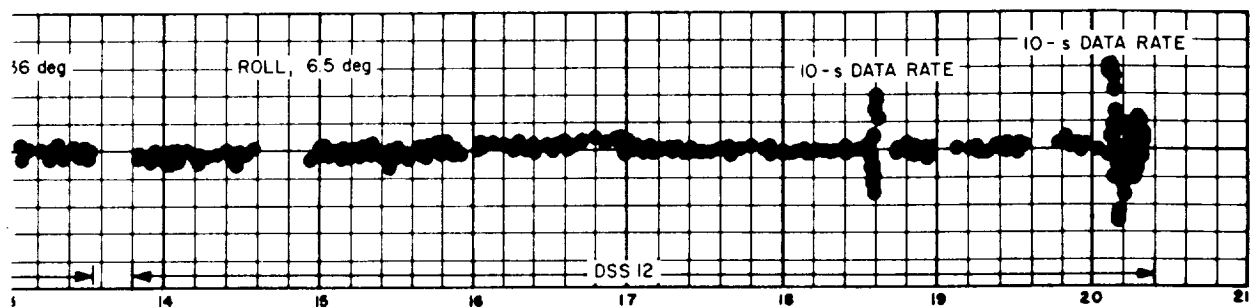
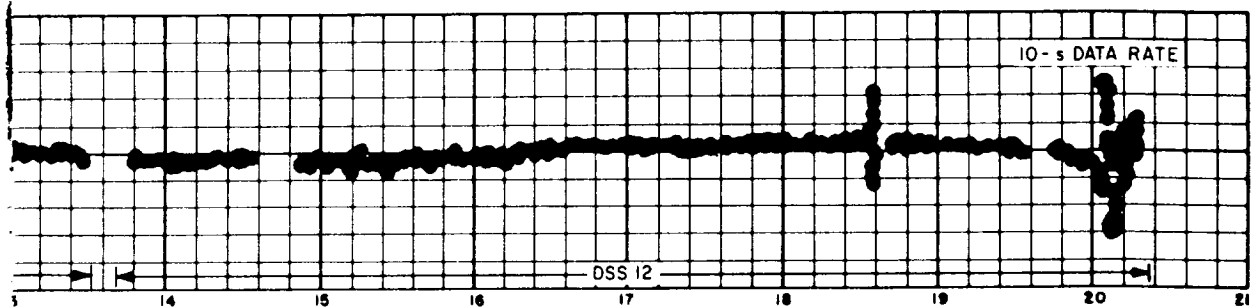
22-3

22-4



~~22-5~~

22-5



When the two data types are combined, much of the ranging bias is deleted. However, definite systematic errors appear in the doppler data. Probably most of what is seen in the doppler data is due to the biases in the ranging data. In general, this is a fairly good fit, with only small biases evident.

Solutions and statistics for the physical constants and other solve-for parameters are displayed in Table 5, and are compared with the combined *Ranger* solutions (SPS 37-43, Vol. III, pp. 3-18). The *a priori Ranger* values used for the *Lunar Orbiter* analysis appear at the bottom of the table.

There is an apparent decrease in GM_{\oplus} from the *Ranger* value; this is undeniably so in the case with the ranging fit, as the GM_{\oplus} is below the *Ranger* value at its $1-\sigma$ limit. Correspondingly, GM_{ζ} has increased beyond its $1-\sigma$ limit with respect to the *Ranger* value. Column 10 shows a comparison of the two *Lunar Orbiter* solutions. The GM_{\oplus} for the doppler-only solution is greater than for the doppler and range solution, while the reverse is true for GM_{ζ} . These differences are within the *Lunar Orbiter II* minus *Ranger* comparisons (columns 5 and 8), but are of opposite sign. Also note that column 10 results are within the *Lunar Orbiter II* doppler-only standard deviations (column 6). However, these *Lunar Orbiter* values, especially GM_{\oplus} , are consistent with those presented in Ref. 3.

The estimates of tracking station locations are presented in Table 5. With the exception of DSS 61, the *Ranger* values were taken from SPS 37-43, Vol. III, pp. 3-18, and updated to the *Lunar Orbiter II* instantaneous pole. Since DSS 61 never tracked a *Ranger*, its *Ranger* reference location was obtained indirectly from *Mariner IV* data. A *Mariner* solution for the difference between DSS 12 and DSS 61 was added to the DSS 12 *Ranger* solution to obtain the absolute DSS 61 location (with consideration given to polar motion; see Ref. 4).

A comparison of the *Lunar Orbiter II* station solutions with the *Ranger* values reveals agreement within about 14 m in distance off the spin axis r_s , and within 20 m in longitude for all but r_s at DSS 12 in the doppler-only fit. The reason for this rather large departure may be due to the fact that DSS 12 was tracking just prior to lunar encounter, where the spacecraft is most strongly perturbed by the moon. However, the ranging data fit would not allow r_s of DSS 12 to change as it does in the doppler-only fit, as is evidenced by the results in column 8. This may also be seen on the doppler residual plots for the

doppler and ranging fit, as shown by a dip just prior to the 10-s data at encounter. The doppler fit does not show this dip, and possibly r_s of DSS 12 was changed to accommodate the data. When the ranging data are added to the fit, this was prohibited and possibly forced changes in GM_{\oplus} , GM_{ζ} , and station longitudes, but did not affect relative longitudes (i.e., 3 m). This is evident in column 10. The doppler-only solutions for absolute longitudes agree to within 9 m with the *Ranger* estimates, adding more confidence to these values.

4. Conclusions

Having seen the solutions and their statistics, and recalling previous remarks about the size of the ranging bias and its possible effects on station locations, it may be concluded that fitting ranging data with doppler data has served to prevent changes in some parameters (i.e., r_s of various tracking stations) but has created changes in other parameters (i.e., absolute longitudes). Encouraging results were present in the doppler-only fit with the ranging residuals, when a bias of only 30 to 40 m was seen throughout the entire 90-h trajectory. Relative longitude estimates compared with those of *Ranger*; also, the various data combinations agreed to within 10 m. The GM_{\oplus} and GM_{ζ} estimates were somewhat different from the combined *Ranger* estimate, but are still in the same range as previous individual *Ranger* and *Mariner* estimates.

E. Results of the Doppler-Ranging Calibration Experiment, Phase I, A. Liu

1. Introduction

Interim results from Phase I of the doppler-ranging calibration experiment as described in SPS 37-44, Vol. III, pp. 28-33, are presented here. This experiment is concerned with the discrepancies between two methods of measuring the difference in range between a spacecraft and a tracking station which builds up over an interval of time. The range change can be measured either by continuously counting doppler over the time interval (integral of range rate) or by simply differencing the range measurement at the start of the time interval from that at the end. At this stage of the experiment the principal effort has been devoted toward analyzing error sources that affect the doppler and ranging system differently. Among these are the differential electrical path length of the two data types (through both the tracking stations and the spacecraft transponder) versus temperature and the effect of the ionosphere. The goal here is

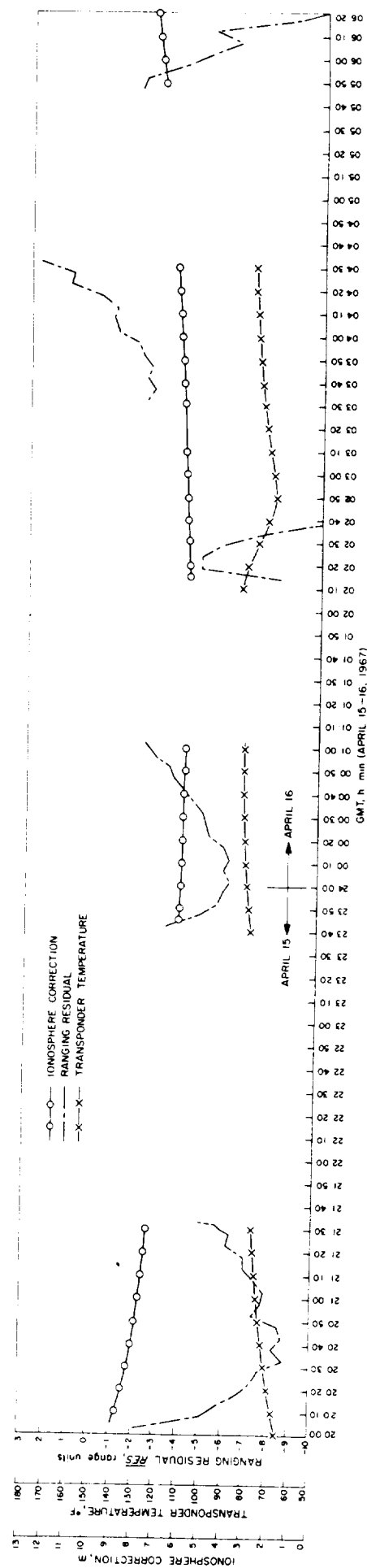
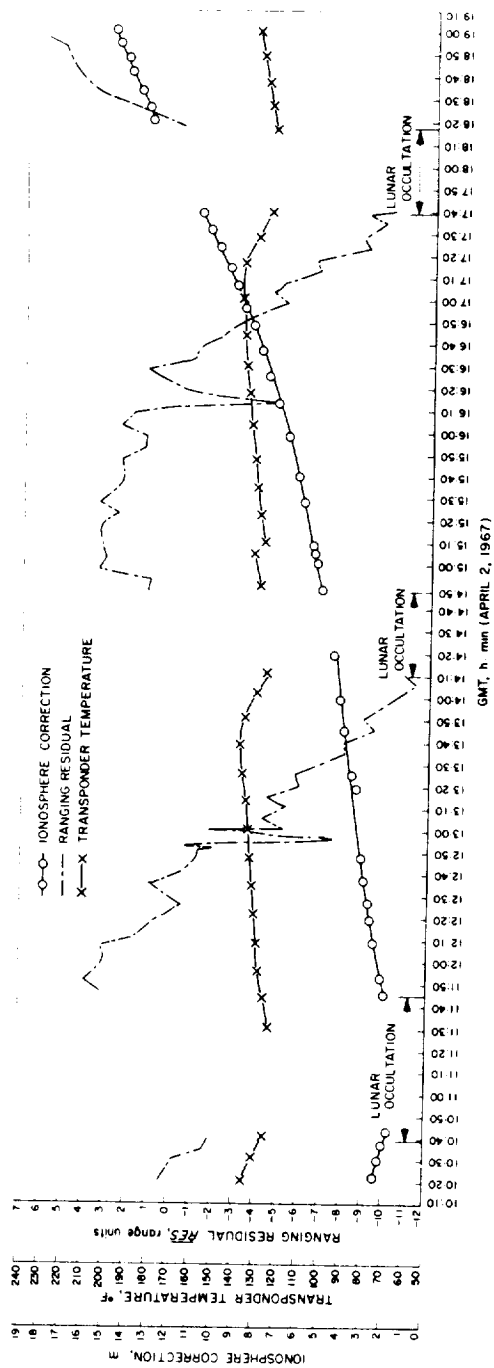
Table 5. Comparison of physical constant estimates from Lunar Orbiter II and Ranger

Estimated parameter	Nominal value ^b	Based on doppler-only fit				Based on doppler and ranging fit			Lunar Orbiter II solution differences, col. (7) — col. (3)	A priori standard deviation on all fits
		Lunar Orbiter II	Ranger	Lunar Orbiter II minus Ranger	Lunar Orbiter II standard deviation	Lunar Orbiter II	Lunar Orbiter II minus Ranger	Lunar Orbiter II standard deviation		
(1)	(2)	(3)	(4)	(5)	(6)	(7)	(8)	(9)	(10)	(11)
GM_{\oplus} , km^3/s^2	398601.27	398600.88	398601.22	-0.34	1.23	398600.37	-0.85	0.263	-0.51	10
GM_{\oplus} , km^3/s^2	4902.6249	4902.6605	4902.6309	0.03	0.191	4902.7562	0.13	0.055	0.096	5
r_{\oplus} , km } DSS 12 ^a	—	5212.0577	5212.0284	0.0293	0.00921	5212.0332	0.0048	0.0031	-0.0245	0.5
λ_{\oplus} , deg } DSS 41 ^a	243.19487	243.19468	243.19477	-0.00009	0.00044	243.19489	0.00012	0.000043	0.00021	0.005
r_{\oplus} , km } DSS 41 ^a	—	5450.1873	5450.1942	-0.0069	0.00951	5450.1849	-0.0093	0.0027	-0.0024	0.5
λ_{\oplus} , deg } DSS 41 ^a	136.88789	136.88775	136.88777	-0.00002	0.000432	136.88799	0.00022	0.000039	0.00024	0.005
r_{\oplus} , km } DSS 61 ^a	—	4862.5967	4862.5883	0.0084	0.0096	4862.6019	0.0136	0.0034	0.0052	0.5
λ_{\oplus} , deg } DSS 61 ^a	355.75106	355.75122	355.75126	-0.00004	0.000444	355.75145	0.00019	0.000040	0.00023	0.005
$\lambda_{12} - \lambda_{41}$, deg	—	106.30693	106.30700	-0.00007	0.000071	106.30690	-0.00010	0.000026	-0.00003	0.007
$\lambda_{12} - \lambda_{61}$, deg	—	-112.55654	-112.55649	-0.00005	0.000055	-112.55656	-0.00007	0.000027	-0.00002	0.007
$\lambda_{41} - \lambda_{61}$, deg	—	-218.86347	-218.86349	0.00002	0.000071	-218.86346	0.00003	0.000025	0.00001	0.007

^aStation locations are referenced to the instantaneous pole at the time of the data (i.e., Nov. 8, 1966); Ranger values referenced to 1905 pole were incremented to this date for comparison.

^bNominal values for DSS 12, DSS 41, and DSS 61 latitude are 35.117495, -31.212091, and 40.238607, respectively; nominal values for geocentric radii are 6371.8775, 6372.6030, and 6369.9970, respectively; DSS 61 longitude determined by adding Mariner IV difference $\lambda_{12} - \lambda_{41}$ (Ref. 5) to Ranger DSS 12 longitude.

Note: 0.001 deg in $\lambda = 100$ m.



to demonstrate, by the use of ground calibration tests and actual flight data, the extent to which the effects of the above error sources can be determined.

Phase I of the doppler-ranging calibration experiment utilized the Mark IA ranging system at DSS 12 (Goldstone Echo) and was restricted to two-way doppler and ranging measurements of *Lunar Orbiters II* and *III*. Two sets of horizon-to-horizon measurements of the *Lunar Orbiters* were accomplished. The first set of measurements of *Lunar Orbiter III*, called Track 1, was taken on April 2, 10:19 to 19:50 GMT; the second set of measurements of *Lunar Orbiter II*, called Track 2, was taken from April 15, 1967, 19:50 to April 16, 1967, 06:27 GMT. The data were used for the following purposes:

- (1) To demonstrate the difference between counted doppler and differenced range measurements.
- (2) To correlate the observed differences (after calibrating out the effects due to the tracking station) with the spacecraft temperature and the ionospheric effects.

2. Discussion

The ranging data received are in terms of round-trip time or range units (RU). For the S-band system configuration used in this experiment, each RU corresponds *exactly* to 16 doppler counts and *approximately* to 1.06 m. An independent RU measurement is considered as that RU datum taken at the beginning of each "lock-up." In order to compare the differences between counted two-way doppler and RU, each successive independent RU measurement is differenced from the initial RU measurement at the beginning of the pass, and each successive doppler count is likewise differenced from the initial doppler count. The doppler measurements are converted to RU, and the two data types (doppler count and RU) differenced at each measurement time. This difference is termed here as a residual (*RES*).

Ideally, $RES = 0$. This is not the case, however, because the hardware through which the doppler and ranging signals pass is not completely common (both on the ground and in the spacecraft); therefore these signals experience different time lags. Also, in a dispersive medium, such as the ionosphere, the effect on ranging (propagated with group velocity) is different from the effect on doppler (propagated with phase velocity). In fact, the ionospheric effects are nearly equal in magnitude but opposite in sign for ranging differences and counted doppler. Therefore, the ionospheric effects can

be self-calibrated from the data if the other effects, such as variations of doppler and ranging time lags through the hardware versus hardware temperature, can be properly taken into account.

RES at time t is given as

$$RES(t) = R(t) - R_0 - \frac{1}{16} [D(t) - D_0 - B(t - t_0)] \quad (1)$$

where

$R(t)$ = ranging measurement at time t

$D(t)$ = doppler count at time t

t_0 = GMT at beginning of the pass

R_0 = ranging measurement at time t_0

D_0 = doppler count at time t_0

B = doppler bias frequency = (10^6 Hz)

It was observed (SPS 37-44, Vol. III) from Mark I ranging data taken during the translunar phase of *Lunar Orbiter II* that a phase jitter of ± 5 deg in the 498-kHz clock loop of the ground system caused a ± 3 -m scatter of the ranging system. The ability of the Mark IA ranging system to measure an independent RU every second afforded a method of reducing the scatter. Phase jitter is then averaged out by calculating the mean of *RES*, \overline{RES} , over 60-second time blocks:

$$\overline{RES} = \sum_{i=1}^{60} RES(t_i) / 60 \quad (2)$$

The resultant high frequency noise on \overline{RES} is less than $\frac{1}{2}$ m.

3. Data Analysis, Track 1

Figure 15 is a plot of \overline{RES} versus time for Track 1; the marked reduction in the effect of phase noise over that of the 1-second data is seen. This figure shows a set of horizon-to-horizon measurements taken from DSS 12 which represent four revolutions of *Lunar Orbiter III*. In all four revolutions, periodic effects can be seen. At the beginning of each revolution, there is a short increase in \overline{RES} , followed by a gradual decrease toward the end

of the revolution. These periodic changes from orbit to orbit are not due to the ionosphere. Also shown (Fig. 15) is a theoretical \overline{RES} for an assumed Chapman ionosphere with an electron concentration of 2×10^5 electron/cc and a sunspot activity index R of 100. A ground calibration test performed subsequent to this experiment showed a peak station delay of ± 1 RU; thus it appears that the periodic effects are associated with the spacecraft environment.

4. Data Analysis, Track 2

Figure 16 is a plot of \overline{RES} versus time for Track 2. The reduction in phase noise on the 1-second data is still quite evident. The periodic effects of the \overline{RES} seen in Track 1 are even more pronounced in this experiment. At the minima of each group of data taken from each revolution, a small protrusion can be seen. These protrusions are separated from each other by $3\frac{1}{2}$ hours, which is the orbital period of *Lunar Orbiter II*. For this experiment the effects of the ionosphere are negligible. Theoretical \overline{RES} for an assumed Chapman ionosphere with an electron density of 2×10^5 electrons/cc and a solar activity index R of 100 show almost no variation in \overline{RES} during the middle of the experiment (Fig. 16). Spacecraft transponder temperatures in $^{\circ}\text{F}$ are also plotted. Even though the minima in the \overline{RES} do not match the minima in the temperature measurements, there could be lags in the sensitivity to temperature changes of some or all of the spacecraft transponder components.

5. Conclusions

The \overline{RES} plots of Figs. 15 and 16 show that a transponder differential delay versus temperature does exist. However, the time lag in the sensitivity of the transponder to temperature changes has not yet been analyzed.

The noise is greatly reduced in the ranging data by using high data rates and then averaging. The averaging of 60 points has reduced the noise from 3 m to less than $\frac{1}{2}$ m.

There are differences between the counted doppler and range increment measurements, but these seem to be due primarily to the equipment. Until these systematic errors can be removed, the effects of the ionosphere will not be evident.

Track 2 concludes Phase I of the doppler-ranging calibration experiment. Phase II was resumed in June 1967, with the Mark IA system tracking *Lunar Orbiter IV* as well as *Lunar Orbiters II* and *III*. The new Mark II

system (planetary ranging system) will be used to track *Lunar Orbiter IV*. *Lunar Orbiter IV* should provide long periods of fairly steady temperature because the spacecraft is in a high inclination orbit and will not usually be occulted over several revolutions from either the sun or the earth by the moon. Phase II will also afford an opportunity to test the new Mark II system and to see if the periodic effects of \overline{RES} in Phase I still exist after a lapse of time.

F. Theoretical Basis for the Double Precision Orbit Determination Program: IX. Statistical Formulas, T. D. Moyer

1. Introduction

This ninth article in the series presenting the theoretical basis for the double precision orbit determination program (DPODP) gives the formulation for computation of the estimate of the parameter vector \mathbf{q} and the statistics of this estimate; namely, the covariance matrix for \mathbf{q} .

The estimate for \mathbf{q} minimizes the sum of weighted squares of residual errors between observed and computed quantities where *a priori* parameter estimates are treated as observed quantities.

There may be functional relations (constraints) between the members of \mathbf{q} . These constraints may be applied by an exact procedure or an inexact procedure. For the exact treatment, the estimates of the parameters related by the constraint are required to satisfy the constraint. For the inexact treatment, the estimates of the parameters related by the constraint are allowed to deviate from values that would satisfy the constraint. This deviation contributes a weighted residual error to the sum of squares, which is minimized by the parameter estimate.

The formulation is given for mapping the covariance matrix from the injection epoch to any other epoch. The parameter vector corresponding to the mapped covariance matrix is \mathbf{q} , with the injection position and velocity components (referred to a selected body, not necessarily the center of integration) replaced by the position and velocity components relative to the center of integration at the map time. The formulation is also given for converting the mapped covariance matrix (relative to the center of integration at the map time) to a covariance matrix relative to any other body (planet, moon, or sun) at that time.

2. Categorization of Parameters and Constraints

The parameter vector \mathbf{q} consists of those parameters required to compute observable quantities; \mathbf{q} is composed of three subvectors:

$$\mathbf{q} = \begin{bmatrix} \mathbf{x} \\ \mathbf{y} \\ \mathbf{s} \end{bmatrix} \quad (1)$$

where

\mathbf{x} = solve-for parameters: those parameters whose estimates are obtained from the least squares fit

\mathbf{y} = "consider" parameters: those whose *a priori* estimates are not corrected, but whose errors are considered when computing the covariance matrix for \mathbf{q}

\mathbf{s} = exactly "constrained" parameters: parameters that are functionally related to the $(\mathbf{x} | \mathbf{y})$ parameters; one parameter from each exact constraint is placed in \mathbf{s}

The parameter estimation formulation allows constraints (functional relations between the parameters) to be treated as exact or inexact. A constraint may be represented by

$$f_i(\mathbf{x}, \mathbf{y}, \mathbf{s}, \mathbf{N}_i) = 0 \quad i = 1, 2, \dots, n \quad (2)$$

where \mathbf{N}_i = vector of constants which appear in the *i*th constraint. A constraint is considered to be exact or inexact as \mathbf{N}_i is considered to be exact or inexact. Estimates for parameters related by a constraint that is considered to be exact are required to satisfy the constraint. Estimates for parameters related by a constraint that is considered to be inexact are allowed to deviate from values that would satisfy the constraint.

One parameter from each exact constraint is designated as a constrained parameter and is placed in \mathbf{s} . The exactly constrained parameter vector is given by

$$\mathbf{s} = \mathbf{s}(\mathbf{x}, \mathbf{y}) = \begin{bmatrix} s_1(\mathbf{x}, \mathbf{y}) \\ s_2(\mathbf{x}, \mathbf{y}) \\ \vdots \\ s_i(\mathbf{x}, \mathbf{y}) \\ \vdots \\ s_n(\mathbf{x}, \mathbf{y}) \end{bmatrix} \quad (3)$$

where $s_i(\mathbf{x}, \mathbf{y})$ represents the solution of the *i*th exact constraint for the constrained parameter as a function of the related parameters of the constraint. The derivative of \mathbf{s} with respect to $(\mathbf{x} | \mathbf{y})$ is denoted by

$$\begin{bmatrix} \frac{\partial \mathbf{s}}{\partial \mathbf{x}} & \frac{\partial \mathbf{s}}{\partial \mathbf{y}} \end{bmatrix} = \begin{bmatrix} \frac{\partial s_1}{\partial x_1} & \dots & \frac{\partial s_1}{\partial x_n} & \frac{\partial s_1}{\partial y_1} & \dots & \frac{\partial s_1}{\partial y_n} \\ \vdots & & \vdots & & & \vdots \\ \frac{\partial s_n}{\partial x_1} & \dots & \frac{\partial s_n}{\partial x_n} & \frac{\partial s_n}{\partial y_1} & \dots & \frac{\partial s_n}{\partial y_n} \end{bmatrix} = [\mathbf{S}_x | \mathbf{S}_y] \quad (4)$$

The *i*th exact constraint may be specified as either of the following:

- (1) The functional relation $s_i = s_i(\mathbf{x}, \mathbf{y})$, in which case the *a priori* value of $s_i = s_i(\tilde{\mathbf{x}}, \tilde{\mathbf{y}})$, where $\tilde{\mathbf{x}}$ is the *a priori* estimate of \mathbf{x} .
- (2) The derivative of the constrained parameter with respect to each related parameter of the constraint; i.e., specifying the *i*th row of Eq. (4). In this case, the *a priori* value of s_i must be given.

As opposed to the exact treatment of constraints, all parameters related by an inexact constraint are members of $(\mathbf{x} | \mathbf{y})$. One parameter from each inexact constraint is designated a constrained parameter and will have a "computed" value and an "observed" value. The computed value is the estimate for the parameter; the observed value is calculated from the constraint as a function of the estimates of the related parameters. Since parameter estimates are obtained by minimizing weighted squares of residual errors between observed and computed quantities, the degree to which each inexact constraint is satisfied will depend upon the weight applied to the constraint (see Section 3).

The observed inexactly constrained parameter vector is given by

$$\mathbf{c}(\mathbf{x}, \mathbf{y}) = \begin{bmatrix} c_1(\mathbf{x}, \mathbf{y}) \\ c_2(\mathbf{x}, \mathbf{y}) \\ \vdots \\ c_i(\mathbf{x}, \mathbf{y}) \\ \vdots \\ c_n(\mathbf{x}, \mathbf{y}) \end{bmatrix} \quad (5)$$

where $c_i(\mathbf{x}, \mathbf{y})$ represents the solution of the i th inexact constraining equation for the constrained parameter as a function of the related parameters of the constraint. For a given constraint, the functions $s_i(\mathbf{x}, \mathbf{y})$ of Eq. (3) and $c_i(\mathbf{x}, \mathbf{y})$ of Eq. (5) are the same. The symbol used depends on whether the constraint is treated as exact or inexact.

The computed inexactly constrained parameter vector is given by

$$\mathbf{c}(\mathbf{x}, \mathbf{y}) = \begin{bmatrix} c_1(\mathbf{x}, \mathbf{y}) \\ c_2(\mathbf{x}, \mathbf{y}) \\ \vdots \\ c_i(\mathbf{x}, \mathbf{y}) \\ \vdots \\ c_n(\mathbf{x}, \mathbf{y}) \end{bmatrix} = [D'_x \mid D'_y] \begin{bmatrix} \mathbf{x} \\ \mathbf{y} \end{bmatrix} \quad (6)$$

The element of the i th row of $[D'_x \mid D'_y]$ corresponding to the member of $(\mathbf{x} \mid \mathbf{y})$ which is the constrained parameter for the i th inexact constraint is unity, and the remaining elements of that row are zero.

The derivative of $\mathbf{c}(\mathbf{x}, \mathbf{y})$ with respect to $(\mathbf{x} \mid \mathbf{y})$ is denoted by

$$\left[\frac{\partial \mathbf{c}(\mathbf{x}, \mathbf{y})}{\partial \mathbf{x}} \mid \frac{\partial \mathbf{c}(\mathbf{x}, \mathbf{y})}{\partial \mathbf{y}} \right] = [D_x \mid D_y] \quad (7)$$

From Eq. (6),

$$\left[\frac{\partial \mathbf{c}(\mathbf{x}, \mathbf{y})}{\partial \mathbf{x}} \mid \frac{\partial \mathbf{c}(\mathbf{x}, \mathbf{y})}{\partial \mathbf{y}} \right] = [D'_x \mid D'_y] \quad (8)$$

The differences of the matrices in Eqs. (7) and (8) are denoted by

$$\Delta D_x = D'_x - D_x \quad (9)$$

$$\Delta D_y = D'_y - D_y \quad (10)$$

3. Error Function

Treating *a priori* estimates of the solve-for parameters as observed quantities, and using Eqs. (5) and (6) for the observed and computed values of the inexactly constrained parameters, the sum of weighted squares of

residual errors between observed and computed quantities is given by

$$Q = (\hat{\mathbf{z}} - \mathbf{z})^T W (\hat{\mathbf{z}} - \mathbf{z}) + (\tilde{\mathbf{x}} - \mathbf{x})^T \tilde{\Gamma}_x^{-1} (\tilde{\mathbf{x}} - \mathbf{x}) + [\mathbf{c}(\mathbf{x}, \mathbf{y}) - \mathbf{c}(\mathbf{x}, \mathbf{y})]^T W_c [\mathbf{c}(\mathbf{x}, \mathbf{y}) - \mathbf{c}(\mathbf{x}, \mathbf{y})] \quad (11)$$

where the superscripts T and -1 indicate the transpose and inverse, and

$\hat{\mathbf{z}}$ = column vector of observables

$\mathbf{z} = \mathbf{z}(\mathbf{x}, \mathbf{y}, \mathbf{s}) = \mathbf{z}(\mathbf{x}, \mathbf{y})$ = vector of computed observables

W = data weighting matrix (diagonal); the weight for each observable is one divided by the input variance for the observable

$\tilde{\mathbf{x}}$ = *a priori* estimate of \mathbf{x}

$\tilde{\Gamma}_x$ = covariance matrix of $\tilde{\mathbf{x}}$

W_c = diagonal constraint weighting matrix

$$W_c = \begin{bmatrix} \frac{1}{\sigma^2 c_1(\mathbf{x}, \mathbf{y})} & 0 & \dots & 0 \\ 0 & \frac{1}{\sigma^2 c_2(\mathbf{x}, \mathbf{y})} & 0 & \dots & 0 \\ \dots & \dots & \dots & \dots & \dots \\ 0 & \dots & 0 & \frac{1}{\sigma^2 c_n(\mathbf{x}, \mathbf{y})} \end{bmatrix} \quad (12)$$

where $\sigma^2 c_i(\mathbf{x}, \mathbf{y})$ is the input variance of $c_i(\mathbf{x}, \mathbf{y})$ calculated from the variances and covariances of the constants N_i of the i th inexact constraining equation and the *a priori* estimates of \mathbf{x} and \mathbf{y} .

4. Parameter Estimation Formula

Since $\mathbf{s} = \mathbf{s}(\mathbf{x}, \mathbf{y})$ and $\mathbf{y} = \text{constant}$, the sum of squares Q is a function of \mathbf{x} only:

$$Q = Q(\mathbf{x}) \quad (13)$$

The estimate of \mathbf{x} is the vector that minimizes Q . If Q is a minimum,

$$\frac{\partial Q}{\partial \mathbf{x}} = \left[\frac{\partial Q}{\partial x_1} \quad \frac{\partial Q}{\partial x_2} \quad \dots \quad \frac{\partial Q}{\partial x_n} \right] = 0 \quad (14)$$

Noting that Q is a scalar and that each term may be transposed,

$$\begin{aligned} \frac{\partial Q}{\partial \mathbf{x}} = & -2 \left\{ (\hat{\mathbf{z}} - \mathbf{z})^T W \frac{\partial \mathbf{z}}{\partial \mathbf{x}} + (\tilde{\mathbf{x}} - \mathbf{x})^T \tilde{\Gamma}_x^{-1} \right. \\ & - [\mathbf{c}(\mathbf{x}, \mathbf{y}) - \mathbf{c}(\mathbf{x}, \mathbf{y})]^T W_c \left[\frac{\partial \mathbf{c}(\mathbf{x}, \mathbf{y})}{\partial \mathbf{x}} \right. \\ & \left. \left. - \frac{\partial \mathbf{c}(\mathbf{x}, \mathbf{y})}{\partial \mathbf{x}} \right] \right\} = 0 \end{aligned} \quad (15)$$

The partial derivative of \mathbf{z} with respect to \mathbf{q} is designated the A matrix

$$A = \frac{\partial \mathbf{z}}{\partial \mathbf{q}} = \left[\frac{\partial \mathbf{z}}{\partial \mathbf{x}} \left| \frac{\partial \mathbf{z}}{\partial \mathbf{y}} \right| \frac{\partial \mathbf{z}}{\partial \mathbf{s}} \right] = [A_x \mid A_y \mid A_s] \quad (16)$$

Noting Eqs. (3) and (4),

$$\frac{\partial \mathbf{z}}{\partial \mathbf{x}} = A_x + A_s S_x \quad (17)$$

Similarly (for use in computing the covariance matrix for \mathbf{q}),

$$\frac{\partial \mathbf{z}}{\partial \mathbf{y}} = A_y + A_s S_y \quad (18)$$

Substituting Eqs. (7), (8), (9), and (17) into Eq. (15) gives

$$\begin{aligned} & (\hat{\mathbf{z}} - \mathbf{z})^T W (A_x + A_s S_x) + (\tilde{\mathbf{x}} - \mathbf{x})^T \tilde{\Gamma}_x^{-1} \\ & + [\mathbf{c}(\mathbf{x}, \mathbf{y}) - \mathbf{c}(\mathbf{x}, \mathbf{y})]^T W_c \Delta D_x = 0 \end{aligned} \quad (19)$$

which is a row vector with the number of elements equal to the number of solve-for parameters. Let the transpose of this vector (a column vector) be denoted by $F(\mathbf{x})$:

$$\begin{aligned} F(\mathbf{x}) = & (A_x + A_s S_x)^T W (\hat{\mathbf{z}} - \mathbf{z}) + \tilde{\Gamma}_x^{-1} (\tilde{\mathbf{x}} - \mathbf{x}) \\ & + \Delta D_x^T W_c [\mathbf{c}(\mathbf{x}, \mathbf{y}) - \mathbf{c}(\mathbf{x}, \mathbf{y})] = 0 \end{aligned} \quad (20)$$

The estimate of the solve-for parameter vector \mathbf{x} must satisfy this equation. Assuming the partial derivatives are constant, the derivative of $F(\mathbf{x})$ with respect to \mathbf{x} is

$$\begin{aligned} \frac{\partial F(\mathbf{x})}{\partial \mathbf{x}} = F'(\mathbf{x}) = & -[(A_x + A_s S_x)^T W (A_x + A_s S_x) + \tilde{\Gamma}_x^{-1} \\ & + \Delta D_x^T W_c \Delta D_x] \end{aligned} \quad (21)$$

Defining

$$J = (A_x + A_s S_x)^T W (A_x + A_s S_x) \quad (22)$$

and

$$K = \Delta D_x^T W_c \Delta D_x \quad (23)$$

Eq. (21) becomes

$$F'(\mathbf{x}) = -[J + \tilde{\Gamma}_x^{-1} + K] \quad (24)$$

The solution of Eq. (20) for the estimate of \mathbf{x} is obtained by using the Newton-Raphson iteration:

$$\mathbf{x}^{(n+1)} - \mathbf{x}^{(n)} = -\{F'[\mathbf{x}^{(n)}]\}^{-1} F[\mathbf{x}^{(n)}] \quad (25)$$

where $\mathbf{x}^{(n)}$ is the n th estimate of \mathbf{x} , and $\mathbf{x}^{(n+1)}$ is the $n+1$ st estimate. Substituting Eqs. (24) and (20) into Eq. (25) gives the parameter estimation formula

$$\begin{aligned} \mathbf{x}^{(n+1)} - \mathbf{x}^{(n)} = & [J + \tilde{\Gamma}_x^{-1} + K]^{-1} \\ & \times [(A_x + A_s S_x)^T W \{\hat{\mathbf{z}} - \mathbf{z}[\mathbf{x}^{(n)}, \tilde{\mathbf{y}}]\} \\ & + \tilde{\Gamma}_x^{-1} [\tilde{\mathbf{x}} - \mathbf{x}^{(n)}] + \Delta D_x^T W_c \{\mathbf{c}[\mathbf{x}^{(n)}, \tilde{\mathbf{y}}] \\ & - \mathbf{c}[\mathbf{x}^{(n)}, \tilde{\mathbf{y}}]\}] \end{aligned} \quad (26)$$

For exact constraints specified by a functional relation,

$$s_i^{(n+1)} = s_i[\mathbf{x}^{(n+1)}, \tilde{\mathbf{y}}] \quad (27)$$

For exact constraints specified by a row of Eq. (4) and the *a priori* estimate of the exactly constrained parameter,

$$s_i^{(n+1)} = s_i^{(n)} + S_{x_i} [\mathbf{x}^{(n+1)} - \mathbf{x}^{(n)}] \quad (28)$$

where S_{x_i} is the i th row of S_x .

The simplified form of Eq. (26) obtained by deleting constraints and consider parameters has also been derived by Anderson (Ref. 6) using maximum-likelihood estimation. Conrad has shown⁸ that the form of Eq. (26) obtained by deleting consider parameters and exact constraints only is a minimum variance estimate.

⁸Minimum Variance Estimation With Inexact Constraints, DPODP Technical Note 1; informal document submitted to JPL by Informatics, Inc., Sherman Oaks, Calif., Nov. 4, 1966 (N-700-16-1).

5. Covariance Matrix

This section gives the formulation for computation of the covariance matrix Γ_q for the estimate of the parameter vector \mathbf{q} . Let the error in an estimate of \mathbf{q} be denoted by

$$\delta \mathbf{q} = \begin{bmatrix} \delta \mathbf{x} \\ \delta \mathbf{y} \\ \delta \mathbf{s} \end{bmatrix} \quad (29)$$

where $\delta \mathbf{y} = \delta \tilde{\mathbf{y}}$, the *a priori* error. Then, the covariance matrix is given by

$$\Gamma_q = \overline{\delta \mathbf{q} \delta \mathbf{q}^T} = \begin{bmatrix} \overline{\delta \mathbf{x} \delta \mathbf{x}^T} & \overline{\delta \mathbf{x} \delta \mathbf{y}^T} & \overline{\delta \mathbf{x} \delta \mathbf{s}^T} \\ \overline{\delta \mathbf{y} \delta \mathbf{x}^T} & \overline{\delta \mathbf{y} \delta \mathbf{y}^T} & \overline{\delta \mathbf{y} \delta \mathbf{s}^T} \\ \overline{\delta \mathbf{s} \delta \mathbf{x}^T} & \overline{\delta \mathbf{s} \delta \mathbf{y}^T} & \overline{\delta \mathbf{s} \delta \mathbf{s}^T} \end{bmatrix} \quad (30)$$

where a bar indicates the ensemble average or expected value of the function. This may be written as

$$\Gamma_q = \begin{bmatrix} \Gamma_x & \Gamma_{xy} & \Gamma_{xs} \\ \Gamma_{xy}^T & \Gamma_y & \Gamma_{ys} \\ \Gamma_{xs}^T & \Gamma_{ys}^T & \Gamma_s \end{bmatrix} \quad (31)$$

If the true value of the solve-for parameter vector \mathbf{x} were substituted into the parameter estimation formula (Eq. 26) along with true values for $\hat{\mathbf{z}}$, $\tilde{\mathbf{y}}$, $\tilde{\mathbf{x}}$, and the constants in the inexact constraints, we would have

$$\hat{\mathbf{z}} = \mathbf{z}[\mathbf{x}^{(n)}, \tilde{\mathbf{y}}] \quad (32)$$

$$\tilde{\mathbf{x}} = \mathbf{x}^{(n)} \quad (33)$$

$$\mathbf{c}[\mathbf{x}^{(n)}, \tilde{\mathbf{y}}] = \mathbf{c}[\mathbf{x}^{(n)}, \tilde{\mathbf{y}}] \quad (34)$$

and $\mathbf{x}^{(n+1)}$ would equal $\mathbf{x}^{(n)}$, the input true value. However, the vectors $\hat{\mathbf{z}}$, $\tilde{\mathbf{x}}$, and $\tilde{\mathbf{y}}$ are in error by $\delta \hat{\mathbf{z}}$, $\delta \tilde{\mathbf{x}}$, and $\delta \tilde{\mathbf{y}}$, and the errors in the constants of the inexact constraints give an error in $\mathbf{c}(\mathbf{x}, \mathbf{y})$ of $\delta \mathbf{c}_N$. Substituting the true value of \mathbf{x} into Eq. (26) and using Eqs. (7), (8), (10), and (18) gives the following erroneous correction $\delta \mathbf{x} = \mathbf{x}^{(n+1)} - \mathbf{x}^{(n)}$, which is the error of the estimate:

$$\begin{aligned} \delta \mathbf{x} = & [J + \tilde{\Gamma}_x^{-1} + K]^{-1} \{ (A_x + A_s S_x)^T \\ & \times W[\hat{\mathbf{z}} - (A_y + A_s S_y) \delta \mathbf{y}] \\ & + \tilde{\Gamma}_x^{-1} \delta \tilde{\mathbf{x}} + \Delta D_x^T W_c [\delta \mathbf{c}_N - \Delta D_y \delta \tilde{\mathbf{y}}] \} \end{aligned} \quad (35)$$

Let

$$L = (A_x + A_s S_x)^T W (A_y + A_s S_y) + \Delta D_x^T W_c \Delta D_y \quad (36)$$

Then

$$\begin{aligned} \delta \mathbf{x} = & [J + \tilde{\Gamma}_x^{-1} + K]^{-1} [(A_x + A_s S_x)^T W \delta \hat{\mathbf{z}} + \tilde{\Gamma}_x^{-1} \delta \tilde{\mathbf{x}} \\ & - L \delta \tilde{\mathbf{y}} + \Delta D_x^T W_c \delta \mathbf{c}_N] \end{aligned} \quad (37)$$

In order to derive the submatrices of Eq. (31), the assumption is made that the data covariance matrix Γ_z is the inverse of the data weighting matrix:

$$\Gamma_z = \overline{\delta \hat{\mathbf{z}} \delta \hat{\mathbf{z}}^T} = W^{-1} \quad (38)$$

Also, from the definition of the weighting matrix W_c for inexact constraints,

$$\overline{\delta \mathbf{c}_N \delta \mathbf{c}_N^T} = W_c^{-1} \quad (39)$$

Postmultiplying Eq. (37) by its transpose and averaging, using Eqs. (38) and (39), gives

$$\begin{aligned} \Gamma_x = & [J + \tilde{\Gamma}_x^{-1} + K]^{-1} \\ & + [J + \tilde{\Gamma}_x^{-1} + K]^{-1} [L \tilde{\Gamma}_y L^T - \tilde{\Gamma}_x^{-1} \tilde{\Gamma}_{xy} L^T - L \tilde{\Gamma}_{xy}^T \tilde{\Gamma}_x^{-1}] \\ & \times [J + \tilde{\Gamma}_x^{-1} + K]^{-1} \end{aligned} \quad (40)$$

where $\tilde{\Gamma}_x$ and $\tilde{\Gamma}_y$ are *a priori* covariance matrices for $\tilde{\mathbf{x}}$ and $\tilde{\mathbf{y}}$, and $\tilde{\Gamma}_{xy}$ is the *a priori* cross-covariance of $\tilde{\mathbf{x}}$ and $\tilde{\mathbf{y}}$.

Postmultiplying Eq. (37) by $\delta \tilde{\mathbf{y}}^T$ and averaging gives

$$\Gamma_{xy} = [J + \tilde{\Gamma}_x^{-1} + K]^{-1} [\tilde{\Gamma}_x^{-1} \tilde{\Gamma}_{xy} - L \tilde{\Gamma}_y] \quad (41)$$

Since the estimate of the consider parameters is not changed,

$$\Gamma_y = \tilde{\Gamma}_y \quad (42)$$

The remaining submatrices of Eq. (31) are Γ_s , Γ_{xs} , Γ_{ys} . From Eqs. (3) and (4),

$$\delta \mathbf{s} = S_x \delta \mathbf{x} + S_y \delta \mathbf{y} \quad (43)$$

Postmultiplying $\delta \mathbf{s}$ by $\delta \mathbf{s}^T$ and averaging gives

$$\Gamma_s = S_x \Gamma_x S_x^T + S_y \Gamma_y S_y^T + S_x \Gamma_{xy} S_y^T + S_y \Gamma_{xy}^T S_x^T \quad (44)$$

Postmultiplying $\delta \mathbf{x}$ and $\delta \mathbf{y}$ by $\delta \mathbf{s}^T$ and averaging gives

$$\Gamma_{xs} = \Gamma_x S_s^T + \Gamma_{xy} S_y^T \quad (45)$$

$$\Gamma_{ys} = \Gamma_{xy}^T S_x^T + \Gamma_y S_y^T \quad (46)$$

The covariance matrix for \mathbf{q} is evaluated from Eq. (31) using the submatrices given by Eqs. (40), (41), (42), (44), (45), and (46).

6. Mapping Covariance Matrix to New Epoch

This section gives the formulation for mapping the covariance matrix for the parameter vector \mathbf{q} from the injection epoch to any other epoch. Section (a) gives the mapped covariance matrix relative to the center of integration at the map time. In Section (b) this covariance matrix is used to compute the covariance matrix relative to any specified body other than the center of integration at the map time. There is a slight difference in either formulation, depending on whether the map epoch is specified in the ET time scale or in another time scale (A1, UTC, UT1, or ST).

a. Mapped covariance matrix relative to center of integration. The solve-for parameter vector \mathbf{q} will be denoted as \mathbf{q}_0 in this section. However for purposes of mapping the covariance matrix to a new epoch, dividing the parameters into the solve-for, consider, and exactly constrained categories is inappropriate. The appropriate categories are

\mathbf{X}_0^B = probe state vector (1950.0 earth equatorial rectangular position and velocity components) at injection epoch t_0 (specified in a time scale other than ET) relative to a specified body B which is not necessarily the center of integration at t_0

\mathbf{a} = all parameters that affect the probe state vector \mathbf{X} relative to the center of integration C

\mathbf{b} = all parameters that affect data but do not affect \mathbf{X}

Thus, the probe state vector $\mathbf{q} = \mathbf{q}_0$ is given by

$$\mathbf{q}_0 = \begin{bmatrix} \mathbf{x} \\ \mathbf{y} \\ \mathbf{s} \end{bmatrix} = \begin{bmatrix} \mathbf{X}_0^B \\ \mathbf{a} \\ \mathbf{b} \end{bmatrix} \quad (47)$$

where the second form of the vector is obtained from the first by reordering the elements.

The mapped parameter vector relative to the center of integration C at the map time is denoted by \mathbf{q}^C :

$$\mathbf{q}^C = \begin{bmatrix} \mathbf{X} \\ \mathbf{a} \\ \mathbf{b} \end{bmatrix} \quad (48)$$

where

\mathbf{X} = probe state vector relative to center of integration C at map time.

The mapped covariance matrix Γ_q^C relative to the center of integration at the map time corresponds to the mapped parameter vector \mathbf{q}^C .

The injection covariance matrix is given by Eq. (31). Reordering the rows and columns and partitioning according to the second vector of Eq. (47) gives, suppressing the subscript and superscript on \mathbf{X}_0^B ,

$$\Gamma_{q_0} = \begin{bmatrix} \Gamma_X & \Gamma_{Xa} & \Gamma_{Xb} \\ \Gamma_{Xa}^T & \Gamma_a & \Gamma_{ab} \\ \Gamma_{Xb}^T & \Gamma_{ab}^T & \Gamma_b \end{bmatrix} \quad (49)$$

The state vector of the probe relative to the center of integration is a function of ET and the parameter vector \mathbf{q}_0

$$\mathbf{X} = \mathbf{X}(\text{ET}, \mathbf{q}_0) \quad (50)$$

The variation in \mathbf{X} at an ET epoch is given by

$$\delta \mathbf{X} = U \delta \mathbf{X}_0^B + V \delta \mathbf{a} \quad (51)$$

where the U and V matrices are obtained from the solution of the variational equations (see Part VII: Eqs. 11, 12, and 13; SPS 37-44, Vol. III, p. 34). If the epoch is specified in a time scale other than ET (i.e., A1, UTC, UT1, or ST), the variation in \mathbf{X} is

$$\delta \mathbf{X} = U \delta \mathbf{X}_0^B + V \delta \mathbf{a} + \dot{\mathbf{X}} \delta \text{ET} \quad (52)$$

where, from Part II (SPS 37-39, Vol. III, p. 37), Eq. (3),

$$\delta \text{ET} = \delta(\Delta T_{1958}) - \frac{(\text{JD} - 243,6204.5)(86,400)}{9,192,631,770} \delta(\Delta f_{\text{cesium}}) \quad (53)$$

Thus, Eq. (52) may be written as

$$\delta \mathbf{X} = U \delta \mathbf{X}_0^B + V^* \delta \mathbf{a} \quad (54)$$

where V^* is the V matrix with the ΔT_{1958} column incremented by

$$\dot{\mathbf{X}}$$

and the Δf_{cesium} column incremented by

$$- \frac{(\text{JD} - 243,6204.5)(86,400)}{9,192,631,770} \dot{\mathbf{X}}$$

where both $\dot{\mathbf{X}}$ and JD are evaluated at the map epoch.

Using Eq. (51), the variation of \mathbf{q}^c at an ET map epoch due to a variation in \mathbf{q}_0 is given by

$$\delta \mathbf{q}^c = \begin{bmatrix} \delta \mathbf{X} \\ \delta \mathbf{a} \\ \delta \mathbf{b} \end{bmatrix} = \begin{bmatrix} U & V & 0 \\ 0 & I & 0 \\ 0 & 0 & I \end{bmatrix} \begin{bmatrix} \delta \mathbf{X}_0^B \\ \delta \mathbf{a} \\ \delta \mathbf{b} \end{bmatrix} = \theta \delta \mathbf{q}_0 \quad (55)$$

where 0 and I represent null and identity matrices. The variation of \mathbf{q}^c at a map epoch specified in a time scale other than ET is given by Eq. (55), with V replaced by V^* .

Using Eq. (55), the mapped covariance matrix for \mathbf{q}^c is given by

$$\Gamma_q^c = \overline{\delta \mathbf{q}^c [\delta \mathbf{q}^c]^T} = \theta \Gamma_{q_0} \theta^T \quad (56)$$

Substituting Eqs. (49) and (55) into Eq. (56) gives

$$\Gamma_q^c = \begin{bmatrix} U\Gamma_X U^T + V\Gamma_{Xa}^T U^T + U\Gamma_{Xa} V^T + V\Gamma_a V^T & U\Gamma_{Xa} + V\Gamma_a & U\Gamma_{Xb} + V\Gamma_{ab} \\ \Gamma_{Xa}^T U^T + \Gamma_a V^T & \Gamma_a & \Gamma_{ab} \\ \Gamma_{Xb}^T U^T + \Gamma_{ab}^T V^T & \Gamma_{ab}^T & \Gamma_b \end{bmatrix} \quad (57)$$

This equation may be simplified by using the following combined submatrices of Eq. (49):

$$\Gamma_{X,ab} \equiv [\Gamma_{Xa} \mid \Gamma_{Xb}] \quad (58)$$

$$\Gamma_{a,ab} \equiv [\Gamma_a \mid \Gamma_{ab}] \quad (59)$$

$$\Gamma_{ab,ab} \equiv \begin{bmatrix} \Gamma_a & \Gamma_{ab} \\ \Gamma_{ab}^T & \Gamma_b \end{bmatrix} \quad (60)$$

With these definitions, Eq. (57) simplifies to

$$\Gamma_q^c = \begin{bmatrix} U\Gamma_X U^T + V\Gamma_{Xa}^T U^T + U\Gamma_{Xa} V^T + V\Gamma_a V^T & U\Gamma_{X,ab} + V\Gamma_{a,ab} \\ [U\Gamma_{X,ab} + V\Gamma_{a,ab}]^T & \Gamma_{ab,ab} \end{bmatrix} \quad (61)$$

This equation gives the mapped covariance matrix relative to the center of integration for an ET map epoch. If the map epoch is specified in any other time scale, Eq. (61) is used with the V matrix replaced by the V^* matrix.

b. Mapped covariance matrix relative to body other than center of integration. The mapped parameter vector relative to the center of integration at the map time is denoted by

$$\mathbf{q}^c = \begin{bmatrix} \mathbf{X} \\ \mathbf{q}' \end{bmatrix} \quad (62)$$

where

$$\mathbf{q}' = \begin{bmatrix} \mathbf{a} \\ \mathbf{b} \end{bmatrix} \quad (63)$$

The mapped parameter vector relative to a body B other than the center of integration at the same map time is given by

$$\mathbf{q}^B = \begin{bmatrix} \mathbf{X}^B \\ \mathbf{q}' \end{bmatrix} = \begin{bmatrix} \mathbf{X} - \mathbf{X}_B^c(\mathbf{q}') \\ \mathbf{q}' \end{bmatrix} \quad (64)$$

where

\mathbf{X}^B = probe state vector relative to body B at map time

\mathbf{X}_B^c = state vector of body B relative to center of integration C at map time

The variation of \mathbf{q}^B is given by

$$\delta \mathbf{q}^B = \frac{\partial \mathbf{q}^B}{\partial \mathbf{q}^c} \delta \mathbf{q}^c \equiv M \delta \mathbf{q}^c = \begin{bmatrix} I & -\frac{\partial \mathbf{X}_B^c}{\partial \mathbf{q}'} \\ 0 & I \end{bmatrix} \delta \mathbf{q}^c \quad (65)$$

where the identity matrices are 6×6 and $n \times n$, where n is the number of elements of \mathbf{q}' . For an ET map epoch, the columns of $\partial \mathbf{X}_B^c / \partial \mathbf{q}'$ are nonzero only for the reference parameters: A_E , R_E , \mathbf{E} for each ephemeris, μ_E , and μ_M . For a map epoch specified in a time scale other than ET, the ΔT_{1958} and Δf_{cesium} columns will also be nonzero. They are given by

$$\frac{\partial \mathbf{X}_B^c}{\partial \Delta T_{1958}} = \dot{\mathbf{X}}_B^c \quad (66)$$

$$\frac{\partial \mathbf{X}_B^c}{\partial \Delta f_{cesium}} = - \frac{(\text{JD} - 243,6204.5)(86,400)}{9,192,631,770} \dot{\mathbf{X}}_B^c \quad (67)$$

Using Eq. (65), the mapped covariance matrix relative to body B is given by

$$\Gamma_q^B = \overline{\delta \mathbf{q}^B [\delta \mathbf{q}^B]^T} = M \Gamma_q^c M^T \quad (68)$$

7. Solar and Lunar Constraints

There are two constraints stored within the DPODP: the so-called solar and lunar constraints. The user specifies whether each of these constraints is to be applied, and also specifies the exact or inexact treatment. The user may also apply exact constraints by inputting the information listed under item 2, p. 29.

The lunar constraint is given by

$$R_E = C(\mu_E + \mu_M)^{1/3} \quad (69)$$

where

R_E = scaling factor for lunar ephemeris, km per dimensionless unit of length

μ_E = earth's gravitational constant, km^3/s^2

μ_M = moon's gravitational constant, km^3/s^2

and the constant C is given by

$$C = \frac{F_2}{n_M^{2/3} a_M} \quad (70)$$

where

n_M = sidereal mean motion of moon (1900)

$$= 2.661,699,489 \times 10^{-6} \text{ rad/s}$$

a_M = perturbed mean distance of moon (the perturbation is due to the sun), dimensionless units of length

$$= \frac{1}{\sin \pi_\epsilon (\text{dimensionless})} = \frac{206,264.80625}{\sin \pi_\epsilon (\text{seconds of arc})}$$

$\sin \pi_\epsilon$ = sine of lunar parallax (the value used to generate the lunar ephemeris). The term $\sin \pi_\epsilon$ is dimensionless; however, it is usually expressed in seconds of arc by multiplying by the number of seconds of arc in one radian.

$$F_2 = 0.99909,31419,75298 \text{ (Brown, 1897)}$$

= ratio of perturbed mean distance of moon to two-body mean distance (sun not present and mean motion remains constant)

The lunar constraint is Kepler's equation constraining μ_E , μ_M , and R_E to the observed mean motion of the moon. Kepler's equation is a two-body equation, and the factor F_2 is necessary to remove the third-body perturbation of the sun.

The following table lists values of $\sin \pi_\epsilon$ used in three different JPL lunar ephemerides and the corresponding values of the constant C for the lunar constraint:

Ephemeris	$\sin \pi_\epsilon$	C
Lunar ephemeris 2 (Development ephemeris 3)	3422'5400	86.315,746,3
Lunar ephemeris 3 (Development ephemeris 15)	3422'452	86.313,527,0
Lunar ephemeris 4 (Development ephemeris 16 and 19)	3422'451	86.313,501,8

From Eq. (69), holding $\mu_E + \mu_M$ constant, the value of R_E will be different for each of these ephemerides. However, from Eqs. (69) and (70), $R_E a_M$, the mean distance to the moon in kilometers, is constant. Thus the value for $\sin \pi_\epsilon$ used in both the lunar ephemeris and C is arbitrary.

The solar constraint is given by

$$\mu_S = \frac{k^2 A_E^3}{(86,400)^2} \quad (71)$$

where

μ_S = sun's gravitational constant, km^3/s^2

k = Gaussian gravitational constant

= 0.017,202,098,95 $\text{AU}^{3/2}/\text{day}$ (exactly)

A_E = number of kilometers/astronomical unit (AU)

The gravitational constant of the sun k^2 in units of astronomical units cubed per day squared is a defined mathematical constant. The solar constraint is simply a

conversion of the sun's gravitational constant from AU^3/day^2 to km^3/s^2 .

G. Sun-Earth Line Plots and DSN Planning,

J. F. Gallagher

It is anticipated that within the next few decades space missions will increase in number and duration. Consequently, it will be necessary for the DSN to make preliminary estimates of tracking coverage capability. This requires a knowledge of the position relative to the earth of any spacecraft that may require tracking during a given period. A device that is proving very useful in DSN planning is the so-called sun-earth line plot.

A sun-earth line plot is a plot of the trajectory of a spacecraft relative to a coordinate system centered at the sun, with the X-Y plane lying in the ecliptic and its X-axis through the earth. This system rotates with the orbital motion of the earth. A conventional plot of the orbits of the earth and *Pioneer VII* is compared with a sun-earth line plot in Fig. 17. As can be seen, a rather complicated drawing extending over much of the available space in Fig. 17a is simply and compactly represented in Fig. 17b. Although some information is lost in the sun-earth line plot, the essential requirement for tracking is position relative to the earth, and this can be shown neatly and concisely and for much longer periods with a sun-earth line plot. A few samples of the many sun-earth line plots which have been made in recent months are shown in Figs. 18-26.

These plots become valuable when used in conjunction with special-purpose computing tools. One such tool* employs a transparent sheet on which straight-line scales are drawn. These straight-line scales radiate from one point which is placed at the earth in the sun-earth line plot and, by means of a pin or similar device, the transparent sheet can pivot around the earth. Each scale is calibrated with different range-dependent quantities, such as the distance to the probe in millions of kilometers, the round-trip light time in seconds, the carrier power received at the antenna, telemetry rate regimes in bits/s, etc. The various range-dependent quantities are determined for any mission and for any date by merely placing the device over the proper sun-earth line plot and rotating the desired scale into position over the point on the trajectory corresponding to the desired date. A sketch showing the principal features of such a device appears in Fig. 27.

*Devised by A. J. Siegmeth, JPL Section 441.

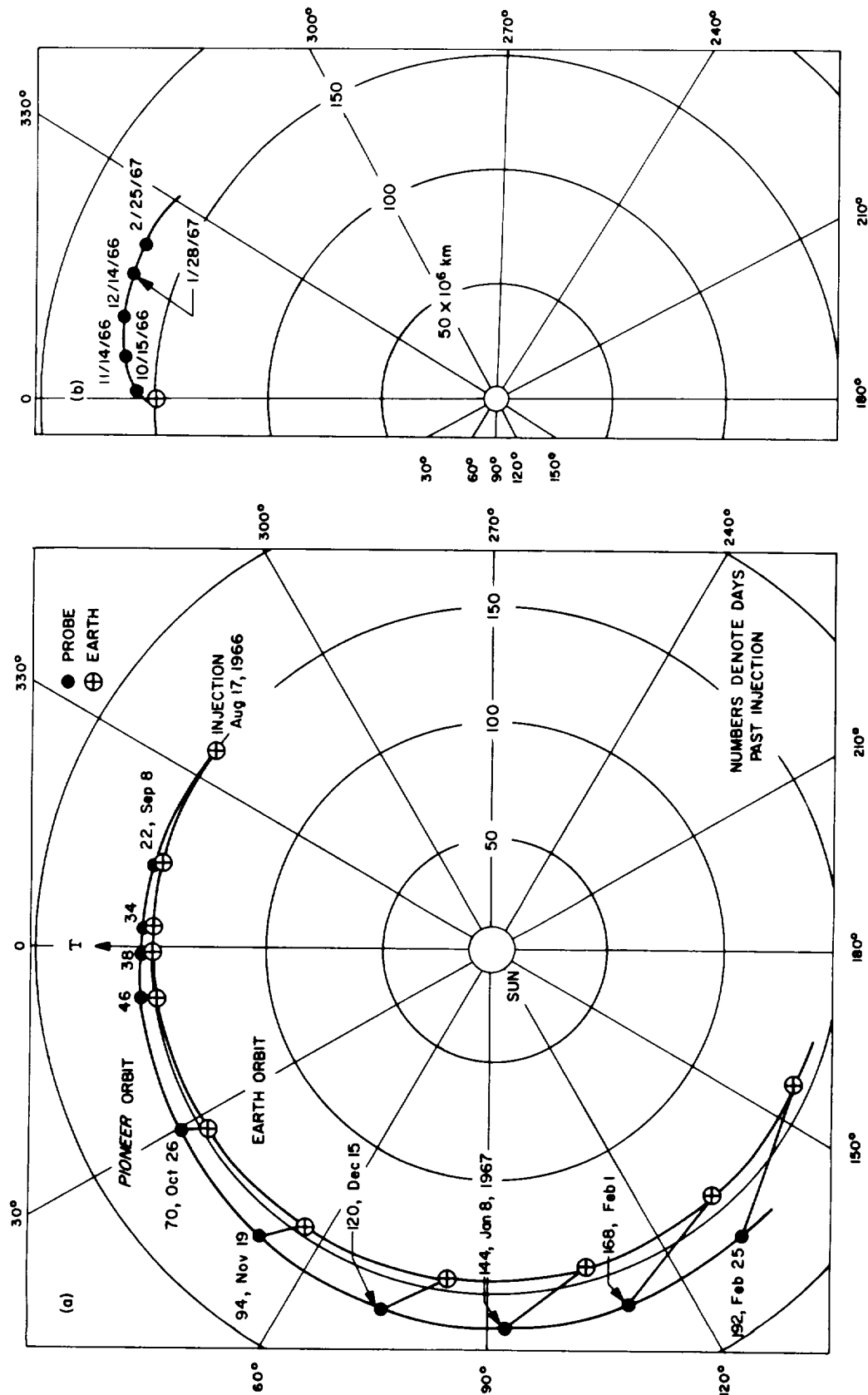


Fig. 17. Conventional heliocentric plot of the orbits of Pioneer VII and the earth compared with sun-earth line plot of Pioneer VII

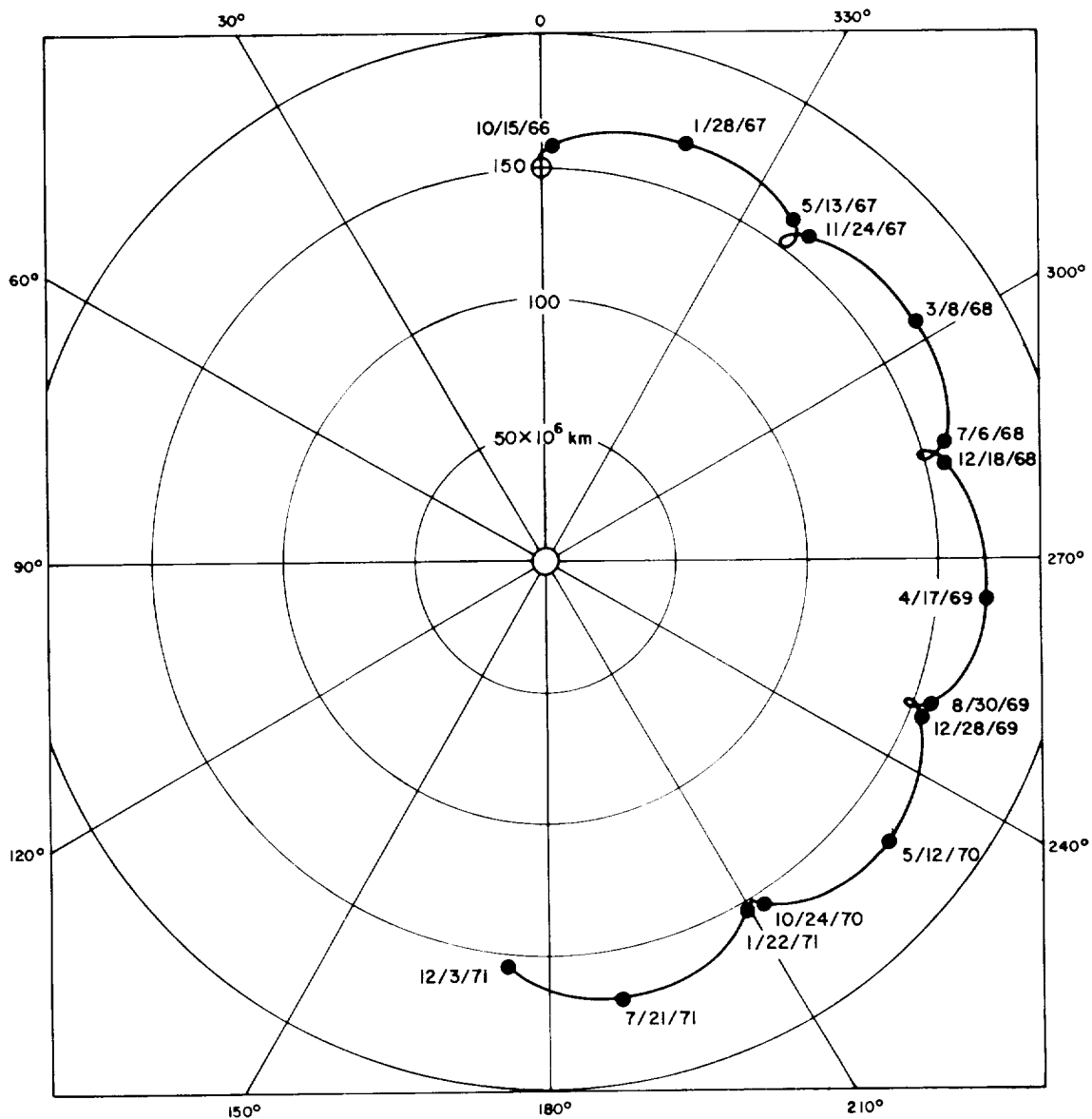


Fig. 18. Sun-earth line plot of Pioneer VII for October 1966 to January 1972

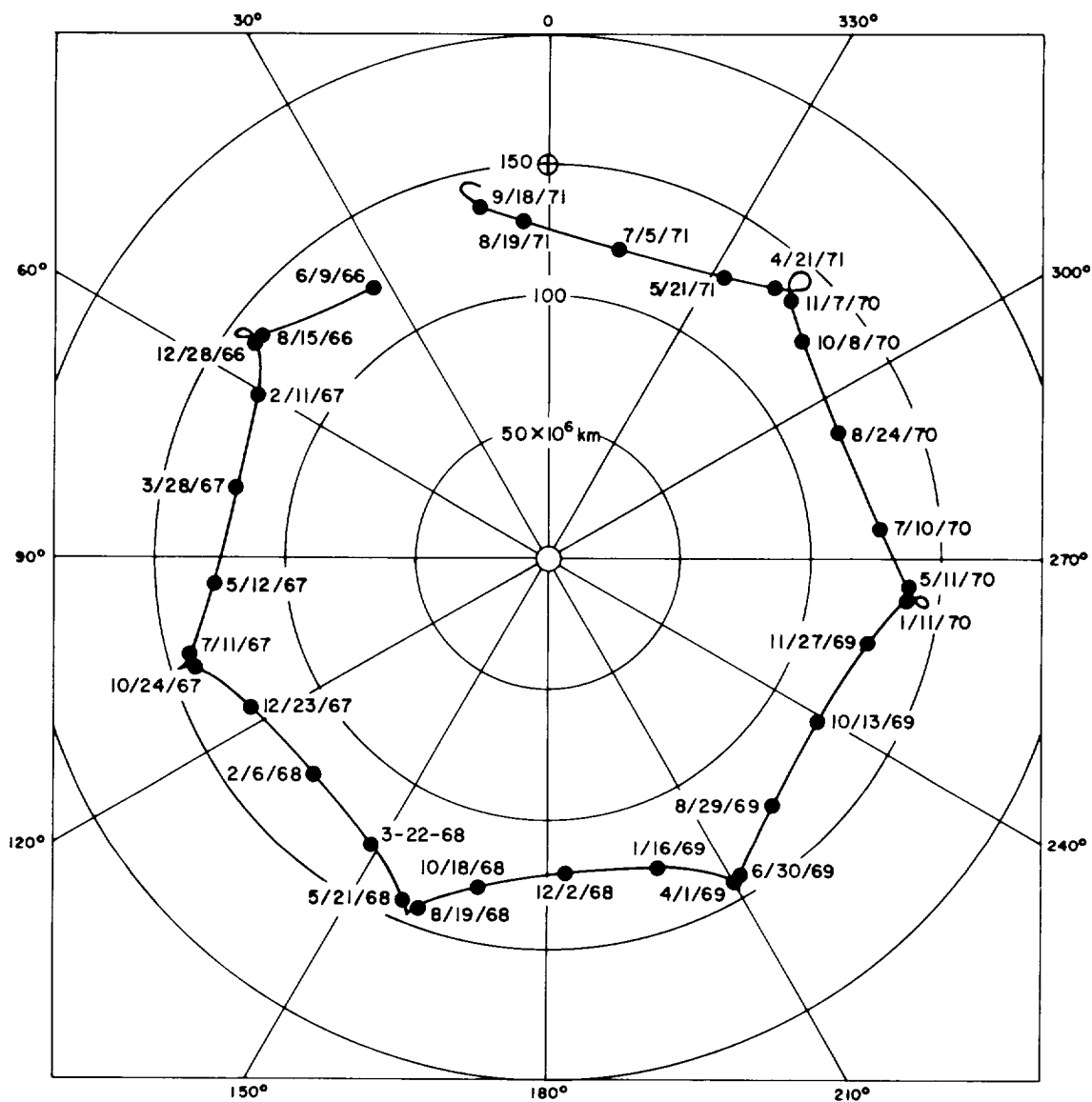


Fig. 19. Sun-earth line plot of Pioneer VI for June 1966 to January 1972

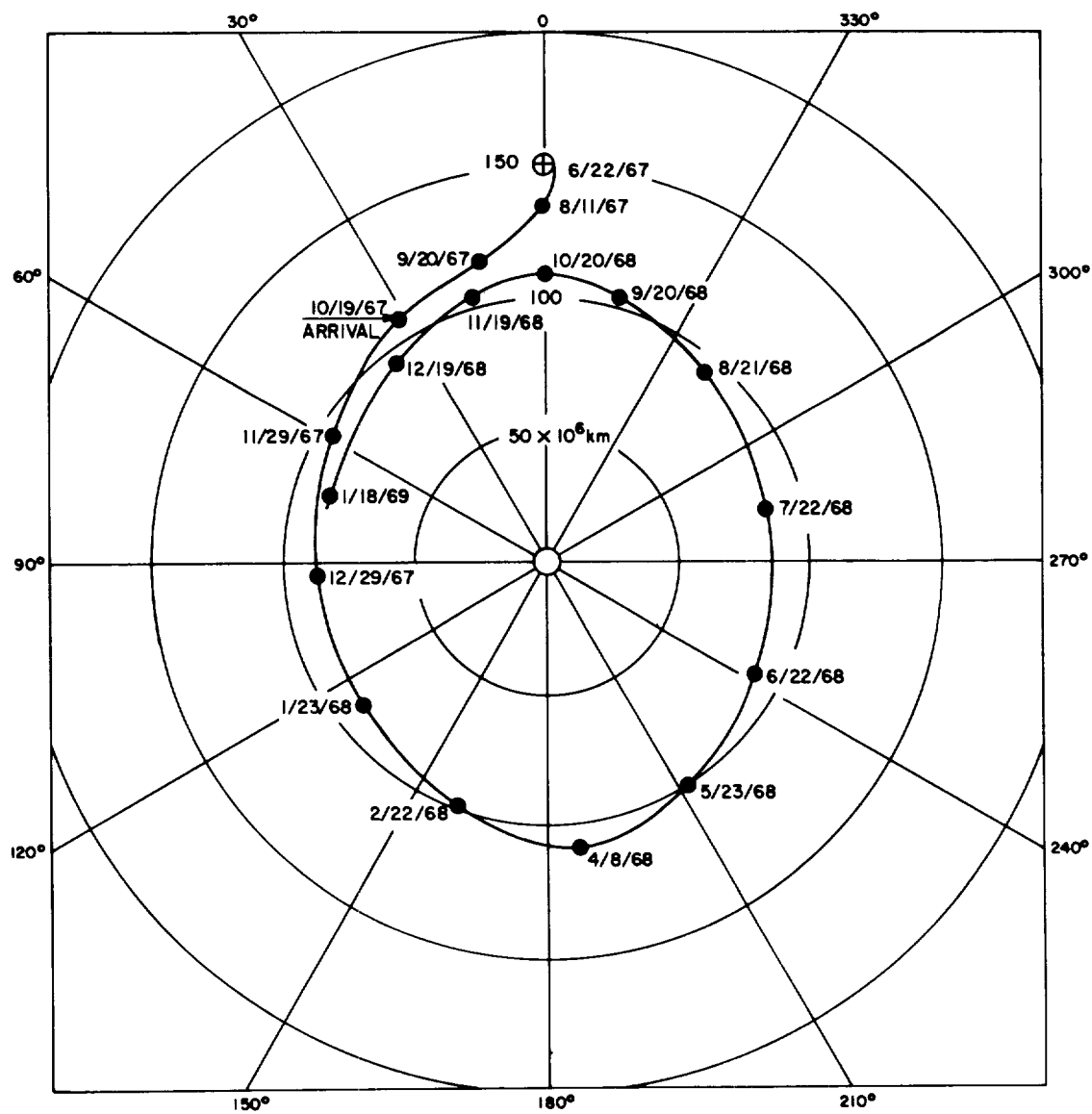


Fig. 20. Sun-earth line plot of *Mariner Venus 67* for June 1967 to January 1969

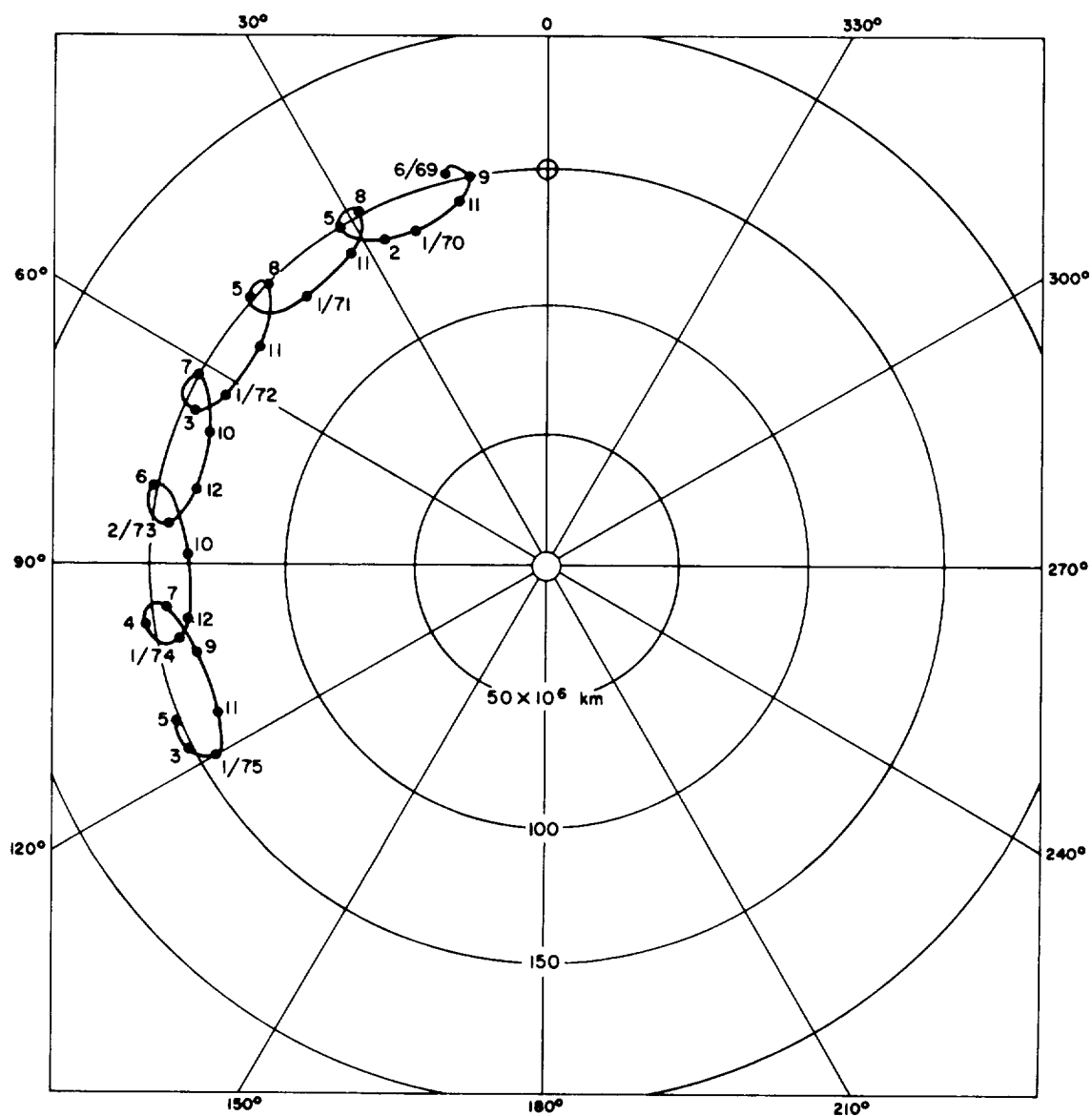


Fig. 21. Sun-earth line plot of Pioneer E for June 1969 to May 1975

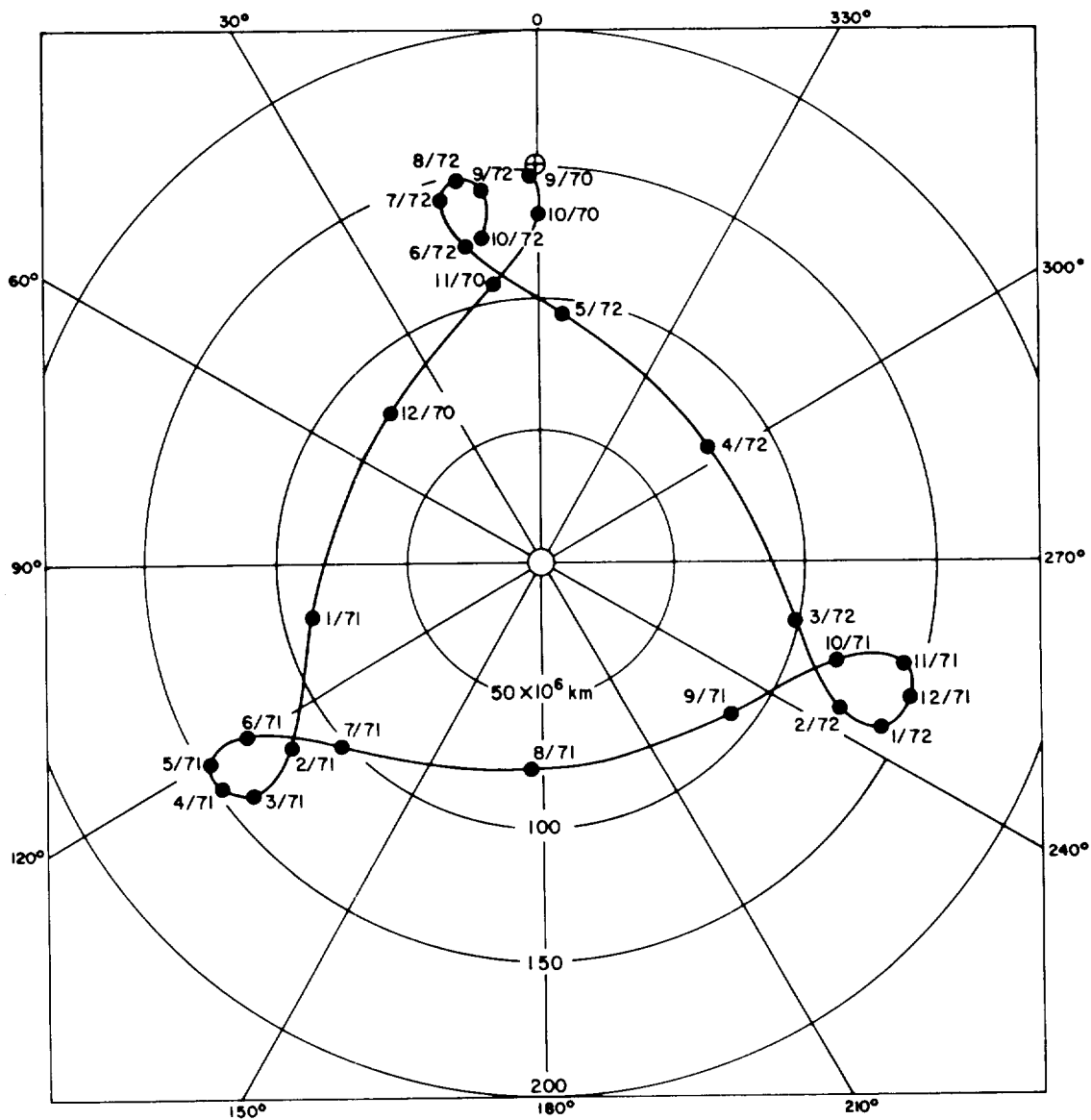


Fig. 22. Sun-earth line plot of Pioneer F for August 1970 to October 1972

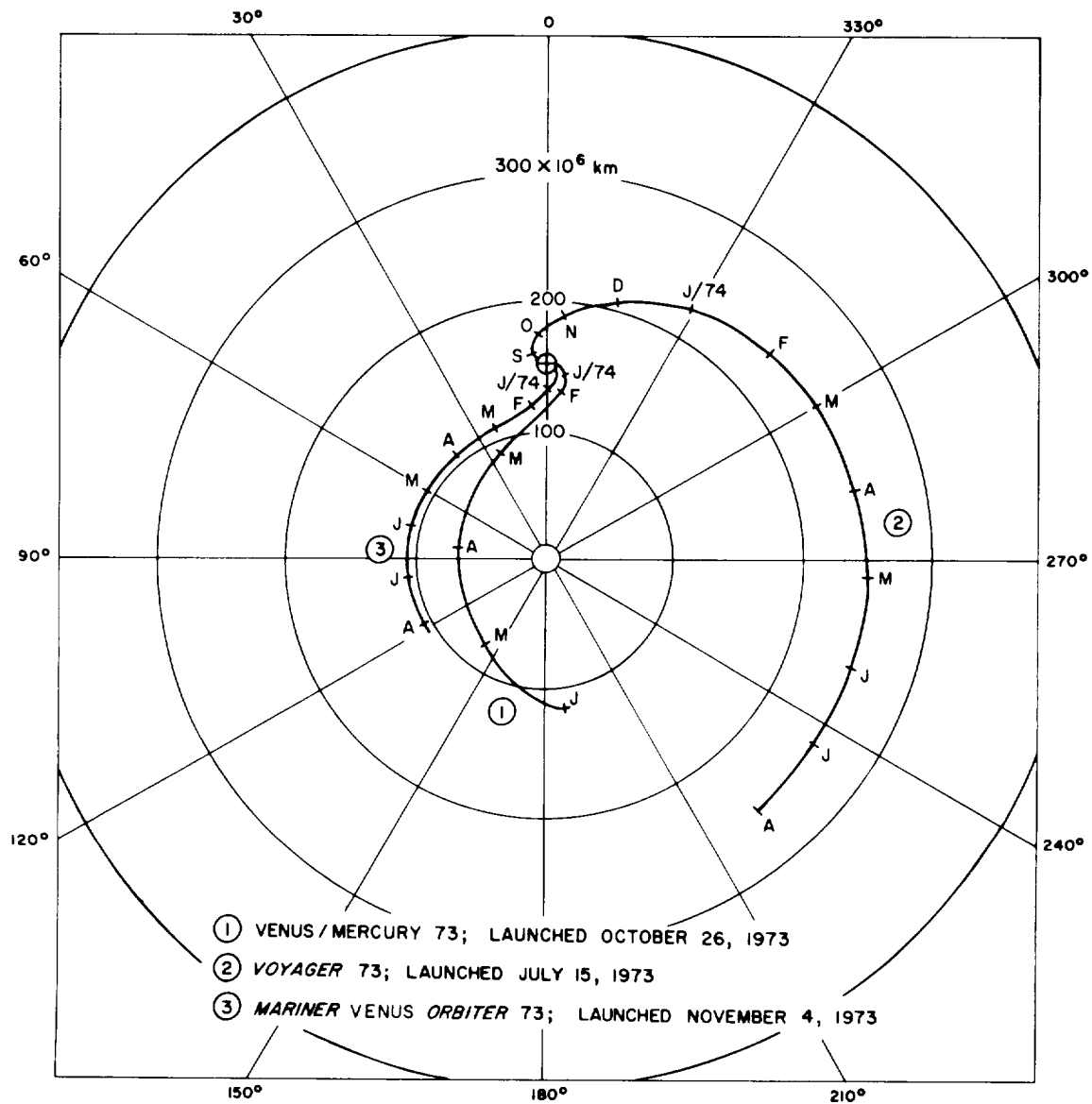


Fig. 23. Sun-earth line plots for some 1973 missions

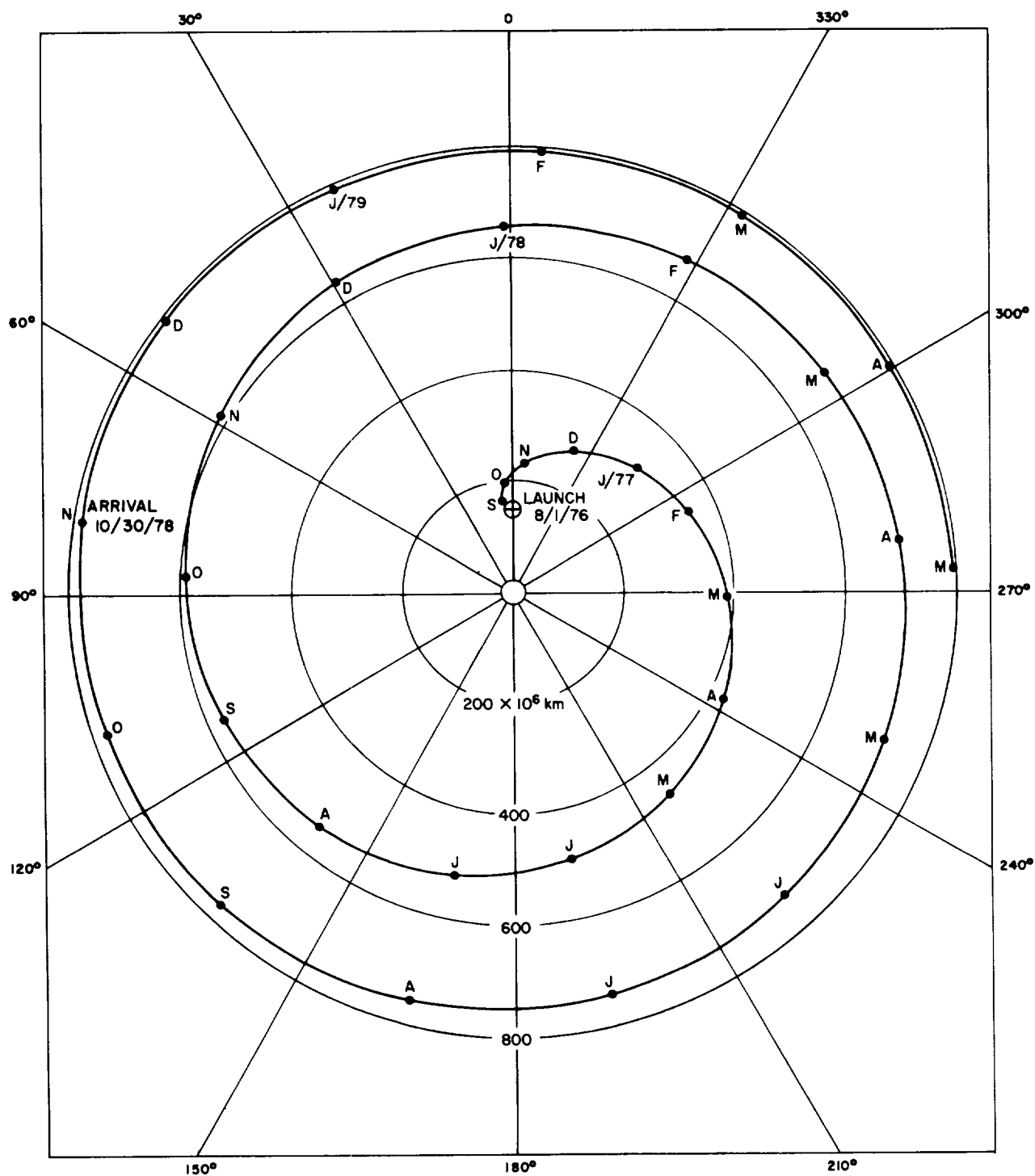


Fig. 24. Sun-earth line plot for Voyager Jupiter 1976

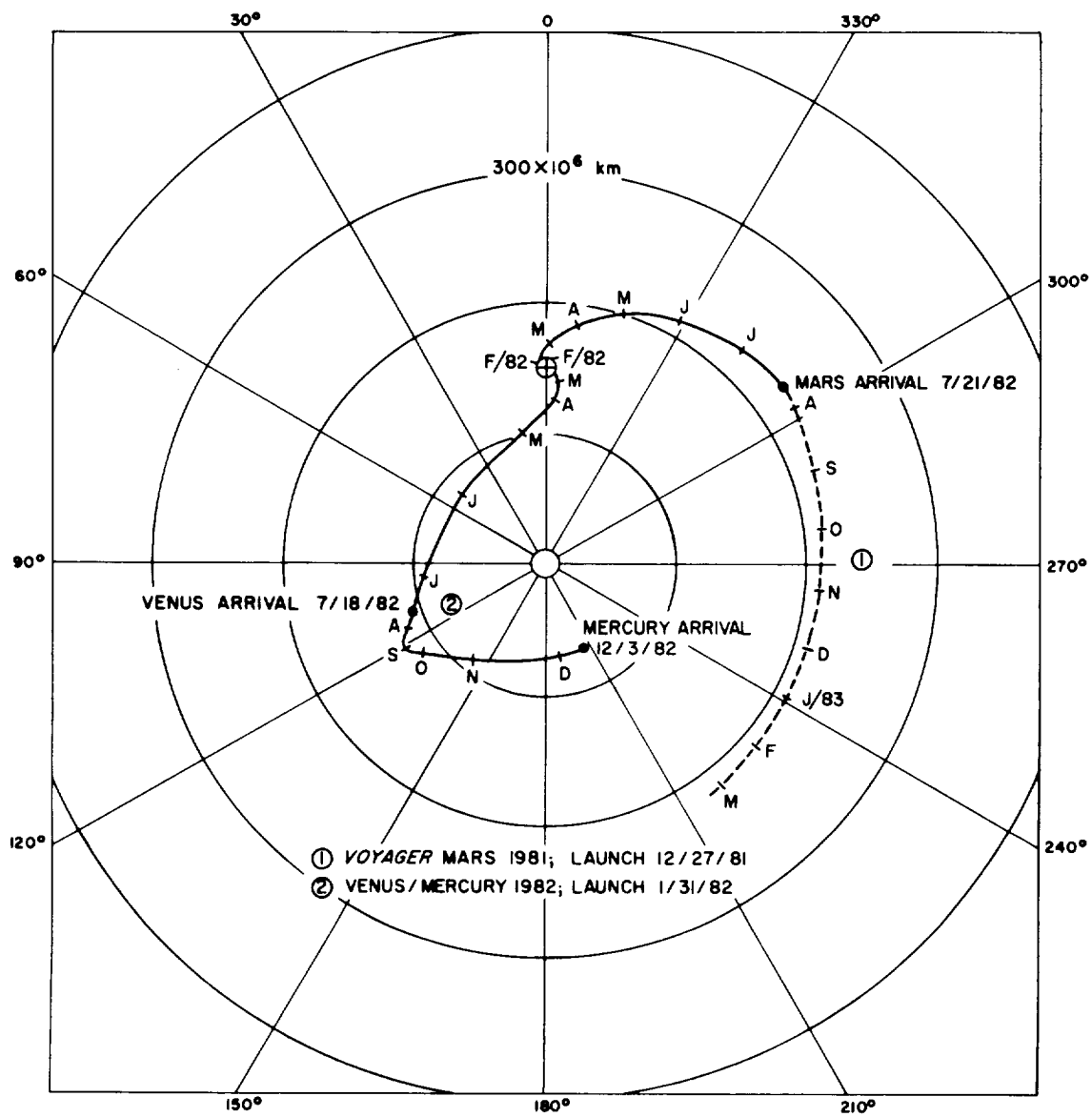


Fig. 25. Sun-earth line plots for Voyager Mars 1981 and Venus Mercury 1982

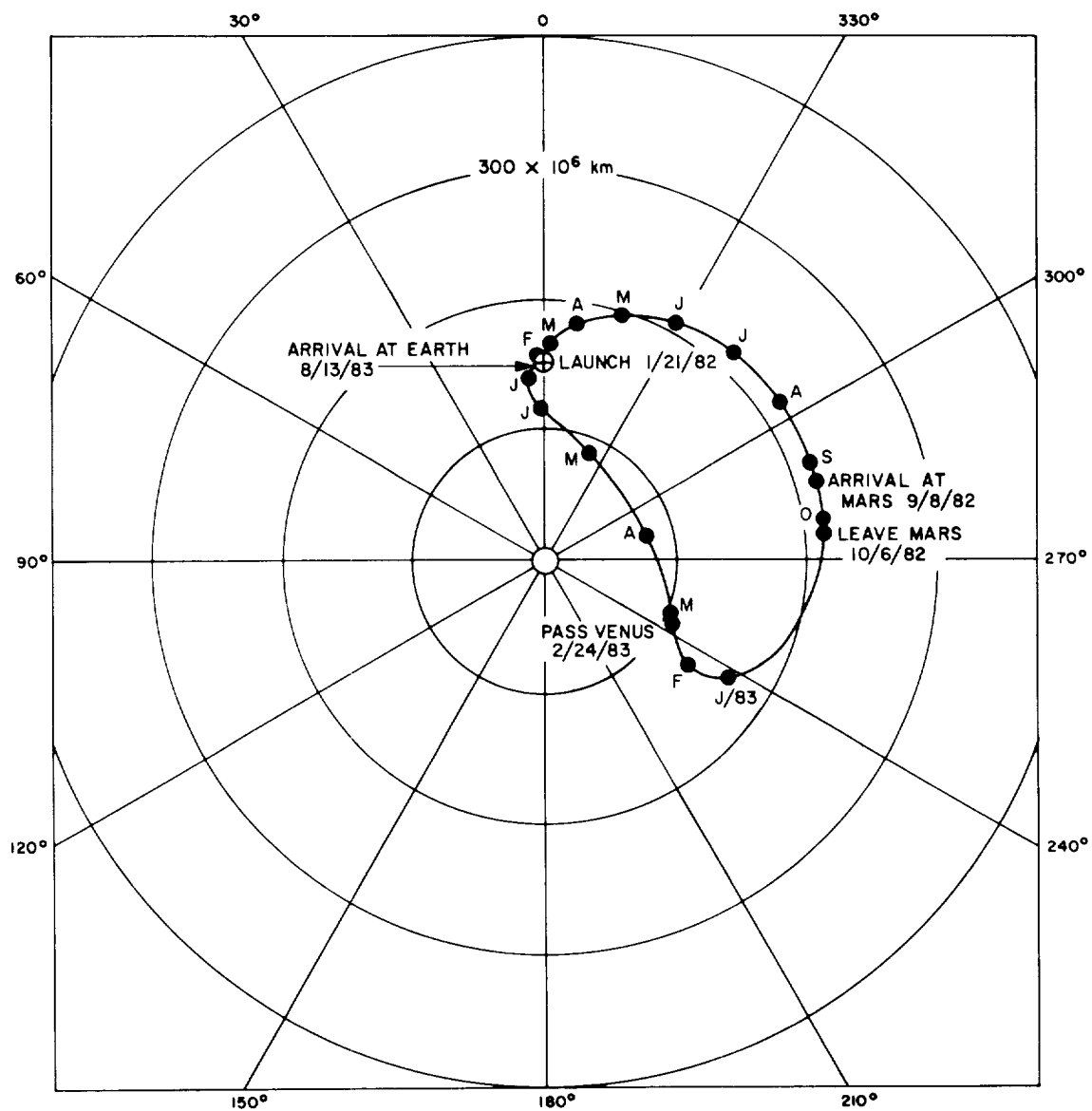


Fig. 26. Sun-earth line plot of manned mission to Mars in 1982

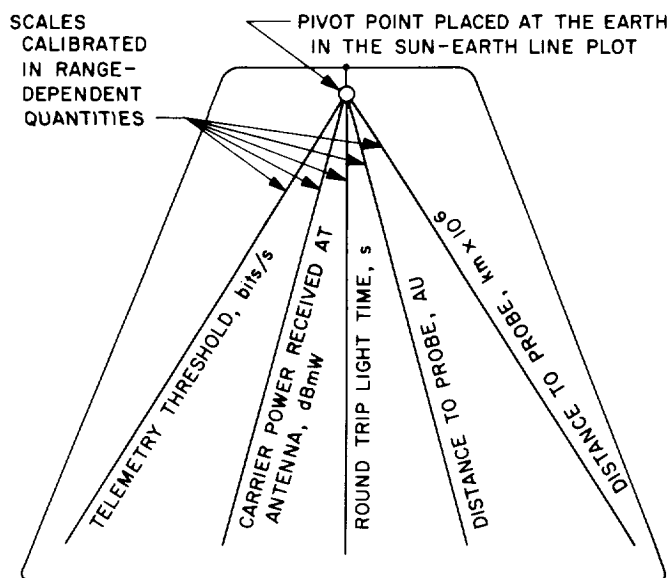


Fig. 27. Rotatable transparent sheet with straight-line scales showing various range-dependent quantities

Another computing tool¹⁰ can be used to calculate approximate view periods for various tracking stations. This tool consists of a transparent wheel on which are drawn a GMT clock and radial lines that represent the rise, maximum elevation, and set of various tracking stations. This wheel is really an analog of the rotating earth. The approximate time of a station rise, maximum elevation, or set can be determined for any mission and any day by placing the radial line that represents the desired event over the desired point on the sun-earth line plot, and then reading the time on the clock in GMT. The time is given by the intersection of the sun-earth line and the clock itself. The sketch in Fig. 28 indicates the use of this view-period wheel.

¹⁰Devised by J. A. Borrás, JPL Section 312.

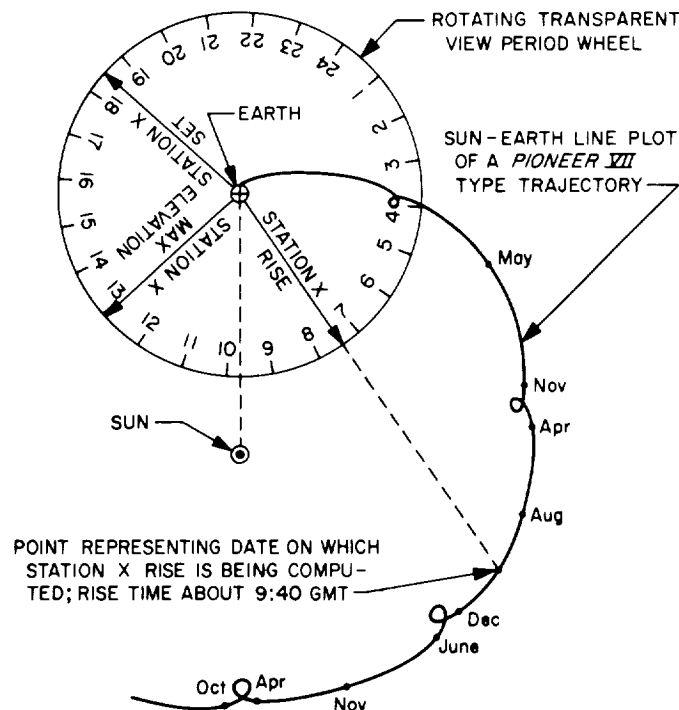


Fig. 28. Illustration of use of a transparent rotating wheel and a sun-earth line plot to estimate station view periods

Another auxiliary device,¹⁰ which uses the synodic month, is a nonrotating circular scale placed over the sun-earth line plot and centered at the earth. The scale gives the age of the moon in days, 0 to 29.5. From an ephemeris, it is possible to obtain the age of the moon at any date, and thus the direction of the moon from the earth in the sun-earth line plot. In this fashion, possible conflicts between lunar- and planetary-mission tracking requirements can be detected. A similar device could be used for the planets when orbiting missions are being tracked.

References

1. Warner, M. R., and Nead, M. W., *SPODP—Single Precision Orbit Determination Program*, Technical Memorandum 33-204, Jet Propulsion Laboratory, Pasadena, Calif., Feb. 15, 1965.
2. Sjogren, W. L., et al., *The Ranger VI Flight Path and Its Determination From Tracking Data*, Technical Report 32-605, Jet Propulsion Laboratory, Pasadena, Calif., Dec. 15, 1964.

References (contd)

3. Sjogren, W. L., et al., *Physical Constants as Determined From Radio Tracking of the Ranger Lunar Probes*, Technical Report 32-1057, Jet Propulsion Laboratory, Pasadena, Calif., Dec. 30, 1966.
4. Markowitz, W., "Latitude, Longitude, and the Secular Motion of the Pole." Reprinted by the U.S. Naval Observatory from *Methods and Techniques in Geophysics*, edited by Runcorn, Interscience Publishers Ltd., London, 1960.
5. Null, G. W., and Gordon, H. J., *The Mariner IV Flight Path and Its Determination From Tracking Data*, Technical Report 32-1108, Jet Propulsion Laboratory, Pasadena, Calif. (in press).
6. Anderson, J. D., *Theory of Orbit Determination: Part II. Estimation Formulas*, Technical Report 32-498, Jet Propulsion Laboratory, Pasadena, Calif., Oct. 1, 1963.

III. Communications Research and Development

A. Digital Communication and Tracking: Specification of Parameters of Phase Locked Receivers at an Arbitrary Design Point, R. Tausworthe

The content of Chap. 10 of Ref. 1 was concerned, in the main, with the performance of a double heterodyne receiver at a given signal level. Threshold was defined as a signal power $A_0^2 = N_0 w_{L_0}$ to be computed mathematically for a given noise density N_0 and linear-theoretic bandwidth w_{L_0} occurring at this signal level. It was shown that all loop parameters could be referenced to the threshold condition, and specified in terms of the loop margin, or signal level relative to threshold. It is often the case, however, that an engineer wishes to specify bandwidth, damping factor, etc., at some point above threshold, in which case the formulas in Chap. 10 may prove a bit cumbersome. In order to analyze performance, the engineer must translate the design-point parameters back to the equivalent threshold bandwidth, damping factor, etc., before he can proceed with the formulas given.

In this article the formulas of Chap. 10 are expanded to include an arbitrary design point.

1. Definition of Design Point

The *design-point signal level*, denoted A_0^2 , is defined to be

$$A_0^2 = \rho_0 N_0 w_{L_0} \quad (1)$$

where the parameters involved are

N_0 = double-sided spectral density of input noise
($= kT/2$)

w_{L_0} = two-sided linear-theoretical loop bandwidth at the design signal level A_0^2

ρ_0 = the loop passband signal-to-noise ratio (SNR) at design point

In the notation hereafter all quantities subscripted "0" refer to the value of that particular parameter at design point.

2. Operation at Levels Other Than Design Point

As in Chap. 10, the *performance margin* m is defined as the ratio of actual signal level A^2 to design-point level A_0^2

$$m = \frac{A^2}{A_0^2} \quad (2)$$

In terms of this m , the predetection SNR ρ_H is

$$\rho_H = \frac{A^2}{N_0 w_H} = \left(\frac{A^2}{A_0^2} \right) \left(\frac{w_{L_0}}{w_H} \right) \rho_0 = m \rho_{H_0} \quad (3)$$

Under the condition $\rho_0 w_{L_0} \ll w_H$ (or $\rho_{H_0} \ll 1$), the value of the signal suppression factor α_0^2 is approximately $\pi w_{L_0} \rho_0 / 4 w_H$; so the value of the design-point damping parameter $r_0 = \alpha_0 K \tau_z^2 / \tau_1$ is given by

$$r_0 = \left(\frac{U - \tau_z / \tau_1}{2} \right) \left\{ 1 + \left[\frac{4U}{(U - \tau_z / \tau_1)^2} \right]^{1/2} \right\} \\ \approx \frac{U}{2} \left[1 + \left(1 + \frac{4}{U} \right)^{1/2} \right] \\ U = \frac{\pi (K_d K_{VCO} M F)^2 \tau_z^3 \rho_0}{8 \tau_1^2 w_H} \quad (4)$$

We can also express U in terms of r_0 ,

$$U = \frac{r_0 (r_0 + \tau_z / \tau_1)}{r_0 + 1} \approx \frac{r_0^2}{r_0 + 1} \quad (5)$$

3. Receiver Performance

The formulas contained in (10-6) of Ref. 1 specify both the linear (with η and γ set to unity) and nonlinear behavior of the double-heterodyne receiver at any margin above threshold. For a receiver designed at $\rho_0 \neq 1$, these formulas are modified as follows:

$$\rho_H = m \rho_0 \left(\frac{w_{L_0}}{w_H} \right) = m \rho_{H_0} \quad (6a)$$

$$\alpha = \left[\frac{0.7854 \rho_H + 0.4768 \rho_H^2}{1 + 1.024 \rho_H + 0.4768 \rho_H^2} \right]^{1/2} \quad (6b)$$

$$\Gamma = \frac{1 + 0.345 \rho_H}{0.862 + 0.690 \rho_H} \quad (6c)$$

$$r = \frac{\alpha K_d K_{VCO} M F \tau_z^2}{\tau_1} = \frac{\alpha}{\alpha_0} r_0 = \tau_z^2 \beta^2 = \tau_z^2 \left(\frac{\alpha}{\alpha_0} \right) \beta_0^2 \quad (6d)$$

$$\sigma^2 = \frac{\pi^2}{3} \left\{ 1 - \exp \left[\frac{-3a^2}{\pi^2} (1 + 0.13a^2) \right] \right\} \\ \approx a^2, \quad (\text{for } \sigma^2 < 1) \quad (6e)$$

$$\gamma^2 = a^{-2} e^{-a^2} \sinh a^2 \quad (6f)$$

$$\eta = e^{-a^2/2} \quad (6g)$$

$$w_L = \frac{1 + r}{2 \tau_z \left(1 + \frac{\tau_z}{r \tau_1} \right)} \approx \frac{1 + r}{2 \tau_z} = \left[\frac{1 + (\alpha / \alpha_0) r_0}{1 + r_0} \right] w_{L_0} \quad (6h)$$

$$w_{L(eq)} = \frac{1 + r \gamma}{2 \tau_z \left(1 + \frac{\tau_z}{r \gamma \tau_1} \right) \left[1 + \frac{2(\gamma - \eta)(1 - \tau_z / \tau_1)}{\gamma^2 r (1 + \tau_z / r \gamma \tau_1)^2} \right]^{1/2}} \quad (6i)$$

$$\zeta = \frac{1}{2} \left(1 + \frac{\tau_z}{r \tau_1} \right) r^{1/2} = \frac{1}{2} \left(1 + \frac{1}{\tau_1 \tau_z \beta^2} \right) \tau_z \beta \\ \approx \frac{r^{1/2}}{2} = \frac{\tau_z \beta}{2} \quad (6j)$$

$$\zeta_{eq} = \frac{1}{2} \left(1 + \frac{\tau_z}{r \gamma \tau_1} \right) \left\{ r \gamma \left[1 + \frac{2(\gamma - \eta)(1 - \tau_z / \tau_1)}{r \gamma^2 (1 + \tau_z / r \gamma \tau_1)^2} \right] \right\}^{1/2} \\ \approx \frac{1}{2} (r \gamma)^{1/2} \approx \zeta \gamma^{1/2} \quad (6k)$$

$$\beta_{eq} = \frac{(r \gamma)^{1/2}}{\tau_z} = \beta \gamma^{1/2} \quad (6l)$$

$$a^2 = \frac{N_0 w_{L(eq)} \Gamma}{A^2 \gamma^2} = \frac{1}{m} \left(\frac{w_{L(eq)} \Gamma}{\rho_0 w_{L_0} \gamma^2} \right) \approx \sigma^2, \quad (\text{for } a^2 < 1) \quad (6m)$$

$$\beta \approx \frac{2 w_L r^{1/2}}{r + 1} = \left(\frac{\alpha}{\alpha_0} \right)^{1/2} \frac{2 w_{L_0} r_0^{1/2}}{r_0 + 1} \quad (6n)$$

Although only Eqs. (10-6a) and (10-6m) of Ref. 1 have been altered¹ by this procedure, the entire set is relisted here for reference.

4. The Value of Margin at $\sigma^2 = 1$

Holding the rest of the loop parameters fixed, the margin m producing 1 rad rms phase error can be computed from the equations in (6) above. The value of σ^2 is within 0.5% of unity when $a^2 = 1$; hence, to the accuracy we require, the values of m_1 and r_1 at $a^2 = 1$ suffice. It then

¹The reader may note some other differences between (10-6) of Ref. 1 and Eq. (6) above: (10-6d) and (10-6n) contained typographical errors, and experiments showed that γ_{tp} in Chap. 9 was more effective than the γ in (10-6f). Hence, γ_{tp} is listed as γ in Eq. (11-6f).

follows that the value $x_1 = A_1/A_0 = m_1^{1/2}$ producing this condition satisfies

$$x_1 = \frac{\Gamma_1(r_0 + \tau_2/\tau_1)(x_1 + 1/r_0\gamma_1)}{\rho_0\gamma_1(r_0 + 1)(x_1 + \tau_2/r_0\gamma_1\tau_1) \left[1 + \frac{2(\gamma_1 - \eta_1)(1 - \tau_2/\tau_1)x_1}{\gamma_1^2 r_0(x_1 + \tau_2/\gamma_1 r_0\tau_1)^2} \right]^{1/2}} \quad (7)$$

The "1" subscripts on x , Γ , η , γ , etc. refer to evaluations at $\sigma^2 = 1$. Under the usual $\gamma_1 r_0 \tau_1 \gg \tau_2$ assumption, m_1 is approximately

$$m_1 = \left[\frac{r_0 \Gamma_1}{2\rho_0 \gamma_1 (r_0 + 1)} \right]^2 \left\{ 1 + \left[1 + \frac{4\rho_0(r_0 + 1)}{\Gamma_1 r_0^2} \right]^{1/2} \right\}^2 \quad (8)$$

The curves in Fig. 1 show how m_1 varies as a function of r_0 and τ_2/τ_1 . It is interesting to note from these plots that at $\rho_0 = 1$, the value of m_1 is closer to threshold at higher values of τ_2/τ_1 than it is at lower values of τ_2/τ_1 . But at $\rho_0 = 2$, just the reverse is true — m_1 is nearest threshold at $\tau_2/\tau_1 = 1$. It thus follows that there is some value of ρ_0 producing virtual independence between m_1 and τ_2/τ_1 . The value of m_1 at $\tau_2/\tau_1 = 1$ (a first-order loop) is

$$m_1 = \left(\frac{\Gamma_1}{\rho_0 \gamma_1} \right)^2 \quad (9)$$

whereas the value of m_1 for $\tau_2 \ll \tau_1$ is given in Eq. (8). The value of ρ_0 making these the same is

$$\rho_0 = \Gamma_1 = 1.16 \text{ (or 0.65 dB)} \quad (10)$$

This value of ρ_0 introduces 1 rad rms phase jitter at a margin $m_1 = 1/\gamma_1^2 = 2.31$ (or 3.64 dB) regardless of τ_2/τ_1 and r_0 .

5. The Design Point Producing $\sigma_0^2 = 1$

Sometimes one desires to set the design point SNR ρ_0 so that 1 rad rms actual phase jitter occurs at zero dB

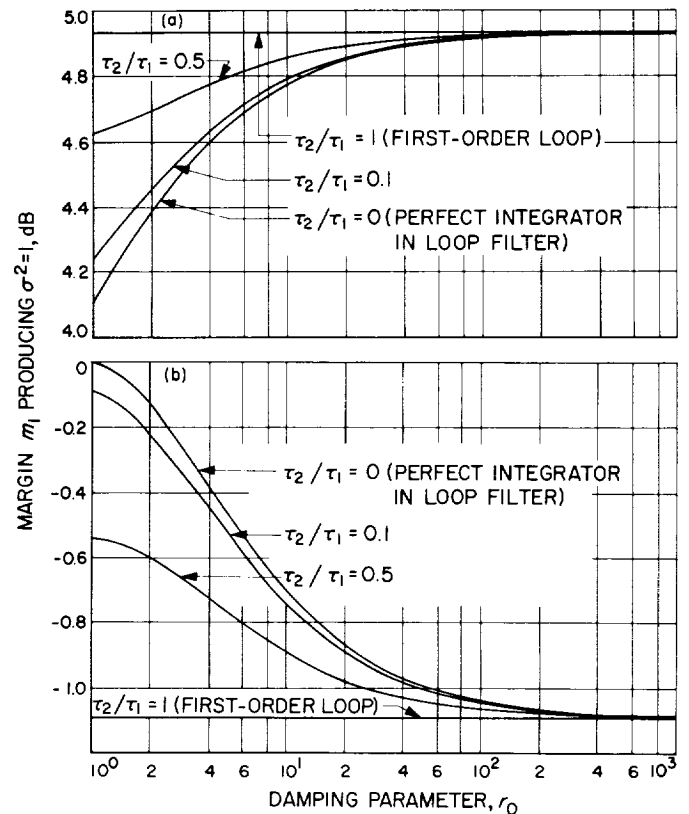


Fig. 1. Value of margin producing 1-rad rms phase jitter: (a) loop design SNR $\rho_0 = 1$; (b) loop design SNR $\rho_0 = 2$

margin — at the design point. The value of ρ_0 so required, denoted here as ρ_{01} , is readily found by inserting $x_1 = 1$ into Eq. (7)

$$\begin{aligned} \rho_{01} &= \frac{\Gamma_1(r_0 + \tau_2/\tau_1)(1 + 1/r_0\gamma_1)}{\gamma_1(r_0 + 1)(1 + \tau_2/r_0\gamma_1\tau_1) \left[1 + \frac{2(\gamma_1 - \eta_1)(1 - \tau_2/\tau_1)}{\gamma_1^2 r_0(1 + \tau_2/\gamma_1 r_0\tau_1)^2} \right]^{1/2}} \\ &\approx \frac{\Gamma_1(r_0\gamma_1 + 1)}{\gamma_1^2(r_0 + 1) \left[1 + \frac{2(\gamma_1 - \eta_1)}{\gamma_1^2 r_0} \right]^{1/2}} \end{aligned} \quad (11)$$

When $r_0\gamma_1\tau_1 \gg \tau_2$, it is seen that ρ_{01} depends only on r_0 ; but otherwise ρ_{01} is a function of τ_2/τ_1 as well. Figure 2 shows how ρ_{01} , r_0 , and τ_2/τ_1 are interrelated.

Note that the value of ρ_{01} for $r_0 \leq 4$ (i.e., at damping factor $\zeta \leq 1$) and small τ_2/τ_1 is $\rho_{01} \approx 2$. With such a design, the SNR within the receiver pass band ($w_{rec} = 2w_L$) takes the approximate value

$$\rho_{rec_0} = \frac{A_0^2}{N_0 2w_{L_0}} = \frac{\rho_{01}}{2} \approx 1 \quad (12)$$

That is, a unity SNR into the receiver produces 1 rad actual phase jitter; the linear theory, however, would predict only $\sigma^2 = 0.5$.

6. Translating Design Points

Suppose the original design specifications for a receiver were ρ_0 , w_{L_0} , ζ_0 , etc. Once this loop has been fabricated, the receiver has built into it a fixed set of resistors, capacitors, gains, etc., which produce a certain operating characteristic. It is quite clear upon reflection that the set $\rho_0, w_{L_0}, \zeta_0, \dots$ is not unique in specifying the receiver because any arbitrary operating point has its own SNR, bandwidth, damping, etc., and these values could have been used equally as well as the original set, and the various resistors, capacitors and gains in the device would be unaffected. The question we consider here is, "How are these various design specifications related?"

Let us consider a design set ρ'_0 , w'_{L_0} , and ζ'_0 which produces the same receiver as ρ_0 , w_{L_0} , and ζ_0 . For conveni-

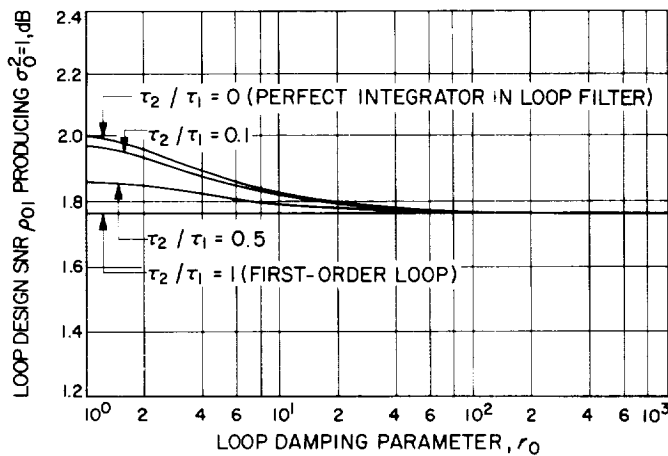


Fig. 2. The value of loop SNR ρ_{01} producing 1 rad actual phase error at design point

ence, we assume $r_0\tau_1 \gg \tau_2$ and $r'_0\tau_1 \gg \tau_2$ and, further, that $\rho_0 w_{L_0} \ll w_H$ and $\rho'_0 w'_{L_0} \ll w_H$. The first of these restrictions produces the linear theoretical parameters

$$w_L \approx \frac{1+r}{2\tau_2}$$

$$\zeta \approx \frac{1}{2} r^{1/2} \quad (13)$$

and the second provides $\alpha/\alpha_0 \approx A/A_0 = m^{1/2}$.

Now let us suppose that the loop is operating at an SNR equal to ρ'_0 in its bandwidth at that point, w'_{L_0} , and

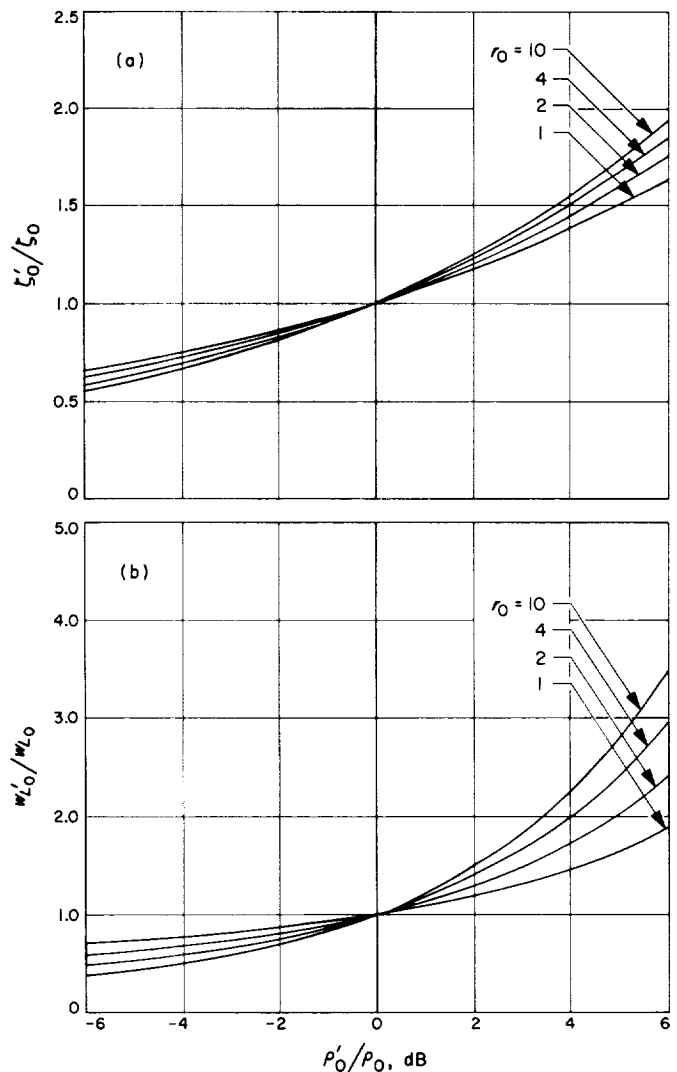


Fig. 3. Translation of bandwidth and damping factors between design points: (a) ζ'_0/ζ_0 vs ρ'_0/ρ_0 ; (b) w'_{L_0}/w_{L_0} vs ρ'_0/ρ_0

a damping factor ζ'_0 is evident. Referred to the original design, these are

$$\begin{aligned}\frac{w'_{L_0}}{w_{L_0}} &= \frac{1 + (m')^{1/2} r_0}{1 + r_0} \\ \frac{\zeta'_0}{\zeta_0} &= (m')^{1/4} \\ \frac{\rho'_0}{\rho_0} &= \frac{m' (1 + r_0)}{1 + (m')^{1/2} r_0}\end{aligned}\quad (14)$$

where m' represents the signal margin relative to the original design

$$m' = \left\{ \frac{(\rho'_0/\rho_0) r_0}{2(1 + r_0)} \left[1 + \left(1 + \frac{4(1 + r_0)}{(\rho'_0/\rho_0) r_0^2} \right)^{1/2} \right] \right\}^2 \quad (15)$$

Substitution of Eq. (15) into Eq. (14) produces the curves given in Fig. 3. These show as a function of the design SNR ρ'_0/ρ_0 just how the bandwidth and damping factors change. Figure 4 shows the way the receiver margin for a design at ρ_0 varies as a function of ρ'_0 . As a specific example, with $r_0 = 2$ and $\rho_0 = 2$ (i.e., an SNR = 1

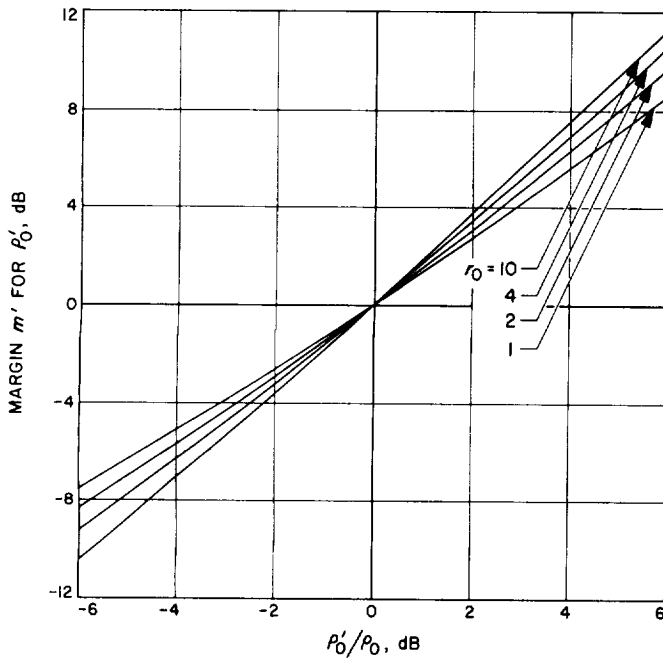


Fig. 4. Value of loop margin for receiver designed at ρ_0 to have a loop SNR equal to ρ'_0

in the receiver passband) and with $\rho'_0 = 1$ (i.e., an SNR = 1 in the loop bandwidth), we have

$$\begin{aligned}\frac{w'_{L_0}}{w_{L_0}} &= 0.738 \\ \frac{\zeta'_0}{\zeta_0} &= 0.784 \\ m' &= 0.368 = -4.3 \text{ dB}\end{aligned}\quad (16)$$

At larger values of r_0 , the values of w'_{L_0}/w_{L_0} and m' are somewhat more drastic.

B. Digital Communication and Tracking: Analysis of the Tracking Loop of the Mariner V Ranging System, R. M. Gray

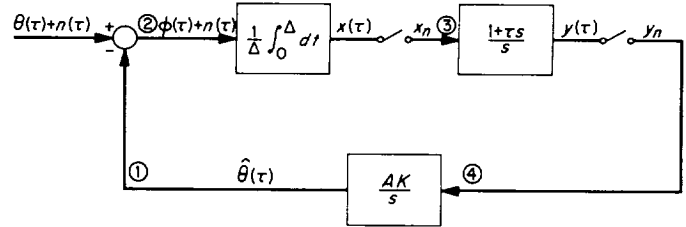
1. Introduction

The sample-data tracking loop of the *Mariner V* ranging system is analyzed.

Pertinent results are compared with those predicted by synthesis of the loop, assuming continuous sampling.

2. The Tracking Loop and Its Transfer Function

A simplified linear-equivalent block diagram and equations for signals at each point in the loop are given in Fig. 5. The input signal $\theta(t)$ is assumed to be some



$$\hat{\theta}(n\Delta) = \hat{\theta}_n$$

$$N = \frac{1}{\Delta} \int_0^\Delta n(\tau) d\tau$$

$$\textcircled{1} \quad \hat{\theta}_{n+1} = \hat{\theta}_n + AK\Delta y_n$$

$$\textcircled{2} \quad \phi(\tau) = \theta - \hat{\theta}(\tau)$$

$$\textcircled{3} \quad x_{n+1} = \theta - \hat{\theta}_n - \frac{1}{2} AK\Delta y_n + N_{n+1} = \phi_n - \frac{1}{2} AK\Delta y_n + N_{n+1}$$

$$\textcircled{4} \quad y_{n+1} = y_n + (\Delta - \tau)x_n + \tau x_{n+1}$$

Fig. 5. Tracking loop block diagram and signal equations

constant θ . The noise $n(t)$ is assumed to be stationary, white Gaussian noise, and in direct analogy with a continuous loop, with double-sided spectral density N_n/A^2 ; x_n and y_n are samples at $\tau = n\Delta$ of the loop error signal $x(t)$ and the VCO input $y(t)$, respectively.

The z -transforms (Laplace transforms with $z = e^{s\Delta}$) of the system equations listed in Fig. 5 yield the corresponding transformed equations

$$\begin{aligned} (1) \quad Y &= \frac{1}{AK\Delta} \left\{ \frac{1-z}{z} \right\} \Theta \\ (2) \quad \Phi &= \Theta - \hat{\Theta} \\ (3) \quad \Phi &= X/z + \frac{1}{2} AK\Delta Y - N/z \\ (4) \quad Y &= (\tau - \Delta) \frac{z - \alpha}{z - 1} X \end{aligned} \quad (1)$$

where $\alpha = 1/(1 - \Delta/\tau)$. The capital letters represent the z -transforms of the corresponding signals denoted in lower case as, for example,

$$\Theta = \sum_{n=0}^{\infty} \theta(n\Delta) z^{-n\Delta} = \theta \frac{z}{z-1}$$

Combining the first three of the above equations into the last we obtain

$$\Theta = \left\{ 1 + \left(\frac{1-z}{z} \right) \left[\frac{1}{AK\Delta z} \left(\frac{z-1}{z-\alpha} \right) \frac{1}{\tau\Delta} + \frac{1}{2} \right] \right\} \hat{\Theta} - \frac{N}{z} \quad (2)$$

Rearrangement of terms gives

$$\hat{\Theta} = L(z) \Theta + \frac{1}{z} L(z) N \quad (3)$$

where the z -transfer function $L(z)$ is given by

$$L(z) = \frac{2z^2(z-\alpha)}{z(z+1)(z-\alpha) - \frac{2\alpha}{AK\Delta\tau}(z-1)^2} \quad (4)$$

The *Mariner V* ranging loop design was based on continuous sampling theory to have critical damping and a noise bandwidth of $w_L = 0.1$ Hz, leading to values

$\tau = 25$ s, $\Delta = 1$ s, $AK = 4/625 = 0.0064$, and producing the loop z -transfer function

$$L(z) = \frac{2z^2(z-25/24)}{z(z+1)(z-25/24) - \frac{1250}{96}(z-1)^2} \quad (5)$$

3. Loci of Poles of the Loop z -Transfer Function

In order to investigate stability of the loop and the allowable margin for the parameters τ and AK , we may plot the loci of the poles of $L(z)$ both as a function of AK with τ fixed and vice-versa. Thus, we plot the root-loci of the equations

$$\begin{aligned} AK \left[\frac{12z(z+1)\left(z - \frac{25}{24}\right)}{(z-1)^2} \right] &= 1 \\ \tau \left[\frac{z(z+1)(z-1)}{z^3 + \left(1 + \frac{625}{2}\right)z^2 - \frac{4}{AK}z + \frac{625}{2}} \right] &= 1 \end{aligned} \quad (6)$$

To allow the use of an available computer program, the substitution $w = 1/z$ was made and the loci of the equations

$$\begin{aligned} AK \left\{ \left(\frac{25}{2} \right) \frac{(w+1)(w-24/25)}{w(w-1)^2} \right\} &= -1 \\ \tau \left\{ \frac{(w^2-1)}{\frac{625}{2}w^3 - \frac{625}{2}w^2 + \left[\frac{627}{2} \right]w + 1} \right\} &= -1 \end{aligned} \quad (7)$$

were plotted. Sketches of these plots appear in Fig. 6. Note in the figure that the conformal mapping $w = e^{-z\Delta}$ maps the left half of the s -plane inside the unit circle, with the j -axis becoming the unit circle.

The poles of $L(z)$ for $AK = 0.0064$ and $\tau = 25$ are indicated in Fig. 6. They are within the unit circle of the w -plane (and therefore within the left half of the s -plane) so that the loop is stable.

4. Allowable Margin of AK and τ

It can be seen from Fig. 6 that AK can increase to 0.082, or by roughly a factor of ten without affecting stability; τ can increase to approximately 312, also roughly a factor of ten without affecting stability.

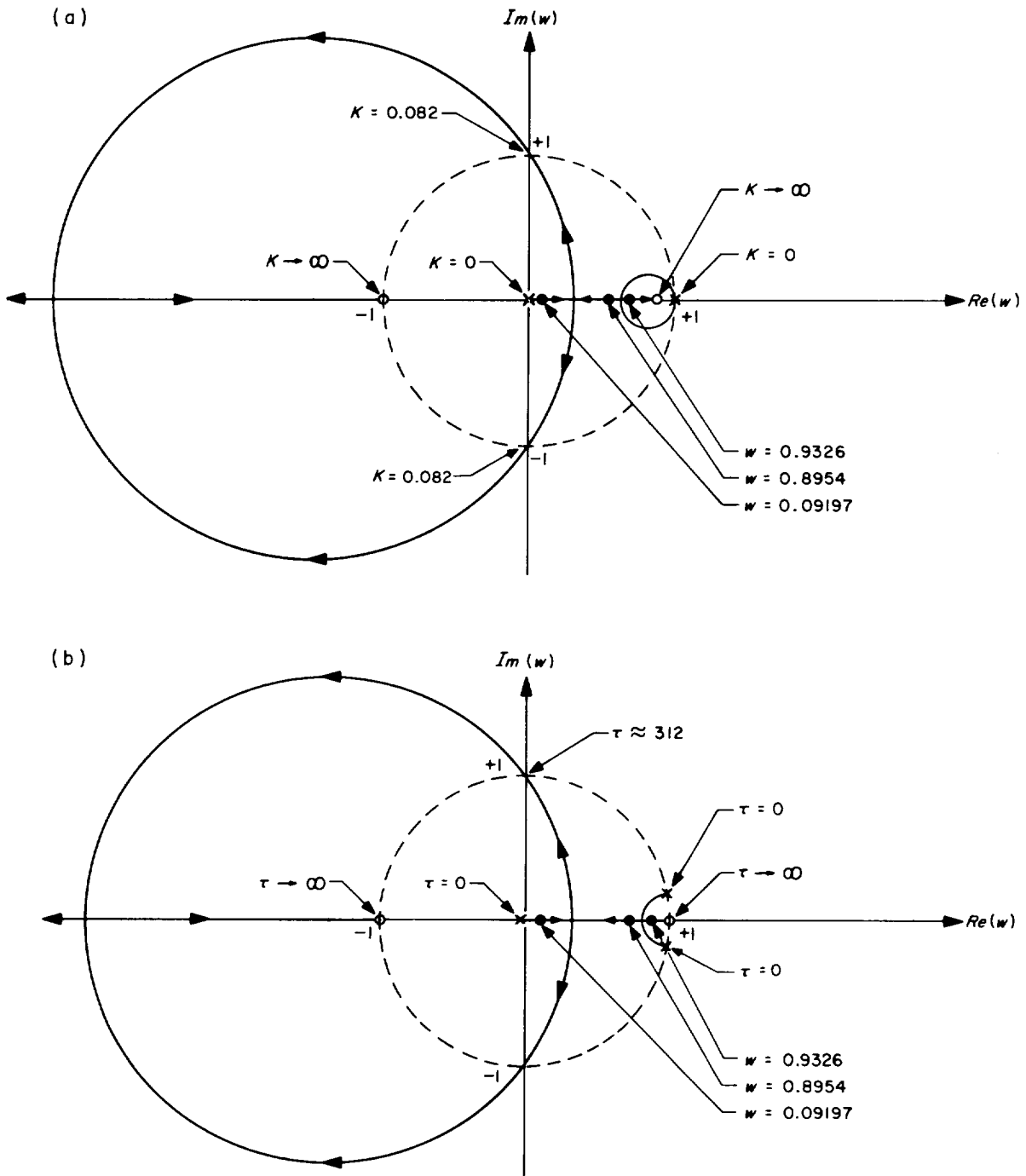


Fig. 6. Loci of the poles of $L(z) = L(1/w)$: (a) $K = 0.0064$, (b) $\tau = 25$

5. Noise Bandwidth

The noise bandwidth of the loop, w_N , is given by the equation

$$\text{Total noise power} = \oint_{|z|=1} L(z) L\left(\frac{1}{z}\right) S_{NN}(z) dz = w_N \frac{N_0}{A^2} \quad (8)$$

Note that this is merely the standard expression for the noise bandwidth transformed into the z -plane [where $L(-z) \rightarrow L(1/z)$, $L(s) \rightarrow L(z)$]. Since

$$R_{NN}(n\Delta) = \begin{cases} E[N^2] = \frac{1}{\Delta^2} \int_0^\Delta \int_0^\Delta E[n(t_1)n(t_2)] dt_1 dt_2 = \frac{1}{\Delta} \frac{N_0}{A^2}, & n = 0 \\ (E[N])^2 = 0, & n \neq 0 \end{cases} \quad (9)$$

we have

$$S_{NN}(z) = \frac{1}{\Delta} \frac{N_0}{A^2} = \frac{N_0}{A^2} \quad (10)$$

Therefore,

$$w_N = \oint_{|z|=1} L(z) L(w) dz = \sum \text{residues of } L(z) L(w) \quad (11)$$

where the summation is taken only over those poles lying inside the unit circle of the w -plane (outside the unit circle in the z -plane), i.e., over the poles of $L(w)$. We therefore, have

$$w_N = \sum_{\substack{\text{poles of} \\ L(w)}} \text{residue of } L(z) L(w) = 0.1029$$

The noise bandwidth concurs very well with that predicted by the synthesis, assuming continuous sampling.

C. Information Systems: Addition of Conditional-Compile Option to SDS FORTRAN-II and Real-Time-FORTRAN-II Compilers, W. B. Kendall

1. Description of the Conditional-Compile Option

It has been found that the real-time-FORTRAN-II (Ref. 2) programming language provided by Scientific Data Systems (SDS), Santa Monica, California, for their nine-hundred series computers is a valuable tool for working with experimental real-time programs. To

extend the usefulness of this language, a feature of SDS FORTRAN-IV has been incorporated into the FORTRAN-II and Real-Time-FORTRAN-II compilers of the SDS MONARCH operating system. This feature is the so-called conditional-compile, or X-option.

To use the X-option, an X is placed in column 1 of any input record of a FORTRAN program. These X-records will then be compiled as if the X's were C's (i.e., the X-records will be treated as comments and *not* compiled) *unless* the parameter list² passed to the compiler from MONARCH contains the parameter X. When the list of parameters from MONARCH *does* contain X (e.g., Δ FORTRAN SI, BO, X, LO), the X's in column 1 are treated as blanks, and the X-records are compiled. Thus, it is possible to include diagnostic statements in a program with X's in column 1, and then when the program is debugged the diagnostic statements can be converted to comments by not directing the compiler to compile the X-records.

The JPL implementation of the X-option has one degree of flexibility that is not in SDS FORTRAN-IV. In FORTRAN-IV, symbolic and Boolean statements require an S or B in column 1, and this precludes use of the X-option with these statements. However, now in real-time-FORTRAN-II, if column 1 contains an X and X-records are being compiled, then an S or B in column 2 will be compiled, as if it were in column 1.

²See SDS publication 90 05 66, *SDS MONARCH Reference Manual*, for a description of MONARCH parameter lists.

An example of part of a program using the X-option follows:

Column: 1234567

```

X      PRINT 10
      PRINT 1, A, B, C

X      C          , D, E
      1 FORMAT ($ HEADING $, 5F10.0)
      10 FORMAT ($ CHECK OUT $)

S      LDA N
S      STA I
XS     STA ITEST

```

2. Implementation

The changes to the MONARCH system required to implement the X-option can be divided into two groups: (1) changes to the FORTRAN and Real-Time-FORTRAN compilers, and (2) other changes required to enable MONARCH to process the parameter X. First we will describe the compiler changes.

a. Compiler programmed operators. The FORTRAN-II and Real-Time-FORTRAN-II compilers use an extensive set of programmed operators (POP's) to process input records. Incorporation of the X-option into these compilers involves the following POP's.

CSA (character scan or alternate). This POP determines if the next character in the input record is the character pointed to by the address field of this POP. If it is not, an "answer flag" is set false. If it is, the answer flag is set true and the next character of the input record is fetched for future processing.

JAT (jump if answer true). This POP checks the answer flag, and if it is true, branches to the location pointed to by the address field of this POP.

JAF (jump if answer false). Same as JAT, except this POP branches if the answer flag is false.

CSF (character scan or fail). This POP determines if the next character in the input record is the character pointed to by the address field of this POP. If it is not, a "fail" exit is taken. If it is, the next character of the input record is fetched to be processed next, and the program continues at the location following the CSF POP.

FET (fetch). This POP fetches the quantity pointed to by the address field of this POP, and places it at the bottom of the "work list." In the main part of the compiler, the address of the bottom of the work list is contained in the index register, so that the last item put into the work list can be found by addressing location 0,2.

JRS (jump recursively to subroutine). This POP causes a branch to the subroutine pointed to by the address field of this POP. The branch is made via the compiler's recursion monitor, so that the subroutine to which the branch is made can return to the location following the JRS POP by making a branch to a location named EXIT. In other words, JRS to a subroutine is analogous to BRM (branch and mark place) to a subroutine, and BRU EXIT is analogous to BRR (return branch) from a subroutine.

b. Compiler changes. The first time an input record is examined by the compiler is when it looks ahead to see if the next input record is a continuation record (which should be processed as part of the preceding record). A continuation record is one which has spaces in columns 1 through 5 and a legal continuation character in column 6. The code which checks for this is the following:

```

Q211  BRM  NXINCH  GET NEXT CHARACTER INTO A-REGISTER
      SKA  CARRFG  SKIP IF CHARACTER IS NOT END OF RECORD
      BRU  Q211    TRY NEXT RECORD
      LDX  FOUR    WILL COUNT FIVE CHARACTERS
      STX  ACHTP2  TEMPORARY STORAGE
Q213  SKE  SPACE   SKIP IF CHARACTER IS A SPACE
      BRU  Q214    NOT A CONTINUATION RECORD
      BRM  NXINCH  GET NEXT CHARACTER INTO A-REGISTER
      SKR  ACHTP2  DECREMENT COUNT, SKIP IF THEN NEGATIVE
      BRU  Q213    GO CHECK FOR ANOTHER SPACE
      SKA  CNCHFG  SKIP IF SIXTH CHARACTER IS NOT A CONTINUATION CHARACTER
      BRU  Q208    GO PROCESS REST OF RECORD AS CONTINUATION OF PRECEDING
      *          RECORD
Q214  . . .      NOT A CONTINUATION CARD; RESET POINTERS AND EXIT.

```

For the conditional-compile option, a flag whose address is XFLAG is set negative by the compiler initialization routine of X-records are to be compiled, and nonnegative if X-records are to be treated as comments. The code for checking for continuation records was modified to use this flag in the following way. Location Q213-1 was changed to BRU QX3, where QX3 is a patch containing:

```

QX3  STX   ACHTP2
      SKE   X           SKIP IF COLUMN ONE CONTAINS AN X
      BRU   Q213        PROCESS RECORD IN THE NORMAL WAY
      SKN   XFLAG       SKIP IF X-RECORDS ARE TO BE COMPILED
      BRU   Q214        TREAT X IN COLUMN ONE AS NONSPACE
      BRU   Q213+2      TREAT X IN COLUMN ONE AS SPACE

```

If an input record is not disposed of as a continuation record, then it is checked again in the comment-statement translation part of the statement-initialization routine. The statement-initialization routine resets some flags and pointers, gets the first character of the next record, and then enters the comment-statement translation routine, which is:

```

COMTSX  CSA   C        SET ANSWER FLAG TRUE IF CHARACTER IS C
        JAF   EXIT     IF NOT C, THE INITIALIZATION IS FINISHED

```

* CHARACTER IS C; PRINT AND REINITIALIZE

...

The changes needed to check XFLAG at this point were made by changing location COMTSX+1 to JAF QX1, where QX1 is the location of the following patch.

```

QX1  SKN   XFLAG       SKIP IF X-RECORDS ARE TO BE COMPILED
      BRU   $+2
      BRU   EXIT       IGNORE NON-C UNTIL LABEL-FIELD TRANSLATION
      CSA   X          SET ANSWER FLAG TRUE IF CHARACTER IS X
      JAT   COMTSX+2   IF CHARACTER IS X, TREAT AS IF C
      BRU   EXIT       CHARACTER NOT C OR X, INITIALIZATION IS FINISHED

```

Finally, if the X-record is not treated as a comment, then X-records are to be compiled, and columns 1 through 6 will be examined by the label-field translation routine. In Real-Time-FORTRAN-II this routine differs from FORTRAN-II, since FORTRAN-II does not allow B or S in column 1 for Boolean or symbolic statements. In FORTRAN-II this routine is:

```

LBFLDX  FET   FOUR     PUT COUNT OF FOUR IN WORK LIST
        JRS   DGCVIN   INITIALIZE DIGIT-CONVERSION ROUTINE
        BRU   Q69
Q68     BRM   NXINCH   GET NEXT CHARACTER INTO A-REGISTER
Q69     . . .
        Routine to "fail" unless A-register contains space or digit; process if digit.
        . . .

```

Q71	SKR	0,2	DECREMENT WORK LIST, SKIP IF NEGATIVE
	BRU	Q68	GO BACK FOR ANOTHER CHARACTER
	BRM	NXINCH	GET SIXTH CHARACTER INTO A-REGISTER
	CSA	SPACE	SET ANSWER FLAG TRUE IF CHARACTER IS SPACE
	JAT	Q72	IF CHARACTER IS SPACE, OK
	CSF	NO	NOT SPACE, FAIL UNLESS CHARACTER IS ZERO
Q72	...		PROCESS RESULTING LABEL

The modification to allow an X in column one consists of replacing the contents of location Q68-1 with BRU QX2, where QX2 contains the patch:

QX2	CSA	X	SET ANSWER FLAG TRUE IF CHARACTER IS X
	JAF	Q69	IF NOT X, PROCESS AS USUAL
	BRU	Q71	IF X, TREAT AS IF SPACE

For Real-Time-FORTRAN-II the label-field translate routine is as follows:

LBFLDX	FET	FOUR	PUT COUNT OF FOUR IN WORK LIST
	JRS	DGCVIN	INITIALIZE DIGIT-CONVERSION ROUTINE
	CSA	B	TEST FOR BOOLEAN STATEMENT
	JAF	Q67A	NOT BOOLEAN
	CLA		IS BOOLEAN
	STA	BOOLFG	SET BOOLEAN FLAG
	BRU	Q71	GO GET NEXT CHARACTER
Q67A	CSA	S	TEST FOR SYMBOLIC STATEMENT
	JAF	Q69	NOT SYMBOLIC, EITHER
	CLA		IS SYMBOLIC
	STA	SYMFLG	SET SYMBOLIC FLAG
	BRU	Q71	GO GET NEXT CHARACTER
Q68	BRM	NXINCH	GET NEXT CHARACTER INTO A-REGISTER
Q69	...		
			Routine to "fail" unless A-register contains space or digit; process if digit.
	...		
Q71	SKR	0,2	DECREMENT WORK LIST, SKIP IF NEGATIVE
	BRU	Q68	GO BACK FOR ANOTHER CHARACTER
	BRM	NXINCH	GET SIXTH CHARACTER INTO A-REGISTER
	CSA	SPACE	SET ANSWER FLAG TRUE IF CHARACTER IS SPACE
	JAT	Q72	IF CHARACTER IS SPACE, OK
	CSF	NO	NOT SPACE, FAIL UNLESS CHARACTER IS ZERO
Q72	...		PROCESS RESULTING LABEL

So that an X in column one could be processed, the contents of location LBFLDX+2 were changed to BRU QX2, where QX2 is the location of the following patch.

QX2	CSA	X	TEST COLUMN ONE FOR X
	JAF	QX2A	IF NOT X, PROCESS AS USUAL
	SKR	0,2	IF X, REDUCE COUNT AND TEST NEXT CHARACTER
	BRM	NXINCH	GET NEXT CHARACTER INTO A-REGISTER
QX2A	CSA	B	TEST FOR BOOLEAN STATEMENT
	BRU	Q67A-4	

The only other compiler change was one to allow the monitor to communicate the status of the X-option to the compiler. The monitor now records the status of the X-option in location 072, setting it negative if X-records are to be compiled, and nonnegative if not. Since location 072 is used by the compiler for temporary storage, the compiler initialization sequence (starting at INIT) was modified to store the contents of location 072 in a location called XFLAG.

c. Other changes. To enable the MONARCH system to process the parameter X in Δ FORTTRAN and Δ RTFTRAN statements, it was necessary to make three changes to the subroutine "Monarch Tables" (Catalog No. 042005D). These are:

(1) Under CODES, the number of parameters acceptable for Δ FORTTRAN statements was changed from 0-3 to 0-4.

(2) Under CODES, the number of parameters acceptable for Δ RTFTRAN statements was changed from 1-8 (!) to 0-4.

(3) Under PARAMS, the addition of the parameter X was made with X = 067606060.

It was also necessary for the "Fortran Action Routine" (Catalog No. 042014E) to be changed:

(1) To have room to receive up to four parameters instead of only three.

(2) To initialize location 072 to 037777777 (non-negative).

(3) To increment location 072 (making it negative) once for each of the four parameters found to be X (=067606060).

Because the Fortran Action Routine loads either the FORTRAN-II compiler or the Real-Time-FORTRAN-II compiler, the above changes were sufficient to properly process both Δ FORTTRAN and Δ RTFTRAN statements.

D. Precision Time Synchronization Development: The Central Frequency Synthesizer, G. U. Barbani

1. Introduction

The central frequency synthesizer (CFS) has been in continuous operation at DSS 13 since May 3, 1966. A general report on performance, phase noise and component aging follows. The CFS block diagram has been updated to reflect the addition of a 100-k Hz amplifier.

2. CFS Performance

The CFS completed 13,727 h of continuous operation as of March 30, 1967. During the past two quarters, no system or subsystem failures have occurred. However, a loose power cord in the cable wrap-up (SPS 37-40, Vol. III, p. 57, Fig. 24) caused a total loss of dc power to all the modules on the number 2 cold plate. This had the effect of leaving system relays in the "off" position, indicating all systems "normal," consequently, no alarm was activated. Since the station was not on mission control at that time, support personnel were not available for surveillance. This off situation lasted for approximately 6 h. Reconnection of the loose power connector by maintenance personnel returned the system to normal operations.

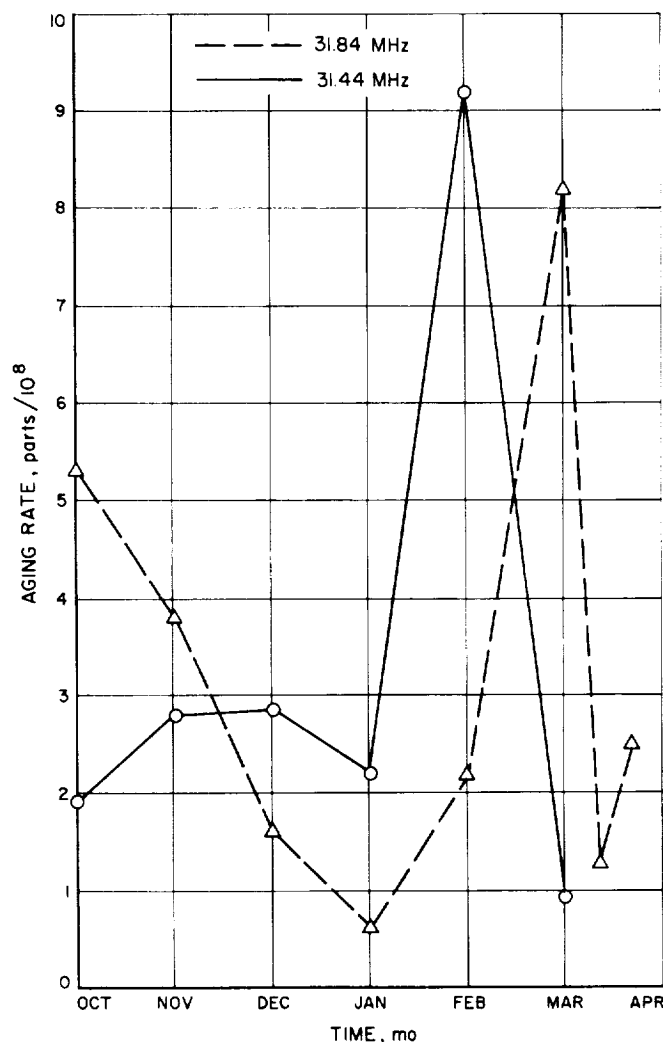


Fig. 7. VCO frequency aging characteristics for 31.44 and 31.84 MHz VCO

The effect of this partial shut down was to disturb the aging characteristics of the 31.44- and 31.84-MHz VCOs. See Fig. 7 during the January–February period. The data for March 1967 show that the 31.44 MHz VCO has apparently returned to a normal condition, while the 31.84 MHz VCO demonstrates a delayed return to normal. Two additional data points were obtained at 10-day intervals to verify the aging rate return of the 31.84 MHz VCO. The phase noise does not show any deviation caused by this thermal disturbance. Figure 8 shows a cyclical behavior in the 35.075 MHz VCO, indicating a possible malfunction in either the oven or thermal control circuitry.

The phase noise characteristics of all four phase-lock loops are shown on Figs. 9 and 10 which show the standard deviation (σ) for the last two quarters. The variations appear to be random and within expected limits. A downward trend in phase noise is evident for all VCOs, thus indicating circuit equilibrium. Refer to SPS 37-42, Vol. III, pp. 71–74 for the first quarter report.

The rubidium vapor frequency standard (Rb 87), serial No. 20, has been operating continuously with the CFS. No failures have ever occurred, and its operation is normal.

3. CFS Additions

A 100-kHz distribution amplifier has been added to supply standard signals to interface with existing equipment used for monitoring station clocks. The amplifier is identical to the existing 125-kHz amplifier, and the

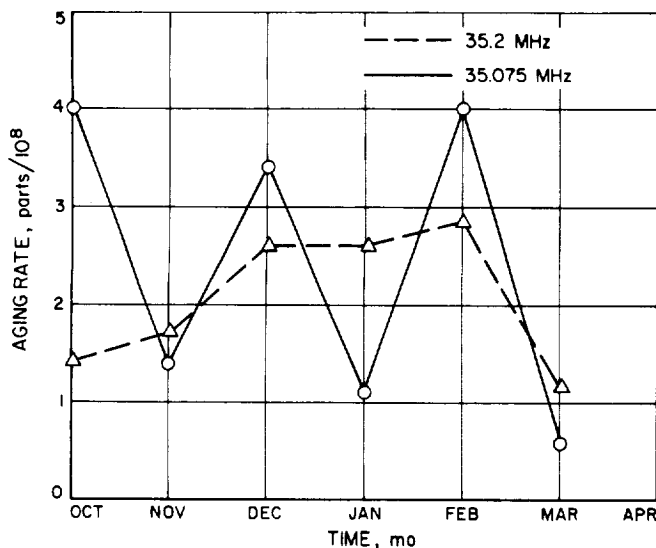


Fig. 8. VCO aging characteristics for 35.075 and 35.2 MHz VCO

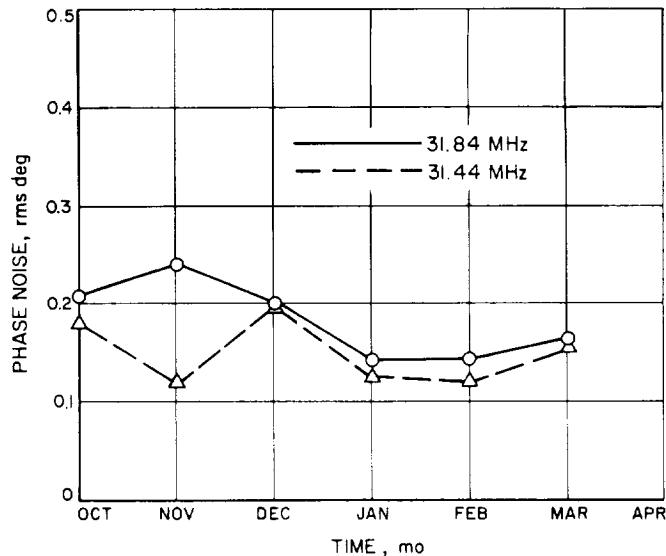


Fig. 9. Phase noise characteristics of 31.44 and 31.84 MHz phase-lock loops

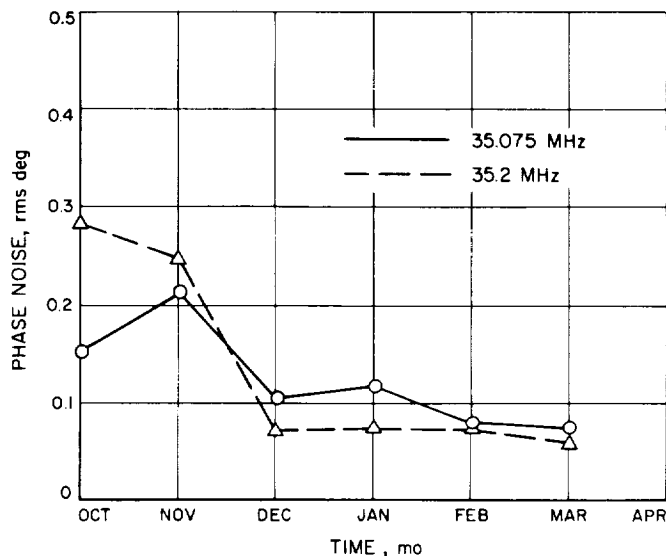


Fig. 10. Phase noise characteristics of 35.075 and 35.2 MHz phase-lock loops

performance data are very nearly identical. Refer to SPS 37-35, Vol. III, pp. 68–71. An updated CFS block diagram appears as Fig. 11.

4. Summary

This report will conclude any further discussion of the CFS. Future reports will be conducted only as part of the deep space station engineering and operations.

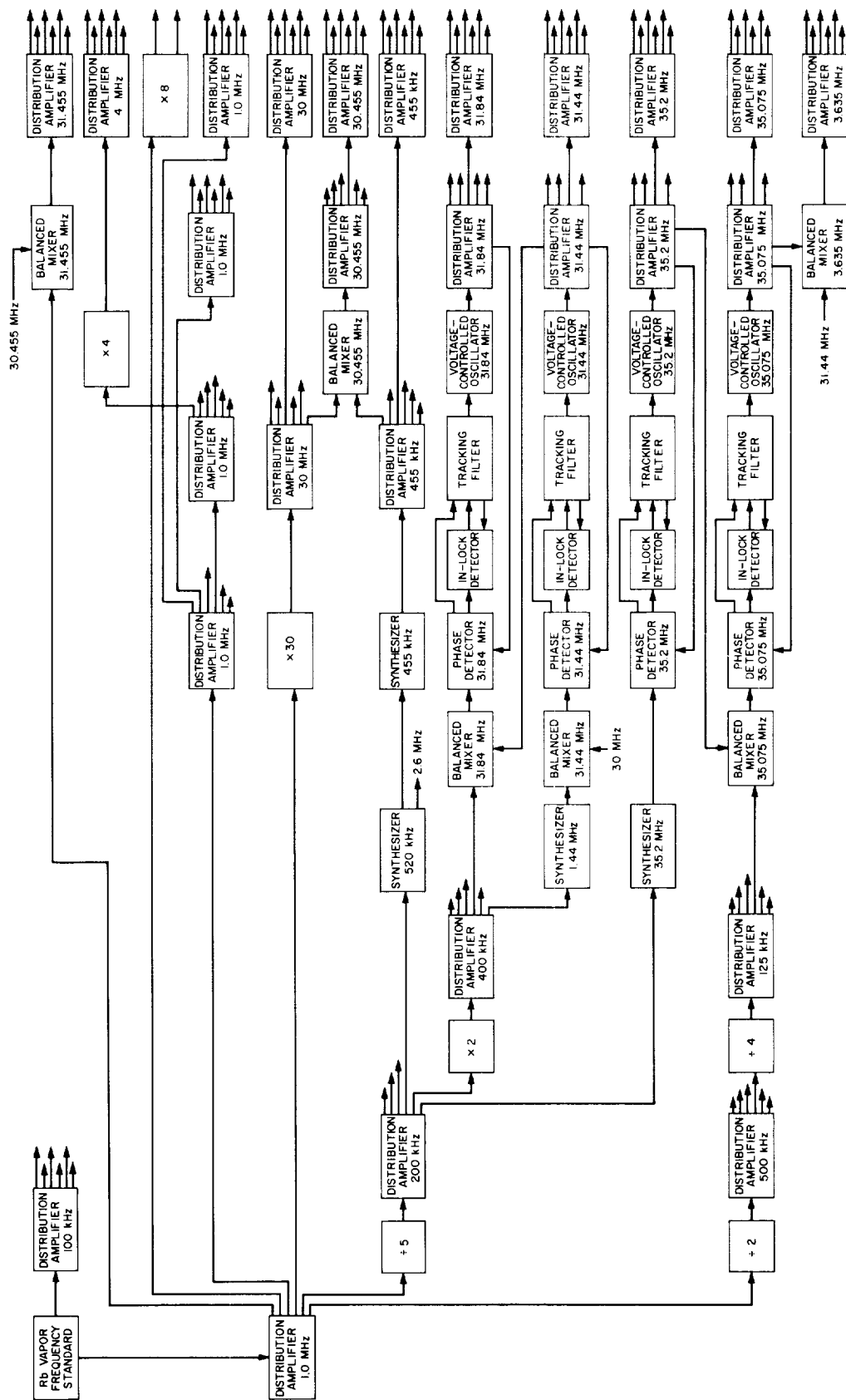


Fig. 11. Updated CFS block diagram

**E. Efficient Antenna Systems: Ultracone, G. S. Levy,
D. A. Bathker, R. E. Cormack, and F. E. McCrea**

1. Introduction

The ultracone is a Cassegrainian feed and front end system designed to yield a total zenith system noise temperature of 18°K. This low temperature is achieved by eliminating all but the most necessary microwave components. The objective of the ultracone project is the determination of minimum practical obtainable temperature and the identification of all remaining temperature sources in the system. The first application of the ultracone will be as a low noise front end for the DSS 13 for *Mariner V* planetary encounter. The Venus DSS will serve as a high-performance backup for the advanced antenna system (AAS).

2. System Description

The ultracone will be capable of reception in either the 2295 or 2388 MHz bands. It was optimized, however, for 2295. It also has satisfactory performance at 2115, if trans-

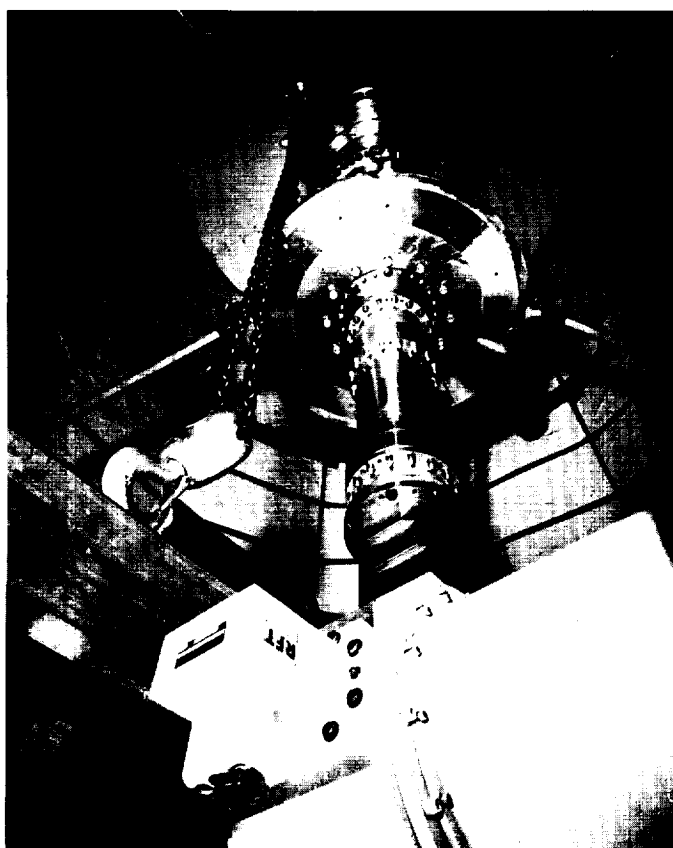


Fig. 12. Ultracone low loss waveguide transmission line from transfer switch to horn

mit capability is required at some future date. Figure 12 is a photograph of the waveguide system between the transfer switch and the radiating horn. Figure 13 is a block diagram of the microwave system in the cone. The feed horn patterns are identical to those now being used in the multifrequency cone of the AAS (SPS 37-35, -38, Vol. IV, pp. 268 and 192, respectively).

The mode generator has been modified from the AAS configuration by shortening and retuning. Figure 14 is a Smith chart plot of the tuned mode generator/horn voltage standing wave ratio (VSWR). The quarter-wave plate is similar in design to the AAS, but its overall length was reduced from 35.25 to 12.12 in. This reduction was accomplished by heavier loading.

A broad band rectangular to circular waveguide transition (Ref. 3) was used to transform from 5.040 in. circular guide to WR 430. This transition allows one mode of polarization, normally right-hand circular polarization (RCP); however, this polarization can be changed by manually unbolting the quarter-wave plate and rotating it with respect to the broad band transition.

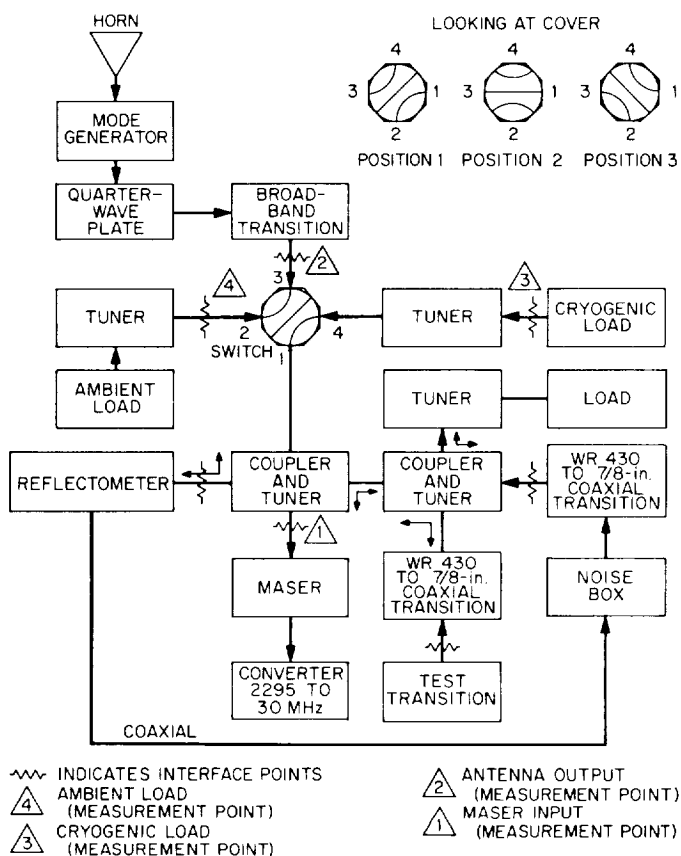


Fig. 13. Ultracone block diagram

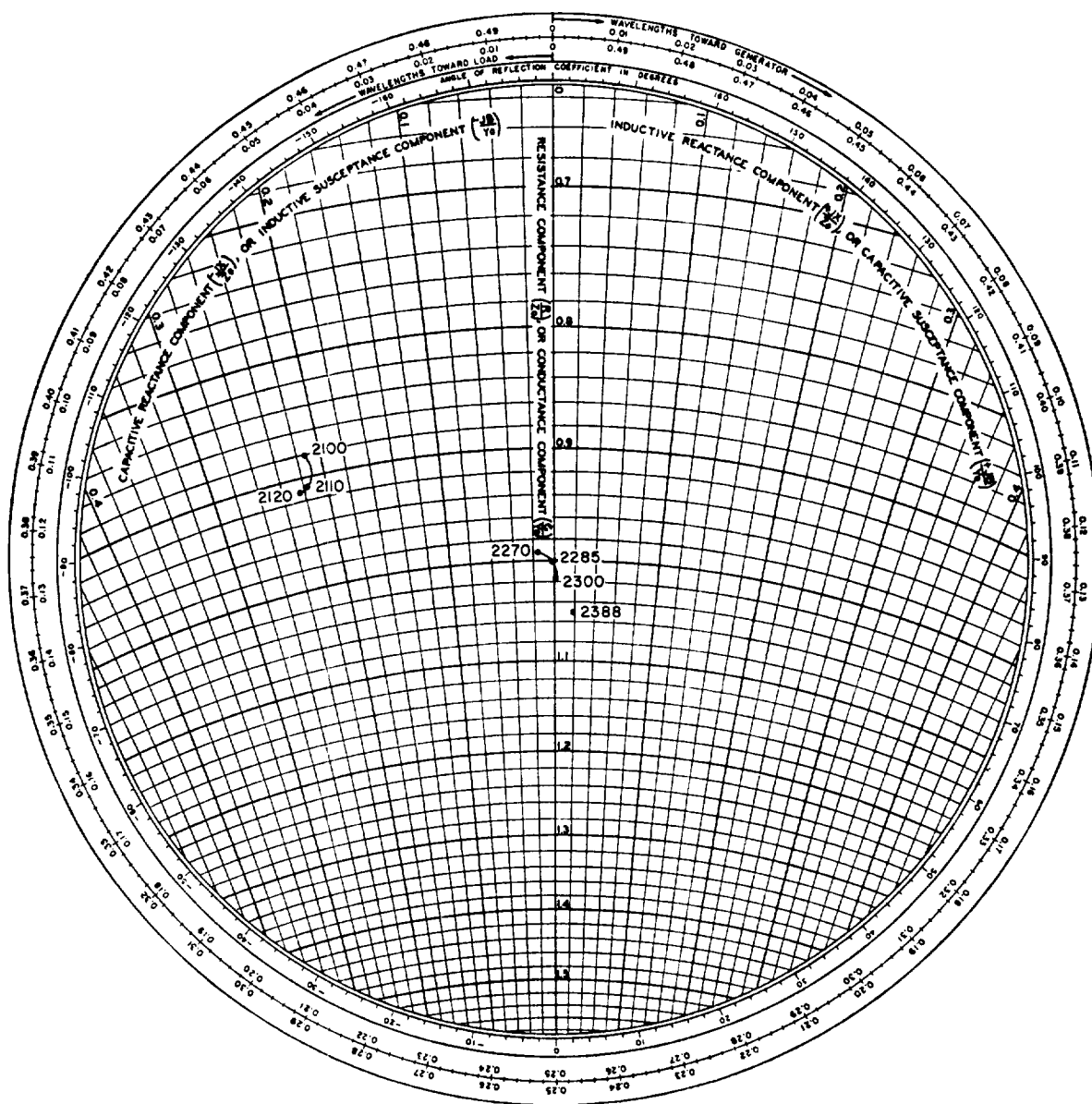


Fig. 14. Smith chart of tuned mode generator and horn

The VSWR and ellipticity were measured, as a function of frequency, in the RCP mode; the results are given in Table 1. These values were optimized by using short 5.040 in. circular waveguide spacers between the mode generator, quarter-wave plate and broad-band transition. It can be seen that the match at 2215 MHz was very much better for the overall system than for the horn-mode generator combination, shown in Fig. 14. This improvement can be explained by the multiple reflections occurring in the system. The RCP energy is reflected as left-hand circular polarization (LCP). The quarter-wave plate converts this polarization to linear polarization with its polarization vector rotated such that the broad-band transition appears to be a waveguide beyond cutoff. Therefore, the energy is again reflected and emerges from the quarter-wave plate as LCP. This energy deteriorates the ellipticity; however, at the frequencies of interest the ellipticity is satisfactory.

Table 1. Final feed horn system data

Frequency, MHz	VSWR	Ellipticity, dB
2115	1.015 ± 0.015	1.18
2270	1.020 ± 0.020	0.30
2285	1.017 ± 0.013	0.28
2297.5	1.012 ± 0.009	0.18
2300	1.014 ± 0.014	0.19
2398	1.025 ± 0.015	0.33

At the output of the transition a three-position waveguide transfer switch is used for noise temperature calibrations. In the future this switch could be used as a transmit-receive switch. A 33-dB cross-guide coupler and tuner unit is used for calibration purposes. From the coupler a waveguide-to-coaxial transition leads to the maser. The maser and the instrumentation of the ultracone are discussed in the following subsections of this article.

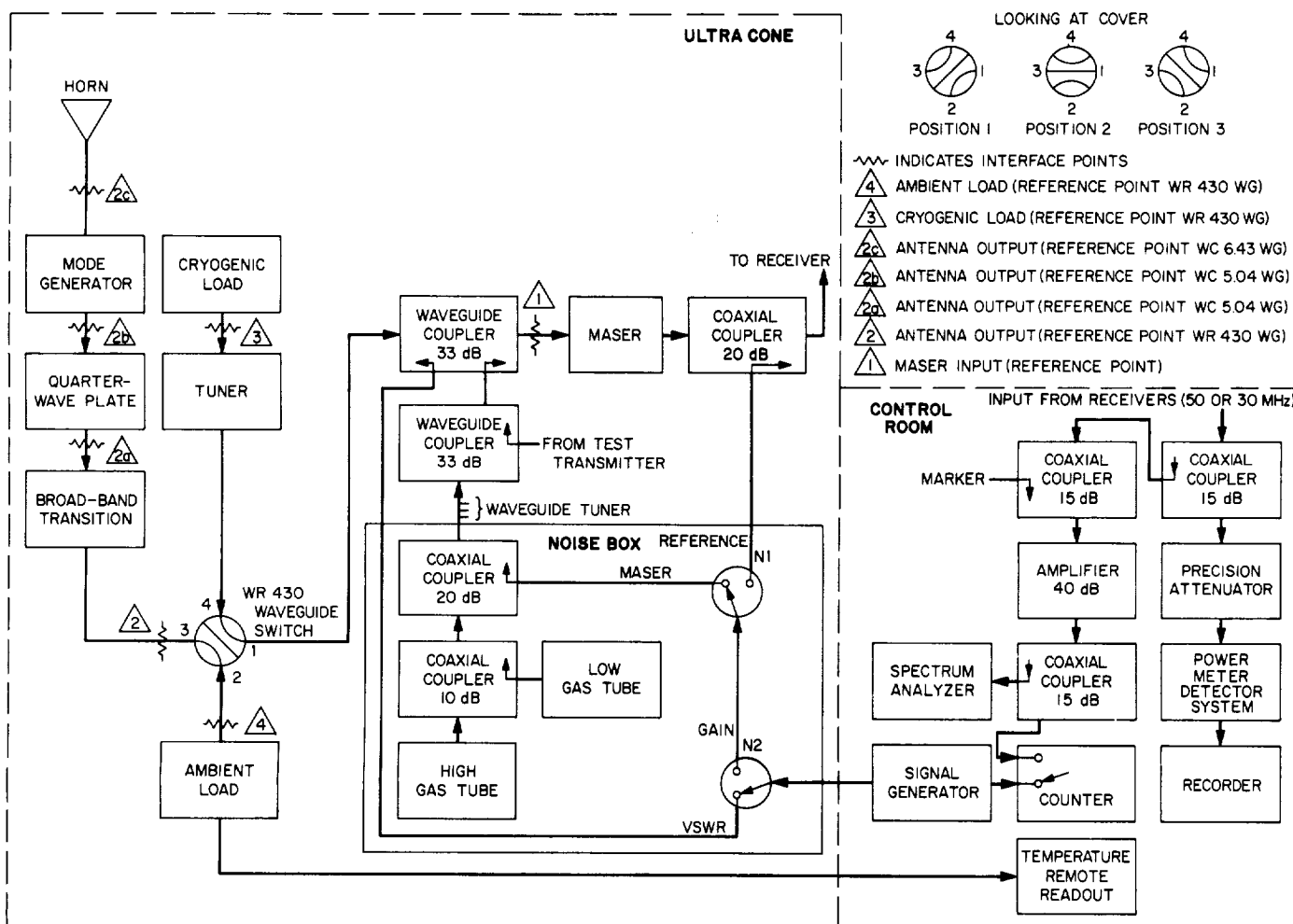


Fig. 15. Block diagram of the S-band ultracone and RF instrumentation rack

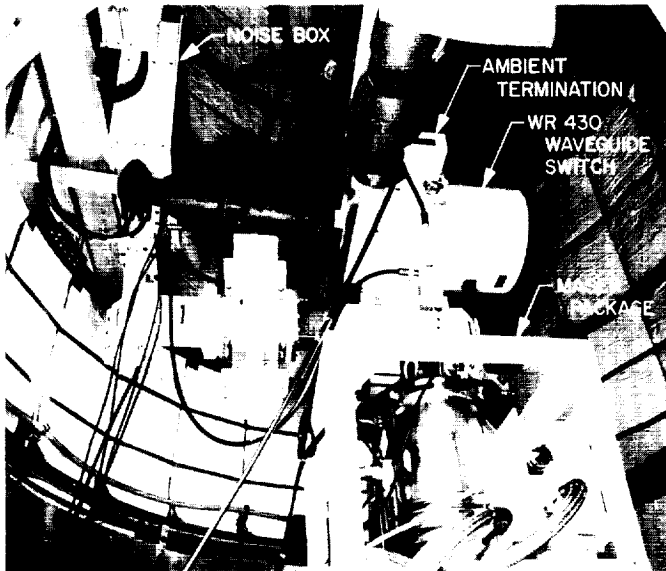


Fig. 16. Lower portion of the ultracone interior

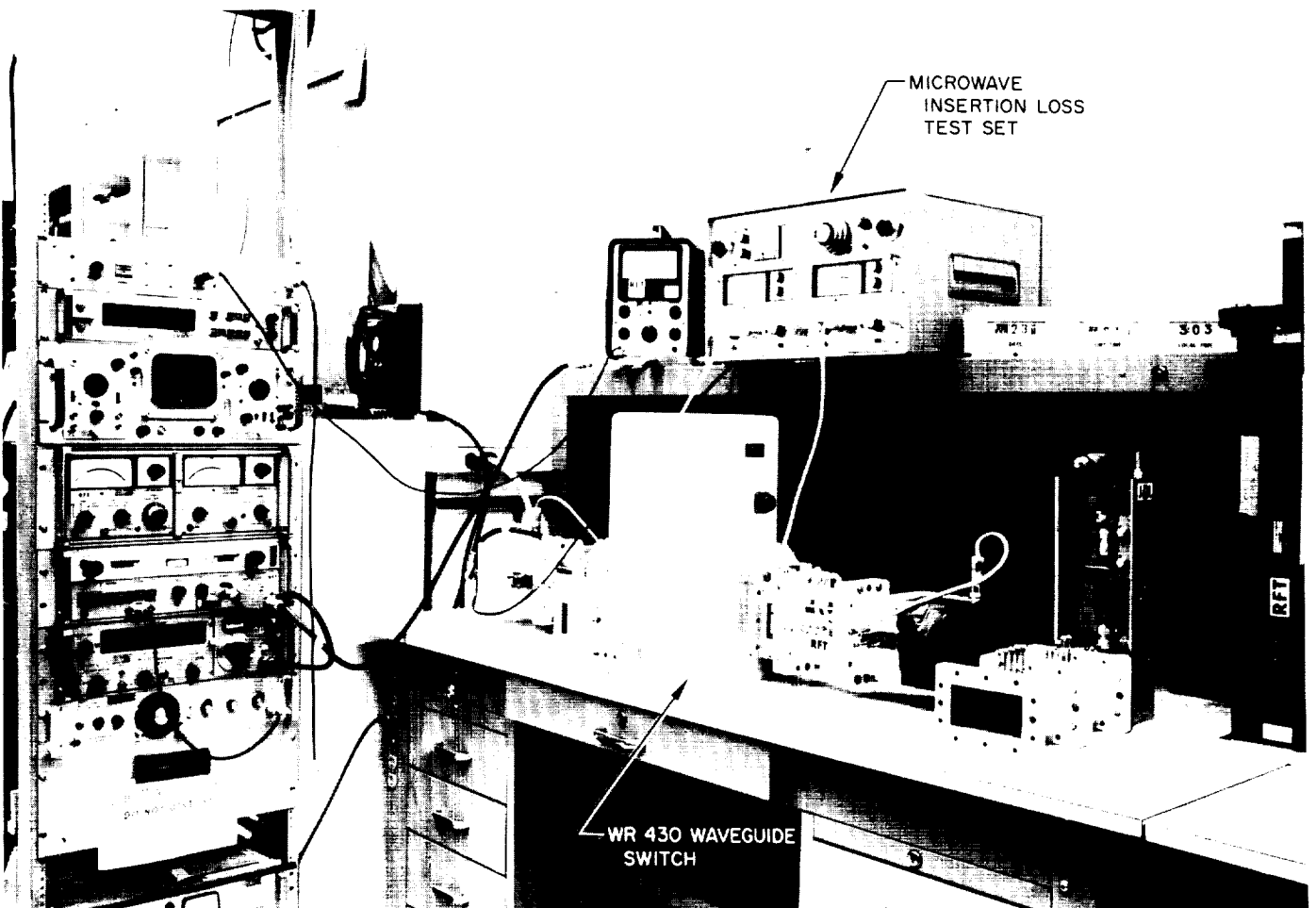


Fig. 17. Ultracone waveguide switch undergoing laboratory insertion loss and VSWR measurements

F. Improved RF Calibration Techniques: S-Band Ultracone RF Instrumentation, D. V. White and C. T. Stelzried

1. Introduction

The S-band Cassegrain ultracone (SCU) project is described in the preceding subsection of this article. The RF instrumentation is similar to that employed in the multifrequency-cone (SPS 37-38, Vol. IV, p. 188) and the Venus DSS R&D cone (SPS 37-40, Vol. III, p. 93). Total system noise temperature, reflectometer and maser gain instrumentation is provided. In addition, there are provisions for absolute antenna, transmission line, and receiver noise temperature calibrations with the use of an all-waveguide liquid nitrogen cryogenically cooled termination. Considerable effort has been expended in insertion loss calibrations of the input waveguide to insure the accuracy of these calibrations.

2. Description

A block diagram of the complete antenna cone and control room RF instrumentation rack is shown in Fig. 15.

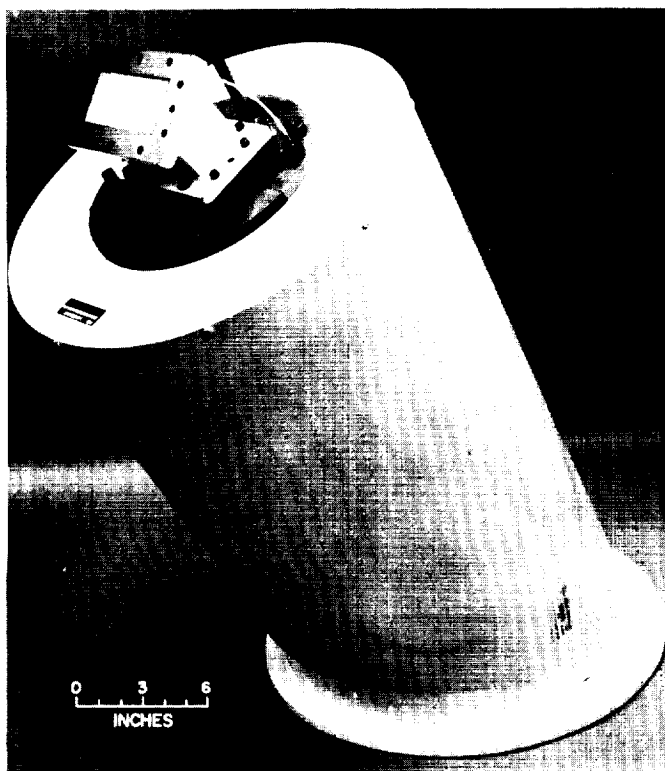


Fig. 18. Liquid nitrogen cooled WR 430 waveguide calibration termination

A photograph (Fig. 16) of the lower portion of the ultracone interior during assembly shows the input transmission line, maser, and calibration instrumentation. Figure 17 shows the cone waveguide switch undergoing laboratory insertion loss and VSWR measurements. Figures 18 and 19 show the liquid nitrogen cooled WR 430 waveguide termination and the noise box interior. The noise box is equipped with a waveguide output to provide the stability obtainable from a waveguide run to the maser input.

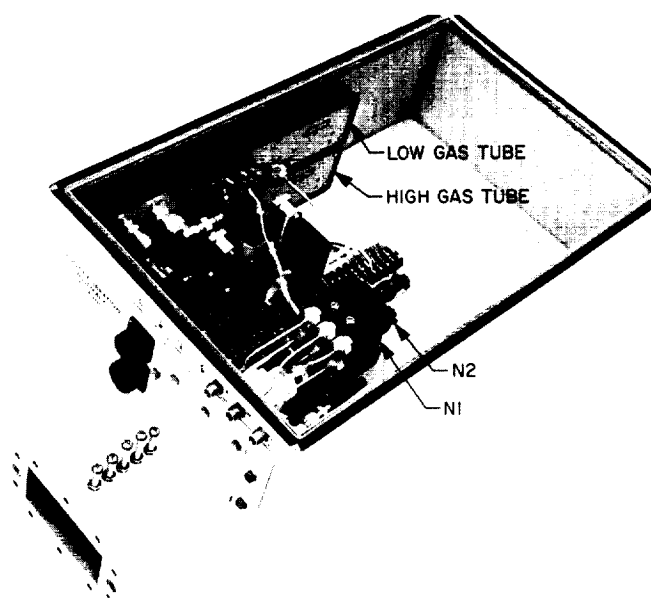


Fig. 19. Noise box instrumentation interior

G. Low Noise Receivers: Ultracone Maser Development, R. C. Clauss

1. Introduction

A tunable traveling wave maser (TWM) for use in the ultracone has been completed. Low noise temperature at 2295 MHz has been the primary consideration in this work. Operational capability at 2388 MHz has also been achieved without noticeably degrading performance at 2295 MHz.

At 4.4°K the TWM provides more than 35 dB net gain in a tunable range from 2230 to 2430 MHz. The use of single crystal yttrium iron garnet (YIG) isolator material, ruby of improved quality, and a figure eight magnetic field staggering coil has substantially improved the performance over existing S-band TWMs. The predicted equivalent input noise temperature (at 2295 MHz) at the waveguide interface to the maser package is 4.1°K.



Fig. 20. Czochralski grown ruby slab during inspection

2. Description

The maser comb structure, the refrigerator, and the maser package are identical with advanced-design units previously installed at the Mars and Venus DSS (Ref. 4).

3. Ruby

The recent development of 0-deg ruby grown by the Czochralski process (by Crystal Products Department, Union Carbide Corp., 270 Park Ave., N.Y.) has given a necessary break-through to the production of high performance S-band traveling wave masers. Ruby slabs used on the forward side of the comb structure were fabricated from a Czochralski ruby boule approximately 1 in. in diameter and 7¼ in. in length. A typical slab is shown during inspection in polarized light in Fig. 20. A previously used type of disc boule ruby is shown in Fig. 21. There is a direct correlation between visible flaws and degradation in maser performance.

Magnetic Q (Q_m) of the maser material can be determined from the electronic gain, slowing factor and filling factor of a TWM. Electronic gain in dB is given by (Ref. 5)

$$G_{dB} = 27.3 \frac{SNF}{Q_m} \quad (1)$$

where

$$S = \text{slowing factor} = \frac{\text{velocity of light}}{\text{group velocity}}$$

$$N = \text{active length of TWM in free space wavelengths}$$

$$Q_m = \text{magnetic } Q$$

$$F = \text{filling factor}$$

The filling factor of a TWM has been discussed in detail by Okwit and Smith (Ref. 6) and Chen and Tabor (Ref. 7). The filling factor for the TWM described in this article approaches unity at the low frequency cut-off. In the usable portion of the maser band-pass the filling factor varies from approximately 0.8 to 0.5.

Figure 22 is a graph of magnetic Q divided by filling factor (Q_m/F) as a function of frequency for three identical comb structures. Improved ruby quality has produced a reduction in slowing factor, resulting in a larger tuning range in each successive case. Case 1, the Mars DSS

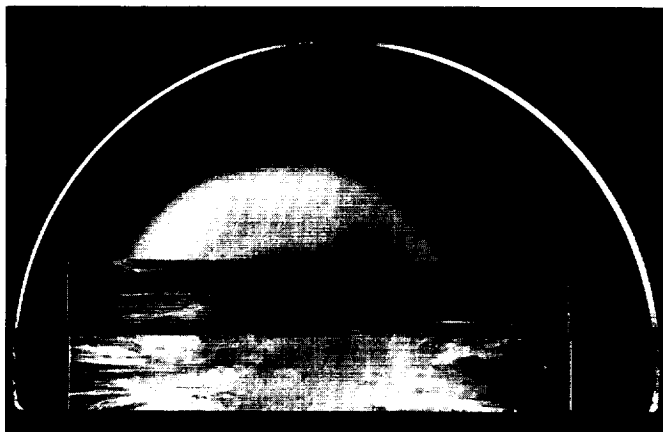


Fig. 21. Disc boule ruby slabs during inspection

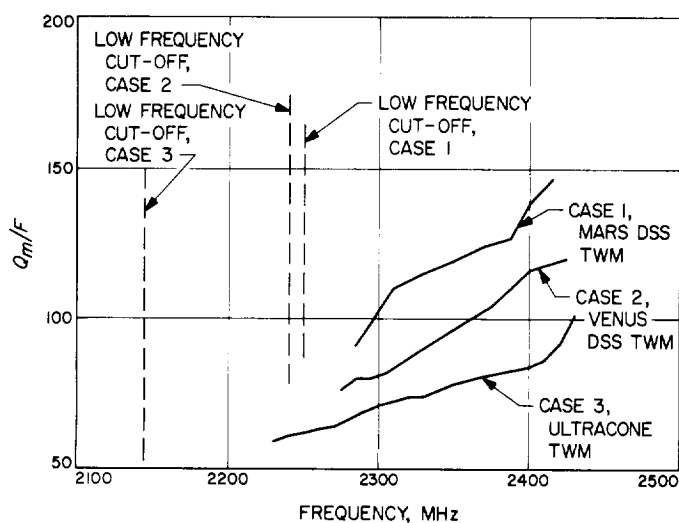


Fig. 22. Magnetic Q of ruby in comb structure of TWM

TWM, was loaded with ruby slabs cut from a disc boule. Case 2, the Venus DSS TWM, was loaded with a combination of disc boule ruby and short 0-deg slabs cut from a 60-deg Czochralski ruby boule (ruby location is shown in Fig. 23). Case 3, the ultracone TWM, was loaded with a combination of disc boule ruby and long slabs cut from a 0-deg Czochralski ruby boule (ruby location is shown in Fig. 24).

The process for growing disc boules has yielded some ruby which has given better maser performance than obtained with the disc boule ruby described here. This occurrence, however, is not typical; it is, in fact, quite rare. The quality observed in several Czochralski process ruby boules indicates that the performance shown can be considered typical of the process.

4. Isolator

The use of single crystal YIG was suggested in a report by Chen and Tabor (Ref. 7). Fabrication of single crystal YIG isolators and performance data for use in the block II TWM test unit was reported in SPS 37-44, Vol. III, pp. 69-72. This is the first use of single crystal YIG in an operational TWM. The resonance linewidth of the YIG isolator was deliberately broadened to approximately 150 MHz at 4.4°K. A comparison of the isolator figure of merit (ratio of reverse loss in dB to forward loss in dB) for the Venus DSS TWM (polycrystalline YIG) and the ultracone TWM (single-crystal YIG) is shown in Fig. 25.

5. Magnetic Field Adjustment

The 150-lb alnico V maser magnet has been temperature compensated (SPS 37-43, Vol. III, pp. 51-52) and is temperature controlled for stability. Two coils connected to form a figure eight can be used to provide magnetic field staggering. This staggering technique provides a more efficient gain versus bandwidth trade-off than the single coil previously reported (Ref. 4). Figure 26 shows the method by which the magnetic field is shifted, providing three sections of amplification which operate alternately at two different frequencies (F_1 and F_2).

6. Performance

Table 2 shows the ultracone TWM performance data in a uniform magnetic field. Both magnetic field strength

Table 2. Ultracone TWM performance

Frequency, MHz	Net gain, dB	Forward loss, dB	Predicted equivalent input noise temperature, °K
2230	52	17.5	5.2
2240	52	15.0	4.9
2250	52	14.0	4.7
2260	53	13.0	4.5
2270	53	11.5	4.4
2280	52	10.0	4.2
2290	51	8.8	4.2
2295	51	8.5	4.1
2300	50.5	8.3	4.1
2310	50	8.0	4.1
2320	49	7.8	4.1
2330	49	8.0	4.1
2350	47.5	9.5	4.3
2370	45	12.0	4.7
2390	42.5	13.5	5.1
2400	41	15.0	5.4
2410	40	16.5	5.7
2420	38	17.0	5.9
2430	35	19.0	6.4

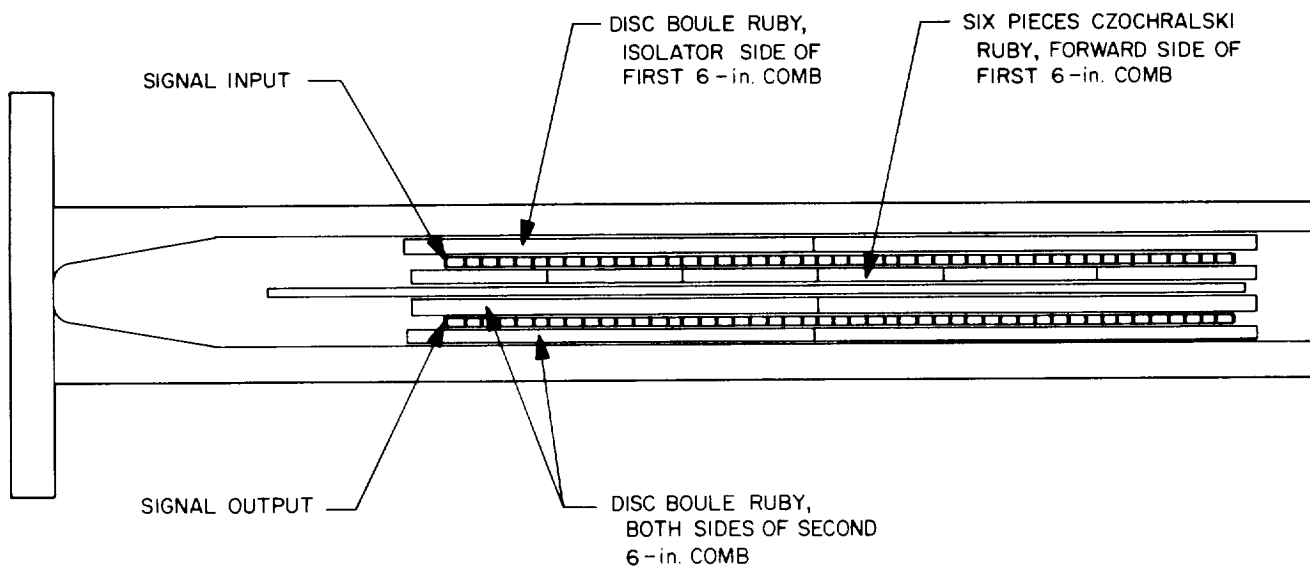


Fig. 23. Venus DSS TWM ruby location

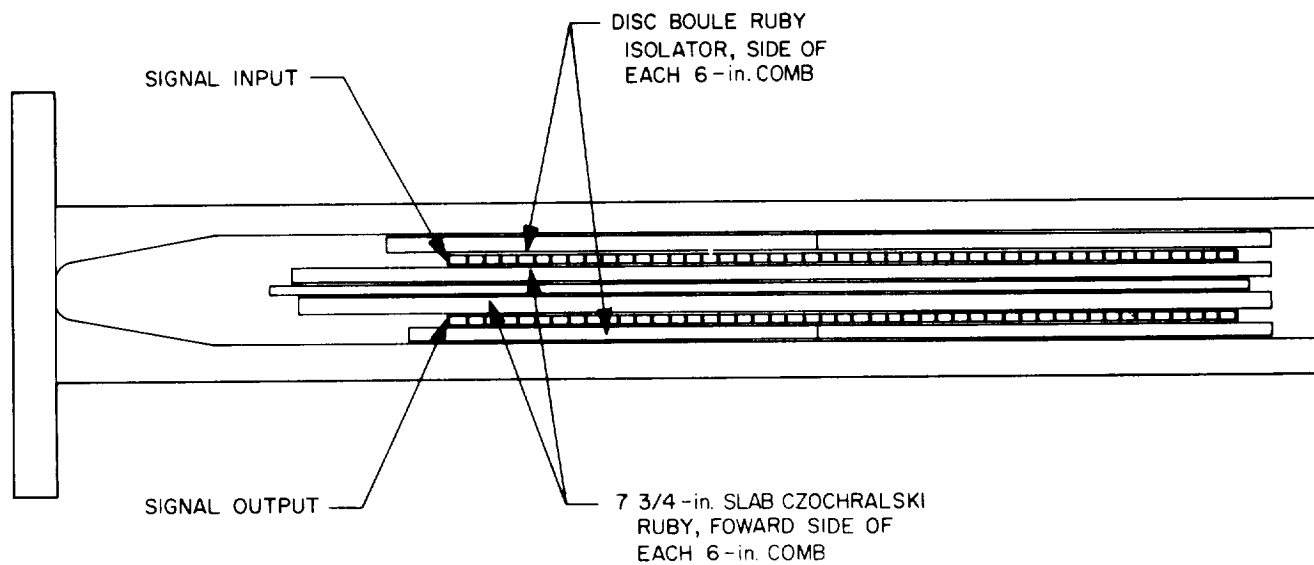


Fig. 24. Ultracone TWM ruby location

and pump frequency have been adjusted to give maximum gain at each frequency shown. The pump klystron supplied with the maser package for use at 2295 MHz is tunable over a limited range (electronic tuning only); this

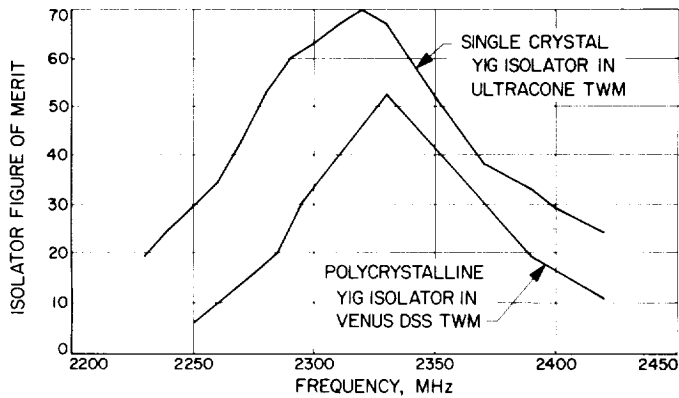


Fig. 25. Isolator comparison

range is not sufficient for proper maser operation at frequencies above 2320 MHz or below 2260 MHz.

Table 3 shows various gain and bandwidth combinations obtained by reducing gain with the figure eight field staggering coil.

Table 3. Gain and bandwidth combinations ultracone TWM

Center frequency, MHz	Net gain, dB	Bandwidth, MHz	
		-1 dB	-3 dB
2255	29	22	31
2280	29	30	39
2280	31	20	31
2280	36	13	22
2280	51	7	12
2295	51	7	12
2320	30	21	33

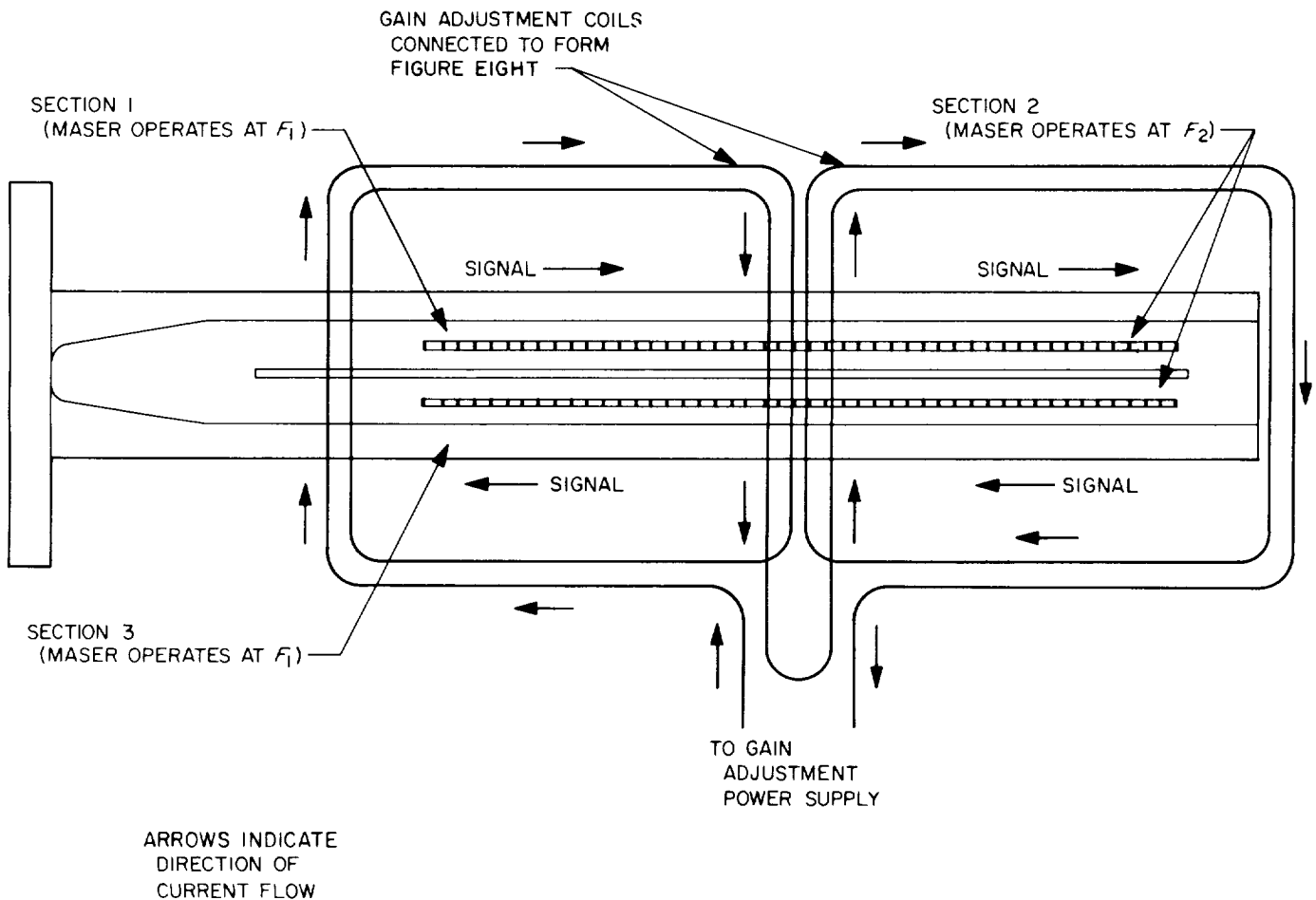


Fig. 26. Gain adjustment coil

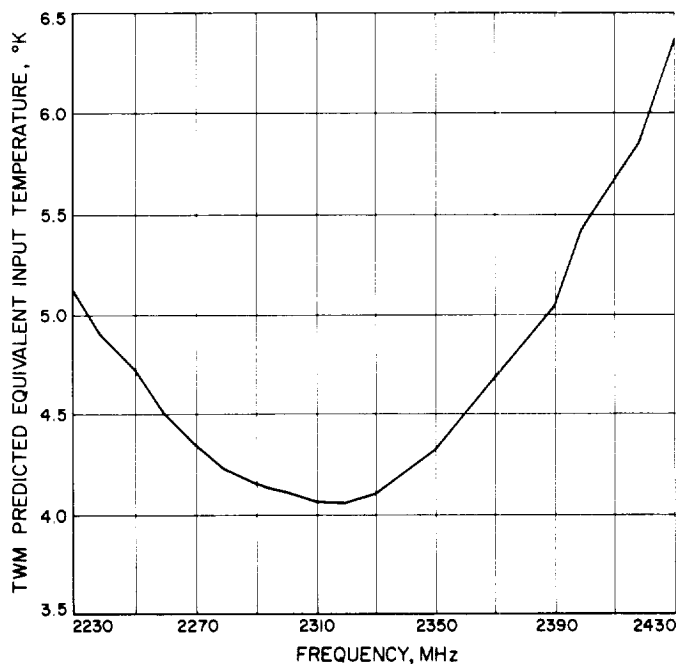


Fig. 27. TWM predicted equivalent input temperature

Figure 27 shows the equivalent input noise temperature (predicted values) at the waveguide interface when the maser is operated in a uniform magnetic field. The values shown represent results of computations using laboratory test data. A mechanically tunable pump klystron was used to cover the entire tuning range.

Stagger-tuning to reduce gain degrades the TWM noise temperature. At 2295 MHz a net gain reduction from 50 to 42 dB will increase the equivalent input noise temperature from 4.1 to 4.3 °K.

H. Improved RF Calibration Techniques: Daily System Noise Temperature Calibration With Ambient Termination, C. T. Stelzried

The daily noise temperature calibration, using the ambient load technique at the Mars and Venus DSSs, has been discussed in detail (SPS 37-42, Vol. III, p. 25). Noise temperature calibrations are made by switching the maser input by means of a waveguide switch between the antenna and a waveguide ambient termination. The principal advantage of this technique is long-term stability and reliability of the ambient waveguide termination. Another advantage is that it is not necessary to evaluate the waveguide losses when the system temperature is defined at the maser input. This technique depends on a previous calibration of the maser input noise temperature;

however, a 10% error in this parameter results in only about a 1% error in the system temperature measurement for a typical Goldstone installation.

A tabulation of the principal results of the daily noise temperature calibrations is presented in Table 4 for the period from February 10 to May 29, 1967 for the Goldstone Mars and Venus DSSs.³ This does not include the data taken at the Mars DSS when used in the standard DSN mode of operation. The probable errors of the measurement dispersions are identified as $(pe_i)_D$ for the individual measurements and $(pe)_D$ for the mean. These errors do not include bias errors, such as those due to nonlinearities, etc. The system temperature averages were computed using only data obtained when

- (1) Antenna was at zenith.
- (2) Weather was clear.
- (3) No RF spur in receiver passband.

The reflectometer readings on the ambient termination and the maser gain averages were computed, using all data points. The maser gain was optimized prior to each daily track precalibration.

The 2292-MHz data at the Venus DSS was taken during special tracking tests of the *Pioneer* spacecraft (see subsection J., p. 82, this SPS).

³All measurements were taken by Venus station personnel.

Table 4. Summary of the reflectometer, maser gain and total system temperature parameters for the Venus and Mars DSSs for the operating period from February 10 to May 29, 1967

DSS	Frequency, MHz	Reflectometer reading or ambient termination, dB	Maser gain, dB	System temperature, °K
Venus	2292		40.1 $\pm 0.2(pe_i)_D$ $\pm 0.1(pe)_D$ 9 data points	30.8 $\pm 2.9(pe_i)_D$ $\pm 1.1(pe)_D$ 7 data points
	2388	40.4 $\pm 0.3(pe_i)_D$ $\pm 0.1(pe)_D$ 72 data points	39.3 $\pm 0.6(pe_i)_D$ $\pm 0.1(pe)_D$ 72 data points	23.5 $\pm 1.3(pe_i)_D$ $\pm 0.2(pe)_D$ 60 data points
Mars	2297	44.1 $\pm 2.4(pe_i)_D$ $\pm 0.6(pe)_D$ 21 data points	40.8 $\pm 1.0(pe_i)_D$ $\pm 0.2(pe)_D$ 21 data points	26.0 $\pm 0.8(pe_i)_D$ $\pm 0.2(pe)_D$ 16 data points
	2388		38.5 $\pm 0.4(pe_i)_D$ $\pm 0.1(pe)_D$ 21 data points	25.1 $\pm 1.4(pe_i)_D$ $\pm 0.3(pe)_D$ 19 data points

The system temperature averages for this reported time period of approximately 4 mo do not agree with those reported for the previous 4-mo period to the accuracy expected. The averages for the Mars DSS at 2297 MHz are $[26.0 \pm 0.3 (pe)_D]^\circ\text{K}$ and $[28.1 \pm 0.2 (pe)_D]^\circ\text{K}$ for this and the previous period, respectively. This is a difference of 2.1°K ; whereas it is to be expected that the difference should be less than 1.0°K (twice the sum of the probable errors of the means). The disagreement between the time periods is undoubtedly due primarily to

- (1) Atmospheric contribution variations.
- (2) Actual equipment contribution changes.
- (3) Measurement error (equipment nonlinearity, operator performance, etc.).

An effort is being made to interpret the measured differences and to determine the relative magnitude of the various contributions.

I. Improved RF Calibration Techniques: WR 430 Waveguide Precision Rotary Vane Attenuator Calibration, T. Y. Otoshi and C. T. Stelzried

1. Introduction

An absolute gain measurement of the Mars DSS 210-ft antenna has recently been completed (SPS 37-44, Vol. III, p. 100). A 2.297 GHz earth-received signal, transmitted from the *Surveyor* spacecraft on the lunar surface, was compared at the output reference ports of a gain standard horn (Ref. 8) and the Mars DSS antenna. A WR 430 waveguide rotary vane attenuator (SPS 37-25, Vol. IV, p. 128) was used as the attenuation transfer standard.

The use of rotary vane attenuators for primary and interlaboratory attenuation standards has been discussed in several papers (Refs. 9-11). A rotary vane attenuator provides an excellent attenuation standard because it can be designed to obey an idealized mathematical law over a large attenuation range. Major types of errors of a rotary vane attenuator which cause deviations from the idealized mathematical law are

- (1) Vane angle readout error.
- (2) Vane misalignment errors.
- (3) Transmission error (Ref. 10).
- (4) Mismatch errors.

The vane angle readout error is the principal factor which limits the overall accuracy of most rotary vane attenuators. If the magnitude and phase of any of the above types of errors can be calibrated, then the error is no longer an uncertainty and can be applied as a correction to the idealized mathematical law. The corrected *theoretical* attenuations can often be more accurate than the attenuations measured with existing microwave insertion loss calibration instrumentation.

In this article a precision theoretical loss is derived in terms of angle setting, with corrections which account for boresight error, runout error, and transmission error. The theoretical attenuation is combined statistically with the previously reported calibration data (SPS 37-44, Vol. III, pp. 90-95).

2. Theory

A photograph of the S-band rotary vane attenuator, taken during calibrations with an ac insertion loss test set, is shown in Fig. 28 with its principal parts identified. The rotary vane attenuator consists of three sections of waveguide mounted in tandem. The center section is composed of a circular waveguide rotor that is free to rotate between two end stator sections. The signal flows through an input rectangular-to-circular waveguide transition stator, circular waveguide rotor, and the output circular-to-rectangular transition stator section. Across the center of each waveguide section is a thin dielectric card which has been deposited with lossy resistive films.

The rectangular waveguide TE_{10} mode is launched at the input stator to establish a vertical electric field \mathbf{E}_o at the input to the rotor, as shown in Fig. 29. This is decomposed into electric vectors $\mathbf{E}_o \cos \theta$ perpendicular and $\mathbf{E}_o \sin \theta$ parallel to the rotor card. Although the derivation closely follows that of A. V. James (Ref. 10), the present treatment differs in that attenuator finite loss and phase shift are treated as first-order correction factors rather than as unknown errors.

Propagation constants γ_o and γ_d are defined for the electric field vectors perpendicular and parallel to the rotor card. The vertical component of the electric field at the output of the rotor is

$$\mathbf{E}_y = \mathbf{E}_o (e^{-\gamma_d l} \sin^2 \theta + e^{-\gamma_o l} \cos^2 \theta) \quad (1)$$

where

$$l = \text{rotor length}$$

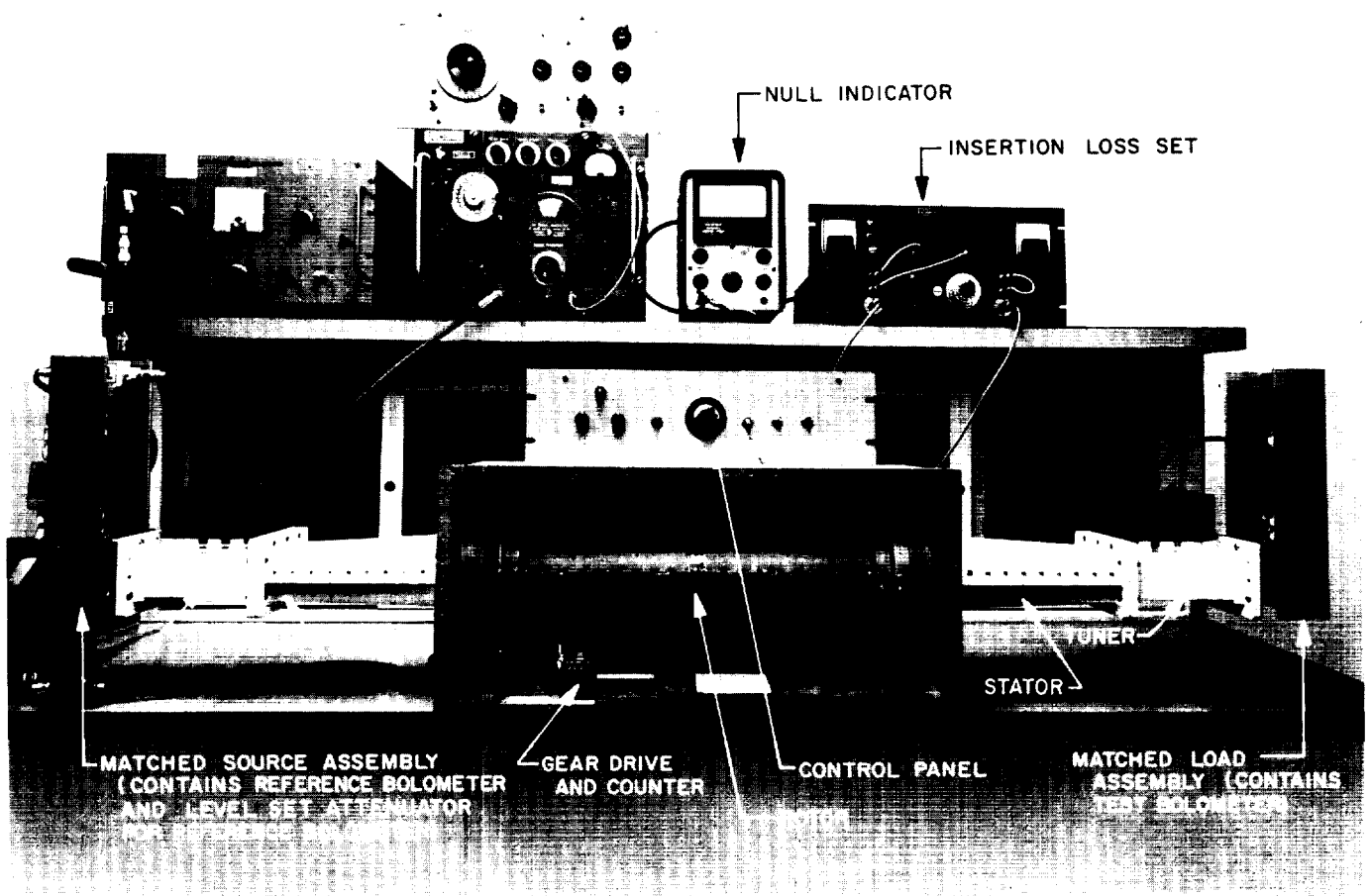


Fig. 28. S-band WR 430 rotary vane attenuator and ac-ratio transformer insertion loss test set

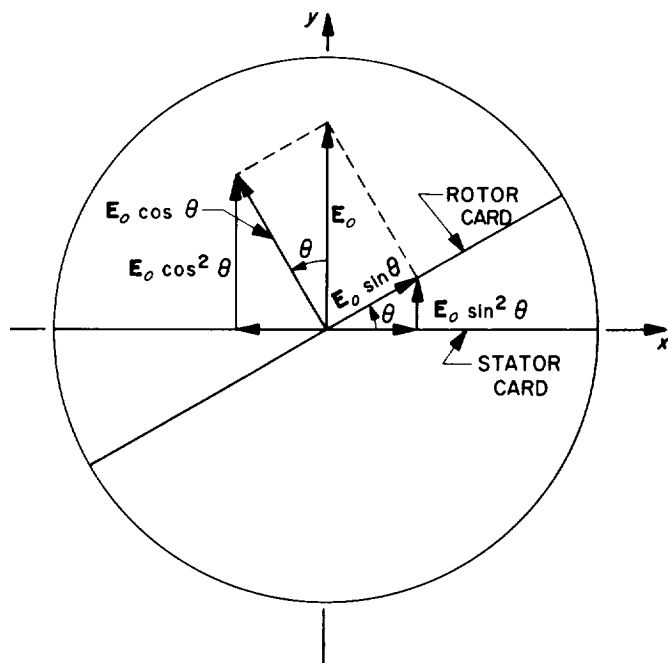


Fig. 29. Rotary vane attenuator voltage vectors at the input to the rotor

This is the only component of interest, since the horizontal component is attenuated in the output stator. The output power ratio due to rotating the rotor from the horizontal to the angle θ is the relative attenuation

$$A = \left| \frac{E_y(\theta=0)}{E_y(\theta)} \right|^2 = \frac{1}{|\cos^2 \theta + e^{-\gamma l} \sin^2 \theta|^2} \quad (2)$$

where

$$\gamma = \gamma_d - \gamma_o$$

Substituting

$$\gamma = \alpha + j\beta$$

$$L = e^{\alpha l}$$

$$\phi = \beta l$$

where

α = difference between the attenuation constants of the normal and tangential electric field components in the rotor

β = difference between the phase shift constants of the normal and tangential electric field components in the rotor

L = power loss ratio of the normal to the tangential components at the rotor output

ϕ = angular phase shift difference between the normal and tangential electric field components at the rotor output, degrees

results in

$$A = \frac{1}{\cos^4 \theta + \left(\frac{2 \cos \phi}{L^{1/2}} \right) \sin^2 \theta \cos^2 \theta + \frac{1}{L} \sin^4 \theta} \quad (3)$$

The last two terms in the denominator of Eq. (3) are correction terms which account for the presence of a transmission error signal appearing at the attenuator output. Note that the correction terms are functions of the differential phase shift and finite loss of the rotor card. If L is made very large we have the usual idealized mathematical law

$$A = \frac{1}{\cos^4 \theta} \quad (4)$$

or

$$A_{dB} = -20 \log_{10} \cos^2 \theta \quad (5)$$

Equation (3) does not account for misalignment between stator cards but accounts for transmission, boresight, and other readout errors. The actual angle θ is given by

$$\theta = \theta_I + \alpha_1 + \alpha_2 \quad (6)$$

where

θ_I = indicated angle

α_1 = boresight error

α_2 = additional readout errors (due to gearing errors, bearing runout, nonlinearity, etc.)

Boresight error is the actual vane angle when the indicated angle is set to zero (α_2 goes to zero at this setting). The boresight error can be determined very precisely from a series of insertion loss readings versus vane angle settings. A computer program (CTS29A) has been written to best fit, in a least squares sense, these data to Eq. (3), treating α_1 as the unknown. The values of α_2 , whose calibrations will be described later, are included in these computations. Four sets of measurements taken in 5-deg steps over a range of ± 30 deg result in $\alpha_1 = [-0.0554 \pm 0.0008 (pe)_D]$ deg. The probable error is that due only to measurement dispersion.

3. Calibration of Alpha 2

Lee Brubaker of the JPL mechanical inspection department suggested a method of calibrating α_2 , defined by Eq. (6), which does not require partial disassembly of the rotary vane attenuator. All mechanical measurements were performed using instruments capable of measuring linear distances accurately to within $\pm 50 \mu\text{in.}$ and having resolutions of a few microinches.

The calibration technique is described as follows:

(1) The rotary vane attenuator was leveled on a flat surface plate, such that the stator cards were parallel to the surface plate. Then a high-precision steel ball, accurate in diameter to a few microinches, was mounted to the principal gear on the circular waveguide rotor. The calibration setup may be seen in Fig. 30.

(2) Maximum and minimum heights h_{\max} and h_{\min} were measured (Fig. 31). These respective heights are measured from the surface plate to the top of the ball when the vane angle is near 90 and -90 deg.

(3) Other height measurements were made from the surface plate to the top of the ball with the rotary vane set at the various desired indicated vane angles.

The calibrated angular position of the rotary vane relative to the 0-deg indicated vane angle setting can be calcu-

lated from the equation

$$\theta_r = \sin^{-1} \left(\frac{h - h_r}{r_m} \right) + \sin^{-1} \left(\frac{h_r - h_o}{r_m} \right) \quad (7)$$

where

r_m = radius from the center of rotation to the center of the ball

h = vertical distance variable from the surface plate to the top of the ball (Fig. 31)

h_r = vertical distance from the surface plate to the top of the ball when the center of the ball is aligned with the horizontal centerline of the waveguide (stator cards)

h_o = vertical distance from the surface plate to the top of the ball when the counter reads 0.000 deg

The radius r_m and reference height h_r were determined from maximum and minimum height measurements using the equations

$$r_m = \frac{h_{\max} + h_{\min}}{2} \quad (8)$$

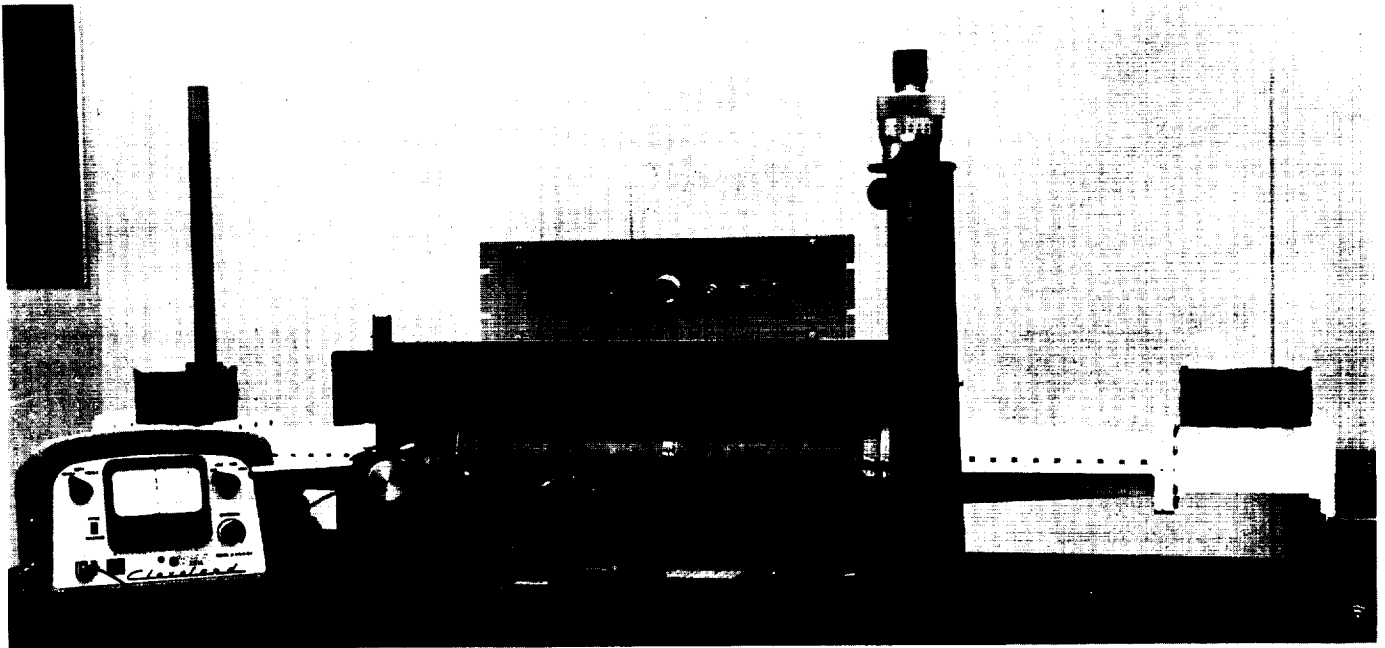


Fig. 30. Setup and instrumentation for calibration of rotary vane angle

and

$$h_r = \frac{h_{max} - h_{min}}{2} \quad (9)$$

where

h_{max} = maximum vertical distance from the surface plate to the top of the ball, measured in the region of 90-deg indicated vane angle

h_{min} = minimum vertical distance from the surface plate to the top of the ball, measured in the region of -90-deg indicated vane angle

For the particular calibration setup, the ball was mounted such that $h_o = h_r$, so that for this special case, Eq. (7) becomes

$$\theta_r = \sin^{-1} \left(\frac{h - h_o}{r_m} \right) = \tan^{-1} \left(\frac{h - h_o}{[r_m^2 - (h - h_o)^2]^{1/2}} \right) \quad (10)$$

The correction term α_2 is calculated from

$$\alpha_2 = \theta_r - \theta_i \quad (11)$$

By differentiating Eq. (10) with respect to the independent height parameters, the following error formula can be derived

$$\epsilon_h = \frac{2\Delta h}{r_m \cos \theta_r} \quad (12)$$

where

ϵ_h = maximum error on the calibrated vane angle θ_r , due to height measurement tolerance of Δh , radians. It is also equal to the maximum error on α_2 due to this tolerance

A second error or uncertainty in the mechanical calibration of vane angle position by the described method results from the assumption that the ball travels in a perfect circular path about the bearing center of rotation at all indicated vane angles and that, therefore, the radius is a constant. The assumption of a constant radius is erroneous due to the existence of runout error of the ring bearing assemblies on which the circular waveguide rotates. The error in angle calibration is a function of this bearing runout error and also, to a lesser extent, a function of any nonconcentricity of the center of the circular

waveguide section and the center of rotation governed by the bearing assemblies.

If it is assumed that the bearing runout error occurs gradually and the deviation of the radius from the assumed constant radius can be expressed in terms of an elliptical equation, then some estimates can be made of worst-case errors in the mechanical vane angle calibration. An analysis made on the basis of the above assumption produced the following error formula for the particular calibration technique involved.

$$\begin{aligned} \epsilon_b &= \theta'_r - \theta_r \\ &= \theta'_r - \sin^{-1} \left(\frac{r(\theta'_r) \sin \theta'_r}{r_m} \right) \end{aligned} \quad (13)$$

where

ϵ_b = vane angle calibration uncertainty due to bearing runout and eccentricity, radians. It is also equal to the uncertainty of α_2 due to this source of error

θ'_r = true angular difference between the vane angle positions at the indicated 0-deg and θ_i vane angle settings, radians

θ_r = calibrated angular difference between the vane angle positions at the indicated 0-deg and θ_i vane angle settings as determined from Eq. (10), radians

r_m = measured radius defined by Eq. (8)

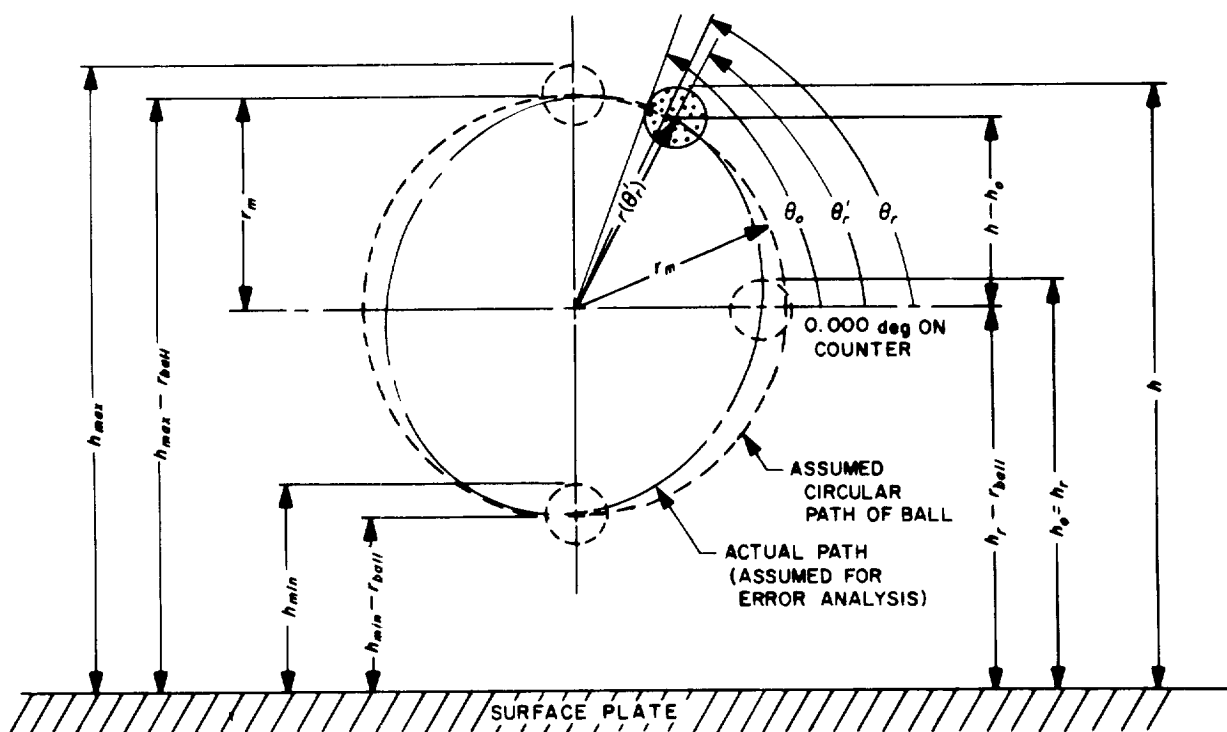
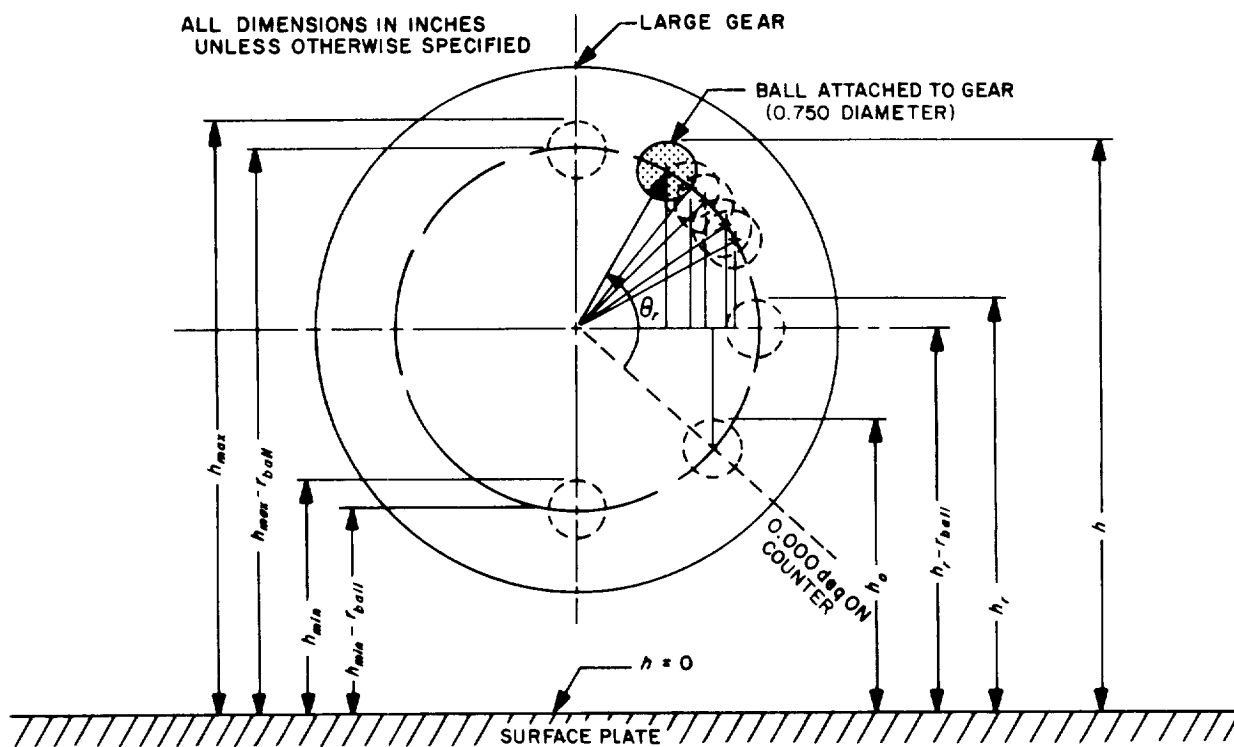
The expression for $r(\theta'_r)$, which is the actual radius vector measured from a reference center of rotation to the center of the ball (Fig. 32), is assumed to be of the following form:

$$r(\theta'_r) = r_m + \underbrace{[\rho(\theta'_r) - \rho(90 \text{ deg})]}_{\text{error term}} \quad (14)$$

where

$$\rho(\theta'_r) = \frac{ab}{[b^2 \cos^2(\theta'_r - \theta_o) + a^2 \sin^2(\theta'_r - \theta_o)]^{1/2}} \quad (15)$$

$$\rho(90 \text{ deg}) = \frac{ab}{[b^2 \sin^2(\theta_o) + a^2 \cos^2(\theta_o)]^{1/2}} \quad (16)$$



where

a = bearing eccentricity or the distance between the bearing center of rotation and the center of the circular waveguide rotor

b = maximum bearing runout minus a

θ_o = angle at which the maximum runout is assumed to occur

It can be seen that the expression for $\rho(\theta'_r)$ is that of an ellipse which has been rotated by an angle θ_o with respect to the horizontal reference plane (Fig. 32). Since the error, as determined from Eq. (13), is slowly varying, and since $\theta_r \approx \theta'_r$, then θ_r may be used in place of θ'_r in Eq. (13) with negligible difference in the calculated error values.

4. Calibration Results

The IBM 1620 computer was used to compute the corrected theoretical attenuations as defined by Eq. (3), which accounts for total readout and transmission errors. Nominal corrected theoretical attenuations are first computed using nominal values of α_1 , α_2 , L and ϕ . Deviations from the nominal corrected theoretical attenuations are then calculated as caused by the following major sources of errors: (1) tolerances on the nominal values of α_1 , L , and ϕ ; (2) uncertainties in the α_2 calibrations; (3) vane angle resetability; and (4) internal mismatch error.

A sample computer printout of the nominal corrected theoretical attenuations case is shown in Fig. 33. The printout is useful for studying the change in attenuation values due to the α_1 , α_2 and the transmission error correction terms.

Figure 33 shows only vane angle calibrations made in the JPL inspection department setup No. 1. A second setup was later made to calibrate the angle readout errors at indicated vane angles of 25.710, 30.600, and 35.500 deg, which were used during the antenna gain calibrations. For the second setup, r_m was slightly different. Although a similar printout is not shown for the second setup, the α_2 values corresponding to the above mentioned vane angles were within expected values, as based on the trend of alpha 2 values shown in Fig. 33.

Figure 34 shows a tabulation of the total probable error and peak deviations associated with the nominal corrected theoretical attenuations. A JO case refers to a deviation caused by a specific perturbation made to a

nominal parameter in Eq. (3). Even and odd JO numbers refer to plus and minus deviation cases, respectively.

Case $JO = 2$: 0.005 deg added to nominal boresight error of -0.055 deg.

Case $JO = 5$: -5 dB added to nominal L_{dB} value of 88 dB, where $L_{dB} = 10 \log_{10} L$. This minus perturbation value was found to produce a larger deviation than that produced by a plus 5-dB perturbation.

Case $JO = 6$: 0.6 deg added to nominal ϕ value of 1.0 deg.⁴

Case $JO = 8$: 50 μ in. used for Δh in Eq. (12).

Case $JO = 10$: $a = 0.010$ in.; bearing runout = 0.005 in.; $\theta_o = 70$ deg in Eqs. (15) and (16). This θ_o was intentionally chosen to produce the largest attenuation error for the region of 40-dB attenuation.

Case $JO = 12$: Indicated vane angle resetability = 0.002 deg.

Case $JO = 14$: $|\Gamma| = 0.015$ was used to calculate a peak internal mismatch uncertainty defined by the following equation (Ref. 10).

$$\text{Peak dB mismatch error} \simeq 20 \log_{10} [1 + 2|\Gamma|^2 \sin^2 \theta] \quad (17)$$

where

$|\Gamma|$ = amplitude of the resistance card reflection coefficient (assume that the resistance cards are the major factors causing internal mismatch error)

The printout given in Fig. 34 is useful for analyzing the individual error contributions to the total error produced by the various sources of error. The tabulation also permits the total maximum error to be determined from the sum of the absolute values of all peak deviations. However, since the individual deviations shown are peak deviations and would, in most cases, occur in a random manner with equal probability for negative or positive values, the total probable error is computed rather than the total peak error. The total probable error for this tabulation was computed by taking the square root of the sum of the squares of the peak deviations and dividing this

⁴Nominal phase shift and tolerances measured by Rantec Corp., Calabasas, Calif., Rantec Test Report 70122-FR, March 27, 1967.

AI = INDICATED THEORETICAL ATTENUATION

AR = AI CORRECTED FOR ALPHA2

AR3 = AI CORRECTED FOR ALPHA2, AND ALPHA1 (BURESIGHT ERROR)

A = AI CORRECTED FOR ALPHA2, ALPHA1, AND TRANSMISSION ERROR

AM = MEASURED ATTENUATION

ANUM = NOMINAL CORRECTED THEORETICAL ATTENUATION

S-BAND R.V.A., JPL INSP. DEPT. SETUP 1 (CASE JO = 1)									
ALPHA1 = -.055 DEG, ATTENUATION AT 90 DEG = 88.0000 DB, DIFF PHASE SHIFT (0-90 DEG V.A.) = 1.0000 DEG									
RM = 4.918000 INCHES HO = 6.868400 INCHES									
THI (DEG)	H (IN)	H-HO (IN)	THR (DEG)	ALPHA2 (DEG)	TH (DEG)	AI (DB)	AR (DB)	ARB (DB)	A (DB)
0.000	6.86840	0.00000	0.0000	0.0000	-0.0550	0.00000	0.00000	0.00000	0.00000
2.749	7.10470	.23630	2.7540	.0050	2.6990	.02000	.02007	.01928	.01928
3.887	7.20220	.33380	3.8918	.0048	3.8368	.04000	.04010	.03897	.03897
4.559	7.25970	.39130	4.5635	.0045	4.5085	.05505	.05516	.05383	.05383
5.000	7.29770	.42930	5.0078	.0078	4.9528	.06623	.06643	.06498	.06498
5.495	7.34030	.47190	5.5062	.0112	5.4512	.08001	.08034	.07874	.07874
6.142	7.39560	.52720	6.1538	.0118	6.0988	.10000	.10039	.09860	.09859
6.674	7.41160	.54320	6.6917	.0137	6.6367	.12002	.12065	.11811	.11810
10.000	7.72340	.85500	10.0118	.0118	9.9568	.26594	.26657	.26363	.26362
12.248	7.91300	1.04460	12.2632	.0152	12.2082	.39997	.40098	.39736	.39734
14.972	8.14040	1.27200	14.9894	.0174	14.9344	.59997	.60139	.59693	.59691
17.255	8.32850	1.46010	17.2708	.0158	17.2158	.79997	.80146	.79629	.79625
19.255	8.49130	1.62290	19.2682	.0132	19.2132	1.00001	1.00141	.99559	.99555
20.000	8.55140	1.68300	20.0117	.0117	19.9567	1.08056	1.08186	1.07579	1.07575
26.969	9.10010	2.23170	26.9865	.0175	26.9315	1.99997	2.00269	1.99421	1.99412
30.000	9.32870	2.46030	30.0174	.0174	29.9624	2.49877	2.50183	2.49221	2.49209
32.712	9.52800	2.65960	32.7373	.0253	32.6823	2.99994	3.00489	2.99418	2.99403
37.408	9.85800	2.98960	37.4370	.0290	37.3820	3.99996	4.00670	3.99395	3.99374
41.419	10.12410	3.25570	41.4523	.0333	41.3973	5.00005	5.00897	4.99426	4.99399
44.932	10.34400	3.47560	44.9678	.0358	44.9128	6.00000	6.01086	5.99422	5.99387
48.061	10.52860	3.66020	48.0943	.0333	48.0393	7.00012	7.01138	6.99282	6.99239
50.879	10.68550	3.81710	50.9093	.0303	50.8543	7.99992	8.01122	7.99071	7.99019
53.440	10.82050	3.95210	53.4751	.0351	53.4201	8.99993	9.01432	8.99183	8.99120
55.782	10.93700	4.06860	55.8211	.0391	55.7661	9.99994	10.01738	9.99285	9.99210
59.921	11.12590	4.25750	59.9624	.0414	59.9074	11.99977	12.02148	11.99268	11.99165
63.469	11.27050	4.40210	63.5212	.0522	63.4662	14.00006	14.03181	13.99838	13.99699
66.540	11.38180	4.51340	66.5965	.0565	66.5415	15.99993	16.03950	16.00102	15.99918
69.218	11.46830	4.59990	69.2797	.0617	69.2247	18.00000	18.04944	18.00542	18.00302
71.565	11.53570	4.66730	71.6268	.0618	71.5718	19.99995	20.05634	20.00621	20.00309
76.282	11.70880	4.77900	76.3453	.0633	76.2903	24.99956	25.07849	25.00999	25.00418
79.757	11.76230	4.84040	79.8082	.0512	79.7532	30.00045	30.08674	29.99423	29.98365
82.337	11.74310	4.87470	82.3913	.0543	82.3363	35.00077	35.12373	34.99935	34.98027
84.261	11.76230	4.89390	84.3254	.0644	84.2704	40.00051	40.19613	40.02912	39.99485
84.650	11.76550	4.89710	84.7159	.0659	84.6609	41.21600	41.43072	41.25135	41.21185
84.970	11.76790	4.89950	85.0287	.0587	84.9737	42.28450	42.48808	42.29743	42.25285
85.300	11.77030	4.90190	85.3625	.0625	85.3075	43.46047	43.69288	43.48851	43.43735
85.699	11.77300	4.90460	85.7694	.0704	85.7144	44.99844	45.28491	45.06093	44.99958
86.776	11.77890	4.91050	86.8353	.0593	86.7803	49.99827	50.32057	50.02156	49.91298
87.583	11.78230	4.91390	87.6602	.0772	87.6052	54.99899	55.56311	55.15971	54.96424
88.188	11.78420	4.91580	88.2861	.0981	88.2311	60.00147	60.98865	60.42009	60.06493

Fig. 33. Computer output: nominal corrected theoretical attenuation case

S-BAND ROTARY VANE ATTENUATOR USED IN GAIN MEAS.

THI (DEG)	NOM CORRECTED ATTEN (DB)	TOTAL PE (DB)	PEAK DEVIATIONS FROM NOMINAL CORRECTED ATTENUATION						
			JO= 2 (DB)	JO= 5 (DB)	JO= 6 (DB)	JO= 8 (DB)	JO= 10 (DB)	JO= 12 (DB)	JO= 14 (DB)
0.000	0.00000	0.00000	-1.38900E-06	-2.60576E-10	0.00000E-99	-3.35448E-07	0.00000E-99	0.00000E-99	0.00000E-99
2.749	0.01928	0.00001	7.15286E-05	-5.98011E-07	1.73000E-10	1.66738E-05	2.64180E-05	2.91448E-05	8.70243E-06
3.887	0.03897	0.00002	1.01732E-04	-1.21028E-06	3.44400E-10	2.74699E-05	5.26253E-05	4.11285E-05	1.73882E-05
5.000	0.06498	0.00003	1.31433E-04	-1.67305E-06	4.71700E-10	2.79438E-05	7.21468E-05	4.82516E-05	2.43373E-05
4.559	0.05383	0.00003	1.19599E-04	-2.02071E-06	6.41900E-10	3.07300E-05	8.66792E-05	5.32900E-05	2.95497E-05
5.495	0.07873	0.00003	1.44729E-04	-2.45045E-06	7.67400E-10	3.38670E-05	1.04497E-04	5.85005E-05	3.56287E-05
6.142	0.09859	0.00004	1.62039E-04	-3.07197E-06	9.76300E-10	3.79627E-05	1.30011E-04	6.52741E-05	4.43145E-05
8.678	0.19810	0.00007	2.30322E-04	-6.20800E-06	1.90900E-09	5.42773E-05	2.54821E-04	9.27238E-05	8.86120E-05
10.000	0.26362	0.00009	2.66186E-04	-8.29244E-06	2.53400E-09	6.29693E-05	3.34655E-04	1.06966E-04	1.17275E-04
12.248	0.39734	0.00012	3.28048E-04	-1.25958E-05	3.84500E-09	7.82090E-05	4.92657E-04	1.31636E-04	1.75469E-04
14.972	0.59691	0.00017	4.04400E-04	-1.91428E-05	5.86700E-09	9.75332E-05	7.17394E-04	1.62209E-04	2.60589E-04
17.255	0.79625	0.00022	4.69783E-04	-2.58343E-05	7.88200E-09	1.14616E-04	9.29628E-04	1.88442E-04	3.43103E-04
19.255	0.99555	0.00026	5.28362E-04	-3.26797E-05	9.98000E-09	1.30402E-04	1.13006E-03	2.11895E-04	4.24746E-04
20.000	1.07575	0.00028	5.50522E-04	-3.54787E-05	1.08500E-08	1.36502E-04	1.20744E-03	2.20756E-04	4.56883E-04
25.710	1.80509	0.00042	7.28663E-04	-6.21576E-05	1.89700E-08	1.88629E-04	1.82661E-03	2.91979E-04	7.34811E-04
26.969	1.99412	0.00045	7.70193E-04	-6.94453E-05	2.12100E-08	2.01370E-04	1.95896E-03	3.08655E-04	8.03425E-04
30.000	2.49209	0.00052	8.73966E-04	-8.94212E-05	2.73000E-08	2.35165E-04	2.25924E-03	3.50002E-04	9.76256E-04
30.600	2.59747	0.00054	8.95095E-04	-9.37973E-05	2.86400E-08	2.42556E-04	2.31492E-03	3.58513E-04	1.01273E-03
32.712	2.99403	0.00058	9.72617E-04	-1.10749E-04	3.38100E-08	2.69400E-04	2.48091E-03	3.89435E-04	1.14126E-03
35.500	3.56603	0.00063	1.08019E-03	-1.36604E-04	4.16900E-08	3.09538E-04	2.63167E-03	4.32523E-04	1.31756E-03
37.408	3.99374	0.00065	1.15832E-03	-1.57081E-04	4.79600E-08	3.39887E-04	2.66373E-03	4.63613E-04	1.44175E-03
41.419	4.99399	0.00067	1.33640E-03	-2.09095E-04	6.38400E-08	4.15433E-04	2.47599E-03	5.35015E-04	1.71010E-03
44.932	5.99387	0.00064	1.51138E-03	-2.67434E-04	8.16500E-08	4.97719E-04	1.89189E-03	6.04681E-04	1.94891E-03
48.061	6.99239	0.00060	1.68598E-03	-3.32796E-04	1.01580E-07	5.88135E-04	8.95722E-04	6.74866E-04	2.16166E-03
50.879	7.99019	0.00064	1.86234E-03	-4.06064E-04	1.23940E-07	6.88147E-04	-5.19218E-04	7.45571E-04	2.35183E-03
53.440	8.99120	0.00083	2.04271E-03	-4.88531E-04	1.49130E-07	7.99662E-04	-2.35716E-03	8.17840E-04	2.52116E-03
55.782	9.99210	0.00118	2.22777E-03	-5.81059E-04	1.77360E-07	9.23947E-04	-4.60167E-03	8.91671E-04	2.67138E-03
59.921	11.99165	0.00221	2.61582E-03	-8.01117E-04	2.44500E-07	1.21754E-03	-1.02186E-02	1.04681E-03	2.92580E-03
63.469	13.99699	0.00357	3.03581E-03	-1.07902E-03	3.29400E-07	1.58639E-03	-1.71882E-02	1.21428E-03	3.12811E-03
66.540	15.99918	0.00517	3.49296E-03	-1.42848E-03	4.36100E-07	2.04891E-03	-2.52648E-02	1.39740E-03	3.28787E-03
69.218	18.00302	0.00697	3.99529E-03	-1.86892E-03	5.70400E-07	2.63105E-03	-3.42962E-02	1.59771E-03	3.41550E-03
71.565	20.00309	0.00895	4.54857E-03	-2.42245E-03	7.39500E-07	3.36226E-03	-4.41597E-02	1.81905E-03	3.51622E-03
76.282	25.00418	0.01466	6.21102E-03	-4.51725E-03	1.37860E-06	6.13039E-03	-7.25368E-02	2.48360E-03	3.68726E-03
79.757	29.98365	0.02170	8.37774E-03	-8.22046E-03	2.50780E-06	1.10330E-02	-1.07195E-01	3.35511E-03	3.78363E-03
82.337	34.98027	0.03069	1.12447E-02	-1.48161E-02	4.51740E-06	1.97932E-02	-1.50945E-01	4.50678E-03	3.83746E-03
84.261	39.99485	0.04256	1.50557E-02	-2.65834E-02	8.09660E-06	3.54999E-02	-2.07462E-01	6.03353E-03	3.86871E-03
84.650	41.21185	0.04600	1.61546E-02	-3.06150E-02	9.32100E-06	4.09016E-02	-2.23579E-01	6.47527E-03	3.87305E-03
84.970	42.25285	0.04916	1.71562E-02	-3.45395E-02	1.05122E-05	4.61692E-02	-2.38223E-01	6.88958E-03	3.87740E-03
85.300	43.43735	0.05302	1.83696E-02	-3.96136E-02	1.20508E-05	5.29931E-02	-2.55918E-01	7.37567E-03	3.88087E-03
85.699	44.99958	0.05857	2.00985E-02	-4.74510E-02	1.44247E-05	6.35615E-02	-2.81061E-01	8.06320E-03	3.88521E-03
86.776	49.91298	0.08040	2.66335E-02	-8.35741E-02	2.53207E-05	1.12686E-01	-3.75651E-01	1.07665E-02	3.89476E-03
87.583	54.96424	0.11284	3.54771E-02	-1.49144E-01	4.49060E-05	2.03443E-01	-5.03216E-01	1.43694E-02	3.89997E-03
88.188	60.06493	0.16286	4.71820E-02	-2.66709E-01	7.93786E-05	3.70875E-01	-6.72199E-01	1.91743E-02	3.90344E-03

Fig. 34. Computer output: tabulation of total probable errors and peak deviations from the nominal corrected theoretical attenuations

Table 5. Comparison of measured and theoretical attenuations for the S-band rotary vane attenuator at 2295 MHz

Indicated vane angle, deg	Indicated theoretical attenuation, dB	Weighted average of measured attenuations relative to 0-deg indicated vane angle, ^a dB				Attenuations relative to 0-deg indicated vane angle, dB	
		Ac substitution system	Dc substitution system	IF substitution system	Grand mean of measured values	Corrected theoretical	Grand mean of measured and corrected theoretical values
25.710	1.8110	1.7988 ± 0.0018	1.8007 ± 0.0018	1.7978 ± 0.0065	1.7997 ± 0.0013	1.8051 ± 0.0004	1.8046 ± 0.0004
30.600	2.6050	2.5900 ± 0.0026	2.5924 ± 0.0026	2.5954 ± 0.0061	2.5916 ± 0.0018	2.5975 ± 0.0005	2.5970 ± 0.0005
35.500	3.5726	3.5562 ± 0.0036	3.5594 ± 0.0034	3.5954 ± 0.0077	3.5615 ± 0.0024	3.5660 ± 0.0006	3.5657 ± 0.0006
55.782	9.9999	9.974 ± 0.010	9.979 ± 0.010	—	9.9763 ± 0.0071	9.992 ± 0.001	9.992 ± 0.001
71.565	20.0000	19.965 ± 0.020	19.936 ± 0.027	—	19.955 ± 0.016	19.992 ± 0.009	19.992 ± 0.008
79.757	30.0005	29.936 ± 0.030	29.905 ± 0.035	—	29.923 ± 0.023	29.984 ± 0.022	29.955 ± 0.016
84.261	40.0005	39.896 ± 0.040	39.843 ± 0.044	—	39.872 ± 0.030	39.995 ± 0.043	39.911 ± 0.024
84.650	41.2160	41.099 ± 0.041	41.045 ± 0.045	41.033 ± 0.031	41.054 ± 0.022	41.212 ± 0.046	41.082 ± 0.020
84.970	42.2845	42.165 ± 0.043	42.106 ± 0.046	42.109 ± 0.030	42.123 ± 0.021	42.253 ± 0.049	42.143 ± 0.020
85.300	43.4605	43.347 ± 0.044	43.263 ± 0.047	43.289 ± 0.031	43.298 ± 0.022	43.437 ± 0.053	43.319 ± 0.020
90.000	—	—	—	88.49 ± 0.72	88.49	88.0 ± 1.0	—

^aTolerances shown for the ac, dc, IF systems and corrected theoretical attenuations are total probable errors associated with the average values. Tolerances shown for the grand mean values are grand mean probable errors (Ref. 12).

result by 5. As may be seen from the tabulation, the $JO = 8$ and 10 cases (uncertainties associated with the α_2 calibrations) produced the largest deviation and, therefore, was the dominant contributor to total probable error.

Table 5 is a tabulation of final attenuation data, which are pertinent to the 210-ft antenna gain calibrations. The corrected theoretical attenuations and associated probable errors were weighted with previously measured values obtained through measurements with ac, dc, and IF substitution systems. Note that the corrected theoretical attenuation has the lower probable errors at vane angle settings below 30 dB but about the same total probable errors as the measured values at 40 dB. When the corrected theoretical values were weighted with measured values, the new grand mean values were found to be approximately 0.005 dB higher in the region of 2 dB and 0.03 dB higher in the region of 40 dB. Therefore any corrections which could be made to previously reported gain values should not be significant.

J. Efficient Antenna Systems: Venus DSS Polarization Tests, D. E. Neff

The 2388-MHz R&D cone (SPS 37-31, Vol. III, p. 56) has been tested for its linear polarization characteristics at 2292 MHz for use with the *Pioneer* spacecraft. A 6-ft paraboloidal antenna with vertical polarization was used at the 100-ft collimation tower to transmit a test signal. The 85-ft antenna was boresighted and the ellipticity measured by rotating the polarization basket assembly in the R&D cone. The measured ellipticity at 2292 MHz was 9.8 dB with the standard 2388-MHz circularly polarized configuration. The 9.8-dB ellipticity is a reasonable compromise with the 2388-MHz system, because no mechanical changes are required in the cone for conversion to 2292-MHz linear-polarized operation.

System noise temperature measurements at 2292 MHz indicated a $30 \pm 5^\circ\text{K}$ temperature, as compared to the 2388-MHz 22°K system temperature. Star track data indicate an antenna efficiency of about $55 \pm 10\%$.

K. Measurement of Signal Power in Real Time With an SDS 920 Computer, H. Mack, Jr.

1. Introduction

This article describes a program that measures the signal strength in the output of the receiver. The method is to compare the spectrum of the signal plus noise with the spectrum of the noise only and to estimate the signal-to-noise ratio (SNR).

The spectrums are computed by first sampling the dynamic automatic gain control (AGC) voltage and then computing the autocorrelation function. The spectral density function is then computed by finding the Fourier transform of the autocorrelation function. The power spectral density is then normalized to make the resulting estimate of the spectrum of the AGC voltage insensitive to the gain variation in the receiver.

2. Method

The two special estimates that must be computed in order to obtain a corresponding estimate of the SNR are designated $P(f)$ and $Q(f)$. $P(f)$ is the normalized spectrum of the signal plus noise, and $Q(f)$ is the normalized spectrum of the noise only. The spectral estimates are normalized in the sense that

$$\int_0^B P(f) df = 1$$

and

$$\int_0^B Q(f) df = 1$$

where B is the total bandwidth of the estimate. Then

$$P(f) = \frac{S(f) + N(f)}{P_s + P_n}$$

$$Q(f) = \frac{N(f)}{P_n}$$

where $N(f)$ is the noise spectrum; $S(f)$ is the signal spectrum; and P_s and P_n are the signal power and the noise power, respectively.

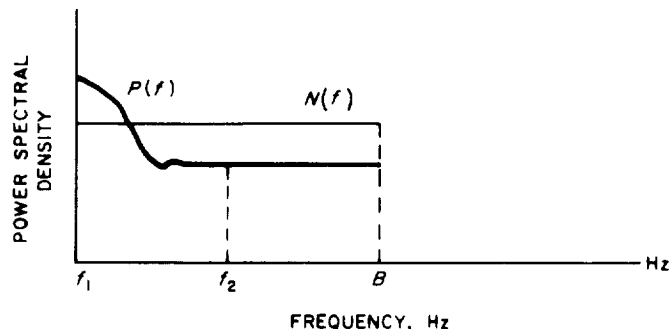


Fig. 35. Normalized spectrum of $P, N(f)$

In Fig. 35, C is defined as the intervals $(0, f_1)$ and (f_2, B) . Estimates of the true signal spectrum $S(f)$ are obtained as follows:

$$W(f) = P(f) - aQ(f)$$

where $W(f)$ is an estimate of $S(f)$, and a is a constant to be determined such that

$$\int_C W(f) df = 0$$

From this equation

$$a = \int_C P(f) df / \int_C Q(f) df$$

and by definition of the estimator

$$\text{SNR} = \frac{P_s}{P_n} = \frac{1}{a} - 1$$

The accuracy of this estimator has been determined in SPS 37-28, Vol. IV, pp. 219-222, and is discussed later in this article.

3. Computational Procedures in Program

a. Autocorrelation function. The first step in the program is the computation of the estimated autocorrelation function $R(t)$, using the N data values $\langle y_n \rangle$, $n = 0, 1, 2, \dots, N$. The function $R(t)$ is defined by the equation

$$R(t) = \lim_{T \rightarrow \infty} \left(\frac{1}{T} \int_{T/2}^{T/2+t} y(t_1) y(t_1 + t) dt_1 \right) \quad (1)$$

at a lag or displacement of t . The discrete form of this equation for a constant sampling rate h^{-1} and at a lag of $t = ih$ is

$$R(ih) = \frac{1}{N-i} \sum_{n=0}^{N-i} y_n y_{n+i}, \quad i = 0, 1, 2, \dots, K < N \quad (2)$$

In Eq. (2) h is the sampling rate in real time and is equal to N/T , and $K+1$ is the number of computed autocorrelation points. For all cases K is chosen such that it is much less than N ; therefore, Eq. (2) may be approximated by

$$R_i = R(ih) = \frac{1}{N} \sum_{n=0}^{N-i} y_n y_{n+i}, \quad i = 0, 1, 2, \dots, K \quad \text{B10}^5 (3)$$

Use of Eq. (3) gives a biased estimate for the autocorrelation function. However, for large N , and small K with

respect to N , the values obtained by using Eq. (3) differ very little from those obtained by using Eq. (2).

Since $R(0) \geq R(ih)$ for all i , a normalized value for the autocorrelation function is obtained by dividing R_i by R_0 , i.e.,

$$r_i = \frac{R_i}{R_0} \quad \text{B8 (4)}$$

where

$$R_0 = \frac{1}{N} \sum_{n=0}^N (y_n)^2 = y^{-2} \quad (5)$$

and where r_i is the normalized estimate of the autocorrelation function and is theoretically between plus and minus one.

b. Power spectral density function. An estimate $P(f)$ of the true power spectral density function is defined for an arbitrary frequency f within the range $0 \leq f \leq f_c$ by

$$P_j = P(f_j) = 2h \left[r_0 + 2 \sum_{i=1}^{K-1} r_i \cos\left(\frac{\pi i f_j}{f_c}\right) + r_K \cos\left(\frac{\pi K f_j}{f_c}\right) \right], \quad j = 0, 1, 2, \dots, L \quad \text{B10 (6)}$$

where f_c is the cutoff frequency. The cutoff is chosen to be $\frac{1}{2}h$ in the program, which in this case makes f_c the same as the bandwidth of the estimate B . The quantity $L+1$ is the number of points on the power spectral density curve and is an input to the program. This equation is derived by taking the Fourier transform of $R(t)$.

After the Fourier transform is taken by using the equation for $P(f_j)$ or Eq. (6) above, the transformation is checked for accuracy by using

$$\int_0^B P(f) df = r(0) = 1 \quad (7)$$

or

$$r(0) = \frac{1}{2hL} (\frac{1}{2}P_0 + \sum_{j=1}^{L-1} P_j + \frac{1}{4}P_L) = 1, \quad L = K \quad \text{B2 (8)}$$

⁵ $B(N)$ indicates the binary scaling of the quantity in the computer program. For instance, B10 indicates that the binary point is located at bit ten of the 24-bit fixed point word.

The estimate of the autocorrelation function $R(t)$, as computed by the program, is actually an estimate $\tilde{R}(t)$ of the autocorrelation function for samples of data values taken from

$$\tilde{y}(t) = y(t) D(t) \quad (9)$$

where

$$D(t) = \begin{cases} 1, & 0 \leq t \leq T \\ 0, & \text{otherwise} \end{cases}$$

This is accounted for in the estimate of the power spectral density by using the "Hanning lag window" weighting function defined by

$$D_i = D(ih) = \begin{cases} \frac{1}{2} \left[1 + \cos\left(\frac{\pi i}{K}\right) \right], & i = 0, 1, \dots, K \\ 0, & \text{otherwise} \end{cases} \quad (10)$$

and

$$\tilde{y}_i = D_i y_i$$

The power spectral density $PS(f)$ associated with $y(t)$ is then obtained from the computed estimate $P(f)$ of the power spectrum of $\tilde{y}(t)$ by smoothing or "Hanning" as follows:

$$PS(0) = \frac{1}{2}P_0 + \frac{1}{2}P_1$$

$$PS(j) = \frac{1}{4}P_{j-1} + \frac{1}{2}P_j + \frac{1}{4}P_{j+1}, \quad j = 1, 2, \dots, L-1$$

$$PS(L) = \frac{1}{2}P_{L-1} + \frac{1}{2}P_L \quad B2(11)$$

This particular smoothing method is very adaptable to a binary digital computer, since the multiplication involves only register shifts.

c. Estimate of system performance. At the beginning of a program run the spectrum of the noise only

$$Q(f) = \frac{N(f)}{P_n}, \quad 0 \leq f \leq B$$

is first computed using the method outlined above. The integral

$$INQC = \int_0^C Q(f) df \quad B2$$

is then calculated by summing as follows:

$$INQC = \sum_{j=L/2}^{L-1} PS_j + \frac{1}{2}PS_L \quad B2$$

where C is the interval $(\frac{1}{2}B, B)$, and B is equal to one-half the sampling rate. This same procedure is followed in computing

$$INPC = \int_0^C P(f) df \quad B2$$

The SNR of the dynamic AGC is then estimated by calculating

$$\begin{aligned} \text{SNR} &= \frac{INQC - INPC}{INPC} \\ &= \frac{P_s}{P_n} \end{aligned} \quad B11$$

The performance of this estimator has been determined in SPS 37-28, Vol. IV, pp. 219-222. For the present case

where f_1 is zero and f_2 is $B/2$

$$\sigma_{SNR}^2 = \frac{2}{TB}$$

where T is the total sampling time.

4. Conclusion

The following conclusions are based on results obtained by simulating, within the computer, signal and noise conditions that would be expected at a station. These conditions consist of having the dynamic AGC voltage with a signal represented by some dc level mixed with white noise. It is expected that the signal will, in general, be completely masked by the noise and that the noise background will be stable for long periods of time.

In the simulation of the noise conditions, random numbers are generated by a random number generation sequence. These random numbers are distributed uniformly over some plus and minus full scale range. This range is adjusted by a multiplier that is read in from the typewriter. Curves for the case where the numbers are uniformly distributed between plus and minus one are shown in Figs. 36 and 37. These curves were plotted by a line printer plotting subroutine, and the ordinate is printed in the right-hand column. For this test a total of 12,000 samples was taken, and 50 autocorrelation points were computed.

There are two indications, besides the curves themselves, of the accuracy of the results. One is I , the integral of the estimate of the power spectral density over the bandwidth of the estimate. From Eq. (7) I should be 1.00, the results show I to be 0.9785. This is an indication of the accuracy of the Fourier transformation subroutine, which is written in fixed point single precision arithmetic. The other indication is the value of R_0 for this test. Theoretically, for uniformly distributed numbers between plus and minus one, R_0 is $\frac{1}{3}$ or 0.3333. From Fig. 36, R_0 is 0.3325, which is not only an indication of the accuracy of the program but is also an indication of the value of the simulation itself. After testing the random numbers, a series of simulated test runs was carried out on the computer. The tests were performed as follows:

- (1) The power spectrum of the random numbers was calculated to obtain an equivalent noise background. From this spectrum the integral $INQC$ was calculated.

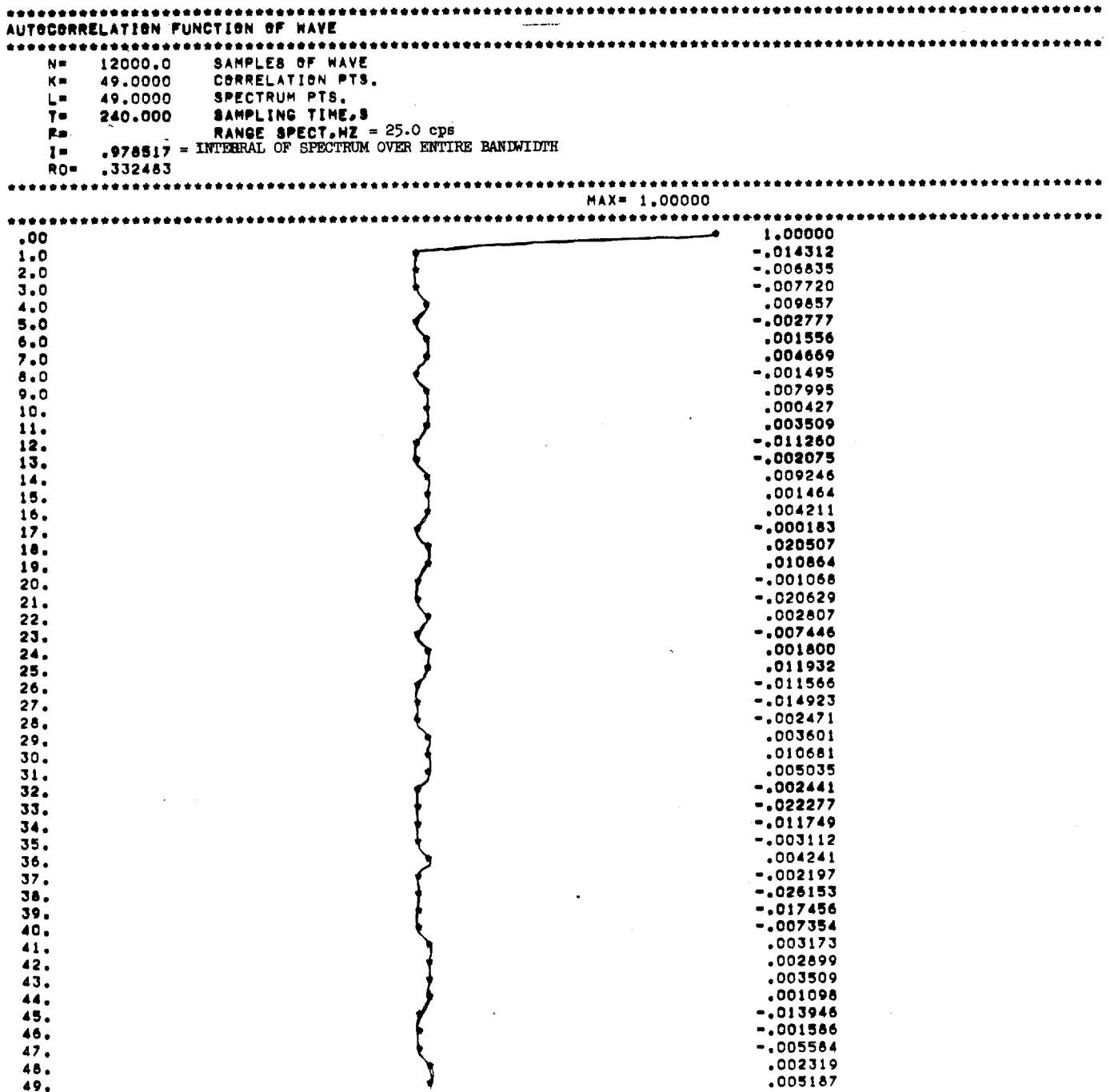


Fig. 36. Autocorrelation function of wave (noise only, -- 1.0, 1.0)

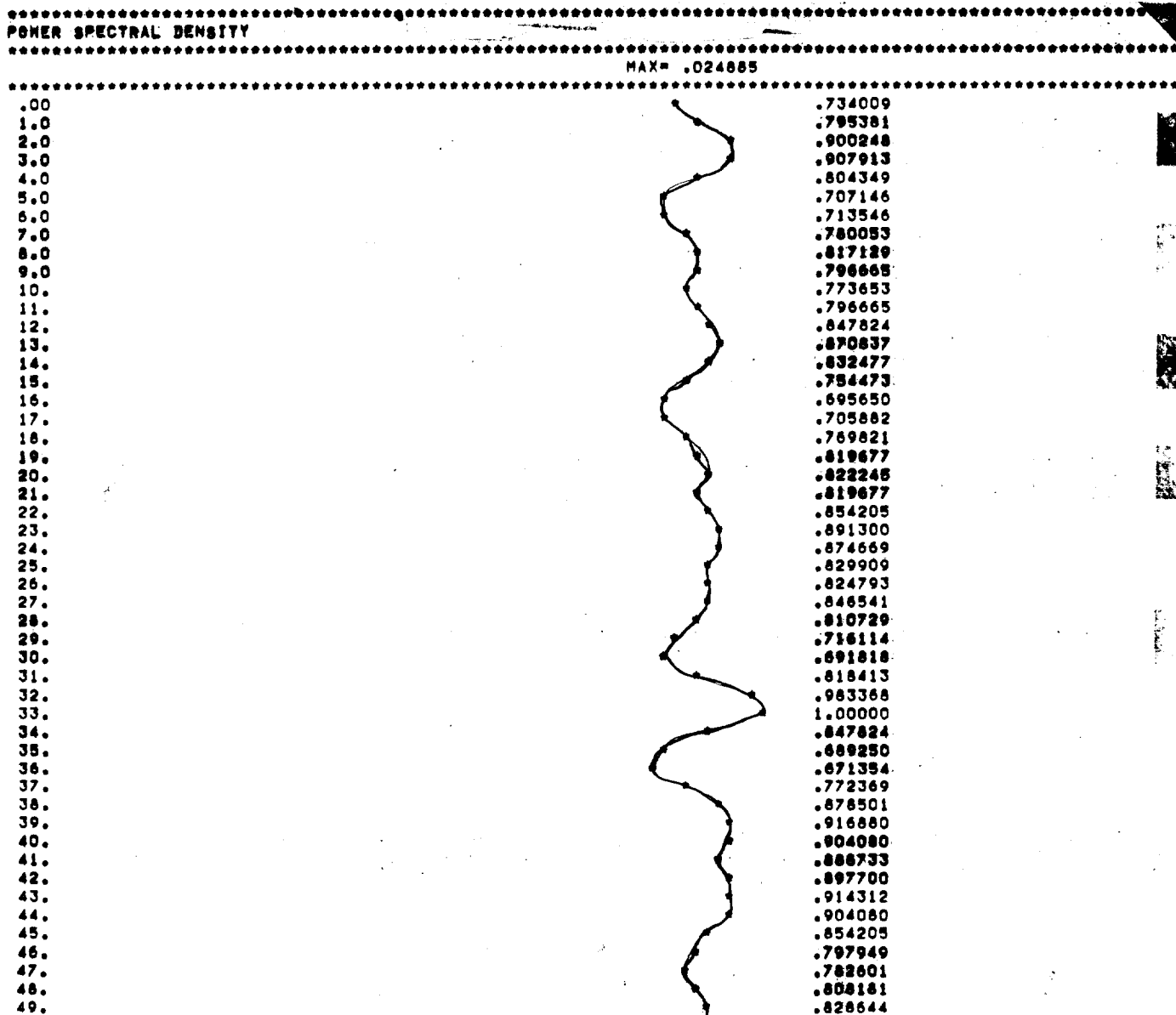


Fig. 37. Power spectral density (noise only)

- (2) A dc level and the range of variation of the random numbers were input to the program from the typewriter. This range of variation is the interval over which the random numbers are uniformly distributed.
- (3) The integral *INPC* was then calculated and using *INQC* from item (1) the estimator SNR was calculated.
- (4) The dc level was decreased by some predetermined value and item (3) was repeated until the results became insignificant. The range of variation of the random numbers was held constant during each test.

During all ten tests the value of N was 6000 and T was assumed to be 120 s. This is equivalent to a real time sampling rate of 50 s^{-1} . With this particular sampling rate approximately 200 autocorrelation points could have been computed; however, during the test only 50 were actually computed. Therefore, plenty of time is provided for the computer to perform other functions. The results from the ten tests are plotted in Fig. 38. The ordinate is the quantity a , where from subsection 2

$$a = \frac{INPC}{INQC}$$

The abscissa is the amplitude of the dc level. The numbers on each of the curves represent the range of varia-

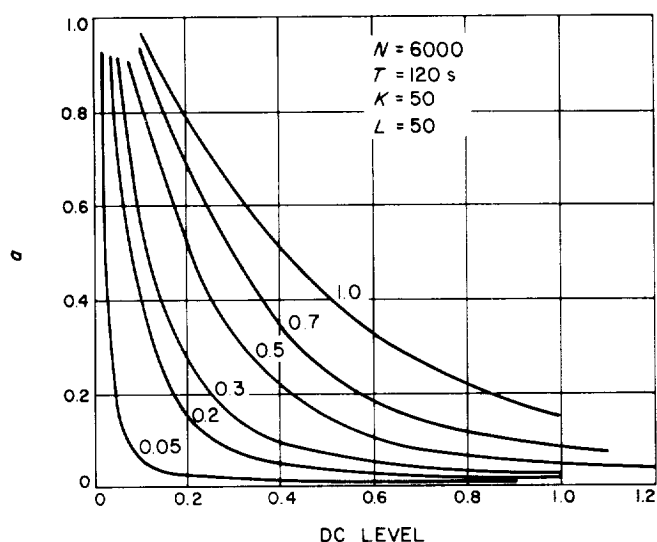


Fig 38. Simulated signal and noise test series results

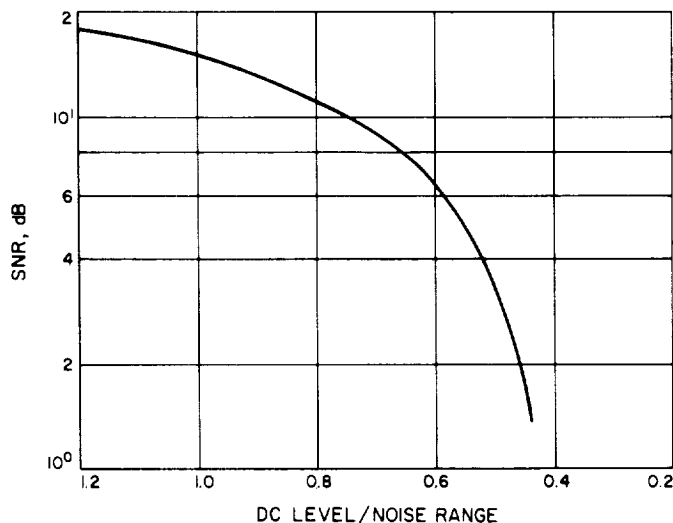


Fig. 39. Plot of the ratio of the dc level to range of the random numbers versus the estimated SNR

tion of the random numbers. Figure 39 was plotted to show the variability of the estimator. For instance of the ten points computed for a ratio of one, the maximum variation of all ten estimates of SNR was $< 1 \text{ dB}$.

L. Advanced Development of Microwave Antenna Subsystems: 500-kW Component Prototypes,

R. W. Hartop

Initiation of a program to develop microwave components capable of handling 500 kW of CW power, with a design goal of 2000 kW CW, was reported in SPS 37-40, Vol. III, p. 80. Contracts have now been placed for the following prototype units:

- (1) Megawatt cassegrain monopulse (MCM) feed system.
- (2) Megawatt cassegrain diplexer (MCD).
- (3) Megawatt transmitter filter (MTF).
- (4) Megawatt receiver filter (MRF).
- (5) Megawatt waveguide switch (MWS).

Table 6 presents some of the critical specifications for these units. The design goals are not shown, but will be discussed from time to time as the units are received and tested.

All of the prototype units except the MWS will be either fabricated from oxygen-free high-conductivity (OFHC)

Table 6. Partial specifications for prototype components

Unit	Frequency bands, MHz	Maximum insertion loss, dB	Minimum isolation, dB	Maximum VSWR
MCM feed system	2110 \pm 10	0.075	$\left\{ \begin{array}{l} 36 \text{ (Sum)} \\ 20 \text{ (Error)} \end{array} \right\}$	$\left\{ \begin{array}{l} 1.10 \text{ (Sum)} \\ 1.50 \text{ (Error)} \end{array} \right\}$
	2250 \pm 50	0.075		
	2388 \pm 5	0.075		
MCD	2110 \pm 10	0.030	90	1.10
	2285 \pm 15	0.070	25	1.15
MTF	2110 \pm 10	0.040	—	1.05
	2285 \pm 15	—	100	—
MRF	2110 \pm 10	—	110	—
	2285 \pm 15	0.10	—	1.20
MWS	2110 \pm 10	0.035	60	1.05
	2285 \pm 15	0.035	60	1.05

copper or will be electroformed in copper. An attempt is being made to arrive at a successful MWS design using a water-cooled aluminum rotor because of the excessive weight of a copper switch in WR-430 waveguide. The first attempt in this direction failed when the prototype MWS jammed after being exposed to a circulating power level of 466 kW in the traveling wave resonator (TWR). The unit has been returned to the manufacturer for rework.

The prototype MTF has been delivered by the Rantec Division of Emerson Electric Company and is awaiting high-power testing. Figure 40 shows the MTF installed in the TWR. The filter exceeds the requirements of the JPL specification with regard to insertion loss and VSWR. Its measured insertion loss of 0.027 dB compares to a design goal of 0.015 dB, and the measured VSWR is 1.03 maximum.

The prototype MCD has been completed by Rantec and will be shipped to JPL and tested during the next reporting period. The MRF will also be completed during this period.

All of the above prototype units, together with the MCM feed, will be incorporated into a complete cassegrain cone assembly (the MCM cone) for complete field testing, including operation on the Venus 85-ft antenna and/or the Mars DSS 210-ft antenna.

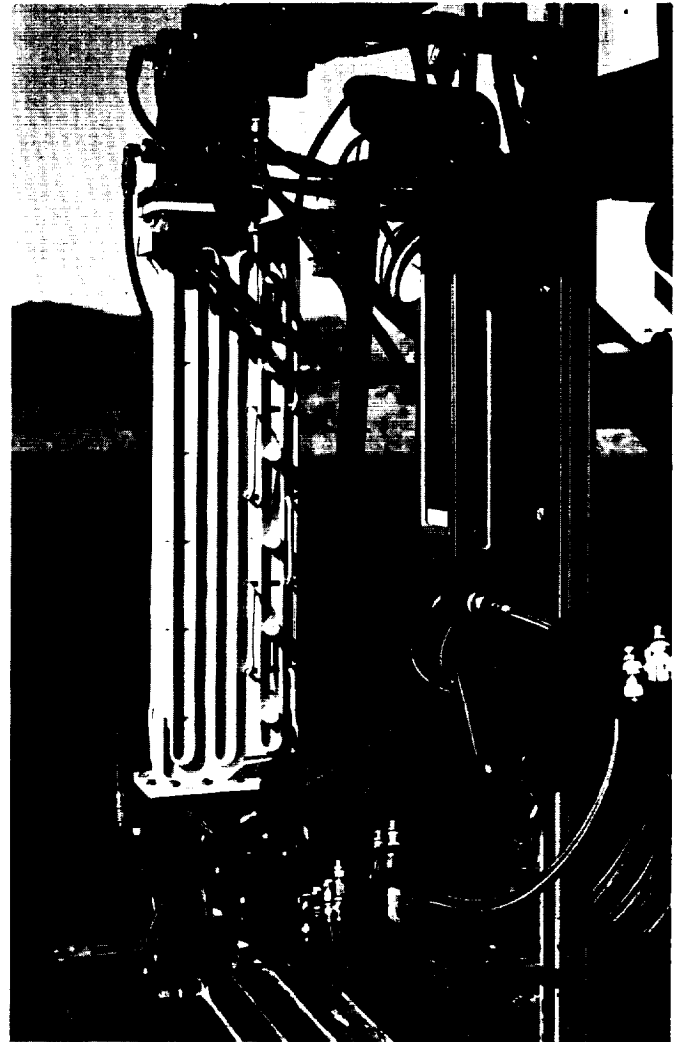


Fig. 40. Megawatt transmitter filter

M. A 1-MHz Cleanup Loop for Mariner Venus 67 Precision Ranging and Occultation Experiments, R. B. Crow

1. Introduction

The 1-MHz cleanup loop was designed to provide spectrally pure references derived from either a local or a remote (via microwave link) rubidium standard. This cleanup loop employs a precision quartz oscillator and is designed to automatically phase-lock to a 1 MHz \pm 60 mHz signal (Fig. 41) and has coherent 100 kHz, 1 and 5 MHz outputs available through distribution amplifiers.

Several interesting problems presented themselves in the design of this loop. To produce the desired spectral purity, it is necessary to use a narrow loop bandwidth to

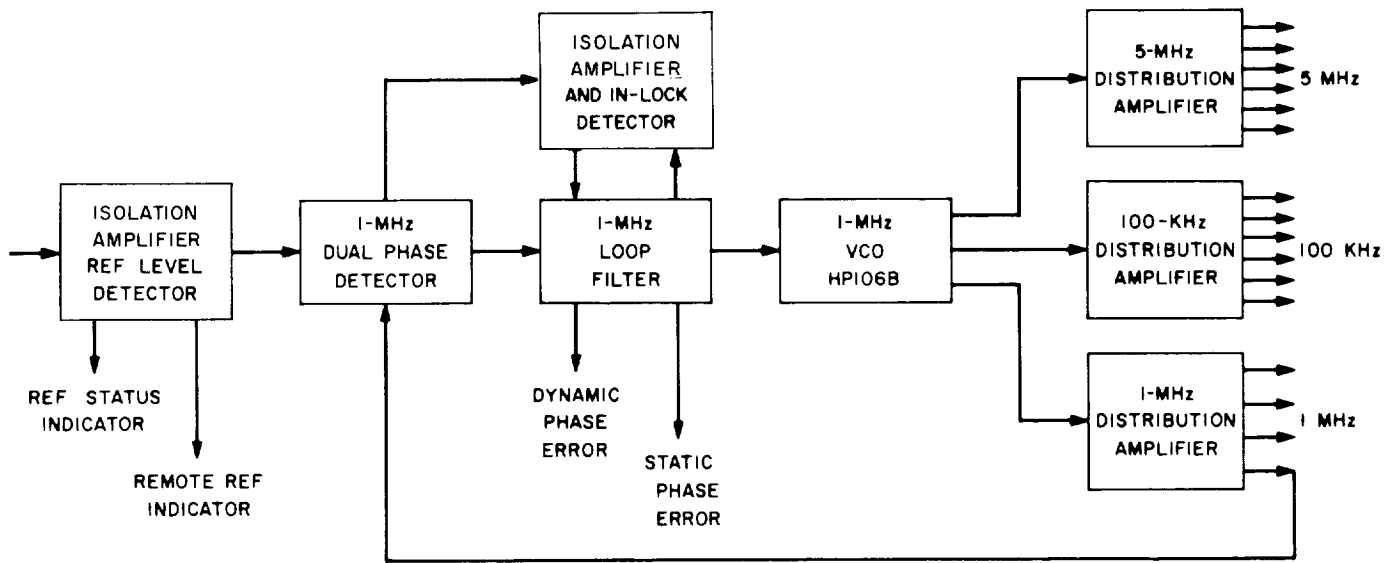


Fig. 41. 1-MHz cleanup loop

reduce the short-term jitter caused by the microwave link/rubidium standard. Past experience with the microwave link (SPS 37-39, Vol. III, p. 106) indicated that a $2B_L \leq 0.03$ Hz was desired in order to yield a pure reference signal. A bandwidth of $2B_L = 0.02$ Hz was decided upon after evaluating the short-term phase stability of the quartz oscillator to be used as the loop VCO. This narrow bandwidth presents an acquisition problem, since the time required for phase lock with an initial offset of only 30 mHz is 67 min. To overcome this problem, the bandwidth is increased to 0.08 Hz automatically when the loop is unlocked and allowed to decrease logarithmically toward 0.02 Hz upon achieving lock. This bandwidth change shortens the acquisition time from 67 min to less than 30 s for a 30-mHz offset.

2. System Description

The loop was designed to have a loop bandwidth ($2B_L$) of 0.02 Hz and a loop damping factor of 1 (i.e., $r = 4$, as described in Ref. 13). To widen the loop bandwidth to 0.08 Hz, the photoresistor (Fig. 42) is placed around R1 and R2. This allows the filter capacitor C1 to quickly charge to the required voltage so that no transient is observed when the loop bandwidth is reduced. It should be noted that the loop damping is unchanged in the wide-band condition. This is done by changing both τ_1 and τ_2 in the correct ratio so that the damping factor

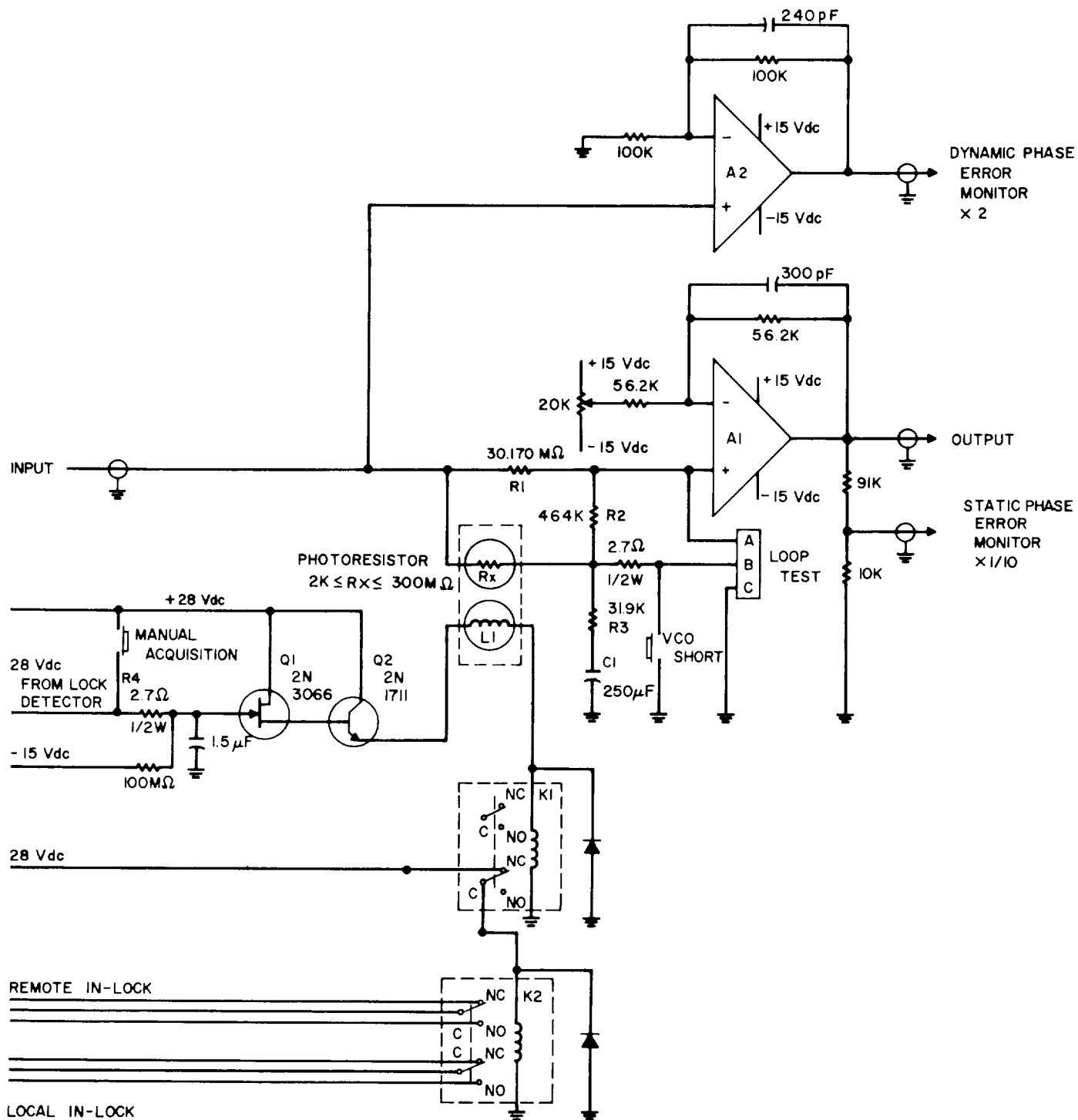
$$\zeta = \frac{1}{2} \left[\frac{1 + AK\tau_2}{(AK\tau_1)^{1/2}} \right]$$

remains unchanged.

The acquisition circuit operates as follows: Assume the loop to be in a locked condition. If the input signal is removed, the reference status will show no input and the loop will indicate an unlocked condition. As soon as an input of 1 MHz (input power between +3 to +13 dBmW) is applied to the loop, the loop automatically begins to acquire. A relay in the lock detector places +28 Vdc on R4. This causes Q1 and Q2 to turn on, thus turning on the photoresistor light source. The photoresistor changes resistance from 300 M Ω to 2K when the light is turned on. This widens the bandwidth from 0.02 to 0.08 Hz and allows the loop to lock to the input frequency (offset by as much as ± 60 mHz) within 1 min (Fig. 43).

As the quadrature phase detector indicates phase lock, the relay in the lock detector drops out removing the +28 Vdc from R4. This allows the photoresistor light source to dim slowly as the gate of Q1 charges toward -15 Vdc. This gradual change in resistance allows a smooth bandwidth reduction so the loop remains in lock. As the voltage to the light is reduced, relay K1 drops out (after approximately 3 min), indicating: (1) that the quadrature phase detector indicates lock, and (2) that an acquisition cycle has been completed and that the loop bandwidth is very close to 0.02 Hz.

Operational amplifier A1 was used to allow a dc offset to the HP106B so that the VCO slope and linearity could be optimized. The HP106B quartz oscillator used in this loop as the VCO is a precision oscillator intended for use as a frequency or time standard. Sinusoidal output frequencies of 5 MHz, 1 MHz, and 100 kHz are provided.



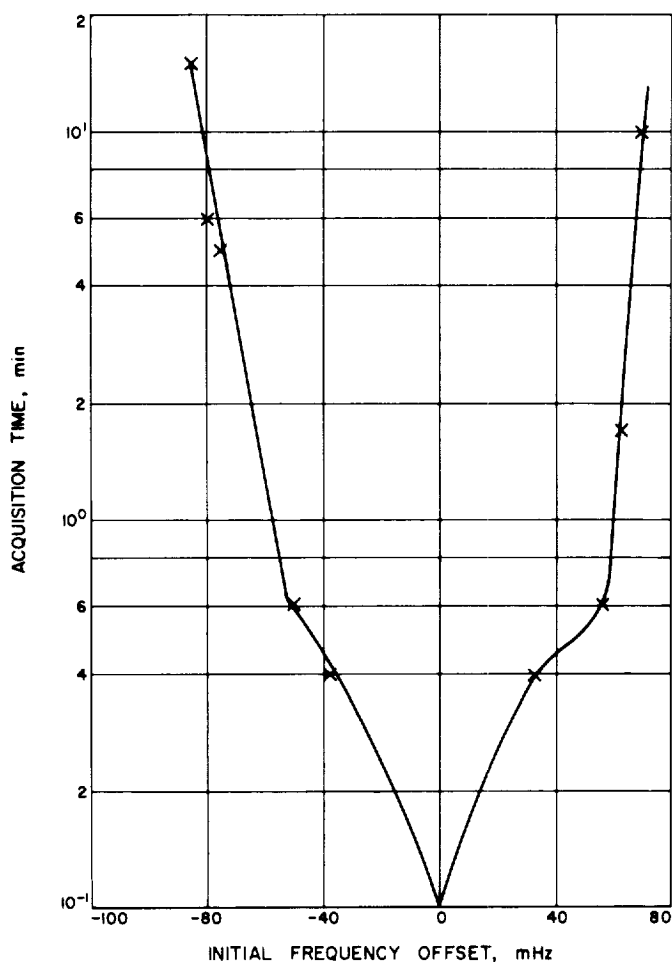


Fig. 43. Acquisition time as a function of original frequency offset

Short-term stability of the 5-MHz output is 1.5 parts in 10^{11} (rms), averaged over a 1-s sample period. Aging rate is less than ± 5 parts in 10^{11} per 24 h. The oscillator frequency can be electrically varied over a range of 12 parts in 10^8 with a dc voltage of ± 5 V.

The basic 2.5-MHz signal is generated by the 2.5-MHz crystal oscillator, amplified and leveled by the AGC circuits, further amplified, doubled, and filtered by the buffer, and supplied to the output amplifier stages. The 5-MHz signal is supplied to the 5-MHz output connectors on the front and rear panels; also to the 1-MHz regenerative

divider. The 1-MHz regenerative divider will not have an output until the 1-MHz start button is depressed. The 1-MHz signal is supplied to the 1-MHz output connectors on the front and rear panels; also to the 100-kHz regenerative divider. (The 100-kHz regenerative divider must also be started manually to obtain an output.) The 100-kHz signal is supplied to the 100-kHz output connectors on the front and rear panels; also through an emitter follower to a rear panel clock connector.

The HP106B can be operated from ac line voltage of 115 or 230 V. An external power supply or batteries can be connected as an alternate supply. When operated from the ac line, the ac interruption light on the HP106B front panel indicates ac line voltage interruption or failure, and the internal battery operates the instrument for approximately 8 h. If the internal battery voltage drops below 20 V, relay K1 is de-energized, and its contacts open the battery supply circuit to prevent complete battery discharge. When ac line voltage is restored, the instrument receives power from the ac line, and the internal battery is charged at a rate determined by the battery charge switch position (float or fast). The ac interruption lamp is turned off when the reset button is pushed. If ac line voltage is present, the lamp stays off. The time required for the inner oven of the HP106B to stabilize its temperature is $8\frac{1}{2}$ h; however, phase lock of the loop is possible after approximately $3\frac{1}{2}$ h.

The meter indications for all positions of the switch are intended to be 80% of full scale with the 5-MHz, 1-MHz, and 100-kHz outputs unloaded.

New 100-kHz and 5-MHz distribution amplifiers were developed for this loop, since none was available among the standard DSIF modules.

The loop bandwidth was measured as 0.021 Hz (design nominal was 0.20 Hz) with a $1-\sigma$ jitter of 0.04 deg rms when locked to the local rubidium frequency standard. A jitter test was conducted at the Mars DSS when the system was installed by measuring the amount of receiver jitter (when locked to a strong test signal) using the local reference and the reference from the 1-MHz cleanup loop. No difference could be seen in this test, indicating that the reference noise is less than the receiver noise.

References

1. Tausworthe, R., *Theory and Practical Design of Phase Locked Receivers*, Technical Report 32-819, Jet Propulsion Laboratory, Pasadena, Calif., Feb. 15, 1966.
2. SDS 900 Series Real-Time FORTRAN II, No. SDS 90 10 48B, Scientific Data Systems, Santa Monica, California, Jan. 1966.
3. Bathker, D. A., "A Stepped Mode Transducer Using Homogeneous Waveguides," *IEEE Trans. Microwave Theory and Techniques*, Vol. MTT-15, No. 2, pp. 128-130, Feb. 1967.
4. Clauss, R. C., *A Traveling Wave Maser For Deep Space Communication at 2295 and 2388 MHz*, Technical Report 32-1072, Jet Propulsion Laboratory, Pasadena, Calif., Feb. 15, 1967.
5. DeGrasse, R. W., Schultz-DuBois, E. O., and Scovil, H. E. D., "Three-Level Solid-state Traveling-wave Maser," *Bell Syst. Tech. J.*, Vol. 38, No. 2, pp. 305-334, March 1959.
6. Okwit, S., and Smith, J. G., "Packaged Electronically Tunable S-Band Traveling-Wave Maser System," *Proc. IRE*, Vol. 50, pp. 1470-1483, June 1962.
7. Chen, F. S., and Tabor, W. J., "Filling Factor and Isolator Performance of the Traveling-Wave Maser," *Bell Syst. Tech. J.*, Vol. 43, No. 3, pp. 1005-1033, May 1964.
8. Potter, P. D., *A New Horn Antenna with Suppressed Sidelobes and Equal Beamwidths*, Technical Report 32-354, Jet Propulsion Laboratory, Pasadena, Calif., Feb. 25, 1963.
9. Larson, W., "Analysis of Rotation Errors of a Waveguide Rotary Vane Attenuator," *1962 IRE International Convention Record*, Mar. 1962.
10. James, A. V., "A High-Accuracy Microwave-Attenuation Standard for Use in Primary Calibration Laboratories," *IRE Trans. Instrumentation*, Vol. I-11, pp. 285-290, Dec. 1962.
11. Larson, W., "Gearing Errors as Related to Alignment Techniques of the Rotary Vane Attenuator," *IEEE Trans. Instrumentation and Measurement*, Vol. IM-14, No. 3, pp. 117-123, Sept. 1965.
12. Worthing, A. G., and Geffner, J., *Treatment of Experimental Data*, John Wiley & Sons, Inc., New York, pp. 195-196, Dec. 1960.
13. Tausworthe, R. C., *Theory and Practical Design of Phase-Locked Receiver*, Vol. I, Technical Report 32-819, Jet Propulsion Laboratory, Pasadena, Calif., Feb. 15, 1966.

IV. Communications Engineering

A. DSN 10-kW Transmitters, B. W. Harness and R. L. Leu

1. Summary

The DSN employs seven 20-kW transmitters and five 10-kW transmitters. In this report, the operational limits and capabilities of the 4KM50SI klystron used in the 10-kW transmitters are explained, and it is concluded that specifications will be met only when operated at the designed power. The transmitter was designed to operate at a fixed output power of 10 kW; deviation from this will result in reduced gain, lower efficiency, narrow bandwidth, and power instability. Many requirements placed on the 10-kW transmitter by *Mariner*, *Surveyor*, *Pioneer*, and *Lunar Orbiter* projects are not compatible with the transmitter design. Extensive tests were conducted to verify the operation of the 4KM50SI klystron across the DSN transmitter 10-MHz frequency band without retuning and at reduced power levels. Some of the capabilities and limitations of the 10-kW transmitters, as determined by test, are as follows:

- (1) The best results at reduced power levels are obtained when the klystron is tuned at 10 kW with 10- to 50-mW drive power.

- (2) The klystron cannot be saturated across an 8-MHz frequency band at 10 kW when tuned with 10- to 50-mW drive power at desired center frequency. The design specification requires 10 MHz at the -3-dB points, with a constant drive power of 1 W.
- (3) The klystron cannot be saturated across an 8-MHz bandpass at power levels below 5 kW and cannot be operated in saturation below 500 W with the DSN exciter; e.g., 10 W are required to saturate the klystron across 3 MHz at 500-W output.

2. Klystron Drive Power

The 10-kW transmitter stations have a nominal drive power of 1 W available at the klystron. Although the Block I exciter buffer amplifier output is 3 W, there is a 4.5-dB insertion loss from the buffer amplifier output to the klystron input. The drive circuit of the transmitter has an insertion loss of 3.2 dB, which includes cable, diode switch, variable attenuator, isolator, and directional coupler. The additional insertion loss is in the cable connecting the buffer amplifier output to the transmitter input. The Block I buffer amplifier bandwidth is less than 10 MHz at the -1-dB points.

The future Block III buffer amplifier specification calls for a capability of greater than 3-W output with a 20-MHz, -1 -dB bandwidth. The additional bandwidth of the new buffer amplifier should increase the bandwidth capability of the 10-kW klystron.

3. Klystron Passband

In general, the definition of a bandpass is power out versus power in, at a constant power input. Since in this service klystrons are operated in saturation, this definition is not useful. The klystron power output is more susceptible to variations in input power, temperature, and voltage during nonsaturated operation. Unless nonsaturated operation is absolutely required, the klystron should be operated in saturation. The saturated stability is better than ± 0.1 dB. Operation of a klystron in saturation across a given frequency band will result in a completely different bandpass characteristic than with constant input power operation. Figure 1 represents the klystron frequency response with a constant drive and with the klystron in saturation. As indicated in Fig. 1, operating

the klystron in saturation gives a broader bandpass and higher output power than constant drive operation. When operating the klystron off the center frequency of 2115 MHz, the output power may be less than 10 kW. This low power condition can be corrected by simply raising the beam voltage (500 Vdc should be sufficient). There are two primary types of klystron tuning: synchronous and high efficiency. To synchronous-tune a klystron, all cavities are tuned to the center frequency, resulting in maximum gain with minimum drive, narrow bandwidth, and lower output power. High-efficiency tuning is similar to synchronous tuning, except that cavity 3 is tuned higher in frequency, resulting in maximum power out, but requiring more drive power because of the broader bandwidth.

4. Klystron Frequency Response Tests

Although the allocated transmitter band is 2110–2120 MHz, the usable coherent band for a DSN mission is reduced to 8 MHz. This reduction in the band is due to the 240/221 spacecraft translator ratio and the assigned

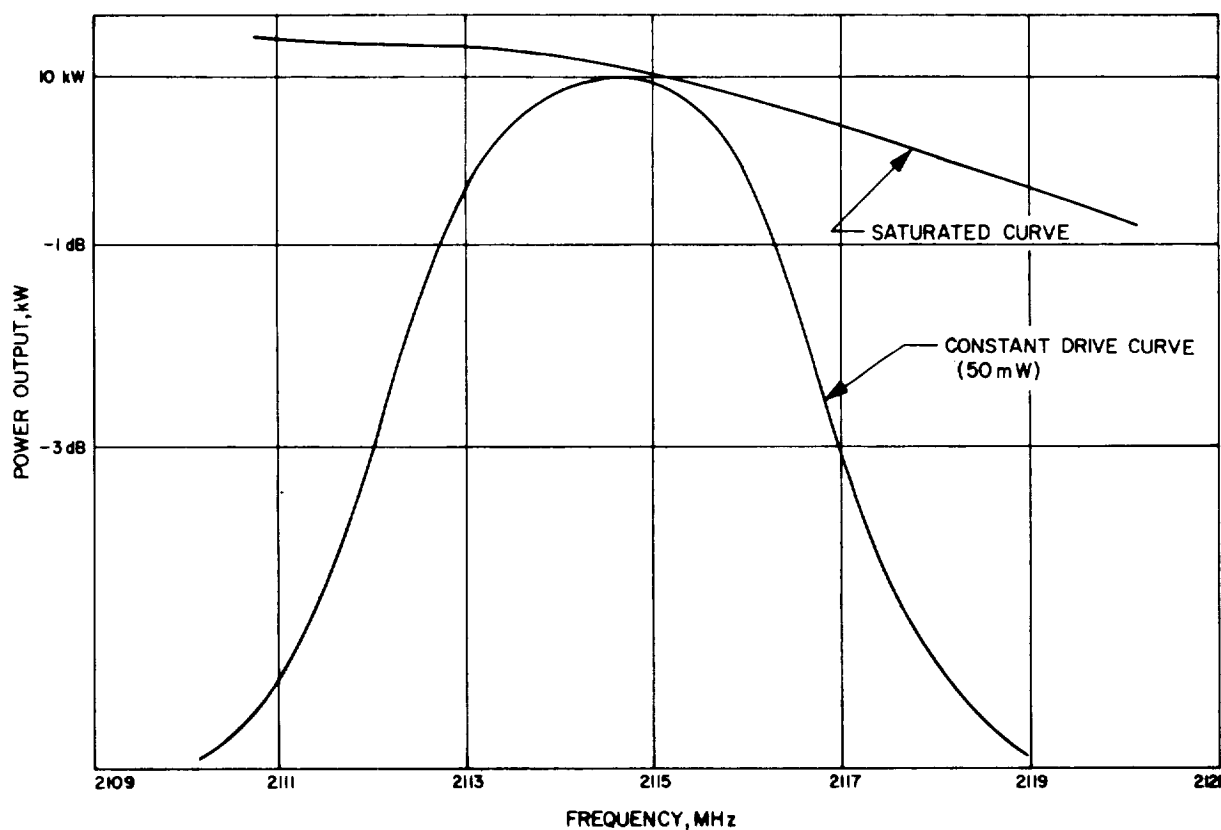


Fig. 1. Klystron power output versus frequency; response when operated in saturation and with constant drive power

receiver band of 2290–2300 MHz. For an uplink frequency of 2113 MHz, the down link is 2295 MHz, limiting the usable transmit band to 8 MHz (2110–2118 MHz).

It is desirable to operate the klystron amplifier over the assigned 10-MHz band without retuning. The cavity tuning mechanism is rated for 200 cycles of operation. With two separate missions per day for a station, if retuning is required, the cavities may be worn out or broken in a very short period of time. Tests were conducted to determine the limitations of the klystron operation with the following constraints:

(1) Klystron not to be retuned.

(2) Use drive power available from the exciter (1 W).
(However, the available drive power for these tests was 20 W.)

(3) Bandpass to be 8 MHz at -1 -dB points.

Available drive power is the limiting parameter in operating this klystron (4KM50SI) in saturation across an 8-MHz bandpass in the DSN transmitter. As discussed previously, the available drive power at the input to the klystron is nominally 1.0 W at center frequency, and the bandpass of the Block I buffer amplifier is much narrower than the klystron. Several saturation bandpass curves are plotted in Figs. 2, 3, and 4 for various conditions of klystron tuning.

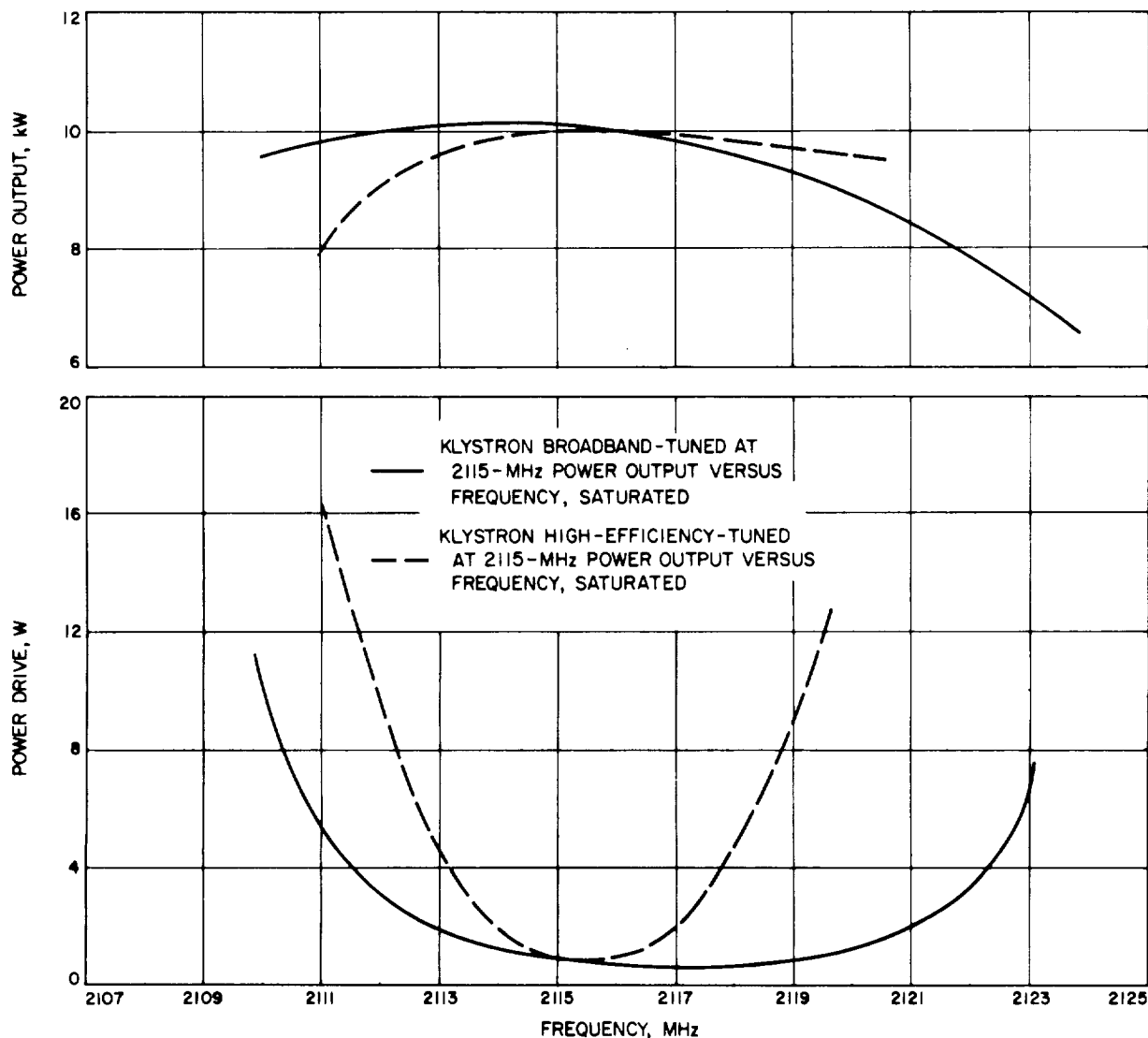


Fig. 2. Klystron power output and drive power versus frequency; broadband and high-efficiency tuning

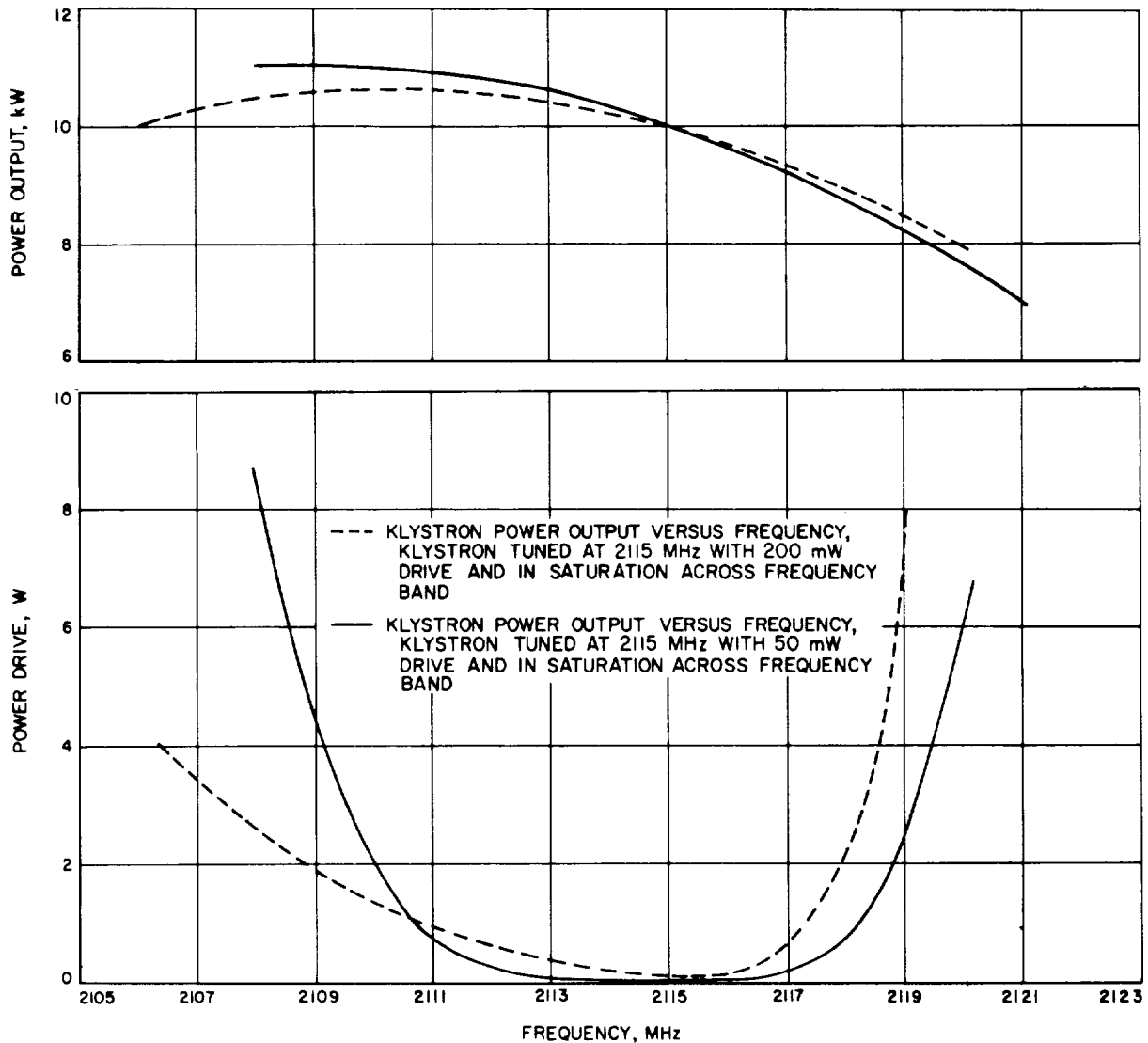


Fig. 3. Klystron power output and drive power versus frequency; 2115-MHz tuning, 50- and 200-mW drive, saturated

represent the drive power required to saturate the klystron at that given frequency.

Figure 2 shows the saturated bandpass curves when the klystron is broadbanded and high-efficiency-tuned. Examination of the drive curves shows that the required drive across the frequency band is much higher than the 1-W drive power available. The curves of Figs. 3 and 4 are derived from tuning the klystron for a given drive of 200, 50, and 10 mW at 2115 MHz and plotting the saturation bandpass for each tuned condition. This condition of tuning is nonstandard but easy to achieve. Basically, it is a modified version of the synchronous tuning condition. The drive into the klystron is set at

the desired level (200, 50, or 10 mW) and center frequency, with the beam voltage on and the cavities adjusted for maximum power out. The results are depicted in the saturation curves of Figs. 3 and 4.

When tuned at 50 and 10 mW, the klystron can be saturated across a 7-MHz frequency band without exceeding 1 W of drive power across the frequency band. With some fine-tuning of the cavities, the 8-MHz band is obtainable. However, when operated at off-center frequency, the drive power of the buffer amplifier will fall below the 1-W level, and it is impossible to achieve a response greater than 6 MHz without tuning the buffer. An appropriate drive level for tuning the klystron is

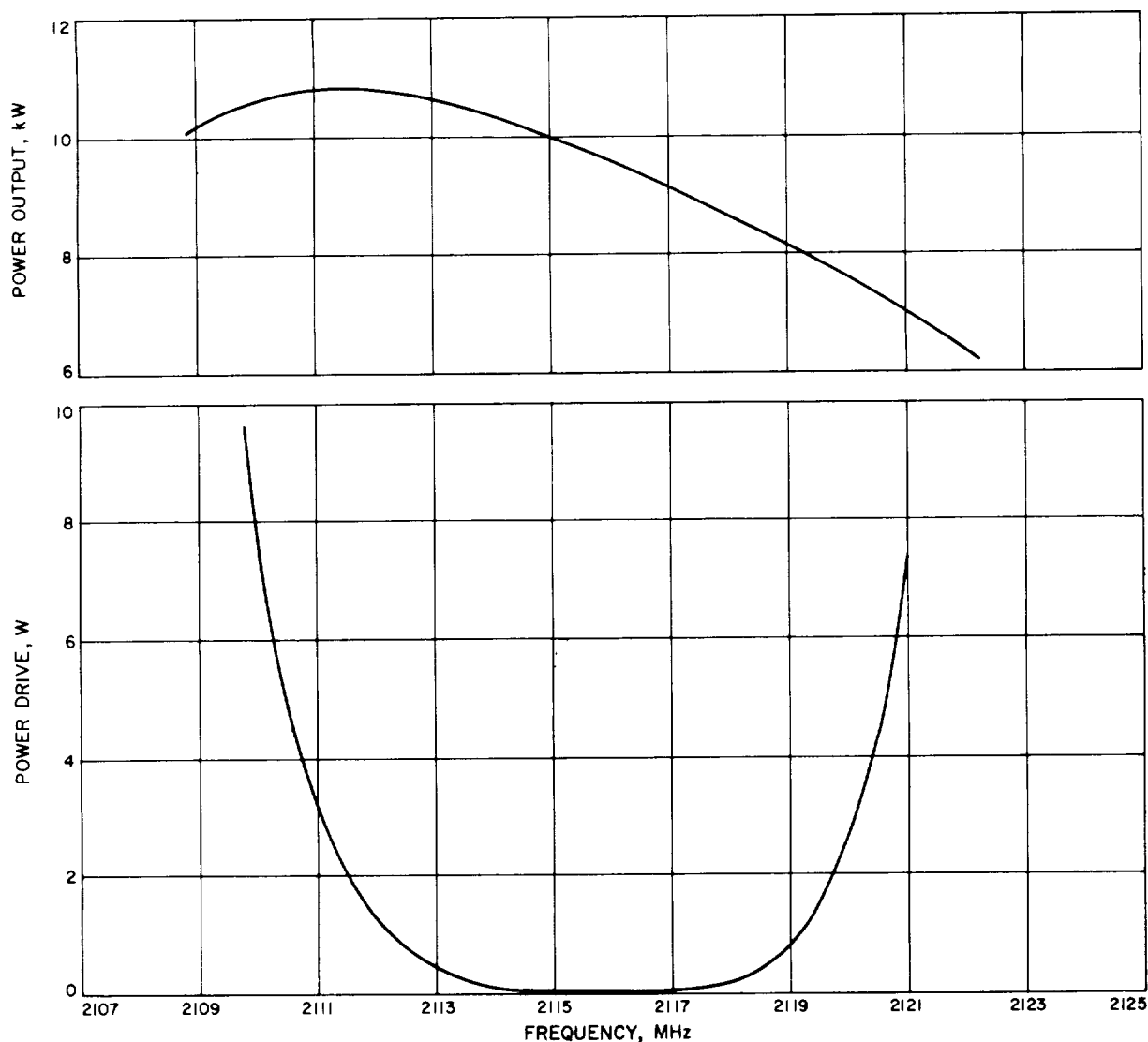


Fig. 4. Klystron power output and drive power versus frequency; 2115-MHz tuning, 10-mW drive, saturated

between 10 and 50 mW. This will vary for each klystron, and as a klystron ages, its performance may deteriorate to the point that the klystron cannot be operated across an 8-MHz band without retuning.

5. Reduced Power Operation

The flight projects *Lunar Orbiter*, *Surveyor*, *Pioneer*, and *Mariner* have placed a requirement on the 10-kW transmitter to operate at reduced power levels. In most cases, the low power radiation was restricted to earth orbit or special tests, but during some missions, the low power mode is a "standard" mode of operation. Tests were conducted to determine the operation of the kly-

stron at reduced power levels. The klystron tests were conducted on the basis that the tube was operated in saturation. Figure 5 is a series of saturated bandpass curves from 10 kW to 100 W for klystron tuning at 2115-MHz and 10-mW drive. As the beam voltage is reduced to lower power levels, the bandpass of the klystron is reduced, limiting the operational frequency range of the klystron. The klystron was not retuned as the beam voltage was lowered.

Also, as the beam voltage was lowered and the output power level was reduced, the drive level necessary to saturate the klystron across the frequency band became increasingly greater (Fig. 5). As shown in Table 1, when

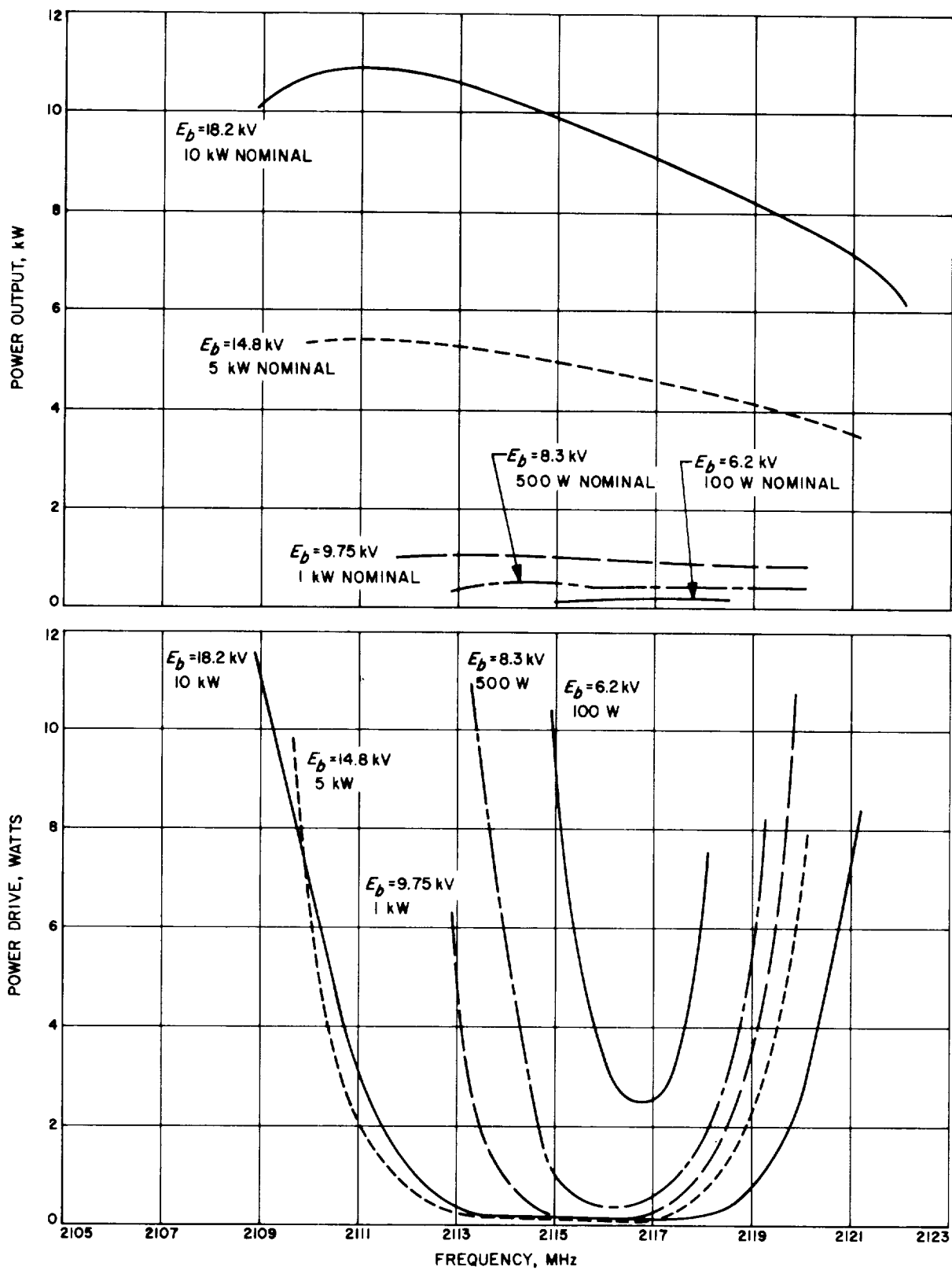


Fig. 5. Klystron power output and drive power versus frequency; reduced power operation

Table 1. Power output, drive power, beam voltages and beam current for various klystron-tuned conditions^a

Klystron tuning	P_o , kW	P_d , W	E_b , V	I_b , A
Broadband tuned	10.3	1.2	17.3	1.78
	5.	2.2	14.0	1.35
	1.	14.5	9.9	0.83
	0.5	20.0	8.8	0.70
	0.100	20.0	7.8	0.60
Efficiency tuned (saturated)	10.	1.0	16.8	1.75
	5.	1.7	14.5	1.42
	1.	8.5	11.0	0.96
	0.5	16.0	9.8	0.84
	0.10	20.0	7.6	0.58
Tune 200-mW drive (saturated)	10.	0.200	18.0	1.9
	5.	0.410	14.6	1.44
	1.	2.7	9.7	0.80
	0.5	13.0	8.1	0.64
	0.10	20.0	6.8	0.50
Tune 50-mW drive, constant drive, no retuning	10.	0.050	18.0	1.9
	5.	0.092	14.7	1.45
	1.0	0.900	9.6	0.79
	0.500	3.6	8.2	0.64
	0.100	14.2	6.5	0.48
Tune 50-mW drive, constant drive, tune for best response at each power level	10.	0.050	18.0	1.9
	5.	0.038	14.5	1.44
	1.	0.200	9.7	0.81
	0.500	0.265	8.3	0.65
	0.100	6.15	6.0	0.43
Tune 10-mW drive, retune cavities for best response	10.	0.016	18.2	1.89
	5.	0.028	14.8	1.45
	1.	0.155	9.75	0.81
	0.5	0.350	8.3	0.66
	0.1	3.8	6.2	0.44
^a All data recorded at center frequency (2115 MHz). P_o = Power output. P_d = Drive power. E_b = Beam voltage. I_b = Beam current.				

the output power was reduced below 100 W, it was not possible to saturate the klystron with the available 20 W of drive power. Table 1 shows the drive power required to saturate the klystron at center frequency for various modes of tuning. In the 10-kW transmitters, the output power is monitored with a power meter connected to a -63-dB port of a waveguide directional coupler. To measure the klystron RF output, the lower scales on the power meter must be used; for *Lunar Orbiter*, the lowest scale is required. The quality of the RF power measurement is questionable because of power meter accuracy on the low range and the instability of the klystron in the nonsaturation operation.

When operating at reduced power levels at lower beam voltages, the incidental phase modulation of the klystron increases considerably. For example, for 10-kW ($E_b = 18.2$ kV) operation, the phase-pushing figure for the klystron is 0.058 deg/V; for 1 kW ($E_b = 9.75$ kV) operation it is 0.17 deg/V. With a small change in the dc beam voltage due to ripple or modulation, the klystron incidental phase noise contribution will be greater at reduced power levels.

6. Conclusion

Since the 4KM50SI klystron was designed to operate at 10 kW and the test results indicate adherence to the specification only above 5 kW, operation below 5 kW is not recommended. If there is a definite low power radiation requirement, a new low power transmitter should be designed.

It can be concluded from the test data plotted in Figs. 3 and 4 that the 4KM50SI klystron can only be saturated across a 7-MHz bandpass. In comparison, the 5K70SG 20-kW klystron used in the 20-kW DSN transmitters can be saturated across a 14-MHz, -1-dB bandpass, with a maximum of 700-mW drive power to the klystron. Even so, the 20-kW klystron is not expected to function properly when operated at reduced power levels.

Similar tests will be conducted on the 5K70SG klystron to establish the capabilities and limitations of the 20-kW transmitter.

B. Modification of a Cassegrain Cone Assembly To Reduce System Noise Temperature, R. W. Hartop

An experimental modification of a GSDS S-band cassegrain monopulse (SCM) cone assembly to reduce the system noise temperature was described in SPS 37-45, Vol. III, pp. 65-66; the observed decrease of $11.5 \pm 1.0^\circ\text{K}$ in total system noise temperature was shown to agree with theory.

During the week of May 7, 1967, the low-noise bypass kit was shipped to DSS 51 and installed in the SCM cone. To further improve the ground system performance in tracking the *Pioneer VII* spacecraft, a receiver modification kit to provide a 3-Hz tracking loop bandwidth was also installed.

Because of limitations in the system noise temperature measurement technique, the results for DSS 51 are less accurate than those obtained with the special techniques used at Goldstone. However, the reduction in noise temperature shown in Table 2, although less than that measured at Goldstone, still falls within the predicted value of $11.5 \pm 1.0^\circ\text{K}$ if a 1.0°K tolerance is applied to the measured values.

Table 2. Improvement in system noise temperatures

Receiver	System noise temperature, $^\circ\text{K}$		Improvement	
	GSDS	Low noise	$^\circ\text{K}$	dB
1	42.5	33.1	9.4	1.09
2	43.3	33.5	9.8	1.12

Receiver threshold measurements before and after installation of the low-noise modification kit gave the results shown in Table 3, which are in closer agreement with the Goldstone results reported earlier.

Table 3. Receiver threshold measurements

Receiver	Bandwidth, Hz	Threshold, dBmW		Improvement, dB
		GSDS	Low noise	
1	12	-172.3	-173.8	1.5
2	12	-172.0	-174.5	2.5

The measurements show some scatter, indicating the difficulty of making precise threshold measurements with phase-locked-loop receivers. Nevertheless, the obvious improvement in system performance demonstrates that the modifications can be used successfully for certain marginal telemetry operations.

C. Results of Signal Acquisition Dynamic Tests Performed at the DSS 11 MSFN Wing, R. L. Weber

1. Summary

This report will show the recorded data and summarize the results of the S-band acquisition aid (SAA) signal acquisition and SAA-to-S-band tracking antenna hand-over tests performed during the DSS 11 MSFN wing and Goldstone MSFN Station integration tests of January 1967. The effects of multipath ground reflections on low-elevation-angle SAA antenna signal acquisition and

tracking are explored, with special emphasis on the performance required by the SAA tracking system when operating in conjunction with the 85-ft narrow-beam S-band cassegrain monopulse (SCM) antenna. A typical tracking trajectory was simulated by a high-altitude aircraft on an east-west track. The target was tracked in the SCM mode, and SAA angle performance was judged by reference to the recorded SAA HA-dec error voltages.

2. Discussion

In the course of testing the *Apollo* communications system at the Goldstone MSFN Station and the DSS 11 MSFN wing, a fixed-wing aircraft was flown at a high altitude on an east-west course south of DSS 11. The airborne equipment included a full complement of test transmitters and test transponders for both the *LEM* and *CSM* frequencies. The tracking servo was operated exclusively in high-speed, wide-bandwidth position to accommodate the moderately high angle rates. The aircraft was tracked in the SCM auto track mode while the SAA angle error voltages were recorded. The SAA angle error voltages were applied to analog recording pens through a 1-sec time constant to simulate the servo integrator and to aid in the data reduction. The effects of multipath-induced antenna jitter and boresight shifts were recorded by making analog recordings of the angle detector output voltages and applying the voltage-to-angle scale factor obtained from collimation tower calibrations. Thus, the total tracking error, comprised of the mean boresight shift and angle channel jitter of the SAA tracking system, was recorded for a large number of tracking passes on a typical trajectory. The angle jitter is a function of the irregularity of the local terrain and is time-dependent (variation occurring as a function of the angular rate of the signal source); hence, it is filtered to some extent by the tracking system loop bandwidth.

Tracking of the aircraft in the SCM auto track mode provided an accurate method of keeping the antenna pointed at the airborne target for both high and low elevations. The narrow SCM antenna beam ($\pm 0.18^\circ$ deg at half-power) and the high loop gain of the SCM angle tracking system made possible the accurate recording of multipath-induced angle errors experienced by the SAA antenna at low elevation angles.

Figure 6 is a pictorial display of the multipath geometry that contributes largely to the received signal path error due to phase additions and phase cancellations for various positions of the spacecraft along its trajectory. Figure 7 is a plot of the theoretically derived angle error as a function of terrain clearance.

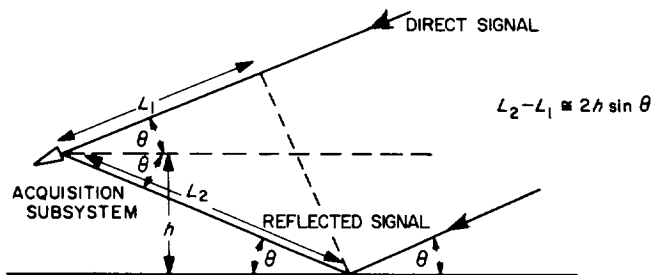


Fig. 6. Geometry of the multipath problem

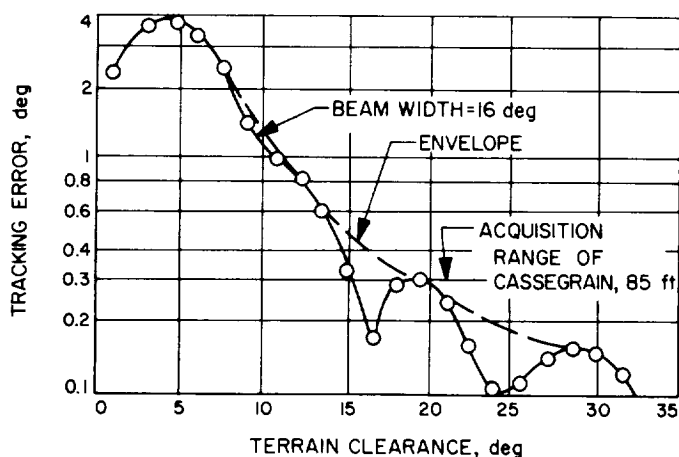


Fig. 7. Theoretical calculation of multipath-induced antenna jitter

Seven useful data runs were recorded on the same nominal trajectory (Fig. 8). Each data run consisted of analog recordings of SAA HA and dec tracking error voltages (open loop), SCM HA and dec closed-loop tracking error voltages, and SAA and SCM automatic gain control (AGC) levels. In addition, the Datex readout of HA and dec angles, while in SCM auto track, was periodically annotated to the strip chart. Thus, the mean RF boresight variations and $3\text{-}\sigma$ angle jitter variation of the SAA antenna were recorded as a function of HA. The HA marks provide a convenient method for locating the position of the radiating vehicle on the nominal trajectory.

The SAA and SCM signal levels and terrain clearance are also plotted with the recorded angle data. There was good correlation between tracking runs regardless of the flight direction of the aircraft. The mean angle is observed to undergo a large departure from the nominal predicted geometric value when the terrain clearance is

below 10 deg. This was especially noticeable when the target was southwest of the station.

The $3\text{-}\sigma$ angle jitter variations, terrain clearance, and signal level shown in Fig. 9 represent the average of four closely repeated west-to-east runs. The effect of low-elevation multipath on SAA boresight jitter about the mean, and to a lesser extent on the signal level, is readily apparent in the region covered by 20 to 40 deg of HA (abscissa). The limits of SCM acquisition are indicated (± 0.3 deg), and the antenna error contribution to SCM acquisition difficulties at low angle is obvious.

In addition to the tracking difficulties introduced by multipath-induced antenna jitter, the more serious effects of mean RF boresight shifts must be accommodated to effect efficient SAA-to-SCM handover. Figure 10 illustrates the average mean RF boresight as a function of the reference HA which resulted from recordings obtained during similar trajectories when SAA-to-SCM misalignment and cross-coupling effects were present. (These were corrected later.) The limits of SCM antenna acquisition are indicated on the HA and dec plots. The terrain clearance angle is also shown for reference. The variation of SAA mean RF boresight is easily evaluated as the most severe problem when contemplating SAA tracking and SAA-to-SCM handover. The SAA boresight shifts depart several degrees beyond the SCM lock-in range when low elevation angles are experienced. In addition, the resultant bias effects (due to misalignment and cross-coupling) in the high elevation range are significant, and can vary a substantial amount throughout the trajectory (see, especially, dec mean angle in Fig. 10). Therefore, the correction of these SAA bias effects is mandatory to achieve the best SAA-to-SCM handover performance.

The mean variations and $3\text{-}\sigma$ limits of SAA HA and dec RF boresight angles are plotted in Fig. 11. The very limited range of SCM lock-in is indicated on this chart. The areas of automatic SCM acquisition, possible SCM acquisition, and impossible SCM acquisition are illustrated diagrammatically in Fig. 12. Figure 13 illustrates the mean and $3\text{-}\sigma$ variations of the SAA RF boresight about the optimum SAA angle bias error correction. The obvious improvement in SCM acquisition probability is indicated in Fig. 12. The "reliable zone" is shown and defined with a terrain clearance angle of at least 11 deg. Table 4 illustrates the effects of optimum bias correction to the SAA tracking system. As a result of the correction, the percentage of the reliable zone that will provide automatic SCM acquisition and possible SCM acquisition is greatly increased.

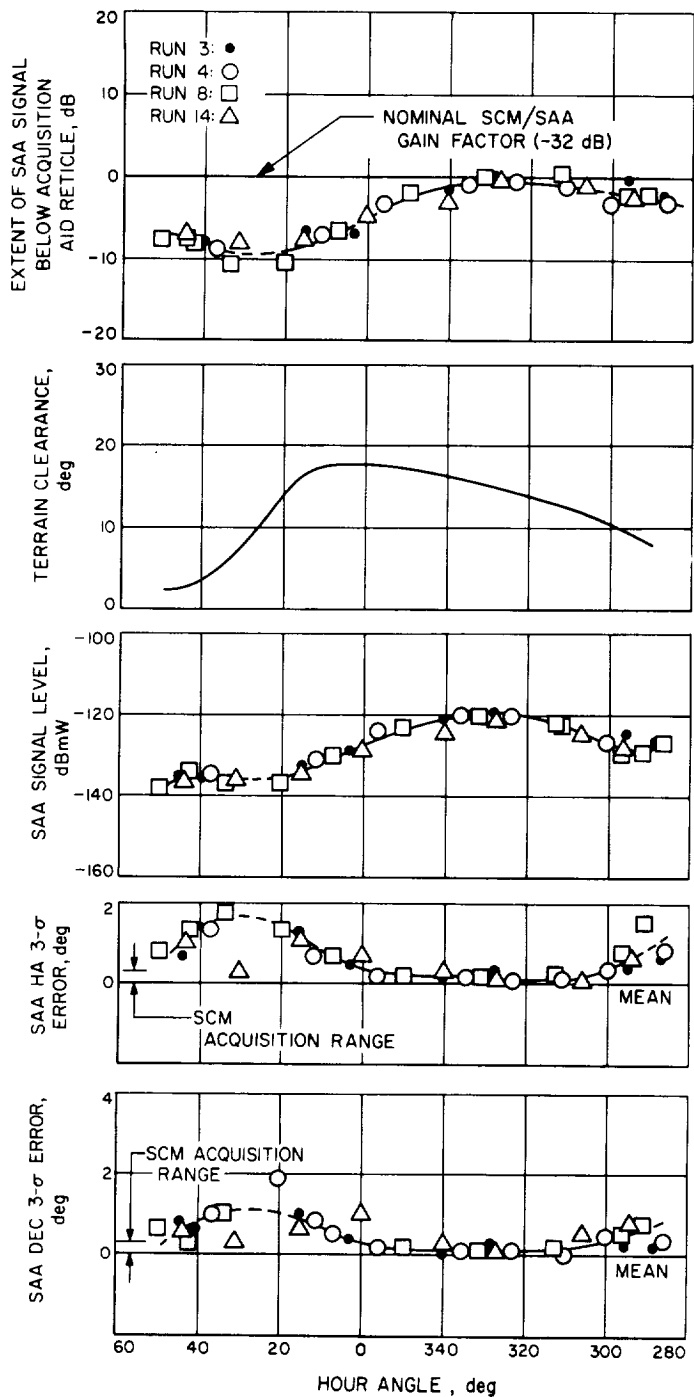


Fig. 9. Variation of angle jitter and signal level with terrain clearance (west-to-east composite of four runs)

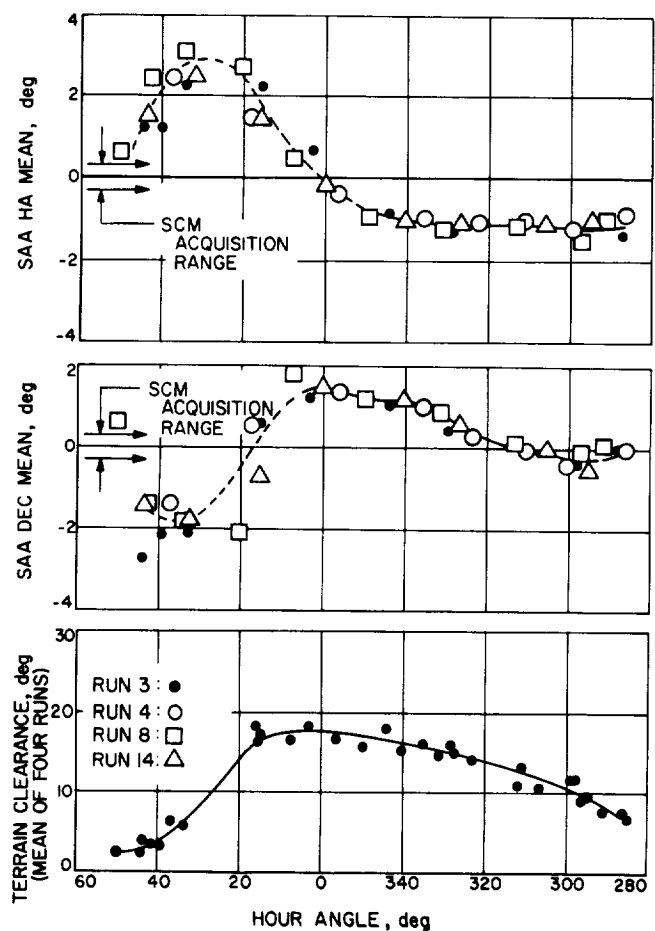


Fig. 10. Variation of mean RF boresight with terrain clearance (west-to-east composite of four runs)

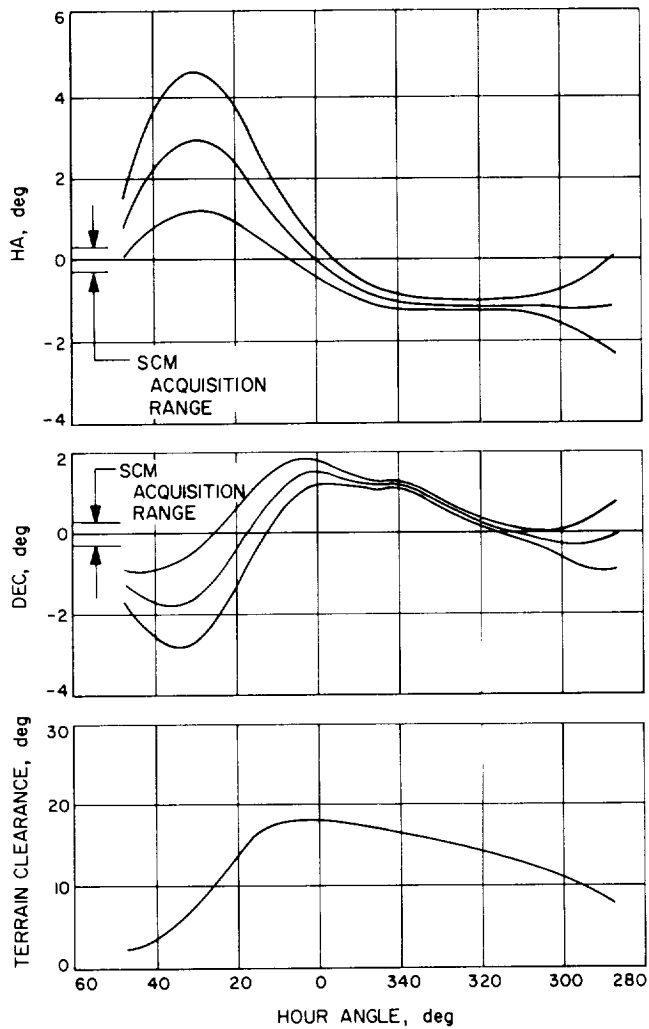


Fig. 11. Variation of SAA boresight about SCM boresight (mean $\pm 3\sigma$)

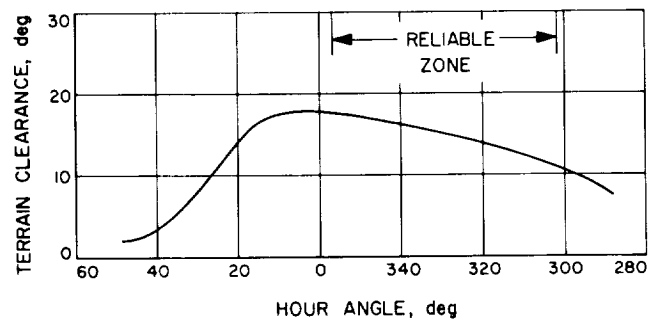
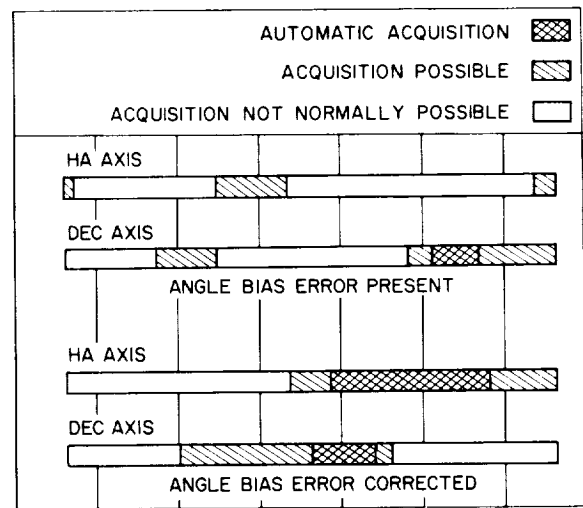


Fig. 12. SCM acquisition problem

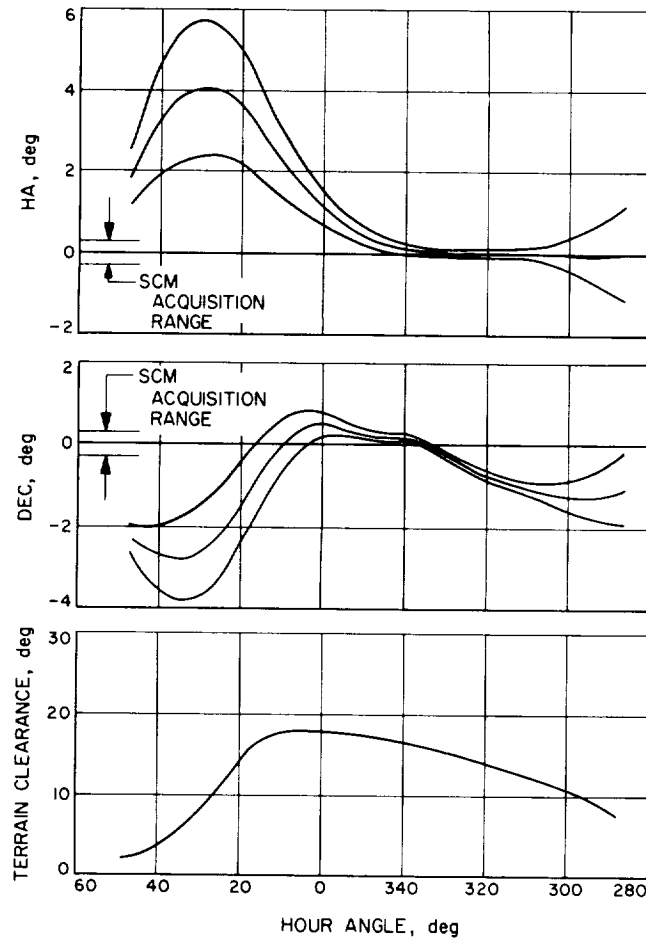


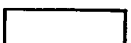





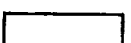


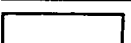


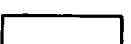


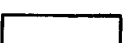


Fig. 13. Variation of SAA boresight about SCM boresight
(mean $\pm 3\sigma$; angle bias error corrected)

Table 4. SCM acquisition possibilities in the reliable zone^a (predicted from recorded data)

Bias error	Automatic SCM acquisition	SCM acquisition possible	SCM acquisition impossible
Bias error present	HA  0%	 8.3%	 91.7%
	Dec  20%	 37.3%	 62.7%
	Both  0%	 0%	 100%
Bias error corrected	HA  71%	 91%	 9%
	Dec  28.2%	 54.5%	 45.5%
	Both  20%	 45.5%	 54.5%
^a Definition of reliable zone: Terrain clearance ≥ 11 deg. Signal level above -127 dBmW. 3- σ deviation ≤ 0.3 deg.			

Automatic acquisition is defined as the SAA auto tracking condition in which the SCM narrow beam tracking system will pick up the angle tracking function with no operator intervention, except for the actuation of the auto track switch. In this area, the target vehicle is always maintained within the beamwidth of the SCM antenna while the SAA system is auto-tracking. The area of possible acquisition is defined as the SAA auto tracking condition wherein the SCM antenna beamwidth is repeatedly passing over the target vehicle in the SAA tracking mode with the SCM antenna orientations, relative to the target, consecutively producing true-lock and false-lock (side lobe) conditions. The zone of impossible SCM acquisition is the condition where the antenna biases produced by maladjustments or boresight shifts are sufficient to entirely exclude the target from the main SCM beam during SAA auto tracking. When this condition exists, the operator is forced to break SAA auto-track and manually search about the presumed target position to obtain some indication, however momentary, of SCM main-beam reception. Table 4 illustrates the percentage of the reliable trajectory in each of these three categories for both the existing and optimum angle bias cases. The cases where SAA tracking actually impeded SCM acquisition, with intuitive operator action resorting to manual antenna pointing, are not insignificant in number.

The existence of large areas of station view angles that comprise categories two and three has given rise to the development and use of some nonstandard acquisition aids at several tracking sites. The usefulness of these aids has been established over a period of many months, and was subsequently more fully appreciated and evaluated at DSS 11 during the MSFN backup system verification flight tests. To effect proper SCM auto-tracking, astute operator techniques and judicious use of auxiliary devices for avoiding side lobe lock are necessary. A keen sense of timing is required to select the proper moment to actuate the SCM auto track switch.

The analog recording display for SCM angle error, along with SAA and SCM AGC voltages, has been used at DSS 51 for some time to enhance SAA-to-SCM hand-over. The more recently implemented display at DSS 42, utilizing an oscilloscope display of SAA and SCM AGC voltages on orthogonal axis with the locus of the respective gain points drawn in, appears to be the most promising contribution at this time. This device was effectively used during the recent flight tests at the DSS 11 MSFN wing, saving both acquisition time and false-lock time. Figure 9 contains a plot of the signal strength differential between the SAA antenna and the SCM antenna as a function of the terrain clearance. The variation

of SAA signal strength is included for reference. Although the gain advantage of the SCM antenna over the SAA antenna is greater at low elevations, the criterion is still valid for selecting the main SCM beam over the SCM side lobes which present an inferior gain advantage. (The first SCM side lobe level is approximately 12 dB below the main beam.)

The tracking ability of the SCM narrow-beam antenna was assumed to be much better than that of the SAA; the error voltages of the SAA angle detectors, with an integrator time constant similar to the servo system, were assumed to indicate the angle errors that would exist if the SAA system was performing the auto tracking. To verify the tracking performance of the SCM antenna, data were obtained from the November 1966, NASA-Goddard acceptance test of the DSS 11 MSFN wing. Figure 14 is a plot of the optical-to-encoder errors developed from numerous star tracks. Figure 15 is a plot of RF-to-optical errors obtained from filmed aircraft tracks on and near the trajectory previously under study. Figure 16 combines the two previous figures to provide the overall RF-to-encoder errors along the trajectory. The existence of SCM tracking errors is evident; however, the SAA tracking errors are easily an order-of-magnitude larger.

3. Conclusion

The basic factors that inhibit the efficient attainment of SCM auto tracking on first-pass trajectories have been

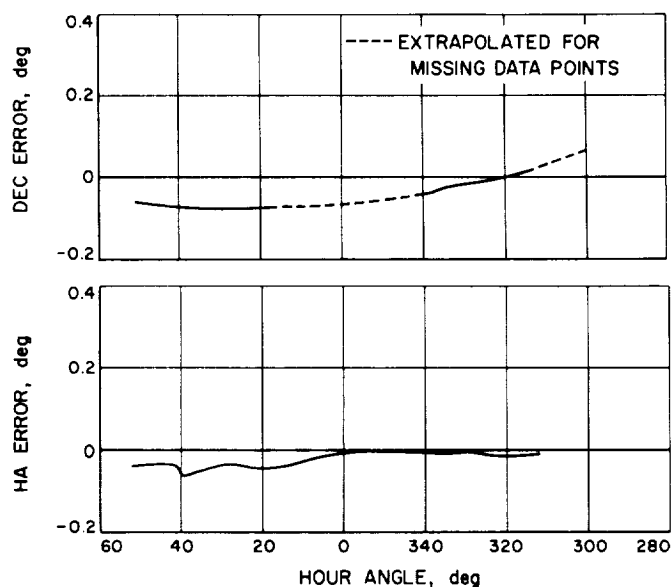


Fig. 14. Optical-to-encoder star tracks recorded November 13, 1966

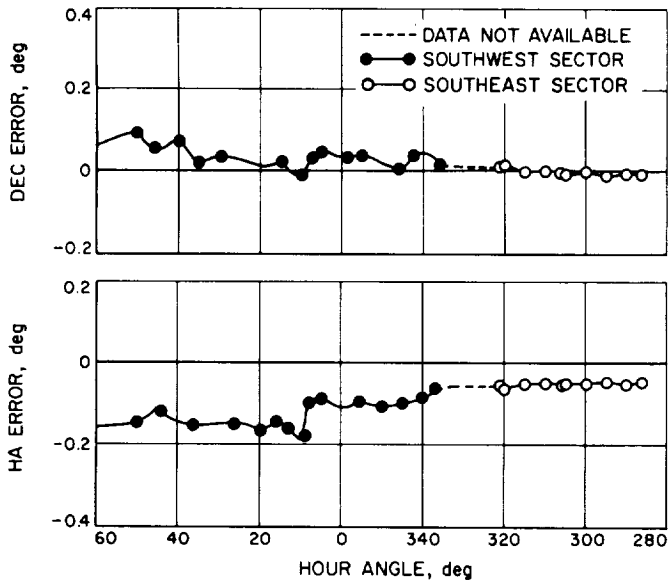


Fig. 15. Optical-to-RF SCM tracking on skew courses during aircraft tracks recorded November 16-22, 1966

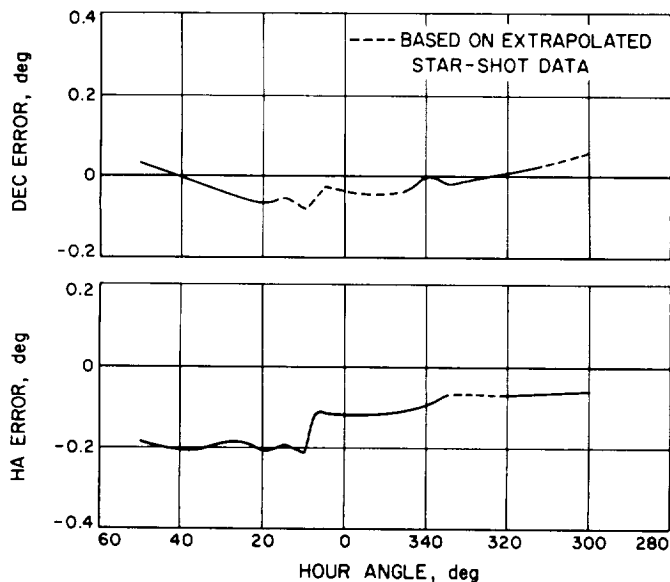


Fig. 16. RF-to-encoder SCM tracking total error during aircraft tracks recorded November 16-22, 1966

largely due to SAA-to-SCM boresight alignment errors, multipath-induced antenna jitter, and RF boresight shifts at low elevations. These effects were shown to be more severe than anticipated in the range of acquisition situations in which the DSN is presently engaged. SAA boresight shifts of as much as ten times the SCM acquisition

range were recorded at terrain clearance angles as large as 10 deg.

When using the DSN acquisition antenna with its large aperture, the interjection of auxiliary devices to prevent SCM side lobe lock appears to be a necessity. The most promising device experimentally in use is an oscilloscope that provides an orthogonal presentation of the SAA and SCM AGC voltages, with the locus line inscribed on the face of the screen. The rapidity of obtaining true SCM lock is greatly improved with the concomitant avoidance of evaluating side lobe tracking and reacquisition.

The information gathered from these tests indicates that future performance may be improved by additional study and testing of the SAA system in such areas as optimum SAA antenna aperture size, SAA tracking performance, and auxiliary acquisition aid devices.

D. Four-Foot HA-Dec Time-Synchronization Antenna Mount, M. Kron

1. Introduction

The design parameters of the 4-ft time-synchronization receiving antenna mount were established at the outset of the program (SPS 37-43, Vol. III, p. 92) by extracting the general environmental design requirements from the DSIF antenna specifications; namely, wind loading conditions. In addition, on the basis of the prime requirements of this program, specific requirements such as drive rates, axes motions, drive control system, and antenna mount configuration were established.

An HA-dec configuration was selected as more suitable for lunar tracking than an az-el configuration, because while the moon's declination varies between ± 28 deg about the celestial equator throughout the year, it varies only slightly from hour to hour. An az-el configuration would have required an elevation drive system as well as the azimuth drive to position the reflector; an HA-dec mount required only a drive system in HA and a manual adjustment in dec. A manual adjustment in dec was considered adequate, since the beam width of the system is 2 deg and the moon subtends an angle of 0.5 deg, thus affording at least 6 h of tracking without further adjustments of the dec axis.

2. Drive System

The drive system for this specific application required that the antenna be capable of tracking the moon for

extended periods up to 8 h. A simple open-loop system using off-the-shelf motors and mechanical components was conceived. Figure 17 shows an isometric view of the drive system. The system employs both tracking and slew modes. The track mode utilizes a synchronous motor driving through one input to a differential. Since the lunar rate varies throughout the year, provision had to be made to vary the antenna output rate without using a complex closed-loop servo system. A standard ac motor, whose speed could be varied in discrete steps by resistance loading, was included as an additional input to the differential. With the synchronous motor the main contributor, the variable speed motor contributes differential increments of speed so that the final output at the HA axis can vary between 14.36 and 14.8 deg/h. A

twelve-position switch on the control panel allows the operator to select the proper rate closest to the moon's rate for that particular time and day. Each switch position allows for an incremental rate increase of 0.04 deg/h, thus making a broad range of speeds available to the operator.

3. Structure Sizing

All components have been sized to accept loads greater than calculated in the event of a requirement for a larger reflector. The sizing of the reflector and mount structures was dictated by the size of components to be packaged rather than stress or deflection considerations. The section properties of the various weldments analyzed were found to be far in excess of those that would have

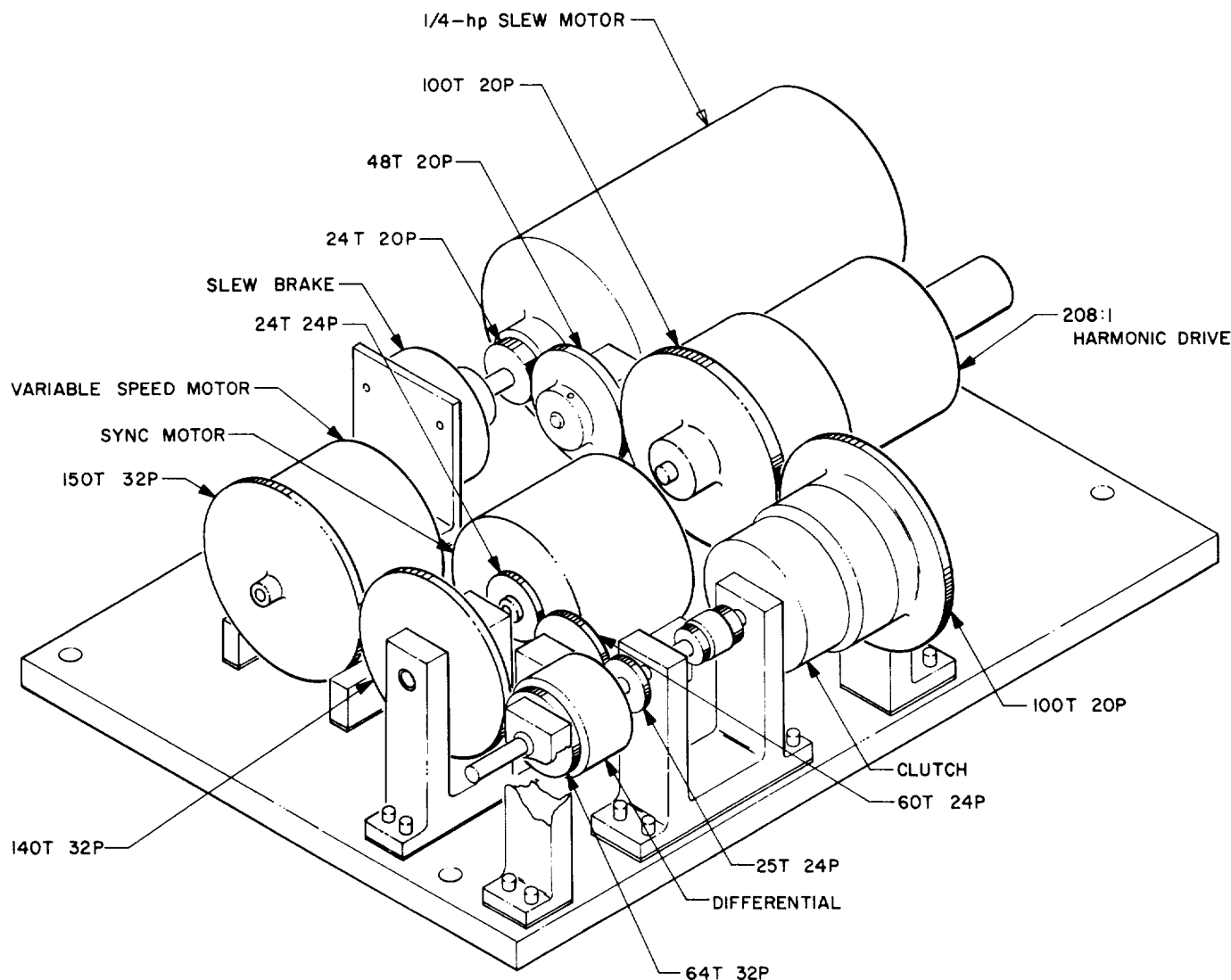


Fig. 17. HA drive machinery

been required had allowable stresses or maximum deflections been used as the criteria for establishing the sections and sizes.

4. Safety Devices

In order to determine the requirements and extent to which safety and limit switches or stops were necessary, the operating methods were established and outlined so that adequate safety devices could be incorporated into the antenna mount design. The stow pin interlocking device was added to prevent the accidental operation of the HA drive with the stow pin engaged. Historically, stow pins on small antennas are normally left hanging from a chain or lanyard, or are simply removed and eventually lost. Other systems used have the stow pin engage a normally closed microswitch which cuts all power to the drive system until the pin has been removed. The system finally used incorporates both a storage device and a switch interlock. It is therefore necessary for

an operator to remove the stow pin and insert it into a storage space to provide power to the control panel.

5. Antenna Control

Since lunar tracking requires operation of the entire system during hours of the day or night where shutdown would be inconvenient or while tracking continues to the horizon limits, east and west limit switches were provided. The circuitry allows the antenna to slew out of the east limit in the track mode (northern hemisphere only; reversed for antennas located in the southern hemisphere). The location of the limit switches and cams allows the HA wheel to travel ± 112 deg from the 0-deg position.

The control panel shown in Fig. 18 contains the function switches and speed control. The antenna is capable of two modes, either track or slew. The track mode can be selected by positioning the toggle switch to the "up" position. When in this mode, the brake is released and the magnetic clutch engaged.

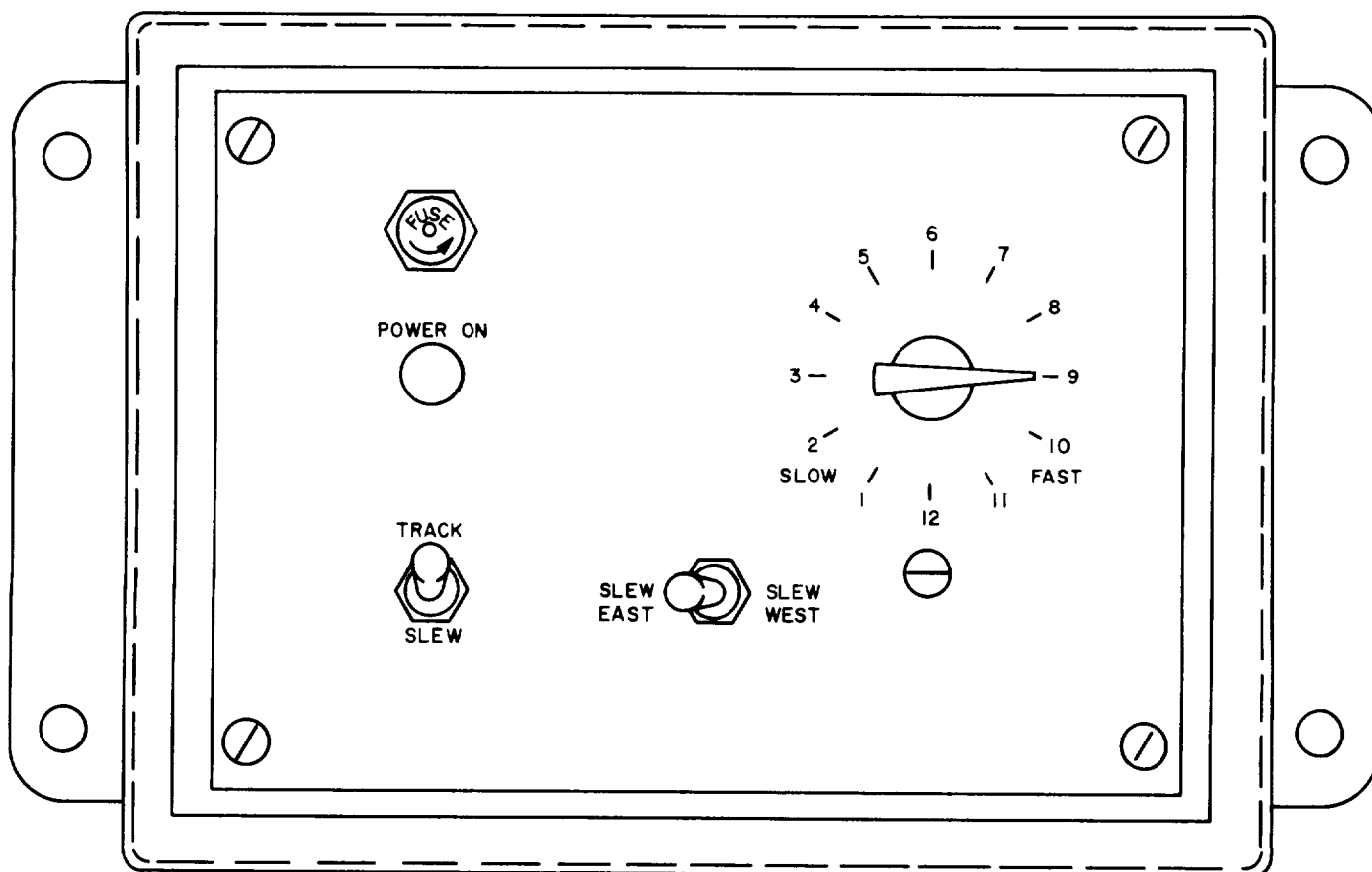


Fig. 18. Control panel

The slew mode is selected by placing the mode selection switch in the "down" position. In this position, the clutch is engaged. To the right of the mode selection switch is an east-west spring-loaded toggle switch. The operator must hold the switch in the direction of slew until the desired position is reached and the switch released.

6. Antenna Mount Installation and Alignment at DSS 11

Prior to the installation of the antenna mount, a survey of the site was conducted and two permanent stations were established. These data are required to compute the geocentric location of the antenna on the "165 NASA Earth Model" spheroid.

The survey data are required to second-order Class II accuracy, as defined by the U.S. Department of Commerce Coast and Geodetic Survey. The requirements are as follows:

- (1) Geodetic latitude.
- (2) Geodetic longitude.
- (3) Astronomical latitude.
- (4) Astronomical longitude.
- (5) Height above local base mean sea level (i.e., above the geoid).
- (6) Reference datum for (5).
- (7) Height of local geoid above assumed ellipsoid.
- (8) Astronomical azimuth of station A to station B.
- (9) Geodetic azimuth station A to station B.

The site selected for the installation of the antenna mount was at the southeast corner of the control building at DSS 11.

A foundation frame (Fig. 19) was designed to support the antenna above the roof and to transfer dead load and wind loading to the roof structure. Threaded jack screws were installed to secure the antenna mount to the foundation frame. These jacking screws allow for adjustments during final alignment. The HA axis alignment procedure determines the precise alignment of the HA axis relative to astronomical north, as defined by the site survey monument, and relative to an elevation angle, as defined by the station's astronomical latitude. Deviations from exact alignment are evaluated in terms of standard errors of the axis, together with the effects of nonorthogonality

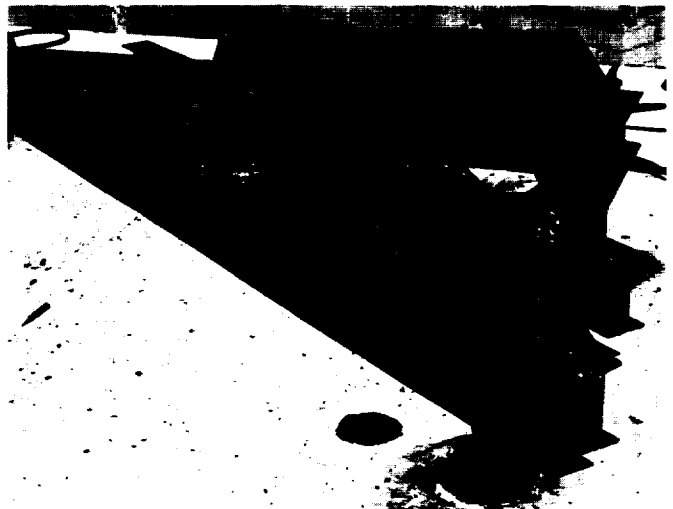


Fig. 19. Antenna foundation frame

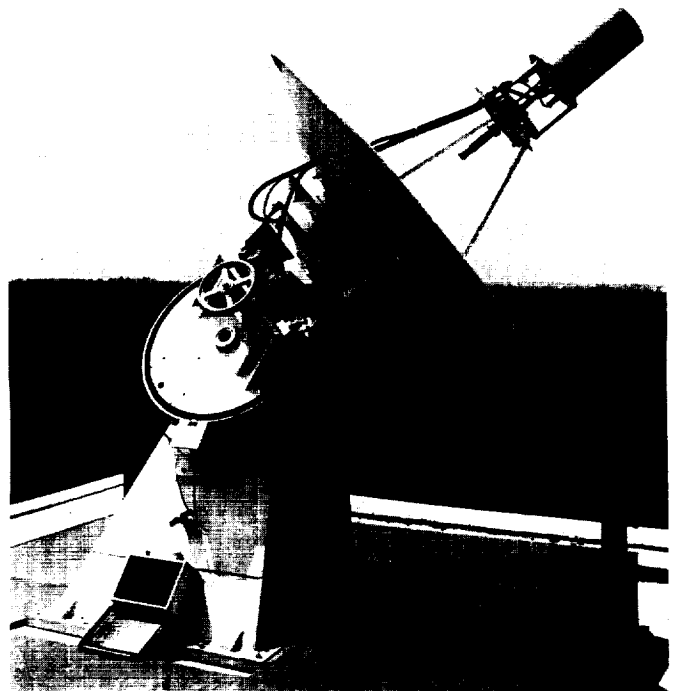


Fig. 20. Antenna mount assembly

of HA and dec axes. The standard error may be treated with a correction factor in data reduction operations or, if within specified limits, may be accepted untreated.

The HA axis datum was established by installing a reference mirror perpendicular to the mean HA axis. Mirror plugs were used for both the HA and dec shaft

alignments and orthogonality determination. The actual horizontal alignment of the HA axis is expressed in azimuth bearing angle to seconds of arc relative to the reference north-south line of the site survey monuments-reference stations, and does not deviate from this reference by more than ± 20 sec of arc. The vertical alignment of the HA axis is expressed in elevation angle to seconds of arc relative to local gravity. During this installation, the elevation angle did not deviate from the astronomical latitude of the antenna station by more than ± 30 sec of arc. At this point, all base jack bolts were locked in place and grout was poured between the base and foundation frame. The completed antenna installation is shown in Fig. 20.

E. Techniques for Evaluation of Antenna Reflector Structures—STAIR Computer Program, M. S. Katow

1. Introduction

Previous reports (Vol. III of SPS 37-17, SPS 37-25, and SPS 37-44) have been made on the use of the STAIR computing program (Ref. 1) to evaluate the deflection behavior of antenna reflector structures subject to gravity and wind loads. The STAIR program was originally formulated to analyze antenna structures where rigidity of the truss due to the bending resistance of individual truss members is negligible. The STAIR program thus assumes a truss structure whose bar members resist axial forces only and are connected by frictionless pin joints. In other words, the joints of the structure are considered to have only three degrees of motions (all translations). The truss assembly must, of course, be stably supported with suitable restraints.

STAIR's unique usefulness for antenna analysis is its capability of analyzing a large reflector structure with 750 joints and 2600 bar members for structural "dead" gravity loads, where the loads are computed from the geometry of the bar members. This capability proved to be adequate for analyzing the advanced antenna system (AAS) 210-ft antenna with one quadrant of structural data. The IBM 7094 Mod 2 computing time has been reasonable. For the 750 joints and three loading conditions problem, the total computing time was 53 min. Also, the computing time is directly proportional to the number of joints.

2. History

The STAIR was received from Lincoln Laboratory in an exchange of programs with JPL in 1962 (Ref. 2). As

the original coding was not adaptable to the JPL closed-shop computing system, it was modified and directly converted to run under the IBM chain subroutine.

After the STAIR's use in feasibility studies of the AAS 210-ft antenna, modifications were made to add (1) the data checking chain subroutine, CHETA, to check the input data as well as to generate duplicate data to reduce the quantity of input cards; and (2) a new chain subroutine to plot a plan view of the joints and the bars of each unit on the SC-4020 plotter. This addition served as a good visual check on the accuracy of the structure simulation. Figure 21 illustrates errors of X-Y coordinates in the top row of joints.

Coding was added in CHETA chain to compute the moment of inertia of the "dead load" truss structure about the axes of the coordinate system. Capability for computing thermal loads on the truss structure was added on the basis of information received from Lincoln Laboratory.

3. Modifications

The experience gained during use of the STAIR program has emphasized the need for careful generation of correct input data. When some 750 joints and 2600 bars of a structure must be correctly generated, it is necessary to use every checking effort or method to delineate each error in the input data. With load data, the total card count was 4900 for the structural analysis of 750 joints; this number clearly illustrates the magnitude of the problem.

To complete the modifications, additional coding was added to the checking chain CHETA and to the general program, as follows:

A new subroutine was coded to arrange all the joint numbers and coordinates with the joint numbers sequenced in ascending order.

A new subroutine was coded to sequence all the bar numbers with the first node number arranged smaller than the second node number, and listed with the first node number sequenced in ascending order. When the first node numbers are the same, the second node numbers are sequenced. A check for duplicate bars is made during the sequencing operation.

A subroutine was coded to check the stability of all the joints of the whole structure as well as the effects of

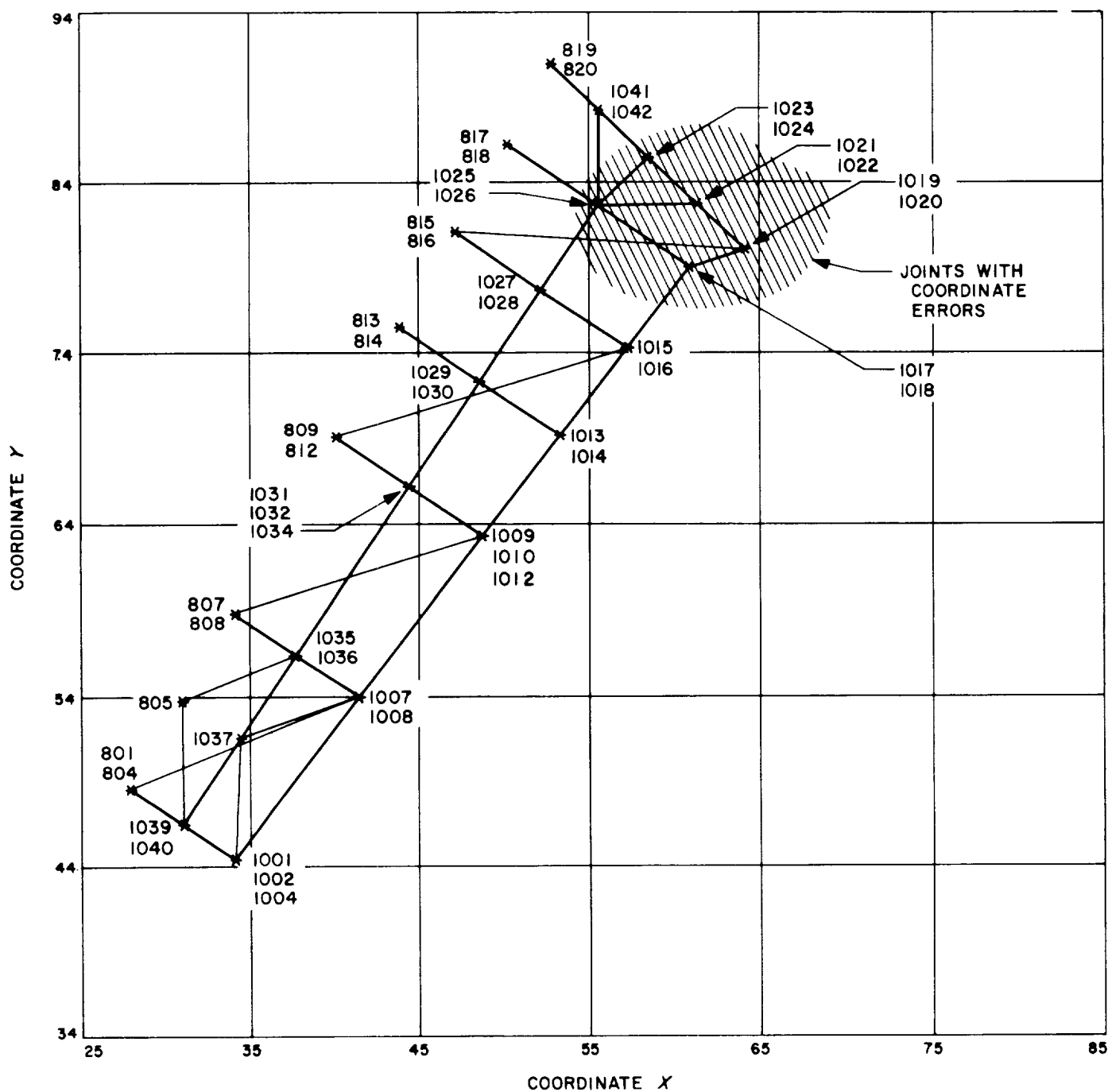


Fig. 21. Sample plot of a unit in the STAIR program

the restraint components. The joint stability is determined by the planar condition of the bars meeting at a joint as originally coded in STAIR. Coding was added to check the planar conditions of joints with restraint components.

Coding was arranged to count and list the number of bars at each joint. This number can easily serve as a check on the symmetry of the structure—or lack of same—which may be caused by missing or wrong bars.

Coding was added to check the joint coordinates when identical joints are input in several units. Also, to prevent errors in joint coordinates in the outputs of deflection cards from the DEFSOL operation, the coordinate data are drawn from the core storage in the CHETA chain.

Coding was included to add an “effixed” joint array in CHETA to keep account of the effixed joints in order to prevent the same joint being effixed twice or more.¹

Coding in CHETA and SLOP was modified to increase the capacity to compute gravity structural bar (“dead”) loads to a limit of 1200 joints and 5100 bars. This was increased from 750 joints and 2600 bars.

Restarting capability that was lost when converting to the IBM chain subroutine was restored in the program. Without the restarting feature, the entire computing time, to the point of occurrence of a machine error such as a tape reading error, can be lost. With preselected restarting points, the program can be restarted at the closest preselected point.

Coding was added to CHETA to compute the total number of loading conditions and the IUADR array, the list of the largest joint number in each unit number. This eliminates two possible control card input errors.

The load computing chain, SLOP, was modified to compute the total weight, center of gravity, and the moment of inertia of all the live loads in each loading condition. These computed values were then added to the structural dead-load data. Thus the effects of the

reflector panels, as well as any counterweights, can be calculated.

In order to economize on the computing time, the driver chain was loaded on tape unit 2 and the remaining chain subroutines were loaded on tape unit 3, with the sort order of chain subroutines arranged to minimize tape searching time. The driver chain tape was always ordered to rewind as soon as it was read into the core of the computer. Since the matrix interpretative routine of each unit called for three successive subroutines used in the same order, these were placed at the head of tape unit 3 and read successively into the core as required, with a rewind order inserted into the last of the three subroutines.

It should be noted that although most of the modifications were added to check for JPL-oriented input data errors, other users may and do make errors peculiar to their problems. Since the problems of ferreting errors in input data are basic to all computer programs, the techniques presented here should be useful.

F. Internal Alignment of the 210-ft Antenna Master Equatorial, H. McGinness

1. Introduction

In SPS 37-26, Vol. III, p. 73, an error analysis was applied to a preliminary design of the advanced antenna system (AAS) master equatorial (ME) instrument. The results showed that the defined pointing error was 6 to 7 arc sec. Further study suggested that this first design could be made more compact, and projections from the analysis indicated that an even smaller pointing error could be obtained. Considerations of practicality led to the belief that an ME could be built having a defined pointing error of not more than 10 arc sec. Therefore, although the design specifications called for a guaranteed defined pointing error of not more than 10 arc sec, the design goal was set at 5 arc sec. Following a corroborative analysis by the vendor, the final design and fabrication were undertaken.²

In this report, the latest measurements made on the ME (shown in Fig. 22), as installed in the AAS at DSS 14, are described. These measurements are then interpreted to determine whether the design goal specifications have been achieved.

¹This check was suggested by Lincoln Laboratory in a recent discussion.

²Design, analysis, and fabrication by Boller & Chivens Division, The Perkins-Elmer Corp., South Pasadena, Calif., under contract to JPL.



Fig. 22. Master equatorial

2. Error Determination

The pointing direction of the plane mirror attached to the declination axle is nominally determined by the two axis angles; namely, the hour angle and the declination. These angles are measured by encoders mounted on an end of each axis. The pointing direction of a perfect instrument would be determined exactly by the coordinates of the two axes. The defined pointing error is the angle between the mirror vector of a real instrument and the mirror vector of a perfect instrument at the time the encoder positions of the two systems are identical. The principal factors contributing to the defined pointing error are: alignment of mirror, run out of axle bearings, gravity loading deflections, dimensional changes from temperature gradients, lack of perfect orthogonality between hour angle and declination axes, and dimensional instability of the materials.

The internal alignment of the ME consisted of an adjustment of a special eccentric bearing at one end of the declination axis to obtain the best degree of perpendicularity between the two axes, alignment of the mirror axis to obtain the best degree of parallelism with the hour angle axis, and alignment of the encoders to their proper positions. Extensive use of a two-axis manually operated autocollimator was made to accomplish the internal alignment, the details of which will appear in another report. Subsequently, this same autocollimator was employed to measure the defined pointing error.

Two different positions of the autocollimator were used. These are shown schematically in Fig. 23 as positions A and B. In position A, the autocollimator was attached to a special bracket fixed to the base of the ME and aligned so that its emerging light beam was almost parallel to the hour angle axis of the ME. The returning beam was reflected from the 7-in.-diam mirror attached to the declination axis. In position B, the autocollimator was attached to a special bracket fixed to one fork leg of the ME, and its emerging beam was reflected back from a small auxiliary plane mirror attached to the end of the declination angle.

The autocollimator reads half the angle between the emerging and returning beams, or rather, two orthogonal components of this angle. This half-angle is, of course, equal to the angle between the emerging beam and the normal to the plane mirror.

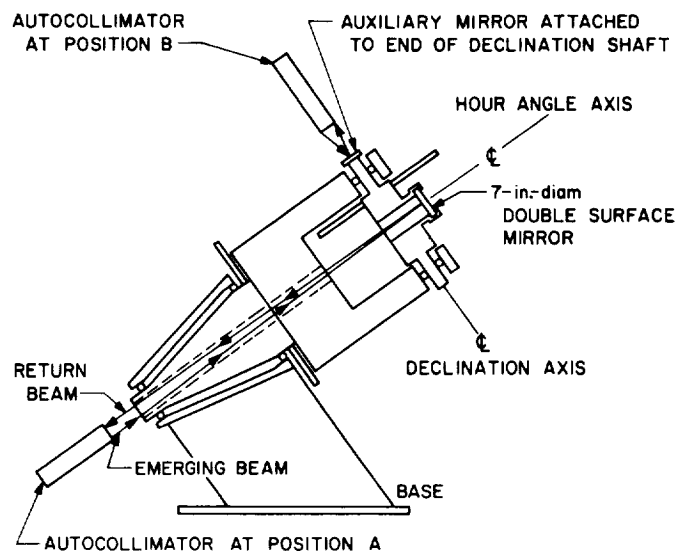


Fig. 23. Autocollimator configurations on master equatorial

The autocollimator readings were made by manually turning two control knobs until the two image lines appeared to be centered between their reference lines. In order to avoid any backlash error, care was always taken to move the image lines in the same direction. Two or more readings were always taken at each position until reading repeatability within 0.1 arc sec was achieved. One division on the readout dials corresponds to 0.2 arc sec. All readings from which the final data were taken were made by the same operator. This technique, although somewhat slow and tedious, is believed to be accurate.

The solid-line plot of Fig. 24 shows the runout of the auxiliary mirror mounted on the end of the declination shaft when it was in the horizontal position. Because of the high torsional stiffness of the shaft, it may be assumed that the runout of the 7-in.-diam mirror is essentially the same as that of the shaft end, and this assumption is substantiated by a deflection analysis. However, it can be demonstrated that a substantial portion of the runout represented by the solid-line curve is a circle caused by the auxiliary mirror not being perfectly aligned with the best-fitted position of the declination axis. This

may be visualized by considering a light beam emerging from the shaft end at an angle to the perfect shaft axis. As the perfect shaft turns, the beam would sweep a conical surface, and its projection onto a screen normal to the shaft axis would describe a circle for each turn of the shaft. Since this circular component has no effect on the accuracy of the shaft, it may be subtracted.

In Fig. 24 are plotted, as solid lines, the rectangular coordinates of the declination shaft runout as measured by a two-axis autocollimator directed toward a plane mirror attached to one end of the shaft. The numbers beside the arrowheads represent the shaft declination corresponding to that point. The dotted curve of Fig. 24 may be described by the following parametric equations:

$$\begin{aligned}\rho &= R [(\cos \theta + \alpha \cos 2\theta)^2 + (\sin \theta + \alpha \sin 2\theta)^2]^{1/2} \\ &= R (1 + \alpha^2 + 2\alpha \cos \theta)^{1/2} \\ \sin \beta &= \frac{\sin \theta + \alpha \sin 2\theta}{\rho} = \frac{(1 + 2\alpha \cos \theta) \sin \theta}{\rho}\end{aligned}\quad (1)$$

where ρ and β are as indicated in Fig 24.

The curve represented by Eq. (1) is the vectorial sum of two rotating vectors; namely, one of radius R and circular frequency of unity, and one of radius αR and circular frequency of two. The specific dotted curve of Fig. 24 is drawn for $R = 1.14$ and $\alpha = 0.75$. Thus, the actual curve of excursion, the solid curve of Fig. 24, consists essentially of a one-cycle circle of radius 1.14 and a two-cycle circle of radius 0.86. Since the one-cycle component is caused by lack of squareness between the mirror and the rotation axis, the instrument error, insofar as bearing runout and gravity loading deflections are concerned, is approximately a circle of radius 0.86. A better and more conservative approximation is obtained by subtracting a one-cycle circle of radius 1.14 from the solid curve of Fig. 24. This result is shown in Fig. 25 from which it may be seen that the maximum declination error is 1.25 arc sec, the distance from the origin to the coordinate labeled 360. Figure 25 illustrates that runout motion is indeed two-cycled and is more or less circular in shape. This is precisely the type of motion to be expected from bearings having elliptical rather than circular races.

The hour angle axis runout is shown in Fig. 26. With the autocollimator in the A position, the hour angle axle was rotated and the autocollimator readings were plotted as rectangular coordinates, as shown by the arrowheads.

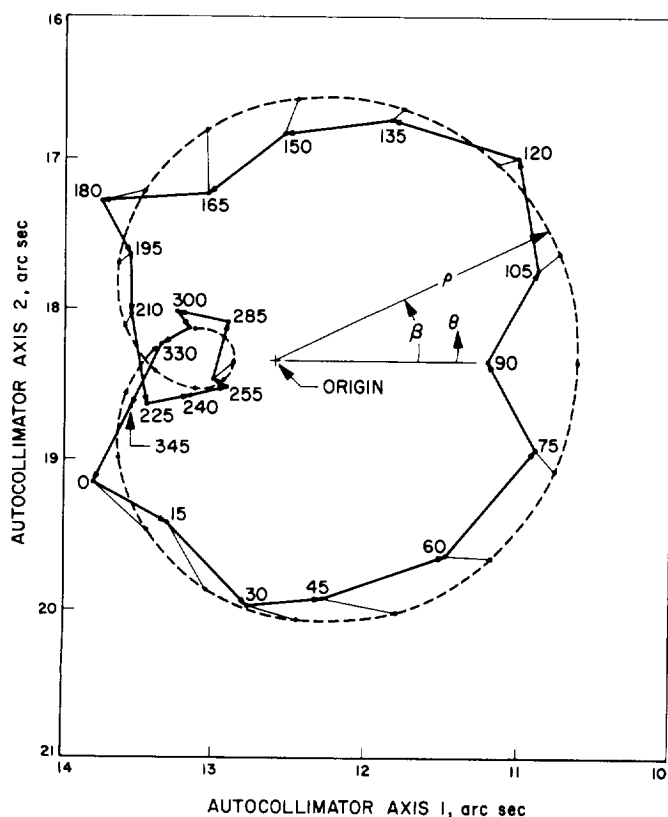


Fig. 24. Declination axis runout

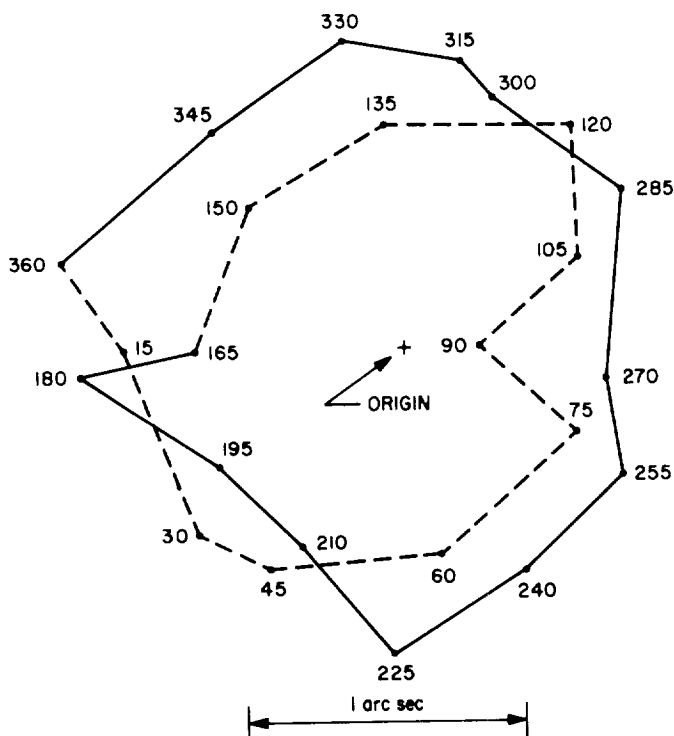


Fig. 25. Net declination axis runout given as distance from curve to origin

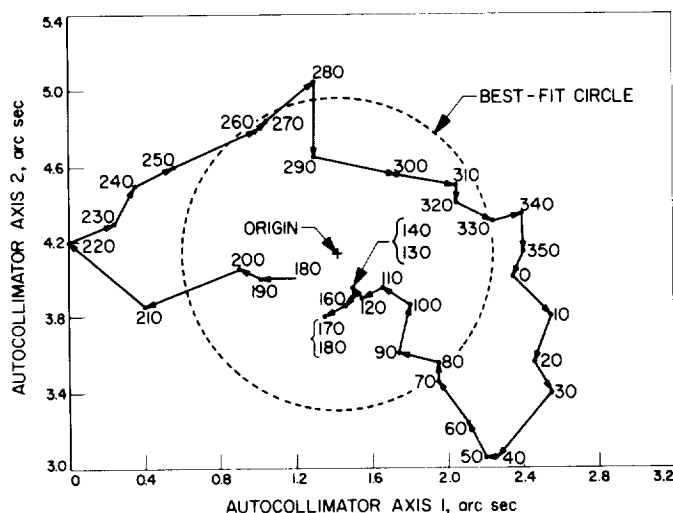


Fig. 26. Hour angle axis error

The numbers near the arrowheads indicate the hour angle. In this case, the resultant runout includes not only the bearing runout and the effect of a misaligned mirror, but also runout caused by gravity loading deflection, since the stiffness of the structure in the vertical direction varies with the hour angle position. If a one-cycle

circle of radius 0.83 sec (represented by the dotted line in Fig. 26) is subtracted from the resultant runout curve, the curve of Fig. 27 is obtained. There is a semblance of a two-cycle curve here, although it is not nearly so clear as in the previous case. The distance from the "origin" of Fig. 27 to the extreme coordinate 40 is 0.75 arc sec.

The axes orthogonality was obtained by first aligning the mirror to the hour angle axis and then rotating the declination axis approximately 180 deg; the exact amount of rotation took into account the angle between the opposite faces of the mirror. The autocollimator reading was proportional to the axes orthogonality error. A series of adjustments was made until the final orthogonality error was 0.15 arc sec.

During the alignment the ME was in the air-conditioned astrodome, where the room temperature remained constant to within $\pm 1^\circ\text{F}$. The axis drive motors were used at slewing speeds, and the antibacklash torquers were always on. Hence, most of the heat sources occurred that would exist during the normal operation of the ME. Calibrated mercury thermometers were taped to both legs of the ME fork structure; the differential between them was never more than 0.5°F , and was usually less than this amount. Since each division on the thermometers corresponded to 1°F , these values are thought to be reliable. A calculation shows that 0.5°F differential temperature produces an angular error of 0.50 arc sec.

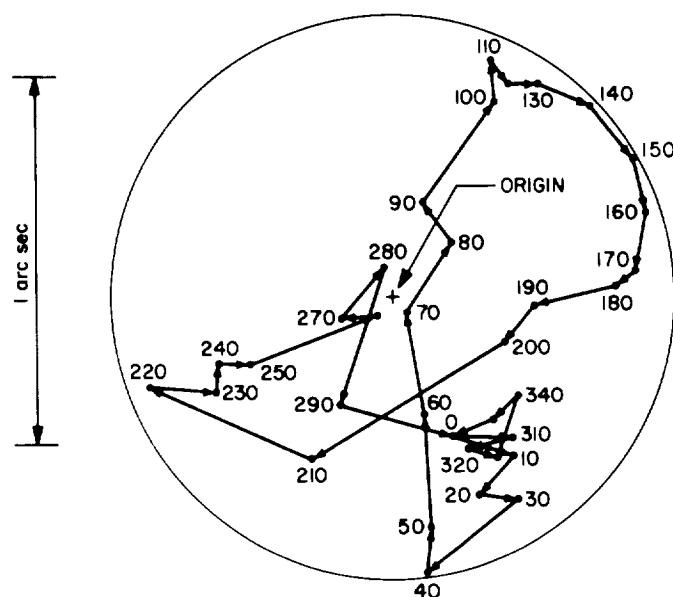


Fig. 27. Net hour angle axis error

3. Interpretations of Measured Errors

The following angular errors have been discussed:

- (1) Declination axle runout error of 1.25 arc sec.
- (2) Hour angle axle runout (including gravity loading deflection error) of 0.75 arc sec.
- (3) Axes orthogonality error of 0.15 arc sec.
- (4) Maximum temperature gradient error of 0.50 arc sec.

These errors are not necessarily additive. Thus far, no attempt has been made to determine their proper combination, and it is doubtful that this could be established experimentally for a large number of axis position combinations. Two obvious combinations are the simple sum, ϵ_s , and the square root of the sum of the squares, ϵ_R . These values are

$$\epsilon_s = 2.65 \text{ arc sec}$$

$$\epsilon_R = 1.55 \text{ arc sec}$$

Either or both could be interpreted as the defined pointing error. Thus it would appear that the design goal has been met with error to spare. These values represent a potential accuracy only; however, they are indicative of the inherent accuracy of the ME instrument.

A more realistic mirror pointing error is obtained by the following consideration. By referring to Figs. 25 and 27, it may be seen that no hour angle or declination coordinate coincides with the origins of the diagrams; hence, no combination of axes settings corresponds to a zero error measured from the origin. Since the encoders are aligned at zero hour angle and +90-deg declination, and the external alignment of the ME is executed under these conditions, these axis coordinates must be considered as having zero error. Hence, error excursions must be measured from these reference points. From Figs. 25 and 27, the maximum declination axis runout error and the hour angle axis runout (including gravity loading deflection) errors are found to be 1.52 and 1.03 arc sec, respectively. Combining these with the axis orthogonality error of 0.15 arc sec and the temperature gradient error of 0.50 sec by simple addition and by the square root of the sum of the squares, the following errors are obtained:

$$E_s = 3.20 \text{ arc sec}$$

$$E_R = 1.91 \text{ arc sec}$$

Thus, even this more conservative interpretation meets the design goal.

It should be emphasized that several other error sources will contribute to the overall error of the angle data subsystem. These will be discussed in future reports.

References

1. *STAIR (Structural Analysis Interpretive Routine) Instruction Manual*, Lincoln Manual 48. Lincoln Laboratory, Massachusetts Institute of Technology, Cambridge, Mass., Mar. 1962.
2. Wada, B. K., *Stiffness Matrix Structural Analysis*, Technical Report 32-774. Jet Propulsion Laboratory, Pasadena, Calif., Oct. 12, 1965.

V. Facility Engineering and Operations

A. Flight Project Support, R. M. Cuberly

1. Lunar Orbiter Missions

a. Lunar Orbiter II and III. The Echo DSS continued providing telemetry and command support operations for both spacecraft. The Mars DSS performed tracking for one pass with the Echo DSS processing the data.

b. Lunar Orbiter IV. The spacecraft was launched from Cape Kennedy, Florida, on May 4, 1967. The Echo DSS provided primary tracking and data command transmissions for all passes until completion of the photographic experiments on June 4. The photographic and scientific data transmitted by the spacecraft was processed by Echo DSS. A voice relay experiment via the spacecraft was conducted according to the requirements of operations order E0-1, dated June 8, 1967, and the results are being evaluated. Also performed were time correlation experiments with Madrid DSS. The spacecraft is on extended mission status and experiments continue.

2. Pioneer Missions

The Mars DSS completed modifications to the hydrostatic bearing on May 1 and resumed tracking of *Pio-*

neer VI and *VII* spacecraft. Echo DSS provided telemetry and command support operations.

3. Mariner Missions

a. Mariner IV. The Mars DSS resumed prime tracking of the spacecraft with Pioneer DSS providing support during two view periods.

b. Mariner V. The spacecraft was launched from Cape Kennedy, Florida on June 14, 1967. Pioneer DSS provided primary tracking and command data transmissions during the first view period and midcourse maneuvers. Mars DSS performed backup tracking. A mutual view time correlation experiment between Canberra DSS, Pioneer DSS, and the spacecraft was performed.

4. Surveyor Missions

a. Surveyor III. The Pioneer DSS continued data transmission and data processing until the end of the first lunar day. Photographic experiments of soil sampling and soil mechanics experiments were performed through May 3. Attempts to revive the spacecraft at the beginning of the

second lunar day were not successful. Eight separate attempts were made through Pioneer DSS between May 24 and June 1.

b. Surveyor D. The Pioneer DSS is performing tests and practice operations in preparation for the *Surveyor D* launch scheduled in July 1967.

B. Facility Construction and Equipment

Installation, R. M. Cuberly

1. Echo DSS

Construction on the communications building, G33, the logistics/stores building, G-38, and on the security building, G-43 (SPS 37-45, Vol. III, p. 77), continues. The slab floors, plumbing, and wiring are roughed-in, and the exterior walls are 90% complete.

2. Pioneer DSS

a. Building construction. Construction on the laboratory, G-18 (SPS 37-45, Vol. III, p. 77), continues. The slab floor, plumbing, and wiring are roughed-in, and work has started on the exterior walls.

b. Equipment. Multimission support recording equipment is being installed in the operations room (Fig. 1). Cable installation and equipment testing are in process. The equipment consists primarily of telemetry and data recording equipment.

3. Mars DSS

a. Hydrostatic bearing improvements. The major portion of improvement work on the azimuth hydrostatic bearing (SPS 37-45, Vol. III, p. 77) was completed by

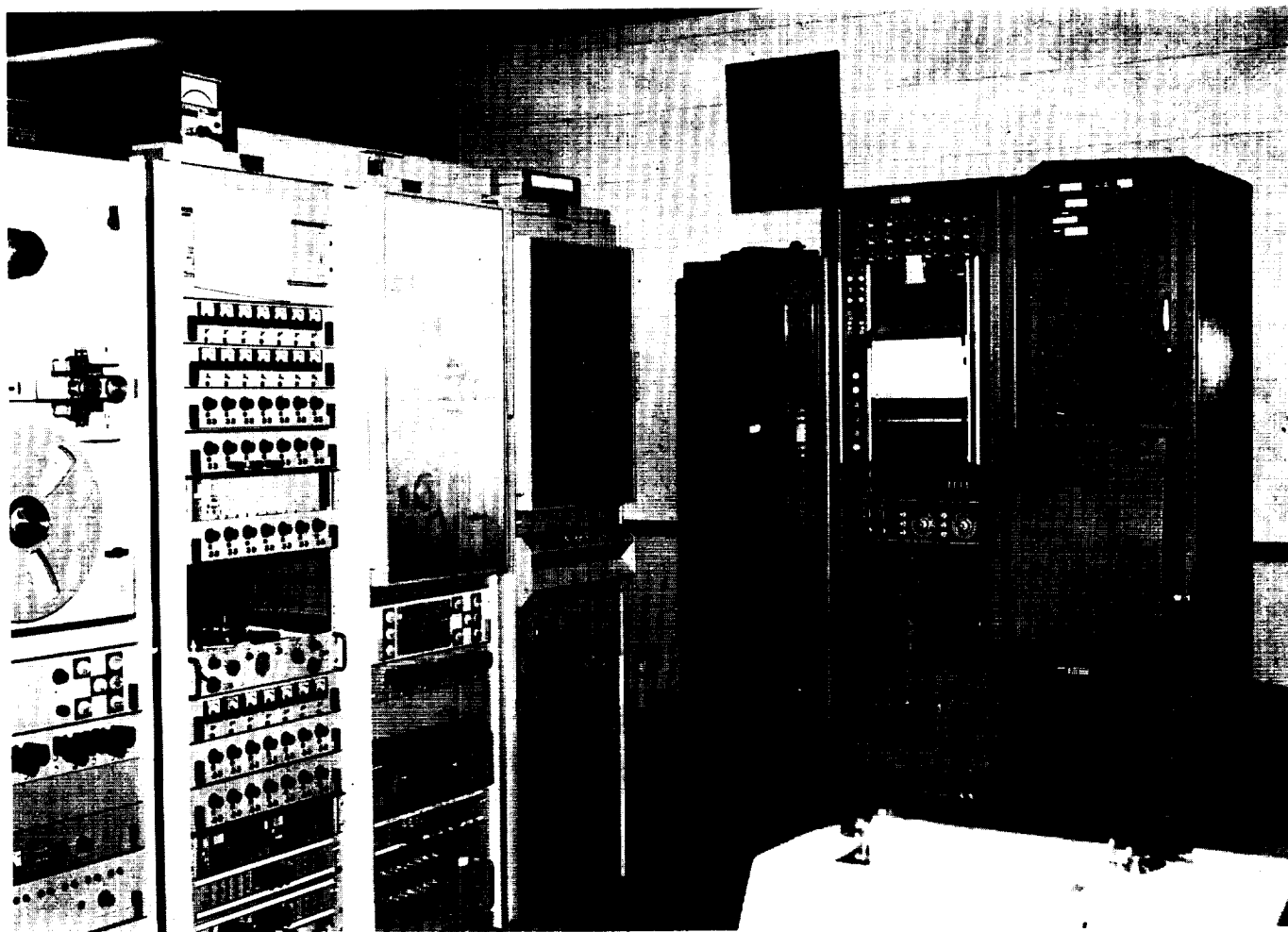


Fig. 1. Multimission support recording equipment installation at Pioneer DSS

May 1 and the station resumed full-time operations. Average film height is 0.005 in. Improvement work continues.

b. Equipment. Ranging subsystem equipment for experiments relative to the *Mariner Venus* project has been installed and is now being tested (Fig. 2). The equipment will be used for research and development projects.

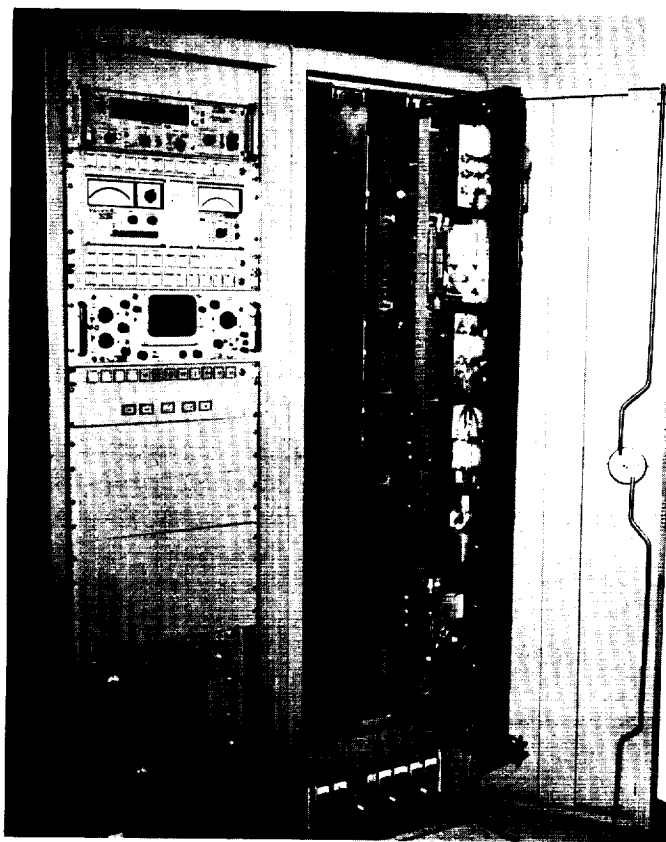


Fig. 2. Ranging subsystem equipment at Mars DSS

C. Venus DSS Operations, E. B. Jackson and A. L. Price

1. Experimental Activities

During the period April 19 through June 14, 1967, the 30-ft az-el antenna at the Venus DSS continued to be used for a time synchronization experiment, the 85-ft az-el antenna was used for a monostatic and bistatic planetary radar experiment, and reception of the *Mariner IV* spacecraft was accomplished utilizing R&D equipment at the Mars DSS.

Time synchronization, with a resolution of better than $\pm 5 \mu\text{s}$, was accomplished between the Venus DSS and

JPL, and between the Venus and Pioneer DSSs, using the moon as a reflector at an operating frequency of 8450.1 MHz. This resolution was made possible by the utilization of a newly developed ephemeris for the moon, developed for this purpose by the Scientific Programming Section of Division 31.

The 85-ft az-el antenna was also utilized for telemetry reception from the *Pioneer VII* spacecraft at 2292 MHz, using rotatable linear polarization to maximize received signal strength. Using matched polarization and a $2B_{Lo}$ bandwidth of 2 Hz in the phase-locked loop tracking filter enabled successful telemetry reception even though the antenna feed system, which is optimized for 2388 MHz, did not deliver maximum performance at 2292 MHz.

The performance of the 85-ft az-el antenna at 8448 MHz is currently being extensively investigated, using radio star tracking to investigate surface and structure deformation as a function of antenna attitude, and using the Tiefort Mountain collimation facility to measure gain and antenna patterns in the horizon look position. Preliminary measurements indicate a gain of 64 dB at 8448 MHz.

The planetary radar experiment, with Mars as the target, has been concluded. Results were very good, as can be seen in Fig. 3. The average round-trip range during

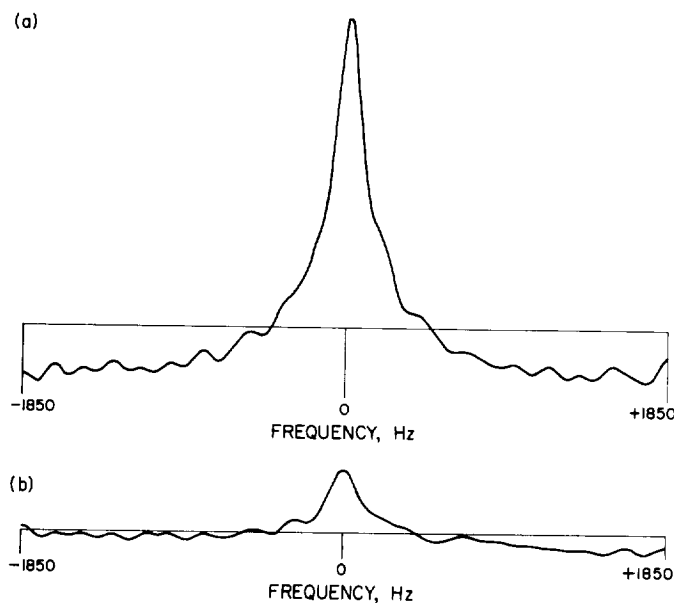


Fig. 3. Cumulative power density spectra from Mars: (a) bistatic (average of 141 runs), (b) monostatic (average of 1088 runs)

this experiment was 640.7 light-seconds so the monostatic spectra shown represent approximately 11,618.5 min of data, while the bistatic spectra represent approximately 1,505.7 min of data. The 6-dB gain superiority of the 210-ft dish on reception can easily be seen in the quality of the data labeled bistatic.

2. Subsystem Performance

a. Receiving systems. The X-band 8448- to 30-MHz converter remained in the 85-ft antenna feed cone during this period. It is presently being used for antenna pattern measurements. In its present configuration, the output of the X-band converter is connected to the 30-MHz input of the MOD IV receiver. This allows phase-locked operation for signal-strength measurements as described in SPS 37-45, Vol. III, p. 79.

The X-band receiver was also used as a monitor in the modulation level adjustment of the X-band transmitter used in the "time zero" experiment. This was accomplished by radiating a signal from the Venus DSS 30-ft antenna, where the X-band transmitter is located, into the 85-ft antenna, where the X-band receiver is located. The received signal is then fed to the range channel of the MOD IV receiver where the carrier suppression is measured utilizing a 10-Hz bandpass filter. The output of the bandpass filter is monitored with a rms voltmeter. The programmed local oscillator was offset to place the received signal within the passband of the 10-Hz filter.

The MOD IV receiver was also used during this period in the Mars planetary experiments at 2388 MHz. Operation was conducted in both the bistatic mode and the monostatic mode. In the monostatic mode, the normal Venus DSS 2388-MHz S-band receiver was used. In the bistatic configuration, the 455-KHz signal from the 2388-MHz R&D receiver at the Mars DSS was fed, via the microwave link, into the AM channel of the Venus DSS MOD IV receiver.

3. System Improvements

a. Receiving system. During this period the *Mariner* receiver, in conjunction with the MOD IV receiver, was used for the reception of signals from the *Pioneer VII* spacecraft. The receiver local oscillator was modified to allow tuning to the *Pioneer* frequency (2292 MHz). This modification involved the substitution of a 24-MHz voltage-controlled oscillator and distribution amplifier and a HP 5100 frequency synthesizer in the main loop channel of the MOD IV receiver.

The AM channel was also modified for use in telemetry detection. This was done by feeding a phased 455-KHz reference signal to the reference input of the AM channel third conversion mixer. The output of the mixer, when the receiver was phase-locked to the received frequency, was telemetry information which was fed via microwave link to the Echo DSS for processing.

b. Frequency and timing subsystem. The Knight crystal oscillator which has been the UT2 frequency reference for the frequency and timing subsystem was replaced with a Varian 4700C rubidium frequency standard which has just been reset to UT2 by the manufacturer. This will provide a more stable frequency reference for timing pulses used in the time synchronization experiment.

D. Antenna Engineering, W. J. Kissane, R. McKee,

A. Nicula, V. B. Lobb, J. Carpenter, and J. O. Breninger

1. Installation and Final Acceptance of DSS 62,

W. J. Kissane and R. McKee

The installation of the antenna mechanical subsystem at DSS 62, Cebreros, Spain, was started on schedule on May 2, 1966. (Figure 4 shows the completed foundation footings and the staging of equipment for the commencement of subsystem erection.) Cebreros is located approximately 90 km west of Madrid and 19 km from DSS 61, Robledo, Spain. DSS 62 is the third DSN 85-ft hour-angle/declination (HA/dec) antenna installation of the new four-legged hi-performance configuration. The others are at DSS 61 and DSS 42, Tidbinbilla, Australia.



Fig. 4. DSS 62 foundation footings and equipment staging

The DSS 62 installation differs from the original DSS 42 and 61 installations in the following areas (Fig. 5):

- (1) A new ladder configuration (wider, better shape) extends from the ground to the lower end (south end) of the hour-angle shaft.
- (2) A modified walkway at east side of declination drive skid area provides improved safety and more area.
- (3) Modified walkways over both declination bearings give improved safety and hour-angle travel.
- (4) New hour-angle and declination cable wrapups are provided.
- (5) Additional double cable trays extend from the antenna support building to the antenna, across the north face of the pedestal and up the west face of the pedestal and up the west side of the hour-angle wheel structure and into the upper electronics room.
- (6) Improved structural connections are provided. All connections, except stitch bolts, were made using

High Strength A490 or A325 interference bolts and Stover lock nuts. This includes all face panel attach bolts. All these connections were made using the new "turn-of-the-nut" bolt tightening procedures, which give more uniform tensioning to all bolts.

- (7) New light towers are provided for night work and emergency repairs.

The total time lapse for the implementation of each of the antenna mechanical subsystems at DSS 42 and DSS 61 was 29¼ and 32¼ mo, respectively. Implementation of the antenna mechanical subsystem at DSS 62, because of station tracking requirements, was expedited (completed in 22¼ mo) and, despite exceptionally bad weather (total lost time was 414 man-hours), was completed on schedule on October 31, 1966. Table 1 gives time breakdowns of the task performance schedules at DSSs 42, 61, and 62. Figure 6 shows the completed antenna mechanical subsystem at DSS 62.

The final evaluation of the DSS 62 antenna mechanical subsystem implementation, relative to specification and drawing requirements, shows that the antenna meets or exceeds all requirements (Table 2).



Fig. 5. New modifications on DSS 62 antenna mechanical subsystem

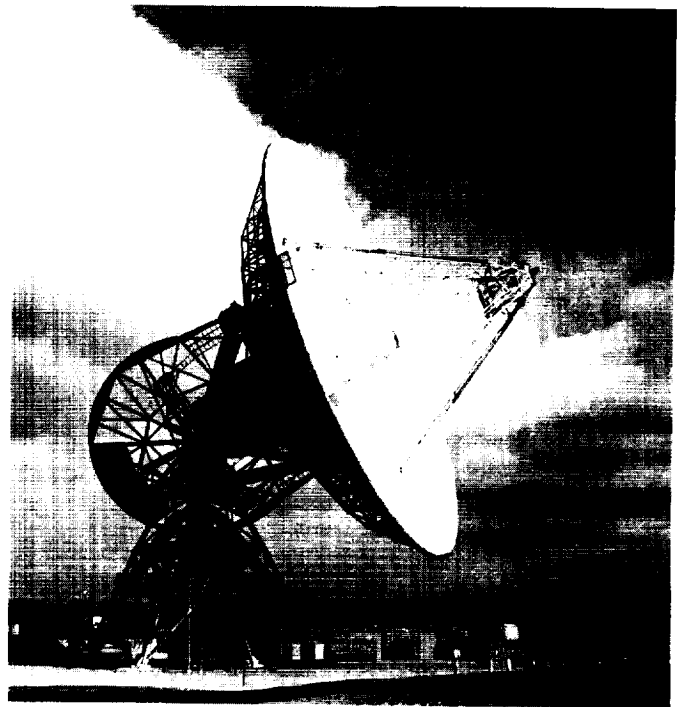


Fig. 6. Completed DSS 62 antenna mechanical subsystem

Table 1. Task performance schedules

Task	DSS 42 ^a		DSS 61 ^b		DSS 62 ^d	
	Time to complete task, mo	Accumulated time from notice to proceed, mo	Time to complete task, mo	Accumulated time from notice to proceed, mo	Time to complete task, mo	Accumulated time from notice to proceed, mo
Write procurement requisitions and statement of work, revise or update specifications, obtain budgetary and scheduling data, gather support specifications and prints, and obtain signatures	2¾	2¾	2¾	2¾	1	1
Procurement effort (request for proposals, vendor bid time, proposal review and evaluation, price analysis, negotiations, etc.)	7½	10¼	7½	10¼	5	6
Contractors' design, detailing, fabrication, testing, quality assurance, and packaging work	7½	17¾	11	21¼	7½	13½
Shipment to station	1½	19¼	2 ^c	23¼	1½	15
Erection	3¼	23	4	27¼	4	19
Acceptance testing; installation and checkout of Cassegrain system, S-band acquisition aid, optics, and air conditioning	1¾	24¾	1½	28¾	2	21
Cable, electronics, and RF hardware installation and checkout	1½	26¼	1	29¾	1	22
Systems tests	1	27¼	1	30¾	1	23
Preliminary training of station operational personnel	2	29¼	2	32¾	1	24
Station operational	—	29¼	—	32¾	—	22¾
^a Effort was expedited in all areas. ^b Effort was partially expedited in all areas. ^c Includes storage time and damage assessment time in Spain. ^d Effort was expedited in all areas.						

Table 2. DSS 62 antenna mechanical subsystem acceptance test data

Item ^a	Specification requirement	Actual achievement
1. Hour-angle axis alignment Azimuth/elevation	Within ± 30 sec of arc with rotational axis of the earth	1 sec of arc west of astronomical north; 20 sec of arc above station astronomical latitude
2. Declination axis orthogonality	Within ± 30 sec of arc with hour-angle axis	Within 16.5 sec of arc; east bearing is north
3. Reflector surface manufacturing setting at zenith	0.020 in. rms 0.010 in. rms	Less than 0.020 in. rms Less than 0.010 in. at zenith
4. Counterbalance Counterweight Hour angle Declination	Antenna Unloaded Loaded +18,000 lb $\pm 6,000$ lb +4,000 lb $\pm 1,000$ lb	Fully loaded antenna Dish +5,100 lb Dish +200 lb
5. Bearing axial end play Hour-angle axis Declination axis	0.005 in. 0.060 in. (total)	0.001 in. 0.032 in. (east bearing) 0.036 in. (west bearing)
6. TIR ^b of gears Declination Hour angle	Unloaded antenna 0.030 in. 0.030 in.	0.021 in. 0.032 in.
7. Running clearances Declination Hour angle	0.025/0.050 in. 0.050/0.100 in.	0.026/0.044 in. 0.091/0.094 in.
8. TIR of bearings Declination Hour angle	0.005 in. 0.005 in.	0.004 in. 0.0015 in.
9. Datex readout packages Hour angle Declination	0.010 in. (TIR) 0.020 in. (TIR)	0.0015 in. (TIR) 0.004 in. (TIR)
10. Cone ring	$6\frac{1}{8} \pm \frac{1}{32}$ in. above vertex; ring attach holes to be concentric within 0.060 in. with dish mechanical axis	6.375 in. above vertex; concentric within 0.030 in. with dish mechanical axis, and parallel within 0.015 in. with dish datum plane
11. Hyperbola	Concentric within 0.030 in. and parallel within 1 min of arc with dish mechanical axis at zenith position	Hyperbola axis is coincident within 0.014 in. with reflector mechanical axis and is parallel within 37 sec of arc with reflector mechanical axis at zenith position
12. Optical tracking aid package	Align optical tracking aid axis within 10 sec of arc with dish mechanical axis	+3 sec of arc in declination and -9.5 sec of arc in hour angle
13. Datex readouts	± 0.004 deg	0.000-deg hour angle and 40.450-deg declination when dish mechanical axis is pointing to zenith
14. Dish mechanical axis primary datum plane	13.000 in. above vertex; parallel within 10 sec of arc with declination axis of rotation	13.000 in. above vertex; parallel within 3 sec of arc with declination axis of rotation
15. Secondary dish mechanical axis datum plane	Parallel within 5 sec of arc with dish mechanical axis primary datum plane	Parallel within 3 sec of arc
16. Spirit levels	± 10 sec of arc	Levels are within 3 sec of arc of being level when dish mechanical axis is pointing to zenith
17. Station coordinates	JPL Drawing 9431720	Astronomical values are 40°27'03.01" or 40.45083° N, 40°21'55.19" or 40.36534° W; Monument 4 is 723.266 m above mean sea level
18. Station base line	JPL Drawing 9431720	Azimuth from Monument 4 to Monument 1 is 08.25 sec of arc east of astronomical north

^aItems 1, 2, 4, 5, 6, 7, 8, 9, 12, and 13 are the results of measurements made after the antenna was fully loaded; items 3, 10, 11, and 16 were measured without the Cassegrain cone in place.

^bTIR = total indicator reading.

2. MSFN Modifications to DSSs 11, 42, and 61, A. Nicula

The modification of DSN stations 11, 42, and 61 was necessary to provide operational support to Manned Space Flight Network (MSFN) project *Apollo*. In order for these stations to fulfill all the DSN tracking commitments and handle the obligation as backup stations for the *Apollo* network, the following modifications to configurations at these stations were necessary:

- (1) Antenna structure: new cable trays, hour angle/declination (HA/dec) wrapups to handle DSN/MSFN cable run installation, service platforms, and safety rails (Figs. 7 and 8).

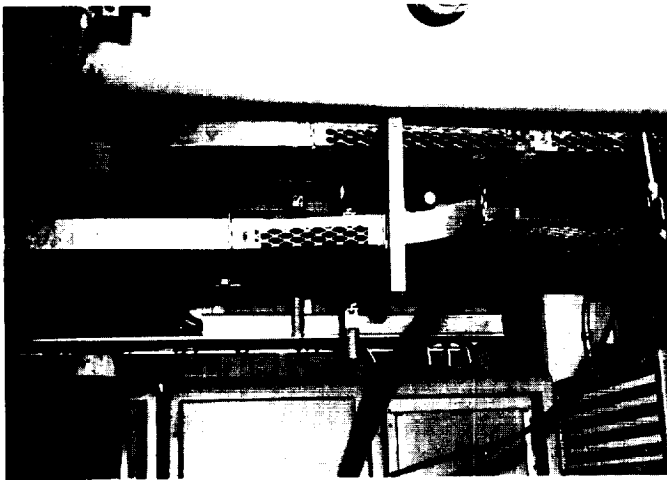


Fig. 7. MSFN cable tray configuration

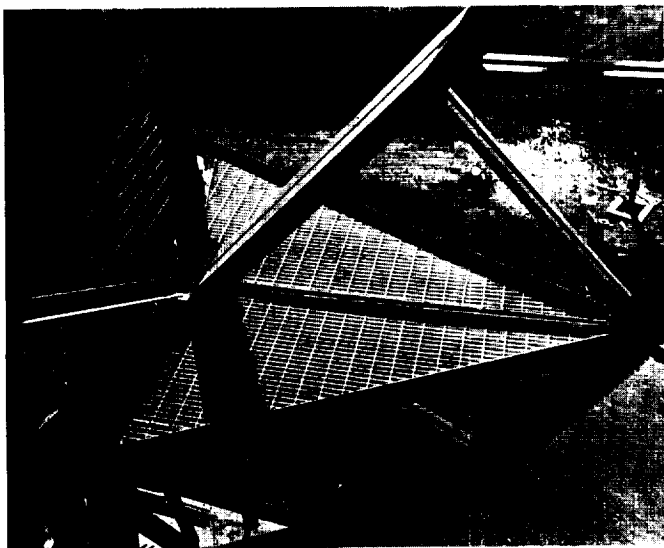


Fig. 8. MSFN declination wheel service platforms

- (2) Upper electronics room: a new maser (1325/UWV-56), MSFN receiver racks (1201A/RCV, 1201B/RCV, 1202A/RCV, 1202B/RCV), and a new MSFN 20-kW power amplifier (1323/TXR-12, etc.) (Figs. 9 and 10).

Due to lack of space available inside the upper electronics room, the RF switching box (1321/UWV-58) was installed on the outer north wall (Fig. 11). The hybrid waterload unit for the MSFN 20-kW power amplifier was installed on the east wall of the upper electronics room by means of a unistrut. To relieve congestion in the electronics room, the cargo hoist control storage box was moved and installed on the east ceiling support beam.

Inasmuch as the new MSFN power amplifier cabinet was overlapping the flange of the access door to the lower electronics room, it was necessary to modify the access door by cutting off the flange and permanently fastening

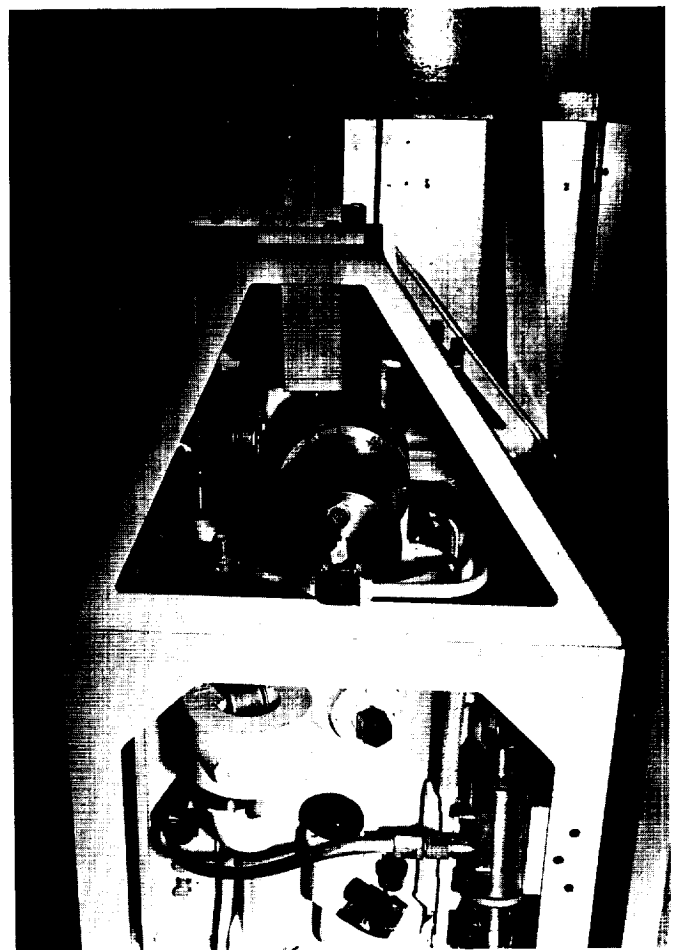


Fig. 9. MSFN maser installation (electronics room)



Fig. 10. MSFN receiver and power amplifier racks (electronics room)

it by means of three $\frac{3}{8}$ -in. flat head screws, thereby making usage possible.

Calculations showed that 1500 lb of counterweight should be removed from the declination room wheel counterweight cage and 4000 lb of lead should be added to the HA counterweight cage, in order to balance the antennas after MSFN equipment installation. However, at DSSs 42 and 61 on the new four-legged antennas, the declination wheel counterweight cage is an integral part of the structure; therefore, no lead billets could be removed from this cage. After MSFN equipment was installed in the upper electronics room, HA and dec counter-

weight measurements were made and a maximum of 5000 lb of lead billets was added to the HA counterweight cage. This weight was sufficient to bring both axes of the antenna to a balance condition.

The optical tracking aid and the collimation tower assembly were modified to accept DSN/MSFN interface. This interface was implemented by paralleling preliminary controls in the operation centers of the DSN and MSFN wings with transfer switching to implement specific control to the wing in configuration control, and by installing required optical boresight targets on the collimation tower.

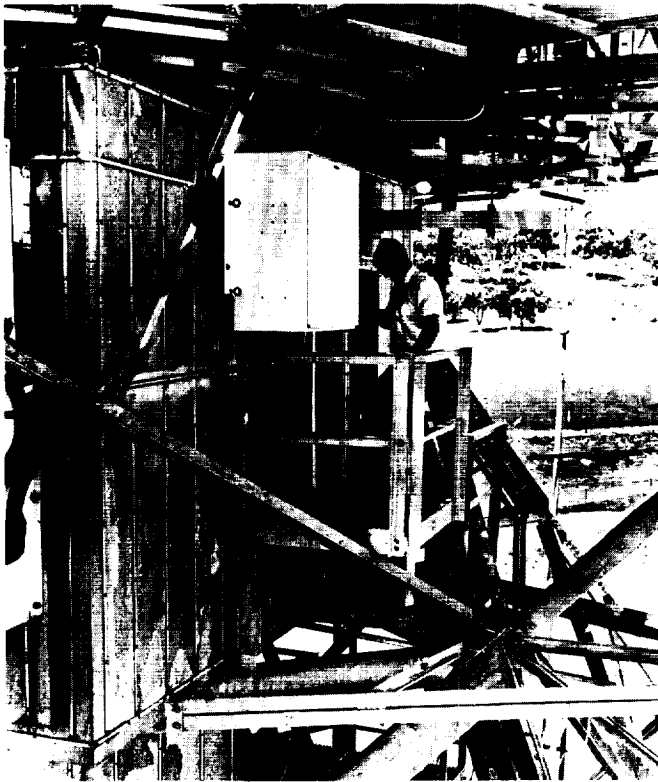


Fig. 11. MSFN RF switching unit and service platforms (electronics room)

In order to achieve RF boresight at MSFN frequencies, it was necessary to install two 4-ft-diameter RF antennas (furnished by Collins Radio Company) on the 100-ft collimation tower, along with an optical target. Using special brackets and channels, the two 4-ft-diameter RF antennas were permanently bolted to the collimation tower structure, at a distance of 20 ft below the DSN 8-ft-diameter RF antenna. The optical target, a red flood lamp (150 W, 120 V) was installed by using rigid conduit fastened to the collimation tower structure. A weatherproof electrical cable was wired into the floodlight socket at one end and routed inside the collimation tower structure to a dimmer inside the collimation tower building. The dimmer is controllable from the MSFN wing.

All DSN/MSFN modifications have been completed at all stations; the DSS 61 modification was completed last. All drawings reflecting DSN/MSFN interface in these areas were released in mid-January. Users drawings are available at each station; and for all modifications, transfer agreements between station managers and cognizant development engineers have been executed.

3. DSIF Cable Wrapping Modifications, V. B. Lobb

New cable wrapups for the 85-ft hour angle/declination antenna were designed to overcome the major difficulties that the old cable loops presented. These difficulties were:

- (1) The danger of a catastrophic cable failure caused by shearing off of the cables since the old loop tended to hang-up on the structure.
- (2) The station requirement that a man must monitor the cables during a track to prevent snagging or shearing of the cable.
- (3) Cable stressing which caused cable wear and reduced the reliability of the antenna.

Numerous ideas were explored concerning a mechanical wrapup system that would solve the difficulties that were plaguing the old cable loops. Initial concepts were explored and finally a prototype wrapup was installed at the Pioneer DSS.

The declination wrapup modification consists of a stainless steel sheet spiral that is bracketed to the declination shaft and to the reflector backup structure. The cables are clamped to the sheet metal spiral and simply expand and contract with the sheet metal spiral for declination movement (Fig. 12).



Fig. 12. Declination axis wrapup drum

The hour-angle wrapup modification consists of a rotating cable tray and a short loop. The rotating tray rotates with the upper antenna structure and is so positioned that the cables leaving the tray rotate on the axis of rotation of the upper structure. An added benefit of this wrapup is that a short loop can be used. The movement of the loop is approximately 1 ft up and down. The cables are securely clamped in the rotating tray (Fig. 13).

A set of cables was installed in the prototype wrapup at the Pioneer DSS to test cable life versus time and to check wrapup function for the following:

- (1) Cable action during movement.
- (2) Wear.
- (3) Clearance to structure.
- (4) Cable stressing.

The life cycle test of the wrapup and cables lasted for a month. The cable wrapup performed well mechanically during the test and passed the function checks.

The hour-angle wrapup design required a change in the ladder and platform in the area of the rotating tray to provide clearance for the tray. The new platform is

wider and improves the safety and access to the antenna (Fig. 14).

The new cable wrapups have been installed at DSSs 11, 42, 61, and 62. The hardware is at DSSs 12, 51, and 41 and will be installed when there are breaks in station commitments.

This wrapup was utilized on the MSFN implementation since it uses two separate loops or paths for the cables. It has the capacity to handle all MSFN cabling on one side and all the DSN cabling on the other side, thus entirely separating the two systems. For the MSFN installations, additional cable trays were required; the original trays were changed to conform to the new wrapups (Fig. 15).

The newly installed cable wrapups have eliminated cables being torn, snagged, or sheared since the cables are securely fastened to the metal wrapup. Elimination of cable loops has relieved station personnel of the monitoring duty. Cable stressing has been eliminated since the mechanical wrapups hold the cables securely and take the stresses.



Fig. 13. Hour-angle axis wrapup rotating tray

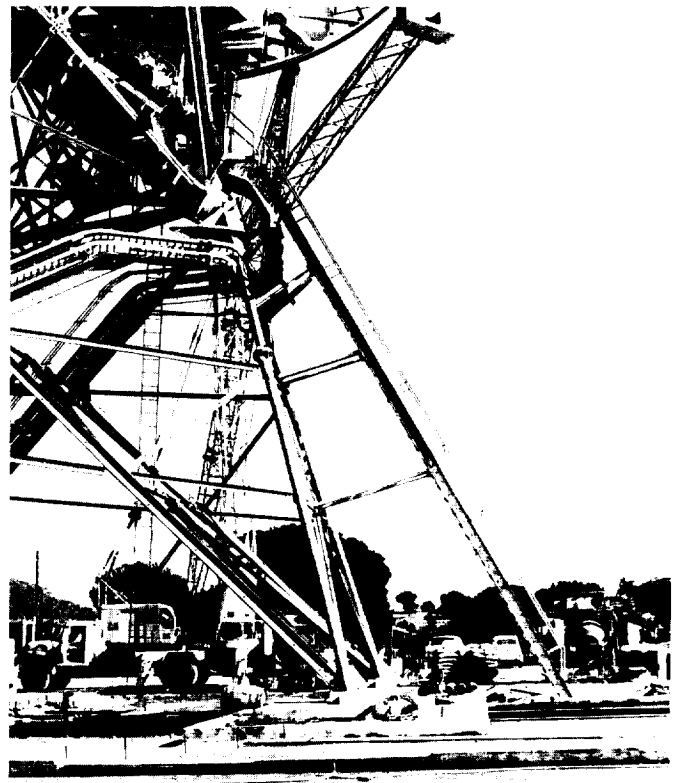


Fig. 14. Modified south hour-angle ladder and platform

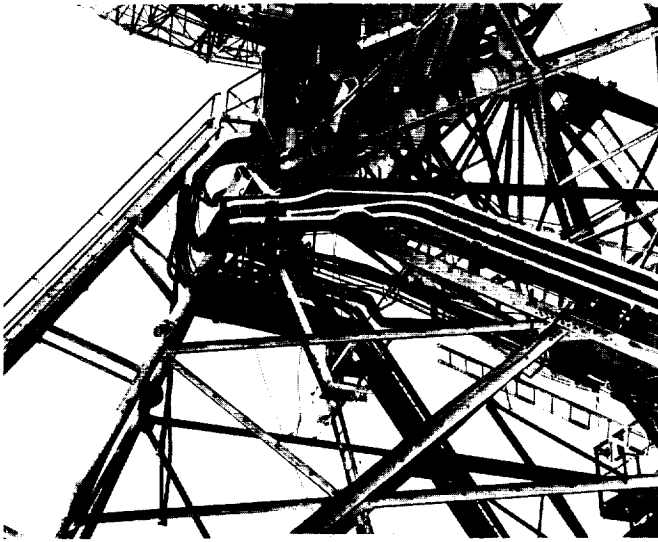


Fig. 15. DSN/MSFN cable tray configuration (hour-angle axis to hydromechanical building)

4. Emergency Repair Light Towers, V. B. Lobb and J. Carpenter

The need for lighting standards first became evident while plans were being made for DSS 62 erection. The scheduled completion date for antenna installation required two-shift, field erection work. In addition, lighting was required for upgrading other DSS antennas and for DSN/MSFN implementation. Therefore, it was decided to provide all DSSs with lighting standards.

The concept used was to station two standards 180 deg apart. This was done to furnish light evenly from both sides to minimize shadows on the antenna. Three banks of lights at levels of 30, 50, and 70 ft from the ground were used on each standard. Each bank contained two 1000-W and two 500-W floodlights (Fig. 16).

The standard was a modified commercial heavy flagpole, which was the most economical structure available. The pole, light banks, and foundation were designed to survive in 120 mph winds.

The foundation for the pole would have been excessively large had not the use of lateral passive soil pressure combined with vertical bearing soil pressure been used. The foundation size, using this survival design assumption, was 5 ft square by 8 ft deep.

One light standard was positioned so that it could be permanently erected. The other standard is removable and is in place only when needed. Complexes, such as Goldstone or Madrid, have one permanent standard in-

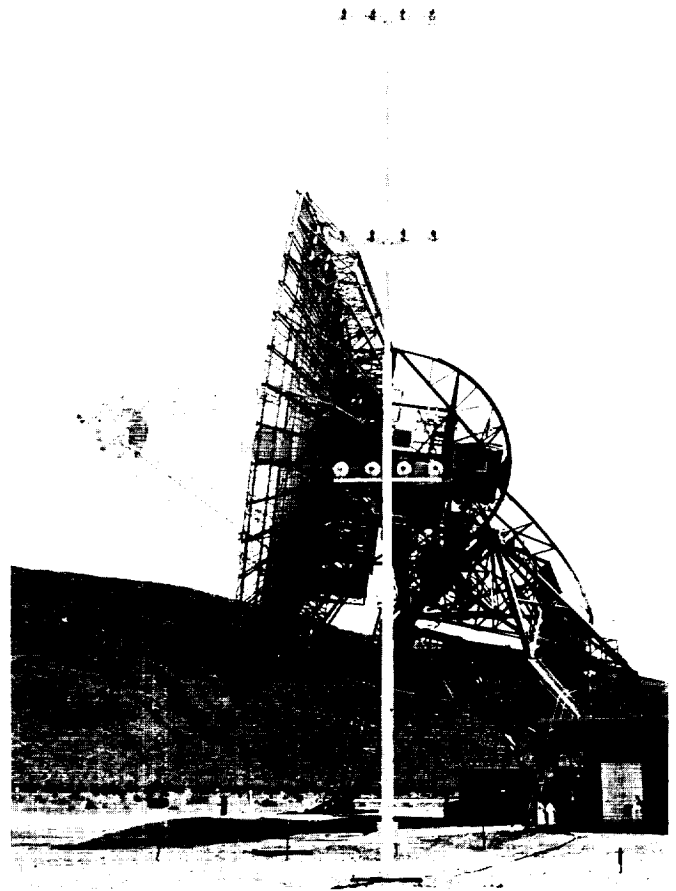


Fig. 16. DSS 11 emergency lighting tower

stalled at each station and one portable standard which can be moved from one station to the other when needed.

The light standards are installed at DSSs 11, 12, 42, 61, and 62. The standards are in the process of being erected at DSSs 41 and 51.

5. Optical Tracking Aid Installation at Table Mountain,

J. O. Breninger

During the last quarter of FY 67 an optical tracking aid (OTA) unit was installed on the 18-ft polar mount antenna at the Jet Propulsion Laboratory Table Mountain radio telescope installation near Wrightwood, California (Fig. 17).

The OTA unit provides optical support for the 18-ft-diameter radio telescope antenna in the areas of (1) star tracking calibration of the apparent geometric axis and tracking axes, (2) angle encoder boresight checks, (3) RF



Fig. 17. Table Mountain radio telescope

boresight checks, (4) optical acquisition and tracking of celestial bodies, (5) RF snap-on tests, (6) radio star optical tracking, where possible, (7) RF horizon mask determination, (8) star track evaluation of angle encoding equipment, (9) RF equipment gain and pattern measurements, and (10) planetary radar optical tracking.

a. OTA description and characteristics. The OTA unit is designed around a cassegrainian, reflecting type, $f/8$, 40-in. Zoomar telescope for maximum light gathering capability. A closed-circuit TV system is used to present the telescope image conveniently to the antenna operator by means of the TV monitor at the control console. An illuminated reticle image, introduced onto the optical axis of the telescope, is registered by the TV monitor and provides a visual reference of the centerline of the antenna geometric axis. Controls for reticle illumination intensity and selection of neutral density filters are provided to compensate for varying light conditions and contrast. The antenna mounted assembly is housed in a weatherproof, rugged weldment for maximum stability with minimum weight. A motor-actuated, slide-mounted cover assembly permits unobstructed viewing through the telescope while protecting the sensitive telescope and TV camera from rain, snow, or wind-blown dust. A manually-viewed $\times 32$ telescope facilitates precise collimation of the Zoomar telescope axis with the antenna reflector geometric axis and provides an auxiliary reference for boresight opera-

tions. Both telescopes are mounted as an optical components subassembly which can be adjusted to precise alignment independently of the exterior housing. The OTA assembly is shown in the manual boresight mode in Fig. 18. The OTA unit at Table Mountain was adapted from a basic design used on the DSIF tracking antennas.

Operation of the OTA unit is remotely controlled from the servo operator's console (Fig. 19). Optical boresight images are presented to the operator on a 14-in. TV monitor adjacent to the filter density, reticle illumination intensity, and automatic door position controls. The TV camera setup controls are located below the console counter top as shown.

b. Radio telescope antenna description. The antenna structure of the radio telescope consists of a high-precision, aluminum reflector mounted on a servo-controlled, two-axis pedestal. The reflector is a cassegrainian design with aluminum honeycomb surface panels, a precision-machined secondary reflector that is movable in three axes, and a backup structure of cast aluminum radial ribs with intercostals of tubing. A tubular aluminum transition structure with radial gussets mount the reflector to the pedestal counterweight arms. The pedestal has been especially adapted to a polar-axis type installation where the vertical axis of the pedestal has been tipped over to a position parallel with the earth's axis and in line with the local meridian. This type of installation permits star tracking while driving the antenna about the polar axis only, at a sidereal rate of rotation, which is advantageous in radio astronomy work. (See Fig. 20 for details of the reflector and pedestal structure.)

c. OTA support structure. The OTA assembly is secured to the transition structure by means of an engine-mount type arrangement using aluminum structural tee members (Fig. 20). Accessibility to the OTA adjustment bolts permits final alignment of the optical components subassembly after the housing has been attached to the support structure.

d. OTA collimation with the antenna geometric axis. The OTA optical axis is brought parallel with the antenna reflector geometric axis with the antenna in the zenith pointing position. The astronomical zenith position is precisely determined under stable night-time environment by means of the "Talyvel" electronic level system placed on the reflector vertex mounting plate. The vertex mounting plate is used to attach the radiometer and RF feed horn in relationship to the reflector geometric axis and is accurately installed in the proper position.



Fig. 18. OTA assembly in manual boresight mode

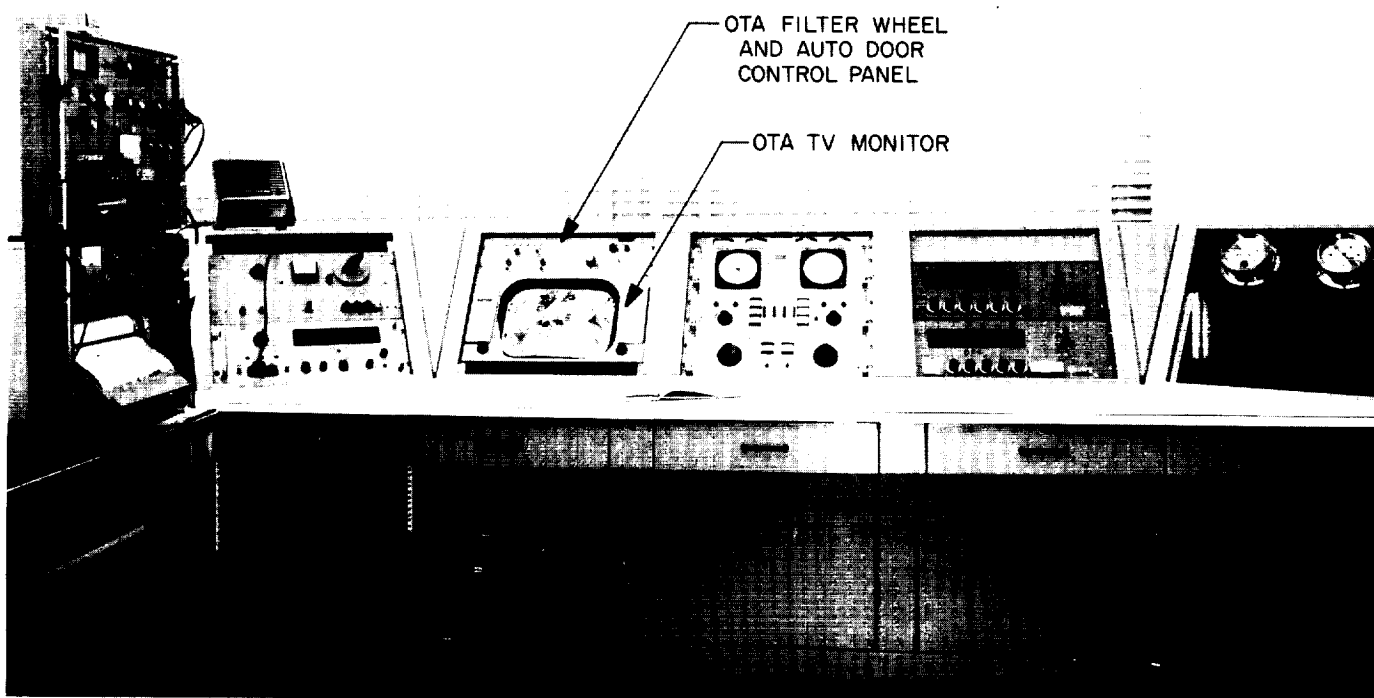


Fig. 19. OTA assembly control room console

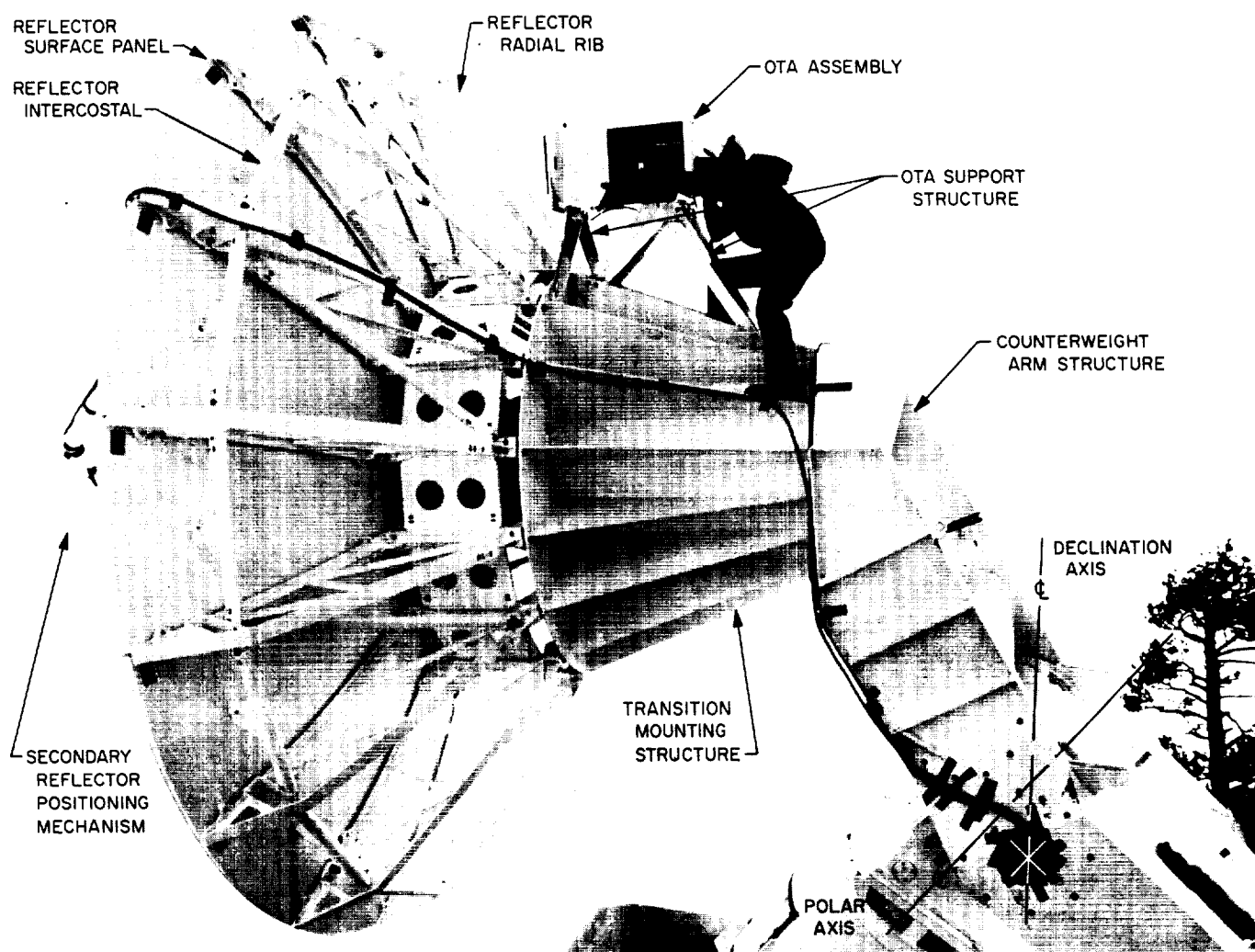


Fig. 20. Radio telescope antenna with optical tracking aid assembly in manual boresight mode

The electronic level is first checked and calibrated in place to indicate a level better than 0.5" of arc (Fig. 21). A pair of coarse and precise spirit levels are used in conjunction with the electronic level, which is operated with full-scale indication of 100" of arc. The antenna is then

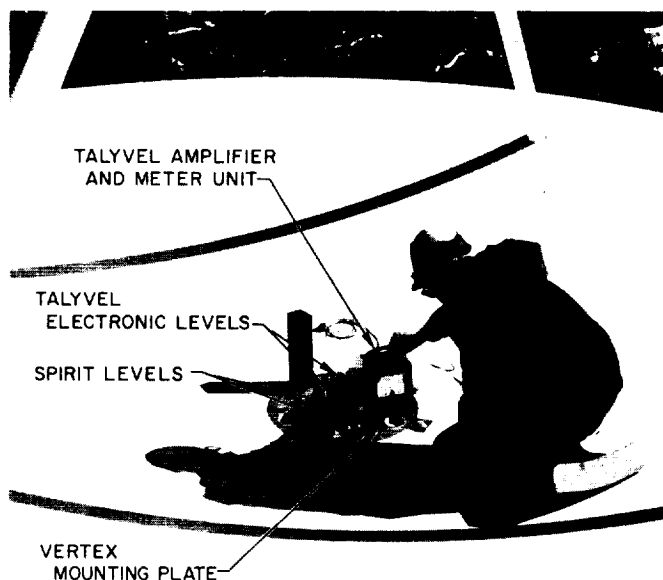


Fig. 21. Talyvel and spirit level setup for zenith position control

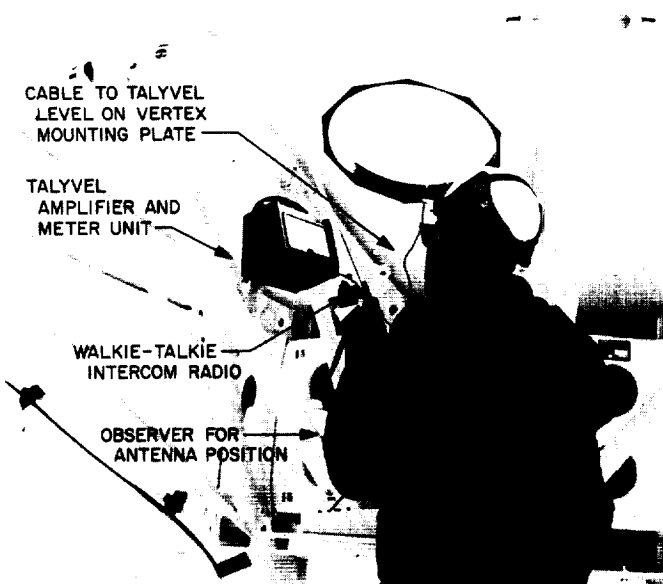


Fig. 22. Observer positioning commands for zenith using Talyvel readout

commanded to approach zenith driving one axis at a time, using the remote readout meter of the electronic level situated outside of the reflector where the weight of the observer can be isolated from the antenna (Fig. 22). Final readings of the astronomical zenith position are verified with the antenna locked in position. Zenith position indicated by the digital readouts of the antenna servo system was established with the antenna position relative to the local vertical within 1" of arc.

With the antenna locked at the precise zenith position, the OTA assembly was then adjusted until the optical axis of the reference telescope was also brought vertical as controlled by a theodolite shown in Fig. 23. The theodolite contains a precise coincidence spirit level and provides angle readout direct to 0.2" of arc. The theodolite telescope is shown directed downward through a hollow spindle into the OTA. The reticle image of the reference telescope is observed by means of a right-angle eyepiece, enabling the observer to work without inducing deflections or vibrations into the OTA assembly. The technician performs the adjustment operations as directed by the theodolite observer until the OTA optical axis is within

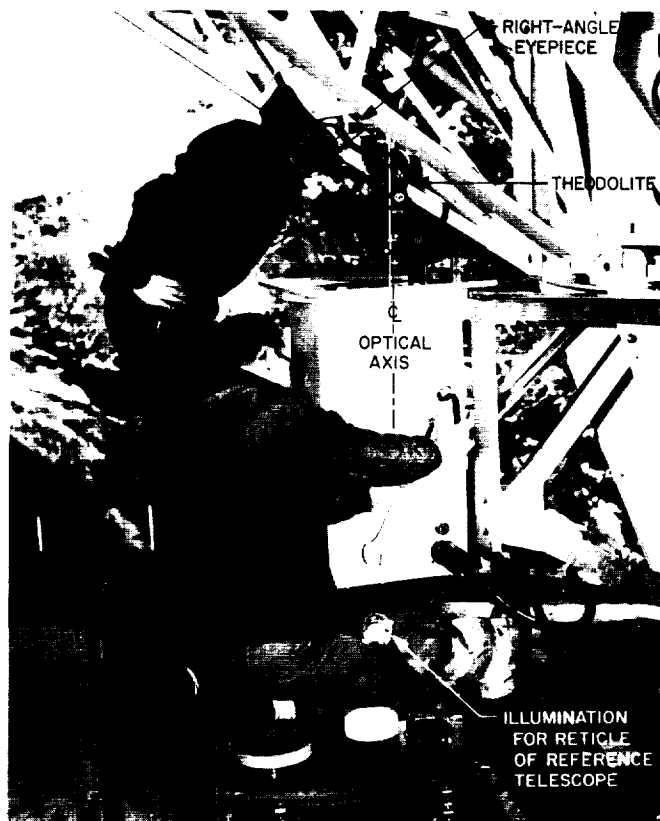


Fig. 23. Hour-angle axis adjustment

10" of arc of the true vertical reference. This adjustment is accomplished in one axis at a time until the specified alignment is achieved. (See Figs. 23 and 24 for adjustment positions in both axes.)

When the precise OTA alignment has been completed, the distance between the reflector geometric axis and the OTA optical axis is measured and recorded (Figs. 25 and 26). This value is used to establish the offset location and orientation of the optical boresight target relative to the RF collimation transmitter. This transmitter is located across the valley on an adjacent mountain and is used for alignment of the RF axis and for performing pattern checks of the radio telescope.

e. Summary. The Table Mountain radio telescope antenna was provided with an optical tracking aid for an optical indication of the antenna geometric axis. Remote operation and display is facilitated by means of a closed-circuit television system with all controls located at the servo control console. The antenna precise astronomical

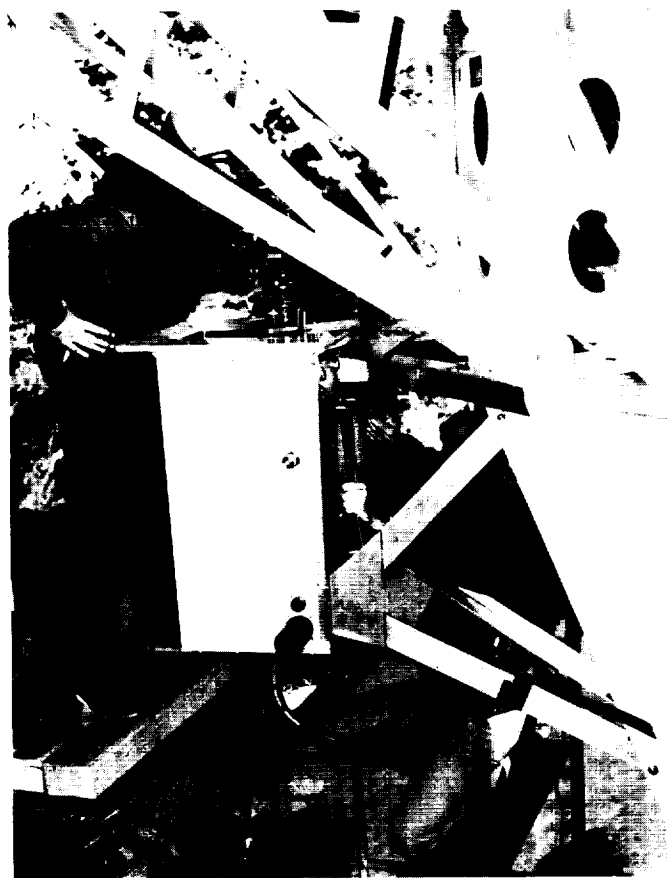


Fig. 24. Declination axis adjustment

zenith position was established to an accuracy of better than 1" of arc and the OTA reference axis was collimated to this reference to better than 10" of arc. The OTA reference axis can be adjusted independently of its mounting to correct for structural deflections or realignment of the antenna on its foundations.

6. DSS 13 Transmitter-Electronics Room Study, V. B. Lobb

The need for a transmitter-electronics room evolved with the development of a 400-kW transmitter to be used at DSS 13. The new transmitter was too large to be housed and serviced in the feed cone location that the existing 100-kW transmitter has now.

The size of the klystron tube and its individual handling requirements, along with the balance of the transmitter hardware and other needed electronic racks in the room, lead to the general size requirement for the proposed transmitter-electronics room.

The design problems associated with the development of the room, transmitter cabinet, and connecting waveguide are many. The following are some of the problems considered:

- (1) Room configuration, location, size, and connection to the existing structure.
- (2) Allowable interconnecting waveguide deflection and stresses.
- (3) Allowable transmitter cabinet deflections for proper support of the klystron tube.
- (4) Allowable heat losses to the room from the transmitter.
- (5) Individual handling of the klystron tube.
- (6) Strength of the existing antenna components to sustain the added loads of the room.

Approaches to the design problems will be discussed in the order listed above.

a. Room configuration, location, size, and connection to the existing structure. The size of the room was developed from the space requirements needed for two 400-kW transmitters and other electronic hardware which



Fig. 25. Measurement of optical axis offset

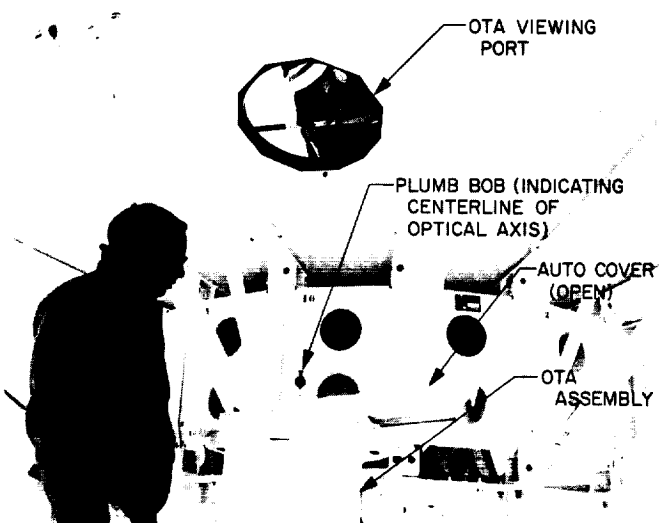


Fig. 26. Location of TV lens axis centerline

were to be placed in the room (Fig. 27). The need to be able to place, remove, and handle a costly and delicate klystron tube, 7 ft long and weighing more than a half ton, required that a bridge-type electric hoist, which could be driven in both directions, be part of the room hardware. The height of the tube plus the handling equipment set the height of the room at 12 ft. The floor area requirement for the needed equipment in the room was 9 ft wide by 24 ft long. The length was increased to 25 ft to facilitate a better structural tie to the existing square girder of the backup structure.

The location of the room on the structure was originally planned to clear the existing structure. However, it was relocated nearer the center of the dish by hinging an existing platform. This resulted in a lower rotation inertia, less new counterweight, and less dish distortion.

The structural configuration was designed so that the room itself was a rigid unit. This was done to allow the

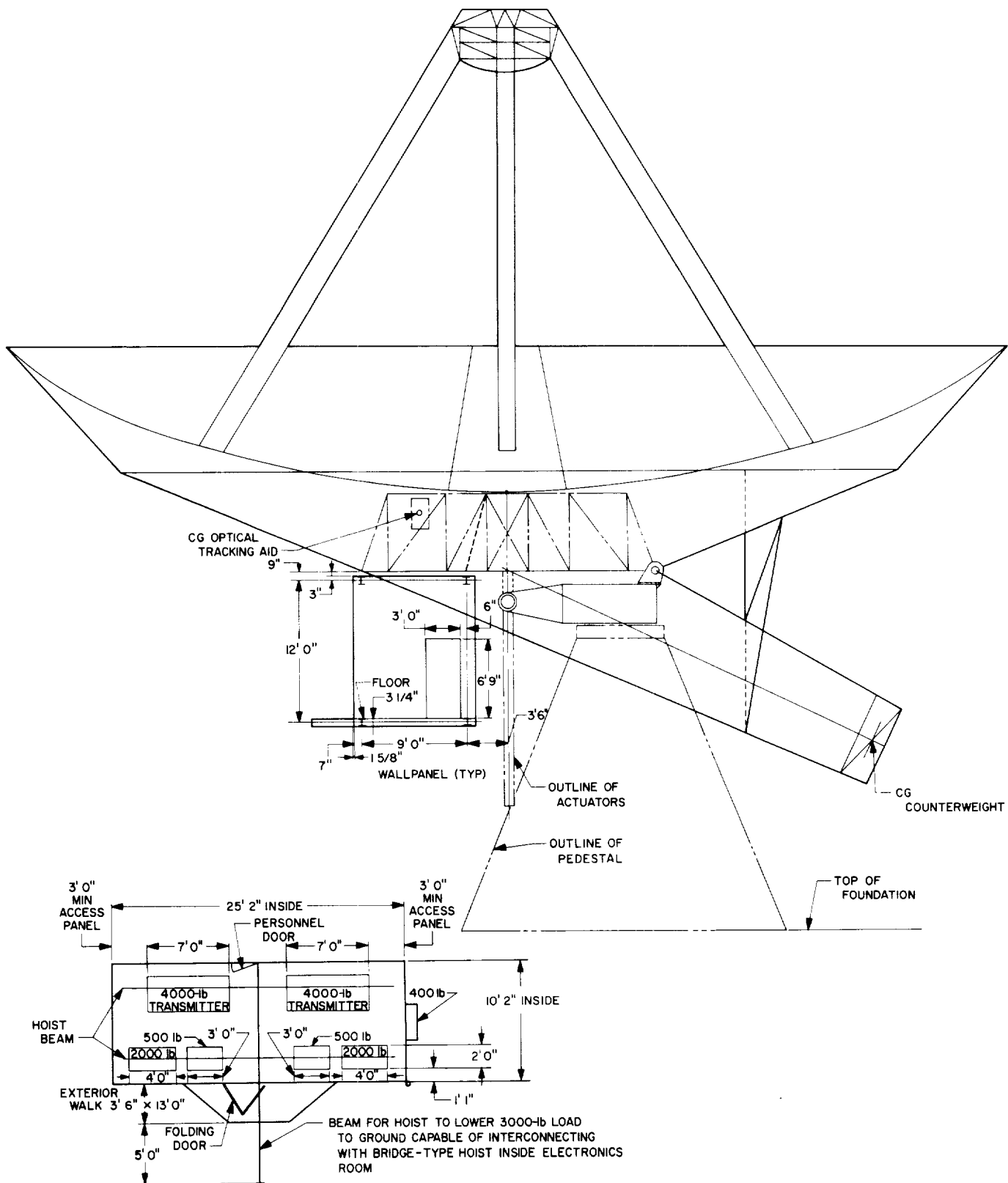


Fig. 27. DSS 13 transmitter-electronics room

room to be assembled on the ground and then installed on the backup structure as a unit. This would result in a shortened erection time and assist in meeting a tight delivery schedule.

A JPL computer analysis of the room structure and the existing square girder of the dish was run to determine the deflection of the room structure in relation to the dish. This was done to compare deflection values with the allowable waveguide distortion, as discussed below.

b. Allowable interconnecting waveguide deflection and stresses. The new room is approximately 23 ft from the cone, and the waveguide is to be run between the transmitter in the room and the cone. Differential deflections between the cone and the room will produce stresses and strains on the waveguide itself and also loadings on the klystron window.

Normally, in a low-power transmitter this differential deflection is handled by a flexible waveguide section which compensates for the deflection. In this 400-kW application, such a section would generate large amounts of heat and would require external cooling. Without a heat exchanger, losses at the flexible section would be too large to tolerate; also, excessive stresses would cause gaps or offsets at waveguide flanges with resultant arcing. To better evaluate the feasibility of using the waveguide run without the problems and expense of a flexible section, an investigation into the ability of the waveguide to distort without permanent damage or excess RF losses was undertaken.

The voltage standing-wave ratio (VSWR) versus waveguide deflection test was set up as shown in Fig. 28 and run at S-band frequency. Results of the test indicated that deflections of the waveguide up to an inch would not cause an appreciable RF problem.

The testing of the waveguide to ascertain its physical properties, as fabricated, was run to determine what kind of strains the waveguide itself could tolerate without failing. The test setup is as shown in Fig. 29. A 5-ft section of waveguide was fabricated with flanges silver-soldered on each end, and one flange rigidly bolted to a support. The other flange had an adapter plate attached and was subjected to an applied load. The free-end deflections were measured by a dial indicator and the applied load by a dynamometer. Possible bolt yielding was checked by a second dial indicator.

The test was run by increasing the load until yielding occurred as noted by failure of the dial indicator to zero-

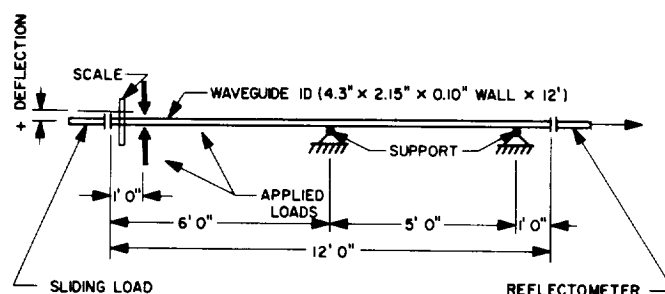


Fig. 28. VSWR vs waveguide deflection test setup

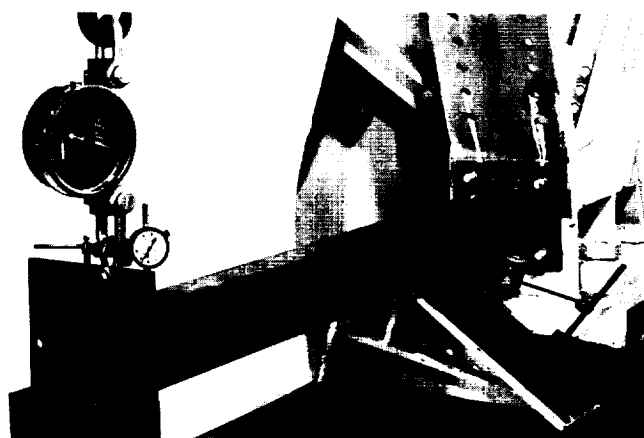


Fig. 29. Waveguide physical properties test setup

set upon releasing the load. The results of testing the waveguide section on its two axes (easy and hard planes) are shown in Table 3. Calculations were made of the theoretical deflections of the waveguide and of the waveguide yielding stress as follows:

Waveguide deflection calculations (typical):

$$I_x \text{ (hard plane)} = 4.58 \text{ in.}^4 \text{ (calculated)}$$

$$I_y \text{ (easy plane)} = 1.85 \text{ in.}^4$$

$$\Delta = \frac{PL^3}{3EI}$$

where Δ = deflection, P = concentrated load, $E = 15.6 \times 10^6$ (copper), and I is given. For $P = 100 \text{ lb}$,

$$\Delta_{\text{easy}} = \frac{100 \times (5)^3 \times 1728}{3 \times 15.6 \times 10^6 \times 1.85} = 0.252 \text{ in.}$$

$$\Delta_{\text{hard}} = 0.252 \times \frac{1.85}{4.58} = 0.101 \text{ in.}$$

Table 3. Waveguide physical properties test

Hard plane					Easy plane				
Applied load, lb	Zero set, in.	Deflection			Applied load, lb	Zero set, in.	Deflection		
		Measured, in.	Calculated, in.	Δ^a , in.			Measured, in.	Calculated, in.	Δ^b , in.
50	0.000	0.049	0.050	0.054	100	0.000	0.280	0.252	0.030
100	0.000	0.103	0.101	0.057	110	0.000	0.310	0.277	0.027
150	0.000	0.160	0.151	0.055	120	0.000	0.337	0.302	0.027
200	Yield → 0.002	0.215	0.201	0.025	130	0.000	0.364	0.327	→ 0.036
225	0.006	0.240	0.226	0.030	140	Yield → 0.004	0.410	0.352	
250	0.078	0.270	0.251	0.028	150			0.377	
275	0.056	0.298	0.276	0.029					
300	0.103	0.327	0.301	0.027					
325	0.186	0.354	0.326	0.033					
350	0.289	0.387	0.351	0.030					
375	0.385	0.417	0.376	0.101					
400	0.456	0.518	0.401						

*The calculated $\Delta = 0.050$ for 50-lb load increase, and 0.025 for 25-lb load increase.
bThe calculated $\Delta = 0.025$ in. per 10-lb load increase.

Waveguide yield stress calculations:

From test yield at 140 lb (easy plane), $P = 140$ lb. Stress $S = Mc/I$ where $M = PL$, $L = 60$ in., $PL = 8400$ in.-lb, $I = 1.85$ in.⁴, and $c = 1.18$. Then

$$S = \frac{8400 \times 1.18}{1.85} = 5400 \text{ psi}$$

From test yield at 200 lb (hard plane), $P = 200$ lb. Then

$$S = \frac{12000 \times 2.25}{4.58} = 5900 \text{ psi}$$

The calculated yield stress for the waveguide near the soldered flange, which is from 5400 to 5900 psi, is close to the handbook value of 6000 psi for annealed copper.

The stresses that will actually occur in the waveguide were determined by a computer analysis. The top connection of the waveguide at the feed cone was free to move in the x , y , and z directions but not free to rotate. The bottom end at the transmitter was fixed in all directions. Intermediate supports were added where expected in the field and restrained accordingly. The free joint was loaded in the x , y , and z direction individually with a 100-lb load, then the dead load of the waveguide itself, and then combinations of the dead load and 100-lb loads were added. From the computer run, the stresses in the waveguide for various differential deflections of the feed cone with respect to the transmitter could be determined. Analysis of the data indicated limits to be placed on the allowable deflections of the new room structure in relation to the feed cone.

c. Allowable transmitter cabinet deflections for proper support of klystron tube. The stiffness of the transmitter cabinet was required to determine the amount of deflection that would occur due to the following:

- (1) The weight of the klystron tube.

- (2) The weight of the cabinet and equipment.
- (3) The weight of the waveguide.
- (4) Applied waveguide loads due to differential deflections.

The transmitter cabinet was modeled for computer analysis during vendor design of the cabinet. JPL furnished the vendor with inputs as to the cabinet structural configuration. The analysis of the structure indicated the need for additional stiffness at the klystron tube to bring the deflections within allowable limits.

As mentioned earlier, the differential deflections between the feed cone and transmitter cause the transmitter cabinet to see loads introduced by the interconnecting waveguide run. These applied loads proved to be too great for the klystron window to withstand. Therefore, the cabinet was redesigned to carry these loads.

d. Allowable heat losses to the room from the transmitter. The 400-kW transmitter has the potential to dissipate a megawatt of heat to its enclosure. It soon was realized that it was not feasible to try and dissipate this quantity of heat by air conditioning. A search for an insulation that would shield the room from this heat resulted in a suitable material that could be placed on the transmitter cabinet and reduce the heat input to the room. The room itself was insulated and an air-conditioning system was selected which would keep the electronic hardware temperature within safe limits.

e. Individual handling of the klystron tube. The handling of the klystron tube was a difficult problem since the tube is a costly and delicate piece of equipment. The original concept was to remove the tube through the top of the cabinet and the dish backup structure. The backup structure (above the room) will not allow this. Instead, a traveling crane will be provided to lift the klystron a few inches off the cabinet floor (after the top and front members of the cabinet have been removed) and remove the klystron horizontally from the cabinet. The klystron is then moved through a cargo door in the room and lowered to the ground. The selection of the hoist must be such as not to subject the klystron to sudden starts, stops, or jerks, yet it must be capable of moving in three directions. The tube has to be carefully placed and aligned in the cabinet. A special custom-machined alignment plate was installed in the transmitter cabinet for this purpose, along with special adjusting fasteners for the tube at its midheight.

f. Strength of the existing antenna components to sustain the added loads of the room. One of the main objec-

tives of the study was to ascertain if the existing major antenna components could sustain the added loads of the room and the equipment it contained. The antenna components that were checked are as follows:

- (1) Azimuth bearings.
- (2) Elevation bearings.
- (3) Alidade.
- (4) Backup structure.
- (5) Counterweight structure.
- (6) Kingpost.
- (7) Ball screws.

The azimuth bearings were found to have the load-carrying capacity needed, but their useful life appeared to be lowered. After a detailed study of the actual past duty cycle (antenna usage) and the predicted future duty cycle, it was found that the useful life of the bearing was sufficient for the expected future life of the antenna.

The elevation bearings were found not to have sufficient capacity for the added load caused by the room and its modifications. The bearings will be replaced by larger capacity bearings. These bearings were found after a thorough search by JPL of bearings that were readily available. To circumvent the long lead procurement time and insure availability of these bearings, they were purchased by JPL and will be government-furnished equipment supplied to the vendor when he is under contract for the DSS 13 modifications.

The alidade, kingpost, and ball screws of the antenna proved to be capable of carrying the added loads and required no modifications.

The dish backup structure will require some beefup of the square girder members. Part of this beefup is required to carry the added room loads, while the other beefup is required for rigidity to maintain the reflector parabola as it was originally, before the room dead loads were added.

The existing counterweight structure will have to be replaced by a new counterweight structure. This was necessitated by the change in the location of the center of gravity of the rotating mass due to the added mass of the room and its equipment. For antenna balance, the center of gravity of the counterweight has to move up approximately 8 ft, which is further than feasible for modification of the existing counterweight structure.

To determine the minimum horizontal spring constant (stiffness) needed for the new counterweight structure, a field test was run. The two existing counterweight flaps were rigged with slings so that a come-along and a dynamometer could be used to apply and measure a force. This force was used to pull the flaps together. Two theodolites, ground mounted, then measured the displacement on scales which were attached to the structure. This was done for 1000-lb load increments. The displacement per 1000 lb was 0.060 in. This gave a spring constant, which was 16,700 lb/in. and is equal to the measured 1000-lb load divided by the measured 0.060 in. displacement.

g. Conclusions. From this study, the following conclusions were reached:

- (1) The room could be located such as to minimize the rotating mass and added counterweight.
- (2) Backup structure modifications and room location can be implemented so that the original reflector characteristics are maintained.
- (3) The room can be designed as a rigid structural unit to be shop fabricated, shipped, and erected as a unit. This will result in significant savings in cost and erection time. The latter is very important since this project is on a very tight schedule.
- (4) The compatibility of the backup structure and room deflection, with interconnecting waveguide, has been tested and analyzed. This analysis demonstrates there is no need for the cost and problems of a flexible waveguide section in the waveguide run.
- (5) The transmitter cabinet can be made stiff enough to support the klystron properly. The cabinet also can withstand the applied waveguide loads.
- (6) Most of the antenna components can withstand the added room loads. The exceptions are: (1) the elevation bearings, which will be replaced; (2) the backup structure, which will be reinforced; and (3) the counterweight structure, which will be replaced.

E. DSS 51 Equipment Replacement, R. C. Rydgig

The Johannesburg, South Africa, tracking, communication, and data acquisition station (DSS 51) started operations in 1961 as an L-band system configuration station. The microwave and the receiver subsystems were subsequently modified (in 1963) to operate within the S-band frequency range; and in March 1967, the modified L-band

receiver was replaced with a GSDS S-band receiver. This article describes the equipment replacement activity, the problems associated with the implementation, and the resultant changes to the station that were made.

The program became active in mid-December 1966, when a MSFN-type receiver/exciter subsystem was delivered to JPL for conversion to a DSN Block II configuration. The conversion was completed in January, the equipment was packaged for overseas shipment, and shipped via sea freight. Packaging and shipment were the first of the problems associated with this implementation. When the packaging process was observed, it seemed as if the packer was over-zealous in his care to protect the equipment with waterproof wrappings; the equipment was dismantled and modules were individually wrapped. Also, much padding was used and stout wooden boxes were secured with nails and steel tape. However, when the loading and off-loading handling techniques were observed, the care in packaging no longer seemed excessive. Another problem was locating the equipment for off-loading. It might be a good idea for JPL to adopt a unique color and paint all boxes for shipment that color.

Shipping by sea freight is another problem in itself. It is reliable in that the equipment will arrive at its destination. The question is when and in what condition. The ship carrying the receiver departed three weeks late because of dock strikes, rain, fog, holidays, and late delivery of other cargo to the ship. These same factors can affect air freight but their delays are a matter of hours instead of weeks. Sea freight is adequate if time is unimportant and the equipment can be packed to stand the abuse.

While the new equipment was enroute, pre-installation activities were started at the station. These consisted of preparing a detailed implementation plan, examining and resolving interface problems, and planning the movement and installation of the equipment according to a building floor plan layout. On March 1, the station was shut down and movement of equipment was begun. A summary of implementation activities is as follows:

- (1) All cabling and cable trays beneath the floor were removed; cable trays were rebuilt to the new configuration and installed.
- (2) All carpeting in the control room was removed and will be replaced at a later date with new carpeting.
- (3) New holes for cabling and air conditioning were cut in the floors for equipment relocation and as equipment was moved the old holes were filled.

- (4) When the equipment that had been moved began tilting, because the floor beams were cracking, the floor was reinforced.
- (5) Since there is less than 3-ft clearance in the basement, it was necessary to dig an 8-ft square by 5-ft deep hole in the basement floor to house the system junction module (Fig. 30).
- (6) Cables to the antenna were removed, examined, replaced as necessary, and relaid.
- (7) Short interface adapter cables were fabricated as needed to connect the standard system cables with the non-standard equipment. This was done to facilitate possible future installation of standard equipment.
- (8) The suitcase telemetry receiver was removed and returned to JPL.
- (9) The L-band transmitter and L/S-band receiver were removed from the electronics cage and the control room. This equipment is in temporary storage at DSS 51 until arrangements can be made to properly dispose of the equipment.
- (10) The analog instrumentation subsystem was rebuilt from an 8-cabinet to a 5-cabinet configuration simulating the standard subsystem.

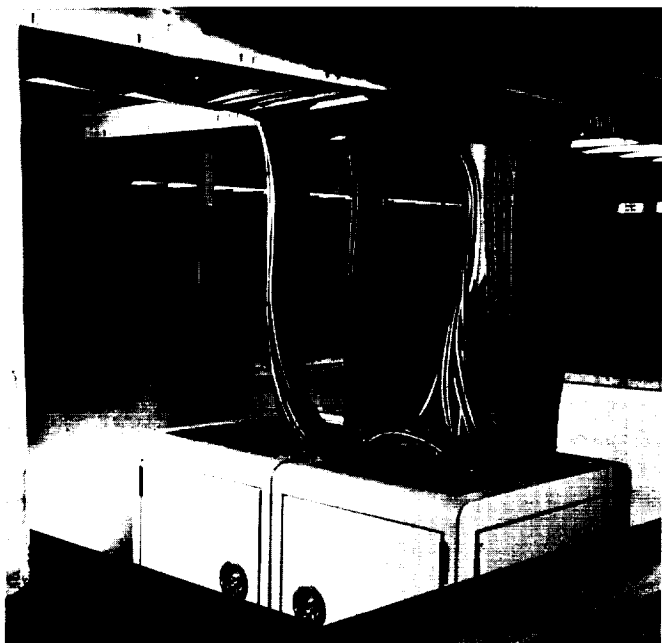


Fig. 30. System junction module installation

- (11) The tracking data handling and frequency and timing subsystems were modified slightly to more closely resemble the standard subsystems; however, at DSS 51 these are combined into essentially one subsystem.

By the time the receiver, system junction module, and system cables arrived (March 8), most of the previously mentioned activities were either completed or well underway. The new equipment was installed, modification to the old equipment was completed, the antenna was rebalanced, all equipment was energized, and minor tests and adjustments were made. On March 28, the station achieved one-way RF phase-lock from the *Pioneer VII* down-link signal. Between that date and April 17, the individual subsystems were tested, mission dependent equipment was tested, and the station resolved discrepancies by participating in the *Surveyor* tests, in lieu of a complete system checkout. As part of the system tests, the system effective noise temperatures with the maser preamplifier were measured at 45 and 46°K for Receivers 1 and 2, respectively, and threshold values for both receivers were approximately -171 dBm for the narrow RF loop bandwidth. Antenna angles (offset from boresight) versus angle error voltages for the S-band Cassegrain-monopulse feed-horn and bridge system (SCM) are shown in Figs. 31 and 32 with the angle tracking function connected in the closed-loop, automatic tracking mode. On April 17, the station successfully participated in the *Surveyor III* mission as a fully operational station.

At the present time, the station can be considered a complete S-band system with the following anomalies:

- (1) The tracking data handling, frequency and timing, analog instrumentation, and antenna mechanical (servo group) subsystems are non-GSDS but are capable of handling standard assignments.
- (2) The station does not have the ranging subsystem, the telemetry and command processor, or the station monitor console.
- (3) The control room is laid out in the standard S-band configuration (Figs. 33 and 34).

To summarize: In less than two months 90% of the equipment in the control room was relocated; all system cabling was replaced; 15% of the equipment was rebuilt; and 10% of the equipment was replaced. All equipment was tested; station personnel learned how to operate and, as needed, repair the new equipment; and the station successfully participated in a mission.

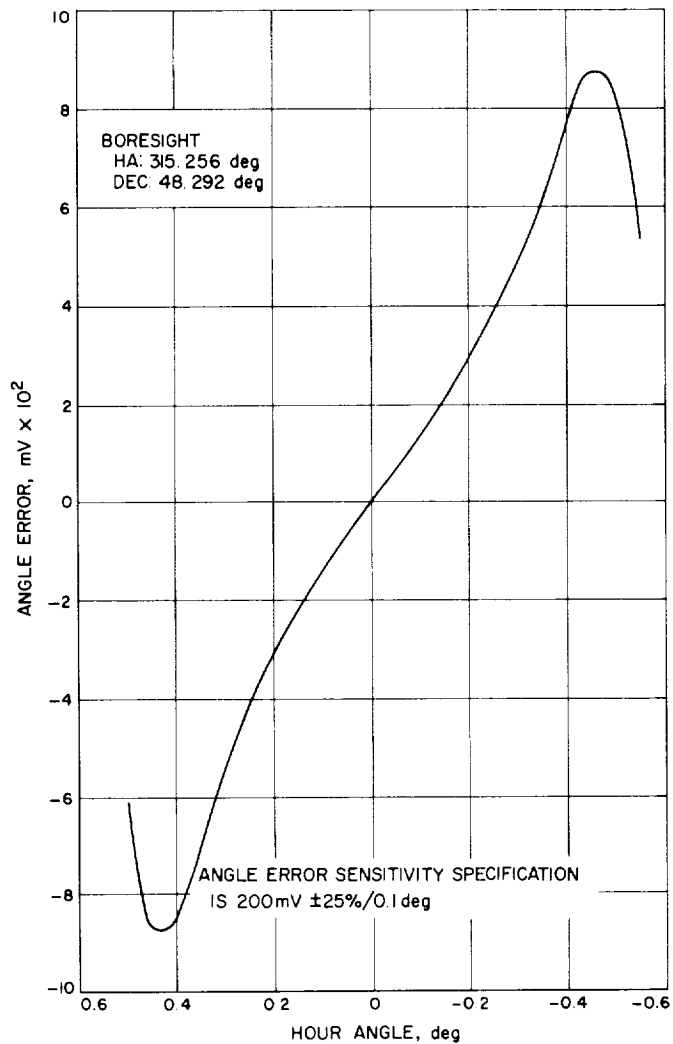


Fig. 31. Hour angle vs angle error

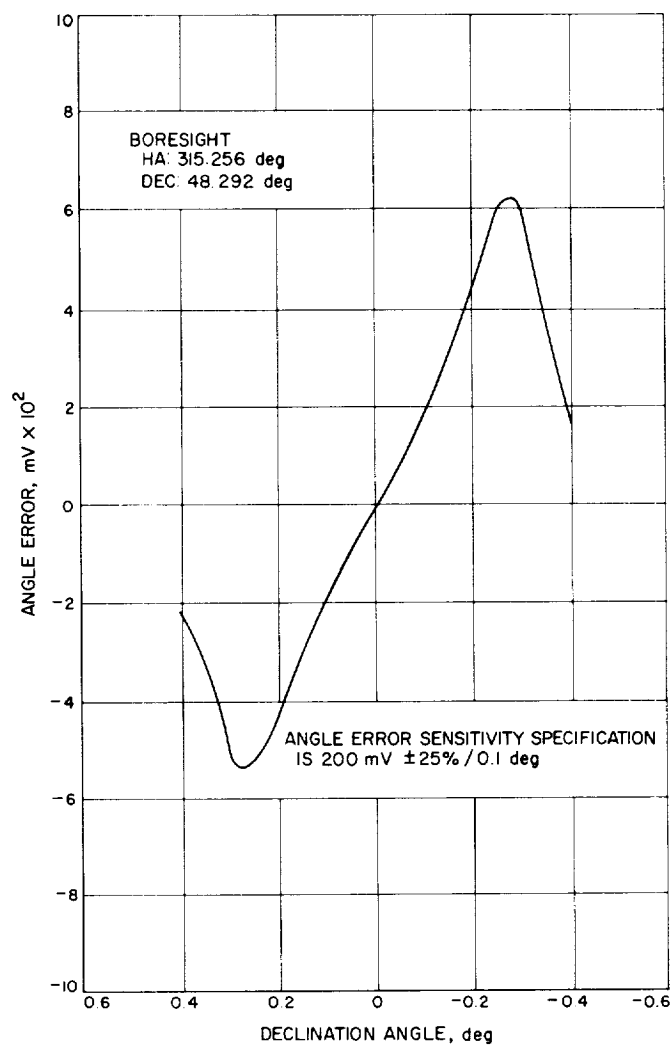


Fig. 32. Declination angle vs angle error

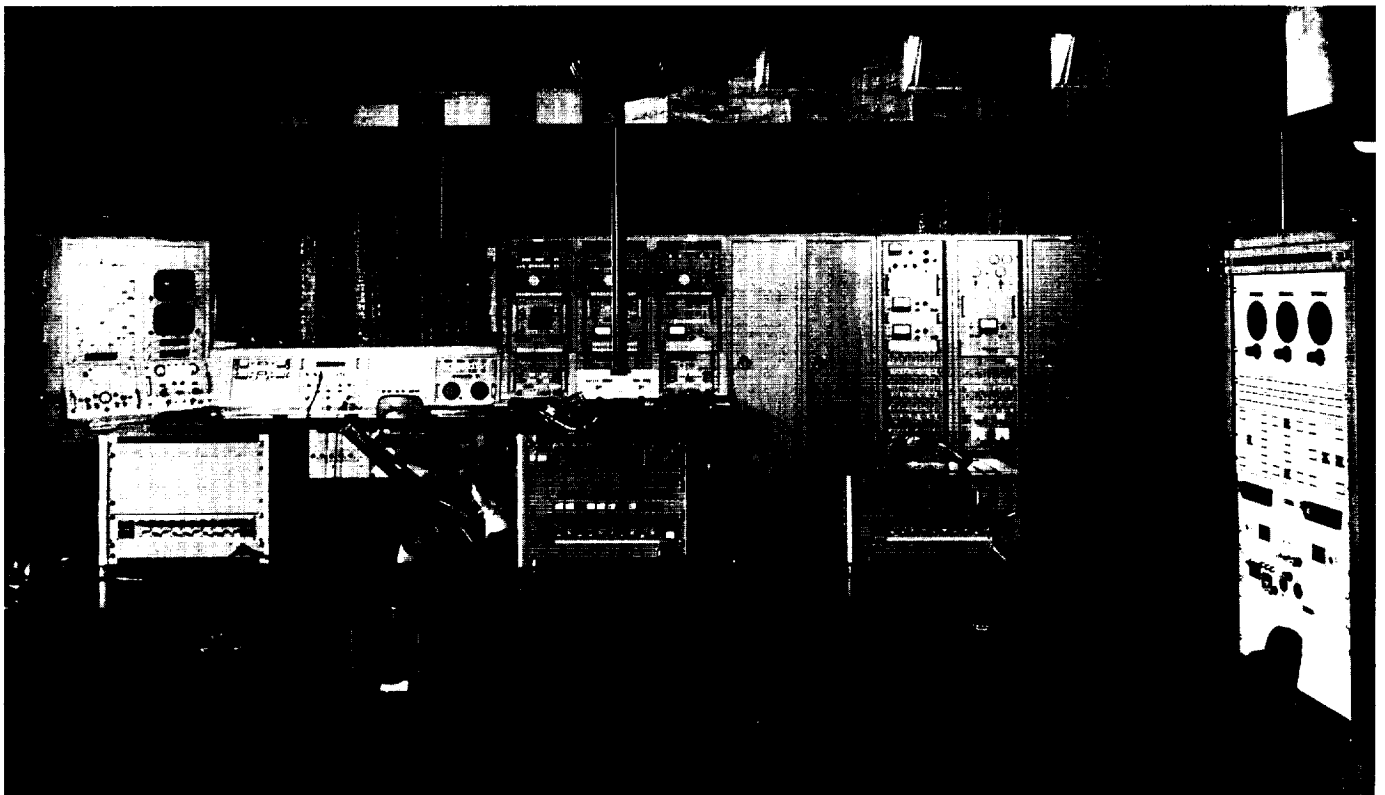
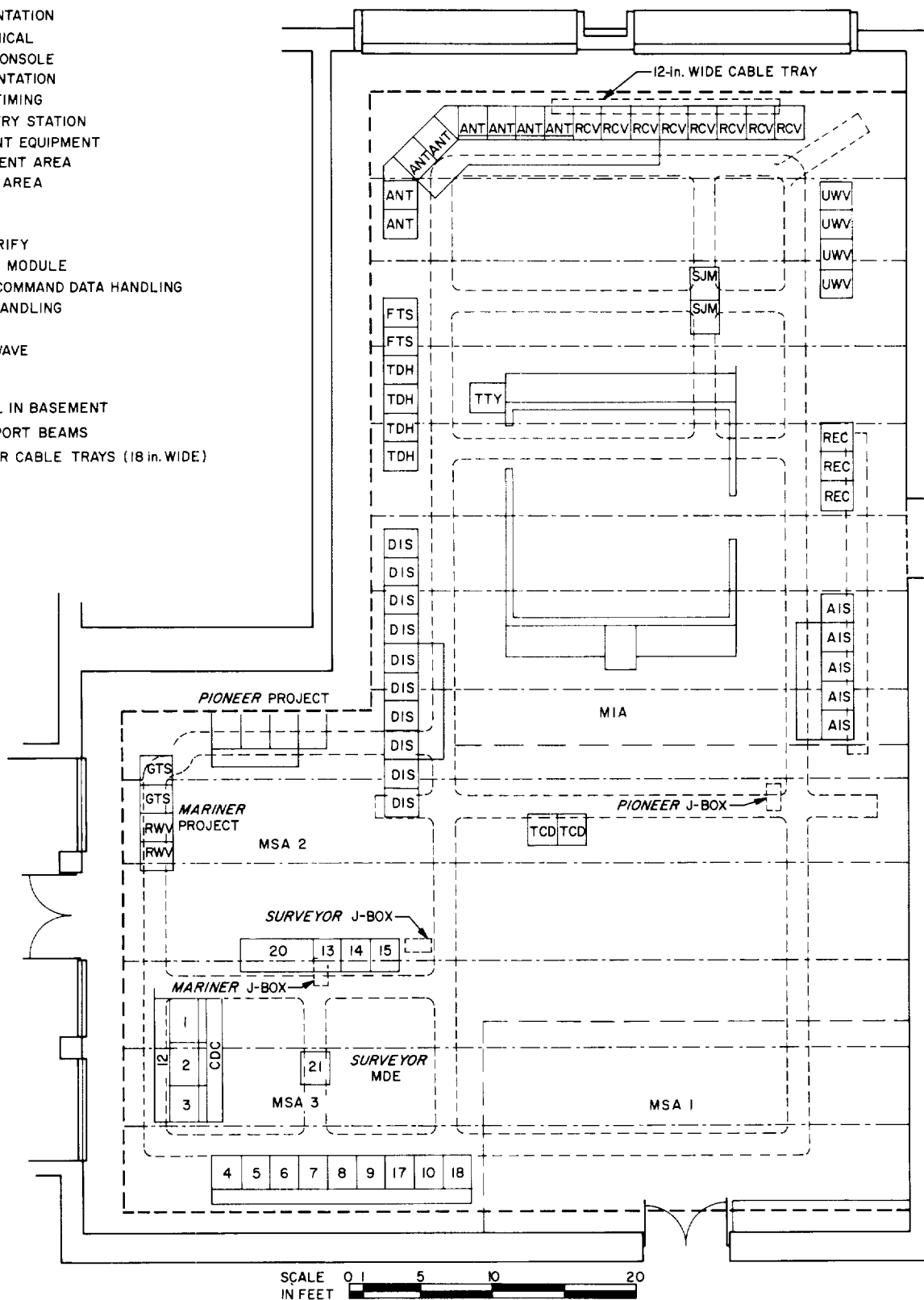


Fig. 33. DSS 51 operations control room

— — — FALSE WALL IN BASEMENT
 - - - - - FLOOR SUPPORT BEAMS
 - - - - - UNDER FLOOR CABLE TRAYS (18 in. WIDE)



148

The fact that this operation was successfully completed in the scheduled time is attributable to the outstanding abilities of the DSS 51 personnel and the excellent support provided by the Lab personnel.

F. DSIF Station Control and Data Equipment,

*R. N. Flanders, E. Bann, G. Jenkins, C. M. Maretzo,
A. T. Burke, and E. Garcia*

1. Introduction

This article gives the status of the DSIF station control and data equipment implementation as of June 1967. The DSIF station control and data equipment includes the antenna pointing subsystem, digital instrumentation subsystem, station monitor and control console, telemetry and command processor, frequency and timing subsystem, and multiple mission support area. This is the sixth status report since the station control and data equipment was introduced in SPS 37-41, Vol. III, pp. 126-129. Reporting will continue in each issue of the SPS.

2. Antenna Pointing Subsystem

The antenna pointing subsystem (APS) has been implemented in the DSIF stations to provide capability to point antennas under computer control. Descriptions of the interim APS and APS Phase I have been given in previous status reports.

APS Phase I has been rescheduled for installation at one-month intervals starting in the early part of February 1968. This coincides with availability of station time and the installation of telemetry and command processor and digital instrumentation subsystem equipment such that station down-time, due to installation of new systems, will be kept to a minimum. Implementation will be performed at DSSs 12, 42, 41, 61, 62, and 72 in the same order. This date represents a change of seven months from the previously reported equipment delivery dates.

The software portion of the APS, which computes an ephemeris from injection conditions at launch, has been completed. This operation mode, known as injection condition mode, enables the antenna to be pointed at the spacecraft by computing the spacecraft ephemeris from seven injection parameters. These parameters, which are sent to the station via teletype or voice line, are fed into the APS computer by either paper tape or typewriter input. If the spacecraft is still below the horizon after ephemeris computation, the antenna will be pointed toward the predicted rise point at the horizon. At space-

craft rise-time, the antenna will be updated to the computed spacecraft ephemeris.

This program has been tested and compared with results obtained from an operational program JPTRAJ-SFPRO which was run on the IBM 7094 computer. The results were extremely satisfactory. Errors between the two programs were in the order of 0.001 to 0.009 deg. The 0.009-deg error was obtained after a 24-hr run and would normally not be encountered since injection condition parameters are periodically updated.

3. Digital Instrumentation Subsystem Phase II

The digital instrumentation subsystem Phase II (DIS Phase II), together with the station control and monitor console Phase II (SMC Phase II), performs the function of system performance and status monitoring, alarm monitoring, maintenance of a permanent record of station performance for post-mission analysis, and preparation of alarm and status messages for transmission to the SFOF. The DIS Phase II, itself, provides for the acquisition, processing, recording, and communication of station data.

The DIS Phase II implementation activities are currently involved in the definition of the hardware and software interface requirements to establish compatibility with the NASCOM automatic data switching system. High-speed data transmission from the DSIF stations will be processed by this multiplexing facility. As such, the DIS Phase II status and alarm messages are to be transmitted by way of the high-speed data communications channel, with a teletype (TTY) mode provided for backup in the event of a failure in the high-speed data line.

Mechanization of this capability requires the determination of electrical and mechanical interface characteristics for the NASCOM modems. The data bit stream signal level and timing constraints are to be determined, together with the control signals, to permit operation in a closed-loop demand and response mode. The latter entails the definition of control signal levels and timing between the DIS Phase II communications buffer and the NASCOM modem. Typically, the DIS Phase II generates a "request to send" signal and awaits acknowledgment by the modem with a "clear to send" signal. This assures that the high-speed data multiplexer and modem are available for transmission of DSIF monitor data to the SFOF.

Software interface characteristics are also being identified, and message format and content defined. Typical messages to be transmitted from the DSIF via high-speed

data line or TTY include DSIF station alarm messages, periodic reports, and summary reports. Format compatibility must be established between the transmitting and receiving terminals to permit the data to be processed, displayed, and analyzed. As such, the message parameters, together with their respective bit assignments, are being established to provide the maximum utility for the analysis activity.

Finally, a procurement is being processed to equip the DIS Phase II communications buffer with the facility to ignore errors in the message header for the incoming high-speed data received from the SFOF. This will allow the message header to be recognized in the presence of an allowable number of bit errors, and synchronization to be established. An allowable bit error switch is to be provided to permit recognition of the header with a total of up to 9 bits failing to correlate. This inequality function is required to allow synchronization of DSIF incoming data messages in the presence of noisy transmissions. The DIS Phase II is to be equipped initially with a high-speed data receive capability to process data messages from the SFOF. The purpose of the DIS Phase II high-speed data receive facility will be to handle monitor criterion data messages, such as tracking data predicts, from the SFOF. Monitor criterion data will be handled initially, however, by TTY communication channels. When the high-speed data communication capability from the SFOF to the DSIF stations is implemented, these functions will be transferred to the high-speed data line, with the TTY communication channel functioning as a backup mode.

4. Station Control and Monitor Console Phase II

The station control and monitor console (SMC) Phase II involves the addition of various assemblies to SMC Phase I as it now exists at all stations. The additional units are as follows: (1) countdown clock, (2) program alarm and control panel, (3) line printer, (4) page printer, and (5) graph plotter. Implementation of the countdown clock has been delayed considerably due to the difficulty of obtaining components for the Hi-Rel modules. All countdown clock logic diagrams, cable drawings, and hardware drawings are complete. All countdown clock cables have been procured. The countdown clock will display time from any selected event. Time will be displayed in days, hours, minutes, and seconds. The symbols L, X, M, I, T, and plus (+) or minus (-) will also be displayed. The clock will be capable of driving 6 remote displays in addition to the local display at the SMC.

The implementation of the program alarm and control panel is also delayed due to Hi-Rel module procurement.

Most mechanical hardware has been purchased for the prototype at this time; however, the modules will not be available for at least 16 weeks. All logic drawings and preliminary wiring and mechanical drawings are available at this time. All cables have been purchased. The program alarm panel provides a horn which sounds an alert upon occurrence of any one of 8 selected station failure modes. The station manager is able to call for a printout (in greater detail) of the failure information. The entire panel will be under DIS computer program control. The prototype panel should be ready for installation and checkout in early November of this year.

The prototype plotter will be delivered during the month of June and evaluation should be complete by mid-July. The plotter is intended to display mission predicted data versus real- or near-real time data. The plotter fits in a standard 19-in. rack and is 17½ in. high. A roll chart of graph paper will fit on the back of the plotter and can be advanced automatically. The plotter is hinged in such a way that it will swing out, thus allowing the refilling of the roll paper from the front of the rack. The plotter will use a ball point pen for tracing, and will have a limited ability to print selected characters.

The prototype line printer is available at the present time and follow-on purchase orders for the line printers and plotters will be issued in early FY 68. The page printers are included in the DIS retrofit procurement.

5. Telemetry Command Processor Phase II

The telemetry command processor Phase II (TCP Phase II) provides the Deep Space Instrumentation Facility (DSIF) with a mission-independent telemetry and command data processing capability for real-time operation. The TCP Phase II assembly interfaces with the mission-dependent project equipment and provides the capability to decommutate, process, edit, alarm monitor, and format spacecraft telemetry data for transmission to the Space Flight Operations Facility (SFOF), and to process and verify command data, received at the DSIF station from the SFOF for transmission to the spacecraft.

The TCP Phase II is in the process of expansion to further its capabilities of digital recording of telemetry and station data (TCP Phase II-B) and telemetry processing support to the mission-independent telemetry demodulation (TCP Phase II-C).

The principal effort in the past two months has been partial implementation of the TCP Phase II-B equipment

into the TCP Phase II, assigned to the *Mariner Venus 67* Project, located in the Spacecraft Assembly Facility (SAF). An analog-to-digital converter, interim junction box, and additional power supplies have been temporarily installed in the magnetic tape assembly cabinet. In its final form the TCP Phase II-B/Phase II-C equipment will be installed in the two new equipment cabinets that are to be installed as part of the TCP Phase II-B/Phase II-C configuration.

With this partial installation of the TCP Phase II-B equipment into the TCP Phase II, it is now possible to provide support to the *Mariner Venus 67* Project in direct demodulation of telemetry data without prior processing by the *Mariner* mission-dependent telemetry subsystem. At the present time the *Mariner Venus 67* Project is performing checkout on the new installation in the SAF.

It is planned to provide DSSs 11, 12, 41, and 62 with the partial TCP Phase II-B equipment by August 15, 1967 and to provide DSSs 42, 61, 71, and 72 with the equipment by September 15, 1967.

6. Frequency and Timing Subsystem Phase II

The basic objective of the frequency and timing subsystem Phase II (FTS Phase II) program is to improve the reliability, accuracy, and flexibility of the frequency and timing equipment used in the DSIF. This report and future reports on the FTS Phase II will place emphasis on a particular element in the subsystem designed to achieve the stated objectives of the project. This report will discuss the digital isolation amplifiers. The flexibility requirement fundamentally calls for the providing of increased drive capability on the pulse rate signal outputs, GMT outputs, and the time code signals. A high-power digital isolation amplifier module has been obtained to accommodate the need for increased output and at the same time permit dc isolation of the basic timing mechanism from the other subsystems. In some cases isolation will be available between subsystems to prevent interaction.

In order to be able to effectively merge this equipment into the DSIF it was necessary to have the digital isolation amplifier designed to be able to handle both positive voltage binary signals and negative voltage binary signals either in true or complementary form. The selection of the desired mode is accomplished by means of a jumper wire change directly behind the front panel. Eventually, when the JPL Hi-Rel modules are used throughout the DSIF, the voltage levels will normally be set at zero

(false) and +10 V (true). The new drive module will therefore provide:

- (1) Increased drive power.
- (2) DC isolation of the FTS clock.
- (3) Waveshape regeneration.
- (4) Independent selection of positive or negative voltage levels.
- (5) Independent selection of true or complementary output.

This equipment should be ready for field test at Goldstone in about one month.

The panel and chassis mechanical layout of the remaining FTS Phase II equipment is 80% completed. The digital electronics construction is being delayed by problems in the procurement of JPL Hi-Rel module components. A complete set of assembled and tested modules for the FTS Phase II prototype are not expected before October 1967. Vendor-supplied equipment for prototype and production FTS subsystems is currently in procurement.

7. Multiple Mission Support Area

a. Introduction. A previous SPS article (SPS 37-45, Vol. III, pp. 82-86) presented, in general, the multiple mission support concept for the DSIF and the Phase I implementation plan. In the following paragraphs, more detailed information is presented on the equipment being added and its function in relation to project support.

b. Phase I MMSA functional description. Implementation of the Phase I multiple mission support area (MMSA) at DSSs 11, 12, 14, 61, and 62 provides the required flexibility needed for proper support of the *Lunar Orbiter*, *Surveyor*, *Pioneer*, and *Mariner Venus 67* Projects. However, the Phase I MMSA has been designed and implemented with limited capabilities that are adequate to support the present projects through the peak DSIF tracking commitments.

The Phase I MMSA, at the stations defined above, is constrained to the local support of the *Lunar Orbiter* and *Surveyor* Projects, while the *Mariner Venus 67* and *Pioneer* Projects may be supported locally or remotely from nearby stations, via the intrastation microwave link. The constraint placed on *Lunar Orbiter* and *Surveyor* is only applicable during TV sequences due to the frequency bandwidth limitations of the intrastation microwave link; however, during emergencies remote tracking support is available.

The Goldstone complex has been organized such that two projects can be supported simultaneously at DSS 11 (*Surveyor*, *Mariner Venus 67*) and DSS 12 (*Lunar Orbiter*, *Pioneer*) by having any one of the three mission-independent equipments (11, 12, 14) available to each other via the intrastation microwave link. However, due to the limitation of antennas only three will be supported in a tracking mode while the fourth may be in a test mode using the system simulation assembly. At DSS 61, as at DSS 11, the *Surveyor* and *Mariner* Projects can be supported simultaneously by using DSS 62's mission-independent equipment remotely. Conversely, DSS 62 will support *Lunar Orbiter* locally and *Pioneer* remotely from DSS 61.

Among the changes at the stations, implemented with a MMSA, the most significant one is in the area of analog recording. In this area, the magnetic tape recorders provided as part of the S-band system will be used solely for the purpose of recording mission-independent data, while the recorders implemented as the mission support recording (MSR) assembly are used to record project-processed data.

The separation of the project data from the mission-independent recorders allows the station's mission-independent equipment (MIE) to remain in a fixed configuration regardless of the project being supported. The standardization of the MIE tracking operations and interface thus provides remote MIE tracking capability to projects located in any of the other stations, within a multi-station complex, via the communications interface assembly and intrastation microwave.

The implementation of the Phase I MMSA allows for three of the stations to have a standard MIE. DSSs 11 and 61 standard MIE was achieved by the implementation of the MSR assembly which supports the *Surveyor* Project, and by having the *Mariner Venus 67* Project recording requirements fulfilled, in digital format, by the TCP Phase II-B. A standard MIE configuration already exists at DSS 14, due to none of the projects being housed within the station.

At DSS 12 a standard MIE will be achieved when the *Lunar Orbiter* is transferred to the MSR and the *Pioneer* Project recording requirements are modified to digital recording on the TCP Phase II-B. DSS 62 was not implemented with a MSR assembly and the MIE recorders will continue to be configured as a function of the project being supported.

c. Mission support recording assembly. Installation of the MSR assembly at DSS 11 completes the analog recording implementation requirement of the Phase I MMSA. The MSR assembly at DSS 11 was installed, tested, and integrated with the *Surveyor* Project equipment during the first lunar night of the *Surveyor III* spacecraft. The MSR assembly was operational during tracking attempts of *Surveyor III* in its second lunar day.

d. Communications interface assembly. The communications interface assembly (CIA), a part of the Phase I MMSA implementation, has been installed at DSSs 11, 12, 14, 61, and 62 since June 1, 1967. The equipment consisted of 4 EMR voltage-controlled oscillators (VCO), 2 EMR ac amplifiers, 4 EMR subcarrier discriminators, and 3 Dynamics dc amplifiers. The above equipment was first installed at DSSs 11 and 14 and successfully integrated with the DSS 14 MIE, intrastation microwave link, and *Mariner Venus 67* Project equipment at DSS 11. Similar installation was carried out at DSSs 61 and 62. The CIA's function is that of providing interface signal conditioning between the project equipment, intrastation microwave link, and mission-independent equipment.

For example, at DSS 14 the receiver-detected telemetry and the receiver status (automatic gain control, static phase error, in-lock) are connected to the 4 VCOs. The mixed VCO subcarriers are transmitted to DSS 11 via one microwave channel, where signal separation is carried out by use of the subcarrier discriminators.

The implementation of the CIA will allow for the remote support of the *Mariner Venus 67* Project at DSS 11 from either DSS 14 or 12 at Goldstone, or at DSS 61 from DSS 62. Similarly, the *Pioneer* Project will be able to operate remotely from DSS 14 or 11 at Goldstone, and from DSS 61 in Madrid.

G. DSIF Phase I Monitor Program, R. N. Flanders

The DSIF Phase I monitor program is the software counterpart of the digital instrumentation subsystem Phase II (DIS Phase II) hardware development. The DIS Phase II, together with the monitor program, dictates the operating modes of the DSIF monitoring subsystem Phase I (DSIF MS Phase I) in the performance of the station monitoring function. The monitor program controls the station instrumentation and system monitoring tasks within each station in the DSIF. The program directs the functions of: (1) station configuration, performance, and status monitoring; (2) alarm monitoring

of selected critical parameters; (3) preparation of a permanent record of station performance and failure data in magnetic tape and tabular form; and (4) communication of alarm messages and periodic reports to the DSIF and the DSN.

The monitor program performs the three primary functions of data input and collection, data processing, and data output.

1. Data Input

The data input function involves the collection and storage of: (1) station monitor parameters, (2) monitor criterion data (predicts), (3) inter-range vector (IRV) parameters, (4) calibration data, (5) initialization inputs, (6) control criteria, and (7) recovery elements (error detection and correction techniques).

The program provides for receipt of monitor criterion data from the SFOF via a teletype receive channel in the DIS Phase II communications buffer. This data consists of performance specifications, alarm limits, tracking data predicts, station configuration specifications, and the monitor data message format and content to be output. The program also provides an on-station predict generation capability for accepting spacecraft position and velocity coordinates as part of the IRV message. The program then computes spacecraft position at periodic intervals for display on the station line printer and output on perforated paper tape.

The monitor program also directs the station data gathering function, which requires the sampling of all system and subsystem parameters at the rates established within the program. Input parameters provided to the DIS Phase II consist of analog and digital data, station time, control signals, and calibration data. Data presented in analog form is converted to digital form for storage and processing, together with the digital input data. The program monitors the following station functions: (1) DSIF system configuration, (2) DSIF subsystem status, (3) signal strength, (4) doppler, (5) angle, (6) range, and (7) transmitter and receiver parameters, and provides the capability for future expansion to include (8) mission-dependent equipment and (9) facilities monitoring. The monitoring function for each of these elements involves the following activities.

a. System configuration. The actual station operating configuration, entered as digital input data, is compared with the required configuration, received as part of the

monitor criterion data message from the SFOF. Any discrepancies are noted by an alarm condition, with the condition being recorded on the station line printer log and an alarm message output to the SFOF.

b. Subsystem status. Subsystem status parameters are monitored, and performance and alarm conditions of specific subsystems are recorded and displayed. Alarms are processed in the manner described above.

c. Signal strength. Ground-received signal strength and static phase error are sampled, and signal strength is converted to dBm for recording and display as a mean, residual mean, and standard deviation. A signal strength alarm will be generated upon detection of an out-of-limit condition for these computed values, or for an out-of-lock condition for the receiver being monitored.

d. Doppler. Doppler data is monitored and the doppler residual, residual mean, and standard deviation are computed, recorded, and displayed. A doppler alarm will be displayed locally and transmitted to the SFOF for an out-of-limit value of the computed results, for doppler bad data condition, or for a blunder point determination.

e. Angle. Angle digital input parameters are sampled and the residuals, means of the residuals, and standard deviations are computed. An angle alarm will result from an out-of-limit value for these calculations, for a bad data condition, or for an error indication from the antenna pointing subsystem.

f. Range. Ranging subsystem input parameters are inspected and the range residual, mean, and standard deviation are computed. An out-of-limit condition, or a range receiver out-of-lock indication will cause a range alarm to be displayed locally and transmitted via teletype to the SFOF.

g. Transmitter/receiver. Digital input parameters representing transmitter and receiver/exciter functions, together with analog input parameters for transmitter power output and total ground receiving system noise temperature (when implemented), are sampled, recorded, and displayed, and alarms are initiated when nonstandard conditions are detected.

h. Mission-dependent equipment and station facilities. The program contains the provision for future expansion to monitor mission-dependent equipment and station facilities functions.

Additional inputs consist of calibration data, initialization conditions, and control signals. Calibration data and

initialization inputs are entered via the DIS Phase II console typewriter. Control signals originate at the station control and monitor console (SMC), as sense switch or interrupt inputs. Error detection and correction techniques will be employed primarily in the areas of communication inputs, where message validation is necessary to detect transmission errors.

2. Data Processing

The data processing functions performed by the monitor program consist principally of: (1) comparison of actual performance against preestablished standards for recognition of nonstandard operating conditions; (2) computation of residuals, means, and standard deviations for input parameters; (3) blunder point determination and rejection from calculations; (4) scaling, editing, linearizing, differencing, normalizing, and conversion of data to engineering units; (5) application of stored calibration characteristic curves to input data; (6) interpolation, extrapolation, and fitting curves to discrete point data; (7) predict computation of spacecraft position message inputs; (8) alarm detection and generation, using correlation and limit checking; and (9) message format structuring and recognition.

Typical parameters requiring the computation of residuals, means, or standard deviations are signal strength, doppler, angle, and range. The ground receiver automatic gain control (AGC) signal is converted to signal strength in dBm through the application of one of fourteen stored calibration curves which are contained as a part of the monitor criterion data message. The selection of the specific curve is a function of the station operating configuration. Doppler monitor data processing requires an interpolation computation, such as least squares or a four point La Grangian interpolation of doppler predict data. A blunder point test is also conducted on the doppler residual to determine if the point is invalid and hence should be rejected from the computation of the mean. Angle monitoring likewise requires interpolation of hour angle and declination angle data. Range data is processed in a straightforward manner. The resultant data for the parameters described above is compared against stored limits and alarms generated locally on the station page printer, line printer, and program alarm and control panel upon detection of an out-of-limit condition. Additionally, an alarm message is assembled for teletype transmission to the SFOF.

The monitor program also processes the IRV message, which includes spacecraft injection position and velocity

parameters, and computes spacecraft position at periodic intervals by integration with respect to time from conditions of injection. This requires the transformation of coordinate systems. Further, the program is responsible for dictating the message formats for all outgoing teletype and high-speed data communications, and for the recognition and disassembly of incoming teletype and high-speed data messages required for the monitoring functions. Finally, the program contains a background diagnostic subroutine to perform a self-checking function to assure proper operation of the monitor subsystem itself. Preflight checkout diagnostics are furnished also, but need not necessarily be an integral part of the monitor program.

3. Data Output

The monitor program output functions are composed of alarm messages (at time of occurrence), periodic reports (at 5-min intervals), summary reports (once per pass), and permanent station performance and failure data in magnetic tape and tabular form. The alarm messages are concise descriptions of the failed function and are displayed locally at the DSIF station via a page printer and line printer. The alarm message is also transmitted to the SFOF by way of a teletype communication channel. Alarm messages will be generated for the following functions: (1) microwave configuration, (2) subsystem configuration, (3) subsystem status, (4) signal strength/static phase error, (5) doppler, (6) angle, (7) range, (8) transmitter and receiver/exciter, (9) mission-dependent equipment (when implemented), and (10) facilities (when implemented). Actuation of the appropriate sense switch on the SMC will provide a high resolution printout of the failed function, at the full sample rate, together with suitably annotated messages.

The periodic report will be output on the station line printer and will be sent by teletype to the SFOF. The periodic report contains a more detailed description of the DSIF station performance and the status of selected critical parameters. The summary report will contain a brief summary of significant events occurring during the pass, together with a tally of the alarm conditions encountered. The permanent record of station performance and failure data will be maintained in magnetic tape and tabular form. The magnetic tape will contain raw, unprocessed data exclusively, with suitable time referencing for postmission analysis. The program contains an on-station magnetic tape listing capability to permit the station magnetic tape log to be output on the station line printer. This mode may be selected under sense switch

control to provide a near-real-time review of a tracking anomaly or subsystem failure.

Outputs are also presented to a visual display on the SMC. An audible alarm may be addressed under program control. An X-Y recorder with a programmable paper change is also located in the SMC, to display selected parameters in graphical form as continuous curves or discrete points.

The DSIF Phase I monitor program is to be implemented concurrently with the hardware development and installation of the DIS Phase II within the DSIF. The completion of both activities is presently scheduled for the third quarter of 1968.

H. Sustaining Engineering, P. T. Westmoreland,

C. N. Wong, and H. W. Baugh

1. Telemetry and Command System, P. T. Westmoreland

The telemetry and command system sustaining engineering provides a follow-on supporting engineering effort for operational DSIF mission-independent telemetry and command data handling equipment. This supporting engineering effort, operating in conjunction with the DSIF trouble and failure reporting system and engineering change requirements program, provides a focal point for all engineering activities related to the operational performance of this equipment. Operational performance is evaluated through trouble/failure reports (TFRs) from the DSIF, and required equipment modifications are initiated through DSIF engineering change requests (ECRs). Modification kits and supporting documentation are designed, procured, and installed in the DSIF in accordance with approved engineering change orders.

The DSIF mission-independent telemetry and command equipment is contained in the telemetry and command data handling subsystem. This equipment consists of the telemetry and command processor assembly (TCP), the simulation assembly (SIM), and the multiple mission support equipment (MMSE). The MMSE is further defined as the mission-dependent equipment (MDE) patch panel, mission support recording (MSR), and the communications interface assembly (CIA). Descriptions of this equipment have appeared in previous SPS articles and appear elsewhere in this issue and thus are not repeated here.

The TCP and MDE patch panel have been operational in the DSIF for several years, while the MSR, CIA, and SIM assemblies are recent additions to the network. Because of this, the major sustaining engineering effort has been dedicated to the TCP and MDE patch panel. ECRs are required for installing and interfacing the new assemblies into the network but this is not considered to be a sustaining engineering effort.

In FY 67 sixteen ECRs were implemented and eight are currently in process. Major ECRs on the TCP that have been implemented are:

- (1) Modify millisecond clock to correct a digital logic problem that caused an incompatibility with flight project requirements.
- (2) Add a fourth teletype channel to the TCP communications buffer to provide a spacecraft telemetry display to the *Mariner Venus 67* read-write-verify operator and to allow the TCP to operate in the multiple mission support configuration.
- (3) Add removable hubs to the TCP magnetic tape transports to allow rapid change of telemetry tapes without first rewinding.

Major ECRs on the MDE patch panel that have been implemented are:

- (1) Add a complementary binary coded decimal time output to the flight projects.
- (2) Transfer one of the two MDE patch panel racks and the precision signal-to-noise mixer to the simulation assembly.
- (3) Install temporary mission support recording capability and microwave communications interface assembly to provide an interim multiple mission support capability to support *Surveyor*, *Mariner Venus 67*, *Pioneer*, and *Lunar Orbiter* Projects.

The above examples represent only the major ECRs that have been implemented. The total ECRs implemented and in process include other minor ECRs that require both hardware and documentation changes. In addition, some approved ECRs are held for incorporation as part of block updates of equipment configuration. These types of ECRs will be incorporated in the TCP Phase II-B and II-C implementation programs and in the MDE Phase II patch panel design.

2. Station Instrumentation and Monitor System, C. N. Wong

The activity of the station instrumentation and monitor system group has been the perpetual improvement of the existing equipment and the development of the modification kits to be incorporated into the system to maintain the state-of-the-art technology in the DSIF. Equipments are being monitored daily, and data are reported weekly to the sustaining engineer for his evaluation. Failure reports are received to be studied for possible failure trend. One hundred thirty engineering change requests have been submitted to the group for approval in the last 18 months, one-half of which were received in the last 6 months, to cope with the increased functional complexity. These requests have been diversified: (1) to change documentation; (2) to upgrade the National Bureau of Standards broadcast reception at a Madrid station with a special antenna or receiver (the difficulty occurred because of a unique geographical terrain or environment); (3) to assure the presence of the last pulse from a prematurely terminated millisecond clock train; (4) to extend the life of a relay which switches once per second or 32 million times a year, by converting from ac to dc power supply to lessen arcing; (5) to add a computer program to direct the antenna towards the target during a temporary support mission; (6) to remove equipment from station configuration for use in the schooling of new trainees; and (7) to redesign interfacing for isolating the response of the individual subsystem.

A program has been initiated to select high reliability components through testing, specification of design guide, and qualification of the manufacturing sources. The components are to be used in the development of reliable standard digital circuit cards. Additional equipments, such as tape recorder reproduce modules and spare parts, are procured for stations to increase their capability to function independently; and rolling test racks are being provided to make test equipments fully available.

The most recent conception of effective usage of the facility is the time-sharing of the existing computer to monitor DSIF system parameters. This interim monitor program interrupts the normal computer program and samples information from various subsystems, then compares it with a precontrived set of standard data. Gross deviation will alert the operator to correct the parameter. Data is continuously displayed visually and logged onto magnetic tapes for later study. Three types of data are presently being monitored with the computer: (1) station operating status at approximately 75 different locations,

- (2) receiver signal strength at a 1-s sampling interval, and
- (3) doppler data on ranging information.

Much of the sustaining engineering effort will be incorporated into the Phase II block designs, which are emerging next year. Sustaining engineering will follow into Phase II operation and will start a new program of improvements.

3. Digital Control and Tracking System, H. W. Baugh

The digital control and tracking system sustaining engineering effort covers the maintenance, modification, and other support services for three subsystems—interim antenna pointing (IAPS), Mark I ranging (RNG), and tracking data handling (TDH I). The cognizant engineers are responsible for making approved changes in their respective subsystems, for maintaining accurate documentation and status information, and for monitoring the performance of the subsystem with the objective of recommending changes which would improve performance, reliability, and overall effectiveness of the equipment.

The IAPS was originally developed by modifying the digital instrumentation subsystem. Special interface equipment, cables, and control panels were added to the SDS 910 computer to adapt it for the new function. As the subsystems were integrated into the DSIF, the sustaining engineer was responsible for changes, both to the hardware and to the computer programs, until the equipment has now reached the state where it can be used in operations. The continuing support effort has kept the cognizant engineer in close contact with the subsystem, and will assist him in the development of the permanent antenna pointing subsystem.

Since the start of the formal engineering change request (ECR) program, there have been six ECRs which pertained to IAPS. Two were cancelled, one by the originator, and one because it was not suitable for ECR procedures. The remaining four ECRs are for minor computer program changes, and are in the process of being implemented.

The TDH I subsystem has required a great deal of effort on the part of the sustaining engineer, because of the manner in which the subsystem has gradually evolved, largely out of components from older versions of the subsystem. For instance, one digital subassembly is known to exist in at least three different configurations, according to available documentation. One aim of the sustaining engineering program has been to attempt to reconcile the

various sets of documentation with the hardware, with a long-range objective of modifying the different units toward a common standard configuration. The need for this has been repeatedly pointed up by instances where a modification kit can be successfully installed at one station, and either cannot be installed at another station or will not work when installed, because of undocumented differences between stations.

This situation came up as the doppler resolver was being installed. A prototype experimental installation had been performing well at one station, so additional equipments were ordered and assembled into modification kits for installation at all stations. The first three installations required to meet tracking commitments have been completed, but in each station a unique set of problems has developed, requiring special attention. In one case the original doppler counter was sufficiently different from the standard configuration that the entire unit had to be rewired.

At the present date, a total of 50 ECRs have been introduced which are related to TDH I. Of these, ten were cancelled by originators or disapproved by the Change Control Board. Six ECRs have been implemented in all affected stations, all the changes being minor wiring, documentation, or operational changes. Twenty-six have been approved for installation, and of these three are major changes in the capability of the subsystem.

The first change was the installation of the angle storage buffer, a change that was necessitated by the installation of the antenna pointing subsystem. The TDH I requires that input data be maintained stationary for a second while it is being sampled, and the antenna pointing subsystem requires fresh angular information up to fifty times per second. This conflict was resolved by the addition of a storage register which would preserve the first sample of each second for the use of TDH, and permit APS to sample as often as needed.

The second major change in capability was made at three stations to permit their facilities to be shared with the MSFN. It is a switching arrangement which permits antenna angles to be read out either by the equipment in the DSN control room or by separate equipments in the MSFN control room at the tracking station.

The third significant change to be implemented in TDH I is the digital resolver modification to the doppler counter. This provides for increased resolution in the doppler frequency measurements that are recorded dur-

ing tracking operations, permitting the detection of velocity changes on the order of a few millimeters per second. This has been implemented in the stations that needed the capability soonest, and will go into the remainder of the DSIF as soon as tracking commitments permit.

The Mark I ranging subsystem has had relatively few problems, since it was developed rather recently and installed in all stations as a block change. A recent modification, known as the Block II-B change, has been installed in all but two stations, where work will be completed as tracking commitments permit. This modification permits the design of the receiver to be changed so that the ranging clock frequency will remain constant when the transmitter frequency is changed. The change was brought on by requirements in the MSFN, which uses identical equipment. This modification required the addition of an extra cage of digital modules, re-wiring of some of the original units, and corresponding changes to drawings, manuals, and test procedures. These have all been accomplished with relative ease, a consequence of the subsystem having been initially built in a standard and well-documented configuration.

Of the twelve ECRs on the ranging subsystem, seven, all minor wiring changes, have been completely implemented. Four were cancelled or disapproved, either as undesirable or because they were inappropriate as ECR material.

I. Digital Tracking System, P. L. Lindley

1. Introduction

Recent developments at JPL have led to the concept, feasibility studies, and in some cases prototype construction and testing of several new subsystems which fall into the general classification of digital spacecraft tracking equipment. These are:

- (1) *Tracking data handling subsystem Phase II (TDH Phase II)*. This subsystem would replace the present TDH Phase I; it would offer considerably greater functional flexibility and greater operational reliability.
- (2) *Ranging subsystem Phase II (RNG Phase II)*. This subsystem would replace the present RNG Phase I at DSS 14 and would be the only ranging subsystem to be installed at the two additionally planned 210-ft-diameter antenna stations (DSS 43 and 63); it would permit range determination to planetary

distances as opposed to the lunar-distance limitations of the present RNG Phase I (Mark I).

- (3) *Programmed local oscillator (PLO)*. This new subsystem would tune the local oscillator of each of the two S-band receivers at a station in accordance with frequency requirements periodically determined by the computer.
- (4) *Programmed exciter (PE)*. This new subsystem would tune the transmitter exciter at a station in the same manner as the receiver oscillators would be tuned by the PLO.

2. System Development

Inasmuch as each of the above subsystems is to include a general-purpose digital computer, it has been decided to consolidate the design of all the subsystems to incorporate but a single computer. The resulting digital tracking system will include TDH Phase II, RNG Phase II, two PLOs, a PE and, at a later stage of development, an antenna pointing subsystem Phase IA (APS Phase IA).

The implementation of the digital tracking system will begin with a TDH Phase II and RNG Phase II configuration. The first use of that configuration is presently planned for the *Mariner* Mars 1969 mission at DSS 14. The philosophy leading to development of the TDH Phase II and RNG Phase II subsystems to date is outlined in the following.

3. Tracking Data Handling Subsystem Phase II

TDH Phase II proposes to overcome the following inadequacies of the presently operational TDH Phase I:

- (1) The present maximum sampling rate of 1/s, which is too slow for some critical phases of a flight such as midcourse maneuver and planetary occultation.
- (2) The lack of a high-speed data line output capability, which limits transmission rates to the SFOF.
- (3) Manual indication of data quality.
- (4) The inherent unreliability and sensitivity to environment of obsolete circuits and components.

The design of TDH Phase II will incorporate the following features and characteristics to provide the improvements required and other desirable capabilities:

- (1) Greater versatility in data acquisition with sampling rates up to 1000/s on some types of input data.

- (2) Versatile data format control and message header flexibility with optional data editing.
- (3) Data conversion and application of station calibration information.
- (4) Addition of a doppler resolver and simplification of doppler mode selection.

The TDH Phase II subsystem will include the following assemblies:

- (1) *Angle encoders*. The angle encoding assembly provides a digital representation of the angular position of both antenna axes. Hour angle and declination are measured for the equatorially-mounted antennas, and azimuth and elevation are measured for the az-el-mounted antennas.
- (2) *Doppler counter and resolver*. The doppler assembly provides a doppler count for distribution and recording. The counting operation is controlled by timing pulses as specified by the selected sampling rate. The digital resolver subassembly is used in conjunction with the doppler counter to make possible a high-resolution computation of the doppler cycles per count interval.
- (3) *Transmitter voltage-controlled oscillator (VCO) frequency counter*. A digital frequency counter provides a measurement of the transmitter VCO frequency over a precise time period. The frequency count is displayed for visual observation and is also supplied to the data format control assembly for distribution and recording.
- (4) *Station status and timing data*. The following data is processed by the data format control assembly for recording and distribution.
 - (a) GMT time data from the frequency and timing subsystem.
 - (b) Data condition information indications for status of tracking data subsystems.
 - (c) Identification data for both spacecraft and the tracking stations.
- (5) *Data format control*. The data format function is provided by a general-purpose digital computer. This assembly receives data from the various information sources, performs code conversions, and adds data correction factors for local station anomalies where required. The versatility inherent in software control of a general-purpose computer

provides great flexibility in meeting the compatibility requirements of different missions, networks, and communication system message headers.

- (6) *Communication buffer.* The communication buffer provides an electrical interface between the data format control assembly and the communication transmission line. The buffer provides termination for multiple low-speed TTY lines and high-speed data lines for both send and receive operation.

4. Ranging Subsystem Phase II

RNG Phase II plans to overcome the following inadequacies of the presently operational Mark I ranging subsystem as part of a ranging system complex:

- (1) The ranging complex with the Mark I ranging subsystem has a signal strength threshold to a spacecraft operating with a 36-in. parabolic dish antenna system transmitting 10 W at a distance of about 3 million km from earth, using an 85-ft-diameter ground antenna. Even with a 210-ft-diameter antenna, signal strength limitations will not permit ranging to planetary distances.
- (2) At lunar distances, typical range code acquisition time with the Mark I is 1 to 2 min. Acquisition time increases sharply with a decrease in ranging sideband power availability.
- (3) The Mark I is constructed of T-PAC digital modules, a line of commercial components representing the state of the art in the late 1950's. Sensitivity to environment and generally lower reliability of circuits and components of that era are not considered compatible with current operational needs.

The design of RNG Phase II will be based on a developmental ranging equipment presently installed at DSS 14 for evaluation in the course of the *Mariner Venus 67* mission. The following improvements over the Mark I are expected to be realized, with certain trade-offs as noted:

- (1) The system design is such as to permit range determination to planetary distances with spacecraft transponders identical to the turnaround type presently used on *Mariner* spacecraft. Calculations have been made which indicate adequate ranging sideband power is available at Venus or Mars with the use of a 210-ft-diameter ground antenna.
- (2) Acquisition time in a ranging subsystem is a function of the length of the overall code used. This, in turn, is a measure of the maximum unambiguous

range that can be determined with the system. The maximum unambiguous range for RNG Phase I is about 800,000 km; that of RNG Phase II is only 100,000 km. This trade-off of desiderata is, however, justifiable when it is realized that the ambiguity corresponds to several hours' flight time of a typical spacecraft and can, therefore, easily be resolved, using known orbit information.

- (3) The acquisition time required for RNG Phase II will be about $\frac{1}{6}$ of that required for RNG Phase I for the same signal strength. The number of code correlation measurements to be made will be $\frac{1}{3}$ of that used now, due to the shortened code length; furthermore, the ranging receiver has two channels operating simultaneously, which will reduce the acquisition time by another factor of 2.
- (4) Subsystem reliability and greater insensitivity to environmental conditions will be ensured by the use in RNG Phase II of the recently developed Hi-Rel digital modules.
- (5) Consolidation of the ranging with other subsystems into a single general-purpose computer with relatively minor peripheral equipment makes this approach particularly attractive in the light of minimizing station space and personnel requirements.

J. Hi-Rel Digital Modules, H. W. Baugh

1. Introduction

The Hi-Rel digital modules are a family of logical building blocks to be used in digital equipment for the DSIF. It is planned that any portion of a subsystem that is designed especially for the DSIF (i.e., not a catalog item) will be built of these modules. On the other hand, catalog items, such as oscilloscopes and computers, will be purchased "off the shelf" and will not use these modules.

2. Developmental Objectives

The development of these modules at JPL was undertaken with several objectives. These are reliability, ease of maintenance, simplicity of design, and standardization of documentation. Many of the modules now in use in the DSIF have failure rates which are excessive for components of such a large and complex system. The diversity of modules now in use requires highly skilled maintenance crews, or crews composed of specialists in the various brands of modules, as well as increasing the size of the inventory of spares. Design constraints on some commercial modules, and the practice of attempting to

minimize the module count, frequently cause a large increase in the time required to design and document a new piece of equipment, and impose a further burden on the maintenance personnel.

In summary, the objectives of this program are to provide a set of reliable, maintainable, well-documented modules.

3. Design History

The designs for these modules have come from several sources. Some were developed by commercial module manufacturers under a competitive procurement, and then modified by JPL; some were designed by JPL personnel, then packaged and documented by outside vendors; and some were designed, packaged, and documented entirely at JPL. Pilot quantities of all modules have been produced, so as to verify the design and the documentation, and small production quantities of the basic modules have been procured for use in R&D efforts. The modules have been used in experiments in coding theory, telemetry demodulation, and in the time synchronization experiment described in SPS 37-43, Vol. III, pp. 92-106. The main effort for the past several months has been the preparation of a complete set of specifications for the family, so that the parts procurement and screening, the fabrication processes, and the inspection and testing criteria are all fully documented for procurement purposes.

4. Available Modules

At the present time there are 13 types of modules available. A listing of the module types and the number of circuits per card is given in Table 4.

5. Subassembly Packaging

a. Modules. The modules are all the same physical size, approximately 4×5 in., using discrete components and printed wiring. The copper is etched off the component side of the board only where necessary to provide insulation around a conductor or a component lead. The remaining surface is connected to the ground system to form a "ground plane" which acts as a shield between cards and a return path for signals on the card. Each module has an integral connector which is used both for mounting and for making electrical connections. The integral connector provides 28 pairs of taper pin receptacles in a molded plastic block, with each pair clearly numbered. The connector assembly is bolted to the printed wiring board for mechanical support, then soldered to assure electrical contact.

Table 4. Hi-Rel digital modules

Type	Name	No. card	Remarks
Basic logic modules			
FF-33	Flip-flop	3	Clocked R-S flip-flop
NG-33	Nand gate	4	Three-input Nand
PA-33	Power amplifier	4	Three-input And
DC-33	Diode cluster	6	Three-input And
Timing sources			
PS-33	Pulse shaper	1	Sine-wave to pulse
CG-33	Clock generator	1	Crystal, phase-locked
Interface devices			
DM-33	Delay multivibrator	1	Adjustable delay
ST-33	Schmitt trigger	1	Adjustable hysteresis
NP-33	Negative-to-positive	6	Level inverter
PN-33	Positive-to-negative	6	Level inverter
Output devices			
LD-33	Lamp driver	8	100-mA output
DD-33	Display driver	4	400-mA output
Utility			
ACB-33	Auxiliary component board	12	Two-lead parts

b. Card files. The connector is mounted to the rails that form the sides of a "card file" assembly, equivalent to a "card cage" or "bin," so that the mounting hardware makes a connection between the ground plane of the module and the metal structure of the card file. This is done to assure that adequate signal return paths are provided in the system, so as to reduce system noise, particularly on the power supply lines. The card file is equipped with one or more multipin cable connectors, with optional capacities of from 50 to 150 wires. It has handles on the front which protect the wiring area, and angle members on the back which protect the edges of the cards, making it possible to remove a card file from the system and place it on a work surface in any position without injury.

c. Replacement. Wherever possible, a card file will be designed as a functional subassembly with a small number of interconnections with other files. With such a structure, the card file can be considered as the lowest replacement level, and a spare card file will be carried as a spare for each unique card file in a subsystem. This feature was initially dictated by the choice of the integral connector, but it has been shown to provide economies in station maintenance. In a conventional digital system, where each module is individually replaceable, and where operators are usually expected to perform emergency maintenance and trouble shooting, the operators must be aware of all details of the logic of the system, so they can locate a particular module when it fails. With replaceable card

files, the operators need only be trained to isolate the trouble to a particular card file and replace it with a tested spare. Malfunctioning card files may be analyzed, repaired, or adjusted as necessary by a local facility and returned to the operating spares stock. Defective modules will be returned to a depot or to the central module repair shop.

6. Larger Packages

Several optional methods of mounting the card files have been designed, and drawings have been released for fabrication. These include drawers, sliding frames, and open racks.

a. Drawers. All the optional drawers are 5¼-in. units. One type holds three card files, another holds one or two files and leaves space for other components, and a third uses short card files and provides enough space for a power supply. There is also a standard power supply drawer that mounts four 7-A supplies and the components necessary for monitoring all supplies and for programming their outputs high and low by 5% for marginal checking.

b. Slide frames. A basic design for a slide frame has been released. This frame provides for mounting card files in pairs, back to back, with the wiring exposed. Such a frame, if built to the full height of the rack, will hold 22 card files. Two of the frames will mount in a DSIF standard rack, for a total of 44 card files.

The design for the slide frame is given in tabular form, so that it may be built to any desired size to accommodate a particular subsystem requirement for modules.

c. Open rack. The simplest method of mounting card files is to attach them to open racks. The dimensions, hole spacing, etc., will accommodate the standard RETMA hole pattern, with each card file occupying 5¼ in. of space in a 19-in. rack.

7. Current Status

To summarize, all documents necessary for procurement of modules are now in released form. Also, all documents pertaining to the standard mounting hardware are released. Several orders have been placed for quantities of modules to be used in various subsystems, among them being the frequency and timing subsystem Phase II, the ranging subsystem Block II, and the tracking and data handling subsystem Phase II, and the multimission telemetry demodulator program.

K. Transmission of Surveyor High-Speed Telemetry Data From DSS to SFOF, R. G. Polansky

1. Purpose

The purpose of this article is to describe the mechanism used for transmission of *Surveyor* high-speed telemetry data from each deep space station (DSS) to the Space Flight Operations Facility (SFOF).

2. Scope

This article contains the following information:

- (1) A discussion of the *Surveyor* Project requirements for high-speed data transmission to the SFOF.
- (2) A description of the physical configuration of the DSN system used to satisfy the requirement.
- (3) A detailed description of the data formats that cross the DSS/SFOF interface.
- (4) A discussion of results.

3. Requirement

During the preliminary planning phases of the data system that would support the *Surveyor* Project, the primary communications capabilities between the DSSs and the SFOF were voice and teletype. Analysts in the SFOF must of necessity have made decisions affecting the spacecraft based upon a very small percentage of the data, since telemetry bit rates received at each DSS could be at least two orders of magnitude higher than teletype transmission rates to the SFOF. The DSN, recognizing the need to improve this operation, had undertaken the development of a high-speed data transmission system between each DSS and the SFOF. It was mutually agreed between the DSN and *Surveyor* managements that these high-speed capabilities could be used for the Project; however, the mission would still be designed to operate using the minimum configuration (the teletype data) until the high-speed system was made operational.

4. Configuration Description

On-station computers (either an SDS 910 or an SDS 920) at each DSS are fed pulse code modulated (PCM) data from mission-dependent equipment. This data is processed in the on-station computer and output to a high-speed data line (HSDL) modem transmitter. The modem output is transmitted via NASCOM high-speed data lines to modem receivers in the SFOF. From these

Present HSDL interfaces between all DSSs supporting *Surveyor* and the SFOF, with the exception of DSS 51, operate at 1200 bits/s. The DSS 51 interface is capable of operating at rates of 137.5, 550, or 600 bits/s.

High-speed data from the on-station computer are received by the TPS in real-time only. These data are received at bit rates of 1200, 600, 550 and 137.5 bits/s consistent with the capabilities of the ground communications system links. Whenever the HSDLs have suffi-

Each sequential group of similar data frames sent from the DSS will be preceded by a data identification (DID) frame. The purpose of this frame is to advise the TPS of the data mode, or editing configuration, to expect in the next frames of data. The construction of the DID frame is shown in Table 5.

Table 5. Format of DID frame

Word No.	Bit configuration											Function	
1	0	1	1	1	1	1	1	1	1	1	1	Unique word used to differentiate DID frame from spacecraft data frame. (Word violates odd parity normally associated with spacecraft data words.)	
2	X	X	X	X	X	X	X	X	X	X	X	Bits 1 and 2 are spares. Bits 3-10 are binary-coded decimal (BCD) DSS number. Bit 11 is chosen for odd parity.	
	S	S	80	40	20	10	8	4	2	1	P		
3	X	X	X	X	X	X	X	X	X	X	X	Bits 1 and 2 are spares. Bits 3-10 are BCD spacecraft ID. Bit 11 is chosen for odd parity.	
	S	S	80	40	20	10	8	4	2	1	P		
4	X	X	X	X	X	X	X	X	X	X	X	Bit 1 = 1 when next data frames are to be nonstandard word-edited. Bit 2 is spare. Bits 3-10 are BCD data mode. Normal spacecraft modes 1-7, as well as preconceived word-edited data modes 8-20, should be indicated here. Nonstandard word-edited modes will be indicated as data modes 1-7; however, the bit-1 position of this word will contain a 1. Bit 11 is chosen for odd parity.	
	E	S	80	40	20	10	8	4	2	1	P		
5	X	X	X	X	X	X	X	X	X	X	X	Bit 1 = 1 if commutator position 1 is to be transmitted. Bit 2 = 1 if commutator position 2 is to be transmitted.	
	1	2	3	—	—	—	—	—	—	—	P	.	
												.	
												.	
												Bit 10 = 1 if commutator position 10 is to be transmitted. Bit 11 is chosen for odd parity.*	
6	X	X	X	X	X	X	X	X	X	X	X	Bit 1 = 1 if commutator position 11 is to be transmitted.	
	11	12	—	—	—	—	—	—	—	—	20	P	.
												.	
												.	
												Bit 10 = 1 if commutator position 20 is to be transmitted.	
												.	
												.	
												.	
												.	
												.	
7	X	X	X	X	X	X	X	X	X	X	X	.	
	21	—	—	—	—	—	—	—	—	—	30	P	.
.												.	
.												.	
.												.	
.												.	
.												.	
.												.	
.												.	
16	X	X	X	X	X	X	X	X	X	X	X	.	
	111	—	—	—	—	—	—	—	—	—	120	P	.

*Words 5 through 16 contain a mask defined manually to the on-station computer for nonstandard word-editing, if this mode of operation is chosen. These words contain a similar mask initialized into the on-station computer program for preconceived word-edited data modes. For standard data modes 1 through 7, words 5 through 16 are each 11111111110.

When the TPS detects a DID frame, it outputs a DID word to the 7044 computer. This word identifies to the 7044 the data mode to be processed next, the spacecraft number, and the DSS source of the data. No words of the actual DID frame are output to the 7044.

When no high-speed data are available for transmission to the SFOF, the on-station computer will send "dummy frames" to keep the communications link and TPS in lock. Dummy frames are 10 words long, start with a two-word sync sequence followed by a special word (0000011111), and are filled with dummy words (00000000101). Detection of the special word in the number-one word position will cause the TPS computer to recognize the entire frame as a dummy. No words of this frame will be output. Dummy frames are configured such that their receipt by the TPS will be readily recognizable. The physical indication caused by receipt of dummy frames is a repetitive blinking of the TPS PCM out-of-lock indicator. This indication, as opposed to a solid out-of-lock indication, allows the TPS operator to differentiate between data outages from the spacecraft and high-speed data line faults.

The sequence of events required to send HSDL data to the SFOF is as follows:

- (1) First a sync sequence consisting of a Barker complement word, 00011101101, followed by a Barker word, 11100010010, will be sent.
- (2) The sync sequence will be followed by two DID frames as previously defined.
- (3) The on-station computer will then alternately send a sync sequence and the data frame as described in the DID frame. This will continue until the data mode is to change.
- (4) When the data mode is to change, the on-station computer will send a new DID frame instead of the previously defined data frame. This will be followed by the sync sequence. The DID frame and the sync sequence will be repeated twice before starting transmission of the new data mode.
- (5) Alternate data frames and sync sequences will then be transmitted until another DID frame is sent.

The sequence just described is shown in Table 6.

A word-edited data frame contains the same number of words as the spacecraft frame (100 for modes 1, 2, 4; 50 for mode 3; 120 for modes 5, 6). As an example, let us assume that the spacecraft is in mode 2 and we wish to select 49 data words from each spacecraft data frame for

Table 6. HSDL data sequence

S	
DID	
S	
DID	
S	
D ₁	
S	
D ₁	
S	
D ₁	
S	
DID	
S	
DID	
S	
D ₂	S sync sequence
S	DID data ID frame
D ₂	D _N data frame, Nth data mode
S	
D ₂	
S	
DID	
S	
DID	
S	
D ₃	
S	
D ₃	

transmission to the SFOF. The 49 data words from each of two adjacent spacecraft frames will be transmitted as one edited frame. When the 2-word sync sequence is added, the edited frame will be 100 words long. In other words, the selected contents of two or more spacecraft data frames are word-edited into a single-edited data frame, and the 2-word sync sequence added. If it is impossible to construct an edited frame from an integral number of spacecraft data frames, the remaining word slots of the edited frame are filled with dummy words (00000000101).

For completeness, processing of television frame identification data (TVID) will now be described. Whatever number of frames of these data is detected for each picture received by the DSS will be sent to the SFOF TPS. They

will be followed by a video ID trailer frame. Video ID trailer frames are 10 words long. They start with a sync word followed by a special word (11111100000) and are filled with dummy words (00000000101). Detection of the special word in the number-one word position will cause the TPS computer to recognize this as a video ID trailer frame. No words of this frame will be output. Instead, a mode-7 data ID word will be output to the 7044 followed by an external interrupt. This will flush the 7044 high-speed subchannel buffer after each burst of frame ID data, making the data immediately available to the remainder of the system.

6. Results

The results of this venture are presented in two categories; namely, accomplishments and shortcomings.

The accomplishments are as follows:

- (1) The high-speed system has been thoroughly exercised for the unedited, standard frame-edited, standard word-edited, and nonstandard word-edited cases. In all instances, the system performed satisfactorily.
- (2) The system provided much more timely data than its teletype counterpart, allowing more timely command decisions affecting the spacecraft to be made.
- (3) Analysts were able to observe orders of magnitude more data than would have been possible using only teletype.
- (4) Automatic mode changes caused by receipt of DID frames considerably simplified the SFOF real-time operations.
- (5) The dummy frame concept coupled with visual aids in the TPS provided a good on-line quality indicator of HSDL performance.
- (6) The use of dummy frames allowed the transition between Hallicrafter- and NASCOM-type modems to be made without any program changes, even though the HSDL transmission rates were different.

The shortcomings are as follows:

- (1) In order to send a DID frame, a manual entry into the on-station computer is required. If this entry is not made at exactly the time that the data mode being received changes, data in the SFOF will be misidentified for a short period of time. It may be reasonable to consider sending new DID frames as

a function of received telemetry data if the data is clean enough.

- (2) Occasionally, the first word of a dummy frame is not recognized. This is normally due to marginal HSDL quality. When this occurs, the dummy frame is wrongly identified as spacecraft data. This is not too great a problem, since all dummy frame words are chosen such that parity is violated. All such words output from the data processing system are flagged as bad parity words.
- (3) Experience has shown that the preconceived word-edited data modes are seldom, if ever, used. If word-editing is required, a much more reasonable selection of parameters to be observed can be made and requested "on the spot." For *Surveyor D* mission and beyond, the standard word-edited mode initialization will not be updated. This saves a number of reassemblies for on-station, TPS, and 7044 programs and eliminates extensive testing caused by these new program assemblies.

L. SFOF Data Processing System, R. G. Polansky

1. Introduction

This article gives a description of the SFOF data processing system (Fig. 35) as it is expected to be by September 1, 1967.

2. Computer Hardware

a. On-line capability. The on-line computing capability in the SFOF comprises three computer strings (W, X, and Y). Each string consists of an IBM 7044 computer with a drum, an IBM 7094II computer, and a shared disk. Each string is provided with a direct data connection (DDC) between the 7044 and 7094, which is used for direct intercomputer communications. The 7044 is provided with an IBM 7288 data communications channel through which all data input/output (I/O) and user I/O devices are handled.

IBM 7044 computer (I/O processor). The IBM 7044 computer is the input/output processor of the SFOF computer system. It contains a 64K core memory. The 7044 performs the following functions:

- (1) *Input processor.* As the input processor, it accepts all real-time inputs through its 7288 data channel.

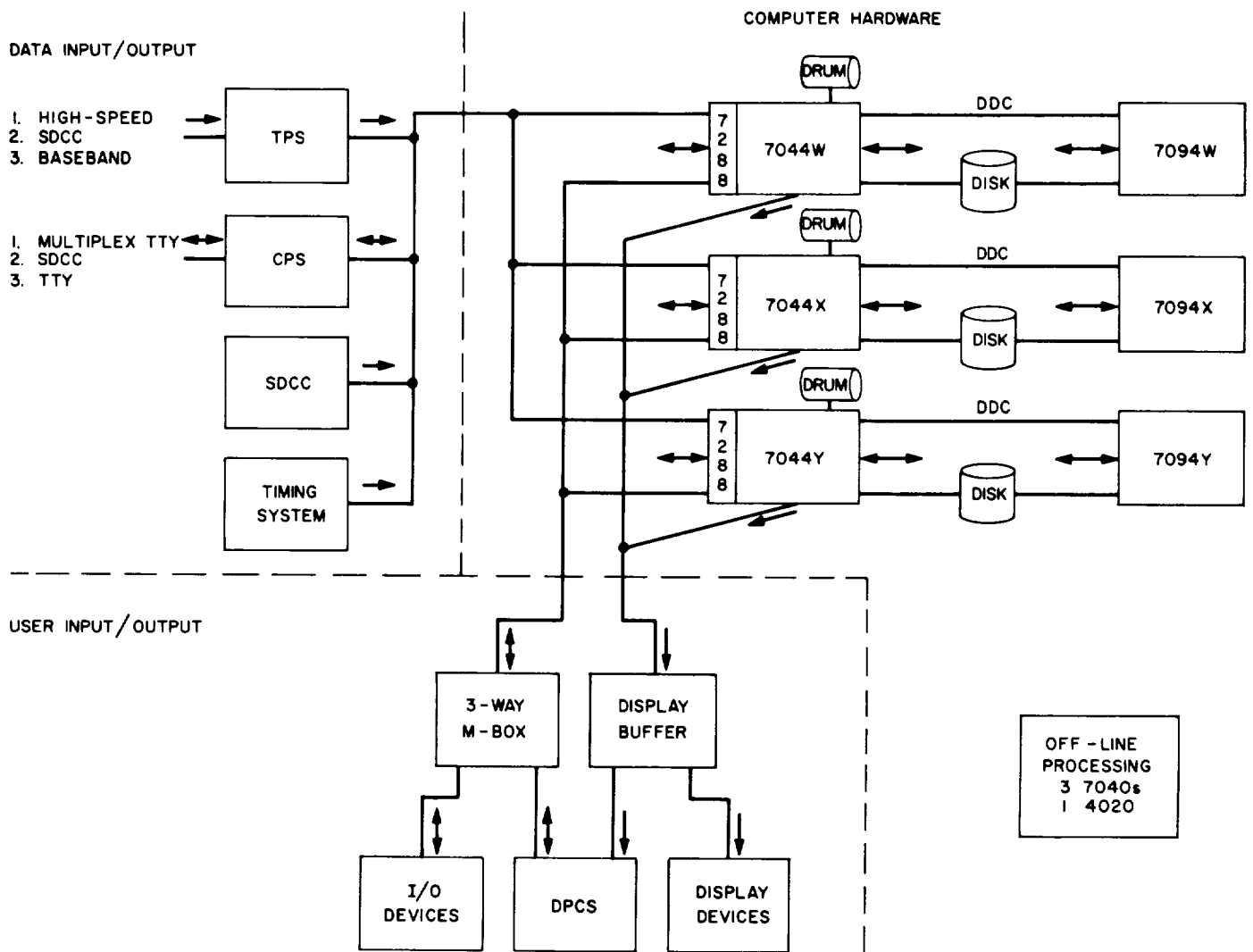


Fig. 35. SFOF data processing system

These inputs consist of messages from inquiry stations and card readers, and data from the telemetry processing station and communications processor (CP). The 7044 formats, time tags, logs, and routes this input data to other parts of the system.

- (2) *Output processor.* As the output processor, it acts as the source and control of all on-line high-speed printers, plotters, and inquiry console displays. Through its 7288 data channel it outputs messages to the communications processor for off-Lab transmission, and for display on TTY machines in the user areas.
- (3) *Quick-look processor.* As a quick-look processor, the 7044 accepts all input data, decommutates the data that has not been decommutated in the telemetry processing system, and converts the data to

engineering units. In response to requests from the user areas, subsets of this data are printed and/or plotted in the user area.

- (4) *Alarm monitor.* As an alarm monitor, the 7044 generates and distributes both spacecraft alarms and data condition or data format alarms to the appropriate area.

IBM 7094II computer (main processor). The IBM 7094II computer is a high-speed digital data processor with a 32K core memory. In the SFOF data processing system, it serves as the primary element for the processing of the complex analysis programs, i.e., the orbit determination, tracking data editing, and guidance and maneuver programs. These programs, because of their size, may require the entire capability of the 7094. All

programs and data are stored on the disk and are transferred to the 7094, as required. Results, in the form of tabulation, plots, commands, and antenna pointing predictions, are returned to the disk when completed. In addition to disk storage, data is also recorded on magnetic tapes for permanent files and off-line bulk processing.

Disk. The disk is the high-volume, medium-access data storage medium in the SFOF computer system. It contains the disk directory, all raw data, all 7094-generated output data, the master data table, the operating and diagnostic programs for both the 7044 and the 7094, planetary and lunar ephemerides, and temporary storage used by 7094 analysis programs.

Each disk complex comprises an IBM 7631IV control unit and two 1301II disks. The 7631IV can communicate with one 7044 and one 7094 on a shared basis. A 1301II comprises two modules, each with 25 disks that rotate on a central shaft (20 are used to store data). Recording is done on the top and bottom surfaces of each disk.

Direct data connection (DDC). The DDC is used to transfer control information between the 7044 executive program and the 7094 executive program, and between remote analysis areas and their associated 7094 analysis programs. A primary function performed by the DDC is the control of shared disk usage. When either of the computers wishes to have access to the disk, the other computer is notified via the DDC.

Drum. Each 7044 in the SFOF has access to its own drum. The drum acts as the source of "overlay program modules" which share the 7044 core on a millisecond level. These program modules operate under control of the 7044 redesign executive routines residing in the machine.

IBM 7288 data communications channel (DCC). The 7288 expands the I/O capabilities of the 7044 computer. The channel can provide direct connection with a variety of external devices operating at various speeds for real-time operation. The data link between the 7288 and the external device is 36 bits parallel; however, special adapters can accommodate serial or parallel transfers of fewer bits. Similar to other overlapped data channels, the 7288 transfers data to and from the computer core storage in a 36-bit parallel fashion concurrent with the operation of the central computer program.

The number of I/O subchannels connected to each 7288 is limited to 48. A maximum of 32 of these can be

used for inputs and a maximum of 32 can be used for outputs. Several classes of devices, such as status modules, administrative printers, card readers, and message composers are multiplexed onto individual subchannels as opposed to using N subchannels for N similar devices. This saves output subchannels and more efficiently uses the overall system capabilities.

b. Off-line capability. In addition to the on-line printing and display devices in the SFOF data processing system, there are three IBM 7040s and one SC 4020, which are used for generation of off-line prints and plots. Each uses as an input source data tapes generated by on-line computers, such as the 7044 and the 7094.

IBM 7040 computer. The function of the IBM 7040 computer is to produce large volume tabular outputs in non-real time. Each 7040 consists of a 7040 central processor, a 1402 card reader/punch, two 1403 printers, and two 729 tape units.

SC 4020 computer. The function of the SC 4020 computer is to produce, at high speed, large volume tabular printouts and plots in non-real time. Magnetic tape output from the 7044 or the 7094 is carried to the 4020 for processing. Output from the 4020 is in the form of 35-mm film or exposed $7\frac{1}{2} \times 7\frac{1}{2}$ in. paper.

3. Data Input/Output

There are four sources of data input, other than from user devices, into the SFOF data processing system: (1) the telemetry processing system, (2) the communications processor, (3) the timing system, and (4) the simulation data conversion system. A short description of each will now be presented.

a. Telemetry processing system (TPS). The TPS does all preliminary processing of telemetry data, other than that received by TTY, before passing the data to the 7044 I/O processor.

Functions performed. The functions performed by the TPS are to:

- (1) Convert telemetry data received in analog, digital, or composite subcarrier form to a 36-bit parallel format that is compatible with a 7288 high-speed subchannel and to IBM compatible digital magnetic tape.
- (2) Provide the capability for recording all composite and high-speed data entering the SFOF.

- (3) Provide the capability for producing strip chart recordings of analog discriminator outputs and of selected pulse-code-modulated channels in real time.

Station configuration. The TPS contains 3 general purpose stations (PDP-7s with appropriate I/O), 2 special purpose stations (discriminators, decommutation equipment, digital-to-analog converters, etc.), and 3 phone line formatters (PLFs) (Fig. 36). Each PDP-7 and PLF provides two possible outputs that can be patched into 7288 high-speed subchannels.

To provide telemetry processing capability for a given mission, it is necessary to:

- (1) Patch inputs to the special and general purpose stations as necessary.
- (2) Patch a general purpose station to the required equipment (if any) from a special purpose station.
- (3) Patch appropriate outputs from the general purpose station to the 7288 high-speed subchannels.

Note that the phone line formatters run independently of the remainder of the general purpose stations, subject only to input and output patching constraints.

b. Communications processor system (CPS). The CPS does all routing of incoming and outgoing TTY information in response to routing information contained in each message header.

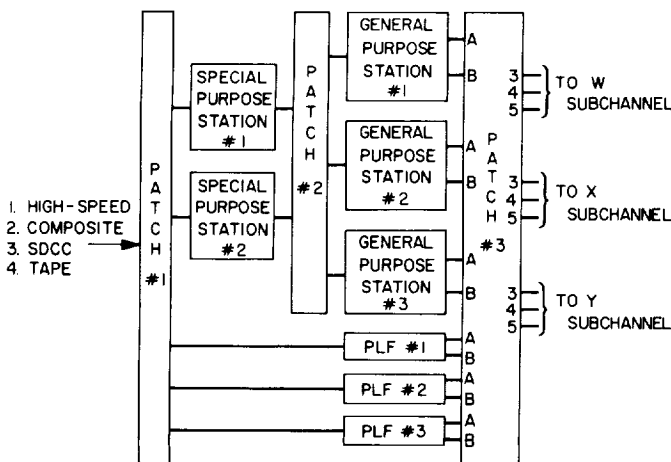


Fig. 36. Telemetry processing system

Functions performed. The CPS is capable of routing data as follows:

- (1) Off-Lab TTY inputs can enter the CPS from individual TTY lines or from a high-speed multiplexed channel connecting the JPL and Goddard Space Flight Center communications processors. Messages received in the JPL CPS may be routed to either the 7044 I/O processors via high-speed block transfer or to user area TTY machines.
- (2) Messages generated by the 7094 main processor may be sent via the 7044 to the CPS for transmission to off-Lab destinations. Data transfer from the 7044 to the CPS is again by high-speed block transfer. Messages leaving the communications processor may exit via individual TTY lines or via the high-speed multiplexed channel to Goddard Space Flight Center.
- (3) Data that has been converted to engineering units by the 7044 can be output to any 100-wpm user area TTY machine if requested by the I/O console operator. These data are again transferred to the CPS from the 7044 via high-speed block transfer. The communications processor then keys the lines to individual TTY machines at the 100-wpm rate. Each user TTY machine has a unique address, which is referenced in the header preceding the data. The inclusion of the machine address in the routing indicator portion of the NASCOM header ensures proper routing of the data.

CPS configuration. The CPS contains two stations, each centered around a Univac 490A computer (Fig. 37). Each communications processor communicates with 6 communications terminal module controllers (CTMCs), one multiplex channel, and one adapter channel. All channels have full duplex capability. All incoming and outgoing TTY lines, as well as SFOF TTY machines, are interfaced with the communications processor via the CTMCs. Thirty-two full duplex lines are available in each CTMC. The duplex multiplex line between the Goddard Space Flight Center and the SFOF is interfaced to the communications processor via the multiplex channel. Full duplex communications with all 7044s simultaneously are handled by the adapter channel.

All inbound (to SFOF) lines are normal through to both the active and backup communications processors. Data is output from both communications processors; however, only data from the active communications processor gets transmitted through the communications line switcher.

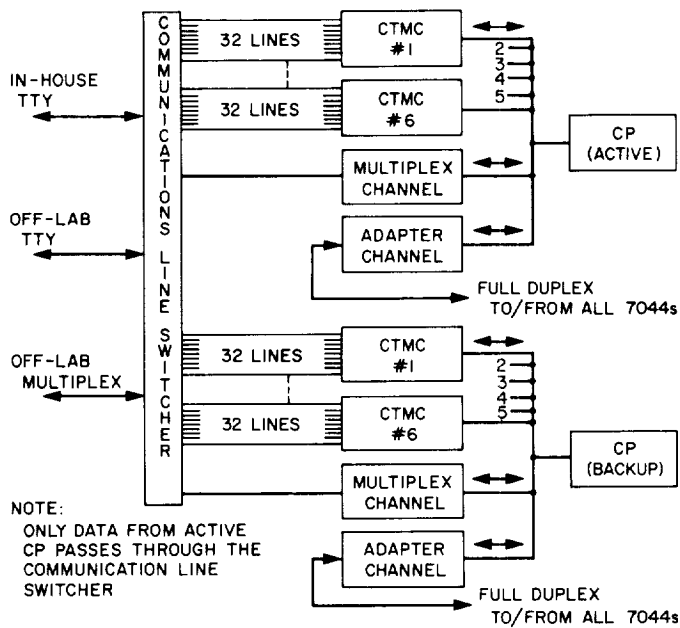


Fig. 37. Communications processor system

Any of the 8 channels communicating with each communications processor can be cross-switched with the same channel on the other communications processor for recovery purposes. Switching capability on an individual line basis can also be effected in the communications line switcher. Normally, interchanging channels requires modifications in communications processor program initialization.

c. Timing system. Two groups of equipment are available for timing. The first is on-line with the SFOF computers and provides the GMT reference for the SFOF. The capability exists to synchronize the on-line generators to time signals received from Goldstone, the JPL Standards Laboratory, and the National Bureau of Standards radio signals from WWV and WWVB.

The second group of equipment is off-line and provides facility time displays during simulations and missions.

Function performed. The functions performed by the timing system are to:

- (1) Provide parallel GMT data to all SFOF 7044 computers to a precision of 1 ms.
- (2) Provide serial NASA 36-bit time codes, rate signals, and parallel time-of-day information to SFOF users.
- (3) Provide SFOF users with simulated time generators, and down/up presetable time counters, along with their displays.

Timing system configuration. The on-line timing system is shown in Fig. 38. In this system, two Astrodata time code generators (TCGs) provide the GMT reference for the SFOF. Their serial outputs are continuously compared so that failures can be rapidly detected.

The output of one of the two generators is manually selected and sent to buffered line drivers, from which the clock subchannels in all 7044s are simultaneously driven. Serial time codes, rate signals from 1 to 1 million pulses/s, and parallel GMT data are provided to SFOF systems as necessary from these generators.

One of four sets of off-line timing system hardware is shown in Fig. 39. The four sets are identical with the exception that two of the time code generators are in fact translator/generators. The typical equipment set comprises a time code generator, two down/up presetable time counters, a live presentation of the three outputs on the mission status board, a display of the three outputs for closed-circuit TV, and a preset and control box for all three "clocks." Each time code generator has the same output capability as the on-line generators.

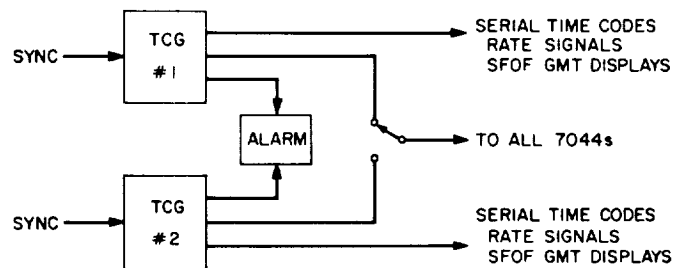


Fig. 38. On-line timing system

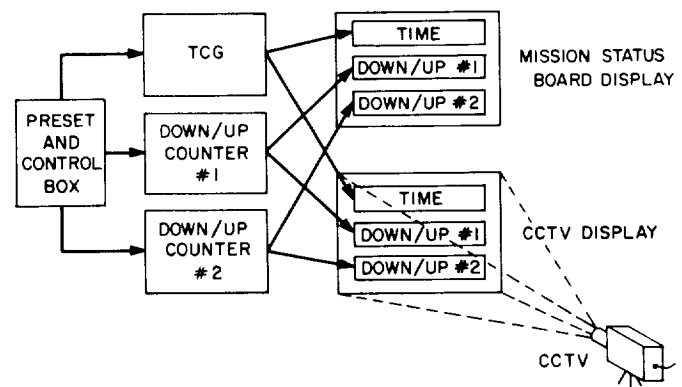


Fig. 39. Off-line timing system (1 of 4 sets)

d. Simulation data conversion center (SDCC). The simulation data conversion center (SDCC) provides simulated data directly or via the deep space stations into the SFOF for systems checkout and for training of mission operations teams. It provides simulated data inputs to the TPS, the communications processor, the 7044s, and to the deep space stations via real-time interfaces and analog magnetic tapes. Data is generated in serial digital, parallel digital, modulated subcarrier, or teletype forms.

SDCC configuration. The SDCC is designed to provide simulation capabilities for two simultaneous missions. This is accomplished through the use of a PDP-1 computer-based system, an ASI 6050 computer-based system, and a pool of system support equipment.

PDP-1 system. The PDP-1 system comprises the original SDCC capability. This system contains the following hardware capabilities:

- (1) One pulse-code-modulated output with program selectable rate.
- (2) One pulse-code-modulated output with manually selectable rate.
- (3) Eight TTY output lines.
- (4) One TTY input line.
- (5) Analog-to-digital inputs (18 channels, multiplex) at 10-kHz maximum rate.

Actual capabilities available are dependent upon software operating in the machine.

ASI-6050 system. The ASI-6050 system is the newest addition to the SDCC. It contains extensive data I/O capabilities and has associated with it four consoles for real-time control of the simulation. This system contains the following hardware capabilities:

- (1) Two pulse-code-modulated outputs with program or manually selectable rates.
- (2) Two pulse-code-modulated inputs at rates up to 100K bits/s.
- (3) Sixteen full duplex TTY channels.
- (4) Analog-to-digital inputs (16 channels, multiplex) at 10-kHz maximum rate.
- (5) Sixteen channels of digital-to-analog output.
- (6) Twenty-four channels of computer-driven relays.

(7) One channel of time code input.

(8) 7288 subchannel input capability.

Actual capabilities available are dependent upon software operating in the machine.

SDCC support equipment. To supplement the PDP-1 and ASI-6050 systems just described, the following support equipment is available in the SDCC.

- (1) Analog tape recorders.
- (2) Voltage-controlled oscillators.
- (3) Amplifiers.
- (4) Modems.
- (5) Discriminators.
- (6) TTY page printers and transmitter drivers.

This equipment is all patchable as required.

4. User Input/Output

a. Three-way M-box. All user I/O devices in the SFOF, with the exception of the data display teleprinters, are interfaced with the 7288 subchannels through the three-way M-box. The position of a given M-box switch determines with which string (W, X, or Y) a given I/O device will communicate. The position of each such M-box switch can be determined locally at the M-box, or remotely at the data processing control and status (DPCS) consoles.

The M-box is made up of three types of modules: (1) switching modules, (2) multiplexing modules, and (3) status generating modules. The switching module switches the data and control lines to or from an I/O device, from one 7288 to another (W, X, or Y). The multiplexing module provides the sequencing or priority of those devices (card readers, inquiry devices, administrative printers, and status displays) which time-share a 7288 subchannel. The status generating modules convert the contact closures, which indicate the status of the computer I/O equipment, into displays for the DPCS consoles.

I/O devices. Each user area in the SFOF has a complement of I/O devices: an I/O console, a card reader, and some number of printers and plotters.

I/O console. A standard I/O console in the SFOF comprises a message composer, a status module, and an administrative printer. Unlike any other user I/O device

in the facility, the I/O console may be switched from the user area to either the W, X, or Y computer string. Descriptions of the I/O console components are as follows:

- (1) *Message composer.* The message composer contains a 48-character alphanumeric keyboard, a 72-character message/character display assembly, 36 binary program option switches, and 25 binary special function buttons. Messages sent to the computing equipment from the message composer contain a preamble, a variable data portion, and a program option word.
 - (a) The preamble is one 36-bit word which contains the console address and the selected bits from the 25 special function switches.
 - (b) The variable portion of the message consists of twelve 36-bit words (seventy-two 6-bit characters). This data is inserted, via the alphanumeric keyboard, and stored in a delay line until the delay line is cleared. Data contained in the delay line is continuously displayed and is not destroyed when a message is transmitted.
 - (c) The program option word contains the 36 bits of data set into the program option switches.

When an operator has composed a message to his satisfaction, the transmit switch is depressed and the message is sent to the 7288. The message is transmitted one 36-bit word at a time, on a demand/response basis. All message composers are multiplexed into one 36-bit parallel input subchannel of the 7288, with a once-requested-eventually-served priority scheme.

- (2) *Status module.* Each status module contains 8 alphanumeric indicators, and 36 program option lights. Four alphanumeric indicators display the current operating program in the 7094, while the remaining 4 indicators display the 7094 program to which the 36 program option lights refer. Each alphanumeric indicator is capable of displaying any one of 36 characters (A through Z and 0 through 9). The program option lights are binary indicators. The display decoder and driver, located in each status module, can easily be expanded to drive additional displays, as they become necessary. All the above status displays for all I/O consoles are driven by one 36-bit output subchannel with the update priority under 7044 program control. The

status module also contains equipment status indicators reflecting the status of all I/O equipment located in that particular user area.

- (3) *Administrative printer.* The administrative printer is a Motorola TP-3000 electrographic character printer. It communicates messages to the user, as required, for feedback from the analysis programs or the programming system. All administrative printers are driven by one 7288, 6-bit, parallel output subchannel through a multiplexer-decoder module with priority under 7044 program control.

Card reader. The card reader is a Burroughs B-122 device that has been modified to interface with the 7288. It is capable of reading standard IBM Hollerith cards and converting the data to a modified IBM, 6-bit, Fortran binary-coded decimal code. It is a column serial photocell reader capable of reading 200 cards/min. The hopper and stacker have the capability of holding 500 cards. The card reader feeds cards from the hopper, face down and column one first, through the station read and into the stacker.

The card reader serves a function similar to that of the message composer of the I/O console; in fact, the two devices can act as backup to each other. In general, the card reader is used where there is a larger volume of data to be input or where input data can meaningfully be selected from a prepunched set of cards.

All card readers are multiplexed into one 7288, 6-bit, parallel input subchannel. Card read-in can be initiated either from an analysis area, or from the computer programming subsystem. If the programming subsystem initiates the card read, then the multiplexing priority is under program control; if the card read is initiated at the card reader, the multiplexer operates on a simple sequencing priority.

Bulk printer. The bulk printer, an SC 3070, is a high-speed, electrostatic character printer which asynchronously prints one character at a time, upon receipt of character selection and control signals from the 7288. It is capable of printing 120 characters per line at a 300-character/s rate. This printer is used to produce all on-line tabulations of raw and reduced data. Each 3070 printer is driven by its own 7288, 6-bit, parallel output subchannel.

Plotter. The plotter is a Milgo Model 4021D, vertical, X-Y recorder which accepts digital data from a 7288 subchannel, converts it to analog signals, and records the

resultant data. The plotter has the capability of plotting lines, points, or characters. Paper must be changed manually after each plot is complete.

This device is used to plot on-line raw and reduced data. Programming options permit dividing the plotting surface into a maximum of 12 subfields for the plotting of multiple parameters.

Each Milgo plotter is driven by a standard 7288, 36-bit, parallel output subchannel.

Data display teleprinters. A number of standard 100-wpm teleprinters are assigned to the various user areas in the SFOF for the display of spacecraft subsystems telemetry data in the cognizant subsystem engineers' locations. Each teleprinter has its own routing indicator or address. Data to be displayed on each device is queued via the associated I/O console. The data is routed to the teleprinters via the communications processor from the 7044.

b. Display buffer system. The display buffer accepts mission-independent inputs from the SFOF's 7044 computers. These data are manipulated as necessary and output to mission-independent hardware. At present, two hardware displays of this type exist. One is the FPAA No. 2 orbital parameters display and the second is the data processing control and status console. Total capabilities in these areas will not be available until 7044 coding is completed and checked out. It is expected that many mission-independent automatic displays will eventually be driven from the display buffer system.

Display buffer configuration. The display buffer system is built around two CDC 3100 computers (Fig. 40). One acts as the active system and one acts as the backup. The active/backup status of each machine can be interchanged by a simple software command.

Each computer receives input data from all 7044s through a common data input control. Input data transfer takes place on a 36-bit parallel word basis. 7044 communications are multiplexed on a block at a time basis. The active display buffer computer controls the data input control unit.

Each of the system's two data output controls can be driven by either computer, although it is normally the active system that drives both. Each output control provides interface, control, and line drive for up to 8 display devices. The SFOF system has the present hardware capa-

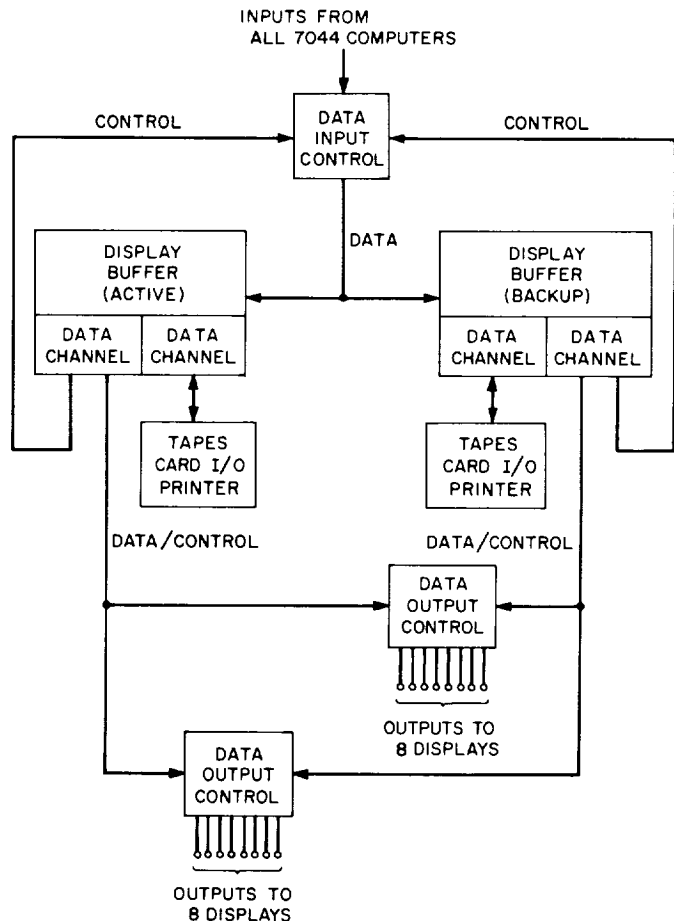


Fig. 40. SFOF display buffer system

bility to drive 16 such displays. All data output from the display buffer is formatted in 12-bit parallel words.

c. Data processing control and status (DPCS) system. The means for monitoring and controlling the SFOF data processing system lies in the data processing control area. The physical hardware used to accomplish this comprises a standard I/O station and an equipment group known as the data processing control and status (DPCS) system. The DPCS system comprises three consoles:

- (1) The equipment status display.
- (2) The processing status display.
- (3) The data status display.

These displays furnish comprehensive and timely indication of the operational status of various systems and equipments throughout the SFOF and also provide control over the assignment of I/O devices to the W, X, and Y computer strings as dictated by operational requirements.

Equipment status display (ESD). The equipment status display permits pushbutton control of the string assignment of individual 3070 printers and 30×30 plotters, as well as the group assignment of card reader, administrative printer, I/O console combinations in the various user areas. It also displays the current operational condition of these individual or grouped equipments.

Further, the ESD monitors the operating condition of the following systems and equipments:

- (1) Off-line equipment (IBM 7040s and SC 4020).
- (2) SDCC direct enable (includes permissive control over TPS subchannels 3 and 4 W/X/Y).
- (3) Timing system (includes permissive control over mission time sources: SDCC or mission control center).
- (4) Display buffer (both systems: on-line, backup, or not operational).
- (5) Displays (maximum of 10 user displays: operational-in use, operational-not in use, not operational).
- (6) Computer status (7044 and 7094 W/X/Y: mission A and B initialization, mode, operational/maintenance/not operational).

Items (4) through (6) are subject to successful software development and checkout in the 7044.

Processing status display (PSD). The processing status display provides dynamic indication of the activity on each of the (up to) 48 subchannels in the IBM 7288 data communications channel as to whether the attached devices are operational (being accessed by the software) or not operational, whether the subchannel has been selected by the software, and whether there is wired buffer activity in the appropriate segment of 7044 memory. Also, the PSD provides indicators which denote the presence of simulated data from SDCC on subchannels 3 and 4, plus lights which monitor the activity of the inquiry, card reader, and status multiplexers.

The PSD console also provides indication, from the 44 redesign software via the display buffer, of program activity in the 7044 I/O processor pertaining to tape, disk, drum, TPS in, communications processor in, message composer (inquiry) in, cards in, mission A, mission B, 3070 out, display out, communications processor out,

administrative printer out, status out, record out, and plot out. The PSD also displays the currently operating 7094 program, along with the 7094 program options and alarms, duplicated for each of the three strings W, X, and Y.

Again, all displays driven from the 7044 software system are available, subject to successful software development and checkout in the 7044.

Data status display (DSD). This capability does not presently exist. It is presently being developed and is included here for completeness only. The data status display will be driven from 7044, so will again depend upon successful development and checkout of the 7044 software.

The DSD consists of three independent cathode-ray-tube (CRT) output stations (W, X, Y) mounted on one console base or desk. These CRTs are driven by the display buffer and graphically offer a running history of the origin and current processing status of TTY input and output messages, and/or TPS data stream entering the data processing system, along with alarm indications if and as necessary. The 20×50 field of characters on each CRT is formatted by means of a four-color overlay to identify and accent the data by type, enabling the observer to monitor these functions with a minimum of attention.

M. SFOF Power System Reliability and Availability, D. C. Card

1. Allocation of Resources to Improve Reliability

This article is the final topic in a series of three which represents results of a study for the SFOF power design team. Concern with the allocation of resources arises from a requirement to design systems with high reliability, yet within some kind of cost criterion. If the criteria to be used can be defined quantitatively, then it is possible to design a system which is "optimum" in some sense.

2. Analysis

System users often express the desire to have at their disposal a system which is "nearly perfectly reliable." If one can imagine the number which "nearly" represents, it can be seen that such an "upper limit" criterion is not reasonable. For example, consider a single-stage system whose single element has reliability r for the time period of interest, such that

$$0 < r < 1$$

and unreliability

$$u = 1 - r$$

Suppose that a parallel redundant scheme is the only reasonable method of enhancing reliability of this unmaintained system, so that system reliability R is given by (the requirement is that at least one element be operable)

$$R = 1 - u^N$$

where $N = 1, 2, \dots$ is the number of parallel elements. Clearly $R \rightarrow 1$ as $N \rightarrow \infty$, but also, cost increases without bound so that there is no workable practical criterion in this case.

Let the criterion of optimality be to minimize a particular function L of the system reliability (or system cost). The function L can be interpreted as expected loss or cost to a series of missions due to the unreliable system. One such function is

$$L = C + MU \quad (1)$$

where C is the total cost of upgrading the reliability of a given system, M is a mission value weighting, and U is the system unreliability function. In most practical cases, the functions are sufficiently well behaved that we can write

$$C = C(U)$$

and

$$U = U(C)$$

For a multistage system, let us suppose

$$C = \sum_i c_i, \quad i = 1, \dots, N \text{ stages}$$

and

$$U = f(u_i)$$

$$u_i = u_i(c_i)$$

We have to solve the system

$$\left(\frac{\partial L}{\partial c_i} \right) = \left(1 + M \frac{\partial U}{\partial c_i} \right) = 0 \quad (2)$$

and demonstrate that this extremal is the minimum.

The function in Eq. (1) has the interpretation of expected loss due to the system, where, for example, M could be the total development cost of the missions to be supported; then, MU represents an expected loss due to system unreliability. This loss is balanced against C , the cost of improving reliability. The solution of Eq. (2) for the c_i gives the appropriate allocation of resources. For most practical problems, L has a minimum in the range (even a unique minimum) since C is usually strictly increasing and U is non-increasing, with M a constant.

A difficulty in solution of the system is that the u_i (or c_i , whichever is most convenient) occur in nonlinear combinations. However, consider u_i to be continuous functions having first partial derivatives. Each u_k is bounded on the range $0 \leq u_k \leq 1$, and, in general, each u_k can be expressed as a nonlinear combination of the remaining u_j ; i.e.,

$$u_k = u_{k0} F(u_j), \quad j \neq k$$

For most meaningful problems, the solution u_k^* (if it exists) is

$$u_{k0} \geq u_k^*$$

Furthermore, let $u_{k1} = u_{k0} F(u_{j0})$; then $u_{k1} < u_{k0}$. Since u_k is bounded, there is a sequence such that

$$|u_{k,m} - u_{k,n}| > |u_{k,m+1} - u_{k,n+1}|, \quad n > m$$

but this sequence defines a contraction mapping; i.e., let us denote the operation by $u_{k,m+1} = Tu_{k,m}$. If T is an operator having the property

$$\rho(Tu_{k,n}, Tu_{k,m}) \leq \alpha \rho(u_{k,n}, u_{k,m})$$

where $0 < \alpha < 1$, then T is called a contraction operator. This property permits the use of the following *fixed point* theorem due to Banach: If T is a contraction operator defined on a complete metric space X , then T has a unique fixed point, $x^* \in X$. (For proof, see Ref. 1.) This theorem says that a unique solution exists, and implies that the construction of an approximate solution is available by using the contraction operator; in the limit the iterative solution approaches

$$x^* = Tx^*$$

Therefore, beginning with the initial values of the element unreliabilities, $u_{i0}, i = 1, \dots, N$, the solution set u^* can be approximated as closely as desired. Numerical economy can be achieved by the following program; for a set $\{u_i\}$, first determine

$$u_{11} = u_{10} F(u_{j0}), \quad j \neq 1$$

then

$$u_{21} = u_{20} F(u_{11}, u_{k0}), \quad k \neq 1, 2, \text{ etc}$$

each time substituting the "latest" information into the independent variable set.

The preceding development has assumed no constraint upon C ; in many practical cases, it will be desired to find the global minimum (over the range). However, if there is a constraint, say $C \leq C^*$, this can be included in the solution (e.g., simplest for continuous functions is to include equality $C = C^*$; the rank of the system $u_{i+1} = Tu_i$ is reduced by one).

Another practical condition is that some of the u_j are fixed at u_{j0} (often all but one); under these conditions, the reduced system is solved (it may become linear in many cases).

An obvious generalization is that unreliability functions are usually distinctly discrete; i.e., no change in u occurs until the value of c is reached which makes a whole element available. This generalization turns the solution surface into N -dimensional polygons, and the solutions always are at vertices. Again, from the function of Eq. (1), we have the finite difference slope

$$\frac{\Delta L}{\Delta C} = 1 + M \left(\frac{\Delta U}{\Delta C} \right)$$

Assuming that each u is non-increasing, and further, $\Delta u_i > \Delta u_{i+m}$, $m \geq 1$, then a minimum exists. The solution can be found iteratively by proceeding in the u_j -direction until a turning point is reached (i.e., a point at which $\Delta L / \Delta C$ goes from negative to positive), then proceeding in another direction, say u_k . The number of steps will usually be few in practical cases.

Reference

1. Liusternik, L., and Sobolev, B., *Elements of Functional Analysis*. Frederick Ungar Publishing Co., Inc., New York, 1961.

VI. Multiple-Mission Telemetry System

A. Introduction, W. S. Baumgartner

The Jet Propulsion Laboratory has been recovering telemetry from space vehicles for ten years. Over this period, wide ranges of subcarrier frequencies, data rates, and types of modulation have been used. Each project has selected parameters for its telemetry requirements, and, because each was different, the ground demodulation equipment has differed. This has necessitated equipping ground stations assigned to a particular mission with "mission-dependent" demodulation equipment which has varied from 5 to 20 racks per station. While providing maximum design freedom, this system was costly in equipment, installation time, and training time. It also limited DSN flexibility, since only stations having the mission-dependent equipment could support that mission.

The *Mariner IV*, *Pioneer*, *Lunar Orbiter*, *Apollo*, *Mariner Venus 67*, *Mariner Mars 1969*, and *Voyager* spacecraft use, or will use, PCM-PM-PM¹ as the telemetry mode. Therefore, this mode is evolving into a standard for deep

space communications. This project recognizes this mode of telemetry transmission as a standard and provides general-purpose mission-independent equipment capable of meeting the requirements of all these projects at each DSN station. The universal nature of this equipment makes it a long-term installation to handle engineering and medium rate science telemetry.

The multiple mission telemetry system (MMTS) consists of a subcarrier demodulation loop which accepts 10-MHz signals from the receiver, phase-modulated with one or more square wave subcarriers which, in turn, are phase-modulated with data. The demodulation is accomplished in a manner which does not lose the power in the square wave harmonics. Bit synchronization is accomplished in a computer operating in conjunction with special-purpose digital equipment by using the transitions in the telemetry data stream. To change from one spacecraft to another, it is only necessary to change the computer program and reset the subcarrier VCO, certain bandwidths, and time constants. Ultimately, this will all be accomplished from the computer program.

¹Pulse code modulated—phase modulated—phase modulated.

A separate channel for subcarrier and bit synchronization is not required from the spacecraft; therefore, this power may be used to increase the power in the information channels. A fixed-phase relationship between subcarrier and bit timing is no longer required. This removes the requirement for rigid bit timing in the various spacecraft data sources and results in simplification of the spacecraft subsystem interfaces. This simplification of spacecraft electronics is expected to increase reliability.

As an additional feature the system also includes dual back-up data recordings for recovery of data in the event of equipment malfunction. Each multiple mission telemetry system can handle one subcarrier. Two systems will be installed at each station, but dual channel operation will be possible only if two computers are available. The entire system will consist of two racks installed with the receiver exciter subsystem housing two subcarrier demodulators and two racks installed with the telemetry and command processor housing digital equipment. The existing SDS 920 computers will be used. One additional rack of signal simulation or test equipment will be provided to each station.

As originally installed, the system will handle the following signals:

Function	Subcarrier	Data rate
Engineering telemetry	20 to 40 kHz	8 to 512 bits/s
Nonvideo science data	40 to 80 kHz	32 to 512 bits/s

These boundaries have been chosen to meet operating and design requirements. By keeping all subcarriers higher than 20 kHz the problem of carrier loop acquisition is simplified. The upper limit of 512 bits/s represents 66% utilization of the SDS 920 computer for bit synchronization, detection, and signal-to-noise computation. The lower limit of 8 bits/s on engineering telemetry represents the lowest bit rate at which adequate predetection bandwidths can be achieved at the standard IF frequency. There is an additional constraint at low data rates related to loop bandwidth versus dynamic capability. The lower limit of 32 bits/s on nonvideo science data represents the lowest bit rate at which the required loop bandwidth can accommodate the doppler on an 80-kHz subcarrier.

In addition to the above requirements, the subcarrier demodulation loop only is designed to handle video science data at subcarriers of 80 to 1000 kHz and rates of 512 bits to 100 kbits/s. This is to provide additional capacity for future high rate requirements. There is an additional con-

sideration to be observed in selecting subcarriers. Exact subharmonics of the 10-MHz intermediate frequency (such as 1000, 100, 50 kHz, etc.) should be avoided. A low bit-rate option, not scheduled for installation at this time, will provide for bit rates down to 1 bit/s.

The first project to use the new system will be *Mariner Mars 1969*. To support this project, a DSN readiness date of September 1, 1968 has been established. By this date, five stations will be equipped, checked out, and operational. The first complete system will be delivered to the Flight Project/Tracking and Data Acquisition Interface Laboratory at JPL in February, 1968 for use in spacecraft check-out.

This article will present a complete system description, a set of specifications, a system analysis, equipment and software descriptions, and results of preliminary tests to date. Future articles will report any design modifications.

B. System Description, W. Frey

1. Equipment Functional Description

Figure 1 shows a functional block diagram of the (MMTS) equipment as it will be implemented into the DSIF. The system consists of three major hardware elements: (1) Subcarrier demodulator assembly (SDA), which tracks the received subcarrier and extracts the telemetry data stream from the subcarrier and 10-MHz carrier input from the receiver-exciter (RE) subsystem. The subcarrier demodulator assembly will form a part of the existing (RE) subsystem when it is implemented into the DSIF. (2) Computer and peripheral digital equipment assembly which accepts the data stream output from the subcarrier demodulator assembly and: (a) generates a clock at the data rate frequency and in phase with the telemetry data transitions (bit synchronization), (b) detects the telemetry data bits at each data clock time (bit detection), (c) searches for telemetry data frame synchronization, and (d) decommutates, formats, and outputs the telemetry data in real-time to the ground communications system (GCS) for transmission to the SFOF for further processing and evaluation. The computer and peripheral digital equipment will form a part of the telemetry and command data-handling subsystem (TCD) when it is implemented into the DSIF and will be known as the telemetry and command processor (TCP) Phase II-C configuration. (3) A rack of test equipment which provides test signals which are used to evaluate the performance of the MMTS.

Detailed functional descriptions of each of the three major hardware elements follow.

a. Subcarrier demodulator assembly. The subcarrier demodulator assembly receives an input from the RE subsystem of a 10-MHz carrier frequency which is phase-modulated by a square wave subcarrier and binary telemetry data generated in the spacecraft. The output of the SDA is an extracted data stream which is sent to the computer and digital equipment for bit synchronization and detection. Figure 1 contains a functional diagram of the SDA. The SDA removes the subcarrier and the 10-MHz IF carrier, in that order, from the input signal to provide the data stream output. The upper portion of the block diagram shows the path of the data stream, and the lower portion is a phase-locked loop which tracks the subcarrier. A local estimate of the data stream is injected in the subcarrier phase-locked loop to remove the modulation by the data on loop phase-error signal.

The input signal (point 1), consisting of 10 MHz modulated with the square wave subcarrier and data plus receiver noise, is applied to two phase switches. When the loop is in lock, the upper phase switch is switched by a square wave that is the local estimate of a subcarrier which is in phase and frequency agreement with the input subcarrier. The lower phase switch is switched by a local subcarrier estimate that is 90 deg out of phase with the input subcarrier. The bandwidth of the phase switches allows the SDA to utilize the power contained in the square wave harmonics of the subcarrier as well as the fundamental. The upper phase switch functions as a 10-MHz amplitude detector when the loop is locked with a 10-MHz output switched 180 deg in phase with the data stream. The lower phase switch functions as a phase detector and provides a signal proportional to loop phase error. This signal is also switched 180 deg in phase with the data.

Since the subcarrier is removed from the input signal first, the predetection filtering bandwidth is required to be only wide enough to pass the data and is centered at 10 MHz. This offers the advantage of relatively narrow band filtering and reduces the possibility of noise overloading of the 10-MHz coherent amplitude detectors, which follow the IF filters.

The upper signal (point 2) is synchronously detected with a 10-MHz reference signal from the RE subsystem which is phase coherent with the 10-MHz telemetry input. The output of this coherent amplitude detector (point 3) is a dc level which is switched plus or minus

with the data. This extracted data stream is: (1) amplified, integrated, and sent to the computer equipment for bit synchronization and detection (point 10), and (2) sent to a postdetection filter and limiter (point 11) to provide a local strong signal estimate of the data. The post-detection filter reduces the amount of noise on the data (i.e., optimizes signal-to-noise ratio) at the input to the limiter. The output of the limiter (point 4) is a strong signal switching plus and minus one with the data. The local data estimate modulates the 10-MHz reference (point 5). This signal is then multiplied with the output of the 90 deg shifted predetection filter (point 6) in a 10-MHz coherent amplitude detector. The multiplication removes the effect of the data phase switching on the loop phase-error signal and provides an output (point 7) of a valid S-curve that is proportional to loop phase error over $\pm\pi/2$ rad. This signal is then narrow-band filtered (point 8) to remove undesired frequency terms and noise. The dc loop phase-error signal is used to drive a VCO to correct the frequency and phase of preselected subcarrier frequency on the synthesizer. The output of the VCO-synthesizer provides a signal that is in phase and frequency agreement with input subcarrier frequency from the spacecraft. This local estimate of spacecraft subcarrier is applied to the signal shaper and quadrature generator to provide 0- and 90-deg phase square wave signals to the phase switches.

The dashed lines on the functional block diagram of the SDA represent the option that will be installed at a later date to allow the SDA to handle low data rates (i.e., 1 bit/s to 8 bits/s). This option introduces a lower intermediate carrier frequency of 100 kHz. The new IF allows the use of very narrow band filters to pass the low data rates centered at 100 kHz rather than 10 MHz. The narrow filtering is more practical to achieve at 100 kHz than at 10 MHz. Other than the lower IF filtering, the loop in the low data rate option operates in an identical manner to the higher data rates previously described.

An additional input to the SDA is shown at point 9 in Fig. 1. This is a baseband input consisting of a subcarrier modulated by a data stream. This signal modulates a 10-MHz reference in the up-converter. The output of the up-converter is identical to the normal 10-MHz telemetry receiver output. This input channel is utilized when the SDA is in the backup recording playback mode or testing is performed on the MMTS equipment.

The SDA provides a loop in-and-out-of-lock lamp indicator and a meter displaying lock voltage. These indications assist the operator in loop acquisition and provide

an output to the digital instrumentation subsystem for monitoring purposes.

A detailed equipment description of SDA hardware is contained in Sect. E-1.

b. Computer and digital equipment

General description. The computer and digital equipment accepts an input of the integrated binary telemetry data stream from the subcarrier demodulator assembly. The primary function of this equipment is to perform bit synchronization and bit detection of the telemetry data stream. In addition, data frame synchronization, data decommutation (engineering telemetry only) and formatting of the telemetry data for output are accomplished in real-time by the computer. The following outputs from computer and digital equipment are provided:

- (1) Formatted telemetry data to the ground communications system. Data is transmitted in real-time on the high-speed data line and teletype lines to the SFOF for central processing and evaluation.
- (2) A digital magnetic tape recording of the formatted telemetry data for back-up in case of ground communications system failure and for historical record.
- (3) A teletype output of MMTS status and performance together with selected spacecraft engineering measurements are transmitted to the station monitor equipment.

Figure 1 contains a functional block diagram of the computer and digital equipment. The computer and digital equipment combine operations executed by a program in the computer. The digital hardware is located external to the computer but under the control of the computer software.

Descriptions of the computer and digital equipment functions of input of data, bit detection and synchronization, and data frame synchronization, decommutation, and formatting follow in this section of the report.

Data stream input. In performing the bit synchronization and detection functions, it is required that the computer sample the data stream output of the subcarrier demodulator assembly. To minimize the effects of noise on the data stream, the input waveform is integrated over a bit time interval before it is sampled by the computer. This input of the data into the computer is accomplished by use of: (1) data integrator filter (located in the SDA),

(2) an analog-to-digital converter (A/DC), and (3) software operating on the input data in the computer. This combination of hardware and software forms an integrate and dump circuit.

Although, for functional clarity, three A/DCs are shown in Fig. 1, in reality only one A/DC is used. It is commanded to sample at three selected times (early, late, and bit timing) during a telemetry bit time interval. The relationship of the sample times is fixed by the timing generator. Once data is integrated over a bit time interval, a command is generated to sample the A/DC which transforms the integrated input voltage to a positive or negative digital value. The command pulse also at this time generates an interrupt to the computer. The interrupted computer then executes software subroutines which read into the computer the digital value of the voltage from the A/DC.

Since the data integrator is not reset at any time, integration is performed over a period of time with an arbitrary initial value. The effect of the integrator time constant and the initial value of the integrator must be taken into consideration in determining the actual value of the sample taken. This is accomplished by the computer program which reduces current sample by the amount of the previous sample (which has been stored in the computer memory) multiplied by decay on the previous sample caused by the integrator time constant over the integration interval. The result is a value that is a function of only the integration of the change of integrator input voltage from previous sample time to the present time and is independent of the initial value of the integrator.

The early and late time inputs are utilized in the bit synchronization loop, and the bit time input is required for bit detection.

Bit detection. Bit detection is accomplished by the computer program operating on the dumped input of the data stream which is sampled by the bit timing command (point 12). A new value of the data is transferred into the computer at the rate of the transmitted data from the spacecraft. The integration, therefore, is over the bit time interval for each input. The software tests the sign of each dumped data input. If the data is positive, a binary *one* is stored in the data table; conversely, if the data is negative, a binary *zero* is stored in the data table (point 13). In order to optimize the probability of correct detection of the data, the integrate and dump input must

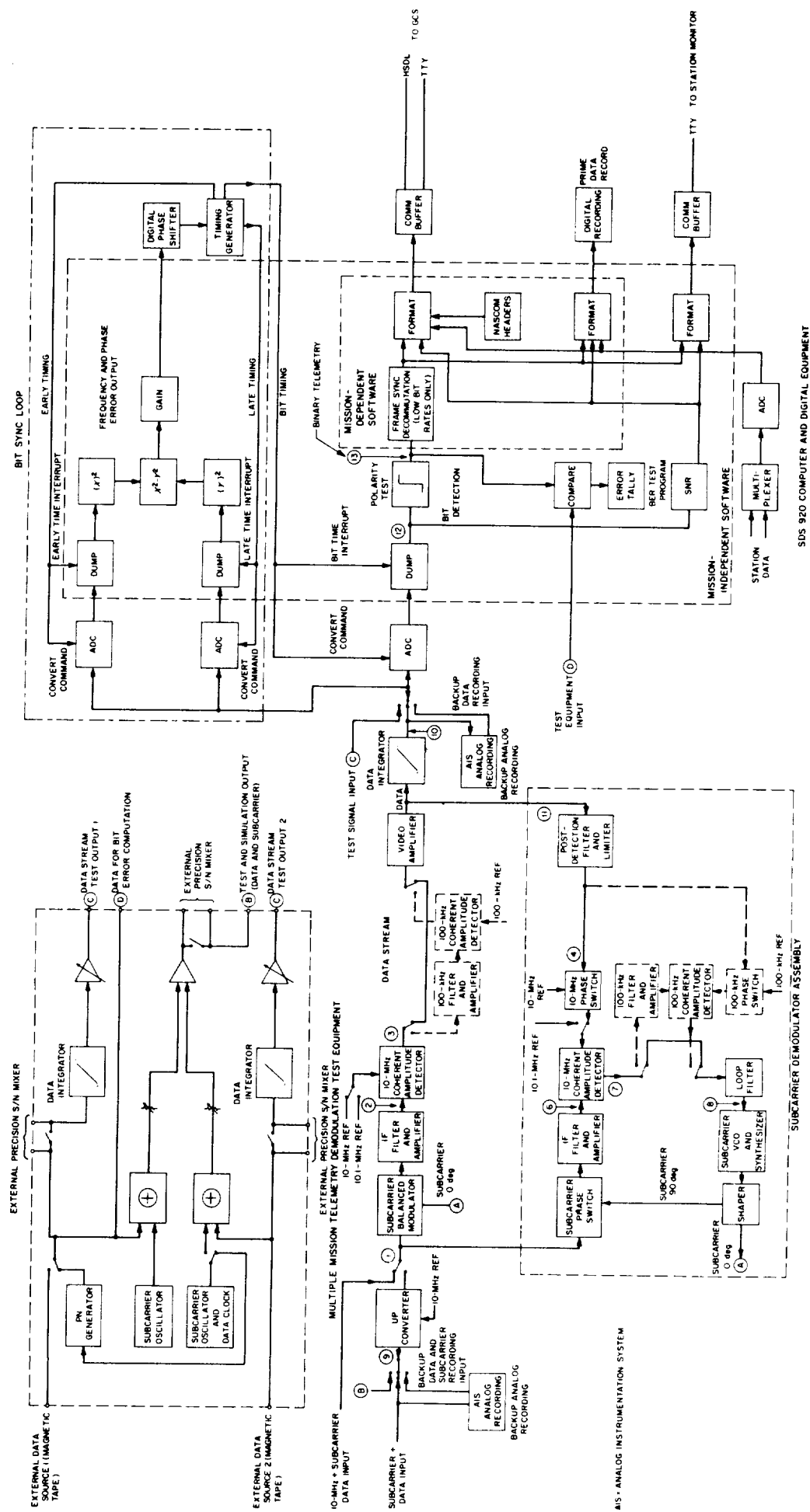


Fig. 1. Multiple-mission telemetry system functional block diagram

produce the maximum or minimum value of the integration of each data bit possible under the prevailing signal-to-noise conditions. To accomplish this, the data stream must be sampled at the same frequency that the data is generated in the spacecraft, and it must be in synchronization (phase) with the clock that originates the data in the spacecraft. When this condition occurs, each bit is integrated over the full bit interval without possibility of any data transitions occurring in the interval to reduce the absolute value of the integral. Therefore, the success of the bit detection depends on the frequency and phase of the bit timing command being identical to the data clock in the spacecraft. The bit timing command is produced in the MMTS by the bit synchronization process.

Bit synchronization. The primary function of bit synchronization is to provide the bit detection hardware and software with a clock which is in phase and frequency with the data clock in the spacecraft. Since the spacecraft data clock is not transmitted to the ground stations, the MMTS must construct a local estimate of the spacecraft data clock. The bit synchronization uses a delay lock loop (analyzed in Section C-4) which, based on the transitions in the incoming data stream, tracks the frequency and phase of the spacecraft data clock. Bit synchronization in the MMTS is accomplished by a combination of computer software and external digital equipment which is under control of the software.

The bit synchronization loop operates by: (1) sampling the early and late integrals of the input data stream, (2) squaring the two integrals, (3) differencing the two squares to obtain a phase-error correction signal, (4) controlling the frequency and phase of the digital phase shifter, and (5) generating the early, late, and bit timing commands. (See Fig. 1, bit synchronization loop.)

The early integral is the integration of the input data stream from $\frac{1}{4}$ of a bit time before the local estimate of the data clock (bit timing command) to $\frac{3}{4}$ of a bit time after the estimated data clock. The late integral is the integration of the data stream from $\frac{3}{4}$ of a bit time before the estimated data clock to $\frac{1}{4}$ of a bit time after the estimated data clock. The sign of the two integrals is removed by squaring to enable the bit sync loop to be independent of both the change of the sign in the integrals due to transitions in the data and the direction of the transitions (i.e., binary 1 to 0 or 0 to 1) in determining phase error. By differencing the squares of the two integrals a loop phase-error signal is obtained. The value of this difference will be zero (neglecting the effects of noise on the data stream) when: (1) no data transitions have occurred during the

early and late integrals, or (2) a data transition occurred at the time of the local estimate of the spacecraft data clock (bit time command). Thus, a phase-error value is not generated when transitions do not appear in the data or the local clock estimate is synchronous with the spacecraft clock. When the difference of the two squares is not zero, there is a phase error in the local estimate of the data clock. The sign of the difference corresponds to the minimum direction to shift the phase of the local estimate of the data clock to correct the phase error. The magnitude of the difference is proportional to the amount of phase shift necessary to correct the phase error.

The phase error signal is scaled to an equivalent number of microseconds of required phase shift. This positive, negative, or zero value is added to the basic data bit interval time in microseconds. The data bit duration (data rate frequency) is *a priori* information supplied to the computer program by the equipment operator at the beginning of the tracking pass. The combined value is then output by the computer to the digital phase shifter.

The digital phase shifter (DPS) performs the function of an oscillator that is programmable in frequency and phase. The DPS accepts an output from the computer consisting of the spacecraft data bit time duration combined with the amount of phase correction in microseconds necessary to bring the local data clock (bit timing command) estimate in coherence with the spacecraft data clock. This value is counted down at a 1-MHz rate by the DPS. When zero count is detected, the DPS is ready to accept new frequency and phase information from the computer. During the countdown, four pulses are output by the DPS to the timing generator. These four pulses are spaced in one-quarter increments of the duration of the countdown. The DPS, by periodically counting down numbers that are either larger or smaller than the expected duration of a telemetry bit interval, can effect a phase shift with a resolution of $1 \mu\text{s}$ on the series of the four output pulses. When a phase shift is not necessary, the DPS simply counts down data bit duration in microseconds.

The timing generator, by utilizing steering circuitry, provides the early, late, and bit timing commands to the A/DC and the computer. These commands control the sampling times of the three integrate and dump inputs to the computer.

Thus, one bit synchronization loop is able to adjust the phase, early, and late timing commands to the point where the difference of the squares of the early and late integrals

is zero (or at least to below correction threshold) to correct the phase of the local estimate of the data clock. When this occurs, the bit timing command is coherent with the spacecraft data clock, and it is a valid signal for use by the bit detection circuit. The computation of the loop phase error and the countdown by the DPS is repeated once during each bit time to either correct the phase of the bit timing command or to maintain the existing phase.

An equipment description of the computer and digital hardware is contained in Sect. E-2.

Telemetry data-frame synchronization, formatting. All formatting and decommutation on the detected telemetry data is accomplished by the computer software. This area contains the only mission-dependent portion of the MMTS. However, since these functions are totally performed by software, no equipment modifications are required to change from one flight project to another flight project. All that will be required is that each flight project

furnish its own operational software to run in the MMTS computer.

Frame synchronization will be performed by examining the data table for the proper sequence of data bits to form the sync word as transmitted by the spacecraft. Thus, the data may be arranged in a table in an orderly sequence starting with each frame with a sync word.

Decommutation of the telemetry data is performed on the spacecraft engineering data as time allows in the computer. MMTS decommutation will extract selected measurements from the spacecraft engineering telemetry and route this information to the station monitor teletype output.

The telemetry data must be formatted for output from the computer. Formatting consists of coding or arranging the data for the various output devices, adding identification messages, and interspersing various MMTS performance indicators between data frames.

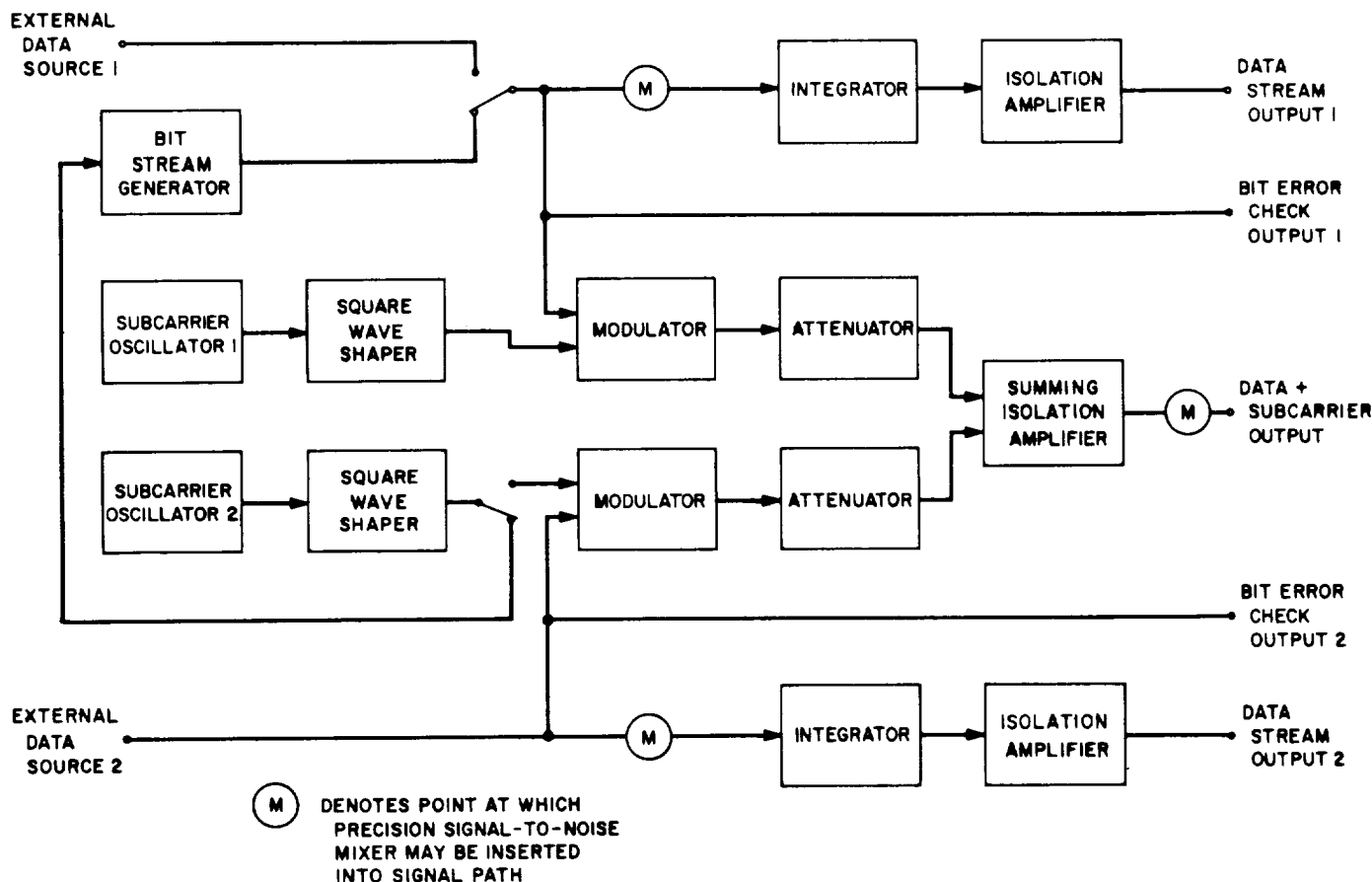


Fig. 2. MMTS test equipment block diagram

c. Test equipment. The objective of the MMTS test equipment is to provide a mission-independent set of equipment to evaluate the performance of the multiple mission telemetry equipment. A functional block diagram of the test equipment is shown in Fig. 2. The test equipment is housed in a rack that is provided to each of the DSIF stations where the MMTS has been implemented. The test equipment has been designed to allow for maximum flexibility in the testing of the MMTS equipment. Test signals provided by the equipment may be inserted into various areas of the receiver and MMTS equipment to evaluate system performance (Fig. 3). The test modes available and types of test signals provided are described in detail in the hardware description (Section E-4) of the test equipment.

Testing of the MMTS equipment consists of performing bit error tests on the telemetry data detected by the MMTS computer. Telemetry data is provided by a pseudo-random code generator located in the test equipment. This data either is integrated or modulates a test subcarrier to

provide test inputs to the computer, the subcarrier demodulator assembly, or the DSIF test transmitter. The test signal is processed by the receiver and/or the MMTS as it would be in an operational configuration supporting a flight project. The test telemetry is recovered in the bit detector in the MMTS computer. The generated test telemetry data is also routed from the test equipment directly to the computer. Each bit that is output by the code generator is then compared with the recovered detected data by a software test subroutine in the computer. The subroutine keeps track of the number of disagreements of the compared data. These errors are counted for a prescribed number of bit inputs. This tally, which is equivalent to bit error rate (BER), is printed out on the computer console typewriter at the conclusion of each test. Tests are performed for various signal-to-noise conditions and subcarrier and data rate frequencies. The bit error-rate data generated by the computer is compared to charts that contain a theoretical performance curve of the equipment to detect performance degradation. These curves plot expected bit error rate versus various signal-

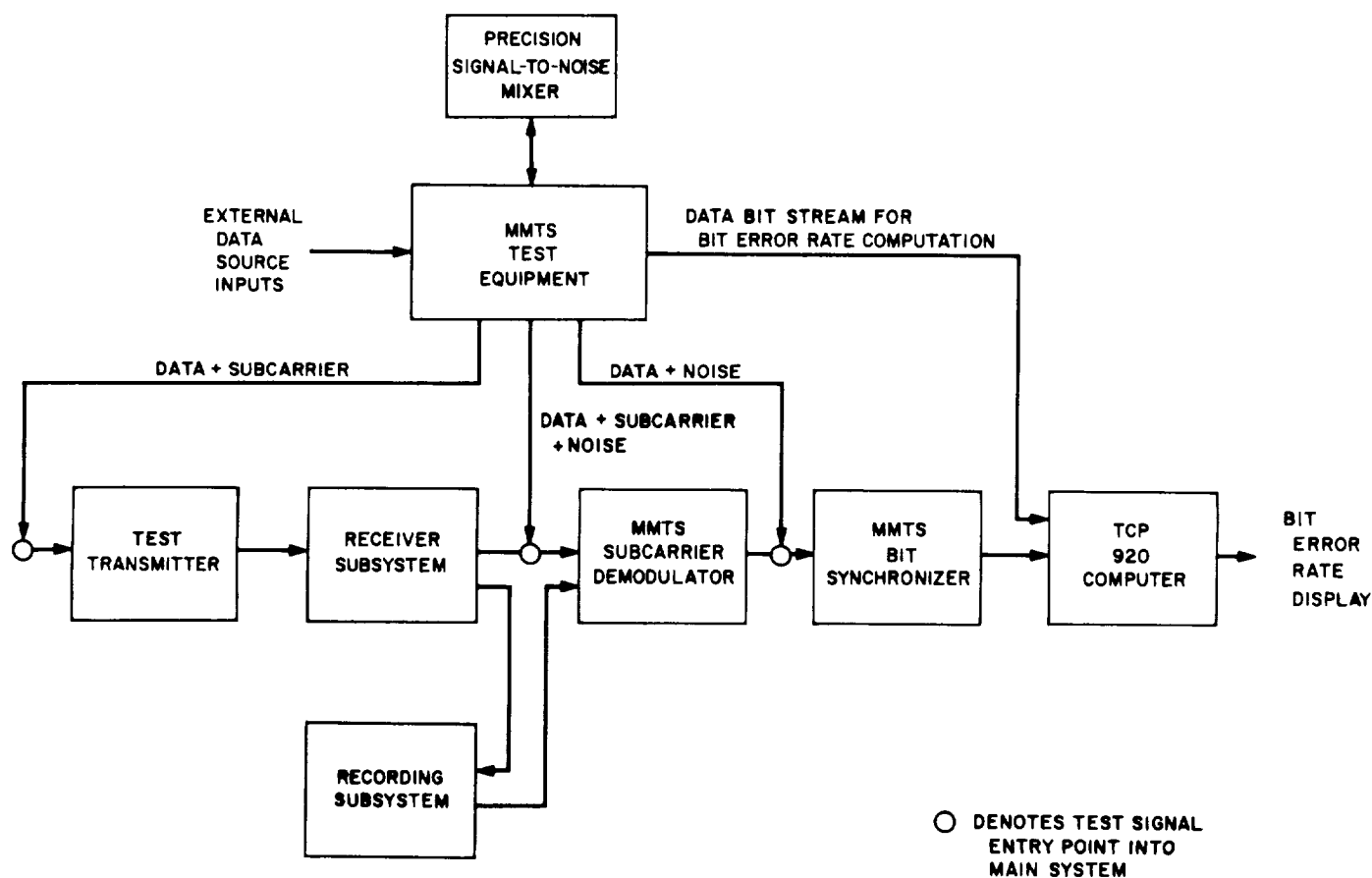


Fig. 3. Functional arrangement of test signals and equipment assemblies

to-noise conditions. The design goal of the MMTS is to allow a maximum of 0.2 of a dB performance degradation from the expected theoretical performance of the equipment over the range of signal-to-noise conditions which the MMTS will encounter in supporting the flight projects.

2. System Backup

The MMTS will have various back-up modes of operation in the event of equipment malfunction. The back-ups are provided to minimize the amount of telemetry data lost in the event of an MMTS equipment failure. Each DSIF station will be supplied with redundant channels of the subcarrier demodulator assembly and the computer and digital equipment assembly. When a flight project is operating with two subcarrier frequencies simultaneously, each channel of the MMTS will be committed to process a subcarrier and data rate. However, during periods when a single subcarrier is being transmitted from the spacecraft, the second MMTS channel serves as a back-up. When both channels are committed, or failure in both channels occurs, the following additional back-ups are available.

a. Subcarrier demodulator back-up recording. In the operational configuration of the MMTS in the net, an analog magnetic tape recording is made of the baseband output (subcarrier modulated with data) from the telemetry channel of the receiver. In the case where a failure occurs in either or both SDAs, the following back-up procedure is taken. The baseband recording is kept intact until such time as the repairs can be made to the SDA. The tape is then played back through the baseband input of the SDA. The baseband input (Fig. 1, point 9) modulates a 10-MHz reference in the up-converter. The output of the up-converter is a replica of the normal 10-MHz IF telemetry output provided by the receiver. Therefore, the tape can be played back through the entire MMTS in non-real-time to recover any of the telemetry data lost in real-time due to failures in the SDAs. A degradation of the performance of the MMTS is encountered in this mode, due to limitations in the bandwidth capability and time base instability of the tape recorder.

b. Computer and digital equipment back-up recording. In the normal operation of the MMTS, a magnetic recording is made of the data stream output of the subcarrier demodulator assembly. Should a failure occur in the computer and digital equipment, this recording is played back in non-real-time into the data stream input of the computer equipment to recover the telemetry data. No

appreciable degradation in performance is encountered in this playback mode.

c. Ground communications system back-up recording. Should a failure occur in the CCS (high-speed data line or teletype lines) which results in loss of the transmitted data, use is made of the digital magnetic tape recording of the formatted telemetry data. This recording is made in real-time at the TCP-IIC equipment. The recording may be played back through the computer and output to the CCS, when communications are restored, or it may be mailed from the station to the SFOF for off-line processing at a later date.

3. MMTS Software

A computer program must be provided to the MMTS computer in order to accomplish bit synchronization, bit detection, formatting, and the output of the telemetry data. Two categories of software will be provided to the system. The first program type is the demonstration software. The demonstration software is being written by and for the MMTS project. This program will be used in the MMTS demonstration system. The demonstration system (described in Sect. D) consists of prototype hardware which will remain at JPL and will be used to test and evaluate MMTS performance and design parameters. The demonstration program will be provided to evaluate the mission-independent software functions and assist in performing hardware tests in the demonstration system. A description of the demonstration program appears in Sect. E-3.

The second type of MMTS software is the operational software. The operational software will be supplied to the MMTS computers at the DSIF stations and will be written under the direction of the flight projects. The operational software performs both mission-independent and mission-dependent functions. The *Mariner Mars 1969* flight project program will be described in a future SPS article. The MMTS project will issue specifications on hardware restrictions and timing constraints placed on the software by the MMTS equipment to assist the flight projects in preparing the operational software.

4. MMTS Implementation into the DSIF

MMTS equipment will be implemented into the DSIF in all stations. Each station will receive two MMTS channels. Initially, the stations that will be supporting the *Mariner Mars 1969* flight projects will be implemented. The remaining stations will be implemented at a later

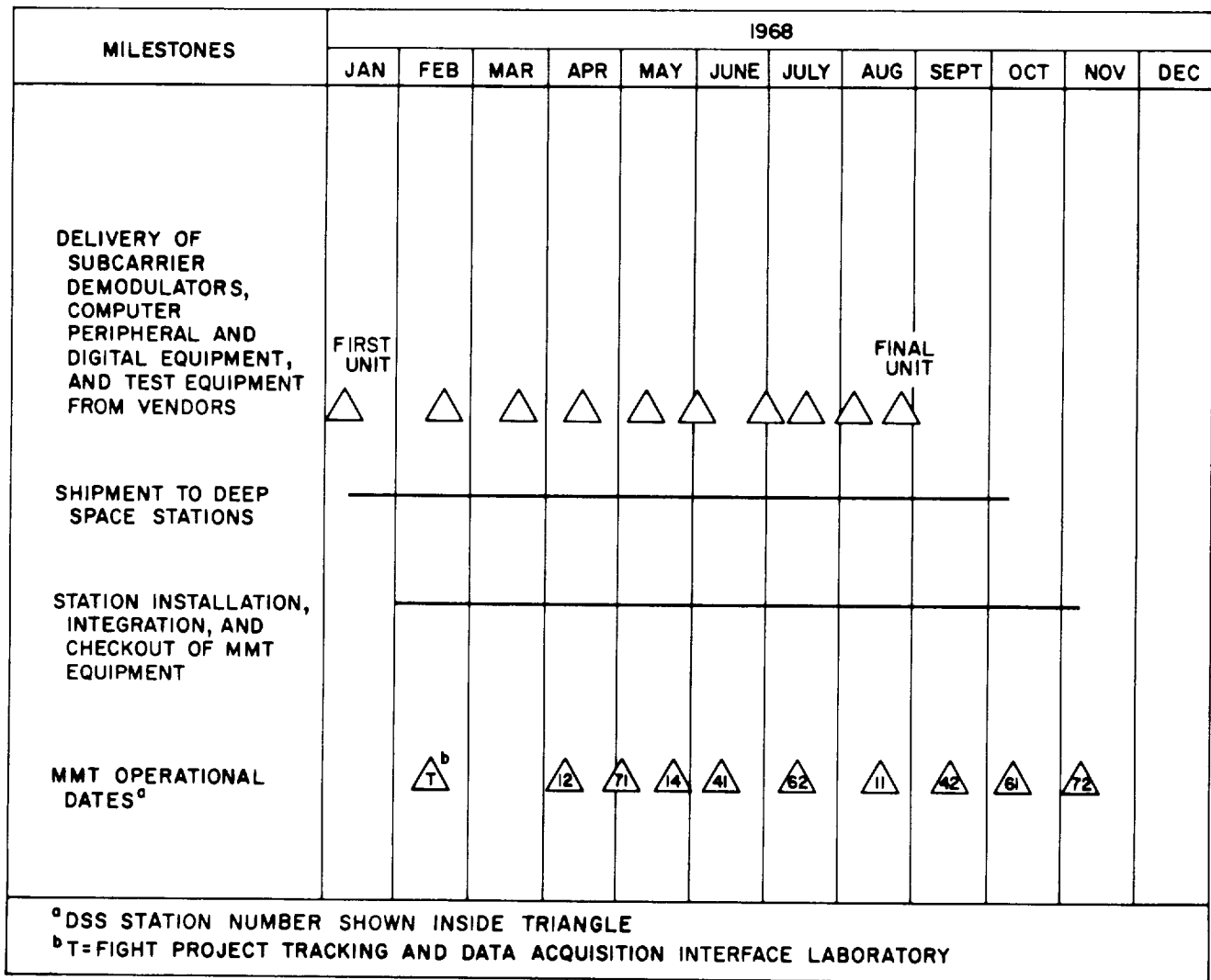


Fig. 4. MMTS implementation schedule

time. Figure 4 contains an implementation schedule showing dates for shipment, installation, checkout, and operational readiness for the MMTS equipment at each of the DSIF stations. In addition to the net systems, the project will supply a single-channel MMTS to the flight project/tracking and data acquisition interface laboratory located at JPL. The delivery of this equipment is also included in the schedule.

5. Operation of MMTS in the DSIF

a. A priori knowledge required for operation. The operation of the MMTS in the net requires *a priori* knowledge to be provided to the operators of the equipment. This required information is obtained from either the Tracking Instruction Manual which is provided to the

station for each project, or from the daily prediction information transmitted by teletype to the station from the SFOF. The operators of the SDA and the computer and digital equipment require the following information for operating the MMTS equipment:

- (1) Spacecraft subcarrier frequency.
- (2) Spacecraft telemetry data rate.
- (3) Nominal signal-to-noise ratio.
- (4) Subcarrier modulation index.
- (5) Doppler frequency rate.

b. MMTS operational procedures. The following description pertains to the procedures used by the operators of the MMTS equipment to obtain an output from the

computer of the detected and formatted telemetry data. The acquisition of the telemetry data by the MMTS is a two-step process. First, the SDA must be locked to the incoming subcarrier and secondly, the computer and digital equipment must lock up the bit synchronization loop. Operational procedures to accomplish these two steps will be described and are based on the assumption that the operators have received the required *a priori* information listed in Sect. B-5-a.

Lock of the SDA. The following steps are taken by the operator to lock the SDA to the incoming subcarrier frequency:

- (1) Verify that the RF carrier loop is in lock.
- (2) Set the SDA input attenuator based on the sub-modulation index information.
- (3) Select the spacecraft subcarrier frequency at the synthesizer.
- (4) Preset the predetection filter, postdetection filter, and the data integrator time-constant selector switch.
- (5) Set the loop bandwidth selector switch based on the signal-to-noise condition, doppler rate, and telemetry data rate.
- (6) Short the output of the loop filter.
- (7) Adjust acquisition control voltage for zero beat frequency of the dynamic phase error.
- (8) Remove the short from the output of the loop filter.

The loop will then pull into lock.

Bit synchronization loop lock acquisition. The following procedures are taken by the operator at the computer and digital equipment to obtain bit synchronization lock:

- (1) Verify that proper patch panel configuration is being used to input data signals from the SDA.
- (2) Load the computer with MMTS operational program.
- (3) Input to the computer values of nominal signal-to-noise ratio and telemetry bit rate. Input is either by paper tape or via computer typewriter.

Once the operator has provided inputs of signal-to-noise ratio and data rate, the remaining portion of the bit synchronization process is automatic and under control of the software. The operator is informed by the program

when acquisition is complete via a message typed out on the computer typewriter.

c. MMTS performance monitoring. After the acquisition phase is complete and the subcarrier and bit synchronization loops are in lock, information is provided by the MMTS to the station monitoring computer to evaluate performance and verify proper configuration. The following indicators are provided:

- (1) Subcarrier demodulator assembly input switch setting.
- (2) SDA predetection filter, postdetection filter, and data integrator switch setting.
- (3) SDA loop bandwidth switch setting.
- (4) SDA output switch setting.
- (5) SDA loop static phase error (SPE)—analog signal.
- (6) SDA loop dynamic phase error (DPE)—analog signal.
- (7) SDA acquisition voltage value—analog signal.
- (8) SDA VCO—synthesizer frequency. (This output must be counted external to the SDA in order to be monitored.)
- (9) SDA data rate option (medium or low).
- (10) SDA in-out lock status.
- (11) Signal-to-noise ratio of the telemetry data stream.

(An estimate of the signal-to-noise ratio of the telemetry data stream is calculated by the MMTS computer. This information is transmitted by the MMTS computer to station monitor equipment. The station monitor computer compares the calculated signal-to-noise ratio to the expected nominal signal-to-noise ratio. If these two numbers agree by a specified tolerance, the performance of the MMTS is considered good. Should the number disagree by more than the specified tolerance, the station monitor will provide an alarm indication of unacceptable performance of the MMTS.)

6. MMTS Testing

The MMTS project is currently in the design and development phase. During this period, it is necessary to verify that the hardware performance meets the design and analysis criteria. To conform to this requirement, a laboratory prototype MMTS will be provided. This equipment will be known as the "demonstration system."

Demonstration software will also be supplied by the project to assist in the evaluation of the hardware performance. A description of the demonstration system verification testing is contained in Section D of this article. Knowledge gained by the demonstration system testing will result in improvements and refinements in the MMTS equipment design before it is implemented to the DSIF.

The first operational MMTS which conforms to the final design will be provided to the new JPL Flight Project/Tracking and Data Acquisition Interface Laboratory. The function of this facility will be to demonstrate telecommunications compatibility of the spacecraft, DSIF ground equipment, ground communications system, and the SFOF. The MMTS will undergo compatibility testing with the existing DSIF ground equipment and the total telecommunications link. This facility will also provide a simulation of the DSIF environment for checkout of the flight project operational software.

The MMTS equipment implemented into the DSIF will be subjected to extensive testing when it is installed and becomes operational. Testing will continue throughout the useful life of the equipment.

a. Installation integration testing. The testing of the MMTS at the time of installation in the DSIF stations will verify proper interfaces with other subsystems in the station and establish that the MMTS is operating to the required design goals. The criteria and procedures for this testing will be originated by the MMTS project.

b. Postinstallation testing. Once installed and operational, the MMTS will undergo the following types of tests:

DSN compatibility testing. For each flight project that the MMTS supports, requirements will exist for compatibility testing. The purpose of this testing is to demonstrate hardware and operational software compatibility of the DSIF, the ground communications system, and the SFOF. Verification of proper MMTS performance and operator training, under simulated mission conditions, will be obtained in these tests. The compatibility tests are performed prior to the launch of a spacecraft and are generated by the DSN project engineer for the flight project.

Performance evaluation testing. This test is performed periodically on the MMTS to verify that the equipment is operating properly and has not suffered any degrada-

tion of performance. These tests will be defined by the MMTS project.

Configuration verification testing. This test is performed on the DSIF station prior to each spacecraft launch to verify that the station (including the MMTS) is in the proper configuration to support the flight project. These tests are originated by the operations engineering group in the DSIF.

Countdown tests. Tests will be performed on the MMTS during the station countdown prior to tracking pass. These tests will provide a daily evaluation of the performance of the MMTS. These tests are defined by the DSIF station managers.

C. System Performance and Analysis,

M. H. Brockman, R. W. Burt, J. W. Layland, and
G. M. Munson

1. Introduction, G. M. Munson and R. W. Burt

This section is divided into three parts. First is a general discussion of the telemetry system bit-error rate performance which is contained in Sect. 2. The other two parts are detailed examinations of the performance of the subcarrier demodulator and the bit-synchronization loop.

An analysis of the subcarrier demodulator is presented in Sect. 3. The first portion of this analysis is a development of a linear model. Design curves are presented relating loop phase error to ST_B/N_0 for various loop bandwidths. Then the parameters associated with low- and medium-rate telemetry are applied to the model.

Section 4 contains an analysis of the bit-synchronization loop. Models for first- and second-order loops are examined, and the expected value and variance of the bit-timing error are derived. The effect of the bit-timing jitter is determined in terms of degradation of ST_B/N_0 . Initial acquisition requires a special procedure. A discussion of this procedure is included. The effects of nonlinearities of the loop are also examined.

2. MMTS Bit Error-Rate Performance

The performance of a digital telemetry receiver is judged by the bit-error rate of the output bit stream, given a received signal power. The output bit-error rate of the MMTS depends on four fundamental parameters in addition to the input sideband signal-to-noise energy ratio in a bit period. These parameters become evident when the simplified block diagram of the system as shown in Fig. 5 is examined.

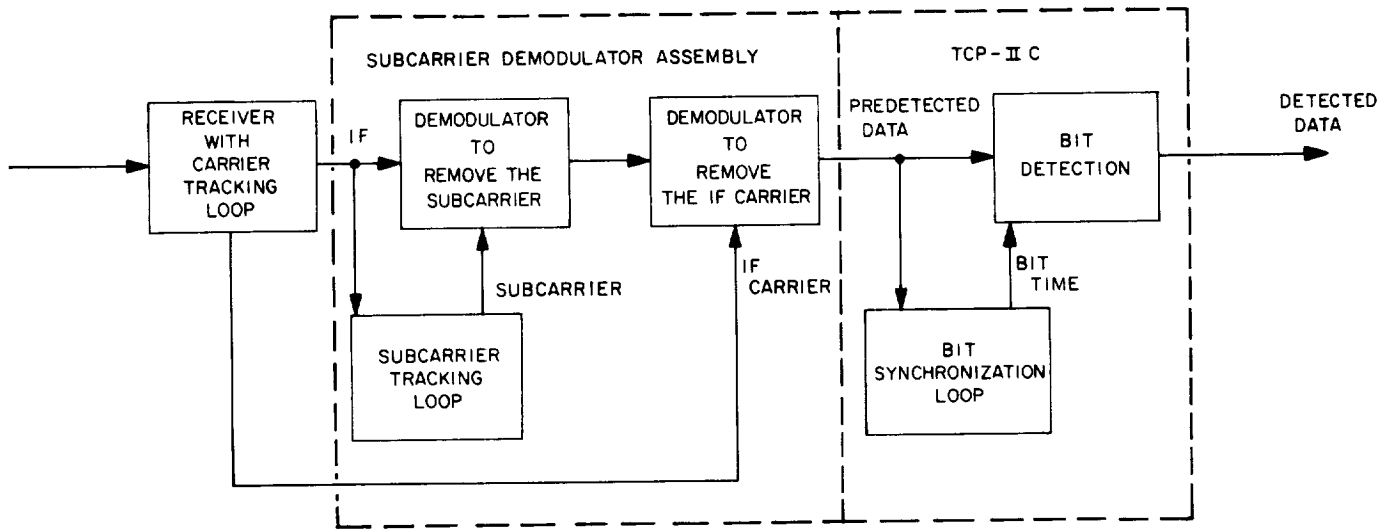


Fig. 5. Simplified block diagram of SDA and TCP-II C

a. The general equation. The general equation for effective sideband signal-to-noise energy ratio is given in Eq. (1).

$$R = \frac{ST_B}{N_0} (\alpha) (\beta) (\gamma) (\delta) \quad (1)$$

where

R = effective sideband signal-to-noise energy ratio per bit.

$\frac{ST_B}{N_0}$ = input sideband signal-to-noise energy ratio per bit.

α = degradation caused by the IF reference error.

β = degradation caused by the subcarrier reference error.

γ = degradation caused by the bit synchronization error.

δ = degradation caused by the bit detection process.

The flight project controls the α parameter by the design of the radio link and the modulation index. A design goal has been established for each of the other three parameters. This goal is 0.1 dB maximum degradation when the probability of bit error for the output bit stream is 0.1. The system will degrade slowly as ST_B/N_0 decreases. The point at which improving signal-to-noise energy ratio does not improve the bit error rate has not been determined at this time.

b. IF reference error α . The phase error between the IF carrier signal and the IF carrier reference results in a degradation of the effective ST_B/N_0 . The degree of degradation may be determined with methods developed by Lindsey in SPS 37-45, Vol. IV, pp. 276-282, using the received signal level, modulation index, and receiver characteristics. The receiver's carrier loop bandwidth is much larger than subcarrier loop bandwidth. This minimizes interaction between the loops and permits usage of Lindsey's analysis.

c. Subcarrier reference error β . The reduction of effective ST_B/N_0 due to the subcarrier phase is caused by two types of phase error. A static error occurs due to doppler and doppler rate tracking. A dynamic phase error occurs due to receiver and oscillator noise. At low values of ST_B/N_0 , the dynamic phase error is the more significant of the two. An analysis of the subcarrier demodulator performance is presented in Sect. C-3. An expansion of this analysis (to be published in a future SPS) will show that

$$\beta = 1 - \left(\frac{2}{\pi} \right)^{3/2} \sigma_{\phi_{n_{sc}}}$$

where $\sigma_{\phi_{n_{sc}}}$ = rms phase noise error in the subcarrier tracking loop and $3 \sigma_{\phi_{n_{sc}}} < \pi/2$ rad.

d. Bit synchronization error γ . The bit synchronization error term γ modifies the input sideband signal-to-noise energy ratio by accounting for errors in estimated transition time. This term is dependent upon the received bit stream. If a transition does not occur, no degradation

results. If a transition does occur, the probability of correct detection is reduced.

For a bit stream which has a probability of transition of approximately 0.5, the degradation of ST_B/N_0 is

$$\gamma = \frac{1}{2} + \frac{1}{2} \int_{-\frac{1}{2}}^{\frac{1}{2}} p(\tau) [1 - 2|\tau|]^2 d\tau$$

where τ is the error between estimated and actual transition time, and $p(\tau)$ is the probability density function of τ , the timing error.

The problems of bit synchronization and the effects of bit error rate are discussed in part 4 of this section.

e. Bit-detection error δ . At this time, the degradation caused by the bit-detection process δ has not been completely analyzed. Initial examinations indicate this degradation will be small with respect to the other parameters.

3. MMTS Subcarrier Demodulator, M. H. Brockman

a. General analysis

Functional description. Figure 6 is a functional block diagram for the MMTS subcarrier demodulator. The input signal is an RF signal at the IF frequency of the DSIF receiver. The DSIF receiver phase tracks the received carrier and heterodynes it to the IF frequency at a fixed phase. The received signal contains telemetry data in the form of a binary waveform which biphase modulates a square-wave subcarrier. The modulated subcarrier,

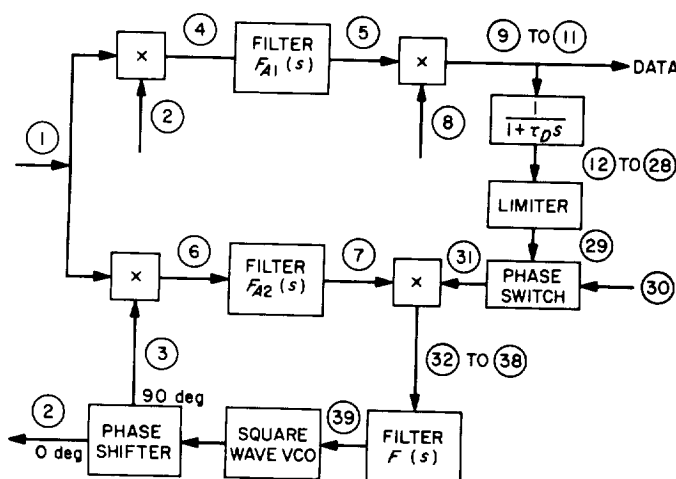


Fig. 6. Telemetry subcarrier demodulator functional block diagram

which is also a binary waveform, in turn phase modulates the carrier. The purpose of the MMTS subcarrier demodulator is to recover the original binary telemetry waveform by synchronously demodulating both the carrier and the subcarrier. The DSIF receiver provides a reference signal at 10 MHz to demodulate the carrier. The reference signal to demodulate the subcarrier is provided by the MMTS demodulator itself, a portion of which acts as a phase-locked loop to track the subcarrier. Both demodulation processes take place in the upper channel of Fig. 6.

For circuitry reasons associated with the need to accommodate a wide range of subcarrier frequencies, the subcarrier demodulation is performed first. The output of the upper channel is the recovered binary waveform which is sent to another part of the overall system for detection. The output waveform is also filtered and limited to provide an estimate of the binary waveform (the recovered waveform is typically contaminated with noise and not strictly binary) that is used in the lower channel. The lower channel operating with the filter and VCO forms the basic subcarrier tracking loop. However, since the original telemetry waveform biphase modulates the subcarrier and thus inverts it whenever the telemetry waveform is negative, the subcarrier tracking loop is trying to track a wave which is inverted part of the time (ideally 50% of the time). The estimate of the telemetry waveform produced by filtering and limiting the output of the upper channel is injected into the tracking loop by modulating the reference of the 10-MHz synchronous demodulator. This has the effect of reinverting the subcarrier, although it actually acts on the error signal in the loop.

Predemodulation signal and noise. In the following simplified analysis, refer to the block diagram shown in Fig. 6.

Assumption. The performance of the various elements of the demodulator are considered ideal, and circuit performance imperfections are not considered. The effect of such imperfections will be considered in a later report. It is also assumed that the RF carrier received from the spacecraft is a spectral line or, alternately, that the phase instability of the spacecraft RF carrier is such that the DSIF RF carrier phase-locked loop can track this phase instability with negligible phase error. In addition, the waveform of the received telemetry subcarrier is assumed to be a perfect square wave.

The input signal is an RF signal (at IF frequency f_2 Hz or ω_2 rad/s) phase modulated with a square wave telemetry subcarrier (ω_{sc}) which is, in turn, biphase-modulated with the data $m(t)$.

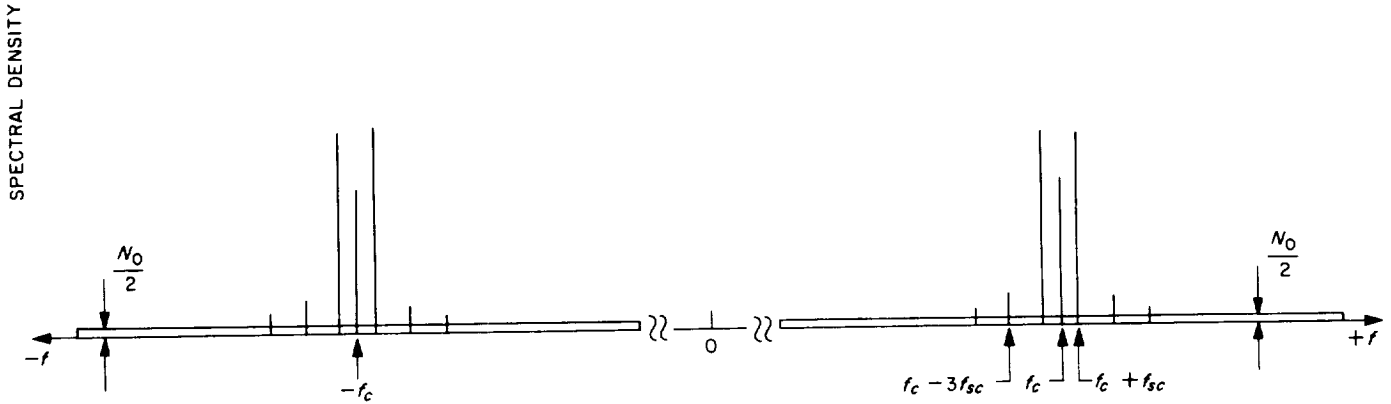


Fig. 7. Spectral power density for input signal to subcarrier demodulator

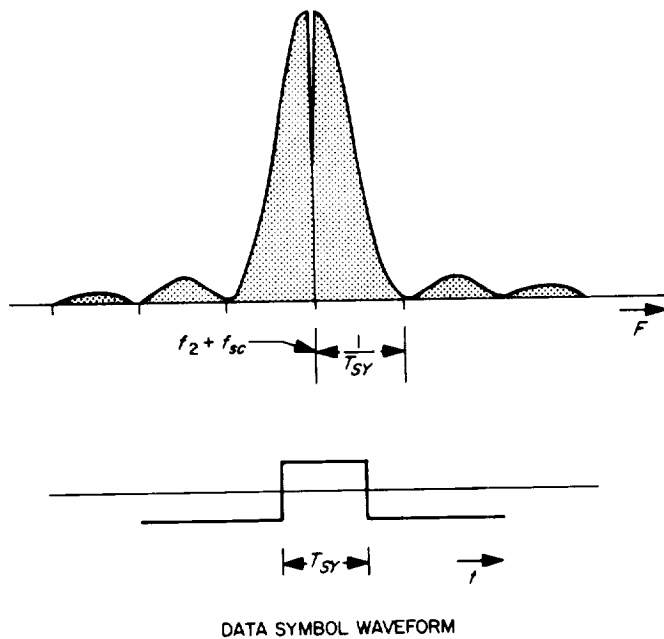


Fig. 8. Data power spectrum about subcarrier fundamental

$$(2)^{1/2} A \cos [\omega_2 t + (m(t) \times m_{ps} \times \cos(\omega_{sc} t + \theta))] + n_2(t) \quad (1a)$$

where m_{ps} is the peak phase-modulation index in radians (due to telemetry), and $m(t)$ is plus or minus 1, depending on the data. The term θ is the input telemetry subcarrier phase, which is considered as nontime varying in this simplified analysis. The term $n_2(t)$ represents input receiver noise (Gaussian and white) for the receiver bandwidth at this point in the system which has a double-sided noise spectral density of $N_0/2$. $N_0/2 = \frac{1}{2}(k \times T \times 1)$ W/Hz, where k is Boltzmann's constant, 1.38×10^{-23} J/°K, and T is the equivalent noise temperature of the

receiving system. Total input signal power is A^2 , where $A \ll 1$ (an impedance of unity is assumed to simplify the expression for power).

Figure 7 shows a spectral power density representation for the input signal and noise for both positive and negative frequencies. A specific modulation index, m_{ps} , is also depicted. In general, the relative magnitude of the RF carrier and subcarrier spectral lines will change with change in modulation index. The subcarrier spectra about the RF signal at f_2 are shown as spectral lines on the scale of Fig. 7. In reality, the subcarrier fundamental spectral line and all its harmonic spectral lines consist of the power spectrum of the data $m(t)$ about them as illustrated in Fig. 8 (for $f_2 + f_{sc}$). The data power spectrum is shown as continuous, which assumes that the data changes somewhat from one data frame to the next. The envelope of the data power spectrum is determined by the square wave shape of the data symbol waveform.

Because the modulation waveform is binary, Expression (1a) can be written as

$$\underbrace{(2)^{1/2} A \cos m_{ps} \cos \omega_2 t}_{\text{carrier}} + \underbrace{(2)^{1/2} A \sin m_{ps} \times m(t) \times \cos(\omega_{sc} t + \theta) \times \sin \omega_2 t + n_2(t)}_{\text{sidebands}} \quad (1b)$$

The signals obtained from the square wave subcarrier VCO at ② and ③ may be written as

$$\cos(\omega_{sc} t + \hat{\theta}(t)) \quad (2)$$

and

$$\sin(\omega_{sc} t + \hat{\theta}(t)) \quad (3)$$

where $\hat{\theta}(t)$ is the loop estimate of θ , the subcarrier input phase. The input signal, Expression (1b), is multiplied by the square wave cosine subcarrier signal, Expression (2), to provide Expression (4):

$$(2)^{1/2} A \cos m_{ps} \cos [\omega_{sc}t + \hat{\theta}(t)] \cos \omega_2t + (2)^{1/2} A \sin m_{ps} \times m(t) \times \cos [\omega_{sc}t + \theta] \cos [\omega_{sc}t + \hat{\theta}(t)] \sin \omega_2t + n_4(t) \quad (4)$$

where the noise term $n_4(t)$ is $n_2(t)$ in Expression (1b) multiplied by $\cos [\omega_{sc}t + \theta(t)]$.

Assumption. The assumption has been made here that the relative broadening of the noise spectrum (shown in Fig. 7) due to this multiplication is small enough to be ignored. Therefore, the noise term, $n_4(t)$, at ④ in Fig. 6 has a double-sided noise spectral density of $N_0/2$ and the same total noise power as $n_2(t)$. This is a conservative assumption.

After passing through the upper predemodulation filter F_{A1} , Expression (4) becomes

$$F_{A1} \{ (2)^{1/2} A \cos m_{ps} \times \cos [\omega_{sc}t + \hat{\theta}(t)] \times \cos \omega_2t + (2)^{1/2} A \sin m_{ps} \times m(t) \times \cos [\omega_{sc}t + \theta] \times \cos [\omega_{sc}t + \hat{\theta}(t)] \sin \omega_2t \} + n_5(t). \quad (5)$$

The noise term $n_5(t)$ represents the receiver noise at the upper predemodulation filter output with a double-sided noise spectral density (positive and negative frequencies) of $N_0/2$. The ratio of noise powers represented by $n_5(t)$ and $n_2(t)$ is equal to the ratio of the noise bandwidths at ⑤ and ① in Fig. 6. The noise term $n_5(t)$ is centered about f_2 . The first term of Expression (5) would normally be removed by the predemodulation filter F_{A1} , although this is not a requirement.

The input signal, Expression (1b), is multiplied in the lower multiplier in Fig. 6 by the square wave sine subcarrier signal, Expression (3), to provide Expression (6):

$$(2)^{1/2} A \cos m_{ps} \sin [\omega_{sc}t + \hat{\theta}(t)] \times \cos \omega_2t + (2)^{1/2} A \sin m_{ps} \times m(t) \times \cos [\omega_{sc}t + \theta] \sin [\omega_{sc}t + \hat{\theta}(t)] \times \sin \omega_2t + n_6(t) \quad (6)$$

where the noise term $n_6(t)$ is $n_2(t)$ in Expression (1b), multiplied by $\sin [\omega_{sc}t + \theta(t)]$.

Assumption. Again the assumption has been made that the relative broadening in the noise spectrum of Fig. 7 due to this multiplication is small enough to be ignored. Therefore, the noise term, $n_6(t)$, at ⑥ in Fig. 6 has a double-sided noise spectral density of $N_0/2$. This is, again, a conservative assumption.

After passing through the lower predemodulation filter F_{A2} , Expression (6) becomes:

$$F_{A2} \{ (2)^{1/2} A \cos m_{ps} \sin [\omega_{sc}t + \hat{\theta}(t)] \times \cos \omega_2t + (2)^{1/2} A \sin m_{ps} \times m(t) \times \cos [\omega_{sc}t + \theta] \sin [\omega_{sc}t + \hat{\theta}(t)] \times \sin \omega_2t \} + n_7(t) \quad (7)$$

The noise term $n_7(t)$ represents the receiver noise at the lower predemodulation filter output with double-sided noise spectral density of $N_0/2$. Ideally, F_{A2} is equal to F_{A1} . Again, the ratio of noise powers presented by $n_7(t)$ and $n_2(t)$ is equal to the ratio of noise bandwidths at ⑦ and ① in Fig. 6. The noise term $n_7(t)$ is centered about f_2 . Further investigation of Expression (7) will be made later in this report.

Coherent demodulation of data waveform

The reference signal at ⑧ in Fig. 6 is

$$(2)^{1/2} \sin \omega_2t \quad (8)$$

Assumption. It is assumed for the present that the received carrier power is such that the phase noise error in the RF carrier tracking loop is small enough so that it can be ignored.

The output of the upper linear coherent demodulator is the multiplication of Expression (5) by Expression (8) which provides (ignoring double frequency terms which are filtered out and orthogonal terms):

$$m(t) A \sin m_{ps} \{ \cos [\omega_{sc}t + \theta] \cos [\omega_{sc}t + \hat{\theta}(t)] \} + n_8(t) \quad (9)$$

Assumption. Assume, for the present, that $\theta - \hat{\theta}(t)$ is small compared to $\pi/2$ rad. Consequently, the product of the two square wave cosine terms is unity.

Since $m(t) = \pm 1$, the signal power in Expression (9) is

$$P_s = A^2 \sin^2 m_{ps} \quad (10)$$

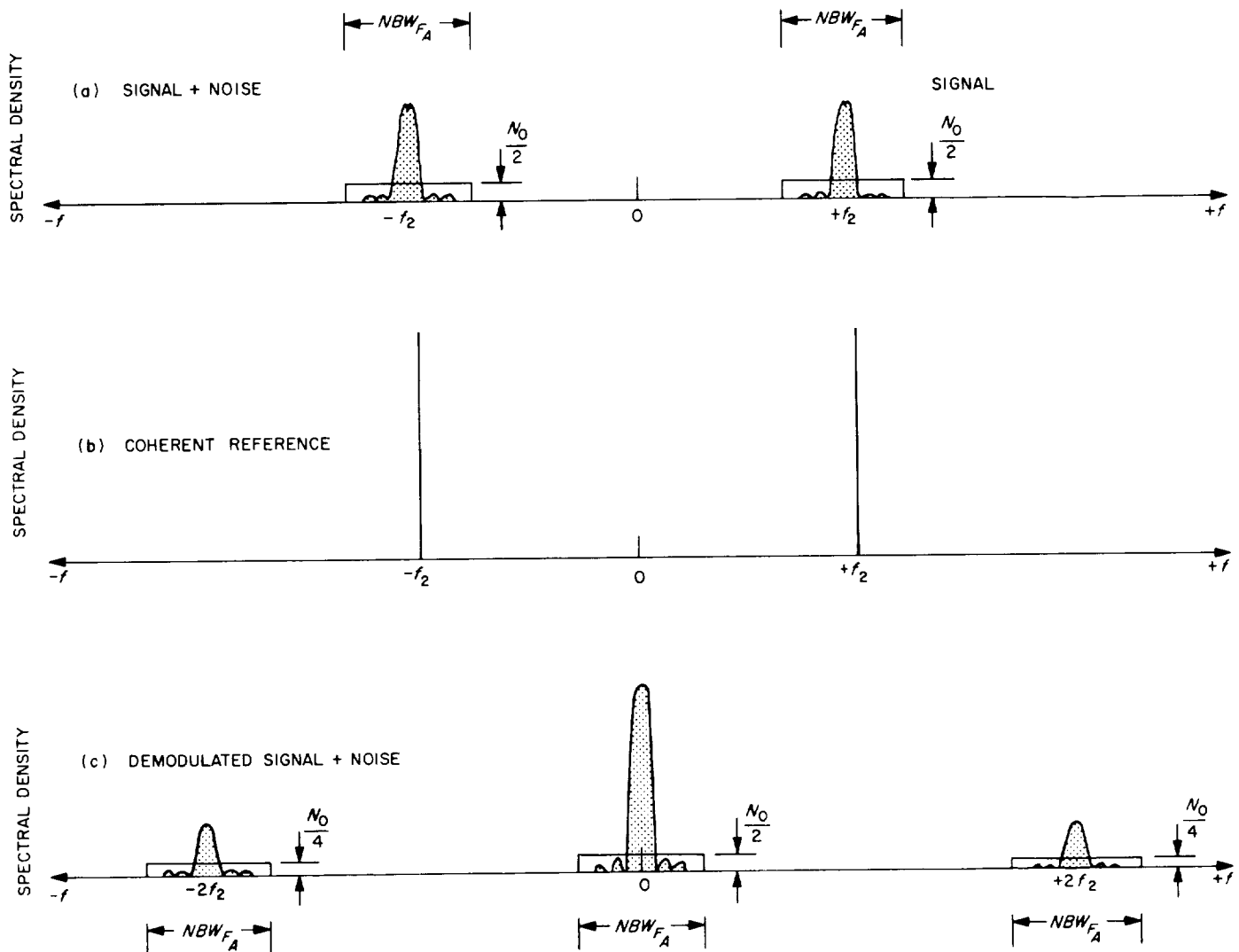


Fig. 9. Coherent data waveform demodulation

Consider next the noise term $n_s(t)$ in Expression (9). Figure 9 is a power spectral density representation of the coherent demodulation process. Figure 9(a) represents the signal plus noise into the coherent detector (second and third terms of Expression 5). The coherent reference signal (Expression 8) is represented by Fig. 9(b). Multiplication of signal plus noise by the coherent reference signal is shown in Figure 9(c). The multiplication process for each of the positive and negative frequency intervals about f_2 reduces the noise spectral density about $\pm 2f_2$ and about zero to $N_0/4$. The noise contributions from each of the positive and negative frequencies centered about zero frequency overlap to provide a resultant noise spectral density of $N_0/2$. Consequently, the power represented by the noise term in Expression (9) is equal to $N_0/2$ times the predetection filter noise bandwidth (NBW_{FA1}). Hence, for

the condition that the upper linear coherent demodulator has an output bandwidth (a low-pass zonal filter) which does not affect the spectral density representation (shown in Fig. 8) about zero frequency, the data signal-to-noise power ratio at ⑨ in Fig. 6 is

$$\frac{P_s}{P_N} = \frac{A^2 \sin^2 m_{ps}}{\frac{N_0}{2} \times NBW_{FA1}} \quad (11)$$

Data waveform filtering. The data waveform filter has a time constant τ_D . Noise power at the output of the filter is

$$P_N = \int_{-\infty}^{+\infty} \Phi_N \frac{1}{1 + \tau_D^2 \omega^2} d\omega \quad (12)$$

which can be expressed as

$$P_{N\tau} = \frac{N_0}{2} \frac{1}{2\pi} \int_{-\infty}^{+\infty} \frac{1}{\tau_D^2} \frac{1}{\frac{1}{\tau_D^2} + \omega^2} d\omega \quad (13)$$

where $\Phi_N = N_0/2 \times 1/2\pi$ is the noise spectral density in units of noise power per radian per second. Evaluation of this integral provides

$$P_{N\tau} = \left(\frac{N_0}{2} \times \frac{1}{2\pi} \right) \times \frac{\pi}{\tau_D} = \frac{N_0}{2} \times \frac{1}{2\tau_D} \quad (14)$$

Since the noise is Gaussian, the noise power is

$$P_N = \sigma_N^2 \text{ (the variance)} \quad (15)$$

Consequently, the rms noise voltage is

$$\sigma_{nv\tau} = \left(\frac{N_0}{2} \times \frac{1}{2\tau_D} \right)^{1/2} \text{ rms amplitude} \quad (16)$$

The amplitude of the demodulated data signal (from Expression 9) is $m(t) A \sin m_{ps}$ where $m(t)$ is ± 1 as determined by the data. Figure 10 shows the detected data signal during a transition of $m(t)$ from -1 to $+1$ which, in turn, is applied to the time constant τ_D . The resultant output signal from the time constant τ_D following such a transition is

$$m(t) A \sin m_{ps} (1 - 2e^{-t/\tau_D}) \quad (17)$$

where $t = 0$ at the transition. This waveform is also shown in Fig. 10. Consequently, the signal-to-noise voltage ratio at the data waveform filter output at time t (following a transition) can be obtained from Expressions (16) and (17)

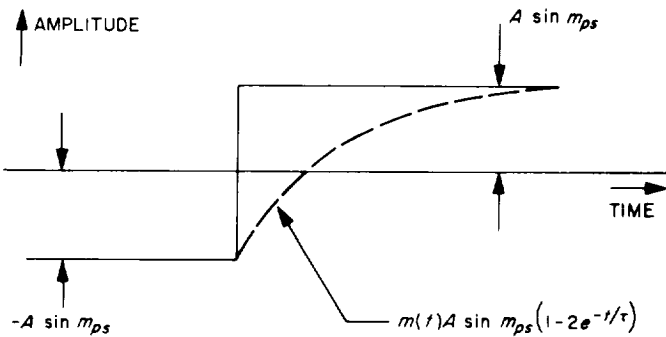


Fig. 10. Data waveform filter signal output waveform

$$(S/N)_v = \left| \frac{A \sin m_{ps}}{\sigma_{nv}} \times (1 - 2e^{-t/\tau_D}) \right| \quad (18)$$

$$= \left| \frac{A \sin m_{ps}}{\left(\frac{N_0}{2} \times \frac{1}{2\tau_D} \right)^{1/2}} \times (1 - 2e^{-t/\tau_D}) \right|$$

Designate the ratio $\tau_D/T_{SY} = \beta$, where T_{SY} is equal to the time duration of a data symbol. The signal-to-noise voltage ratio shown in Expression (18) can now be written as (substituting $\tau_D = \beta T_{SY}$)

$$(S/N)_v = \left| \frac{A \sin m_{ps}}{\left(\frac{N_0}{2} \times \frac{1}{2\beta T_{SY}} \right)^{1/2}} \times (1 - 2e^{-t/\beta T_{SY}}) \right| \quad (19)$$

The variation in relative signal-to-noise voltage ratio (at the data waveform filter output) following a transition is shown in Fig. 11, plotted as a function of the ratio $\tau_D/T_{SY} = \beta$ at time equal to T_{SY} (that is, at the end of a data symbol). The signal-to-noise voltage is maximized when $\tau_D/T_{SY} = 1/2.48$. Relative signal-to-noise voltage ratio at $t = T_{SY}$ normalized to the maximum value for $\tau_D/T_{SY} = 1/2.48$ is

$$\text{Rel}(S/N)_v = \frac{\left| \frac{A \sin m_{ps}}{\left(\frac{N_0}{2} \times \frac{1}{2\beta T_{SY}} \right)^{1/2}} \times (1 - 2e^{-1/\beta}) \right|}{\left| \frac{A \sin m_{ps}}{\left(\frac{N_0}{2} \times \frac{2.48}{2T_{SY}} \right)^{1/2}} \times (1 - 2e^{-2.48}) \right|} \quad (20)$$

$$= \left| (2.48 \beta)^{1/2} \times \frac{(1 - 2e^{-1/\beta})}{(1 - 2e^{-2.48})} \right|$$

$$= \left| \left(2.48 \frac{\tau_D}{T_{SY}} \right)^{1/2} \times \frac{(1 - 2e^{-T_{SY}/\tau_D})}{(1 - 2e^{-2.48})} \right|$$

Maximum signal-to-noise voltage ratio is

$$\text{Max}(S/N)_v = \frac{A \sin m_{ps}}{\left(\frac{N_0}{2} \times \frac{1.24}{T_{SY}} \right)^{1/2}} \times (1 - 2e^{-2.48}) \quad (21)$$

$$= \frac{A \sin m_{ps}}{\left(\frac{N_0}{2} \times \frac{1.24}{T_{SY}} \right)^{1/2}} \times 0.8325$$

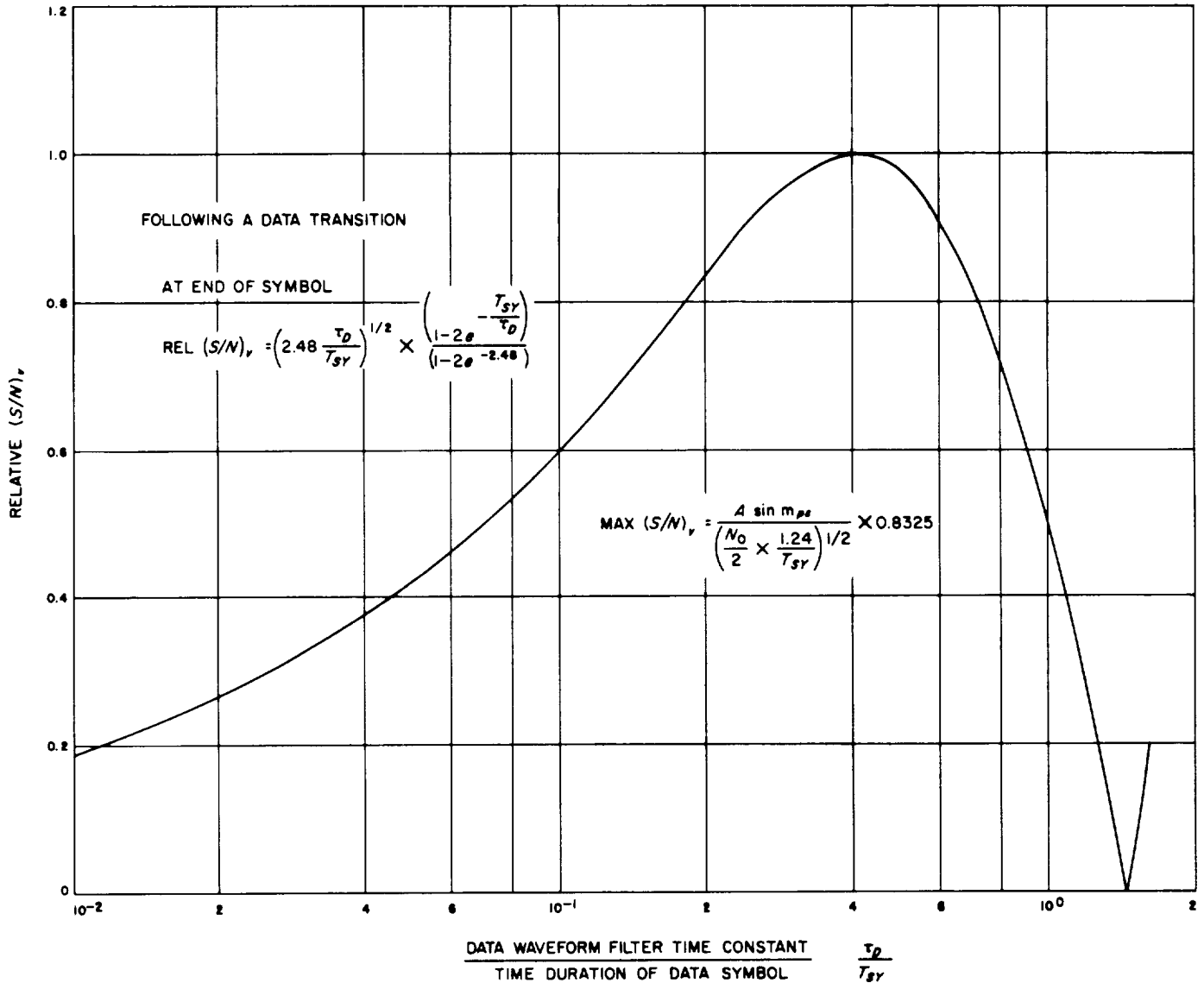


Fig. 11. Relative signal-to-noise voltage ratio versus ratio of data waveform filter time constant to data symbol time duration

Limiter characteristic and subcarrier loop error signal.
The observed voltage at the output of the data waveform filter consists of filtered signal plus noise

$$v(t) = s^*(t) + n(t) \quad (22)$$

At a particular time

$$V = S_v^* + N_v \quad (23)$$

From Expression (17), the filtered signal is

$$s^*(t) = m(t) A \sin m_{ps} (1 - 2e^{-t/\tau_D}) \quad (24)$$

The undistorted or ideal signal is

$$s(t) = m(t) A \sin m_{ps} \quad (25)$$

which is a binary waveform that switches between two values ($\pm S_v$) corresponding to whether $m(t)$, the data, is +1 or -1 which, in turn, corresponds to a binary 0 or 1. Note that for $t \gg \tau_D$ following a data transition, $s^*(t)$ and $s(t)$ become identical; consequently, $S_v^* = S_v$ ($t \gg \tau_D$).

Assume, for the present, that the transition (switching) of the binary data signal waveform from +1 to -1, or vice versa, is random with a 50% probability that it does

not switch from one symbol period to the next and, of course, 50% probability that it does switch² (for example, as determined by a sequence of flips of an unbiased coin). The signal at the input to the limiter (following the data waveform filter, Fig. 6), during any given symbol period, represents either of two situations: Either there has *not* been a transition from $+S_v$ to $-S_v$ (or vice versa) at the beginning of the period, or there has been a transition. Designate the first type of symbol period as $T_{SY_{11}}$ or $T_{SY_{00}}$ and the second type as $T_{SY_{01}}$ or $T_{SY_{10}}$. The observed voltage V given S_v (signal is present) has a probability density function

$$p(V/S_v) = \frac{1}{(2\pi)^{1/2} \sigma_{nv}} \exp \left[-\frac{1}{2} \left(\frac{V - S_v^*}{\sigma_{nv}} \right)^2 \right] \quad (26)$$

which is shown sketched in Fig. 12 for a $T_{SY_{00}}$ type symbol period.

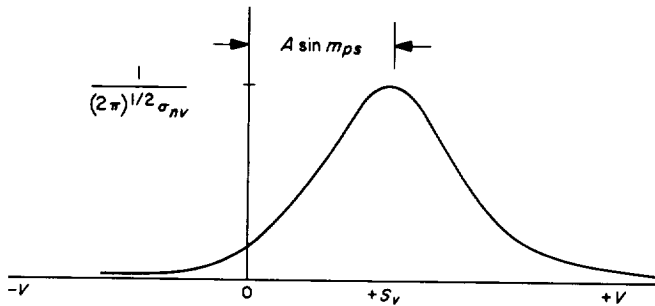


Fig. 12. Probability density function of observed voltage

Consider first a symbol period not preceded by a transition ($T_{SY_{11}}$ or $T_{SY_{00}}$). In particular, Fig. 13 shows a $T_{SY_{00}}$ type symbol period. The probability that the observed voltage V is greater than zero, given S_v , is represented by Expression (27). The $(S/N)_v$ is obtained from Expression (19) for time $t \gg \tau_D$ and $m(t) = 1$.

$$P(V/S_v > 0) = \frac{1}{(2\pi)^{1/2} \sigma_{nv}} \int_0^{+\infty} \exp \left[-\frac{1}{2} \left(\frac{V - S_v^*}{\sigma_{nv}} \right)^2 \right] dV \quad (27)$$

where $V - S_v^* = N_v$ and N_v has rms amplitude σ_{nv} .

Expression (27) defines the probability that the observed voltage V is of the same polarity as the ideal or undistorted signal during a $T_{SY_{00}}$ symbol period. The expression is shown for a positive voltage symbol period.

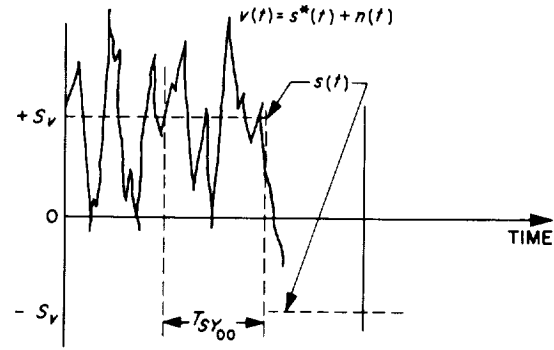


Fig. 13. Type $T_{SY_{00}}$ symbol period

For a negative voltage symbol period ($T_{SY_{11}}$), the probability that the observed voltage V is of the same polarity as the undistorted signal, given S_v , is

$$P[V/S_v < 0] = \frac{1}{(2\pi)^{1/2} \sigma_{nv}} \int_{-\infty}^0 \exp \left[-\frac{1}{2} \left(\frac{+V - S_v^*}{\sigma_{nv}} \right)^2 \right] dV \quad (28)$$

(Note that S_v is negative in this case; therefore, the probability that V is also negative is the item of interest.) For the same $(S/N)_v$, the integrals in Expressions (27) and (28) are equal.

For a symbol period preceded by a data transition, as indicated in Fig. 14 for a $T_{SY_{10}}$ type symbol period, the time constant τ_D provides a time varying S_v^* during T_{SY} where $\tau_D/T_{SY} \leq 1/3$. In this case, the symbol period is divided into increments small enough so that, for all practical purposes, S_v^* can be considered constant during any one of these time increments. Expression (27) is evaluated at each increment to determine the probability that the observed voltage is of the same polarity as the ideal or

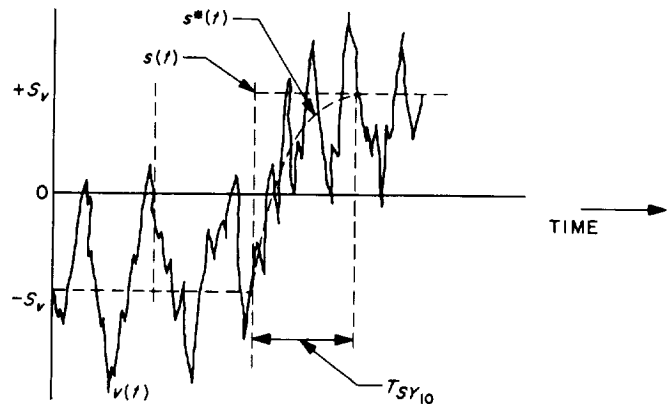


Fig. 14. Type $T_{SY_{10}}$ symbol period

²This provides maximum information rate (Ref. 1).

undistorted signal. Note that the mean value S_v^* in each small time increment is not equal to S_v (Fig. 14). The $(S/N)_v$ is obtained from Expression (19) for each small increment of time starting at $t = 0$ and ending at $t = T_{SY}$. For a $T_{SY_{01}}$ type symbol period, Expression (28) is evaluated at each increment as described above.

The voltage at the output of the hard limiter which follows the data waveform filter assumes either of two states: +1 when $V > 0$ and -1 when $V < 0$, as indicated in Fig. 15. The output of the limiter represents the data symbol stream $m(t)$ with serrations due to noise plus a time delay at transitions due to the time constant τ_D . Designate the limiter output as an estimate of $m(t)$ or

$$\hat{m}(t) \quad (29)$$

The percentage of time that $\hat{m}(t)$ agrees with $m(t)$ can be obtained from Expressions (27) and (28) as an average over many digit periods. Note again that, for the $T_{SY_{10}}$ and $T_{SY_{01}}$ type symbol periods, this average is obtained for each of the small increments into which the symbol period was divided as described above. The overall average of all the small increment averages represents the percentage of time that $\hat{m}(t)$ agrees with $m(t)$ for these $T_{SY_{10}}$ and $T_{SY_{01}}$ periods. The assumption was made earlier that switching of the binary data signal was random with 50%

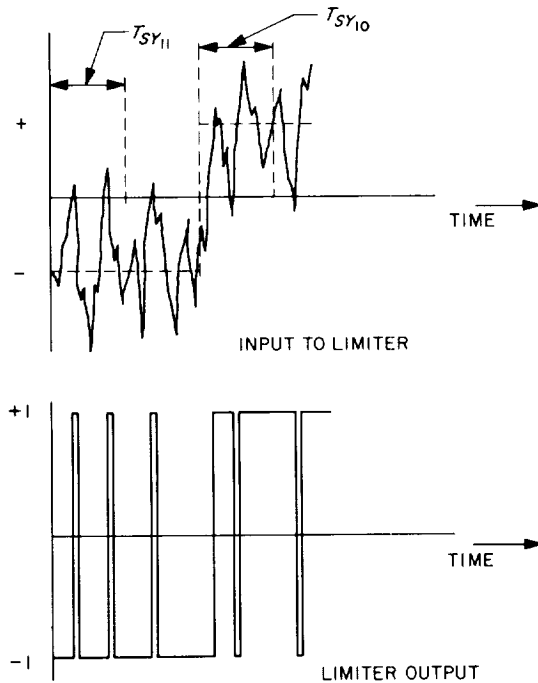


Fig. 15. Limiter input and output waveforms

probability that it does switch from one digit period to the next. This assumption will be altered later.

The data symbol stream estimate $\hat{m}(t)$ biphase modulates the reference signal

$$(2)^{1/2} \sin(\omega_2 t) \quad (30)$$

plus and minus $\pi/2$ rad, which provides

$$\hat{m}(t) (2)^{1/2} \sin(\omega_2 t) \quad (31)$$

The output of the lower linear coherent amplitude detector in Fig. 6 is the detection of Expression (7) with reference signal ③ which provides (ignoring double frequency terms which are filtered out and the orthogonal terms)

$$m(t) \hat{m}(t) A \sin m_{ps} \{ \cos [\omega_{sc} t + \theta] \times \sin [\omega_{sc} t + \hat{\theta}(t)] \} + n_{32}(t) \quad (32)$$

Assumption. Since it is assumed the $\theta - \hat{\theta}(t)$ is much less than $\pi/2$ rad, the portion of the product of the square wave cosine and sine terms centered about dc is proportional to $[\theta - \hat{\theta}(t)]/(\pi/2)$ where the phase difference is expressed in radians.

The other portion of the square wave cosine and sine product is a double frequency square wave which is filtered out by filter $F(s)$. It should be noted that the noise term $n_7(t)$ in Expression (7), which has a double sideband noise spectral density of $N_0/2$, is multiplied by $\hat{m}(t)$.

Assumption. The assumption is made here that relative broadening of the noise spectrum due to this multiplication is small enough to be ignored. Consequently, the noise power represented by $n_{32}(t)$ is equal to $N_0/2 \times NBW_{FA2}$. This is a conservative assumption. Note also that $\hat{m}(t)$ and the noise $n_7(t)$ are statistically independent, since the input noise is multiplied in the upper and lower input multipliers by orthogonal waveforms at the square wave subcarrier frequency (Fig. 6).

From Expression (32), the error signal due to the signal alone out of the lower coherent amplitude detector is linearly related to the difference in phase between the received square wave telemetry subcarrier and the square wave subcarrier voltage-controlled oscillator. Its value is zero when θ and $\hat{\theta}(t)$ are equal, positive in sign when $\theta > \hat{\theta}(t)$, and negative in sign when $\theta < \hat{\theta}(t)$. The product $m(t) \hat{m}(t)$ is unity when $\hat{m}(t)$ is exactly $m(t)$. When $\hat{m}(t)$

does not agree with $m(t)$, the product $m(t)\hat{m}(t)$, when averaged over many symbol periods, is reduced. The average value of $m(t)\hat{m}(t)$ is shown in Expression (33)

$$\overline{m(t)\hat{m}(t)} = \begin{aligned} & \text{[fraction of time } \hat{m}(t) \text{ agrees with } m(t)] \\ & - \text{fraction of time } \hat{m}(t) \text{ disagrees with } m(t) \end{aligned} \quad (33)$$

Consequently, $\overline{m(t)\hat{m}(t)}$ can be considered as a suppression factor which affects the phase error characteristic represented by the first term of Expression (32). Designate the suppression factor as α' , then

$$\alpha' = \begin{aligned} & \text{[fraction of time } \hat{m}(t) \text{ agrees with } m(t)] \\ & - \text{fraction of time } \hat{m}(t) \text{ disagrees with } m(t) \end{aligned} \quad (34)$$

The suppression factor α' , Expression (34), is shown plotted in Fig. 16 as a function of ST_{SY}/N_0 , the ratio of signal energy per symbol to noise spectral density. Note that if one bit of information transforms into l symbols and $ST_B/N_0 = y$ for the maximum permissible bit error rate (Ref. 2), then $ST_{SY}/N_0 = y/l$. ST_{SY}/N_0 can be rewritten as

$$\frac{S}{\frac{N_0}{2} \times \frac{2}{T_{SY}}}$$

If the above expression is related to Expression (19) when $t \gg 1/(\beta T_{SY})$, where $\beta = \tau_D/(T_{SY})$ and $m(t) = \pm 1$, the following is observed by comparison of the numerators

$$(S)^{1/2} = A \sin m_{ps}$$

The denominator of Expression (19) can be written as

$$\left[\frac{1}{4\beta} \left(\frac{N_0}{2} \times \frac{2}{T_{SY}} \right) \right]^{1/2}$$

Consequently, for a given ST_{SY}/N_0 and τ_D/T_{SY} , the $(S/N)_v$ can be calculated from Expression (19) for any time t following a data transition. Suppression factor (α') curves are shown for a 50% probability that the data symbol stream does switch from one symbol period to the next for ratios of τ_D/T_{SY} of $1/3$, $1/6$, and $1/12$. Figure 16 also provides information for other distributions of zeros and ones in the data symbol stream. In particular, the suppression factor characteristic is shown for those cases when the probability is approaching 100 and 0%, respectively, that the data symbol stream does switch from one symbol period to the next (for ratios of τ_D/T_{SY} of $1/3$, $1/6$, and $1/12$).

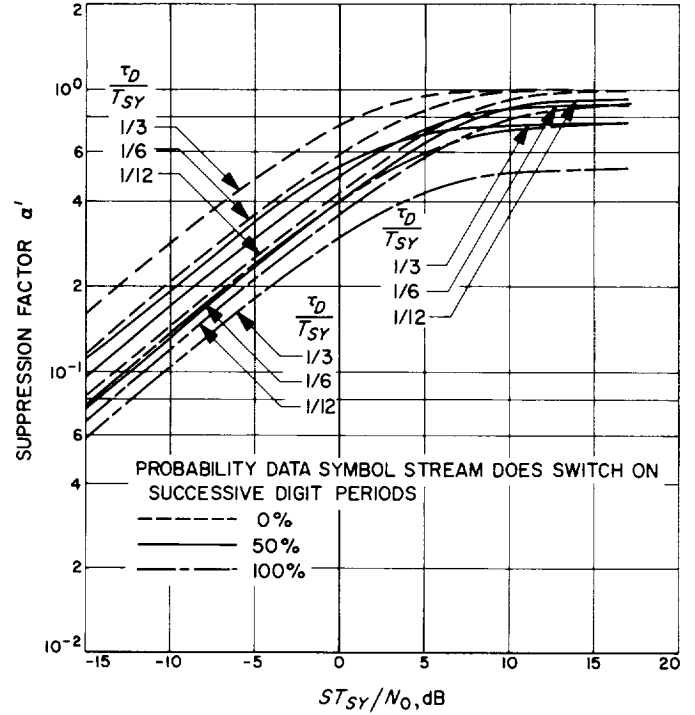


Fig. 16. MMTS subcarrier demodulator suppression factor versus ratio of signal energy per symbol to noise spectral density

Consider next the noise term $n_{32}(t)$ in Expression (32). The noise power represented by the noise term is

$$P_N = \frac{N_0}{2} \times NBW_{FA2} \quad (35)$$

Since the noise is Gaussian, the variance of the noise is equal to the noise power

$$\sigma_{nv_2}^2 = \frac{N_0}{2} \times NBW_{FA2} \quad (36)$$

and, consequently, the rms noise voltage is

$$\sigma_{nv_2} = \left(\frac{N_0}{2} \times NBW_{FA2} \right)^{1/2} \text{ rms amplitude} \quad (37)$$

Consider for a moment the signal portion of Expression (32). Note that if $\theta - \hat{\theta}(t)$ is equal to $\pi/2$ rad, the output voltage from the lower coherent amplitude detector is equal to $\alpha' A \sin m_{ps}$. Consequently, conversion of the rms noise voltage to equivalent phase noise can be accomplished by normalizing the noise voltage to the

signal voltage. The resultant expression at the output of the lower coherent amplitude detector is

$$\frac{\pi}{2} \times \frac{\sigma_{nv_2}}{\alpha' A \sin m_{ps}} \text{ rad rms}$$

or

$$\frac{\pi}{2} \times \frac{\left(\frac{N_0}{2}\right)^{1/2}}{\alpha' A \sin m_{ps}} \times (NBW_{FA2})^{1/2} \text{ rad rms} \quad (38)$$

After passing through the filter $F(s)$, the signal plus noise represented by Expression (39) controls the output

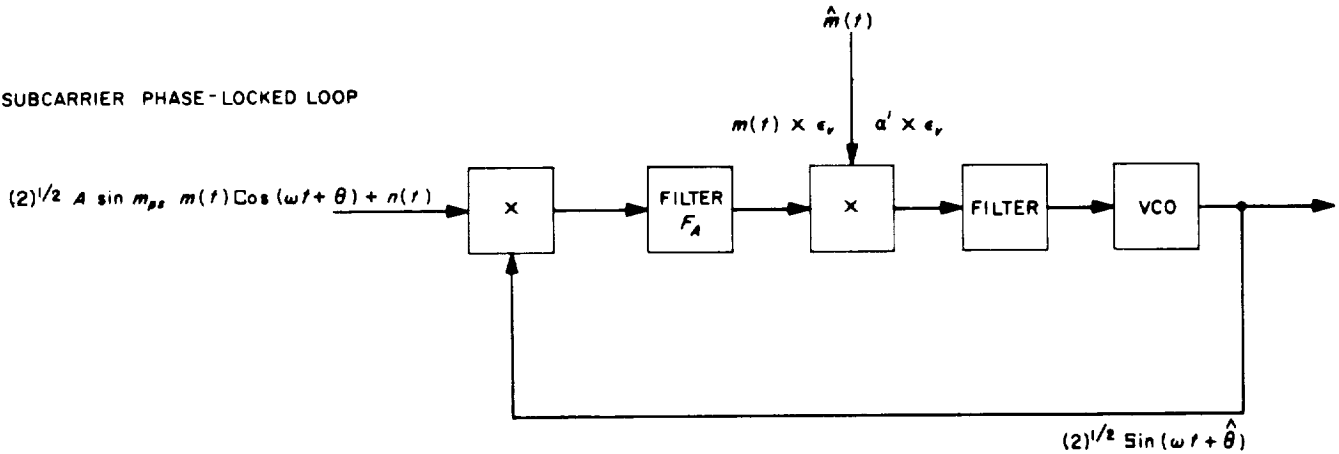
phase of the subcarrier VCO.

$$F(\omega) [\alpha' A \sin m_{ps} \{\cos [\omega_{sc} t + \theta] \times \sin [\omega_{sc} t + \hat{\theta}(t)]\} + n_{32}(t)] \quad (39)$$

Since $\theta = \int \omega dt$, the VCO functions as an integrator.

Linear model of the subcarrier tracking loop. The lower loop in Fig. 6 can now be treated as a linear model of the phase-locked loop (Ref. 3) with the constraint that at minimum signal level the probability of the phase noise

(a) SUBCARRIER PHASE-LOCKED LOOP



(b) RELATIONSHIP BETWEEN ERROR VOLTAGE AND PHASE DIFFERENCE FOR INPUT MULTIPLIER

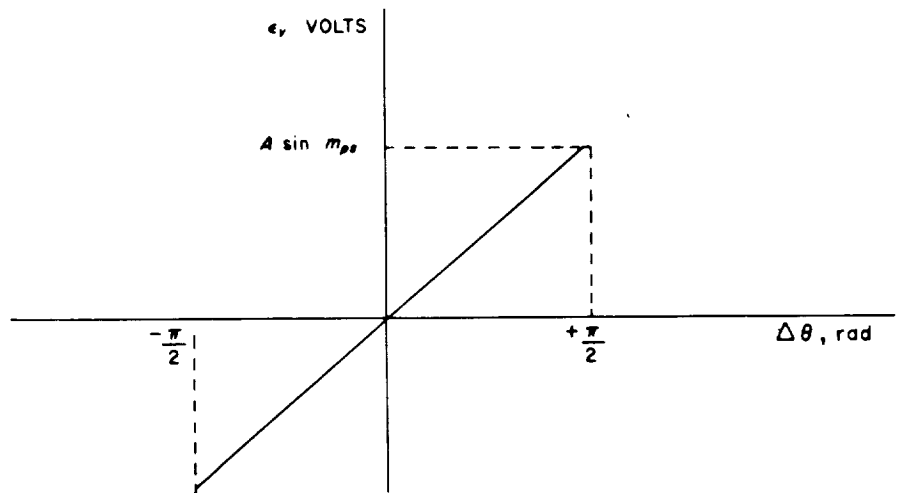


Fig. 17. Simplified block diagram of subcarrier phase-locked loop

error exceeding 90 deg $\ll 1$. Figure 12 shows a simplified tracking loop with an input signal

$$(2)^{1/2} A \sin m_{ps} m(t) \cos(\omega t + \theta) + n(t) \quad (40)$$

and an output signal

$$(2)^{1/2} \sin(\omega t + \theta) \quad (41)$$

The assumption is made that conversion of receiver noise to subcarrier phase noise is accomplished with essentially zero correlation between the two.

Also shown in Fig. 17 is the linear relationship between error voltage (ϵ_v) and phase difference ($\Delta\theta$) as produced by the input multiplier (assuming $m(t)$ is a constant for the moment). As described earlier (Fig. 2), the input noise has a two-sided noise spectral density of $S_N(f) = N_0/2$ in units of noise power per Hz. Since the linear input multiplier changes the input noise voltage $n(t)$ to noise voltage at its output that has the effect of phase noise, the input noise $n(t)$ can be replaced by an equivalent input phase noise $\theta_n(t)$. This equivalent input phase noise $\theta_n(t)$ will have a spectral density $S_{\theta_n}(f)$ which can be expressed in units of rad^2/Hz ; which is flat, since the input noise voltage has a flat spectral density. If $m(t)$ is now considered a function of time and $\hat{m}(t)$ is an estimate of $m(t)$, the linear relationship between error voltage (ϵ_v) and phase difference ($\Delta\theta$) is modified by $\alpha' = m(t)\hat{m}(t)$ which was developed earlier (Fig. 11 and Expression (34)). Consequently, at the output of the second multiplier in Fig. 17, the slope of the ϵ_v vs $\Delta\theta$ linear characteristic varies with α' to provide a family of linear curves.

As developed earlier in Expression (32), the ϵ_v due to the signal is related to the phase difference by

$$\epsilon_{v_s} = \frac{2}{\pi} \alpha' A \sin m_{ps} \times \Delta\theta \quad (42)$$

where $(2/\pi) \alpha' A \sin m_{ps}$ is expressed in units of volts per radian and $\Delta\theta$ in radians. The spectral density of the ϵ_v due to noise is related to the input noise spectral density by (see Expression 36)

$$S_{\epsilon_N} = 1 \times \frac{N_0}{2} \text{ noise power per Hz} \quad (43)$$

Consequently, the noise spectral density of the equivalent input phase noise $\theta_n(t)$ is from Expressions (42) and (43)

$$S_{\theta_n}(\omega) = \frac{\frac{N_0}{2}}{\left(\frac{2}{\pi} \alpha' A \sin m_{ps}\right)^2} \text{ rad}^2/\text{Hz} \quad (44)$$

The expression for $\theta_n(t)$ can now be written as

$$\theta_n(t) = \frac{n(t)}{\frac{2}{\pi} \alpha' A \sin m_{ps}} \quad (45)$$

In light of the development above, the subcarrier phase-locked loop can now be represented by the equivalent block diagram shown in Fig. 18. The multipliers shown in

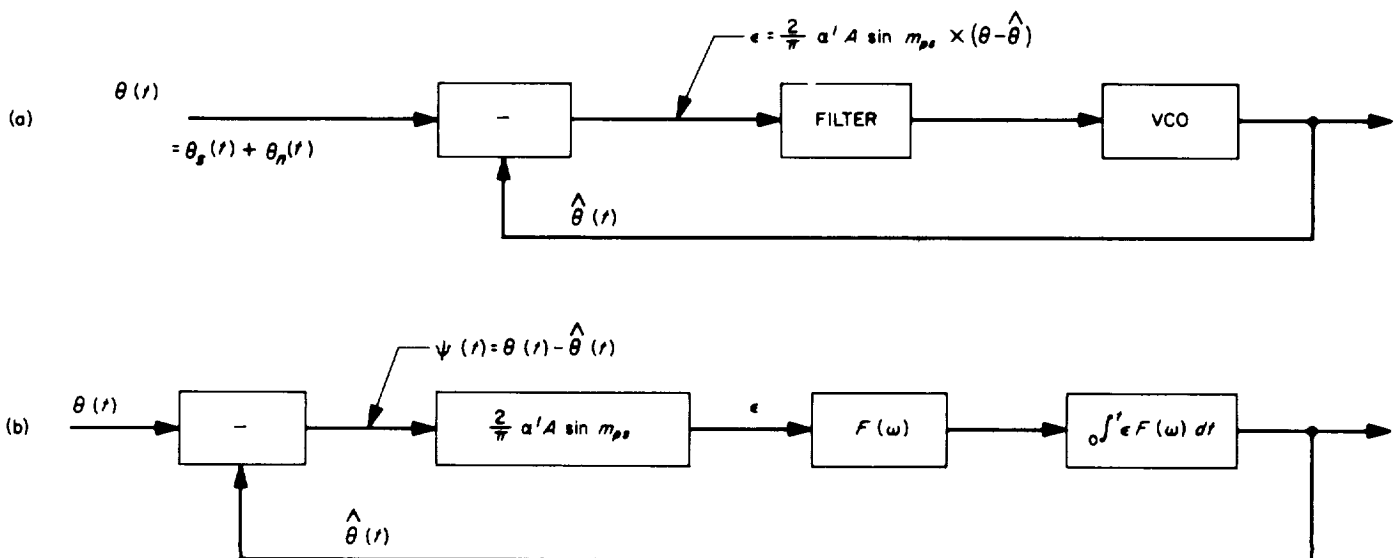


Fig. 18. Equivalent block diagram of subcarrier phase-locked loop

Fig. 17 are replaced by a phase differencing junction in Fig. 18. Figure 18(a) consists of a differencing junction, filter, and square-wave VCO. Figure 18(a) can be further represented by the equivalent block diagram shown in Fig. 18(b). Since the square-wave VCO functions as an integrator to produce the proper output phase, it is represented as

$$\int_0^t \epsilon F(\omega) dt$$

in Fig. 18(b). The phase error is

$$\psi(t) = \theta(t) - \hat{\theta}(t) \quad (46)$$

Applying Laplace transform notation to Fig. 18(b), the linear model of the subcarrier phase-tracking loop becomes the model shown in Fig. 19. The subcarrier square-wave VCO becomes K/s in this mathematical model, where K is the effective gain constant of the VCO in radians per second per volt. Note that the open loop gain at dc is $(2/\pi) K \alpha' A \sin m_{ps}$. Referring to Fig. 19,

$$\hat{\theta}(s) = \frac{2}{\pi} K \alpha' A \sin m_{ps} \times \frac{F(s)}{s} \times [\theta(s) - \hat{\theta}(s)] \quad (47)$$

which becomes, after rearranging terms,

$$\hat{\theta}(s) = \frac{\frac{2}{\pi} K \alpha' A \sin m_{ps} \times F(s)}{s + \frac{2}{\pi} K \alpha' A \sin m_{ps} \times F(s)} \times \theta(s) \quad (48)$$

The transfer function of the subcarrier loop is from Expression (48)

$$H(s) = \frac{\hat{\theta}(s)}{\theta(s)} = \frac{\frac{2}{\pi} K \alpha' A \sin m_{ps} \times F(s)}{s + \frac{2}{\pi} K \alpha' A \sin m_{ps} \times F(s)} \quad (49)$$

Expression (48) provides a relationship which permits determination of an output phase function for a given input signal phase function. However, the equivalent input phase noise cannot be handled in this manner, since Laplace transforms do not, in general, exist for random processes. The noise spectral density of the equivalent input phase noise has been developed in Expression (44). Since the input noise is Gaussian and white,

$$P_N = \sigma_{\theta n}^2 = S_{\theta n}(\omega) BW_{scl} \text{ rad}^2 \quad (50)$$

In addition, for linear filtering (Ref. 2)

$$P_N = \frac{1}{2\pi} \int_{-\infty}^{+\infty} |H(j\omega)|^2 S_{\theta n}(\omega) d\omega \quad (51)$$

which can be expressed as

$$P_N = S_{\phi n}(\omega) \times \frac{1}{2\pi} \int_{-\infty}^{+\infty} |H(j\omega)|^2 d\omega \quad (52)$$

Consequently, the two-sided noise bandwidth of the subcarrier phase-tracking loop is from Expressions (50) and (52)

$$BW_{scl} = \frac{1}{2\pi} \int_{-\infty}^{+\infty} |H(j\omega)|^2 d\omega \text{ Hz} \quad (53)$$

or, in Laplace transform notation

$$BW_{scl} = \frac{1}{2\pi j} \int_{-j\infty}^{+j\infty} |H(s)|^2 ds \text{ Hz} \quad (54)$$

The variance of the phase noise at the output of the loop is from Expressions (44), (50), and (54)

$$\sigma_{\theta n}^2 = \frac{\frac{N_0}{2}}{\left(\frac{2}{\pi} \alpha' A \sin m_{ps}\right)^2} \times BW_{scl} \text{ rad}^2 \quad (55)$$

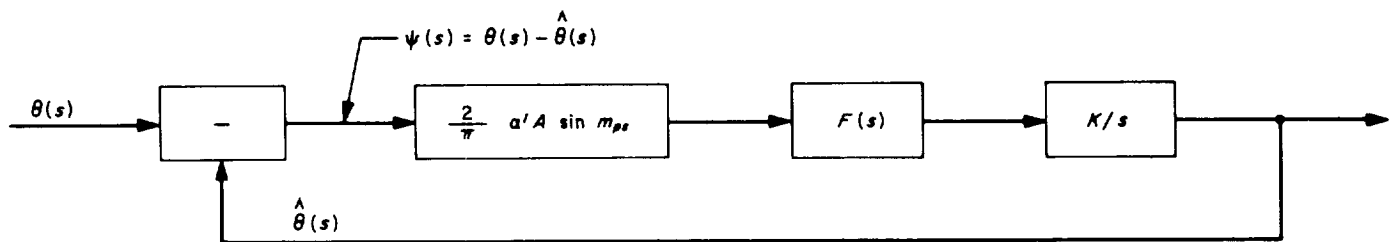


Fig. 19. Linear model of subcarrier phase-tracking loop

The square root of Expression (55) provides $\sigma_{\theta n}$, the rms phase noise at the output of the loop which, for a spectral line input signal, becomes the rms phase noise error in the loop.

First-order subcarrier tracking loop. Although the subcarrier demodulator loop may be designed as a second-order phase-locked loop, examination of the behavior of a first-order loop under noisy signal conditions will provide information on selection of closed-loop noise bandwidths for a large number of designs. The performance of a second-order loop under the same noisy signal conditions will be at least as good, if not better, than that of the first-order loop. The second-order loop will be considered in later reports.

For a first-order loop, $F(s) = 1$; therefore, from Expression (49), the transfer function becomes

$$H(s) = \frac{\frac{2}{\pi} K \alpha' A \sin m_{ps}}{s + \frac{2}{\pi} K \alpha' A \sin m_{ps}} \quad (56)$$

The two-sided closed-loop noise bandwidth is

$$\begin{aligned} BW_{scl} &= \frac{1}{2\pi} \int_{-\infty}^{+\infty} \frac{\left(\frac{2}{\pi} K \alpha' A \sin m_{ps}\right)^2}{\omega^2 + \left(\frac{2}{\pi} K \alpha' A \sin m_{ps}\right)^2} d\omega \\ &= \frac{\left(\frac{2}{\pi} K \alpha' A \sin m_{ps}\right)}{2} \text{ Hz} \end{aligned} \quad (57)$$

At the design point

$$BW_{scl} = \frac{\alpha'_0 \frac{2}{\pi} K A \sin m_{ps}}{2} \text{ Hz} \quad (58)$$

Since the two-sided noise bandwidth of a time constant τ is equal to $1/(2\pi)$ (from Expression 14), the equivalent time constant of the first-order loop is

$$\tau_L = \frac{1}{\alpha'_0 \frac{2}{\pi} K A \sin m_{ps}} \quad (59)$$

Again, at the design point

$$\tau_{L0} = \frac{1}{\alpha'_0 \frac{2}{\pi} K A \sin m_{ps}} \quad (60)$$

Note that the two-sided noise bandwidth is one half the reciprocal of the equivalent time constant of a first-order loop. Designate the ratio τ_{L0} , design point equivalent time constant, to T_{SY} , time duration of a symbol, as γ_0 ; then

$$\tau_{L0} = \gamma_0 T_{SY} \quad (61)$$

For a given design point, ST_{SY}/N_0 , the variance of the phase noise at the output of the first-order loop at the design point is (from Expression 55):

$$\sigma_{\theta n}^2 = \left(\frac{1}{\alpha'_0}\right)^2 \left(\frac{\pi}{2}\right)^2 \times \frac{N_0}{ST_{SY}} \times \frac{T_{SY}}{2} \times \frac{1}{2\gamma_0 T_{SY}} \text{ rad}^2 \quad (62)$$

Now for a given τ_D/T_{SY} , γ_0 , and probability that the data symbol stream does switch on successive symbols, the rms phase noise error at the design point can be calculated from Expression (62) where α'_0 is obtained from Fig. 11. A change in ST_{SY}/N_0 from the design point provides an α' from Fig. 11 which provides, in turn, a new γ and $\sigma_{\theta n}^2$ is recalculated from the expression

$$\sigma_{\theta n}^2 = \left(\frac{1}{\alpha'}\right)^2 \left(\frac{\pi}{2}\right)^2 \times \frac{N_0}{ST_{SY}} \times \frac{1}{4\gamma} \text{ rad}^2 \quad (63)$$

Figure 20 shows the rms phase noise error $\sigma_{\theta n}$ for a first-order loop as a function of ST_{SY}/N_0 for τ_D/T_{SY} equal to 1/3 and 50% probability that the data symbol stream does switch on successive symbols. The design point is chosen for $ST_{SY}/N_0 = -10$ dB. Performance curves are shown for ratios of τ_{L0}/T_{SY} from 50 to 51,200 in octave steps. In general, the phase noise error $\sigma_{\theta n}$ should be maintained to 0.1 rad or less at the ST_{SY}/N_0 which provides a 10% bit error probability (Ref. 2) so as not to materially affect the signal-to-noise ratio of the detected data symbol stream. The effect of $\sigma_{\theta n}$ on the detected symbol stream will be presented in a later report.

b. Low- and medium-rate telemetry subcarrier demodulator. The low- and medium-rate telemetry subcarrier demodulator accommodates the engineering telemetry and nonvideo science data described in the introduction. Both of these data types are transmitted uncoded on a bit-by-bit basis which represents the condition $T_B = T_{SY}$ in the preceding general analysis.

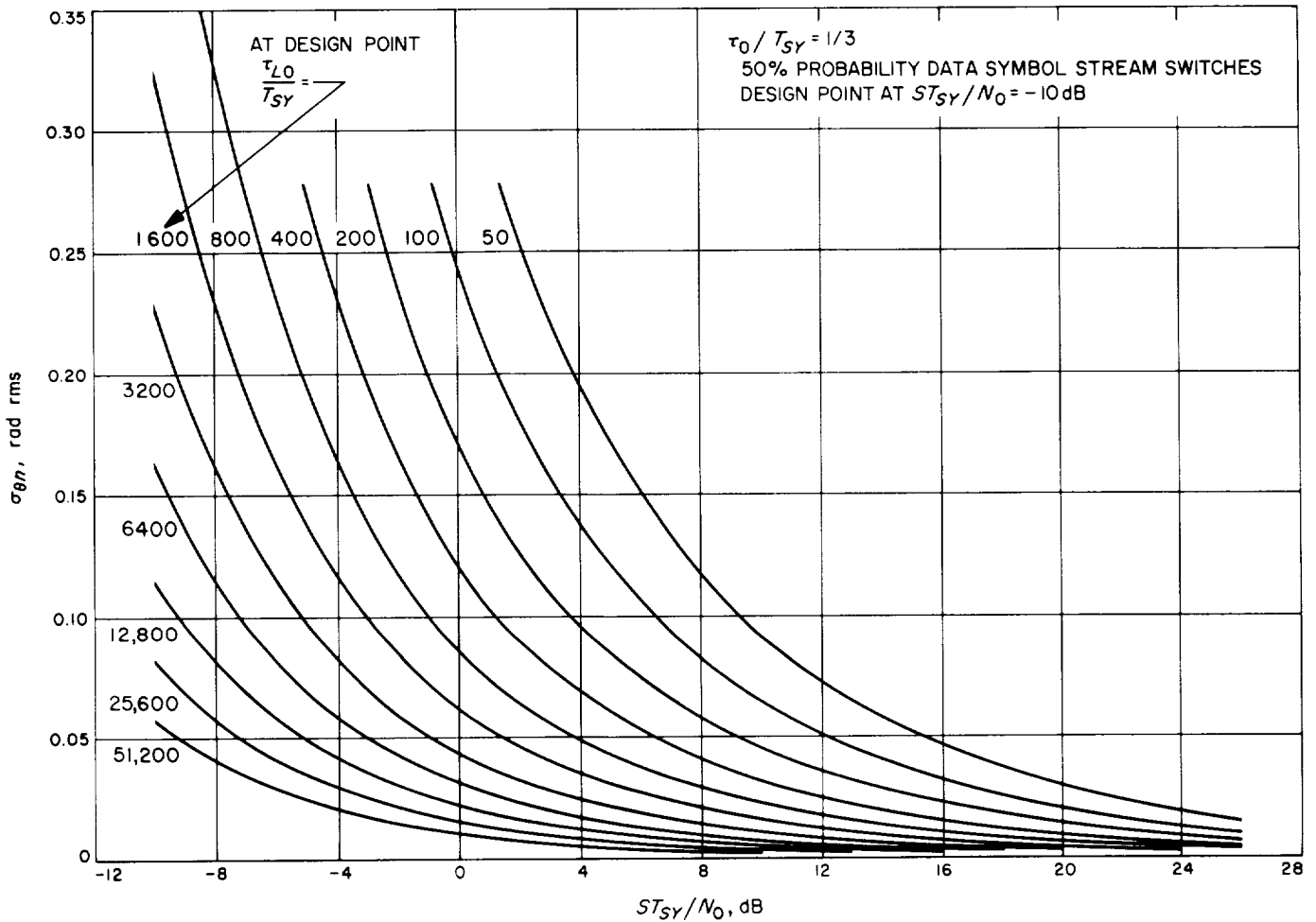


Fig. 20. MMTS subcarrier demodulator first-order loop rms phase noise error versus ratio of signal energy per symbol to noise spectral density

In order to apply the preceding analysis, consider the *Mariner* Mars 1969 mission as typical for a deep space mission. The nominal ST_B/N_0 for the overall telecommunications system design is +5.2 dB at encounter for low- and medium-rate data with a bit error rate of five parts in 10^3 . The allowable degradation which is allocated to the telemetry subcarrier demodulator at this ST_B/N_0 of +5 dB is 0.1 dB. A degradation of 0.1 dB in the demodulated output ST_{SY}/N_0 due to the rms phase noise error in the subcarrier tracking loop results when $\sigma_{\theta n} = 0.02$ rad rms. In general, for the subcarrier demodulator

where $3\sigma_{\theta n} \leq \pi/2$ and ST_{SY}/N_0 is expressed as a ratio. Derivation of this expression will be presented in a later report.

From Fig. 20 the curve for $\tau_{L0}/T_{SY} = 3200$ provides an rms phase noise error $\sigma_{\theta n}$ of 0.02 rad rms at an ST_{SY}/N_0 of +5.2 dB. At an ST_{SY}/N_0 of -1 dB which represents a 10% bit error rate (Ref. 2), $\sigma_{\theta n} = 0.05$ rad rms for the $\tau_{L0}/T_{SY} = 3200$ curve. Make this the design point for the low- and medium-rate telemetry. This provides from Expressions (58), (59) and (60) and from Fig. 16 a design point noise bandwidth of

$$\frac{\text{demodulated } \frac{ST_{SY}}{N_0}}{\text{input } \frac{ST_{SY}}{N_0}} = \left[1 - \left(\frac{2}{\pi} \right)^{3/2} \sigma_{\theta n} \right]^2 \quad (64)$$

$$\begin{aligned} BW_{SCL} &= \frac{1}{2 \times 3200 T_{SY}} \times \frac{0.490}{0.193} \\ &= \frac{1}{2520 T_{SY}} \end{aligned} \quad (65)$$

to meet the requirements relative to phase noise error. Design point two-sided noise bandwidth is shown in Fig. 21 as a function of data rate. The noise bandwidth curve shown is for τ_D/T_{SY} equal to $\frac{1}{3}$ with a 50% probability that the data stream switches from one bit period to the next. Changing τ_D/T_{SY} to $\frac{1}{6}$ with all other conditions the same would reduce the noise bandwidth at any given data rate to 0.9 of that shown in Fig. 21. It should be noted that the subcarrier tracking loop if designed as a second-order loop would result in less than 0.02 rad rms noise error at ST_{SY}/N_0 equal to +5.2 dB. Also, the combined short-term stability of the square-wave telemetry subcarrier oscillator in the spacecraft and the square-wave subcarrier VCO in the DSN ground equipment must be such as to produce a phase error due to oscillator noise which is small compared to 0.05 rad rms in the design point noise bandwidth; for example, 0.015 rad rms.

The telemetry subcarrier demodulator must have sufficient open-loop gain and a maximum closed noise bandwidth capability to accommodate the doppler shift and doppler rate which occurs at injection of the spacecraft on its trajectory. Performance in this respect should be comparable to the RF system. Consider first the problem of accommodating doppler shift. The strong signal open-loop gain ($\alpha' = 1$) versus subcarrier frequency characteristic shown in Fig. 22 is obtained under the constraint that the phase error due to a frequency offset of 4.5 parts in 10^5 shall not exceed 0.1 rad at strong signal levels.

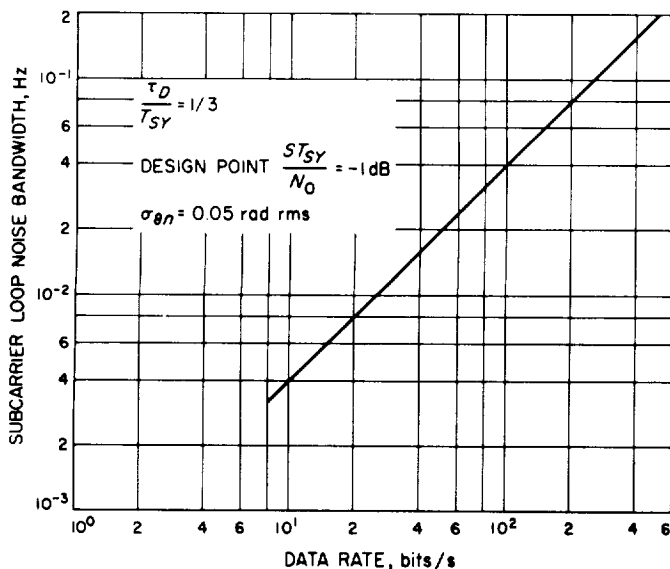


Fig. 21. Low- and medium-rate telemetry demodulator minimum design point noise bandwidth versus data rate

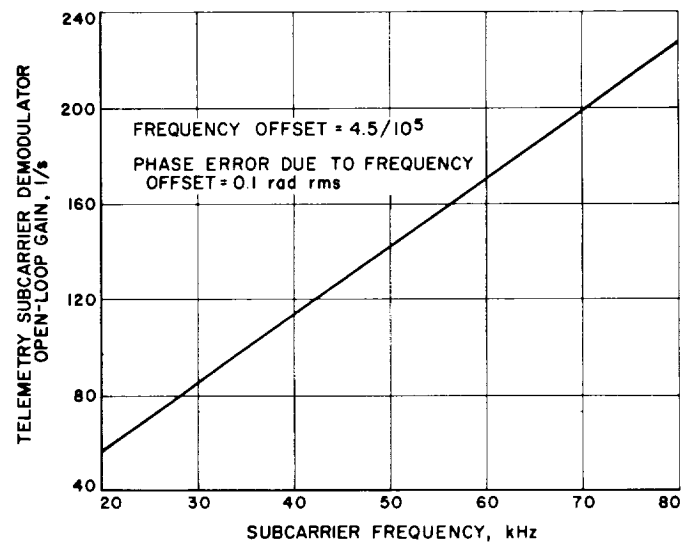


Fig. 22. Low- and medium-rate telemetry demodulator strong signal open-loop gain versus telemetry subcarrier frequency

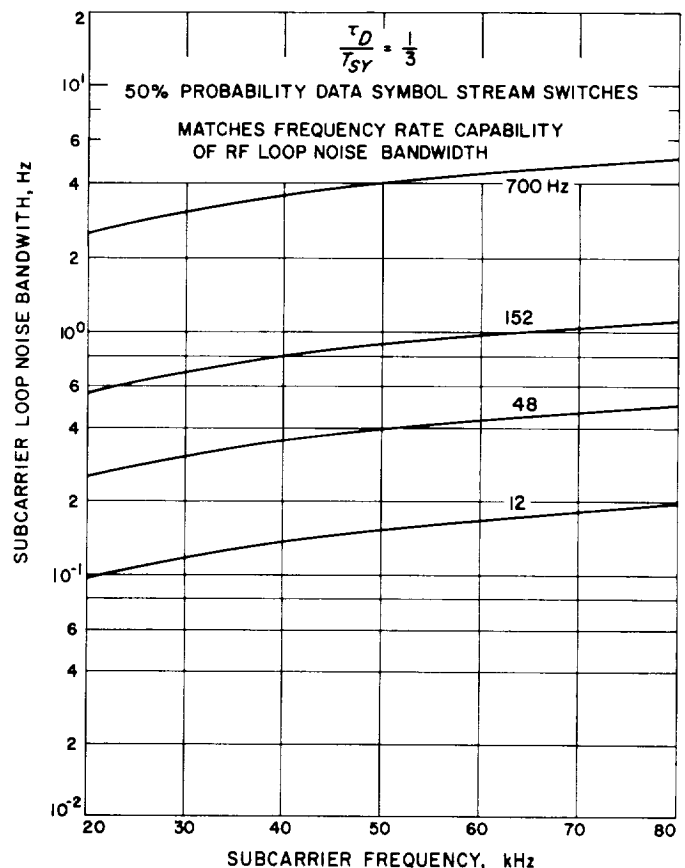


Fig. 23. Low- and medium-rate telemetry demodulator maximum design point noise bandwidth versus telemetry subcarrier frequency

Consider next the maximum design point two-sided noise bandwidth required to provide doppler rate tracking capability commensurate with the RF carrier tracking loop design point two-sided noise bandwidths of 12, 48, 152 and 700 Hz. This characteristic is shown in Fig. 23 as a function of subcarrier frequency. The 700-Hz RF carrier tracking bandwidth accommodates worst-case doppler rates during injection of the spacecraft on its mission trajectory. Figure 23 provides information on the maximum subcarrier design point noise bandwidth which matches the frequency rate capability of the RF carrier tracking system. The characteristic shown in Fig. 23 assumes that the subcarrier tracking loop is designed as a second-order loop with a damping factor of 0.707 at the design point.

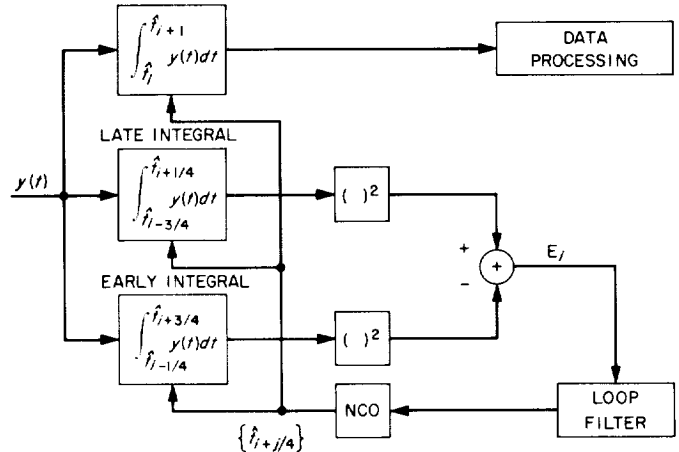


Fig. 24. Functional diagram of bit-timing subsystem

4. Telemetry Bit Synchronization Loop, J. W. Layland

a. General discussion. Bit synchronization for the MMTS must be obtained directly from the data signal. The methods by which this may be accomplished fall into two general categories: (1) The data signal is filtered, or processed nonlinearly and then filtered, to extract a frequency component which is a small ratio harmonic of the bit rate and coherent with the data stream. This frequency component is then tracked by a phase-locked loop to produce the bit-timing reference signal. (2) A bit-time tracking error signal is derived directly from the probabilistic transitions of the data signal, much as a range-code delay-locked loop error signal is derived from the known transitions of the pseudonoise ranging signal (Ref. 4). It is from this second category that the bit-tracking algorithm for the MMTS has been chosen.

The MMTS bit-tracking loop is functionally diagrammed in Fig. 24. An error signal is generated by differencing the squares of integrals of $y(t)$ —the bit stream plus noise—each taken over a bit duration starting one-quarter bit time early and one-quarter bit time late; its operation is as follows:

Let t_i denote the actual epoch of the transition prior to the i th data bit and let \hat{t}_i denote the local estimate of it. Assume that $y(t) = +1$ for $t \leq t_i$ and $y(t) = -1$ for $t > t_i$. Assume further that the numerically controlled oscillator (digital phase shifter) is out of phase such that $\hat{t}_{i+1/4} = t_i$. Then the late integral argument is $+1$ for the entire range; the early integral argument is $+1$ for the first half of its range and -1 for the second half of its range. As a result, the difference-of-squares error signal

E_i is $+1 \cdot T_B^2$, where T_B is bit duration. If $-y(t)$ is substituted for $y(t)$, the same error signal is obtained. Consider now that the numerically controlled oscillator (NCO) is out of phase in the opposite direction by $T_B/4$, such that $\hat{t}_{i-1/4} = t_i$. Then the late integral argument is $+1$ for half of the range and -1 for the second half, giving a zero result. The early integral, however, has a -1 argument over the full range, producing an E_i of $-1 \cdot T_B^2$. Again, changing the sign of $y(t)$ does not change the error signal.

If now \hat{t}_i is equal to t_i , the late integral argument is $+1$ for three fourths of the range and -1 for one fourth of the range, a net value of $T_B/2$. The early integral argument is $+1$ for $1/4$ the range and -1 for $3/4$ the range, for a net value of $-T_B/2$. The difference-of-squares error signal is zero. Similarly, if $y(t)$ has no transition in the range $\hat{t}_{i-1/4}$ to $\hat{t}_{i+1/4}$, the early and late integrals have identical values and the error signal is zero.

The error signal, then, depends only upon the relative positions of the transition time t_i and the estimate of it, \hat{t}_i . It does not depend upon the sign of the data transition, and is therefore a valid error signal to use for tracking data transitions which necessarily occur with random signs and interspersed with nontransitions.

b. Analysis of a first-order linear bit-tracking loop. The relative positions of timing marks for the early, late, and data integrations are shown in Fig. 25. Some simplifications, both in analysis and in computer implementation, may be obtained by reference to the labeling on the bottom line of Fig. 25. The late integral in the vicinity of

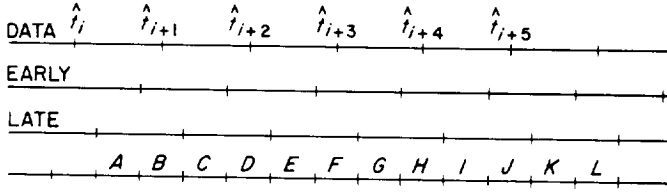


Fig. 25. Time points defining early, late, and data integrals

t_{i+2} is the sum of integrals C and D. The early integral there is D + E. The error signal at t_{i+2} is then

$$\begin{aligned} E_{i+2} &= (C + D)^2 - (D + E)^2 \\ &= C^2 + 2D(C - E) - E^2 \end{aligned} \quad (1)$$

Furthermore, breaking up the adjacent error signals shows

$$\begin{aligned} E_{i+1} &= A^2 + 2B(A - C) - C^2 \\ E_{i+3} &= E^2 + 2F(E - G) - G^2 \end{aligned} \quad (2)$$

Clearly, if the loop filter averages over a large number of bits—as it should—the squared terms drop, and only cross-terms remain at the input to the NCO. Figure 26 shows the reduced bit-timing subsystem. The analysis which follows for it produced results identical to the results obtained by a much more complicated route for the system of Fig. 24.

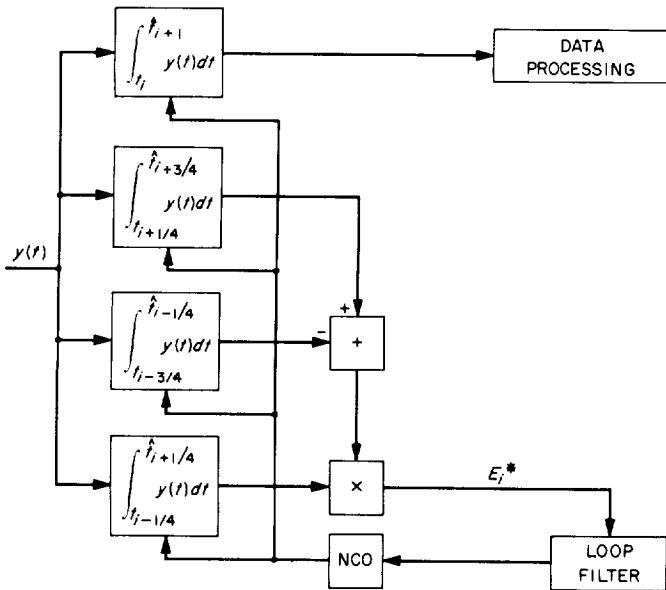


Fig. 26. Reduced bit-timing system

Let the input signal be normalized such that both the mean and variance of the integral of the signal-plus-noise over a bit time are given by $\rho^2 = 2ST_B/N_0$, where S is signal power, T_B is bit duration, and N_0 is the one-sided noise spectral density. Then the integrals, $I_{i,j}$, $j = 1, 2, 3$, which comprise the i th timing error sample, E_i^* , are given by

$$\begin{aligned} I_{i,1} &= \int_{t_i}^{t_{i+1}} y(\tau) d\tau = M_i \frac{ST}{N_0} + n_1 \left(\frac{ST}{N_0} \right)^{1/2} \\ I_{i,2} &= \int_{t_{i+1/4}}^{t_{i+3/4}} y(\tau) d\tau \\ &= 2 \frac{ST}{N_0} \left[M_{i-1} \left(\frac{1}{4} + \tau \right) + M_i \left(\frac{1}{4} - \tau \right) \right] + n_2 \left(\frac{ST}{N_0} \right)^{1/2} \end{aligned} \quad (3)$$

$$I_{i,3} = \int_{t_{i-1/4}}^{t_{i+1/4}} y(\tau) d\tau = M_{i-1} \frac{ST}{N_0} + n_3 \left(\frac{ST}{N_0} \right)^{1/2}$$

where n_1, n_2, n_3 are mutually independent zero-mean, unit variance Gaussian random variables, M_i and M_{i-1} are the values (+1 or -1) of the i th and $i-1$ th data bits, and τ is the timing error—in fractions of the bit duration. T_B —between the (possible) transition time t_i and the estimate of it, \hat{t}_i . The i th timing error sample, E_i^* , and the expected value of it, \bar{E}_i^* , are given in Eq. (4)

$$\begin{aligned} E_i^* &= I_{i,2} (I_{i,3} - I_{i,1}) \\ &= 2 \left(\frac{ST}{N_0} \right)^2 (M_{i-1} - M_i) \left(M_{i-1} \left[\frac{1}{4} + \tau \right] + M_i \left[\frac{1}{4} - \tau \right] \right) \\ &\quad + \text{noise terms} \end{aligned} \quad (4)$$

$$\begin{aligned} \bar{E}_i^* &= \left(\frac{ST}{N_0} \right)^2 \left\{ 2\tau (M_{i-1} - M_i)^2 + \frac{1}{2} (M_{i-1}^2 - M_i^2) \right\} \\ &= 0, \quad \text{if } M_i = M_{i-1} \\ &= 8\tau \left(\frac{ST}{N_0} \right)^2, \quad \text{if } M_i \neq M_{i-1} \end{aligned}$$

The noise terms not explicitly shown in Eq. (4) will produce a jitter in the resulting time estimate from the NCO, and thus cannot be ignored. The mean-squared value of E_i^* is given by

$$\begin{aligned} \bar{E}_i^{*2} &= \bar{E}_i^{*2} + \left(\frac{ST}{N_0} \right)^3 (M_i - M_{i-1})^2 + 2 \left(\frac{ST}{N_0} \right)^2 \\ &\quad + 8 \left(\frac{ST}{N_0} \right)^3 \left[M_{i-1} \left(\frac{1}{4} + \tau \right) + M_i \left(\frac{1}{4} - \tau \right) \right]^2 \end{aligned} \quad (5)$$

Furthermore, $I_{i,1}$ is identical to $I_{i-1,3}$ and $I_{i,3}$ is identical to $I_{i+1,1}$, so each of these is used in producing the $i-1$ th and the $i+1$ th error sample, respectively. The cross-correlations with adjacent error samples are given by

$$\begin{aligned}\overline{E_{i+1} \cdot E_i} &= \overline{E_i} \cdot \overline{E_{i+1}} - 4 \left(\frac{ST}{N_0} \right)^3 \\ &\times \left(\frac{M_i + M_{i-1}}{4} - \tau [M_i - M_{i-1}] \right) \\ &\times \left(\frac{M_{i+1} + M_i}{4} - \tau [M_{i+1} - M_i] \right)\end{aligned}\quad (6)$$

$$\begin{aligned}\overline{E_{i-1} \cdot E_i} &= \overline{E_i} \cdot \overline{E_{i-1}} - 4 \left(\frac{ST}{N_0} \right)^3 \\ &\times \left(\frac{M_i + M_{i-1}}{4} - \tau [M_i - M_{i-1}] \right) \\ &\times \left(\frac{M_{i-2} + M_{i-1}}{4} - \tau [M_{i-1} - M_{i-2}] \right)\end{aligned}$$

E_i is not correlated with timing error samples not adjacent to it. Since the loop filter averages over a large number of error signals, the effective variance of E_i is given by

$$V_{eff}\{E_i\} = \overline{E_i \cdot E_i} - \overline{E_i}^2 + \overline{E_i E_{i+1}} - \overline{E_i} \overline{E_{i+1}} + \overline{E_i E_{i-1}} - \overline{E_i} \overline{E_{i-1}} \quad (7)$$

and if $\tau \approx 0$, the effective variance reduces to

$$\begin{aligned}V_{eff}\{E_i\} &= 2 \left(\frac{ST}{N_0} \right)^2 + \left(\frac{ST}{N_0} \right)^3, & \text{if } M_i M_{i-1} = 1 \\ &= 2 \left(\frac{ST}{N_0} \right)^2 + 4 \left(\frac{ST}{N_0} \right)^3, & \text{if } M_i M_{i-1} = -1\end{aligned}\quad (8)$$

Software timing constraints may make it desirable not to generate a bit-timing sample for every possible transition. If this is done, the correlation for adjacent error samples does not exist, and the effective variance of E_i is

$$\begin{aligned}V_D\{E_i\} &= 2 \left(\frac{ST}{N_0} \right)^2 + 2 \left(\frac{ST}{N_0} \right)^3, & \text{if } M_i M_{i-1} = 1 \\ &= 2 \left(\frac{ST}{N_0} \right)^2 + 4 \left(\frac{ST}{N_0} \right)^3, & \text{if } M_i M_{i-1} = -1\end{aligned}\quad (9)$$

To consider the E_i in the delay-locked loop, normalize the signal such that

$$\overline{E_i} = \tau, \quad \tau \text{ for } |\tau| \leq \frac{1}{4}$$

or

$$\begin{aligned}\overline{E_i} &= 0, & \text{if } M_i M_{i-1} = 1 \\ &= 2\tau, & \text{if } M_i M_{i-1} = -1\end{aligned}\quad (10)$$

Then the effective variance of the i th sample becomes

$$\begin{aligned}V_{Ei} &= \frac{1}{8} \left(\frac{N_0}{ST} \right)^2 + \frac{1}{16} \left(\frac{N_0}{ST} \right), & \text{if } M_i M_{i-1} = 1 \\ &= \frac{1}{8} \left(\frac{N_0}{ST} \right)^2 + \frac{1}{4} \left(\frac{N_0}{ST} \right), & \text{if } M_i M_{i-1} = -1\end{aligned}$$

Let X_i be the sequence of bit-time estimates and Z_i be the sequence of true bit times, and implement the delay-locked loop by the difference equation

$$\begin{aligned}X_{i+1} &= X_i + K \cdot E_i \\ &\cong X_i + K \cdot (Z_i - X_i)\end{aligned}\quad (11)$$

where E_i is the error signal generated by the method just described. To account for the randomness of the data stream, let $d_i = M_i M_{i-1}$ take values $+1$ and -1 with equal probability. The loop closure equation then becomes

$$\begin{aligned}X_{i+1} &= X_i + K(1 + d_i)(Z_i - X_i) \\ &\quad + K[N_{i1} + (1.5 + 0.5d_i)N_{i2}]\end{aligned}\quad (12)$$

where

$$\overline{N_{i1}} = \overline{N_{i2}} = \overline{N_{i1}N_{i2}} = 0$$

$$\overline{N_{i1}^2} = \frac{1}{8} \left(\frac{N_0}{ST} \right)^2$$

$$\overline{N_{i2}^2} = \frac{1}{16} \left(\frac{N_0}{ST} \right)$$

Assume that $Z_i = Z + i\psi$. Taking the expected value of the $\{X_i\}$ as given in Eq. (12), and assuming a steady-state solution produces

$$E\{X_i\} = Z_i - \frac{\psi}{K}\quad (13)$$

In a similar manner, the variance of the $\{X_i\}$ in steady state may be determined to be

$$V_x = V_x(1 + k[1 + d])^2 + K^2 [\overline{N_{i1}^2} + (1.5 + 0.5d)^2 + \overline{N_{i2}^2}] \quad (14)$$

$$V_x = \frac{K}{2(1-K)} \left[\frac{1}{8} \left(\frac{N_0}{ST} \right)^2 + \frac{5}{32} \left(\frac{N_0}{ST} \right) \right] \quad (15)$$

The development of V_x has assumed that the error signal is linear. In reality, symmetries between the integrations involved in Eq. (4) produce an error signal whose expected value is shown in Fig. 27. To verify Eq. (15), a Fortran simulation was run using $K_r = 0.005$, with excellent agreement with Eq. (15), as shown in Fig. 28. Figure 29 shows the error-rate data from the same simulation.

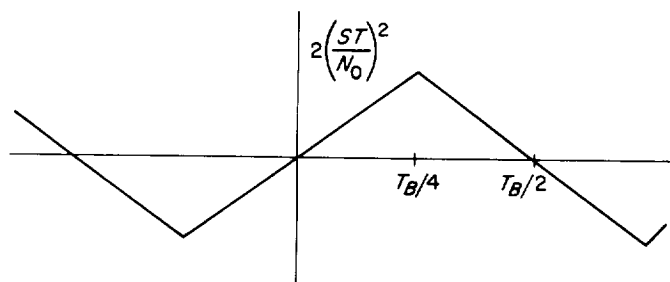


Fig. 27. Error signal of delay-lock loop

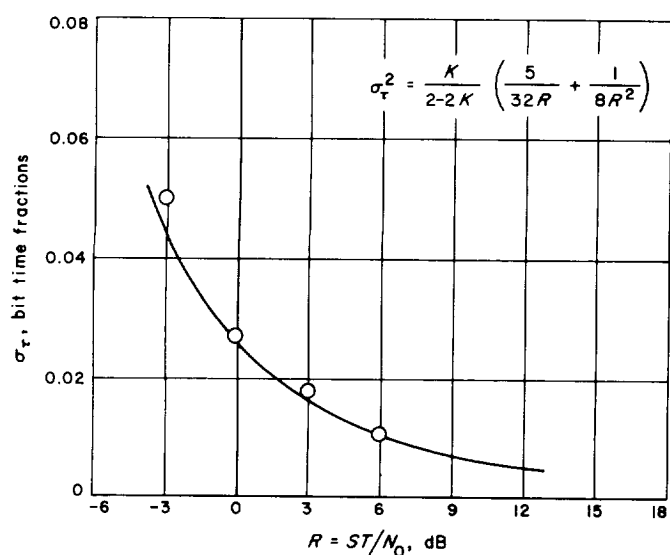


Fig. 28. Timing jitter—theoretical and simulation results for loop gain = 0.005

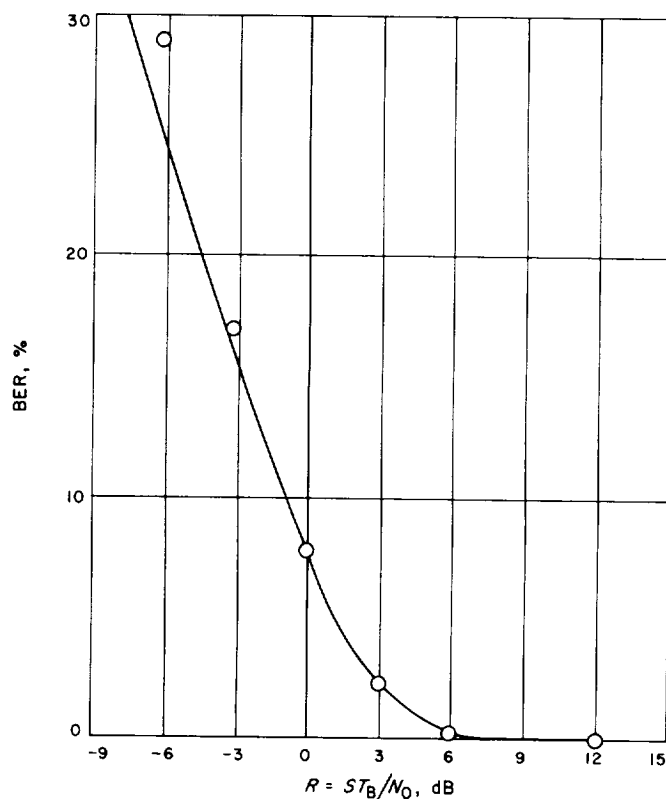


Fig. 29. Comparison of perfectly timed detection BER and simulated results for data-derived sync

Even though the individual error signals are not Gaussian, the timing sequence itself may be treated as if Gaussian with variance given by Eq. (15) for small K . The X_i represent, effectively, an average over $2/K$ of the past E_i , which converges to a Gaussian distribution as K decreases.

The degradation, if any, in bit-error probability due to bit-timing noise may be computed using this approximation to the distribution of the $\{X_i\}$.

c. Effects of bit sync jitter on detection. If the effects of the RF and subcarrier tracking loops are ignored, the effects of bit-timing jitter on the error probability of a correlation detector is a quite simple and well-documented phenomenon (Refs. 5 and 6). Figure 30 shows a possible data waveform, along with an erroneous sequence of estimated transition times and the resultant waveform in the correlation detector. It is evident that the timing offset, $\hat{t}_i - t_i$, has no effect on the correlator output unless a data transition is crossed. If a transition is crossed, the effective signal amplitude is reduced by a factor $(1 - 2|\tau|)$

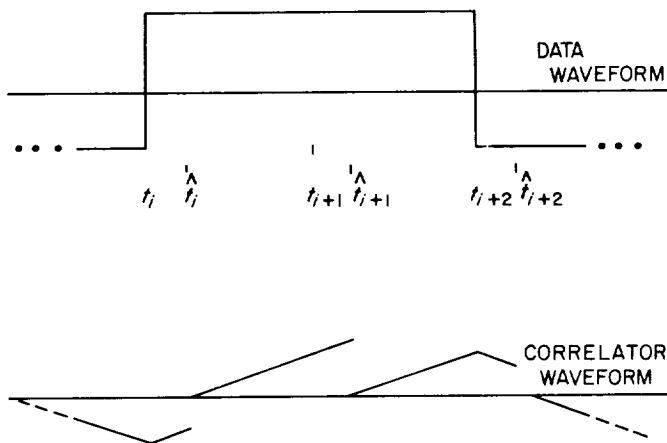


Fig. 30. Effects of bit-timing errors

where τ is the timing error measured in fractions of the bit duration. Since the probabilities of encountering a transition and a nontransition between any two bits may be assumed to be both equal to $\frac{1}{2}$, the probability of bit-detection error is

$$P_e = \frac{1}{2} \int_{-\frac{1}{2}}^{\frac{1}{2}} p(\tau) \operatorname{erfc} \left(\left[\frac{2ST_B}{N_0} \right]^{\frac{1}{2}} x [1 - 2|\tau|] \right) d\tau + \frac{1}{2} \operatorname{erfc} \left(\frac{2ST_B}{N_0} \right)^{\frac{1}{2}} \quad (16)$$

where $\operatorname{erfc}(x)$ denotes the integral from x to ∞ of the standardized Gaussian density function and $p(\tau)$ is the probability density function of τ , the timing error.

Exact evaluation of Eq. (16) would require numerical integration, which is probably not justified without including the effects of the subcarrier loop in the distribution of τ . As an alternative, the effective signal-to-noise ratio (SNR) at the output of the data correlator may be computed. If this effective SNR is only slightly degraded by the timing jitter, the increase in error probability due to timing jitter will also be slight; but the nonlinearity of the $\operatorname{erfc}(x)$ function makes a more quantitative connection difficult. Nevertheless, the convenient degradation-in-SNR model will be used as a performance measure for the remainder of the bit-synchronizer discussion instead of the more exact but cumbersome bit error rate (BER) model as described by Eq. (16). This effective SNR is given by

$$SNR_E = \frac{ST_B}{N_0} \left[\frac{1}{2} \int_{-\frac{1}{2}}^{\frac{1}{2}} p(\tau) [1 - 2|\tau|]^2 d\tau + \frac{1}{2} \right] \quad (17)$$

and if jitter is controlled to a small enough variance for the Gaussian approximation to be valid,

$$SNR_E \approx \frac{ST_B}{N_0} \left[1 - 2 \left(\frac{2}{\pi} V_j \right)^{\frac{1}{2}} \right] \approx \frac{ST_B}{N_0} \left[1 - 2 \left(\frac{K}{\pi(1-K)} \left[\frac{1}{8} \left(\frac{N_0}{ST_B} \right)^2 + \frac{5}{32} \left(\frac{N_0}{ST_B} \right) \right] \right)^{\frac{1}{2}} \right] \quad (18)$$

where the jitter variance in Eq. (15) has been used. The loss in SNR due to timing jitter is plotted in Fig. 31 as a function of ST_B/N_0 for several values of K , the bit-tracking loop gain.

d. The acquisition problem. When it is initially activated, the bit-synchronizer timing generator will produce marker pulses which are at the same rate as the received bits (to a close tolerance) but which have an unknown phase error with respect to the received data bits. Before the data can be reliably detected, this phase error must be reduced to a very small value. One way of doing this is simply to allow the bit-time tracking device to track to a stable node. This process, however, is slow; and at low bit rates may take many minutes. The acquisition procedure introduced and analyzed in the following section

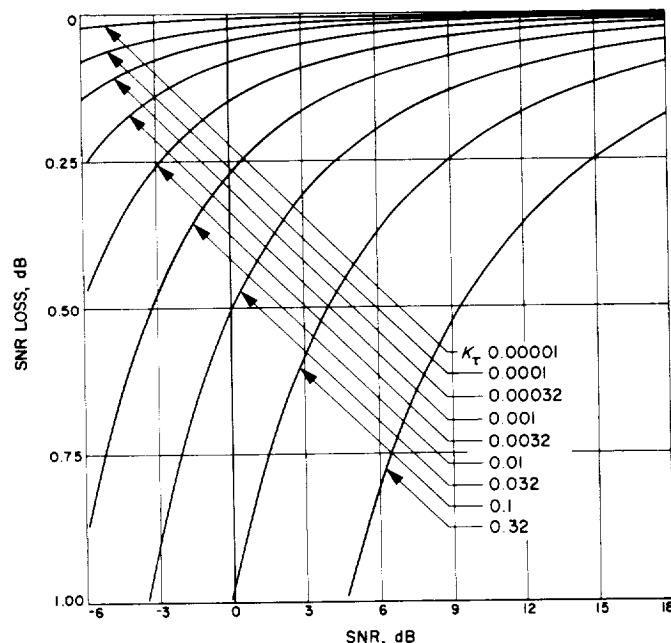


Fig. 31. SNR loss due to timing jitter

has the (possible) disadvantage that no data can be detected while acquisition proceeds, coupled with the advantage that both the acquired timing jitter and the probability of failure can be made as small as desired if there is no rate error between the received signal and the timing generator.

The acquisition process is functionally diagrammed in Fig. 32. The number-controlled oscillator (NCO) used in the bit-tracking process is initialized to run at the proper bit rate; and, as the data is received, the four y_i 's are computed:

$$y_j = \sum_{i=1}^N \left(\int_{t_{i,j/4}}^{t_{i+1,j/4}} y(t) dt \right)^2, \quad j = 0, 1, 2, 3 \quad (19)$$

where $y(t)$ is the received signal; N is the number of bits used in the acquisition process. The y_i 's are differenced to form the δ_j ($j = 0, 1$), which are used to compute τ , the delay shift from y_0 's start to the true bit start time. The expected values of the δ_j are shown in Fig. 33. Let $E\{\delta_j\} = d_j$ ($j = 0, 1$). The d_j 's follow these rules:

$$\begin{aligned} \text{If } d_0 > 0, & \quad d_1 = A \cdot (4\tau) \\ \text{If } d_0 \leq 0, & \quad d_1 = A \cdot (2 - 4\tau) \\ \text{If } d_1 > 0, & \quad d_0 = A \cdot (1 - 4\tau) \\ \text{If } d_1 \leq 0, & \quad d_0 = A \cdot (4\tau - 3) \end{aligned} \quad (20)$$

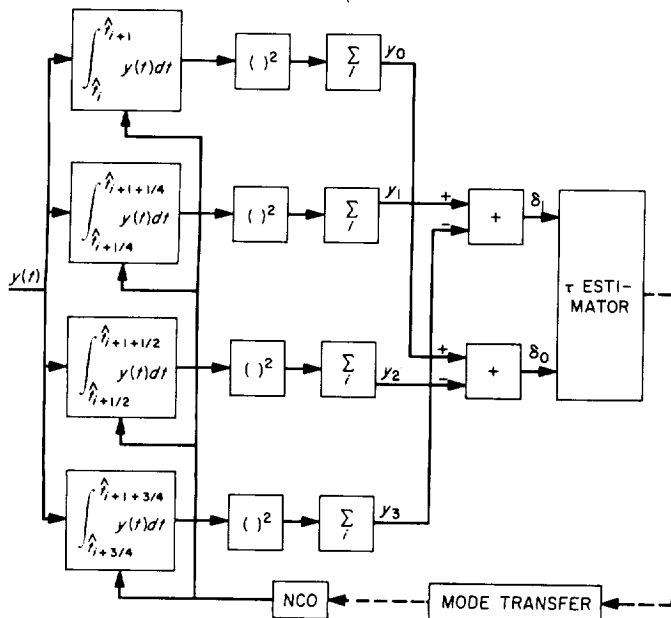


Fig. 32. Functional diagram of acquisition process

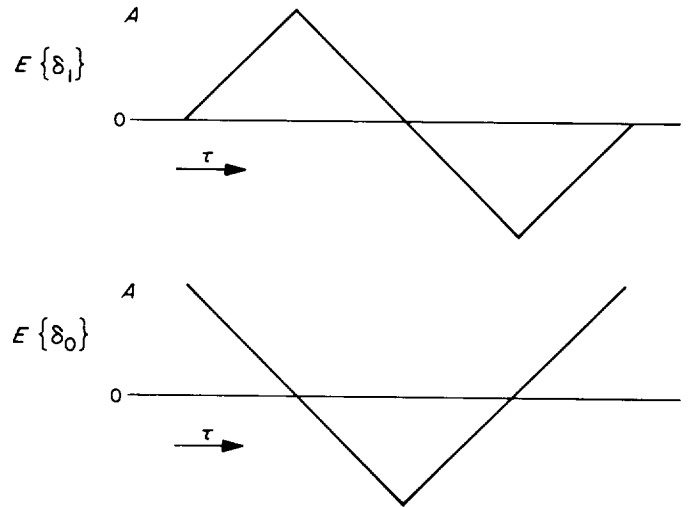


Fig. 33. Expected value of δ_j 's as a function of τ

Either of the two δ_j 's could be selected as a pivot and τ estimated using δ_j and the proper equation from Eq. (20). The probability of the acquisition failure is the probability that the wrong sign is selected for the pivot δ_j , i.e.,

$$P_r \{\text{acq fail}\} = P_r \{d_j \cdot \delta_j < 0 \mid \delta_j \text{ is pivot}\} \quad (21)$$

Since choice of pivot is arbitrary, it should be selected to minimize (if possible) the failure probability. This can be done by selecting that δ_j which is larger in magnitude as the pivot. With this additional constraint

$$P_r \{\text{acq fail}\} = P_r \{(d_j \cdot \delta_j < 0) \cdot (|\delta_j| > |\delta_j|)\} \quad (22)$$

Figure 34 shows the locus of d_j/d_j and the associated failure region in δ_j/δ_j space for τ in one particular quadrant of its range. Since the problem is symmetric, only one quadrant need be considered. The probability of failure is clearly bounded above by the probability of failure when the noises are fully correlated, or

$$P_r \{\text{acq fail}\} \leq P_r \left\{ \delta_j < d_j - \frac{A}{2} \right\} \quad (23)$$

(d_j assumed positive). The statistics of the δ_j were determined in the first-order loop-tracking analysis.

Assume that M data transitions occurred in the signal used to generate the y_i 's, and assume further that both N and M are large enough that end-effects in the summations may be ignored. Then it follows from Eqs. (4)

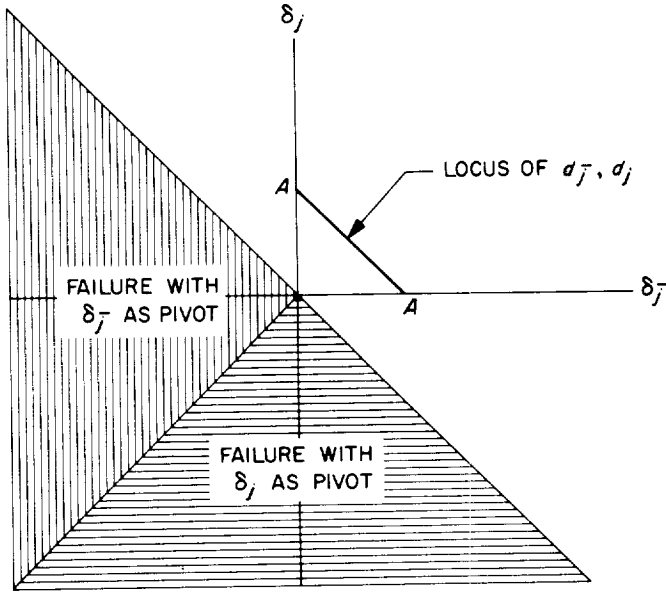


Fig. 34. Locus of d_j , d_j and the acquisition failure region for one quadrant of τ 's range

and (6) that

$$E\{\delta_1\} = 2M \left(\frac{ST_B}{N_0} \right)^2 4\tau \quad (24)$$

$$V\{\delta_1\} = 2N \left(\frac{ST_B}{N_0} \right)^2 + M \left(\frac{ST_B}{N_0} \right)^3 \times \left[6 - 2\frac{M}{N} + 32\tau^2 \left(1 + \frac{M}{N} \right) \right]$$

for $|\tau| \leq 1/4$. Equation (24) may be extended in the obvious manner to apply to δ_0 and to δ_1 with $|\frac{1}{2} - \tau| \leq 1/4$. Applying Eq. (24) to Eq. (23), and taking an upper bound on the variance produces

$$P_r(\text{acq fail}) \leq P_r \left(N_1 > \frac{1}{\left[\frac{N}{2M^2R^2} + \frac{2}{MR} \right]^{1/2}} \right) \quad (25)$$

where N_1 is a zero-mean unit-variance Gaussian-random variable, and $R = ST_B/N_0$. If the data bits are assumed independent and (± 1) equiprobable, the expected value of M is $N/2$. The bound in Eq. (25) is monotonically decreasing in N if M is proportional to N , and can be forced to assume as small a value as desired. One approach to specifying the acquisition process using Eq. (25) would be to set a threshold on M , e.g., $M_T = N/4$, and reject data if the measurements fell below that level. The

proper value of N could then be specified from the acceptable failure probability level, and the SNR.

The failure probability is only one of the two parameters necessarily connected with the acquisition process. The other parameter of interest is the resultant jitter in the estimated τ . To invert Eq. (20), the parameter A must be known. From Eq. (24), $A = 2M (ST_B/N_0)^2$; and since M depends upon the data sequence, it must be estimated. Note from Fig. 33

$$|d_0| + |d_1| = A \quad (26)$$

Then if the SNR of the δ_j 's is high

$$|\delta_0| + |\delta_1| \approx A \quad (27)$$

with high probability. Thus, if δ_0 is selected as the pivot, τ is in 1st or 4th quadrants, assuming no acquisition failure.

$$\hat{\tau} = \frac{\frac{1}{4} \delta_1}{|\delta_0| + |\delta_1|} \quad (28)$$

Let $\delta_1 = d_1 + n_1$, $|\delta_1| = |d_1| + n'_1$, $|\delta_0| = |d_0| + n'_0$,

$$\hat{\tau} = \frac{1}{4} \frac{d_1 + n_1}{|d_1| + |d_0| + n'_0 + n'_1} \quad (29)$$

$$\hat{\tau} = \tau + \frac{\frac{1}{4} n_1 - \tau n'_1 - \tau n'_0}{|d_0| + |d_1|} + \text{higher order terms in } n'_0, n'_1$$

If SNR is high, the higher-order terms in Eq. (29) may be neglected; and either the contribution of the n 's may be neglected because τ is small, or they may be treated as Gaussian because the probability of their affecting the absolute value operation in Eq. (28) is small. In either case, the variance of $\hat{\tau}$ is given approximately by

$$V(\tau) \approx \frac{1}{8MR} + \frac{N}{32M^2R^2} \quad (30)$$

where again, the upper bound on the variance in Eq. (24) has been used. Interestingly enough, comparison of

Eqs. (25) and (30) reveals that

$$P_r \{ \text{acq fail} \} \geq P_r \left\{ \tau - \tau > \frac{1}{4} \right\} \quad (31)$$

under the assumptions of this analysis.

One of the assumptions made throughout this analysis was that τ did not vary as the N bits entering into the δ_i were received. While this restriction is not completely necessary, the expected value of the final time estimate will be the average of the true τ , provided τ varies slowly and over a small range during reception of the block of N data bits. If, for example, a rate error of 10^{-4} bits/bit existed between the timing generator and the actual bit stream, there would be a 2% drift in τ over a block of 200 data bits, and a corresponding 1% systematic error in the estimated τ . In general, the value of N chosen for a particular application will be a compromise between this systematic error, on the one hand, and jitter and acquisition failure probability, on the other. This compromise is the same one which must be made between jitter and static phase error in a first-order tracking loop with ramp input.

e. Second-order loop filter. One way of eliminating the static phase error arising from tracking a ramp input is the use of a second-order tracking filter. Doppler nominally is on the order of 10^{-5} to 10^{-6} bits/bit, but anomalies in the data source can push this to perhaps 10^{-3} bits/bit, which would create a sizeable static timing error for a loop gain of 10^{-2} or less. For this reason, the succeeding paragraphs will explore a few of the properties of a second-order digital tracking filter.

Figure 35 is a functional diagram of the discrete second-order tracking filter. This filter is governed by the set of difference equations:

$$\begin{aligned} E_i &= Z_i - X_i \\ F_i &= F_{i-1} + E_i + A(E_i - E_{i-1}) \\ X_{i+1} &= X_i + KF_i \end{aligned} \quad (32)$$

This filter is the discrete analog of the continuous servo:

$$F(S) = K \frac{1 + A \Delta \tau S}{(\Delta \tau)^2 S^2} \quad (33)$$

$$X(S) = \left[\frac{F(S)}{(1 + F(S))} Z(S) \right]$$

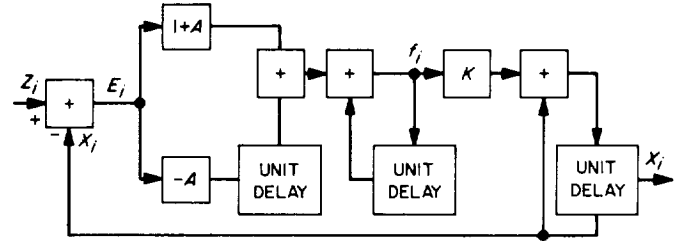


Fig. 35. Second-order sampled data tracking loop

where $\Delta \tau$ is the time-step between the samples of Eq. (32). The behavior of Eq. (33) is well known, and if the response of the filter is slow enough, should closely approximate the behavior of Eq. (32).

The response of Eq. (32) will be investigated by the technique of generating functions. Define

$$G_z(\eta) = \sum_{-\infty}^{\infty} \eta^i Z_i \quad (34)$$

and similarly define the generating functions of the other sequences involved in Eq. (32). Applying Eq. (32) to these and manipulating formally, one gets

$$G_x(\eta) = \frac{K\eta(1 + A - A\eta)}{(1 - \eta)^2 + K\eta(1 + A - A\eta)} G_z(\eta) \quad (35)$$

and

$$G_E(\eta) = \frac{(1 - \eta)^2}{(1 - \eta)^2 + K\eta(1 + A - A\eta)} G_z(\eta)$$

Applying the final value theorem to the second form shows that

$$\begin{aligned} E_\infty &= 0, & \text{if } Z_i &= \delta_{i,0} \\ & & \text{or if } Z_i &= 1, i \geq 0, & 0 \text{ before} \\ & & \text{or if } Z_i &= \alpha i, i \geq 0, & 0 \text{ before} \end{aligned} \quad (36)$$

That is, the filter shows the desired zero steady-state error for a pulse, step, or a ramp input. It shows the expected static error for a double ramp input.

Let the pulse response of the digital filter be H_j . Then for any sequence Z_i the sequence X_n is given by

$$X_n = \sum_{j=-\infty}^n H_{n-j} Z_j \quad (37)$$

Assume that the Z_j are independent Gaussian random variables with variance V_z . Then

$$\begin{aligned} E\{X_n^2\} &= E\left\{\left(\sum_{j=-\infty}^n H_{n-j} Z_j\right)\left(\sum_{i=-\infty}^n H_{n-i} Z_i\right)\right\} \\ &= \sum_{i,j=-\infty}^n H_{n-i} H_{n-j} E\{Z_i Z_j\} \\ &= V_z \sum_{i=0}^{\infty} H_i^2 \\ &\triangleq B_H V_z \end{aligned} \quad (38)$$

where B_H is, by definition, the noise bandwidth of the filter H_j . For any fixed value of open-loop gain K , the noise bandwidth B_H is minimized by selecting A to be

$$A_0 = \frac{1}{K^{1/2}} - \frac{1}{2} \quad (39)$$

at which point

$$B_{H0} \approx K \frac{2 + K^{1/2}}{2 - K^{1/2}} \quad (40)$$

Actual choice of the parameters A and K will depend upon the statistics of the (Z_i) and the constraints upon $(X_i - Z_i)$. If the (Z_i) are relatively stable, and initial acquisition performed as an estimation rather than as a tracking process, B_H can be chosen to satisfy jitter requirements at the detector, and A and K chosen from Eqs. (39) and (40). The resultant jitter variance in question is (see Eq. 15):

$$V_x = B_H \left[\frac{1}{8} \left(\frac{N_0}{ST_B} \right)^2 + \frac{5}{32} \left(\frac{N_0}{ST_B} \right) \right] \quad (41)$$

where B_H defines A and K through Eqs. (39) and (40).

f. Loop nonlinearities. Analysis of the bit synchronizer presented so far has treated the tracking loop as if it were a linear sampled servo. There are, however, two nonlinearities which must be accounted for. One of these is shown in Fig. 27 in the decreasing error signal with increasing $|\tau|$ in the region $\frac{1}{4} \leq |\tau| < \frac{1}{2}$. The exact probability distribution of τ may be determined by a technique similar to that used by Viterbi (Ref. 7) for a continuous servo with generalized restoring force. Such refinement is unnecessary, however, as one of the requirements upon the bit synchronizer is that it contribute negligible degradation to the signal. One of the consequent necessary conditions is that the probability that τ is in the range

$\frac{1}{4} \leq |\tau| < \frac{1}{2}$ must be virtually zero. Since the loop error signal is linear in τ for $|\tau| < \frac{1}{4}$, the linear servo approximations that have been used must be valid for all situations of interest.

The second nonlinearity does not seem to be so easily dismissible. The nonlinearity in this case is the quantization of bit time—the controlled variable—in the timing generator or NCO. This quantization affects the bit-timing subsystem at two levels:

- (1) Bit-time and bit-time-rate offsets due to this discretization will directly affect bit-error rate.
- (2) Quantization of the time variable in the bit-tracking-servo will introduce a "dead zone" and may degrade its performance significantly. These two problems will be treated separately in the following.

Loss due to quantization. Assume that an estimate of bit timing exists separate from the NCO which is exact in rate and phase. Assume further that the NCO is forced to mark the bit time as its allowed state nearest to this correct timing estimate. Any losses (in SNR) arising in this configuration are due directly to the time discretization, and to no other cause. In the absence of noise, a computer-controlled delay-locked loop in which fine time resolution is maintained in software and a coarser resolution in hardware will closely approximate this operation.

Consider the detection of bit B_1 shown in Fig. 36. The start of the integral defining \hat{B}_1 is delayed by τ_p , a phase offset. The end of this integral is delayed by $\tau_p + \tau_R$, where τ_R is bit-duration (rate) error; τ_p and τ_R are measured in fractions of a bit duration. The effective SNR on \hat{B}_1 is given by

$$SNR_E = \frac{ST_B}{N_0} \frac{(1 - |\tau_p| - |\tau_p + \tau_R|)^2}{1 + \tau_R} \quad (42)$$

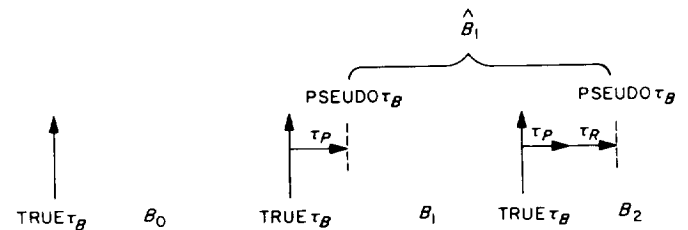


Fig. 36. Detection of a bit stream with improper time references

if the offsets cross a transition, or by

$$SNR_E = \frac{ST_B}{N_0} (1 + \tau_R) \quad (43)$$

if the offset crosses a nontransition. The parameter ST_B/N_0 is the bit energy to noise spectral density ratio.

If the allowed states of the NCO clock times are exactly δ_τ apart, the noiseless selection system will maintain $|\tau_p| \leq \delta_\tau/2$, $|\tau_R| \leq \delta_\tau$; τ_p and τ_R take a sequence of values which is completely determined by δ_τ . An upper bound on the SNR loss is determined by setting τ_p and τ_R at their bounds, i.e.,

$$SNR_E \geq \frac{ST_B}{N_0} \frac{(1 - 2\delta_\tau)^2}{1 + \delta_\tau} \quad (44)$$

This is shown as the upper bound on Fig. 37. For small δ_τ , the expected loss may be approximated by determining the expected value of the SNR_E under the assumption that τ_p and τ_R are independent and uniformly distributed over their allowed range. This is shown as the expected value line on Fig. 37.

It is apparent from Fig. 37 that a δ_τ on the order of 10^{-2} to 10^{-3} will provide the required resolution at the detector.

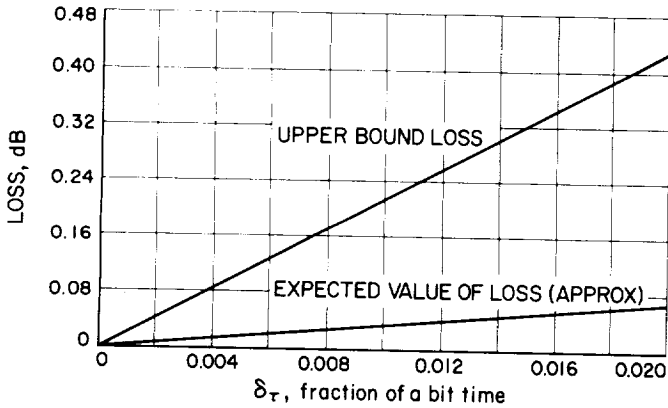


Fig. 37. Loss in signal power attributable solely to discretization of the time estimate

g. Quantization in the bit-tracking system. A discrete servo-system with quantizer is shown in Fig. 38. We wish to determine here for which values of δ_τ the quantizer may be neglected. In the absence of noise, a dead zone of width δ_τ/K exists which can significantly degrade the system's ability to follow variations on the input signal. The noise, however, will act as a "dither" signal and smooth out the quantizer steps.

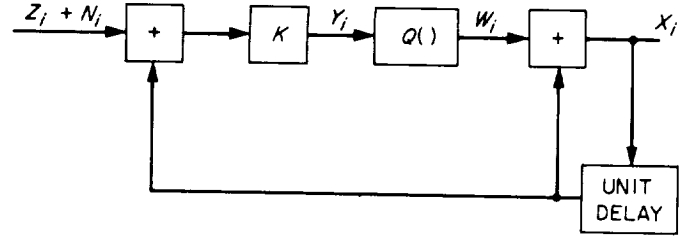


Fig. 38. Discrete servo with quantization:

$$Q(x) = \delta_\tau \left\lfloor \frac{1}{2} + \frac{x}{\delta_\tau} \right\rfloor$$

Let the input x to the quantizer $Q(x)$ be a Gaussian random variable with mean μ and variance σ^2 . The output variable q is defined by

$$q = Q(x) = \left\lfloor x + \frac{1}{2} \right\rfloor \quad (45)$$

where the variables q and x are both normalized with respect to the time step δ_τ .

The expected value of q is

$$E\{q\} = \int_{-\infty}^{\infty} \left\lfloor x + \frac{1}{2} \right\rfloor N_{\mu, \sigma^2}(x) dx \quad (46)$$

where $N_{\mu, \sigma^2}(x)$ is the normal density function for mean μ , and the variance σ^2 . The derivative of $E\{q\}$ with respect to μ is

$$\begin{aligned} \frac{d}{d\mu} E\{q\} &= \int_{-\infty}^{\infty} \left\lfloor x + \frac{1}{2} \right\rfloor \frac{\partial}{\partial \mu} N_{\mu, \sigma^2}(x) dx \\ &= - \int_{-\infty}^{\infty} \left\lfloor x + \frac{1}{2} \right\rfloor \frac{\partial}{\partial x} N_{\mu, \sigma^2}(x) dx \\ &= - \int_{-\infty}^{\infty} \left\lfloor x + \frac{1}{2} \right\rfloor d\{N_{\mu, \sigma^2}(x)\} \\ &= \int_{-\infty}^{\infty} N_{\mu, \sigma^2}(x) d\left\{ \left\lfloor x + \frac{1}{2} \right\rfloor \right\} \\ &= \sum_N N_{\mu, \sigma^2} \left(N - \frac{1}{2} \right) \end{aligned} \quad (47)$$

This series converges rapidly to a function of μ and σ^2 which is periodic in μ with period 1, and symmetric about $\mu = 0$. Figure 39 shows this function for $\mu \in (0, 1/2)$ and several values σ . For $\sigma \geq 1/2$, the function is 1, and the expected value of q is equal to μ . Applying this to the servo

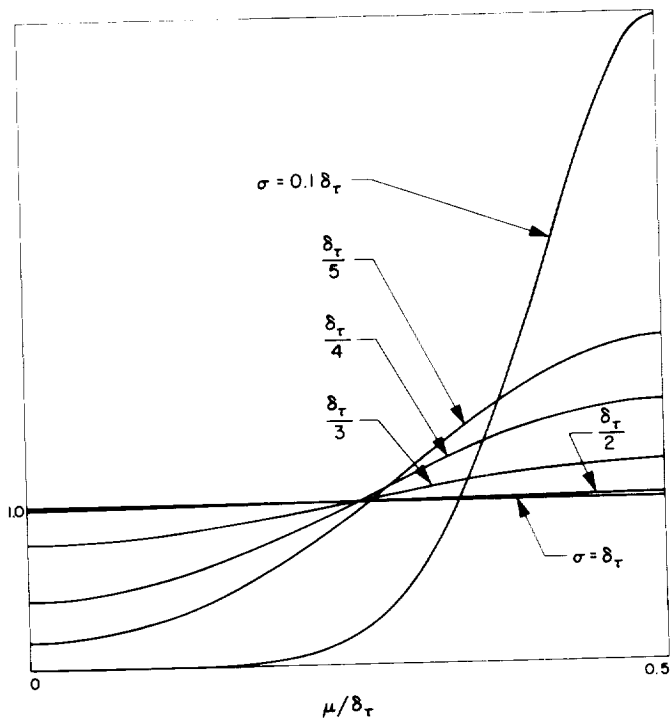


Fig. 39. Derivative of quantizer output with respect to mean of input

of Fig. 38:

$$\text{If } V\{Y_i\} \geq \left(\frac{\delta_\tau}{2}\right)^2$$

$$\text{Then } E\{W_i\} = E\{Y_i\} \quad (48)$$

Furthermore, if this condition holds for all Y_i , the expected value of X_i is equal to the expected value of the output sequence for an unquantized system. The effect of dead zone may be neglected if Eq. (48) holds.

The system of Fig. 38 may always be represented in the form of Fig. 40. In general, however, the nq_i are functions of the W_i . The condition in Eq. (48) guarantees that

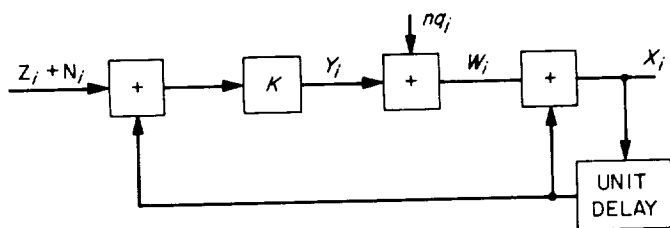


Fig. 40. Discrete servo with quantization noise
 $nq \in (-\delta_\tau/2, +\delta_\tau/2)$

$E\{nq_i\} = 0$ independent of $E\{Y_i\}$. The effect of the nq_i may thus be approximated by assuming that they are independent of the W_i and distributed uniformly in $[-\delta_\tau/2, \delta_\tau/2]$. Under this assumption

$$V\{X_i\} = \frac{K}{2(1-K)} \left\{ V\{n_i\} + \frac{1}{3} \left(\frac{\delta_\tau}{2K} \right)^2 \right\} \quad (49)$$

where the X_i follow a quantized distribution with Gaussian envelope. For any fixed value of SNR, Eq. (48) sets a minimal value of K for which Eq. (49) represents a valid model of the quantized system, i.e.,

$$K_{\min} = \frac{\delta_\tau 2 \frac{ST_B}{N_0}}{\left(2 + 3 \frac{ST_B}{N_0}\right)^{1/2}} \quad (50)$$

Without quantization, loop gain would be selected on the basis of the jitter statistics of the received bit stream. Since K_{\min} is monotonically increasing in ST_B/N_0 , Eq. (50) is most likely to constrain this normal selection process for strong signals. At $ST_B/N_0 = +12$ dB, $K_{\min} = 4.5\delta_\tau$. For $\delta_\tau \approx 10^{-3}$, this constraint $K \geq 4.5 \times 10^{-3}$ which is probably below the level which the tracking requirements would set.

Using $K = K_{\min}$ in the tracking loop produces

$$V\{X_i\} = \frac{\delta_\tau}{\left(2 + 3 \frac{ST_B}{N_0}\right)^{1/2} - 2 \delta_\tau \frac{ST_B}{N_0}} \left(\frac{7}{32} + \frac{N_0}{6 \cdot ST_B} \right) \quad (51)$$

which represents the minimum attainable jitter variance. For $ST_B/N_0 = 0$ dB and $\delta_\tau = 10^{-3}$, $V\{X_i\} \approx 1.75 \times 10^{-4}$, which represents an expected loss of ~ 0.1 dB if the X_i are assumed Gaussian. Equation (51) is plotted as Fig. 41, for various values of δ_τ .

The results of the time discretization analysis are essentially unchanged if the same arguments are applied to the second-order loop. Refer to Eq. (32) and assume that F_i and X_i are quantized, the other terms are not. Then the variance at the input to the quantizer is

$$\begin{aligned} V\{q_i\} &= K^2 (1 + 2A + 2A^2) V_z \\ &\approx 2B_{h_0}^2 V_z \quad \text{if } A = A_0 \end{aligned} \quad (52)$$

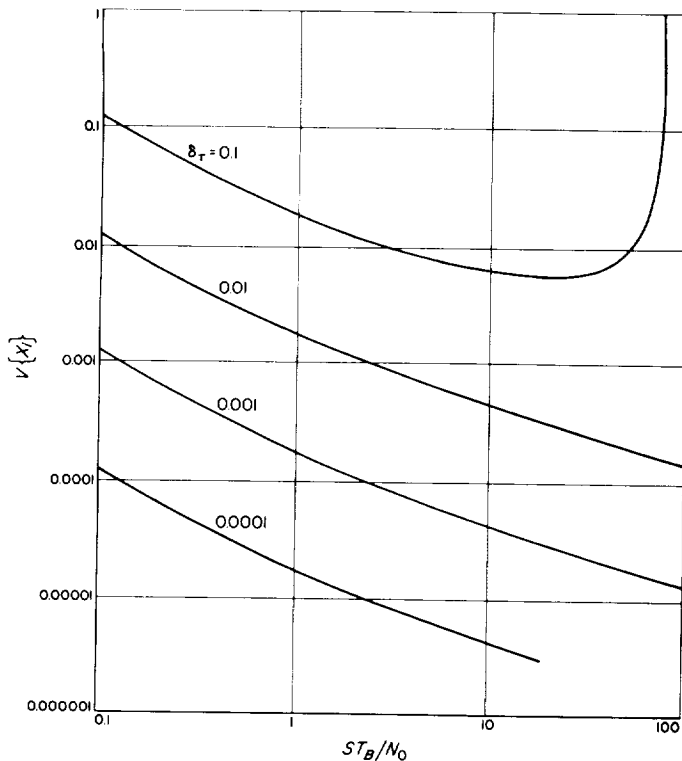


Fig. 41. Irreducible jitter variance versus SNR

Rather than defining a K_{min} , Eq. (48) defines a $B_{H,min}$ using Eq. (52). The results of Eq. (51) are multiplied by a $(2)^{1/2}$ factor in this process.

The digital timing generator being developed for the MMTS has a resolution of $1 \mu s$. The highest bit rate committed is on the order of 500 bits/s making the largest $\delta_\tau = 5 \times 10^{-4}$. The conclusion reached is that which could probably have been assumed: that the quantization of bit-timing in the NCO will have negligible effect upon the bit-timing subsystem under current bit-rate constraints.

D. System Verification and Testing, N. A. Burow, L. Couvillon, and A. Vaisnys

1. Goals

This part of the MMTS project accomplishes the initial integration and the detailed performance testing of a prototype MMT system. The goals are to prove the system concepts and to verify the results of system analysis. While a prototype MMTS was being built, a system model was used to make some required preliminary measure-

ments, the results of which will be described below. Further experiments will be performed with the prototype system now under construction. It is anticipated that this work will produce the final system parameters and specify the system performance for missions using the MMTS.

2. Approach

Shortly after the MMTS concept was generated, work began on the construction of a model of the system to demonstrate its operation and investigate the practical problems of building such a system. A Scientific Data Systems (SDS) model 920 computer was available, but the RF hardware called for in the early conceptual designs was not. It was therefore necessary to model the system at audio-frequencies; i.e., the 10-MHz bandpass filters were simulated by 100-kHz filters having the same bandwidth. The resulting assembly, which will hereafter be called the baseband breadboard (BBB), very closely duplicates the functions of the actual system design except that the input signal is the subcarrier(s) plus low-passed noise, instead of a phase-modulated intermediate carrier plus band-passed noise. In a sense, the 10-MHz IF has been replaced in the BBB by zero frequency.

Figure 42 is a diagram of the BBB. It shows the subcarrier and data source which generates square-wave subcarriers modulated (phase-shift keyed) by data bit streams, which can be alternate *one-zero*, all *ones*, or long pseudonoise (PN) code sequences. As shown, the bit timing clock may be coherent or noncoherent with the subcarrier clock. The subcarrier(s) thus generated is (are) linearly added to noise in a signal/noise mixer and presented to the BBB demodulator.

The remainder of Fig. 42 will be recognized as very similar to the system block diagram previously explained (Sect. B). The input signal (subcarrier plus noise) is impressed on a 100-kHz IF in the first multiplier². The resulting signal is then fed, in parallel, to two multipliers. In one it is multiplied by a square wave subcarrier reference and in the other by a 90-deg shift of the reference. The 0- and 90-deg reference multiplied signals are band-pass filtered at 100 kHz, one is low-pass filtered and limited, and the two are multiplied together to generate a phase-error voltage which is filtered and controls a VCO. Such a system is recognized to be a form of a Costas phase-lock loop.

²The word "multiplier" is used loosely here. In the mechanization, the multipliers are actually choppers.

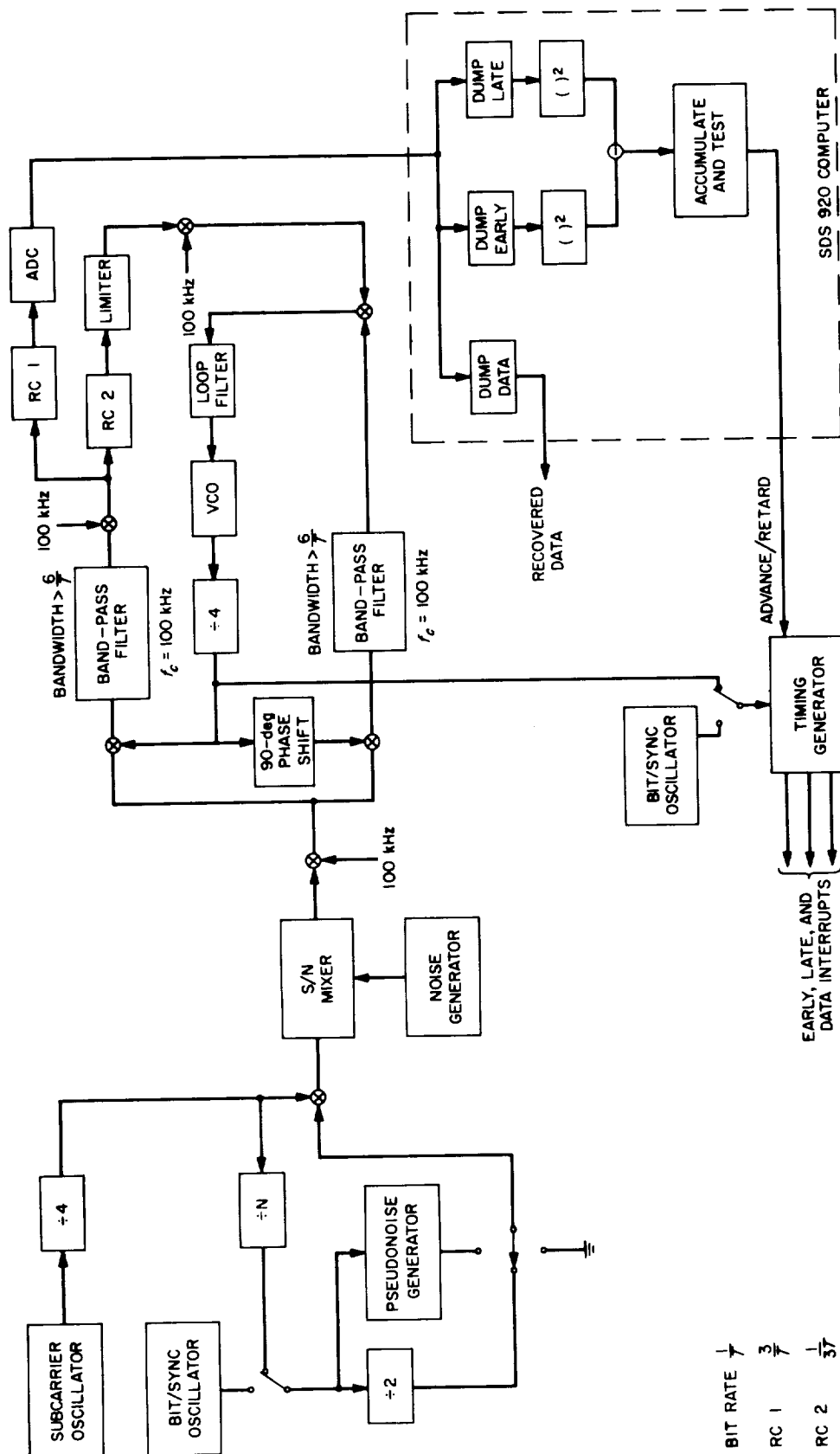


Fig. 42. BBB system diagram

The BBB was built up using Computer Control Co. (3C) digital circuits and operational amplifiers. The choppers are basically operational amplifiers operating in the differential mode. The choppers were designed to operate over a range of 20 mV to 5 V (48 dB). This dynamic range allows operation down to $ST/N_0 = 0$ dB at 6¼ bits/s with a 20-mV signal in a 40-kHz bandwidth, accommodating $\pm 3\sigma$ noise peaks linearly. The band-pass filters are of the Q multiplier type with a bandwidth tunable between 1200 and 200 Hz.

Initially, problems were encountered in interfacing the A/DC with the computer, and in the stability of some components, such as the VCO. For example, with the first VCO used, the best performance was obtained with a 2-Hz loop bandwidth. A newer model VCO allowed going to 1-Hz loop bandwidth, and only by using a HP 5100A frequency synthesizer as a VCO was it possible to go to loop bandwidths below 1 Hz and realize any improvement.

As shown in Fig. 42, data demodulated from the subcarrier by the Costas loop is low-pass filtered and digitized. The A/DC enters data to the SDS 920 computer, in which bit synchronization operations are carried out. The algorithm used in the BBB is the same as previously described (Sect. C-4); early and late samples of data are squared, subtracted, and their difference is used to generate a timing error signal. The timing generator circuitry for the BBB was built from 3C logic.

The computer programs for the BBB were written to accomplish only the required control and instrumentation functions for the equipment on hand; no consideration was given to other operations (e.g., decommutation) necessary in the real world or to integration of the software with other TCP functions. The software is organized as several subroutines, executed under interrupt control. Figure 43 is a flow diagram for the BBB bit synchronization program. It may be seen from Fig. 43 that the computer waits for a new interrupt after it has finished an operation requested by a prior interrupt. When a timing error computation has been made, the correction is outputted (POTted) immediately.

For instrumentation purposes, several additional routines have been added to the main program to allow examination of the system at various points, somewhat increasing the required running time. Four additional routines are: (1) computation of the normalized signal-to-noise ratio averaged over 1000 data bits, (2) printout on the line printer of both the corrected and uncorrected

digitized data from the two integrators, (3) outputting of the bit timing error values to a digital-to-analog converter to generate the open-loop bit sync error curves for observation, and (4) writing the corrected value of data taken at bit sync time on magnetic tape.

Considerable effort has gone into the design and construction of test instrumentation for the BBB. The test setup has been designed so that it may be used with the prototype system with minimal changes. Some of the system parameters which are accurately measurable with the test setup are bit-error rate, bit clock jitter, subcarrier jitter, bit acquisition time, and effective (internal) SNR.

The instrumentation used in evaluating the system is illustrated in Fig. 44. Bit-error rate tests are handled as follows:

As the data bits are recovered by the computer, they are outputted to a storage flip-flop. A bit-error rate monitor is used to compare the recovered bits with the corresponding bits from the modulator and to count the number of bits transmitted. It stops after a predetermined number of total bits and displays an error count.

Another measurement that is valuable in determining system performance is that of the jitter in the subcarrier loop. Both the subcarrier from the modulator and the recovered subcarrier are fed to a time interval counter which measures the time interval between their corresponding edges. This information is sampled and stored on tape for later analysis.

3. Baseband Breadboard Test Results

Initial runs on the BBB were made at a bit rate of 200 bits/s in order to allow debugging of the system with convenient signal levels and test times. Performance at this bit rate was found to be substantially in accordance with theory. Figure 45 is a plot of bit-error rate versus ST/N_0 , the ratio of energy per bit to noise spectral density. The experimental points are seen to be within 0.3 dB of theory; the instrumentation error is estimated at less than ± 0.2 dB at each individual point.

Also measured were the open-loop error curves for the subcarrier and bit-sync loops, Figs. 46 and 47, respectively. Figure 46 is seen to be a sawtooth wave as theoretically predicted; Fig. 47 is a sampled triangular wave, as it should be. These figures are for the case of no noise.

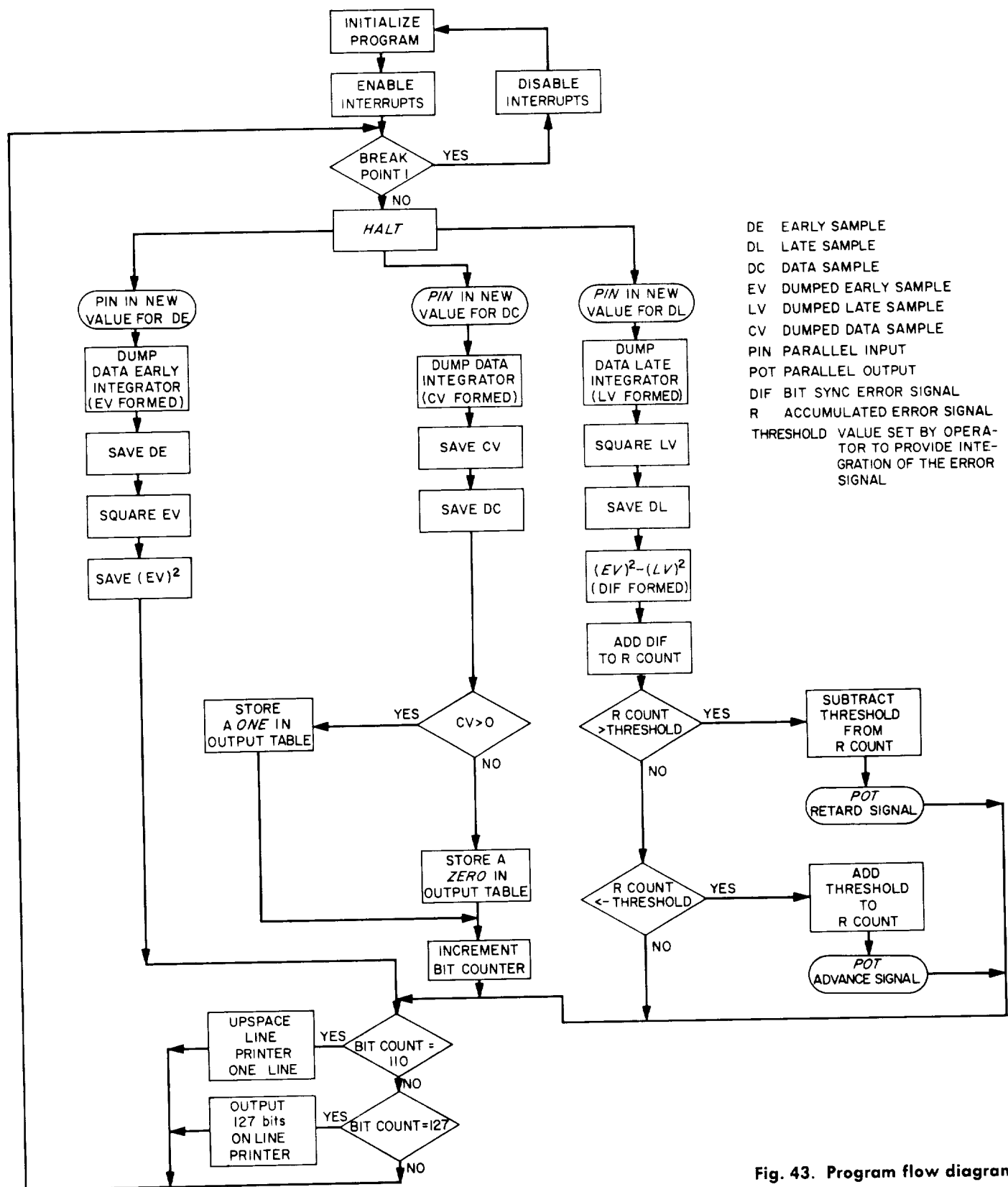


Fig. 43. Program flow diagram

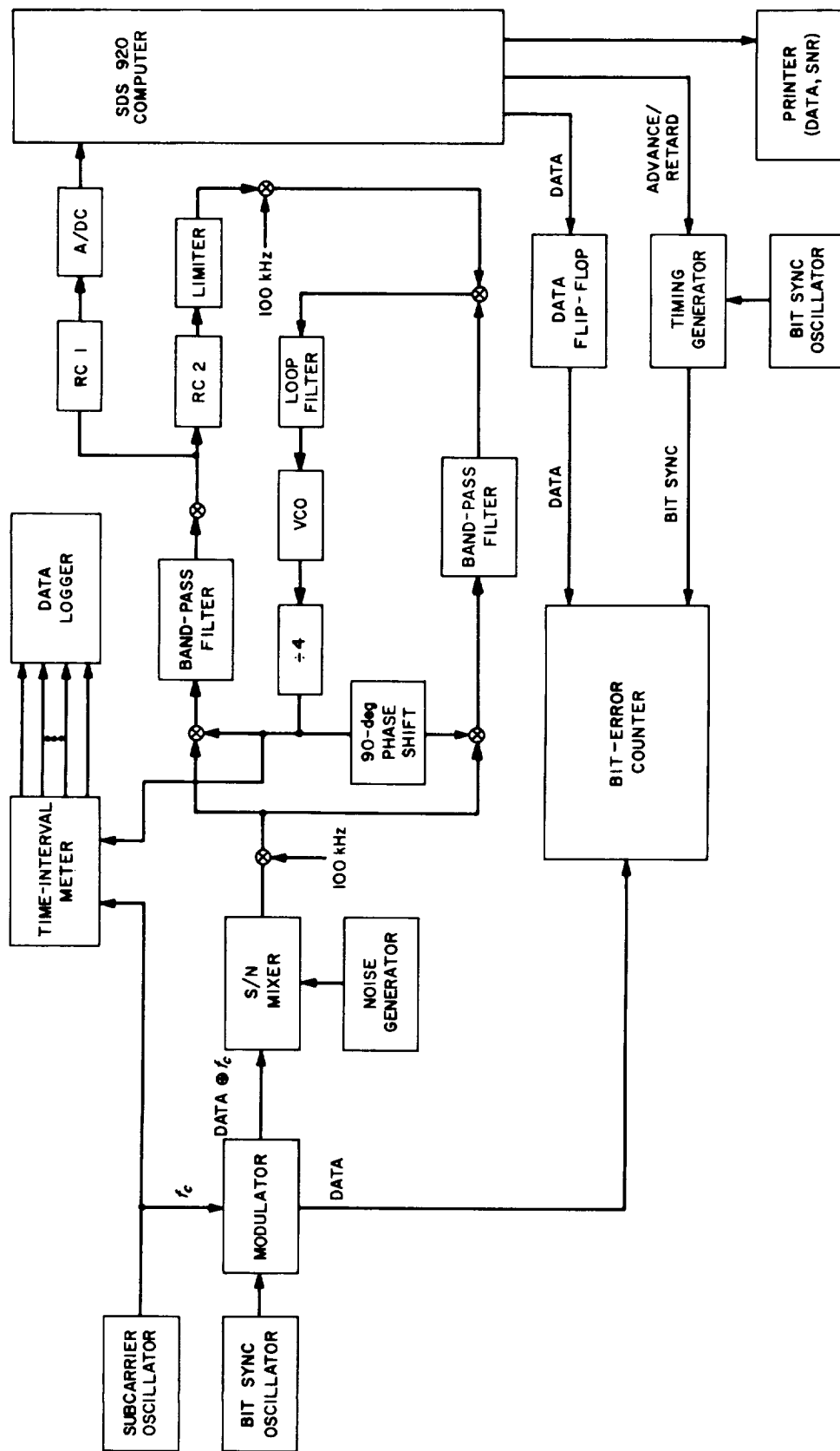


Fig. 44. BBB system test setup

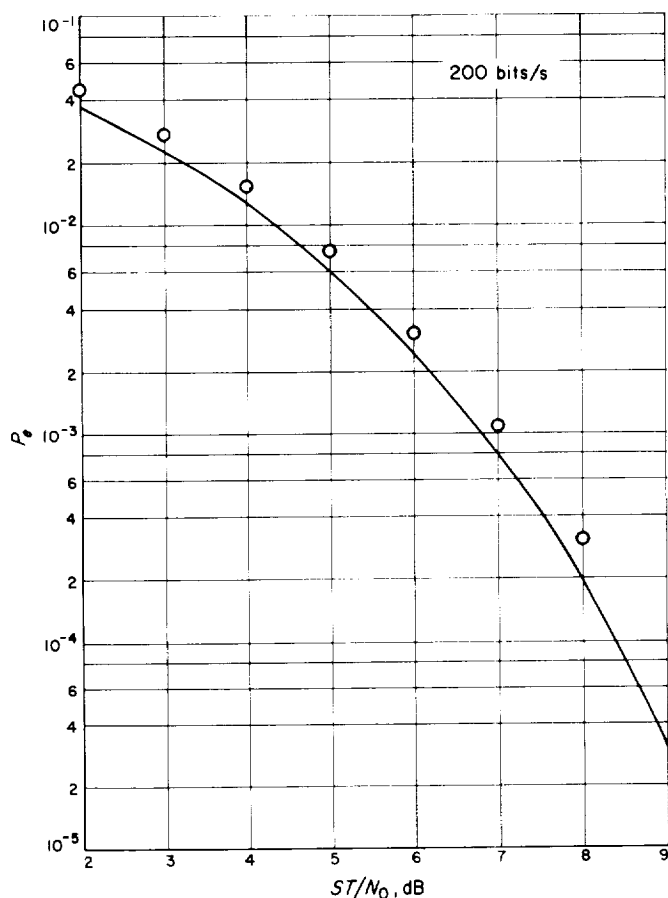


Fig. 45. Error rate versus SNR

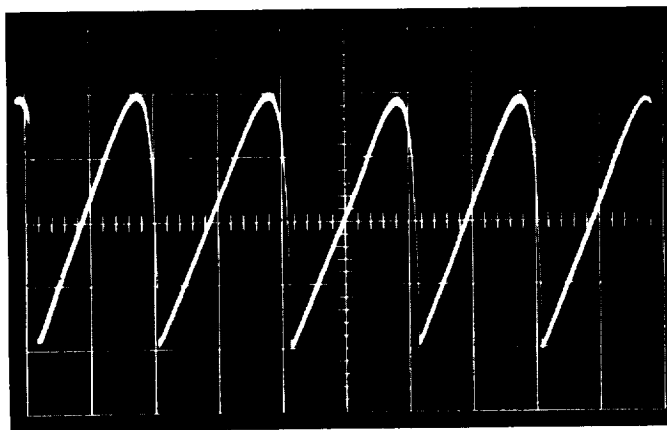


Fig. 46. Subcarrier S-curve

Results of error rate tests at lower bit rates were more pessimistic. Several runs have been made at 6¼ bits/s, but the results are not yet conclusive. At 6¼ bits/s, using a 1-Hz subcarrier loop bandwidth, it was found that the degradation due to jitter was on the order of 3 dB. It was

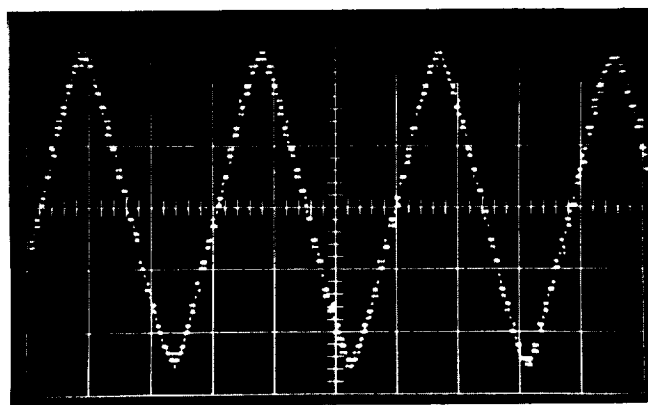


Fig. 47. Bit sync S-curve

difficult to obtain a loop narrower than 1 Hz, apparently, because of the large VCO constant and the large values of loop-filter components. By using the VCO in an HP 5100A synthesizer, it became possible to achieve narrower loop bandwidths. Figures 48 and 49 are plots of subcarrier jitter with loop bandwidths of 1 and ¼ Hz, respectively. Note that there is a substantial dependence of the jitter upon the presence of data modulation.

It is planned, as far as time allows, to further investigate the performance of the loop at low bit rates and to make a trade-off between loop bandwidth, performance degradation, and acquisition time.

4. Net System Verification Plans

A functional description of the net system was given in a previous section of this report. The net system prototype soon to be assembled in the lab is intended to be functionally identical to the systems that will eventually go to the DSN stations. Thus, it is intended to continually update it as design changes or improvements are made.

The test instrumentation to be used in evaluating the prototype will be substantially the same as that used with the breadboard system. A comprehensive test plan is being generated with inputs from each of the groups of the MMT project. The checkout of the prototype system will include, but will not be limited to, the following tests:

- (1) The determination of usable and forbidden subcarrier frequencies in the range of 20 Hz to 80 kHz.
- (2) Bit-error tests at selected bit rates in the range of 1 to 512 bits/s under various signal-to-noise conditions.

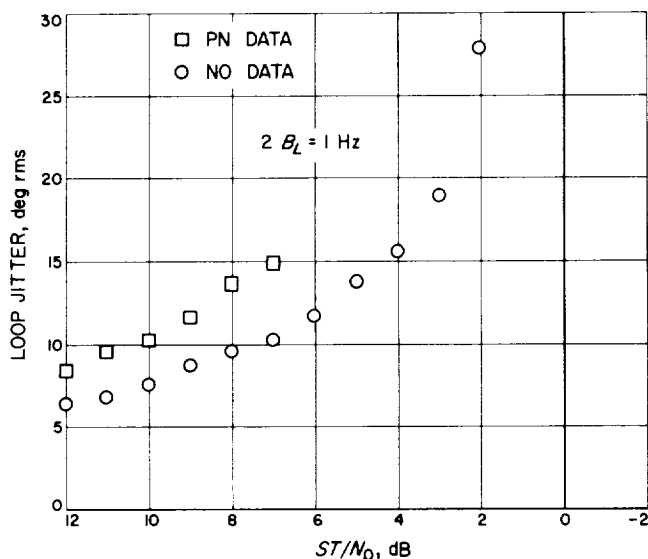


Fig. 48. Subcarrier jitter with 1-Hz loop bandwidth

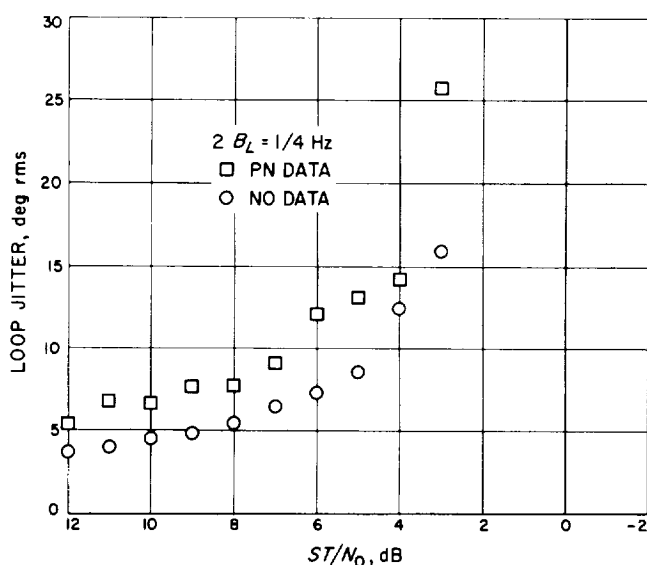


Fig. 49. Subcarrier jitter with 1/4-Hz loop bandwidth

- (3) Bit-error rate performance as subcarrier tracking loop bandwidth ($2 B_{L0}$) varies.
- (4) Subcarrier acquisition time as a function of ST/N_0 , frequency off-set, and $2 B_{L0}$.
- (5) Acquisition properties of the bit-sync loop.
- (6) Investigation of performance degradations as they are found.
- (7) Evaluation of performance in the magnetic tape playback (system backup) modes of operation.

E. Equipment Description, J. W. Layland, R. G. Petrie, J. E. Stelzried, and J. K. Woo

1. Subcarrier demodulator assembly, J. E. Stelzried

a. Electrical characteristics. The basic design philosophy incorporated into the subcarrier demodulator assembly (SDA) was compatibility and maximum equipment interchangeability with the existing receiver-exciter (R-E) subsystem and other DSN equipment.

b. Performance characteristics. This equipment is designed to demodulate data that is biphasemodulated on a subcarrier which is phase-modulated on a 10-MHz IF signal derived from the R-E subsystem. Pertinent parameters of this signal are as follows:

Subcarrier power	-70 dBmW \pm 15 dB
Subcarrier frequency	20 kHz to 1 MHz
Subcarrier doppler	$1 \times 10^{-5} \times F_{sc}$
Subcarrier to noise ratio	-77 dB maximum (bandwidth, 2 MHz at 1 dB)
Data rates	8 to 512 bits/s

A hardware block diagram of the SDA is shown in Fig. 50. This equipment contains a considerable amount of hardware applicable to future expansion capabilities for both high and low data-rate options, as described in more detail later in this report. In order to demodulate the data under all variable conditions of data rates, doppler rates, subcarrier frequencies, and output SNRs, system-selectable parameters were provided for the prototype SDA to evaluate for use in the DSIF. They are listed in Tables 1 to 6.

Table 1. Variable loop bandwidth ($2 B_{L0}$) selector

Selector position	Loop bandwidth $2 B_{L0}$, Hz	Nominal data rate, bits/s
1	0.010	1.0-2.2
2	0.022	2.2-4.7
3	0.047	4.7-10
4	0.10	10-22
5	0.22	22-47
6	0.47	47-100
7	1.00	100-220
8	2.20	220-470
9	4.70	470-1000
10	10.0	1000-2200
11	22.0	2200-4700
12	47.0	4700-10K
13	100.0	10K-22K
14	220.0	22K-47K
15	470.0	47K-100K

Variable loop bandwidth selector. The loop bandwidths and nominal data rates are given in Table 1.

This selector also controls the tracking or acquisition tuning range capabilities of the loop as defined in Table 2

Table 2. Tracking or acquisition tuning range capabilities of the loop

Selector position	Acquisition tuning range, Hz
1-3	± 2
4-6	± 20
7-9	± 200
10-12	± 2000
13-15	$\pm 20,000$

Data-rate selector. The data-rate selector provides variable RC integration time constants (T_D) for the prime data outputs, loop reference RC filter time constants (T_S) that precede the data limiter, the lock indicator relay time constant (T_L), and 10-MHz IF filter bandwidths as noted in Tables 3, 4, 5, and 6.

Table 3. Integration time constants for data outputs

Selector position	Time constant T_D , ms
1-3	3300.00
4-6	330.00
7-9	33.00
10-12	3.30
13-15	0.330

Table 4. Loop data filter time constants and lock detector error-channel signal time constants

Selector position	Time constants T_S and T_E , ms	Data rate, Hz
1	220.0	1.0-2.2
2	100.0	2.2-4.7
3	47.0	4.7-10
4	22.0	10-22
5	10.0	22-47
6	4.70	47-100
7	2.20	100-220
8	1.00	220-470
9	0.47	470-1000
10	0.22	1000-2200
11	0.10	2200-4700
12	0.047	4700-10K
13	0.022	10K-22K
14	0.010	22K-47K
15	0.0047	47K-100K

Table 5. Filter time constants of lock indicator relay

Selector position	Time constant T_L , s
1-3	50.000
4-6	5.000
7-9	0.500
10-12	0.500
13-15	0.500

Table 6. 10-MHz IF filter bandwidth

Selector position	IF bandwidth (-1 dB), kHz
1-2	Low data option
3-5	0.50
6-9	10.00
10-12	100.00
13-15	1000.00

c. Block diagram description. A hardware block diagram of the SDA is shown in Fig. 50. The numbered blocks represent individual subassemblies and indicate their specification numbers, while the large blocks represent panel-mounted equipment with small internal blocks representing separate functions inside these panel-mounted units. For discussion purposes, the block diagram may be broken down into the following categories: input distribution, data channel, error channel, lock detector, and reference distribution.

Input distribution. The input signal to the SDA may be selected from one of four sources:

- (1) 10-MHz input. This is the normal mode of operation. The 10-MHz signal is supplied from receiver 1 of the R-E subsystem, routed through the 10-MHz baseband relay, level set attenuator, and then distributed to the data and error channels via the 10-MHz IF distribution amplifier subassembly (9465). An auxiliary output of this signal is routed to the interface panel. The level set attenuator is variable in 1-dB increments over a 50-dB range. Its setting is dependent upon the modulation index of the subcarrier onto the carrier (0.1 to 1.27 rad); it also equalizes the various baseband inputs to the equivalent 10-MHz input.
- (2) Tape input. This baseband signal is supplied from the recording subsystem as a backup mode of operation. A baseband signal consists of a subcarrier biphase-modulated with data. This signal is routed through the baseband selector relay to the balanced modulator (9577). This unit modulates a 10-MHz reference signal with the baseband signal. The

resultant spectrum is then routed to the 10-MHz baseband relay. From there it is processed as a normal 10-MHz input signal.

- (3) Receiver 2 input. This is a signal supplied from receiver 2 of the R-E subsystem and is considered as an emergency backup mode in case of a failure or malfunction in receiver 1. This baseband signal is routed through the input selector similar to the recorded baseband signal.
- (4) Test input. This is a signal supplied from the SDA test equipment. It simulates the backup baseband input and is used only for equipment checkout and verification tests.

The input configuration is still under study and the switching arrangement shown in Fig. 50 may be revised when requirements are more firm.

Data channel. The signal is processed from the 10-MHz IF distribution amplifier to the data channel. The first subassembly in this channel is the upper 10-MHz signal phase switch (9578). This unit multiplies the 10-MHz input spectrum by the square-wave subcarrier reference frequency. The subcarrier reference is supplied by the subcarrier shaper and $\div 4$ subassembly (9588). This product is filtered by the following 10-MHz selectable bandwidth filter subassembly (9580). The filter eliminates all unwanted products and as much noise as is practical, leaving only the data square-wave modulated on the 10-MHz IF signal. Ideally, this filter is sufficient in width to pass the tenth harmonic of the data rate. Since it is not infinitely selectable, it is, at worst case, approximately ten times this width. The signal is then amplified in the 10-MHz IF amplifier subassembly (9589) to a level sufficient to be detected in the following 10-MHz amplitude detector (9581). This is a coherent detector which receives its reference signal from the reference distribution systems. The output of this detector is then buffered and split into three components. One component is routed via a monitor amplifier to the data oscilloscope input which is used for phasing purposes. A second component is routed through the data RC integrator and amplifier; it is then further split into two more identical components. These two components are then further buffered in the Dynamics Model 7575 isolation amplifier before becoming available as outputs—one for backup analog recording and the other for the TCP equipment. The Dynamics amplifiers ensure adequate signal isolation and capability of handling any common-mode problem caused by a difference in ground potential by the users of these signals. The third component is routed to a low-pass filter. The

time constant of this filter is selectable (Table 4). The output of this filter is routed to the error channel via a limiting amplifier. It is also sent to the lock detector. The power profile of the primary data signal path is shown in Fig. 51.

Error channel. The signal for this also originates in the 10-MHz IF distribution amplifier. It is routed to the lower 10-MHz signal phase switch which functions identically to the switch described in the data channel except that its reference input, which is also derived from the subcarrier shaper and $\div 4$ subassembly, is shifted by 90 deg relative to the reference signal that is fed to the data channel. The resultant data, square-wave modulated on the 10-MHz IF, has a suppressed carrier component due to this quadrature multiplication. This signal is then processed through a filter, amplifier, and coherent amplitude detector—all identical to the data channel units except for the reference signal in the final detector. This reference is derived from a 10-MHz reference source that has been square-wave modulated by the filtered and limited data signal in the 10-MHz reference phase switch (9582).

The multiplied output of these two signals becomes the loop dynamic phase error (DPE) signal. This DPE has a ramp response rather than the normal sine wave response (when out of lock), with a beat note of twice the rate of actual frequency difference of the subcarrier. This is due to the result of multiplying two square waves together. This feature can cause the loop to lock in two modes. One mode causes data to be extracted, and the other mode causes inverted data to be extracted. Either mode of lock is permissible, since the TCP will correct for this factor in the data loop.

After passing through the loop filter, this signal is called the static phase error (SPE). At this point, it is summed with the acquisition control voltage, supplied from the acquisition potentiometer, and becomes the input to the synthesizer. This synthesizer, a Fluke type 314B-7, has incorporated an internal symmetrical search oscillator that serves the purpose of the normal VCO in other phase-locked loops. This technique not only saves the cost of a VCO subassembly, including development, but it is quite functional in that its sweep range may be selected in decade steps, thus varying the K_{VCO} factor in loop gain calculations. This means that for very narrow loop filters the sweep range is made small, causing very little degradation of the loop due to VCO jitter; for wide-loop filter bandwidths, it can be made to have a large sweep range in order to accommodate high doppler rates or signal instability.

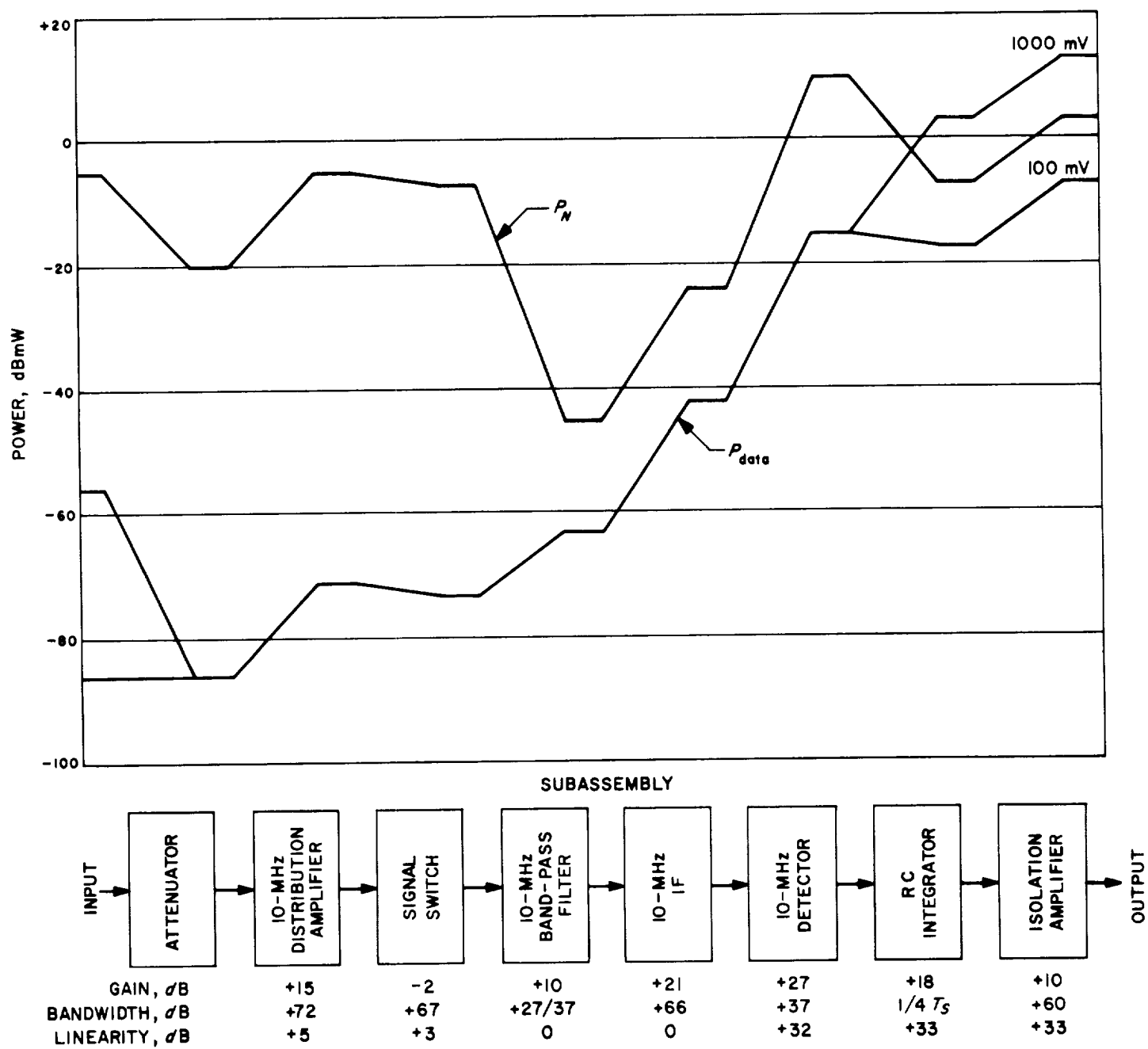


Fig. 51. Power profile curve

This synthesizer is operated at four times the incoming subcarrier frequency. The reason for this is that the synthesizer output must be converted into two signals, separated from each other by 90 deg. This process is accomplished in the subcarrier shaper and $\div 4$ subassembly. This unit accepts the synthesizer output, converts it to a square wave via a shaping circuit, divides by four in a pair of integrated-circuit flip-flops, and then is fed via isolation stages to the two signal phase switches. The purpose of the $\div 4$ portion of this circuit is to ensure accuracy of the 90-deg phasing between the two signals and also to maintain good square-wave symmetry in each signal component. This symmetry ensures 10-MHz carrier suppression in the phase switch which is essential in the operation of this loop. If the loop is stressed due to doppler, the suppress carrier signal will tend to become less suppressed, since the quadrature phasing in the signal switch will not be ideal. This will cause a dc output from the amplitude detector of the proper polarity to be injected into the loop filter. This dc will tend to shift the synthesizer frequency so as to cause a reestablishment of the 90-deg phasing of the signal switch.

Lock detector. The lock detector has two signals input. One is derived from the filtered data amplifier as described in Sect. E-1-c. The other is derived from the error channel 10-MHz IF amplifier. This signal is detected in a 10-MHz amplitude detector which has an input phase coherent to the common 10-MHz system reference. This detector output is also filtered by a low-pass RC integrator. The filter time constant is selectable and is controlled by the data-rate selector switch. The filter time constants are the same for both inputs and are as outlined in Sect. E-1-b. These two filtered inputs are then buffered and sent to two identical squaring circuits. The squared outputs are then subtracted in a combining amplifier. This combined output is then monitored on a correlation meter and further filtered in another RC low-pass circuit. The time constants of this filter are also controlled by the data-rate selector switch. The output of this filter is then fed to an in-lock relay driver-amplifier that also has a dc level set control (internal) input. This control is adjusted for optimum threshold lock indication. The relay actuates a front panel lock-indicator light.

Three alternate systems for in-lock indication and acquisition aid are under investigation (if any of them prove superior to this lock indicator, a substitution will be made):

- (1) Monitor functions. All front panel controls that are normally operated or indicated are monitored by relay closures or voltages by the station monitor.

The only exception to this is the input level set attenuator. This setting is indirectly monitored by the correlation meter voltage. All switch positions are monitored by relay closures except the synthesizer frequencies which must be monitored by a counter via the $\div 4$ subassembly. All three indications (SPE, acquisition, correlation) are monitored by buffer amplifiers that supply ± 5 V maximum to the station monitor.

- (2) Remote control capabilities. All normal operator control functions are capable of remote control for future computer programming of this equipment. The only exception to this philosophy is the input level set attenuator. The reason for this is that no commercial equipment is known that will economically supply this function without introducing objectional phase shift into the signal path. A search for a suitable unit will continue.
- (3) Limitations. There are several limitations to this system that must be observed. One of these is that subcarrier frequencies that are harmonically related to the 10-MHz carrier signal must not be used. This is because even large ratio subcarrier harmonics of 10 MHz will be amplified by the 10-MHz IF amplifier and will saturate the phase detectors. Another limitation is that care should be used in selecting proper data to subcarrier ratios. The fifth harmonic of data rates should be lower than the subcarrier rates or intermodulation products could cause reduced signal power. If high doppler rates are anticipated, high subcarrier frequencies should be utilized in order to better optimize nominal loop filter bandwidths.

Reference distribution. The reference signals (10, 10.1, and 0.1 MHz) are all derived from the R-E subsystem at a nominal level of +10 dBmW. The 10-MHz signal is the only reference needed under present requirements. The other two are for the future low data-rate options. All distributed signals are also at a nominal +10-dBmW level. The input 10-MHz phase shifter (9579) is for establishing correct phase between the incoming 10-MHz carrier and the baseband reference 10-MHz signal. The three output 10-MHz phase shifters are for establishing correct phasing between the data error and lock detector channels relative to the input 10-MHz carrier.

d. Mechanical characteristics. The basic design philosophy incorporated into the SDA was mechanical compatibility with the existing R-E subsystem in the areas of appearance, operator controls, and packaging techniques.

Front panel description. The overall front panel configuration of the SDA is shown in Fig. 52. The following is a list of the panels shown in this view:

- (1) Power panel—includes a running time meter and primary ac power switch.
- (2) Isolation amplifiers—includes two data amplifiers and one spare (Dynamics type 7575).
- (3) Oscilloscope—Tektronix type 503.
- (4) Oscilloscope selector—switch for selecting various monitor displays.
- (5) Control panel—includes the following controls and displays:
 - (a) SPE meter indicator.
 - (b) Correlation meter indicator.
 - (c) Acquisition meter indicator.
 - (d) SDA lock/out-of-lock indicator.
 - (e) R-E lock/out-of-lock indicator.
 - (f) Input selector modes—test/receiver 2/tape/10-MHz.
 - (g) Loop filter selector—short/momentary/normal.
 - (h) Output selector—test/data/tape.
 - (i) Level set attenuator—0–50 dB.
 - (j) Acquisition control potentiometer.
 - (k) System operation—local/remote.
 - (l) Data-rate selector—15-position push-indicate switch.
 - (m) Loop bandwidth ($2 B_{Lo}$) selector—15-position push-indicate switch.
- (6) Synthesizer—Fluke type 314B-7.
- (7) Blank panel—may become remotely controllable variable attenuator.
- (8) Subassembly drawer 1—input signal units.
- (9) Subassembly drawer 2—data channel units.
- (10) Subassembly drawer 3—low rate data channel units.
- (11) Subassembly drawer 4—error channel units.
- (12) Subassembly drawer 5—low rate error channel units.
- (13) Subassembly drawer 6—reference distribution units.
- (14) and (15) Power supplies — HP type 6255A.

Hardware description. There are normally two sub-carrier demodulator assemblies associated with each R-E

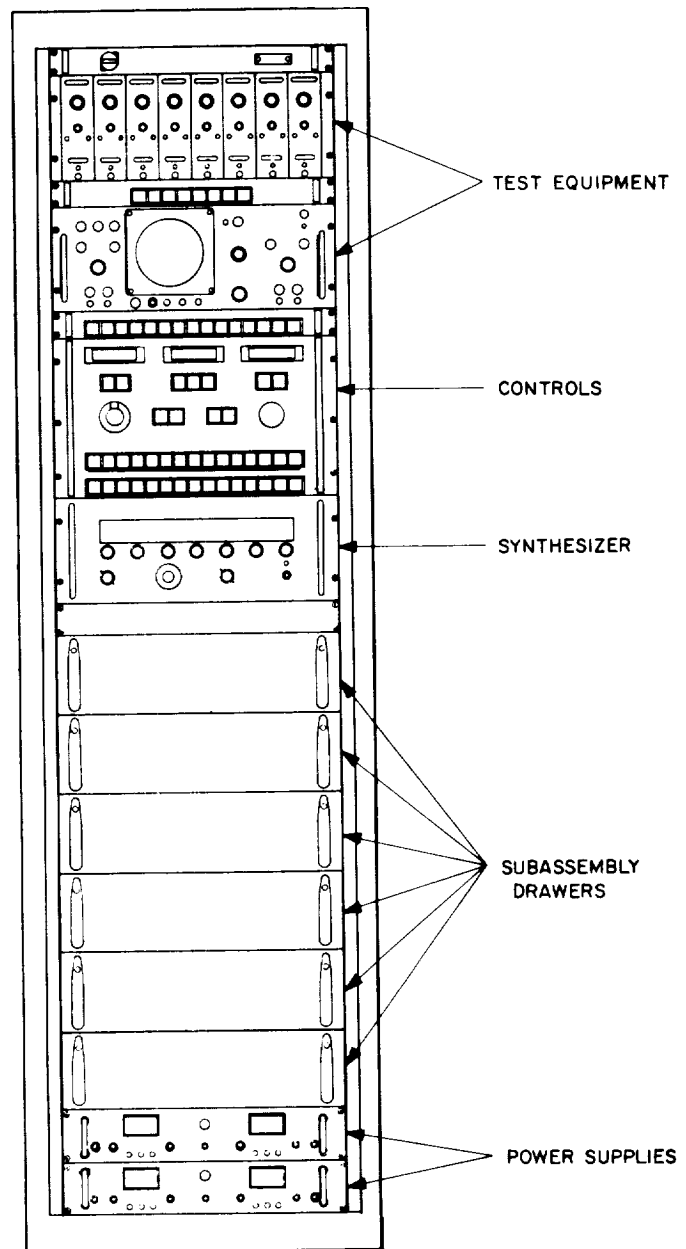


Fig. 52. Front panel configuration of SDA

subsystem. Each is identical and has been designed to be self-contained in the interest of fail-safe operation, except for necessary inputs from other sources. In order to be completely contained in a standard DSIF rack, while providing future low data-rate expansion capabilities, a higher packaging density was found to be necessary than that utilized in the R-E subsystem. One method to be employed is the use of subassembly drawer mounting rather than vertical plate mounting. Careful layout has achieved at least a 40% packaging density capability

increase. Another technique to be employed is packaging the loop filter, data conditioner, and lock detector circuitry in a common drawer, the front panel of which is the operator control panel. This approach will achieve much greater utilization of internal rack space.

e. Expansion capabilities. This equipment has capabilities for future expansion that include both high and low data-rate options.

Low data rate. The definition of low data rates are from 1 to 8 bits/s, biphase-modulated onto existing subcarrier rates.

This option is accomplished by the installation of the shaded subassembly blocks shown on the SDA block diagram (Fig. 50). Operation in this mode is accomplished by signal relays as operated by the existing data-rate selector. It is anticipated that the selectable IF filter bandwidths (as shown in Table 6) will be reassigned to the values shown in Table 7.

Table 7. IF filter bandwidths with low data-rate options

Data rate selector	IF bandwidth (—1 dB), kHz	IF frequency, MHz
1-3	0.10	0.10
4-6	1.00	0.10
7-9	10.00	10.00
10-12	100.00	10.00
13-15	1000.00	10.00

The purpose of these low data-rate subassemblies is that the 100-Hz IF filter shown in Table 7 is beyond the present state of the art at a center frequency of 10 MHz. It is, therefore, necessary to translate the 10-MHz spectrum down to 100 kHz which is accomplished in the 10-MHz signal mixer subassembly (9588).

High data rate. The definition of high data rates are from 512 to 100,000 symbols/s, biphase-modulated onto subcarriers as high as 1 MHz.

This option will be accomplished by the substitution of existing subassemblies with units of wider bandwidths and greater dynamic range. The units that will need substitution, and their parameters, are still under evaluation by the high data-rate project.

f. Engineering evaluation. A preliminary prototype of the SDA has been assembled. It was installed in two low-boy racks for ease of portability (Fig. 53). A typical sub-

assembly drawer is shown in Fig. 54. This drawer is similar to the ones planned for the final version.

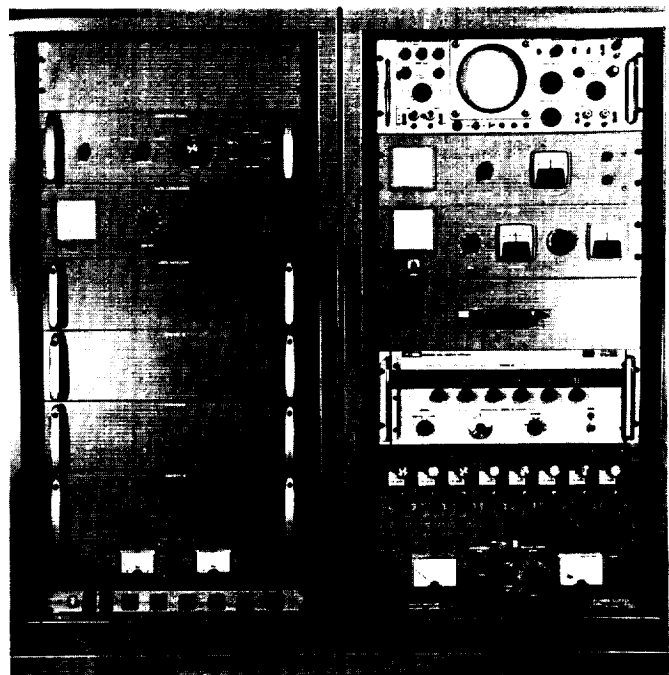


Fig. 53. SDA prototype equipment

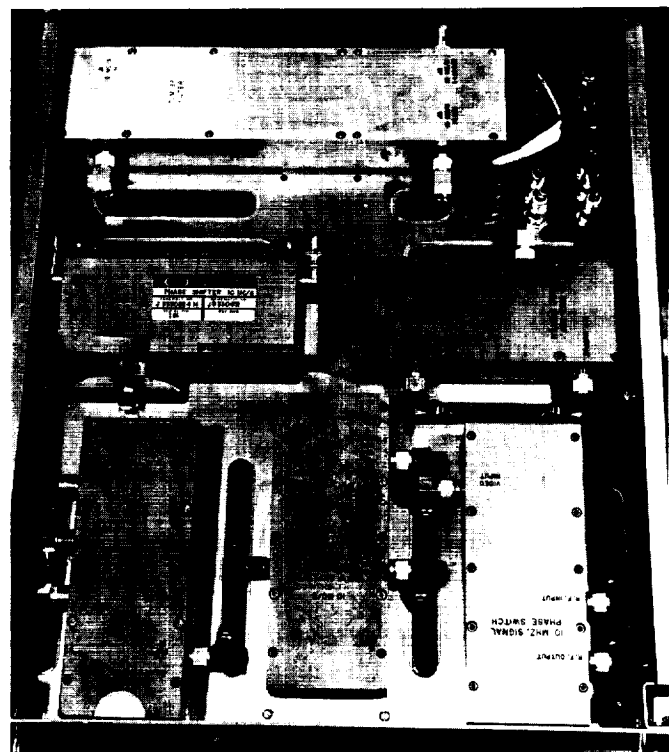


Fig. 54. SDA prototype drawer configuration

This initial assembly is an electrical equivalent of the final design, except no space is provided for the low data-rate option. The unit has been checked out operationally and delivered for system verification testing (see Sect. IV above). Due to time limitations caused by tight scheduling, very little data has been taken on this prototype as of this writing. Capabilities of locking the loop under threshold conditions have been demonstrated with a loop bandwidth of 0.01 Hz.

g. Problem areas. The design process is still continuing on many of the system parameters detailed above. Further system evaluation of several problem areas may cause changes to these parameters. A detailed analysis of these problems is not possible at this time due to lack of sufficient data and definition. The major known problem areas are listed below.

IF bandwidths. Care must be used to select practical bandwidth numbers and sufficient number of filters to protect the dynamic range of the amplitude detectors.

Synthesizer stability. The commercial synthesizer/VCO must be capable of satisfying the stability requirements of low, medium, and high data rates under all conditions of selected subcarrier frequencies, doppler rates, and tape stretch in the spacecraft.

Lock indicator. Threshold resolution of the above detailed indicator may be marginally acceptable. Optional circuits are at present objectionably complex.

2. Computer and Digital Equipment—Telemetry Command Processor, Phase IIC (TCP-IIC),

J. K. Woo and R. G. Petrie

a. Introduction. The TCP-IIC is an expansion of the existing DSIF TCP-II assembly which is described in SPS 37-38, Vol. III, pp. 76, 77. The primary objective of the TCP-IIC is to provide the DSIF station with the capability of converting the undetected data stream from the subcarrier demodulator assembly to a formatted data bit stream for recording and transmission to the SFOF under real-time computer control. In addition to this primary function, the TCP-IIC monitors status of certain receiver assembly and demodulator assembly indicators and converts this station data into the proper format for recording and transmission with the telemetry data.

TCP-IIC will add the following capabilities to the DSIF: (1) determine bit timing and detect bit informa-

tion from the subcarrier demodulator undetected binary data stream, (2) format the detected bit information for digital recording and transmission to the SFOF, (3) monitor the status of receivers in-lock and demodulators in-lock indications, (4) convert station data, receivers automatic gain control, and static phase error for digital recording and transmission with the telemetry data.

The principal elements of the TCP-IIC assembly are two SDS 920 computers, associated peripheral equipment for input/output, magnetic tape recorder, digital phase shifter for bit-timing control, interface equipment for data transfer and conversion, and communication buffer for direct communication with the SFOF. The TCP-IIC is composed of two independent assemblies, designated as Alpha and Beta, providing a completely redundant data-processing capability. In the event of failure in the primary assembly, the alternate assembly may assume the responsibility of data processing. The switchover from one assembly to the other is rapidly and reliably accomplished through a preprogrammed patch board.

The major equipment elements of TCP-IIC are shown in Fig. 55 and their functional characteristics are described in the following sections:

Transfer rack. The transfer rack is part of the TCD subsystem and its primary functions are to: (1) provide an input interface cable terminus for the subcarrier data streams, receiver AGC and SPE, subcarrier demodulator in-lock, carrier loop in-lock indications and test data, and (2) provide quick-patch capability for switching the set of input data between the Alpha and Beta assemblies. Switching is performed by changing programmable patch boards.

Assembly computer and peripheral equipment. The computer and peripheral equipment in collaboration with the analog-to-digital converter and the digital phase shifter perform the primary functions of data detection and formatting for recording and transmission. The data-detection process consists of bit-time determination and bit-detection operations which are controlled by mission-independent software defined by DSIF and implemented by the project. The formatting of detected bit stream is a function of the mission-dependent software supplied by the project.

The computer is a general-purpose SDS 920 computer with the following characteristic features:

- (1) 16,384 words of core memory.

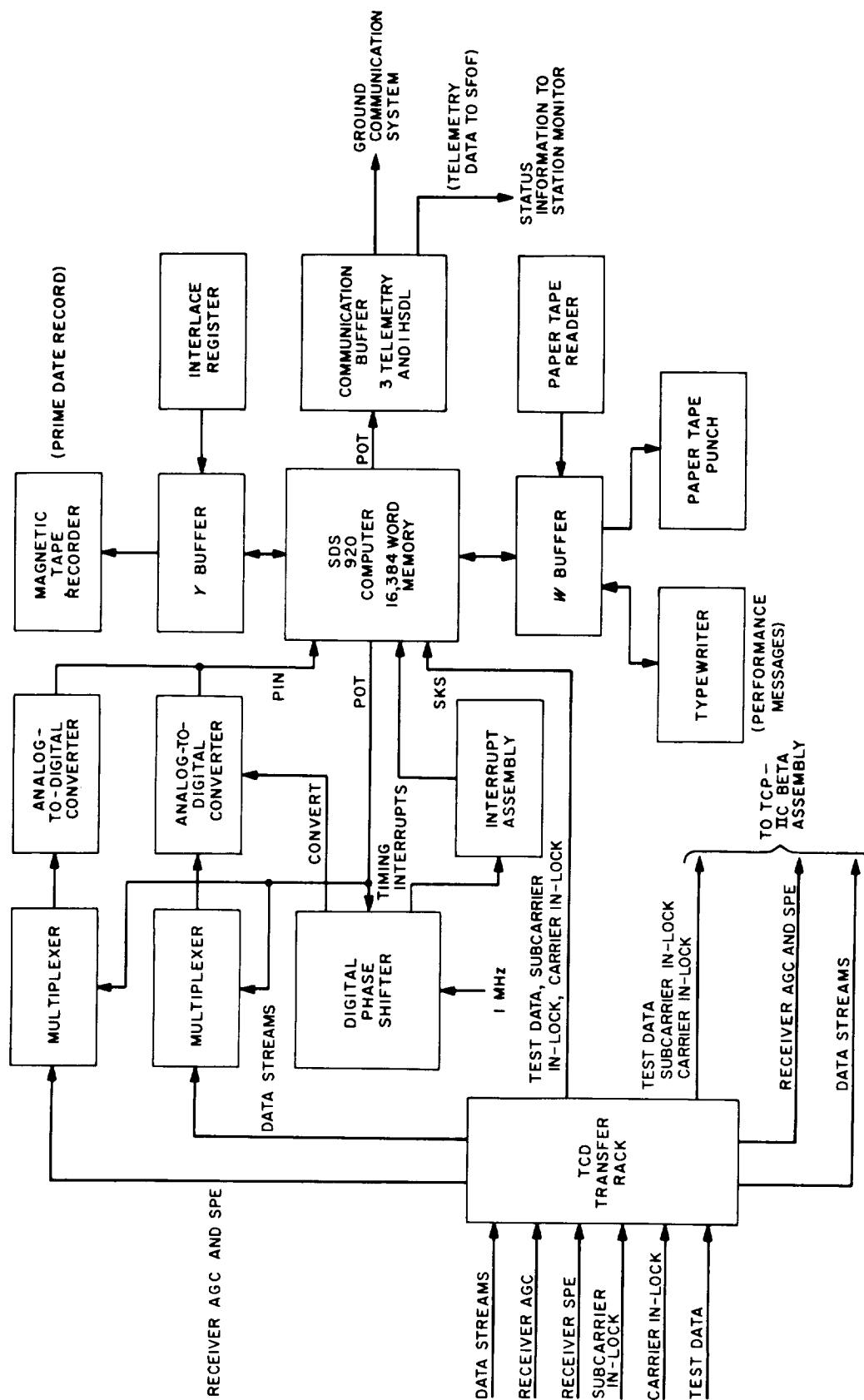


Fig. 55. TCP-IIC Alpha assembly

- (2) Word size: 24 bits plus parity check bit.
- (3) Arithmetic type: binary, *two's* complement for negative numbers.
- (4) 8- μ s memory access time.
- (5) 16- μ s add time (fixed point).
- (6) 32- μ s multiplication time (fixed point).

W-buffer (Input/Output). A 6-bit character buffer operating with a 24-bit word register provides for communication between computer and paper tape reader, paper tape punch, and typewriter.

Paper Tape Reader. Programming information contained on perforated paper tape is optically scanned at a rate of 300 characters/s and presented to the computer in a character serial format. The paper tape reader operates through the *W* input/output buffer.

Paper Tape Punch. Output data may be perforated on paper tape under computer control at a rate of 60 characters/s and presented by the computer in the character serial format. The paper tape punch operates through the *W* input/output buffer.

Typewriter. Computer-generated performance messages are presented in printed form by the typewriter output at a rate of 10 characters/s. Programming information may be entered into the computer by way of the manual keyboard. The typewriter operates through the *W* input/output buffer.

Priority Interrupt Assembly. Early, late, and bit timing interrupt signals generated by the digital phase shifter interrupt the MMTS computer program and perform specific programmed functions established for each interrupt. An interrupt patch panel is provided to allow for arranging these interrupts into any desired priority.

Y-buffer. The Y-buffer is identical to the W-buffer, and its function is to provide communication between computer and magnetic tape recorder for the recording of prime telemetry data.

Magnetic Tape Recorder. A magnetic tape recorder provides the capability of recording digital data in an IBM compatible format (binary or binary-coded decimal, 6-bit plus parity) at 200 characters/in. Under computer program control, the prime telemetry data will be recorded at the rate of 15,000 characters/s.

Interlace Register. A 26-bit register operates in conjunction with the Y-buffer. The register is divided into two parts, a 12-bit counter that holds the number of words in a data block and a 14-bit address designates the initial memory address into which prime telemetry data are to be obtained. Complete data transfer can be accomplished at rates up to 200,000 characters/s without interfering with other activities of the computer. This facility will permit the computer to operate with simultaneous telemetry-data processing and recording.

Parallel Input/Output. The computer system provides the capabilities of: (1) accepting analog-to-digital converter output data in parallel to the computer, (2) presenting timing and telemetry data in parallel to the digital phase shifter and the communication buffer, respectively. Data transfer is accomplished at rates up to 25,000 words/s with a word length up to 24 bits.

Skip an External Signal (SKS). A computer input signal used to test the status of subcarrier in-lock, carrier in-lock indicators and the data input from the test equipment.

Digital phase shifter.

General. The function of the digital phase shifter/timing generator is to provide the computer program timing signals coherent with the data-bit transition times. In order to establish and maintain coherence, the phase-shifting capability permits adjustment of the timing signals as directed by the program. The timing generator also provides a signal every $\frac{1}{4}$ -bit time ($T_b/4$), since the timing algorithm requires early and late signals in addition to the bit time signal. A block diagram of the phase shifter/timing generator is shown in Fig. 56. Additional functions are detailed in the following description of the theory of operation.

Theory of Operation. The phase shifter is composed primarily of two binary registers, a limit detecting gate, and a transfer logic network. One register, the holding register, contains a number, in effect, equal to the number of microseconds in $\frac{1}{4}$ -bit duration. The other register, the counting register, starts initially with the value contained in the holding register, and counts backwards at 1- μ s intervals until the register reaches *zero*, when it is again reset to the value contained in the holding register. The transfer logic network is used to set the counting register to the correct initial value and is energized by the limit detecting gate, which senses when the counter has reached its lower limit.

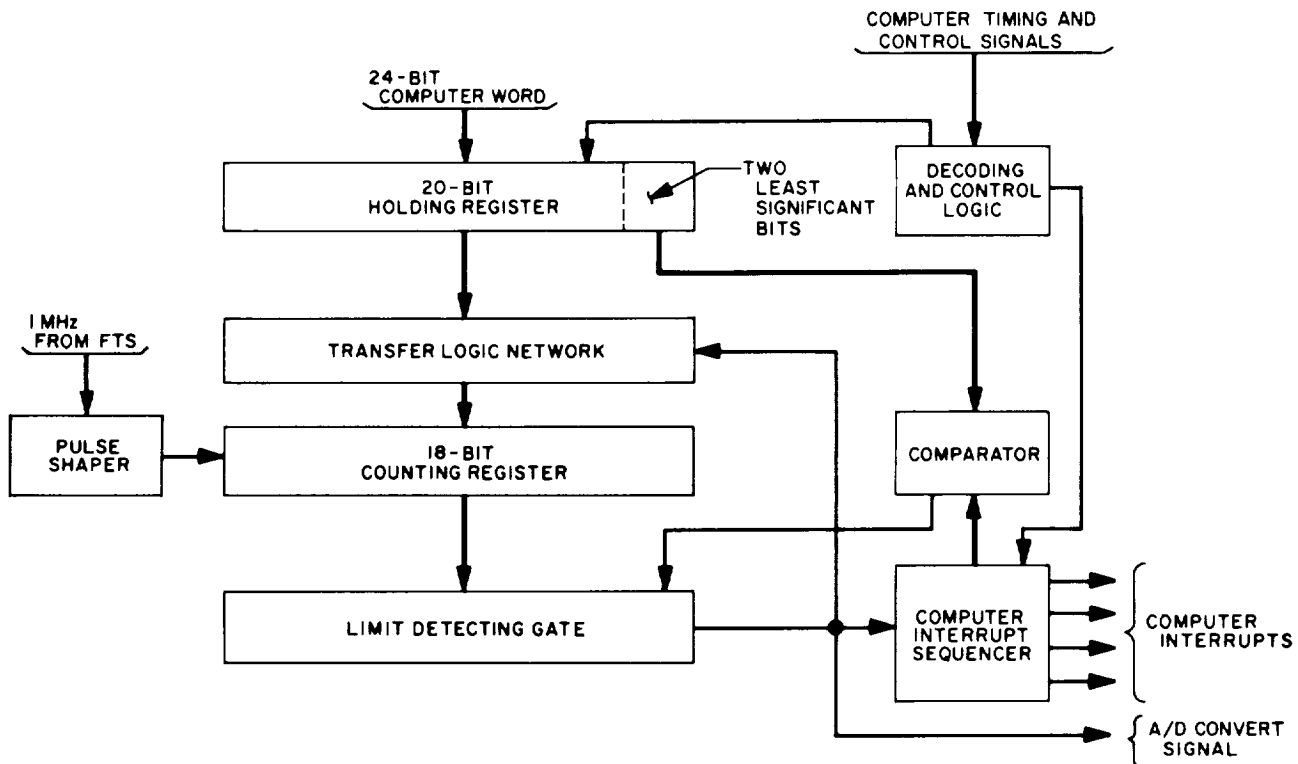


Fig. 56. Digital phase shifter/timing generator block diagram

Since this operation is continuous and cyclic, the limit detecting gate is true and generates an output to the timing generator portion once every $T_b/4$. The holding register is accessed directly by the computer program via an energize output M (EOM) 3 instruction, and a value placed in the register by a following parallel output (POT) instruction from the computer word bits 4 through 23. Since this value is the result of computation by the timing algorithm, and the contents of the holding register can be modified at will by the program, phase shifting of the timing signals can be accomplished by increasing or decreasing, for a given number of $T_b/4$ periods, the value held in the register, and consequently the number of microsecond pulses counted by the counting register. Since varying this count is equivalent to an apparent change in the duration of $T_b/4$, a phase shift of the timing pulse is accomplished.

The timing generator consists of a scale-of-four divider chain which uses the limit detecting gate signal to generate computer interrupts (i.e., the timing signals) and to sequence them in the proper order. In addition, a *convert* signal is generated at each $T_b/4$ time and is sent to the A/DC. This ensures that the incoming data bit stream is sampled coherently with the bit transition time.

In order to obtain the resolution of the basic clock frequency (1 MHz) over the entire bit duration, a comparator circuit is used between the two least significant bits of the holding register and the timing generator divider chain. The holding register has a capacity of two more bits at the least significant end than has the counting register. If these two bits, which are the two least significant bits of the value computed by the timing algorithm, are considered as a number H , ranging from 0 to 3, and if the timing generator divider chain bits are similarly considered a number T , then by comparing H and T such that if $H > T$ the counting register is allowed to count one additional microsecond each $T_b/4$, a total resolution of $1 \mu\text{s}$ is achieved over the entire bit duration. The size of the counting register permits a total range of bit rates from less than 1 to 10^6 bits/s with the resolution of $1 \mu\text{s}$, as described above.

Further control circuitry in the phase shifter/timing generator performs such tasks as EOM decoding, clocking the POT and interrupt signals with the correct computer clock phase or control signals, and shaping of the 1-MHz frequency standard from the frequency and timing subsystem (FTS), for use as the internal clocking and timing signal.

Implementation. The digital phase shifter/timing generator is to be implemented completely with Division 33 standard Hi-Rel digital modules. The complete system will be mounted in a drawer-type card cage and, together with the necessary power supplies, installed in the data conversion equipment rack as part of the TCP-IIC modifications.

Interface signals with the phase shifter will be via the standard computer POT connector, which carries all the necessary control signals as well as the computer word bits. The timing generator will interface via RG-55 cables terminated in TNC connections as will the 1-MHz standard frequency from the FTS.

There are no control devices, e.g., push buttons or switches, associated with this equipment, since in its final configuration it is completely under computer control in its operation.

Multiplexers. The multiplexers accept AGC and SPE from both receivers and integrated data streams from both subcarrier demodulators. Each input is assigned to its corresponding multiplexer input channel. The multiplexers operate under computer program control with the computer selecting the required channel to be sampled. Other features of the multiplexers include:

- (1) Full-scale input voltage of ± 5 V.
- (2) Input impedance of 10K.
- (3) 16 differential input channels.
- (4) Sample rate of 50,000 samples/s.
- (5) Channel selection by random binary address.

Analog-to-digital converters. Analog output voltages of the multiplexers, such as receiver AGC, SPE or integrated data stream are input to the analog-to-digital converters. Two analog-to-digital converters are used and operate in the following manner: (1) One analog-to-digital converter samples input voltages of receiver AGC and SPE. Conversion to digital data is initiated automatically after the proper multiplexer input channel has been selected by the computer program, and (2) a second analog-to-digital converter samples the integrated data stream input from the subcarrier demodulator assembly. Conversion is initiated by timing signals from the digital phase shifter/timing generator. Characteristic features of the analog-to-digital converters include:

- (1) Conversion time of $1.5 \mu\text{s/bit}$.

- (2) Output resolution consists of 11 binary magnitude bits plus sign with *two's* complement for negative numbers.
- (3) Conversion accuracy of 0.025% of full-scale value (± 5 V).
- (4) Sample and hold capability.

Communication buffer. The primary function of the communication buffer is to transmit computer detected and formatted data bit stream to SFOF via teletype send circuits and high-speed data line (HSDL). A communication buffer is provided with each computer assembly (Alpha and Beta) and communication with the computer is via the computer parallel input/output channel. Each communication buffer consists of the following units.

Teletype Communication Equipment. Three full duplex teletype communications channels each capable of simultaneously transmitting and receiving are provided for the Alpha and Beta assemblies. These teletype channels interface with common carrier transmission lines for communications with the SFOF. Telemetry data are transmitted in standard Baudot Code (five information bits per character) at a rate compatible with the teletype terminal equipment at each station. The standard rates are presently 60 or 66.7 words/min. A communications patch panel allows send and receive channels to be connected to selected teletype lines.

HSDL Register. The HSDL register transmits computer data to SFOF via the NASCOM system. Preamble data required by the NASCOM system and formatted bit information are presented to the register via the computer parallel output channel for conversion to a serial bit data. The register serial output bit stream is transmitted to the HSDL modem of the DSIF GCS in synchronism with clock pulses supplied by the modem. The HSDL register is capable of operating at data rates of 660, 1200 or 2400 bits/s synchronous with an external timing source.

3. Demonstration Software, J. W. Layland

A glance at Fig. 1 reveals one important fact about the MMTS: that the SDS 920 computer and its controlling program have become an integral part of the demodulator. In order to perform the system verification tests, some form of the mission-independent software must be coupled with enough output software that the entire system's performance may be observed. This is the primary purpose of the demonstration software. Of nearly equal importance is the intent that the control/detection segments of

the demonstration software serve as a prototype for the mission-independent segments of future software. Associated with these two purposes are the (possibly) conflicting requirements that the control/detection segments be as close to optimal as possible, and that the software package adapt easily to modification in hardware parameters. The succeeding paragraphs describe the specific requirements on the demonstration software and the details of its implementation, particularly of the control/detection (or mission-independent) segments.

The requirements on the demonstration software are most readily describable in terms of the available inputs and required outputs from the software. The outputs required are: (1) the detected data stream, (2) an estimate of signal-to-noise ratio, (3) information of the in-lock status of the RF and subcarrier tracking loops. These must be recorded on magnetic tape as the prime data record, and formatted for other appropriate output. In addition, the program must compute and type the bit-error rate when the data source is the MMTS test equipment.

During real-time operation, the software inputs consist of: (1) the timing marks (interrupts) from the program-controlled timing generator, (2) the sampled and digital value of the MMTS integrator, (3) the status (in-lock/out-of-lock) of the RF and subcarrier phase-locked loops, (4) the transmitted data bits (when input is from the test equipment). A necessary condition for the performance of this input/output processing is that the timing generator be synchronized to, and kept in close synchronism with, the transitions of the received data stream. To minimize loss of data in acquisition, it is desirable that the initial synchronization be done as fast as possible. The program must run "comfortably" at bit rates of up to 512 bits/s.

The demonstration software package being written to satisfy these requirements is a direct descendent of both the audio model software (Sect. D) and the type III demonstration software (SPS 37-45, Vol. III, pp. 51-57). The package is divided into six major blocks (Fig. 57). Block I, entered when the program is loaded and re-enterrable at cell 0240, accepts four parameters from the console typewriter: (1) bit rate, (2) integration time constant, (3) nominal signal-to-noise ratio, and (4) loop bandwidth of the bit-time tracking loop. It then computes thresholds, gain constants, and scaling instructions and sets these for use in and by the real-time processing blocks. Most computations in this block are performed in floating-point mode. Most of the computations performed here would be unnecessary in an operating system where bit

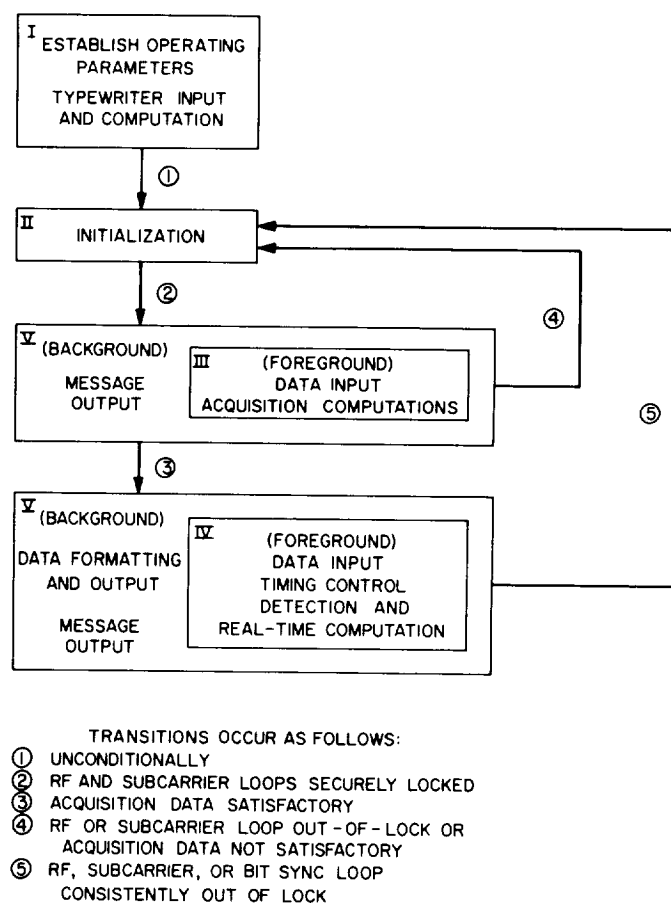


Fig. 57. Demonstration program block

rate, and other parameters linked to it, would be selected from a finite set. When this computation is completed, control is transferred to Block 2, which initializes buffer pointers and flags, conditions the interrupts, and links the initializing interrupt routines of Block 3 to the proper points. When the RF and subcarrier loops have reached a stable in-lock condition, the interrupts are enabled and control transferred to the non-real-time data processing in Block 5. Block 2 may be reentered manually from cell 01, or from a *bad data* condition in the non-real-time data processor. Blocks 3 and 4 comprise the real-time data processor and will be given a complete description shortly. The non-real-time data processor, Block 5, performs all of the output formatting, data validation, bit-error rate computation, etc., in response to flags set by the interrupt routines in Block 4, using data supplied by the interrupt routines on a set of circular cues. Twenty-four received data bits comprise one word of the data cue, while the sum-of-absolute-values and sum-of-squares of the data-integrals of these 24 bits and the number of subcarrier and RF loop *not-locked* responses associated with these bits are entered on parallel cues. Figure 58 is a skeletal

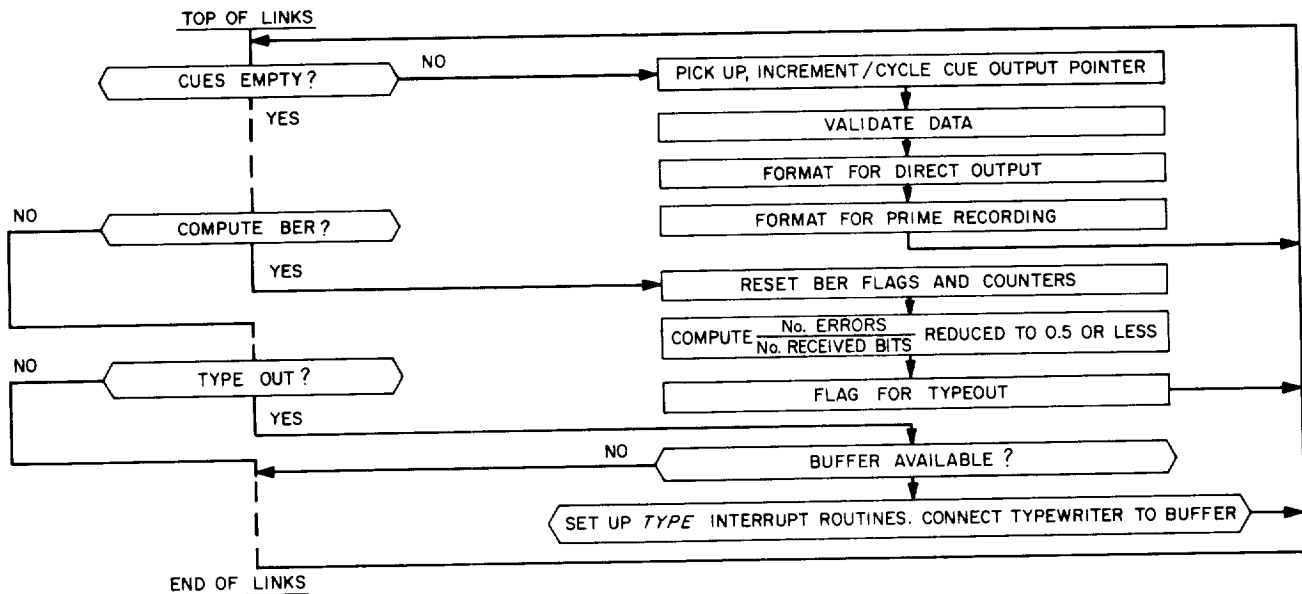


Fig. 58. Block 5 flow diagram

flow diagram of Block 5. The dashed lines represent other processor options which are not shown explicitly, but which are handled similarly to those shown. The *validate-data* routine performs some of the important mission-independent functions and will be described fully later. Block 6 contains storage locations, cues, and data buffers. When the program assumes final form, Block 6 will also be a dictionary of all labels used in the program.

Figure 59 is a flow diagram of the Block 4 real-time processing routines. Subroutine *erlytrk* responds to an interrupt signal occurring $\frac{1}{4}$ -bit time before the data transition time. Subroutine *datatrck* responds to an interrupt signal at the data transition time, while the interrupt signal which energizes *latetrk* occurs $\frac{1}{4}$ -bit time after the data transition time. The basic cost (in machine time) of these routines is 142 cycles for each cycle through the trio (once per bit time). To this must be added an incremental load of 43 cycles for placing the packed data on the cues, an overhead of 21 cycles if the bit-error-rate option is selected, and a scaling cost which may vary from 0 to 13 cycles, depending upon the signal level at the A/D input. Of the basic cost, 37 cycles are spent storing data samples and handling the interrupt routine entry and exit, 32 cycles to compute the timing-error sample, 20 cycles to filter this sample (a double-integrator filter is used) and update the time generator, and 36 cycles to compute the data integral, detect the data bit, and update the sum-of-absolute values and sum-of-squares used in estimating SNR. The remaining time is consumed by performing brief bookkeeping.

If the data stream is at 512 bits/s, there are nominally 244 computer cycles available per bit. To sustain operation, neither the peak level of real-time processing during a given received bit nor the overall average processing cost may exceed this. With scaling taking its maximum load of 13 cycles and the bit-error-rate option active, the peak load is 219 cycles. There may, in addition, be one (and only one) typewriter/buffer interrupt of higher priority than the timing generator which will insert a 12- or 13-cycle overload, bringing possible peak consumption to 232 cycles, quite close to the limit. Since only token typewriter output is required with this option, the average constraint is of no consequence.

Without using the bit-error-rate option, the peak load of the Block 4 routines is reduced to 198 cycles; but the typewriter may again contribute 13 cycles, and an interlaced magnetic tape may require 12 cycles stolen by the interlace for memory access plus a minimum of 7 cycles for an end-of-record interrupt, bringing the peak load total to 230 cycles. It has been assumed (and is probably necessary) that the comm-buffer interrupts be of lower priority than those of the timing generator, thus removing them from this critical timing consideration. Noninterruptable sequences of more than 10 cycles' duration must be avoided in the non-real-time processor, to allow reasonable assurance that the complete package will run. In particular, this eliminates the divide instruction and shifts of more than 16 places. The average cost per bit is a more reasonable 157 cycles in the data transfer mode, leaving a nominal 77 cycles per data bit available for formatting

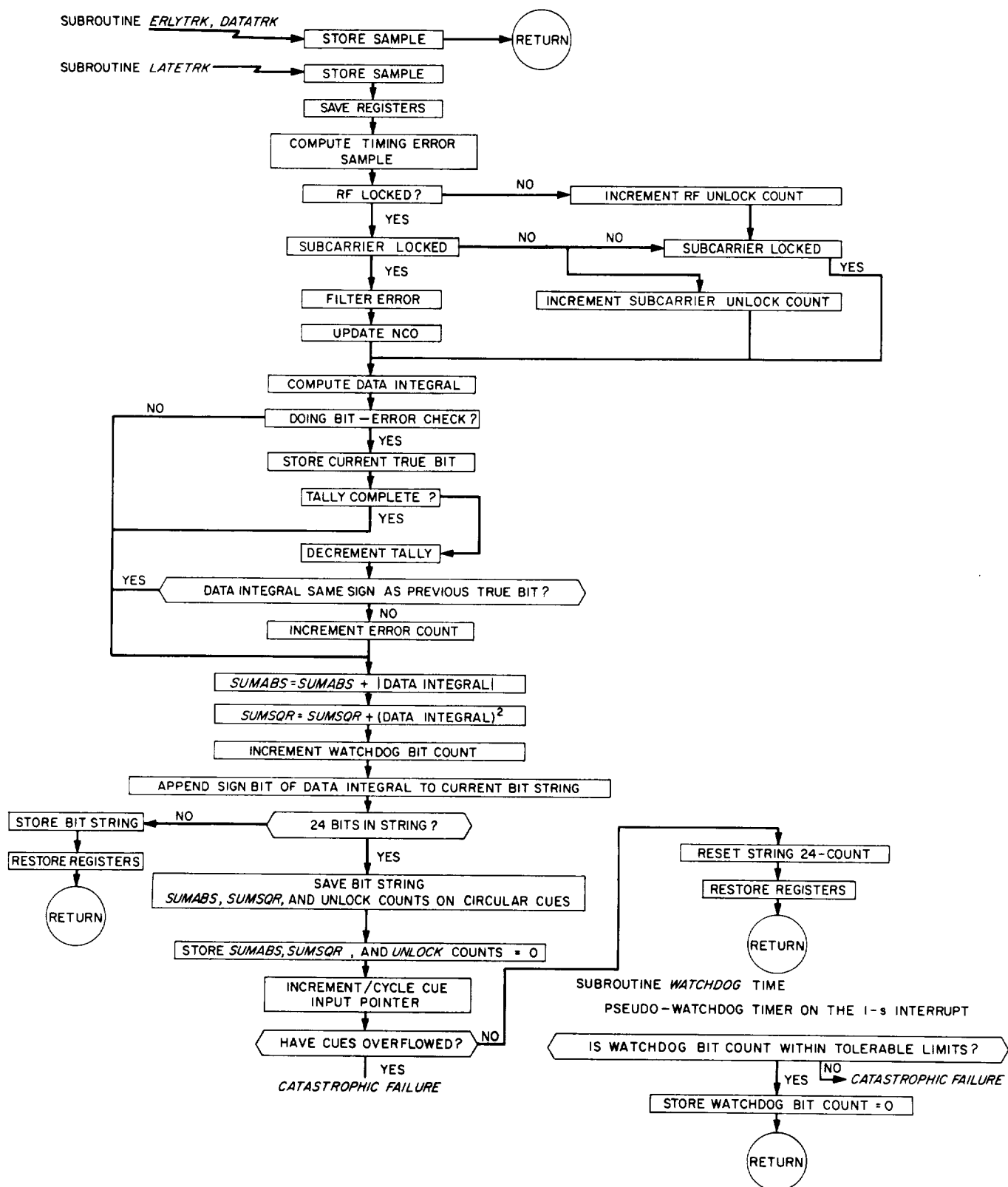


Fig. 59. Block 4 real-time data-processing routines

and output processing. While this figure could never be reached in practice, most of it should be available if the cyclical cues are made long enough to average over the periodic work load for the non-real-time data processing.

Block 3 contains the acquisition and transition real-time processing routines. There are three distinct sub-blocks or phases to this block of routines. The first phase initializes linkages and constants for the second phase and

guarantees that this second phase is initiated at the proper point in the timing generator interrupt cycle. The third phase performs this same task for the Block 4 routines, in addition to shifting the timing generator into synchronism with the data-bit transition. Figure 60 is a flow diagram of the second phase, which computes the delay between the data interrupt signal of the timing generator and the received data transitions. *Quatarun* is alerted by an interrupt signal at the mid-bit or data-quadrature time of

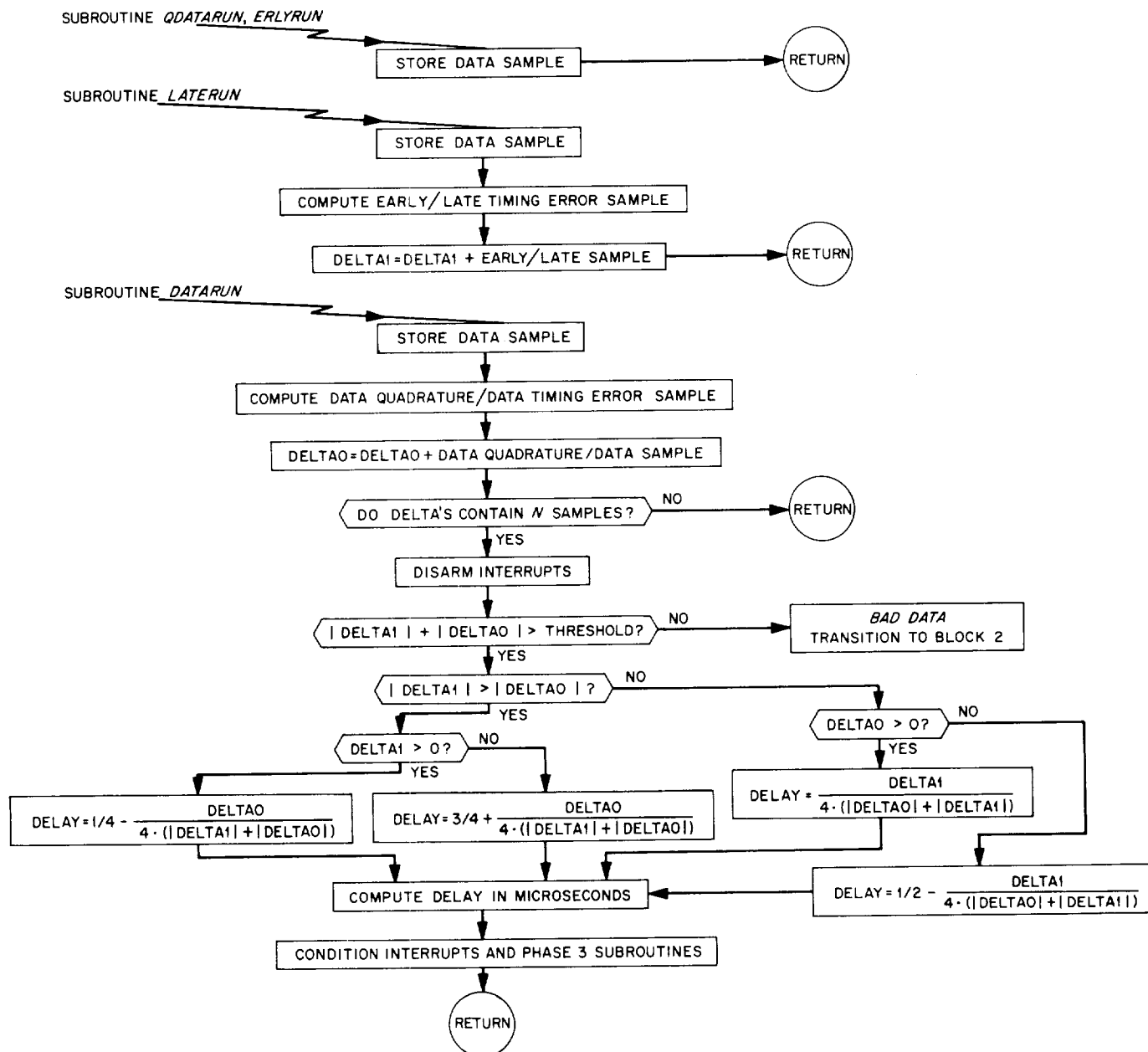


Fig. 60. Block 3, sub-block 2, real-time acquisition routines

the timing generator. The other routines are activated by the interrupt signal which activates their Block 4 counterpart as already described. Computation of "Delta0" and "Delta1," the total real-time load, takes 156 cycles per data bit—well within the 244 cycles available at 512 bits/sec. The final computation of the delay shift takes place with interrupts disarmed and hence does not contribute to the real-time load. In addition to those routines already described, an interrupt routine operating at a 1-ms request rate interrogates the RF and subcarrier lock indicators. If a persistent out-of-lock condition is found at any time during the Block 3 processing, acquisition is aborted and control is transferred to Block 2.

Subroutine *locktest* performs the data validation functions in the non-real-time data processor. Its flow diagram is shown in Fig. 61. The SNR estimated from the sum-of-absolute values and sum-of-squares of the data integrals for the current 24 bits is used as a lock indicator for the overall system. The RF and subcarrier loops are con-

sidered to be out-of-lock if the number of *not locked* responses during detection of these 24 bits exceeds a preset threshold. Any *not locked* condition which is sufficiently persistent to invalidate the bit-timing system status will cause a transfer to Block 2, an appropriate message, and a subsequent reacquisition.

4. MMTS Test Equipment, R. G. Petrie

a. General requirements. A necessary adjunct to any major system development is the special test equipment required to establish and maintain the correct operation of the system. The MMTS is such a system for which special test equipment is needed. The general requirements for the test equipment are as follows:

Baseband output signal. A test signal comprised of a bit stream, with or without superimposed noise, to be used for testing the digital portion of the MMTS only.

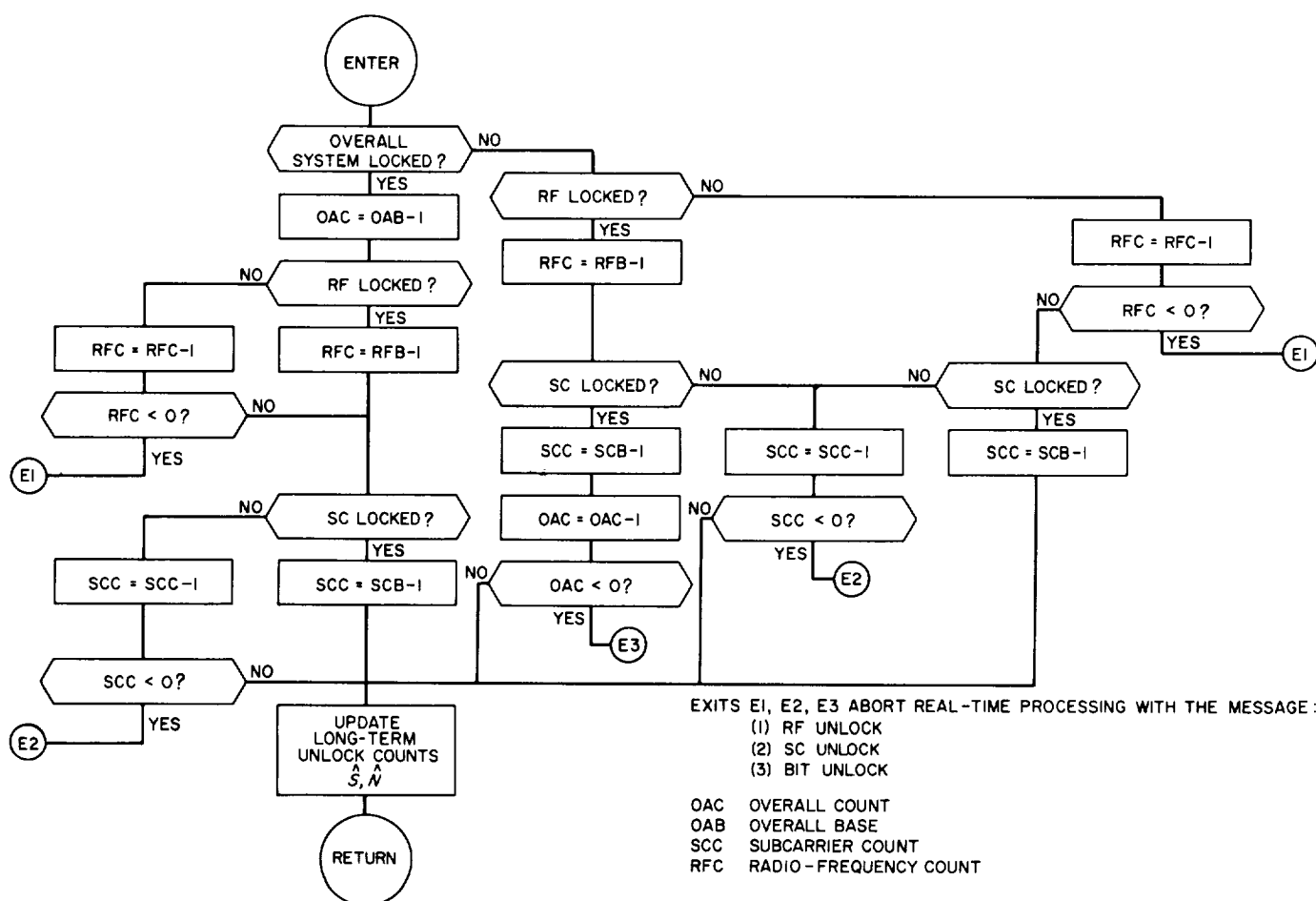


Fig. 61. Subroutine *locktest* flow diagram

required test signals. Additional details not directly connected with the signal generation will be covered in the section on implementation that follows.

Operating modes. The MMTS test equipment has two basic roles to fulfill: (1) to provide a testing and troubleshooting capability for the MMTS, and (2) to aid in simulation and training. While both of these functions are similar, they have distinct differences in the test equipment configurations required to support them. The several operating modes, both test and simulation, are presented in Table 8.

c. Implementation. In addition to the equipment description above, the following implementation details are presented to further describe the MMTS test equipment configuration.

The bit-error rate computation, referred to in the above discussion, will not be implemented through hardware but will instead be a program routine entered in the TCP computer during the time testing or simulation is being done. The bit-error check outputs are directly connected to the computer for this purpose. Display of the bit-error rate computation results will be via the computer console typewriter.

All of the signal switching required to generate specific test signals will be done on a semiautomatic basis. A specific mode setup will require only one action on the part

of the operator, exclusive of attenuator or data format control settings.

An oscilloscope, permanently mounted in the test equipment rack, is used to monitor the various signals being generated. Test points will be brought to a central control and patch panel, thus permitting the operator to locate quickly any problems that may arise in the test equipment itself.

The bit-stream generator will be constructed of JPL Division 33 Hi-Rel standard digital modules with the necessary selecting controls brought out to the central control panel.

All the isolation amplifiers and the integrators shown on the block diagram will be operational amplifiers appropriately connected. There are isolation amplifiers in addition to those actually shown on the block diagram, but they are primarily of a fixed impedance and gain matching function and consequently are not included in the functional diagram.

The entire test equipment is to be mounted in a roll-around standard DSIF equipment rack with all connectors and cables necessary to perform its functions. The test equipment rack is to be complete in itself with no need for auxiliary test devices, except the precision signal-to-noise mixer. Each station that is equipped with the MMTS (either single or dual channel) will be provided with one set of MMTS test equipment.

References

1. Shannon, C. E., and Weaver, W., *The Mathematical Theory of Communication*, University of Illinois Press, Urbana, Ill., 1949.
2. Golomb, S. W., Baumert, L. D., Easterling, M. F., Stiffler, J. J., and Viterbi, A. J., *Digital Communications*, Prentice-Hall, Inc., Englewood Cliffs, N. J., 1964.
3. Jaffe, R. M., and Rechtin, E., "Design and Performance of Phase-Lock Circuits Capable of Near-Optimum Performance Over A Wide Range of Input Signals and Noise Levels," *IRE Transactions on Information Theory*, Vol. 1T-1, pp. 66-76, March 1955.
4. Spilker, J. J., "Delay-Lock Tracking of Binary Signals," *IEEE Transactions on Space Electronics and Telemetry*, Vol. 9, pp. 1-8, March 1963.

References (contd)

5. Stiffler, J. J., "On the Allocation of Power In a Synchronous Binary PSK Communication System," Paper 5-1, *National Telemetry Conference*, June 2, 1964.
6. Kaneko, H., "A Statistical Analysis of the Synchronization of a Binary Receiver," *IEEE Transactions on Communication Systems*, Vol. 11, pp. 498-501, December 1963.
7. Viterbi, A. J., "Phase Locked Loop Dynamics in the Presence of Noise by Fokker-Planck Techniques," *Proceedings of IEEE*, Vol. 51, pp. 1737-1753, December 1963.

the timing generator. The other routines are activated by the interrupt signal which activates their Block 4 counterpart as already described. Computation of "Delta0" and "Delta1," the total real-time load, takes 156 cycles per data bit—well within the 244 cycles available at 512 bits/sec. The final computation of the delay shift takes place with interrupts disarmed and hence does not contribute to the real-time load. In addition to those routines already described, an interrupt routine operating at a 1-ms request rate interrogates the RF and subcarrier lock indicators. If a persistent out-of-lock condition is found at any time during the Block 3 processing, acquisition is aborted and control is transferred to Block 2.

Subroutine *locktest* performs the data validation functions in the non-real-time data processor. Its flow diagram is shown in Fig. 61. The SNR estimated from the sum-of-absolute values and sum-of-squares of the data integrals for the current 24 bits is used as a lock indicator for the overall system. The RF and subcarrier loops are con-

sidered to be out-of-lock if the number of *not locked* responses during detection of these 24 bits exceeds a preset threshold. Any *not locked* condition which is sufficiently persistent to invalidate the bit-timing system status will cause a transfer to Block 2, an appropriate message, and a subsequent reacquisition.

4. MMTS Test Equipment, R. G. Petrie

a. General requirements. A necessary adjunct to any major system development is the special test equipment required to establish and maintain the correct operation of the system. The MMTS is such a system for which special test equipment is needed. The general requirements for the test equipment are as follows:

Baseband output signal. A test signal comprised of a bit stream, with or without superimposed noise, to be used for testing the digital portion of the MMTS only.

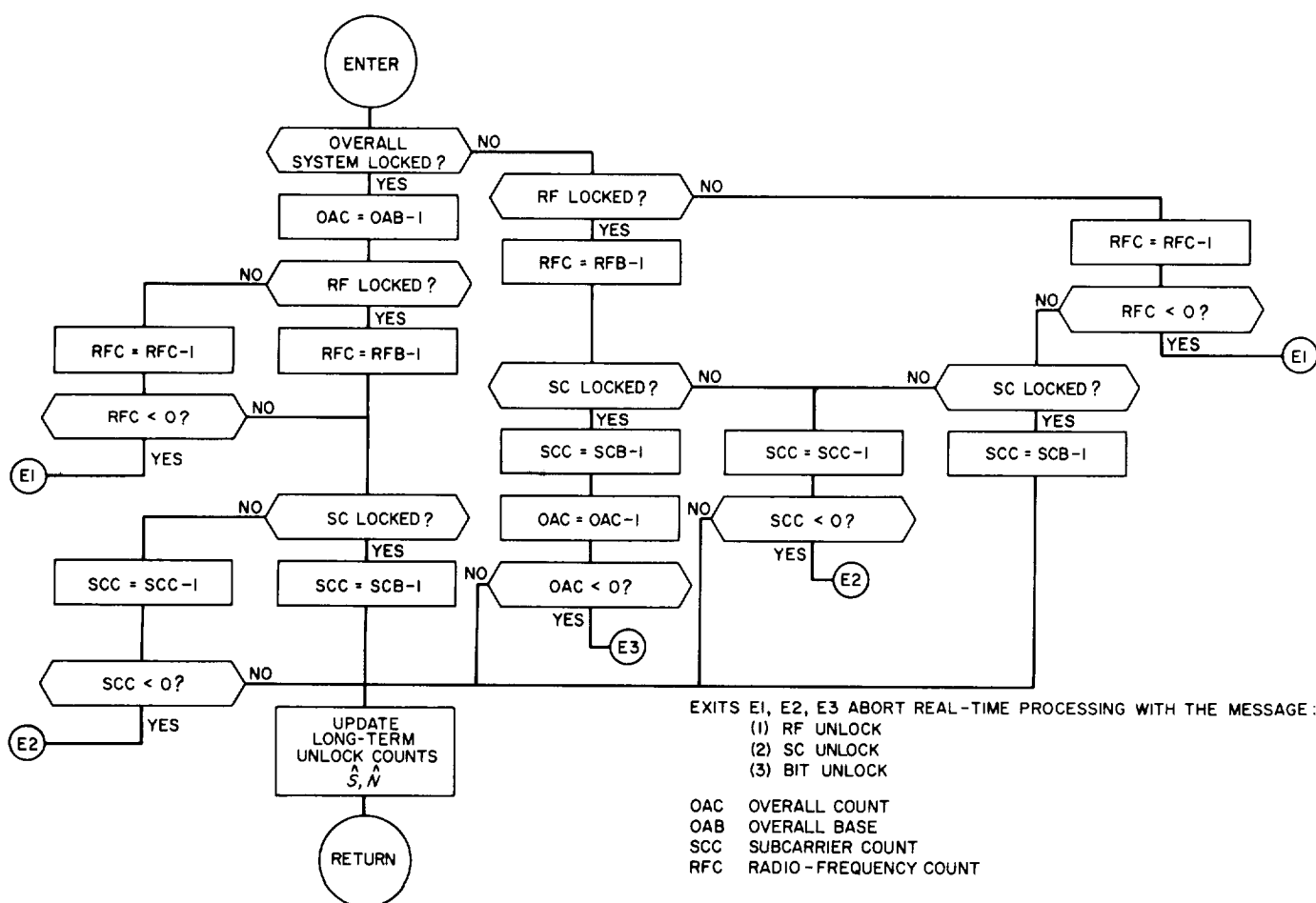


Fig. 61. Subroutine *locktest* flow diagram

Subcarrier output signal. A test signal comprised of a subcarrier, modulated with a bit stream, with or without superimposed noise, to be used for testing the entire MMTS.

Carrier output signal. A test signal comprised of a subcarrier, modulated with a bit stream, to be in conjunction with the test transmitter to modulate an S-band carrier for testing the combined MMTS and S-band receiver system.

Bit-error checking. A method whereby the data stream bits as generated by the test equipment are compared, bit by bit, with the data bits recovered by the MMTS and an error tally or bit error rate computed and displayed.

Simulation input. Provisions are made for external data sources, such as magnetic tape recordings of simulated or actual spacecraft data, to be used in place of the internal bit stream generator.

Test flexibility. The test equipment should be sufficiently versatile to allow tests closely simulating actual operating conditions. Thus, the test equipment should be able to supply, for instance, two subcarriers, each modulated with data, to test the ability of the MMTS subcarrier demodulator to reject the unwanted subcarrier and recover the desired data.

The various test signals and their entry points in the station equipment assemblies are shown in Fig. 3.

b. Equipment description and operating modes. Figure 2 shows a complete block diagram of the MMTS test equipment. This block diagram is referenced in the following description.

Signal sources. Two subcarrier oscillators are shown on the block diagram. Oscillator 1 is the primary oscillator for generating the desired subcarrier frequency and is a precision oscillator of the synthesizer type. Oscillator 2 can be used to generate a second subcarrier frequency when desired, but its primary purpose is to provide a clock frequency at the desired data bit rate. This oscillator is not as precise as oscillator 1, being only a high-quality L-C type oscillator rather than a synthesizer, and consequently should not be used as the main subcarrier generator.

Both subcarrier outputs are converted into square waves by means of the shaper circuits indicated on the block diagram.

The bit-stream generator is a multifunction device having the following capabilities:

- (1) A pseudo-noise (PN) sequence of equally probable *ones* and *zeros*. Several different length PN sequences will be available to the operator through proper setting of a pair of selector switches.
- (2) A square wave, i.e., an alternating series of *ones* and *zeros*.
- (3) A constant stream of either *ones* or *zeros* into which can be inserted a single bit of opposite polarity at the discretion of the operator. This function is desirable in testing the recovery capability of the integrators in the subcarrier demodulation loop.

When in use, the bit stream generator uses subcarrier oscillator 2, which is set at the data bit rate, as a clock pulse generator.

Two additional signal sources are available through use of the external data source inputs 1 and 2, as shown on the block diagram. These inputs would be used if, for example, it is required to have two simultaneous and independent data streams or if two simultaneous subcarrier frequencies are desired. These inputs provide the simulation input capability described above in the list of general requirements.

These various signal sources can then be combined and processed in the following ways:

Signal conditioning and output. A direct output of the data bit stream is provided at the bit-error check outputs 1 and 2. These outputs are used by the computer in determining the bit-error rate and, in normal test configurations, they are reserved exclusively for this use.

The data stream outputs 1 and 2 are used for the base-band testing capability as stated in the general requirements above. Provision is made to allow the operator to first mix noise with the bit stream, if desired, using the precision signal-to-noise mixer available at each DSS station. The signal is next processed through an integrator identical to the one shown in the output of the subcarrier demodulation loop on the MMTS block diagram. This integrator has five switch-selected decade time constants to cover the range of bit rates required. Finally, the signal is processed through a variable gain isolation amplifier for level adjustments and impedance matching.

The test signal available at the data plus subcarrier output is comprised of one or both subcarrier frequencies,

each of which is modulated with a data bit stream and with or without superimposed noise. To achieve this configuration, each subcarrier is first combined with its data stream in a modulator. Since both the subcarrier and the bit stream are square waves, and the desired modulation is biphase, the modulator consists of an *exclusive or* gate or a modulo two adder. The action of this modulator can best be seen by noting the truth table for an *exclusive or* function:

Subcarrier	Data	Modulated output
0	0	0
0	1	1
1	0	1
1	1	0

Note that a "0" can be considered zero or reference phase and a "1" can be considered 180-deg phase in the above table.

The modulated subcarriers are then passed through a precision attenuator for level setting and are summed in a fixed gain isolation amplifier. The output of this amplifier can be switched through the precision signal-to-noise mixer depending upon the use of the test signal at this point. By referring to Fig. 3, it can be seen that the test signal sent to the test transmitter and that sent to the input of the MMTS subcarrier demodulator differ only in the absence or presence of noise, respectively. Either signal can thus be generated by the same modules in the test equipment.

The previous section has described the operation of the test equipment insofar as the generation of the

Table 8. Test equipment operating modes

Mode of operation	Function			Outputs	System entry point (Fig. 1)
	Subcarrier oscillator 1	Subcarrier oscillator 2	Data bit-stream source		
Test					
Baseband single channel	Not used	Data bit-rate clock	Bit stream generator	Data stream output 1	Input to MMT bit synchronizer
Subcarrier single channel	Subcarrier frequency generator	Data bit-rate clock	Bit stream generator	Data + subcarrier with noise	Input to MMT subcarrier demodulator
Carrier	Subcarrier frequency generator	Data bit-rate clock	Bit stream generator	Data + subcarrier	Input to test transmitter
Simulation					
Baseband single channel	Not used	Not used	External data source No. 1	Data stream output 1	Input to MMT bit synchronizer
Baseband dual channel (primary)	Not used	Not used	External data sources 1 and 2	Data stream outputs 1 and 2	Input to MMT bit synchronizer
Baseband dual channel (secondary)	Not used	Data bit-rate clock	Bit stream generator and external data source 2	Data stream outputs 1 and 2	Input to MMT bit synchronizer
Subcarrier single frequency	Subcarrier frequency generator	Not used	External data source 1	Data + subcarrier with noise	Input to MMT subcarrier demodulator
Subcarrier dual frequency	Subcarrier 1 frequency generator	Subcarrier 2 frequency generator	External data sources 1 and 2	Data + subcarrier with noise	Input to MMT subcarrier demodulator
Carrier, single subcarrier frequency (primary)	Subcarrier frequency generator	Not used	External data source 1	Data + subcarrier	Input to test transmitter
Carrier, single subcarrier frequency (secondary)	Subcarrier frequency generator	Data bit-rate clock	Bit stream generator	Data + subcarrier	Input to test transmitter
Carrier, dual subcarrier frequency	Subcarrier 1 frequency generator	Subcarrier 2 frequency generator	External data sources 1 and 2	Data + subcarrier	Input to test transmitter
In all cases, the appropriate bit-error check outputs are used for the bit error rate computation.					

required test signals. Additional details not directly connected with the signal generation will be covered in the section on implementation that follows.

Operating modes. The MMTS test equipment has two basic roles to fulfill: (1) to provide a testing and troubleshooting capability for the MMTS, and (2) to aid in simulation and training. While both of these functions are similar, they have distinct differences in the test equipment configurations required to support them. The several operating modes, both test and simulation, are presented in Table 8.

c. Implementation. In addition to the equipment description above, the following implementation details are presented to further describe the MMTS test equipment configuration.

The bit-error rate computation, referred to in the above discussion, will not be implemented through hardware but will instead be a program routine entered in the TCP computer during the time testing or simulation is being done. The bit-error check outputs are directly connected to the computer for this purpose. Display of the bit-error rate computation results will be via the computer console typewriter.

All of the signal switching required to generate specific test signals will be done on a semiautomatic basis. A specific mode setup will require only one action on the part

of the operator, exclusive of attenuator or data format control settings.

An oscilloscope, permanently mounted in the test equipment rack, is used to monitor the various signals being generated. Test points will be brought to a central control and patch panel, thus permitting the operator to locate quickly any problems that may arise in the test equipment itself.

The bit-stream generator will be constructed of JPL Division 33 Hi-Rel standard digital modules with the necessary selecting controls brought out to the central control panel.

All the isolation amplifiers and the integrators shown on the block diagram will be operational amplifiers appropriately connected. There are isolation amplifiers in addition to those actually shown on the block diagram, but they are primarily of a fixed impedance and gain matching function and consequently are not included in the functional diagram.

The entire test equipment is to be mounted in a roll-around standard DSIF equipment rack with all connectors and cables necessary to perform its functions. The test equipment rack is to be complete in itself with no need for auxiliary test devices, except the precision signal-to-noise mixer. Each station that is equipped with the MMTS (either single or dual channel) will be provided with one set of MMTS test equipment.

References

1. Shannon, C. E., and Weaver, W., *The Mathematical Theory of Communication*, University of Illinois Press, Urbana, Ill., 1949.
2. Golomb, S. W., Baumert, L. D., Easterling, M. F., Stiffler, J. J., and Viterbi, A. J., *Digital Communications*, Prentice-Hall, Inc., Englewood Cliffs, N. J., 1964.
3. Jaffe, R. M., and Rechtin, E., "Design and Performance of Phase-Lock Circuits Capable of Near-Optimum Performance Over A Wide Range of Input Signals and Noise Levels," *IRE Transactions on Information Theory*, Vol. 1T-1, pp. 66-76, March 1955.
4. Spilker, J. J., "Delay-Lock Tracking of Binary Signals," *IEEE Transactions on Space Electronics and Telemetry*, Vol. 9, pp. 1-8, March 1963.

References (contd)

5. Stiffler, J. J., "On the Allocation of Power In a Synchronous Binary PSK Communication System," Paper 5-1, *National Telemetry Conference*, June 2, 1964.
6. Kaneko, H., "A Statistical Analysis of the Synchronization of a Binary Receiver," *IEEE Transactions on Communication Systems*, Vol. 11, pp. 498-501, December 1963.
7. Viterbi, A. J., "Phase Locked Loop Dynamics in the Presence of Noise by Fokker-Planck Techniques," *Proceedings of IEEE*, Vol. 51, pp. 1737-1753, December 1963.

